AD-A173 878 PROCEEDINGS OF THE SCIENTIFIC CONFERENCE ON OBSCURATION 1/7
AND AEROSOL RESEA (U) KOHL (RONALD H) AND ASSOCIATES
TULLAHOMA TN R H KOHL JUL 86 CRDEC-SP-86019
UNCLASSIFIED DAAG29-81-D-0100 F/G 20/6 NL

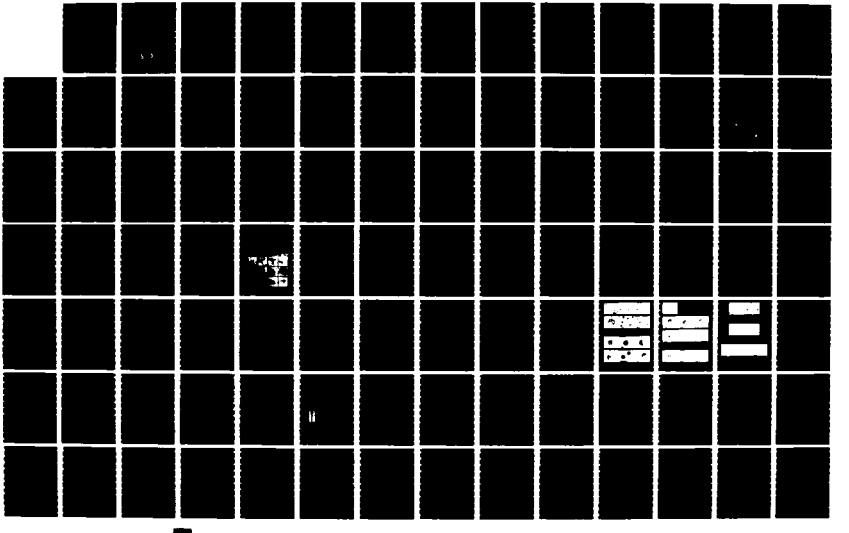

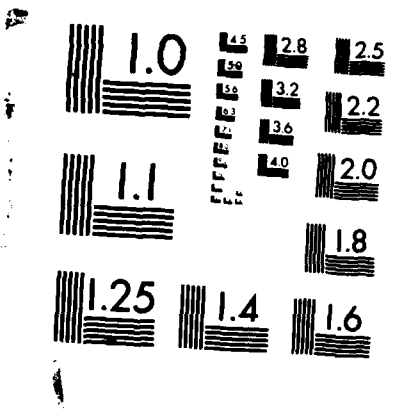

(12)

CHEMICAL RESEARCH, DEVELOPMENT & ENGINEERING CENTER

CRDEC-SP-86019

PROCEEDINGS OF THE 1985 SCIENTIFIC CONFERENCE ON OBSCURATION AND AEROSOL RESEARCH

by Ronald H. Kohl

RONALD H. KOHL & ASSOCIATES
Tullahoma, TN 37388

July 1986

U.S. ARMY ARMAMENT MUNITIONS CHEMICAL COMMAND

Aberdeen Proving Ground, Maryland 21010-5423

Disclaimer

The findings in this report are not to be construed as an official Department of the Army position unless so designated by other authorizing documents.

Distribution Statement

Approved for public release; distribution is unlimited.

UNCLASSIFIED
SECURITY CLASSIFICATION OF THIS PAGE

ADA173878

REPORT DOCUMENTATION PAGE

1a. REPORT SECURITY CLASSIFICATION UNCLASSIFIED	1b. RESTRICTIVE MARKINGS
2a. SECURITY CLASSIFICATION AUTHORITY	3 DISTRIBUTION / AVAILABILITY OF REPORT Approved for public release; distribution is unlimited.
2b. DECLASSIFICATION / DOWNGRADING SCHEDULE	
4. PERFORMING ORGANIZATION REPORT NUMBER(S) CRDEC-SP-86019	5. MONITORING ORGANIZATION REPORT NUMBER(S)
6a. NAME OF PERFORMING ORGANIZATION Ronald H. Kohl & Associates 6b OFFICE SYMBOL (If applicable)	7a. NAME OF MONITORING ORGANIZATION CRDEC
6c ADDRESS (City, State, and ZIP Code) Cook Road, PO Box 1298 Tullahoma, TN 37388	7b. ADDRESS (City, State, and ZIP Code) Aberdeen Proving Ground, MD 21010-5423
8a. NAME OF FUNDING / SPONSORING ORGANIZATION Battelle-Columbus Laboratories 8b. OFFICE SYMBOL (If applicable)	9. PROCUREMENT INSTRUMENT IDENTIFICATION NUMBER Battelle Delivery Order 1441 under Contract DAAG29-81-D-0100
8c. ADDRESS (City, State, and ZIP Code) 200 Park Drive, PO Box 12297 Research Triangle Park, NC 27709	10. SOURCE OF FUNDING NUMBERS PROGRAM ELEMENT NO. / PROJECT NO. / TASK NO. / WORK UNIT ACCESSION NO.
11 TITLE (Include Security Classification) Proceedings of the 1985 Scientific Conference on Obscuration and Aerosol Research	
12 PERSONAL AUTHOR(S) Kohl, Ronald H.	
13a. TYPE OF REPORT Special publication 13b. TIME COVERED FROM 86 Jan TO 85 Dec	14. DATE OF REPORT (Year, Month, Day) 1986 July 15. PAGE COUNT 647
16. SUPPLEMENTARY NOTATION COR: Dr. E. Stuebing, SMCCR-RSP-B, (301) 671-3089	

17 COSATI CODES		
FIELD	GROUP	SUB-GROUP
15	02	

18. SUBJECT TERMS (Continue on reverse if necessary and identify by block number)

Obscurants	Aerosols	Extinction	Smoke
Obscuration	Aerosol properties	Scattering	Light
Aerosol	Absorption	Transmission	Sizing

19 ABSTRACT (Continue on reverse if necessary and identify by block number)

Fifty-two papers on current or recent research are included under the headings of: Physical and Chemical Properties of Aerosols; Aerosol Characterization Methods; Tutorial Reviews; Small Needle-Shaped Filaments Based on Carbon; Nonlinear Interactions at High Energy; and Optical Properties of Aerosols.

20 DISTRIBUTION / AVAILABILITY OF ABSTRACT ☒ UNCLASSIFIED/UNLIMITED ☐ SAME AS RPT. ☐ DTIC USERS	21. ABSTRACT SECURITY CLASSIFICATION UNCLASSIFIED
22a NAME OF RESPONSIBLE INDIVIDUAL TIMOTHY E. HAMPTON	22b. TELEPHONE (Include Area Code) (301) 671-2914 22c. OFFICE SYMBOL SMCCR-SPD-R

DD FORM 1473, 84 MAR 83 APR edition may be used until exhausted
All other editions are obsolete.

SECURITY CLASSIFICATION OF THIS PAGE
UNCLASSIFIED

18. Subject Terms (continued)

Electromagnetic scattering
Microwaves
X-band
Millimeter wave
Submillimeter wave
Infrared
Far-infrared
Visible radiation
Electromagnetic waves
Spherical particles
Mie scattering
Particles
Droplets
Aerosol particles
Particle dynamics
Particle mechanics
Particle fluidization
Particle beds
Atmospheric dispersion
Cloud dynamics
Cloud mixing
Plumes
Plume mechanics
Aerosol plumes
Plume dispersion
Diffusion
Gas-aerosol reactions
Transport phenomena
Particle growth
Particle formation
Solid particle formation
Carbon filaments
Intercalation
Carbon fibers
Graphite
Chemistry
Nucleation
Smoke generation
Aerosol generation
Chemical characterization
Phosphorus smoke
Hygroscopic smokes
Clusters (gaseous)
Coagulation
Condensation
Liquid drop
Drop growth
Spheres
Cylinders
Rough particles
Irregular particles
Nonspherical particles
Particle aggregates
Particle chains
Infrared emission
Chemiluminescence
Cooperative scattering
Dependent scattering
Multiple scattering
Radiative transfer
Atmospheric optics
Scavenging
Aerosol elimination
Aerosol clearing
Smoke clearing
Aerosol characterization
Particle sizing
Aerosol size distribution
Condition numbers
Particle size distribution
Particle orientation
Particle motion
Unsteady motion
Nephelometer
Inversion
Inversion techniques
Inverse scattering
Optical properties
Optical constants
Optical properties
Drude Model
Reflection spectroscopy
Natural minerals
Minerals
Metal
Metallic particles
Powdered minerals
Refractive index
Index of refraction
Complex refractive index
Permeability
Permittivity
Dielectric function
Surface impedance
Conductivity
Laser
High energy laser
Laser-particle interaction
Vaporizing aerosols
Hydrodynamics
Nonlinear interactions
Saturable absorbers
Nonlinear simulations
SERS
Surface Enhanced Raman Scattering
Layered spheres
Bubbles
Forward glory
Glory
Transients
Energy transfer

18. Subject Terms

Interacting particles
Interacting spheres
Diffraction
Diffraction catastrophes
Finite cylinders
Infinite cylinders
CIDS
Helix
Spiral
Dielectric
Cubes
Quadrapole trap
Mueller matrix
Symmetry
Clustering
Surface roughness
Surfaces
Dielectric particles
Conducting particles
Cyclindrical particles
Fibers
Conducting fibers
Spheroids
Spheroidal drops
Clouds
Radiation diffusion
Radiation transport
Random media

PREVIOUS PROCEEDINGS
Of The CSL/CRDC*SCIENTIFIC CONFERENCE
On OBSCURATION And AEROSOL RESEARCH

Year of Conference	Report Number
1979	ARCSL - CR - 81023
1980	ARCSL - SP - 82021
1981	ARCSL - SP - 82022
1982	ARCSL - SP - 83011
1983	CRDC - SP - 84009
1984	CRDC - SP - 85007

*The U.S. Army Chemical Research, Development and Engineering Center (CRDEC) was known as the Chemical Research and Development Center (CRDC) prior to March 1986 and as the Chemical Systems Laboratory (CSL) prior to July 1983.

PREFACE

The 1985 Scientific Conference on Obscuration and Aerosol Research was held 17-21 June 1985* at the Edgewood Area of Aberdeen Proving Ground, Maryland. The Conference is held annually, the last full week in June, under the direction of Dr. Edward W. Stuebing, Research Area Coordinator, Aerosol Science, from whom it receives its unique and productive character.

The Conference is an informal forum for scientific exchange and stimulation among investigators in the wide variety of disciplines required for aerosol research and for description of obscuring aerosols and their effects. The participants develop some familiarity with the Army aerosol and obscuration-science research programs and also become personally acquainted with the other investigators and their research interests and capabilities. Each attendee is invited to present any aspect of a topic of interest and may make last minute changes or alterations in his presentation as the flow of ideas in the Conference develops.

While all Conference participants are invited to submit written papers for the Proceedings, each investigator who is funded by the Army Research Program is requested to provide one or more written papers which document specifically the progress made in his funded effort in the previous year and which indicate future directions. Also, the papers for the Proceedings are collected in the Fall to allow time to incorporate the fresh ideas which arise at the Conference. Therefore, while the papers in these proceedings tend to closely corespond to what was presented at the Conference, there is not an exact correspondence.

The reader will find the items relating to the Conference itself--labeled photographs of the participants, list of attendees, and the agenda--in the appendixes which follow the papers and the indexes pertaining to them.

Acknowledgments

Thanks are extended to Ian Spain, Department of Physics, Colorado State University, on behalf of the Conference attendees and the readers of these Proceedings for organizing the tutorial review, "Small Needle-Shaped Filaments Based on Carbon." See pages 291-324.

*In 1985, as an exception to the rule, the Conference was held one week before its standard scheduled time, which is the last full week in June. Such an exception should not occur in the future.

CONTENTS*

*See also page 607 for the indexes of the authors and the organizations of the authors.

V. OPTICAL PROPERTIES OF AEROSOLS (Continued)

VB. Interaction of Radiation and Nonsperical Particles Including Aggregates (Continued)

I. PHYSICAL AND CHEMICAL PROPERTIES OF AEROSOLS*

IA. Particle Formation, Evolution and Composition

*See also the Tutorial Review, page 291

THE INTERACTION OF CLUSTERS WITH REACTIVE SPECIES: INITIAL STAGES IN THE EVOLUTION OF PARTICLE COMPOSITION

R. G. Keesee and A. W. Castleman, Jr.
Department of Chemistry
The Pennsylvania State University
University Park, PA 16802

RELATED RECENT PUBLICATIONS AND PRESENTATIONS:

A) R. G. Keesee and A. W. Castleman, Jr., "Gas-to-Particle Conversion: The Role of Pre-Existing Dimers in the Formation of Clusters During Supersonic Expansion," Proceedings of the CRDC's 1984 Conference on Obscuration and Aerosol Research, pp. 13-21.

B) J. J. Breen, K. Kilgore, K. Stephan, R. Hofmann-Sievert, B. D. Kay, R. G. Keesee, T. D. Mark, and A. W. Castlman, Jr., "The Use of Similarity Profiles in Studying Cluster Formation in Molecular Beams: Evidence for the Role of Pre-Existing Dimers," Chem. Phys. 91, 305-313 (1984).

C) R. G. Keesee, J. J. Breen, K. Kilgore, L. DiFazio, R. E. Leuchtner, and A. W. Castleman, Jr., "Nucleation and Aerosol Formation in Reative Systems," presentation at the Symp. on Heterogeneous Processes in Source-Dominated Atmospheres, New York City, October 8-11, 1985.

ABSTRACT

Preliminary results on the formation of clusters containing both ammonia and sulfur dioxide are presented. The clusters are produced by expansion through a dual nozzle into vacuum.

INTRODUCTION

Despite their potential importance to the chemistry of the troposphere, and especially source dominated atmospheres, little is known about the details of the transfer of molecules from the gaseous to the condensed state by either new particle formation or heterogeneous processes including adsorption onto or dissolution into aerosol particles. It is becoming well recognized that research on clusters provides a valuable approach in understanding gas-to-particle conversion and the role of small particles in the chemistry of the atmosphere.

Clusters can be produced by supersonic expansion of a gas through a nozzle into vacuum. In our laboratory, we have developed a co-expanding nozzle source as a method for producing clusters consisting of reactive species. The nozzle is designed in such a way that one gaseous species can be introduced and expanded through a small (usually 100 μm diameter) glass nozzle opening. The second species is introduced through a co-axial glass tube surrounding the inner nozzle, where the area of the annular opening is about 5 or 6 times that of the inner opening (see Figure 1). After the nozzle, a skimmer collimates a beam,and species in the beam are then detected via electron-impact ionization mass spectrometry. Earlier we reported use of this dual nozzle in a study of the interaction of SO_3 with water clusters (1) and the reaction of ammonia with nitric acid/water clusters (2).

In view of their atmospheric importance and potential role in particle formation, SO_2 and NH_3 are an interesting pair of gases for study. When a few torr of each gas are mixed, a solid material is produced. This reaction has been known for over 150 years and a variety of colors have been reported

for the solid product (3,4). Decomposition is thought to lead to many of the species responsible for the observed colors. However, a yellow solid which has a stoichiometric ratio of 1:1 and a white solid with a 2:1 ratio for NH_3 to SO_2 have been identified. Both of these solids reversibly sublime back to NH_3 and SO_2 as the pressure of the gas phase is reduced. The thermodynamic quantities for both sublimation processes have been determined (5).

We have performed one series of experiments in which ammonia was expanded from the inner nozzle and SO_2 introduced through the annular opening and another series in which the roles of the gases were reversed. With ammonia introduced via the inner nozzle (500 torr stagnation pressure) and when the SO_2 pressure behind the outer annular opening is 40 torr, ionized clusters of the form $(NH_3)_nSO_2^+$ and $H^+(NH_3)_nSO_2$ are detected. The observed distribution is shown in Figure 2. (The intensity of NH_4^+ is not shown as it would be considerably off-scale.) When the SO_2 pressure is reduced to 20 torr, no evidence of SO_2 incorporation into the ammonia clusters is found (see Figure 3). A peculiar feature is that the unprotonated species exhibit a normal size distribution, whereas the protonated clusters are strongly peaked at $NH_4^+NH_3SO_2$. On the other hand, ionization of pure ammonia clusters results almost exclusively in protonated clusters due to the internal cluster reaction

$$NH_3^+(NH_3)_n \rightarrow NH_4^+(NH_3)_{n-1} + NH_2$$

which occurs following ionization of the neutral ammonia clusters (6).

Figures 4-6 show the resulting ionized cluster distributions when sulfur dioxide is introduced through the inner nozzle and the amount of ammonia behind the annular opening varies from 6 to 50 torr. The intensity of SO_2^+ is very large and not shown. Due to the wider mass range and lower mass resolution, no distinction could be made between protonated and unprotonated clusters. The extent of ammonia incorporation into the clusters dramatically increases with increasing ammonia pressure. Up to two ammonia molecules were observed to be incorporated into the clusters with 20 torr of ammonia behind the annular opening. With 40 torr, up to four NH_3 molecules were observed in the clusters. In addition, clusters containing one NH_3 molecule become more prevalent than the pure $(SO_2)_n^+$ clusters.

In general, the observed cluster distributions are smooth and in neither series of experiments is any preference for a particular stoichiometric ratio apparent, except for $NH_4^+NH_3SO_2$ in the protonated distribution shown in Figure 2. These experiments also demonstrate that the dual nozzle design results in the reaction of the species exiting from the annular opening with clusters of the species introduced through the inner nozzle.

A comparison between Figures 3 and 5 readily demonstrates that incorporation of NH_3 into SO_2 clusters is more extensive than that of SO_2 into NH_3 clusters under similar pressure conditions in the

nozzle source. Since the mass of NH_3 is about four times lighter than SO_2, the flux of NH_3 through the annular opening at a given pressure is expected to be about a factor of two higher; however, the extent of reaction appears to be about an order of magnitude greater. Another possible contribution due to mass differences is that collisions of NH_3 with a SO_2 cluster will result in less scattering or deflection from the beam axis than in the case of SO_2 colliding with NH_3 clusters. Consequently, detection of reaction products may be more efficient in the former case. Buck and Meyer (7) have investigated the scattering of Ar clusters by a He beam; however, with our nozzle arrangement, the collision angle is not well defined so a prediction of the effect of scattering cannot be made. Further study of the effect of the pressure in the annular tube on the total measured ion cluster intensity may help to resolve the importance of scattering. Ionization processes or ion stability may also affect the observed distributions. Ammonia has a considerably higher proton affinity than sulfur dioxide and a lower ionization potential, as well, so that NH_3 is expected to be the preferred charged species in either protonated or unprotonated clusters. Hence, SO_2 may be preferentially lost in dissociation processes. The importance of this phenomenon can be investigated using a reflectron technique as described in reference (6). In summary, the more prevalent incorporation of NH_3 compared to SO_2 may be due to (1) a more efficient or faster transport of NH_3 to the cluster beam region, (2) a higher probability of SO_2 evaporation for the clusters upon ionization, or (3) a greater reactivity (accommodation coefficient) for NH_3 with SO_2 clusters than for SO_2 with NH_3 clusters.

ACKNOWLEDGMENTS

Financial support of the U.S. Army Research Office, Grant No. DAAG29-82-K-0160, is gratefully acknowledged.

REFERENCES

1. R. Sievert and A. W. Castleman, Jr., J. Phys. Chem. 88, 3329 (1984); R. G. Keesee, R. Hofmann-Sievert, and A. W. Castleman, Jr., "The Interaction of Sulfur Trioxide with Water Clusters," Proc. NATO Advanced Study Institute on Chemistry of Multiphoton Atmospheric Systems, Corfu, Greece, September 26-October 8, 1983, in press.

2. B. D. Kay, R. Hofmann-Sievert, and A. W. Castleman, Jr., "A Molecular Beam Electric Deflection Study of the Solvation of HNO_3 and NH_4NO_3 in Microscopic Aqueous Clusters," Chem. Phys., submitted.

3. W. D. Scott, D. Lamb, and D. Duffy, J. Atmos. Sci. 26, 727 (1969).

4. E. McLaren, A. J. Yencha, J. M. Kushnir, and V. A. Mohnen, Tellus 16, 291 (1974).

5. R. Landreth, R. G. dePena, and J. Heicklen, J. Phys. Chem. 89, 1690 (1985).

6. O. Echt, P. D. Dao, S. Morgan, and A. W. Castleman, Jr., J. Chem. Phys. 82, 4076 (1985).

7. U. Buck and H. Meyer, Phys. Rev. Lett. 52, 109 (1984).

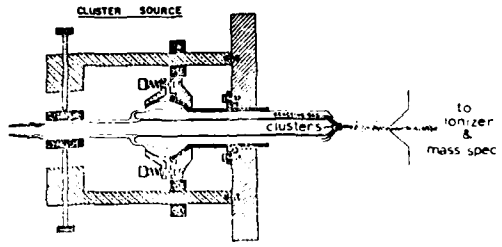

FIGURE 1. Schematic of the dual nozzle source.

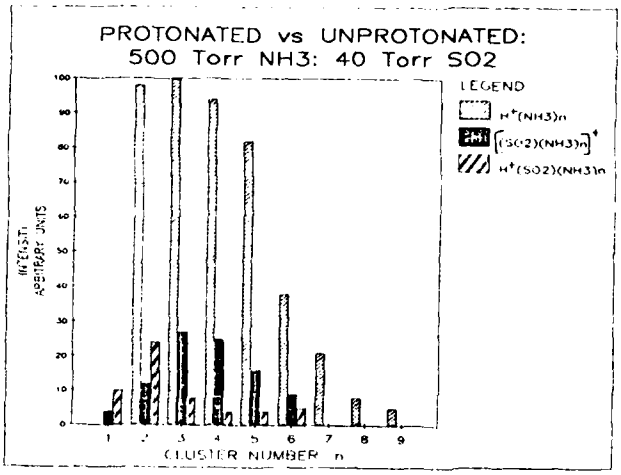

FIGURE 2. Ionized cluster distribution from expansion of 500 torr NH_3 through inner nozzle and 40 torr SO_2 through outer annular opening.

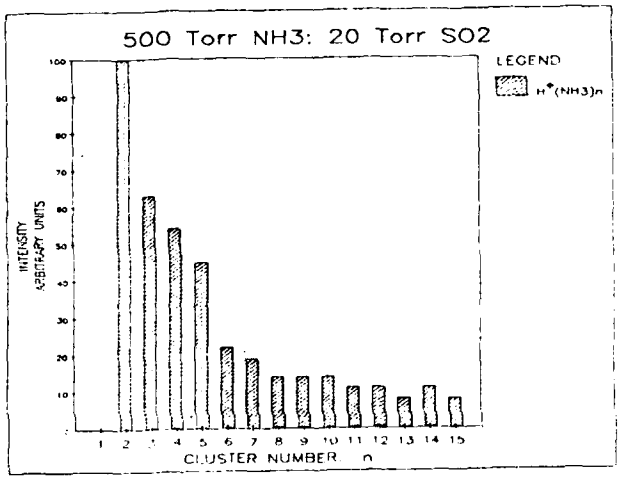

FIGURE 3. Ionized cluster distribution from expansion of 500 torr NH_3 through inner nozzle and 20 torr SO_2 through outer annular opening.

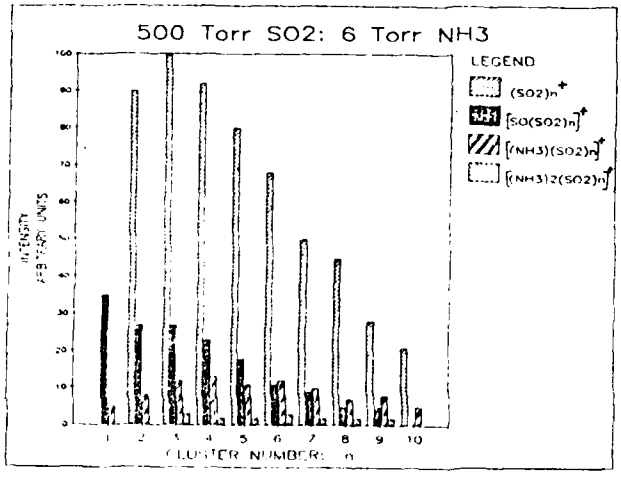

FIGURE 4. Ionized cluster distribution from expansion of 500 torr SO_2 through inner nozzle and 6 torr NH_3 through outer annular opening.

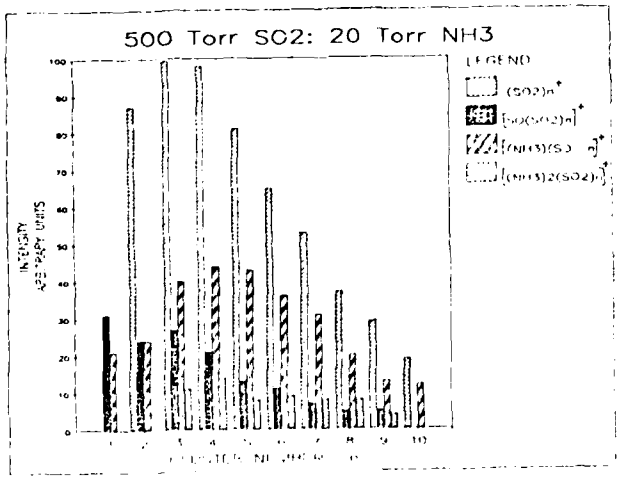

FIGURE 5. Ionized cluster distribution from expansion of 500 torr SO_2 through inner nozzle and 20 torr NH_3 through outer annular opening.

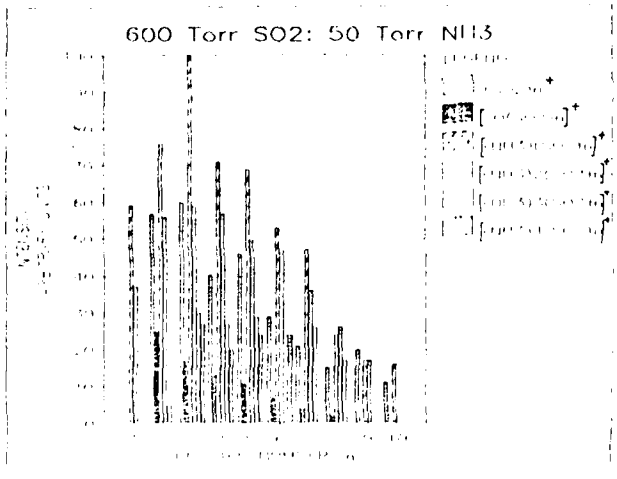

FIGURE 6. Ionized cluster distribution from expansion of 600 torr SO_2 through inner nozzle and 50 torr NH_3 through outer annular opening.

NUCLEATION AND PARTICLE GROWTH

S. G. Kim and J. R. Brock
Department of Chemical Engineering
University of Texas
Austin, Texas 78712

RECENT PUBLICATIONS, SUBMITTALS FOR PUBLICATION AND PRESENTATIONS:
(Contract DAAK11-83-K-0006)

S. G. Kim and J. R. Brock "Chain aggregate aerosols produced by liquid phase reactions", in B.Y.H. Liu et al Eds. Aerosols:Science, Technology and Industrial Applications. Elsevier NY, 1984.

T. H. Tsang and J. R. Brock. "On Ostwald ripening", in B.Y.H. Liu et al Eds. Aerosols: Science, Technology and Industrial Applications, Elsevier NY , 1984.

J. R. Brock, "Remarks on particle size distributions of ultrafine binary particles with one involatile component" , Journal of Aerosol Science 16 436 (1985).

J. R. Brock, D. Zehavi and P. Kuhn, "Condensation aerosol formation and growth in a laminar coaxial jet : experimental", Journal of Aerosol Science, In Press (1985).

J. R. Brock and P. Kuhn, "Multicomponent condensation aerosol formation and growth in a laminar coaxial jet: theoretical", Journal of Aerosol Science, Submitted.

S. G. Kim and J. R. Brock, "On formation of ultrafine ferromagnetic particles by vapor condensation" Aerosol Science and Technology, Submitted.

S. G. Kim and J. R. Brock, "Growth of ferromagnetic particles in liquid phase reactions". Journal of Applied Physics, Submitted.

J. R. Brock, T. H. Tsang and S. G. Kim, "Aerosol plume mechanics and particle growth processes", in R. H. Kohl,Ed. , Proceedings of the CRDC's 1984 Scientific Conference on Obscuration and Aerosol Research, CRDC-SP-85007, June 1985.

S. G. Kim and J. R. Brock, "Chain aggregate aerosols produced by liquid phase reactions" First International Aerosol Conference, Minneapolis, MN September 1984.

T. H. Tsang and J. R. Brock, "On Ostwald ripening", First International Aerosol Conference, Minneapolis, MN September 1984.

Patent Disclosure: "Method for determining vapor pressures of substances with very low vapor pressures", 1985.

ABSTRACT

Work on nucleation and growth of particles under Contract DAAK11-83-K-0006 for the past year is outlined. This work includes: (1) Vapor phase nucleation and growth of ferromagnetic particles ; (2) Liquid phase nucleation and growth of ferromagnetic particles; (3) Vapor phase nucleation and growth of multicomponent liquid aerosols. Experimental findings and theoretical developments in these three areas are summarized. A model has been developed which for the first time explains our own and previous experimental observations of formation of ultrafine solid particles by vapor nucleation near a heated surface. A model, based on detailed chemical mechanisms, has also been developed for nucleation and growth of ultrafine ferromagnetic particles formed in liquid phase borohydride reduction. For the first time, a model has been developed for nucleation and growth of multicomponent aerosols.

INTRODUCTION

Work under Contract DAAK11-83-K-0006 is intended to contribute to the technological base of the U. S. Army's programs in em radiation obscuration, aerosol technology, laser-particle nonlinear interactions, and chemical detection, identification and warning. Progress in theseprograms will continue to require a detailed understanding of the aerosol dynamical processes of nucleation, growth, reaction and removal, as well as other fundamental processes, such as the interaction of particles with em radiation.

This report is divided into two sections. In the first, our work on formation and growth of ferromagnetic particles and chains is summarized for the past year. This work covers nucleation and growth of ultrafine ferromagnetic particles in gas and liquid media. In the second, development of models predicting size distributions of multicomponent aerosols by vapor nucleation is described.

FERROMAGNETIC PARTICLES

Ultrafine ferromagnetic particles (size 50 - 1000 A) have been of considerable interest in various practical areas including their use for catalysts, electroless plating, ferrofluids, and magnetic recording materials, to name a few. However, details of the mechanisms for generation and growth of these particles have been lacking. Our studies have been directed toward conducting experiments to investigate these mechanisms and formulating models to describe the growth processes. Two general methods for formation of ferromagnetic particles have been used: (a) Vapor phase nucleation; (b) Liquid phase nucleation. We discuss these in order.

Vapor phase nucleation and growth

When ferromagnetic source material is heated in static or flowing inert gas, the atoms escaping from the source are cooled down by collisions with the gas atoms. Subsequently, growth takes place by condensation of single atoms and coagulation of entire clusters. In our experiments, sampling of such particles on TEM grids was carried out as a function of distance from the source with varying conditions such as source temperature and inert gas pressure. The following qualitative observations apply to our and others', similar, experimental investigations. Primary particle size of ferromagnetic particles increases with source temperature and inert gas host pressure. The aggregates of the primary particles are approximately linear with some branching. Chain linearity increases and branching decreases as an applied external magnetic field strength is increased.

A model has been developed which permits explanation of the experimental observations cited above. The model has been applied specifically to the nucleation and growth of particles surrounding a heated spherical source of ferromagnetic material. As the material vaporizes, the vapor diffuses outward and at some point undergoes homogeneous nucleation with subsequent growth of particles by condensation of vapor atoms and smaller clusters. At larger distances, as the particles move under the influence of Brownian motion and thermophoresis, particles may begin to collide to form chain aggregates. Figs. 1 and 2 show the vapor concentration and particle number concentration predicted by the model using classical (BDZ) nucleation theory and the appropriate expressions for the aerosol

noted here. The model has proved to be successful in correctly predicting the qualitative observations noted above and in predicting within reasonable bounds the actual experimental observations. This work has been submitted for publication.

Liquid phase nucleation and growth

The salts of ferromagnetic metals such as iron, cobalt and nickel react with the borohydride ion in liquid phase to produce ferromagnetic particles which may contain boron. Since the reaction is fast, mixing of the reactants is very important for obtaining reproducible results. A mixing junction, which is commonly used for stopped-flow reactors, has been used in our experiments. The flow from this junction, on a time scale of 1 msec., is directed to a dilution system in the presence of ultrasonic vibrations where the final phase of growth of particles takes place. Samples of the particles are then taken on TEM grids for study. The effects of cations, anions, solvent, concentration of reactants and temperature of reacting systems have been investigated in this manner. External magnetic fields have been applied to determine effects of field strength on chain linearity and branching. The following qualitative observations have been made in these studies. The size distributions of the primary particles are narrow. Chain linearity increases and branching decreases with increasing external magnetic field strength. Above 500 gauss, chains are linear with no branching. For the various ferromagnetic cations (Fe^{++}, Co^{++}, Ni^{++}) variation of cation concentration leads to large changes in primary particle characteristics, as well as for the chains. The pH appears to play a key role, and the reaction mechanism and particle formation process at low cation concentration at pH greater than 7 appears to change completely, apparently mediated by the formation of "micronets" of hydroxol precipitates where subsequently metallic particles begin to appear. The solvent also is important in determining size and linearity of the ferromagnetic particles. Surface-active agents have been employed which suppress chain formation or which permit partitioning of chains into water insoluble phases (oils, for example). Primary particle size is very sensitive to reaction temperature, but temperature has no apparent effect on linearity and branching of chains. The saturation magnetization of the chain aggregates varies with cation concentration, decreasing with decreasing cation concentration.

The results obtained in the liquid phase have been analyzed in terms of a model describing the reduction step in terms of a published, detailed reaction mechanism. Subsequently, particle formation occurs by a zero activation-energy nucleation process. The effects of van der Waals, hydrodynamic, and electric double layer forces are accounted in the particle growth process. The great sensitivity of the observed primary particle size to cation concentration and temperature is reliably predicted by our model. This work has been submitted for publication.

MULTICOMPONENT AEROSOLS

Work on this subject has been underway in our laboratory for several years. Our aim in the study of multicomponent aerosols has been to answer the question: given a liquid consisting of various chemical species, what will be the characteristics of the aerosol formed from condensation of the vapor formed from this liquid? From another view, which parameters in the nucleation and growth processes can be controlled to produce an aerosol with stated characteristics from such liquids? We have studied

these questions with the experimental, laminar, coaxial jet system described in previous CRDC conference proceedings and in various scientific journals. Briefly, in our experimental system, metered, heated vapor issues from a small nozzle into a coaxial, flowing gas stream. The vapor jet begins to condense by homogeneous nucleation at a certain downstream distance, and the particles formed there continue to grow by condensation of vapor as they are convected further downstream. The aerosol jet formed by this process flows along the centerline of the tube for its entire length of approximately 1.5 meters. The aerosol is sampled with a cone sampler at various downstream distances and the particle size distribution of the sampled aerosol is subsequently determined, after suitable dilution, by means of a calibrated optical particle counter. The optical particle counter is calibrated with an aerosol with the same optical properties as the experimental aerosols, usually the same substances. Binary and ternary liquid mixtures have been studied in this manner, with components varying in their vapor pressures by as much as an order of magnitude. Other variables studied have been the vapor concentration in carrier gas, nozzle exit flow rate, and nozzle temperature. These last two variables, are important determinants of cooling rates in the jet. Cooling rates in turn are important in their effect on nucleation rates and subsequent particle size.

Vapor concentrations have been used in our experiments at sufficiently small values that the vapor and aerosol are passive contaminants. We have carried out detailed numerical studies of the momentum and heat transfer equations under our experimental conditions so that the velocity and temperature fields in the condensation region are accurately known; this has been verified in part by experimental measurements of average temperatures at various downstream distances in the jet. Based on these results a model has been developed for nucleation and growth of aerosol in our experimental system. Reasonable agreement between theory and experiment has been achieved starting with the classical theory of multicomponent nucleation. Information obtained with this model with respect to variation of particle composition in an aerosol particle-size distribution is consistent with our experimental measurements of this variation. Figure 5 shows a typical result for agreement between theory and experiment. It should be noted that classical nucleation theory is known to be in disagreement with nucleation rate measurements at the high nucleation rates occurring in our studies (10^{11} - 10^{12} #/cm^3-sec). The work reported here is now in press.

FUTURE WORK

Future work will be devoted principally to continued investigation of nonspherical particle generation. This will consist of development of continuous processes for production of linear chain aerosols in the liquid phase and means for dispersal of such chains as aerosols. With our new laser facility, we plan to investigate the nonlinear interaction between our chain aerosols and laser beams, as well as to investigate aerosol formation and growth in such em radiation fields.

ACKNOWLEDGMENT

Work performed here was supported under Contract DAAK11-83-K-0006 from the Chemical Research & Development Center, U. S. Army. The advice and assistance of Dr. Edward W. Stuebing and Dr. Glenn O. Rubel of the Chemical Research & Development Center are gratefully acknowledged.

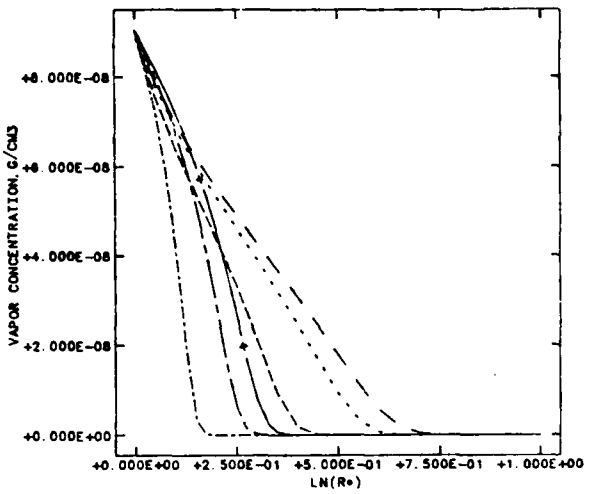

Figure 1. Iron vapor concentration as a function of logarithm of dimensionless distance from surface of evaporating iron sphere in argon host gas for various host gas pressures and time from start of heating. Source temperature = 1900 °C.

— — —	Pressure = 500 dynes/cm^2;		Time=	1. E-5 sec
—·—	"	10000	"	1. E-5
-------	"	500	"	5. E-5
— - —	"	10000	"	5. E-5
— — —	"	500	"	1. E-4
— + —	"	10000	"	1. E-4

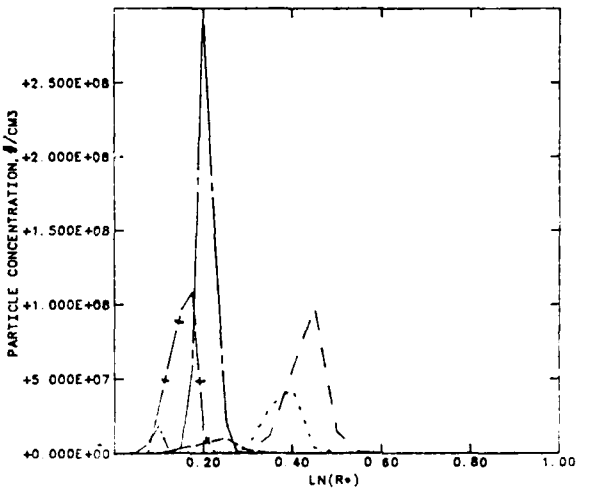

Figure 2. Iron particle concentration as a function of logarithm of dimensionless distance from surface of evaporating iron sphere in argon host gas for various host gas pressures and time from initiation of heating. Source temperature = 1900°C.

— - —	P = 500 dynes/cm^2,	Time=	1. E-5 sec.
—·—	" =10000		1. E-5
-------	= 500		5. E-5
— + —	=10000		5. E-5
— — —	= 500		1. E-4
— - —	=10000		1. E-4

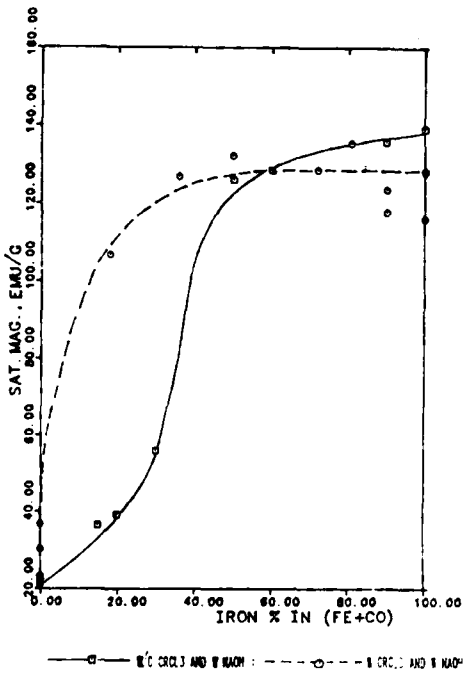

Figure 3. Variation of saturation magnetization of ferromagnetic chain aerosol of Fe+Co alloy particles with iron composition with and without Cr surface oxidation passivation. Ferromagnetic particles formed in liquid-phase reduction of cations by borohydride ion.

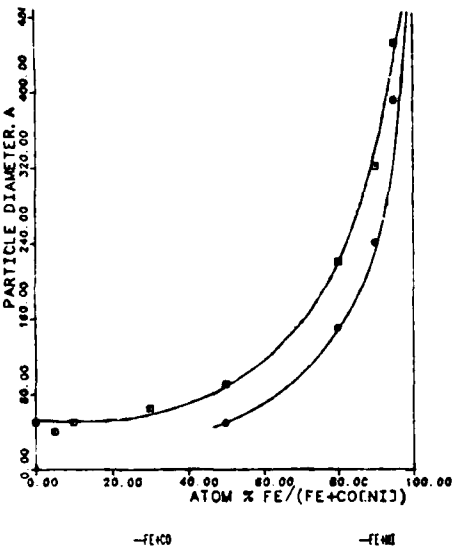

Figure 4. Variation of primary ferromagnetic particle size with particle composition for binary alloys of Fe+Co and Fe+Ni. Ferromagnetic particles formed in liquid-phase reduction of cations by borohydride ion.

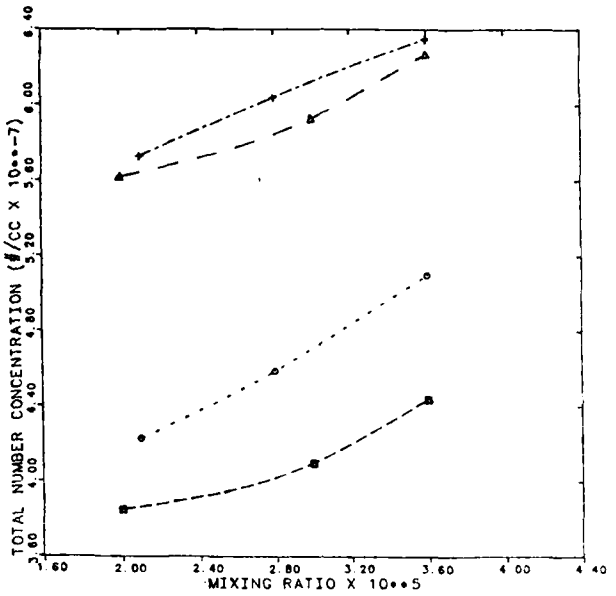

Figure 5. Asymptotic particle number concentration as a function of inlet vapor concentration in carrier gas for condensation of phthalate esters in laminar coaxial jet system.

Dioctyl phthalate aerosol, theory
Dioctyl phthalate aerosol, experiment
Dihexyl phthalate aerosol, theory
Dihexyl phthalate aerosol, Experiment

CHANGES IN PHOSPHORUS SMOKE CHEMISTRY WITH ENVIRONMENTAL CONDITIONS[1]

K. M. McFadden, M. W. Ligotke,
T. R. Garland, P. Van Voris, and R. E. Schirmer

Pacific Northwest Laboratory[2]
Richland, Washington 99352

RECENT PUBLICATIONS, SUBMITTALS FOR PUBLICATION AND PRESENTATIONS:

A) T. M. Poston, R. M. Bean, R. L. Thomas, K. M. McFadden, M. L. Clark, and B. W. Killand, Acute Toxicity of Smoke Screen Materials to Aquatic Organisms, Final Report prepared for U.S. Army Medical Research and Development Command by Pacific Northwest Laboratory, Richland, Washington, submitted October 1985.

B) P. Van Voris, M. W. Ligotke, D. A. Cataldo, T. R. Garland, K. M. McFadden, J. E. Rogers, D. W. Carlile, and S. W. Li, "Transport, Transformation and Ecological Effects of Phosphorus Smokes in an Environmental Wind Tunnel," In Smokes and Obscurants Symposium IX, in press.

C) P. Van Voris, D. A. Cataldo, M. W. Ligotke, T. R. Garland, K. M. McFadden, J. K. Fredrickson, R. M. Bean, D. W. Carlile, R. L. Thomas, and S. M. Li, J. E. Rogers. Environmental Transformations. Fate and Terrestrial Ecological Effects of Red Phosphorus/Butyl Rubber and White Phosphorus Smokes, Final Report, Prepared for U.S. Army Medical Research and Development Laboratory by Pacific Northwest Laboratory, Richland, Washington, submitted October 1985.

D) P. Van Voris and M. W. Ligotke. 1984. Evaluate and Characterize Mechanisms Controlling Transport, Fate and Effects of Army Smokes in an Environmental Wind Tunnel, Presented at the Pacific Northwest Association of Toxicologists Inaugural Meeting, September 28-29, 1984, Seattle, Washington.

ABSTRACT

Physical and chemical characteristics of two phosphorus aerosols were measured under a limited number of environmental conditions. The exposures and measurements were performed in a wind tunnel under various relative humidities, wind speeds and, to a limited extent, aerosol ages. Temperature, another important environmental variable that may influence the chemical form of the aerosols, was not studied in this research program. Steady-state aerosols generated by combustion of red phosphorus/butyl rubber (RP/BR) and white phosphorus (WP) were suspended in a closed-loop wind tunnel to simulate the continuous-generation of these obscurants at Army field training sites.

Measured aerosol characteristics were found to differ significantly from characteristics predicted by simple phosphoric acid models previously thought to represent the chemical form of the suspended particles. As many as 28 individual phosphorus species were detected in aerosol samples. The distribution of linear and cyclic phosphorus species in the sampled aerosol was observed to vary significantly for changes in both aerosol age (0 to 60 min) and relative humidity (<5% to 90%). Hydrolysis toward phosphate occurred as the aerosol aged, and the rate of change was slower for higher humidities. More high-order phosphorus species appeared to be formed during aerosol generation at low relative humidities than at high humidity, as revealed by measurements near the combustion zone. Steady-state aerosols showed decreasing conversion to phosphate with increasing humidity. The highly speciated aerosols hydrolyzed to phosphate in less than 18 hr after deposition onto dry surfaces. Other aerosol characteristics such as mass concentration, water and phosphorus content of the particles, and particle size distribution were also measured.

---

[1] This research is supported by the U.S. Army Medical Bioengineering Research and Development Laboratory, Health and Environmental Effects Research Division, Ft. Detrick, Frederick, Maryland 21701.

[2] Pacific Northwest Laboratory, operated for the U.S. Department of Energy by Battelle Memorial Institute.

INTRODUCTION

Researchers at Pacific Northwest Laboratory (PNL) are studying the transport, transformations, and ecological effects of obscurant smokes used by the U.S. Army to mask troop and vehicular movement during combat training throughout the United States. Aerosols formed by the combustion of red phosphorus/butyl rubber (RP/BR) and white phosphorus (WP) were maintained in a wind tunnel during exposures of terrestrial vegetation and soils. The rate of deposition of the suspended smoke particles to the various specimen surfaces, the chemical and physical characteristics of the aerosols, and the chemical fate of materials deposited onto plant, soil, water, and other surfaces were measured during each exposure test. The resulting ecological effects on several species of natural terrestrial vegetation and soil microbiological communities were also evaluated after each test. Because the deposition rates and the chemical natures of these obscurant smokes are highly dependent on the wind speed and relative humidity of the exposure, the mechanisms controlling environmental impacts can be characterized only by understanding the chemistry of the aerosols produced by combustion of these materials (Van Voris et al. 1985). This paper presents the results of a series of aerosol chemistry measurements that were performed as part of this ecological effects program.

Aerosols were generated from RP/BR and WP and maintained at steady-state conditions in a closed-loop wind tunnel for up to 8 hr under controlled relative humidities and wind speeds. Because the aerosols were steady-state (to simulate the continuous-generation field situation), the age of the individual particles within the aerosols was not uniform. As a result, the average age of each aerosol had to be calculated. Thus, aerosol age was divided, not into specific times, but into several general categories. Because of limitations within the current project, anticipated changes in phosphorus speciation due to temperature were not investigated. It is recommended that future phosphorus speciation research include age, temperature, and relative humidity as variables.

Literature on phosphorus chemistry is extensive (Halmann 1972; Riemann and Beukenkamp 1961; Van Wazer 1958). Phosphorus can form polymeric chain and ring compounds valued as softening, complexing, and solubility-controlling agents in the fertilizer and detergent industries. Although early work with phosphorus smokes was based on the assumption that combustion of phosphorus would yield P_4O_{10}, which would yield phosphoric acid upon contact with atmospheric water vapors, it became apparent that phosphorus aerosol chemistry was more complex. Using nuclear magnetic resonance (NMR) and gross titration data, Tarnove (1980) suggested tetrametaphosphoric and pyrophosphoric acids were present in the smoke at a 1:6 mole ratio and concluded that only P_4O_{10} was formed in the combustion. However, the NMR scans were done on highly concentrated droplets of deposited aerosol, which may be subject to marked acid hydrolysis, and no data were reported that would preclude tetrametaphosphate in favor of

trimetaphosphate. Spanggord et al. (1985) reported that NMR resonances for tri-, tetra-, and hexametaphosphates were broad and virtually indistinguishable. Because the Tarnove (1980) titrations were only reported as totals to pH 9, no estimate of numbers of end versus middle phosphorus groups or of average chain length could be calculated. Determination of differences between first and second acid endpoints before and after acid hydrolysis and after addition of a silver ion to displace the weak third hydrogen from phosphoric acid would have been required to better define the mixture of ortho- and polyphosphates (Van Wazer et al. 1954).

Yamaguchi et al. (1979) first achieved separation of 30 linear and cyclic condensed phosphoric acids via a 6-hr anion exchange chromatography procedure followed by post-column reaction and colorimetric detection. A similar method was used by Katz et al. (1981) to identify polyphosphates of up to eight phosphorus (P) atoms in white phosphorus/felt (WP/F) munitions smoke. Brazell et al. (1984a) used a highly (8%) cross-linked resin with a flow injection detection method to shorten analysis time to 40 min, at the expense of resolution of the >13P polyphosphates.

These earlier studies illustrated that conditions present at combustion and during aerosol sampling influenced the complexity of phosphorus chemical evolution. Our objective has been to build on these earlier findings by using a wind tunnel to more closely simulate field conditions in a controlled manner.

METHODS

Aerosols were produced and characterized during environmental fate and effects testing of obscurant smokes within the wind tunnel of the Aerosol Research Facility at Pacific Northwest Laboratory (Figure 1).

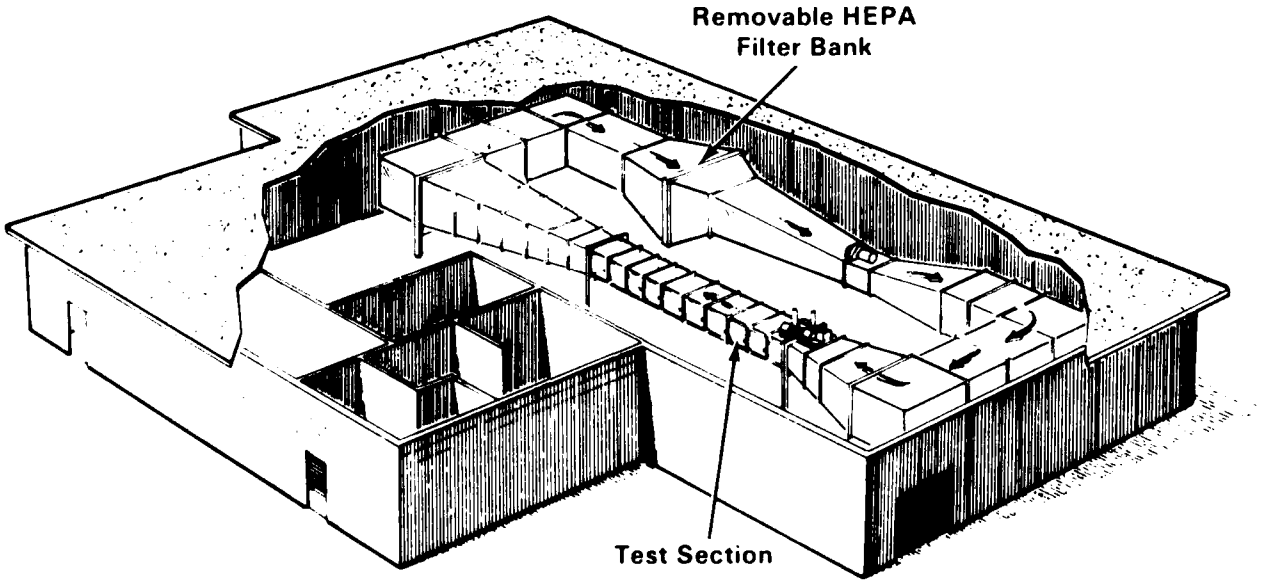

FIGURE 1. THREE DIMENSIONAL PERSPECTIVE OF AEROSOL RESEARCH FACILITY.

The wind tunnel, except for the test section, is constructed of stainless steel and is designed to safely contain aerosols of hazardous, toxic, and radioactive materials. The air flow approaching the test section was uniform, enabling us to study airborne particle transport and deposition phenomena within the flow field of the vegetative canopy in the test section. Metal halide lamps provided illumination through the transparent ceiling and walls of the test section to promote the continuation of plant respiration processes throughout each test. Wind speed was measured with a hot-wire anemometer. Temperature and relative humidity were controlled by operating a pair of stainless steel heat exchange coils located within the wind tunnel. Additional water vapor was added to the wind tunnel atmosphere during testing at high relative humidities. To maintain steady-state aerosols, we allowed air from the laboratory to enter the wind tunnel at the phosphorus combustion chamber and withdrew a similar quantity of air from the wind tunnel to provide an overall pressure difference of 0.25 to 0.50 in-H_2O between the laboratory and the wind tunnel. Most laboratory instrumentation was connected to a centralized computer for control and measurement of aerosol generation procedures, aerosol and gaseous species characteristics, and environmental parameters existing within the wind tunnel.

Aerosol Generation

Bulk pellets of 95% red phosphorus/5% butyl rubber (RP/BR) were obtained from the U.S. Army Chemical Research and Development Center. White phosphorus (WP) was purchased from a commercial supplier because distribution of WP in WP/F munitions is not uniform (Spanggord et al. 1985). Use of pure WP rather than WP/F also eliminated potential complicating effects of felt combustion products in the aerosol during plant and soil testing.

Previously used generation systems (DeFord et al. 1982; Holmberg and Moneyhun 1982) were deemed unsuitable for the present research. A new computer-controlled combustion chamber was designed and constructed for automatic generation of phosphorus obscurant smokes. Smoke generated within this chamber was then passed to the wind tunnel. Up to 22 individual portions of the base material were burned at intervals during each test to maintain approximately constant aerosol concentrations within the test section of the wind tunnel. The RP/BR material was burned on a dry sand surface in stainless steel trays, and WP (initially covered with water) was burned in ceramic cups. The laboratory computer was programmed to drain the water baths prior to ignition of WP and to initiate combustion of both RP/BR and WP by heating a nichrome wire. Various components of the generation system are shown in Figure 2.

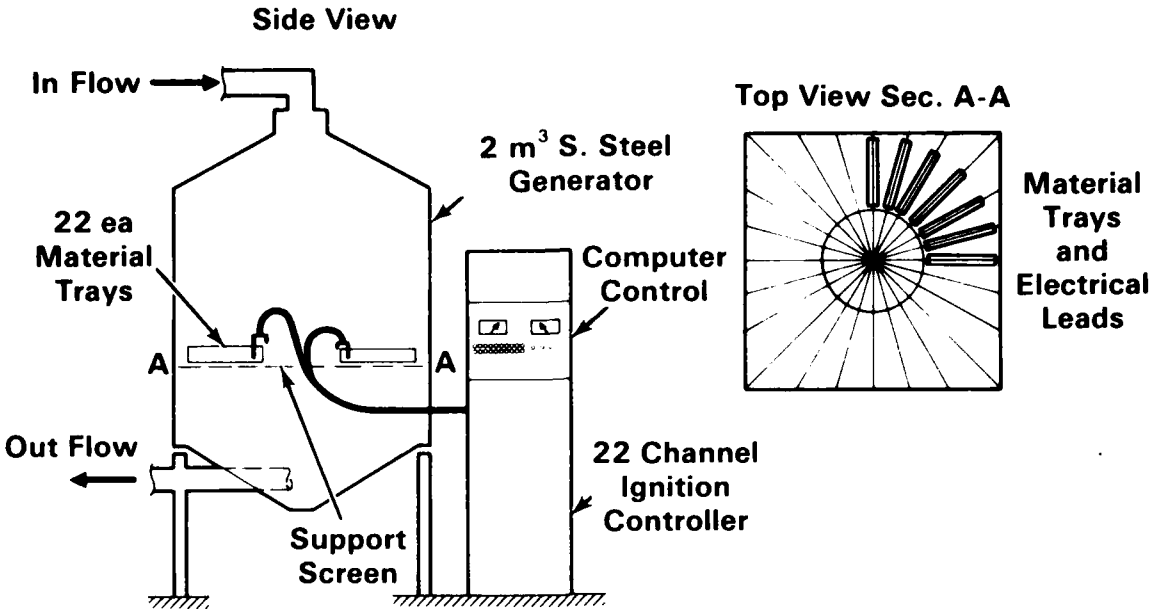

FIGURE 2. AEROSOL GENERATION SYSTEM (Van Voris et al. 1985).

Aerosol Measurement

The mass concentration of RP/BR and WP obscurant aerosols was monitored at 0.5- to 2-min intervals using a He-Ne (632 nm) laser transmissometer. The relative transmittance of the laser beam through a 61-cm path length of aerosol was calibrated during each test against isokinetically obtained filter samples of particulate mass. Transmittance of electromagnetic radiation through an aerosol is a function of many aerosol parameters and the wavelength of the radiation; therefore, calibration of this measuring device is adequate only as long as these parameters remain constant. Changes in particle size and composition will alter the response of the transmissometer. Although the response of the instrument changed slightly with relative humidity, the largest contribution to alterations in instrument response was aerosol age. For aerosols generated from RP/BR, the effectiveness of laser beam obscuration decreased by perhaps 20% during the first 20 min of aerosol aging, presumably due to an increase in particle size resulting from hydration and coagulation. Because the average age describing the steady-state aerosols in the wind tunnel during each test remained constant, the transmissometer calibration remained constant, and actual aerosol mass concentration was obtained from the ratio of laser output intensity to transmitted intensity.

The remote transmissometer was confined to measuring fresh, or actual, concentration because of its dependence on particle size and composition. Fresh, dried (or desiccated), and phosphorus mass concentrations were measured for each test. Dried aerosol mass concentration was measured by

desiccating glass-fiber filter samples over Drierite® for 24 hr to remove free water associated with the particles and then measuring the dried particulate matter on a conventional mass balance. Phosphorus mass concentration was measured by analyzing filter samples for total phosphorus content. Phosphorus mass concentration was measured because plant and soil effects were compared to the total dose of phosphorus each specimen received.

Particle size distributions of the steady-state phosphorus aerosols were characterized during each exposure test using Andersen cascade impactors. Additional measurements were made of fresh and aged aerosols. The particle collection stages were analyzed gravimetrically, and then chemically for phosphorus. No significant differences in the results of the two methods were noted (Figure 3);

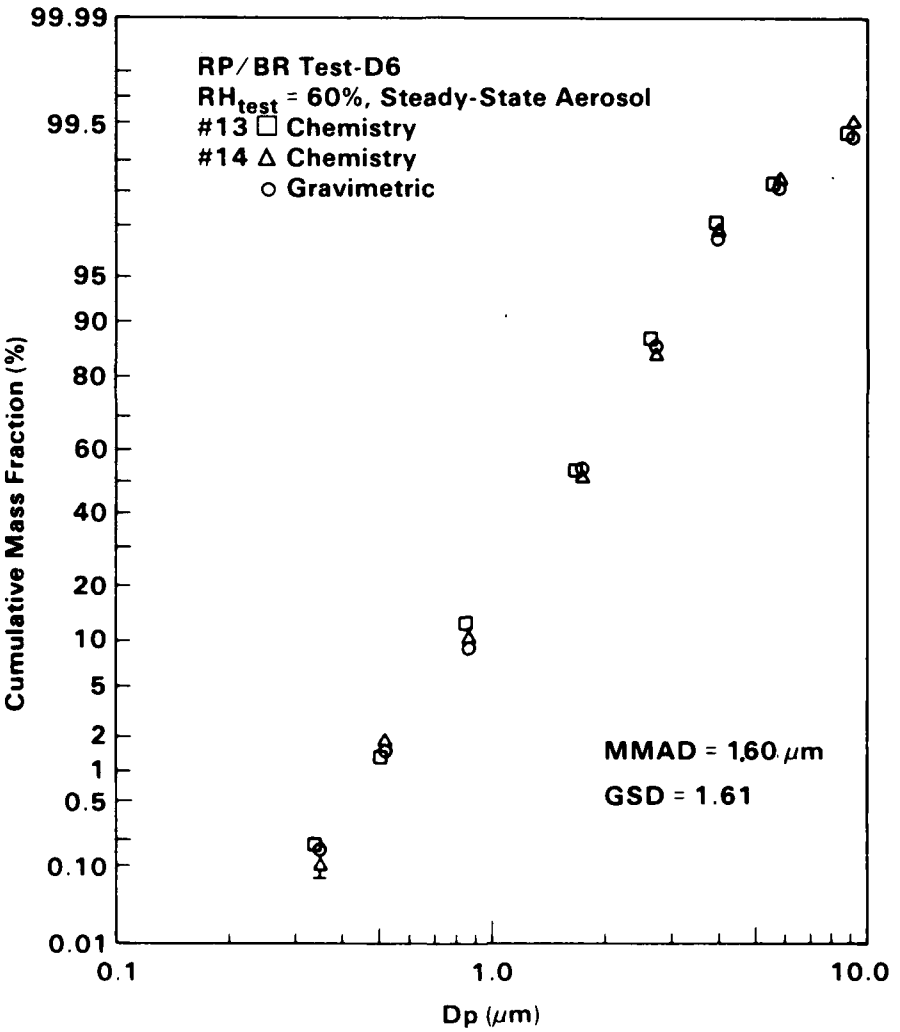

FIGURE 3. PARTICLE SIZE DISTRIBUTION OF RP/BR AEROSOL (VAN VORIS ET AL. 1985). Mass Median Aerodynamic Diameter (MMAD) equals 1.60 μm and Geometric Standard Deviation (GSD) equals 1.61.

® Trademark of W. A. Hammond Drierite.

apparently, evaporative losses did not preferentially affect the gravimetric analysis procedure. Particle size was seen to be approximately log normal in distribution. All impactor results were summarized by mass median aerodynamic diameter (MMAD) and geometric standard deviation (GSD).

Chemical Analysis

Concentration and species distribution of phosphorus compounds were measured after steady-state conditions had been reached in the test chamber, about 30 minutes after initiation of combustion. The aerosol was sampled isokinetically for mass concentration using glass-fiber filters. Particle mass on each filter was measured and then the filters were either desiccated and reweighed or sonicated in deionized water for phosphorus determination by inductively coupled plasma (ICP) emission spectrometry.

Phosphorus speciation measurement involved trapping the aerosol at a flow rate of 150 ml/min in a gas wash bottle containing 50 ml of deionized water. Deposition on dry (polystyrene petri cover) and wet (polystyrene petri dish containing deionized water) surfaces provided an estimate of the total deposition during each of the 1- to 4-hr exposures. Although Brazell et al. (1984a) recommended inclusion of ethylenediaminetetraacetate (EDTA) to inhibit breakdown of the higher polyphosphates, we found little change in either bubbler or static wet deposition samples using pure deionized water when analyzed on the day of preparation. Since the EDTA interfered with other analyses, it was only used in samples that could not be speciated on the day of collection. Aqueous samples were stored at room temperature (21° to 24°C) prior to analysis. Alterations in storage temperature were purposely avoided since hydrolysis rates are dependent on temperature.

Phosphate, phosphite, hypophosphite, and pyrophosphate solutions were prepared from reagent-grade chemicals. Tripolyphosphate was supplied by Monsanto (St. Louis, Missouri). Tetrapolyphosphate, hexammonium salt, and the type 5, 15, and 25 polyphosphate glasses were obtained from Sigma Chemical Company (St. Louis, Missouri). Cyclic trimetaphosphate was prepared according to Ballou (1981). All other chemicals used were reagent grade.

The concentration of phosphorus in solutions generated by burning RP/BR or WP was determined with a Model 975 Jarrell-Ash (Division of Fisher Scientific; now Allied Analytical Systems) ICP emission spectrometer. Aqueous samples were analyzed without modification (i.e., no acid added) and normally did not require filtration. The detection limit by ICP is 0.1 mg/l phosphorus. Relative standard deviation is 50% at the detection limit, 10% at 5 times the detection limit, and 3% at 50 times the detection limit.

The lower oxyphosphoric-acid species were analyzed using a Dionex (Sunnyvale, California) Model 16 Ion Chromatograph (IC) equipped with AG1 and AS1 separator columns and with a continually regenerated fiber suppressor linked to a conductivity detector. Eluent was 3 mM $NaHCO_3$ plus 2.4 mM Na_2CO_3. Detection limits for phosphate, phosphite, and hypophosphite were 0.03 mg/l as phosphorus. Continued analysis of stock and exposure solutions resulted in a loss of column efficiency and an increase in back pressure. Back pressure was presumably caused by binding of the higher polyphosphates onto the column in the basic system. Reasonable column recovery was attained by back-flushing with a series of acid and base washes (0.1 N H_2SO_4, 0.1 N NaOH, 0.2 N Na_2CO_3).

The separation scheme for polyphosphate speciation basically followed that of Yamaguchi et al. (1979). The procedure involved anion exchange using a high-salt eluent containing EDTA to complex any metals in the system, thereby slowing the depolymerization rate. The condensed phosphates were acid hydrolyzed, and the resultant phosphate reacted to form a heteropoly blue complex with Mo (V-VI) detected at 660 nm. Use of a water bath at 94°C for both the acid hydrolysis and the color development loops resulted in good recovery of P species, based on total P analysis by ICP emission spectrometry. Although we have detected up to 28 P species in bubbler samples of the actual aerosol or deposition samples, most samples contained fewer than 20 species.

Phosphite and hypophosphite were not hydrolyzed to phosphate under the conditions used in the test. Since IC analysis is rapid (20 min) compared to the HPLC separation (~4 hours), it was used to monitor phosphate concentrations in most of the samples. In practice, hypophosphite levels were negligible and will not be discussed further.

Aerosol samples were collected for phosphine analysis with a gas sampling bottle attached to the wind tunnel. The bottle was flushed with approximately five volumes of aerosol at a flow rate of about 0.5 l/min before aerosol samples were collected. Analysis for phosphine was conducted using a HP 5880A gas chromatograph (GC) equipped with a 5% phenyl/95% methyl silicon fused-silica capillary column (held at 100°C) and a nitrogen/phosphorus detector. Gas-tight syringes were used to collect samples from the gas collection bottles. A standard gas mix (Union Carbide, Linde Division) containing 104 ppm (w/w) phosphine in argon was diluted to produce standards used in calibration. Detection limits varied somewhat with instrument conditions, but in all cases were better than 43 $\mu g/m^3$. Phosphorus components other than phosphine were observed in some gas samples. Standard addition and reanalysis by both the above procedures and via a 4-ft Porapak-Q glass column followed by flame photometric detection confirmed that the multiple peaks were due to species other than phosphine. Further identification was not pursued.

Elemental white phosphorus (P_4) in the aerosol was trapped in 40 ml of benzene in a gas wash bottle. The aerosol was sampled at a rate of 150 ml/min. Estimated carryover to backup trap was $\leq$0.1%. The entrained phosphorus oxy-anions did not interfere with the determination. A water rinse of the benzene layer and trap walls resulted in essentially complete recovery of the polyphosphate fraction, giving a second check on total aerosol collected in the bubbler. A HP5840 GC equipped with a 4-ft glass column containing 5% OV101 packing (100°C isothermal) and flame photometric detector equipped with a P-specific filter was used for injections of up to 10λ of benzene trap solution. The detection limit for P_4 in benzene was 1 part per billion (ppb).

RESULTS

Physical and chemical characteristics of the aerosols were measured. Physical characteristics such as mass concentration, particle size, and particle water content are important in defining the level of exposure, the mass loading rate of aerosol onto exposed specimens, and the evolution of the particles as they grow by coagulation and water absorption. Results of the chemical composition of the aerosols and of the particles deposited to various surfaces are also presented. The composition of the suspended particles was seen to be significantly affected by aging and by the water vapor content of the surrounding air. The chemical fate of the deposited particles also varied widely with deposition surface and aging conditions.

Aerosol Characteristics

Phosphorus aerosols were characterized in the wind tunnel under a variety of controlled environmental conditions. Particle chemical composition, size distribution, and mass concentration were found to vary with relative humidity and aerosol age, and particle deposition velocity to plant specimens was observed to vary with wind speed, plant species, and relative humidity. As mentioned previously, the effect of temperature on aerosol characteristics was not investigated. Temperature was maintained at 22° ± 1°C, humidity was varied between 20% and 90%, and wind speed was varied between 0.2 and 4.5 m/s (0.5 to 10 mph). For the RP/BR series, a "rainout" test was added, during which a fine water spray (0.4 cm/hr) was generated in the test section of the wind tunnel. Tests were also performed at low (5°) relative humidity within the combustion chamber to provide additional information on phosphorus speciation.

Aerosol mass concentrations were maintained in the wind tunnel at constant levels within approximately 10% for up to 8 hr. Actual average mass concentrations ranged from 200 to 6000 mg/m^3 during the plant and soil exposure tests. The average age of the aerosol during each test sequence was held approximately constant during each exposure test and was controlled by altering the volumetric flow rate into and out of the wind tunnel. The average age of particles in the steady-state WP and

RP/BR aerosols were estimated to be 22 min and 28 min, respectively. Before each test, the aerosol was aged to a steady-state condition by isolating and bypassing the test section from air flow within the wind tunnel.

Data on particle size distribution for both types of phosphorus smokes generated in the wind tunnel are summarized in Table I (Van Voris et al. 1985). The MMAD was larger for increased aerosol age and water vapor availability. The MMAD of WP aerosols increased from 1.5 to 1.75 μm as humidity increased. The results for aerosols generated from RP/BR revealed slightly larger MMAD's possibly caused by the more aged condition of the aerosol during testing. Measurements of MMAD indicated that rapid particle growth occurred in the first several minutes after generation. The initial rapid increase in particle size may have been caused by water vapor absorption and coagulation, and the latter change, between steady-state and aged aerosols, was probably due to a combination of coagulation and preferential deposition of the larger particles onto plant, soil, and wind tunnel surfaces. Aerosols that were aged longer than the 22- and 28-min steady-state conditions exhibited slightly increased MMAD's.

TABLE I. MASS MEDIAN AERODYNAMIC DIAMETER VERSUS RELATIVE HUMIDITY AEROSOL AGE FOR RP/BR AND WP AEROSOLS (GSD = 1.60 ± 0.1). Number of impactor samples shown in parentheses (Source: Van Voris et al. 1985)

Aerosol Condition	Relative Humidity ~25%	~60%	~90%
	MMAD (μm)		
RP/BR Aerosols			
Steady-state[a]	1.6 (1)	1.61 (5)	1.95 (2)
Age ≤5 min	--	--	--
Age ~10 min	1.5 (1)	1.40 (2)	1.85 (1)
Age ≥50 min	--	1.80 (2)	--
WP Aerosols			
Steady-state[a]	1.50 (1)	1.56 (6)	1.75 (1)
Age ≤5 min	1.15 (1)	--	1.10 (1)
Age ~10 min	--	1.30 (1)	--
Age ≥50 min	--	1.62 (1)	--

[a]Steady-State (time = approximately 28 min for RP/BR and 22 min for WP).

Particle density was not measured directly. However, assuming a particle density of 1.8 g/cm^3 (approximate density of H_3PO_4) at low humidity, an increase in particle volume of roughly 2.5 times may be estimated between the low and high humidity conditions. This estimation assumes that the gain in particle mass with increasing humidity was due to water vapor absorption and that the density of the particles decreased to approximately 1.3 g/cm^3 at the high humidity condition. Actual measurement of particle density would allow calculation of particle physical diameter from the present results.

The bulk composition of the phosphorus aerosols remained approximately constant during each exposure test because the aerosol was maintained at nearly steady-state conditions. The ratio of phosphorus mass concentration to fresh aerosol mass concentration was compared to relative humidity (at 22°C). These results are presented in Figure 4 and compared to data calculated from results of other investigators for RP/BR (Holmberg and Moneyhun 1982; Brazell et al. 1984b; Tarnove 1980; and Burton et al. 1982). Additionally, a curve representing equilibrium phosphorus concentration versus relative humidity in an aqueous solution of H_3PO_4 (Tarnove 1980) is presented for comparison. The scatter in these data may result from differing aerosol age at time of sampling and from methods used to store samples prior to actual sample analysis. Figure 4 was plotted using relative humidity rather than water vapor content because the phosphoric acid equilibrium curve was said to be independent of temperature between 10° and 60°C (Tarnove 1980); however, some of the scatter in the data is reduced

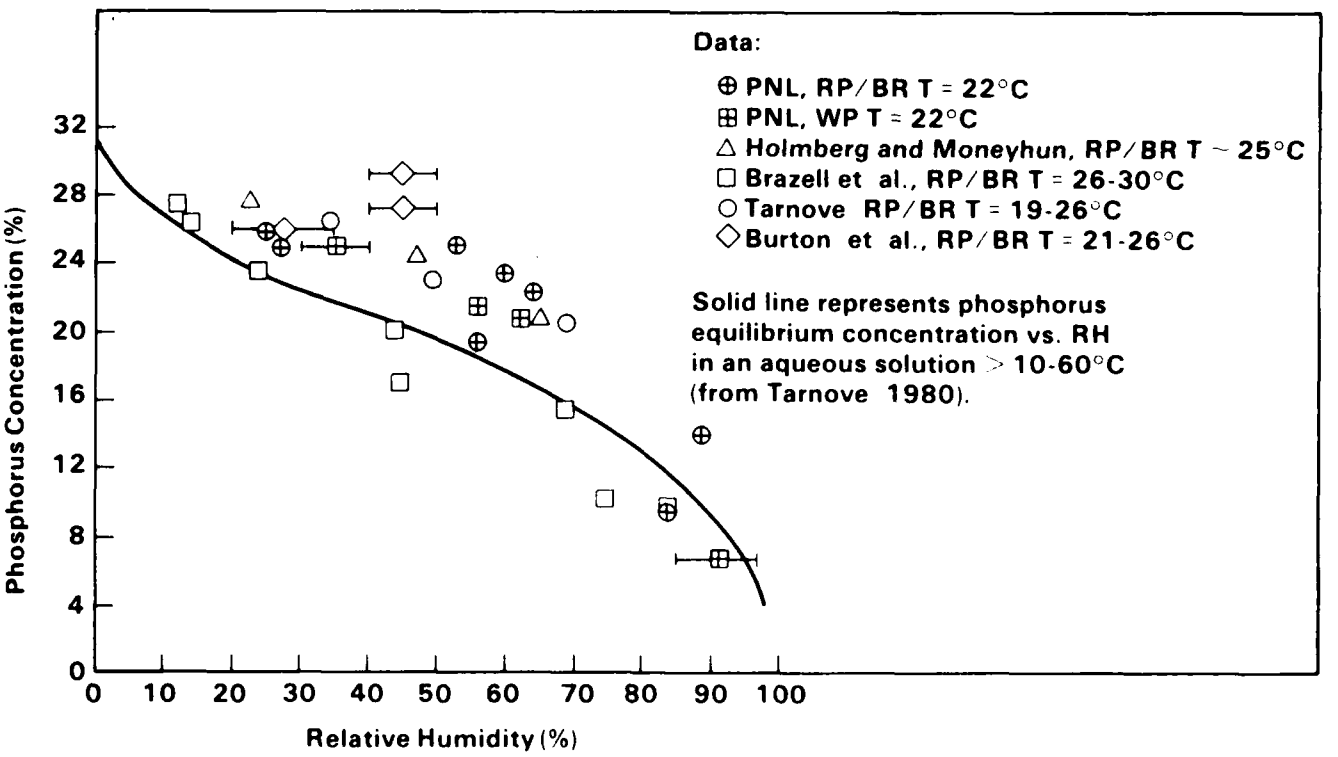

FIGURE 4. CHEMICAL COMPOSITION OF AIRBORNE PARTICLES; PERCENTAGE PHOSPHORUS, BY MASS, IN VARIOUS AEROSOLS GENERATED FROM RP/BR OR WP.

when water vapor content rather than relative humidity is considered. The general trend seen in Figure 4 is that the phosphorus content of these aerosols was slightly greater than that of an aqueous phosphoric acid solution. This further indicates that use of a simple phosphoric acid model is insufficient to predict the complicated chemical composition and evolution occurring within the particles in phosphorus obscurant aerosols.

Distribution of Phosphorus Species

The actual speciation of phosphorus in the particles deposited onto soils or vegetation depends on the humidity of the air, the temperature, and probably the composition of the air during combustion and subsequent aging in the wind tunnel or in a natural environment. As noted earlier, temperature was held constant in this study. It is likely that rates of depolymerization of the higher polyphosphate species have some dependence on temperature. Since the aerosol was sampled after steady-state conditions had been reached in the recirculating wind tunnel, and since fresh smoke was continually added, the aerosol was a mixture of fresh and aging particles, thus complicating the interpretation of the aging phenomenon. Several short-term combustions of RP/BR were performed with the burn plume sampled directly (into bubbler traps) and then a short time later in the exposure section (Table II). Actual water vapor mass measurements corresponded to 20% relative humidity in the plume and 26% in the chamber and tunnel. The high proportion of species that were not recovered during the short sampling periods apparently corresponded to very large polyphosphates, which break down with aerosol aging.

TABLE II. AGING OF P AEROSOL AT CONSTANT HUMIDITY

	PNL Data				ORNL Data[a]		
Sampling Time (min)	0	5	5	30	~0	30	60
Location	Plume	Mixing Chamber	Wind Tunnel	Wind Tunnel	Plume	Test Chamber	Test Chamber
Species	% of Total P						
1P	2.6	5.0	9.9	24.5	9.5	16.6	31.6
2P	1.9	2.5	4.1	10.2	3.6	7.0	14.0
3-4P	5.2	7.7	8.8	14.0	8.4	6.4	10.2
5-13P	34.0	47.2	44.9	44.0	24.3	12.1	15.2
14-20P	9.5	12.2	8.1	7.4	53.3	57.9	29.0
>20P	46.9	25.4	24.3	0			

(a) Data from Brazell et al. 1984a, Oak Ridge National Laboratory (ORNL), Oak Ridge, Tennessee.

The 30-min sampling point would correspond to the earliest sampling time during routine exposures of plants and soils. When these data were compared to those of Brazell et al. (1984a), the same trends are observed. Variations in burn characteristics and more rapid analysis of samples preserved with EDTA amendments in the latter case are likely to have had some effect on the actual distribution.

Aging of particulate mass deposited on dry polystyrene plates or collected on glass-fiber filters repeatedly showed rapid conversion to phosphate. Table III shows a rough estimate of this conversion based on phosphate concentrations compared to total phosphorus. These data were compiled from several tests, performed essentially at room temperature (22°C) and at a relative humidity of between 20% to 30%. For comparison, the zero dry time may be defined by the bubbler samples, where water contact is considered immediate.

TABLE III. HYDROLYSIS VERSUS AGE PRIOR TO WATER LEACH

Time to H_2O Contact (hr)	% of P as PO_4^{3-}
0[a]	19-27
<0.1	20-28
0.5	54
0.8	49-57
2	66
18	100

(a) Bubbler sampler.

The hydrolysis rate we observed for RP/BR and WP was faster than that reported by Spanggord et al. (1985) for WP/F and RP/BR burn residues. A half-life of 49 hr was reported in the latter study for conversion to H_3PO_4; our results indicated that complete conversion occurred within 18 hr. The variation in the conversion rate is not surprising, since such factors as humidity and smoke concentration (and the resulting pH of the residue) have a marked effect on the actual hydrolysis rate. Rapid water contact was necessary to slow the breakdown of polyphosphates.

Hydrolysis to phosphate will slow somewhat in an aqueous medium, but partial hydrolysis of the higher polyphosphates will continue. Brazell et al. (1984a) showed the loss of >13P and peaking of 5P to 13P levels in an aqueous solution in 2 days with a significant increase in trimetaphosphate levels. Katz et al. (1981) showed a 70% drop in 5P to 8P species concentration in 3 days. We found the increase in trimetaphosphate levels to be significant in less than 2 days (Table IV) in smoke-dosed deionized water. Since the metaphosphate elution pattern was superimposed on the polyphosphate elution, the detection limits in fresh solution were higher than those in the absence of interfering

TABLE IV. SPECIATION VERSUS SAMPLE AGE AT ANALYSIS

	Dosed Water			Dosed Soil Leachate		
Sample Age (Days)	0.7	1.7	9.0	0.8	1.7	9.0
Species	- - - - - - - - - % of total P - - - - - - - - -					
1P	23.4	25.8	30.3	41.9	41.9	83.2
2P	9.6	9.2	11.8	4.1	3.3	3.7
3-4P	13.6	17.1	23.9	14.5	16.4	8.8
5-13P	45.0	39.7	19.3	29.5	27.5 (max)	1.4
≥14P	6.7	<1	<1	1.8	<1	<1
3mP[a]	~2 (max)	7.9	13.9	8.4	10.3	<1
4mP	<2	Trace	0.7	<2	0.6	1.3
6mP	<2	<1	0.5 (max)	<2	≤1.2	1.7

[a] mP = metaphosphate ring structure.

peaks. We observed markedly different behavior in a solution containing 10 parts of deionized leachate water and 1 part of exposed soil; trimetaphosphate disappeared entirely, and traces of tetra- and hexametaphosphates were detected. Microbial activity may have combined with chemical weathering effects in the presence of soil minerals to catalyze hydrolysis and influence solubility of these compounds.

Our speciation measurements for phosphorus were conducted using deionized water alone or with EDTA amendments. We must stress, however, that the actual hydrolysis of phosphorus smoke under environmental conditions would be directly dependent on the resulting mixture. Poston et al. (1985) showed that water hardness, ionic makeup, and neutralization caused marked changes in species distribution with time (Figure 5). Two points are shown in Figure 5: 1) the shift to trimetaphosphate as a predominant species under neutralized conditions, and 2) the slow rate of complete hydrolysis to phosphate. Even after 3 months, an unneutralized aliquot contained only 26% phosphate, although the 1P to 4P species accounted for 66% of the total phosphorus.

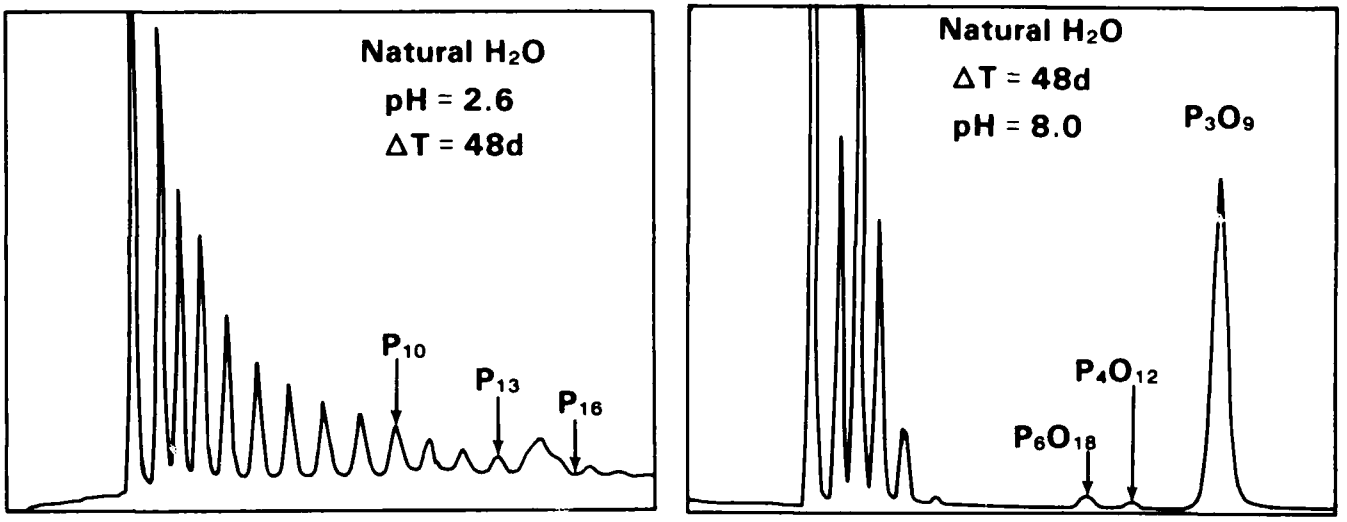

FIGURE 5. PHOSPHORUS SPECIATION ANALYSIS OF HARD WATER AGED 48 DAYS AFTER CONTACT WITH FRESH WP/F SMOKE (Alkalinity - 115 mg/l). (Source: Poston et al. 1985).

When the burn plume of RP/BR was sampled at various humidities (Table V), minor changes were seen in the phosphate ratios. Percentages of the higher polyphosphate species declined markedly as humidity increased. The initial phosphate levels present in the unaged aerosols were low, as expected.

TABLE V. SPECIATION VERSUS HUMIDITY IN FRESH RP/BR AEROSOL

	Relative Humidity		
	5%	20%	95%
Species	- - - - - - - - - % of total P - - - - - - - - -		
1P	2.7	2.6	3.0
2P	0.7	1.9	2.0
3-4P	2.0	5.2	6.6
5-13P	23.5	34.0	39.1
14-20P	ND[a]	9.5	12.2
>20P	72.5	46.9	37.2
HPO_3^{-2}	$\leq$ 0.2	$\leq$ 0.1	0.1

(a) Not detected

When the smoke in the wind tunnel reached steady-state, conversion to phosphate was diminished, while concentrations of 2P to 4P generally increased with increasing humidity. A similar trend was observed for both RP/BR and WP combustion (Table VI).

The decrease in phosphate with increasing humidity was also observed by Brazell et al. (1984a); however, they also reported a marked increase in >13P species with increasing humidity--a phenomena that we failed to see in either fresh or steady-state aerosols. However, when they burned RP/BR and WP/F under free-burn conditions (closely resembled by our steady-state conditions), no metaphosphate species or species greater than 11P were observed (at 38% relative humidity), and concentrations of the lower P species resembled those determined in our study. Katz et al. (1981) studied the effects of humidity ranging from 33% to 67% using a 0.011-m^3 combustion chamber and could not conclusively identify a relationship between humidity and speciation. An identification of such a relationship may have been difficult to determine because of a significant time lapse between sample collection and analysis. It is likely that the hydrolysis to phosphate continued prior to analysis.

In tests using wind speeds of 0.2 to 4.5 m/s, we saw no significant shift in speciation in steady-state aerosols. While this is in agreement with the small-scale test done by Katz et al. (1981) under entirely different burn conditions, it differs from Brazell et al. (1984a). The latter study showed a marked decrease in the >13P and an increase in 5P to 13P fraction as wind speed rose from 2.0 to 8.2 m/s. The Brazell et al. (1984a) study is unique in that the wind speed across the combustion zone was equal to the test velocity. The high air velocities across the burning phosphorus would have resulted in more rapid transport of aerosol to the sampling point; higher-order phosphorus

TABLE VI. SPECIATION VERSUS HUMIDITY IN STEADY STATE AEROSOLS

	RP/BR			WP		
RH (%)	27	53	89	25	60	90
Species	- - - - - - - - - - % of Total P - - - - - - - - - -					
1P	26.0	24.1	18.6	30.2	18.7	16.2
2P	15.4	16.0	19.3	18.4	14.7	15.8
3-4P	16.3	21.8	25.0	18.0	11.5	24.0
5-13P	30.8	34.0	32.8	30.0	33.4	38.7
14-20P	2.4	2.8	1.5	2.5	9.6	2.7
>20P	7.6	[illegible]0	2.7	0.9	12.1	1.8
HPO_3^{-2}	0.6	0.4	0.2	0.2	0.2	0.1

species would be expected to be found in the less aged aerosol. In addition, changes in combustion characteristics, caused by changing air velocities, may have also affected phosphorus speciation in the resulting smoke. In the present study, the motion of air across the combustion zone was independent of actual wind speed in the test section of the wind tunnel.

Differences in phosphorus speciation as a function of particle size were measured by analyzing for phosphate and total phosphorus. In general, the percentage of phosphorus as phosphate tended to peak slightly in the 4.8 to 7.5 μm size and then decrease with decreasing particle size. An impactor taken from a RP/BR burn at 87% relative humidity, 0.9 m/s wind speed, and 22 ± 1°C was chosen for further speciation. Results (Table VII) confirm the drop in phosphate and corresponding increase in higher polyphosphates. A bubbler sample representing an integrated aerosol sample from the same run is included for comparison. Since the particle size increases with age, the smaller particles would be expected to represent a somewhat fresher, or less aged, component of the continuous smoke generation.

The maximum phosphine concentration observed during the WP burns was 70 μg/m³, representing 0.02% of the total phosphorus in the aerosol. The highest values measured were most prevalent at the higher humidities; however, most of these values were at or below the detection limit, resulting in phosphine concentration estimates of $\leq$0.002% of the total phosphorus suspended in the wind tunnel. Katz et al. (1981) reported phosphine levels at less than 0.0001% of total P. Brazell et al. (1984b) detected no phosphine (detection limit 0.1 ppm). Spanggord et al. (1985) generated extremely high (500 ppm) levels of PH_3 in a sealed reactor at 100% relative humidity over a 12-day period following WP/F oxidation in air and adjustment to 1 atm with air. However, such contained conditions hold little resemblance to actual field deployment.

TABLE VII. SPECIATION VERSUS PARTICLE SIZE (RP/BR)[a]

Impactor Stage	2	6	Bubbler Sample
Approx. Particle Size (μm)	4.8	0.65	
Species	- - - - - - % of total P - - - - -		
1P	22.6	14.5	18.6
2P	18.9	20.0	19.3
3-4P	25.4	28.6	25.0
5-13P	29.5	35.9	32.8
$\geq$14P	1.0	0.9	1.5

[a] Conditions: 87% RH, 0.9 m/s wind speed, 22 ± 1°C.

The same study reported no detectable PH_3 generated with RP/BR in a like reactor when RP/BR was initially oxidized in pure oxygen and then adjusted to 1 atm with air. The lower O_2 levels observed in the WP/F study probably encouraged the formation of lower phosphorus oxides (such as P_4O_6), which yield PH_3 upon disproportionation.

Levels of elemental white phosphorus (P_4) in the aerosol ranged from 0.007% to 0.015% of total phosphorus in a series of experiments. Upon deposition to water surfaces, P_4 showed depletion to levels of less than 0.0009% of the total P deposition in the 1-hr tests, and less than 0.0002% in the 4-hr tests. The upper limit of combustion efficiency for WP/F munitions is estimated to be 92%; therefore, significant quantities of P_4 could remain unburned during field use (Spanggord et al. 1985).

CONCLUSIONS

Variations in methods used in this study and by other researchers to generate and collect phosphorus aerosols (Brazell et al. 1984a,b; Katz et al. 1981; Spanggord et al. 1985) have led to some conflicting results. The chemical composition of these aerosols was shown to be dependent on age and environment (e.g., relative humidity). We therefore believe that these conflicting results were caused by the use of different generation, sampling, and analysis methods.

We conclude that phosphorus speciation within RP/BR and WP aerosols is dramatically affected by humidity and age (i.e., time to water contact). The rate of hydrolysis after deposition is also affected by contact with water and by the availability of agents causing complexation or precipitation. Particle size distribution is a function of parameters such as age and humidity, and average particle size will increase with increases in both of these parameters. Wind speed may have a minor effect on species distribution, but the effect would most likely be outweighed by the water-related responses. Wind speed will affect the rate of particle deposition and, thus, will tend to increase the severity of potential ecological and soil chemistry effects of the RP/BR and WP aerosols. (Foliar effects and changes in the solubility of soil components after exposure will be the subjects of future reports.) Since hydrolysis is expected to be dependent on temperature, future studies should examine phosphorus speciation at temperatures other than 20°C (perhaps 0° to 40°C, a range typical of actual field conditions). The effect on phosphorus speciation of co-dispersion with dust particles also has yet to be addressed.

ACKNOWLEDGMENTS

The authors wish to acknowledge individuals who have contributed to the direction and successful completion of this research. First, the guidance and professional experience of Drs. Dominic A. Cataldo and Roger M. Bean, both major contributors to this research project, were invaluable. Donald

C. Klopfer and Berta L. Thomas provided excellent technical assistance in the laboratory. The efforts of Carolynn M. Novich in editing and Bonnie S. Dennis and Joan F. Segna in text preparation were appreciated. This work was supported under contract by the U.S. Army, Medical Bioengineering Research and Development Laboratory, located at Ft. Detrick in Frederick, Maryland. Thanks are also extended to Mr. Jessie J. Barkley, Jr., the Contracting Officer's Technical Representative.

REFERENCES

Ballou, J. E. 1981. Chemical Characterization and Toxicological Evaluation of Airborne Mixture. AD-A102678 DAMD17-79-C9160 S1055, Prepared for U.S. Army Medical Research and Development Command by Pacific Northwest Laboratory, Richland, Washington.

Brazell, R. S., R. W. Holmberg, and J. H. Moneyhun. 1984a. "Application of High-Performance Liquid Chromatography-Flow Injection Analysis for the Determination of Polyphosphoric Acids in Phosphorus Smokes." J. Chromotog. 290:163-172.

Brazell, R. S., J. H. Moneyhun, and R. W. Holmberg. 1984b. The Chemical and Physical Characterization of Phosphorus Smokes for Inhalation Exposure and Toxicology Studies. ORNL/TM-9571, Prepared for the U.S. Army Medical Research and Development Command by Oak Ridge National Laboratory, Oak Ridge, Tennessee.

Burton, F. G., M. L. Clark, and R. E. Schirmer. 1982. "Generation and Characterization of Red Phosphorus Smoke Aerosol for Inhalation Exposure of Laboratory Animals." Am. Ind. Hyg. Assoc. J. 43(10):767-772.

DeFord, H. S., M. L. Clark, and J. R. Decker. 1982. "A Laboratory-scale Conveyor/metering Device and Combustor for Generating Smoke from Solids at a Uniform Rate." Am. Ind. Hyg. Assoc. J. 43(10):764-766.

Halmann, M., ed. 1972. Analytical Chemistry of Phosphorus Compounds. Wiley-Interscience, New York.

Holmberg, R. W. and J. H. Moneyhun. 1982. "System for the Continuous Generation of Phosphorus Aerosol from Red Phosphorus-Butyl Rubber." CONF-820468-1, National Technical Information Service, Springfield, Virginia.

Katz, S., A. Snelson, R. Butler, W. Bock, N. Rajendron, and S. Relwani. 1981. Physical and Chemical Characterization of Military Smokes. Part III: White Phosphorus-Felt Smokes. ADA115657, IIT Research Institute, Chicago, Illinois.

Poston, T. M., R. M. Bean, B. L. Thomas, K. M. McFadden, M. L. Clark, and B. Killand. 1985. Acute Toxicity of Smoke Screen Materials to Aquatic Organisms. Prepared for U.S. Army Medical Research and Development Command by Pacific Northwest Laboratory, Richland, Washington.

Riemann, W. III, and J. Beukenkamp. 1961. "Phosphorus." In Treatise on Analytical Chemistry, ed. I. M. Kilthoff, P. J. Elving, and E. B. Sandell, pp. 317-402. Interscience Publishers Inc., New York.

Spanggord, R. J., R. Rewick, T. Chou, R. Wilson, R. T. Podoll, T. Mill, R. Parnas, R. Platz, and D. Roberts. 1985. Environmental Fate of White Phosphorus/Felt and Red Phosphorus/Butyl Rubber Military Screening Smokes. Draft Final Report, DAMD17-82-C-2320 prepared for USAMRDL by SRI International, Menlo Park, California.

Tarnove, T. L. 1980. Studies of the Chemistry of the Formation of Phosphorus-Derived Smokes and Their Implication for Phosphorus Smoke Munitions. ARCSL-TR-80049, U.S. Army Armament Research and Development Command, Chemical Systems Laboratory, Aberdeen Proving Ground, Maryland.

Van Voris, P., M. W. Ligotke, D. A. Cataldo, T. R. Garland, K. M. McFadden, J. E. Rogers, D. W. Carlile, and S. W. Li. 1985. "Transport, Transformation and Ecological Effects of Phosphorus Smokes in an Environmental Wind Tunnel." In Smokes and Obscurants Symposium IX. (In Press).

Van Wazer, J. R., E. J. Griffith, and J. E. McCullough. 1954. "Analysis of Phosphorus Compounds: Automatic pH Titration of Soluble Phosphates and Their Mixtures." Anal. Chem. 26:1755-1759.

Van Wazer, J. R. 1958. Chemistry. Volume 1 of Phosphorus and Its Compounds. Interscience Publishers, Inc., New York.

Yamaguchi, H., T. Nakamura, Y. Hirai, and S. Ohashi. 1979. "High Performance Liquid Chromatographic Separation of Linear and Cyclic Condensed Phosphates." J. Chromatog. 172:131-140.

MEAN FREE PATH EFFECTS ON PARTICLE COAGULATION

Phil Lawless, Ashok Damle, Parker Reist*, Mike Hsieh*
Research Triangle Institute
Research Triangle Park, NC
and
*University of North Carolina at Chapel Hill
Chapel Hill, NC

Supported by AFOSR

ABSTRACT

-- An experimental study of aerosol growth at reduced pressures
-- Primary aerosol formed in an exploding-wire generator
-- Growth in liquid and solid phases
-- Metallic aerosols

INTRODUCTION

The exploding-wire generator is capable of vaporizing sufficient material that high concentrations of submicron aerosol can be formed, leading to rapid coagulation over a wide range of pressures. The formation of the initial aerosol and its subsequent growth are the focus of this work.

To understand the role of gas mean free path, first consider the molecular (MFP >> particle diameter) and the continuum (MFP << particle diameter) regimes. Here the coagulation is determined by the geometrical collision cross-section of the particles and the relative velocities. The velocities are diffusive in the continuum regime, but there are no size dependent effects .

In the transition regime, molecular slip introduces a size-dependent collision rate, and the result is that the smaller particles "catch up" to the larger particles in the size distribution, changing its shape.

This is expressed in dimensionless coordinates, using the normalized particle volume η, and the volume distribution function ψ. The distribution functions are shown below (Figure 1) for the three regimes discussed here.

What is not shown here is the rate at which a distribution can move from one regime to the other. This is primarily determined by the initial particle concentration, but all closed distributions will eventually grow into the continuum.

For many aerosol systems, combustion sources for one, the initial particle size and concentration lead to a transition-type distribution because the rate of coagulation slows dramatically with time. For time scales on the order of seconds to minutes, the transition distribution is the appropriate one to use at atmospheric pressure. As the gas pressure is reduced, the same aerosol should remain in the free molecular distribution for the same time period.

Steady-State Distributions for Atmospheric Pressure

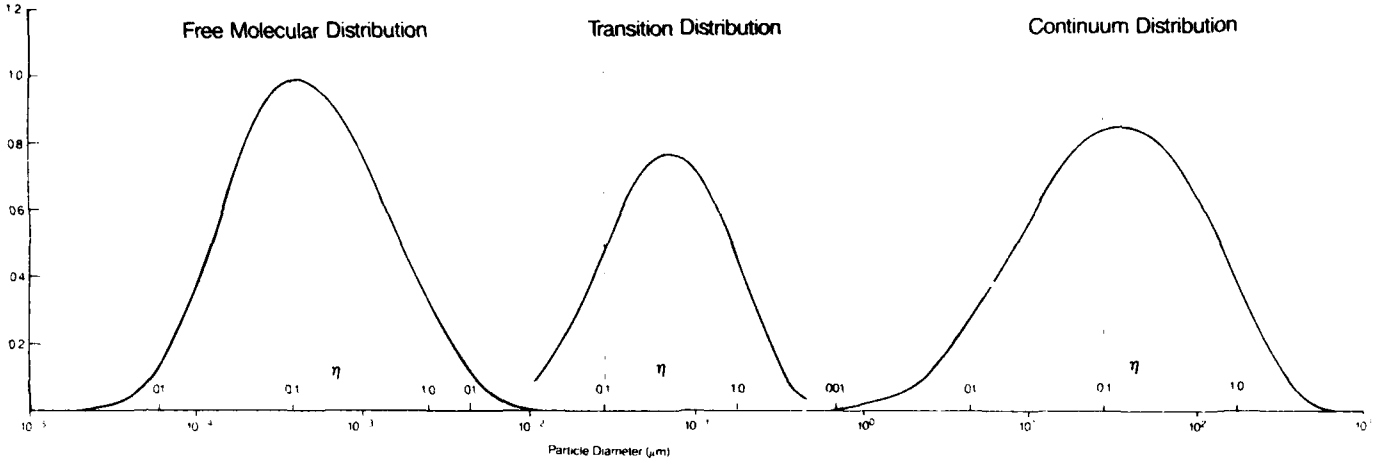

Figure 1.

These models strictly apply only to liquid aerosols because the particle volumes are assumed to be additive. By incorporating a void fraction into the model, we hope to extend the range of validity to particles which remain roughly spherical, even though they may contain a void space.

These models also explicitly assume that no extraneous forces govern the motion of the coagulating particles. Consider now the experimental results that have been obtained in the early stages of the project.

APPARATUS

The exploding wire generator (Figure 2) can produce enough material to grow macroscopic particles (1-10 mm) in tens of minutes, at atmospheric pressure. Lower pressures lead to rapid gravitational settling. For the present, slower growth and extractive sampling are being used to study the effects of pressure. The extracted sample is being analyzed by an optical particle counter, by SEM and video image examination of filter samples, and by Faraday cage filter for particle charge. There are samplers in place for TEM grids, and piezo-mass balance, and an optical scattering system will be added for dynamic monitoring.

FRACTAL ANALYSIS OF AEROSOL

The microscope pictures (Figure 3) show a definite need for an analysis that does more than estimate spherical collision cross-sections. Fractal analysis is a potential tool we are investigating actively for application to this problem.

Sampling Devices

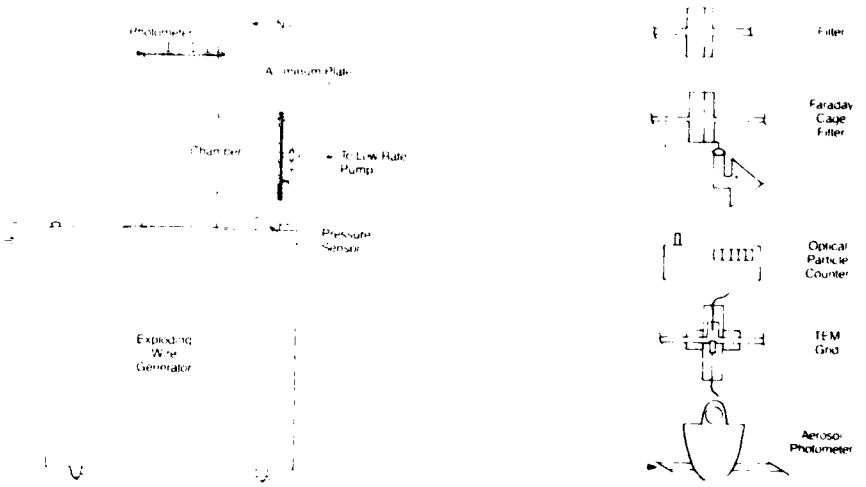

Figure 2.

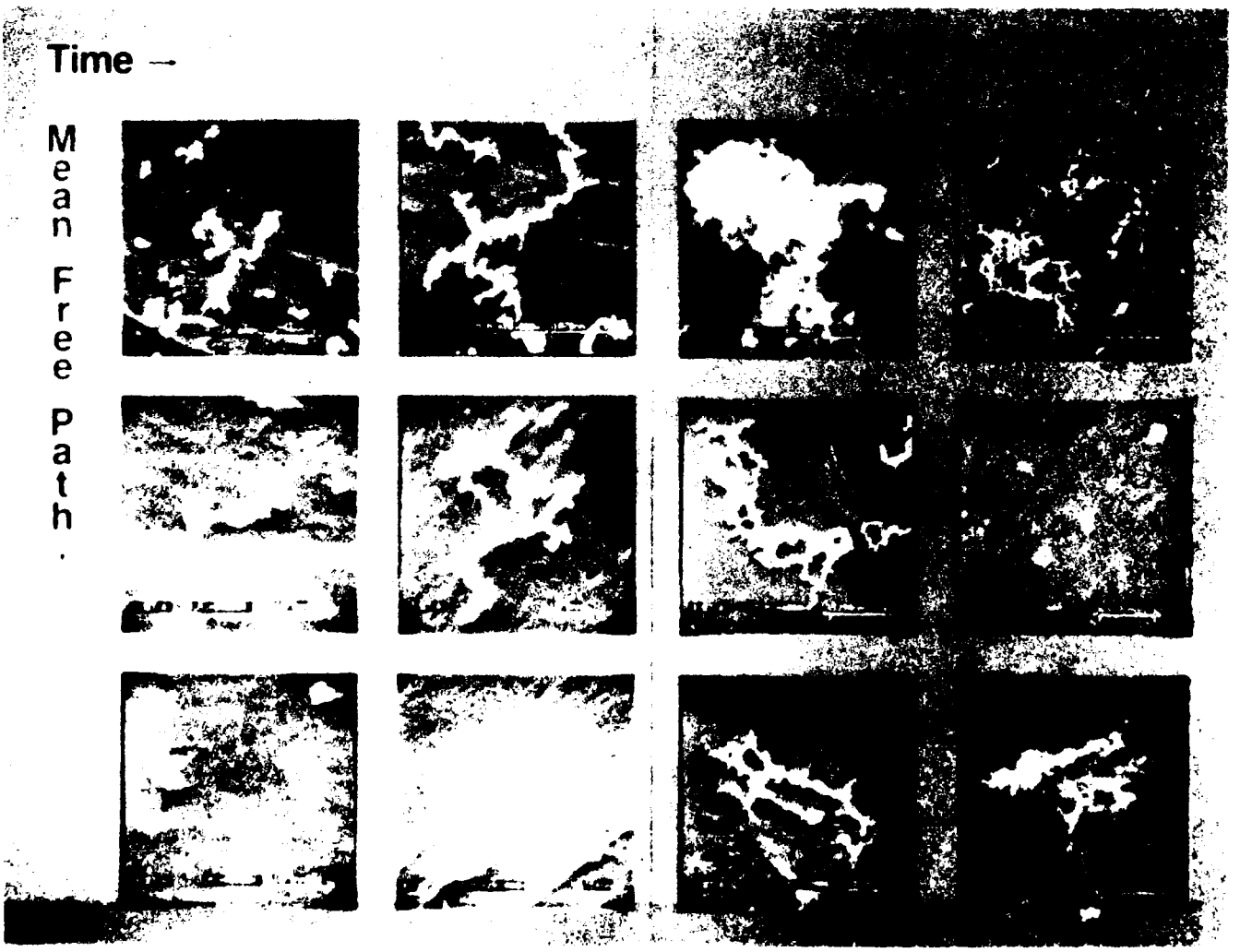

Figure 3.

The heart of the method is the investigation of similarity of properties with the scale of measurement. A typical property is the perimeter of a particle image; when the perimeter is measured in steps of decreasing length, it tends to increase as the step size takes into account the convolutions of the particle. A log-log plot of perimeter versus step size will often reveal a linear relationship over a certain size range, and this region can be said to exhibit a "fractal dimension." See Figure 4.

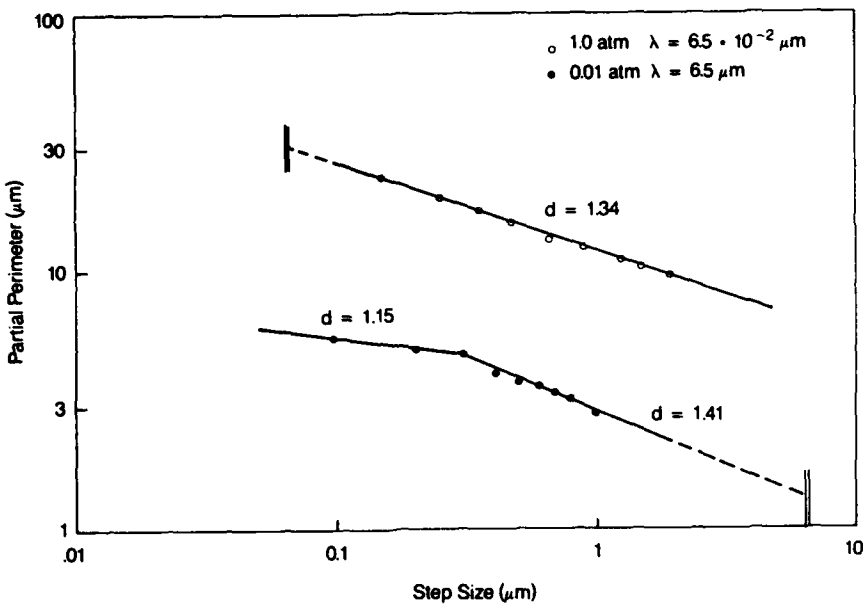

Figure 4.

The value of the fractal dimension should bear some defined relationship to the formation processes for the particle. In particular, the fractal property is related to the occurrence of randomizing effects in the particle formation. Our working hypothesis is that the range of attractive forces must be comparable to the gas mean free path for fractal structure to appear, so that particles can diffuse toward one another, rather than collide ballistically.

Some of the features in the SEM pictures do show up in the fractal analysis. The partial perimeter plots in the figure show a long linear region in the one atmosphere particles, where most of the growth took place above the gas mean free path; but the low pressure particle shows a different appearance and a narrower linear region, all of which were below the gas mean free path.

Computer simulations of particle growth have qualitatively borne out some of these hypotheses, and the references show some of the potential uses of fractals for particle characterization.

REFERENCES

S. K. Friedlander, Smoke, Dust, and Haze, Wiley, New York (1977).

F. S. Lai, S. K. Friedlander, J. Pich, and G. M. Hidy, J. Colloid and Interfacial Sci. 39, 395-405 (1972).

H. R. Pruppacher and J. D. Klett, Microphysics of Clouds and Precipitation, D. Reidel Publishing Co., Dordrechet, Holland (1978).

A. S. Damle and P. A. Lawless, "Pseudo-Self-Preserving Particle Size Distribution for Browning Coagulation in the Transition Regime". To be submitted to J. Aerosol Sci.

R. Richter, L. M. Sander, and Z. Cheng, "Computer Simulations of Soot Aggregation". J. Colloid and Interfacial Sci. 100, 203-209 (1984).

B. H. Kaye, Specification of the Ruggedness and/or Texture of a Fine Particle Profile by Its Fractal Dimension, Powder Technology, 21, 1-16 (1978).

M. Kolb, R. Botet, and R. Julien, Sealing of Kinetically Growing Clusters, Phys. Rev. Lett, 51, 1123-1126 (1983).

SOLID PARTICLE FORMATION MECHANISMS

Philomena G. Grodzka
Lockheed Missiles & Space Company
Huntsville, Alabama 35807

RECENT PUBLICATIONS, SUBMITTALS FOR PUBLICATION AND PRESENTATIONS:

A) P.G. Grodzka, "Solid Particles Formation Mechanisms - Final Report," Lockheed Missiles & Space Company Report LMSC-HEC TR F042444, June 1985.

ABSTRACT

Knowledge of the mechanisms by which solid particles form from various fluid media opens the way for tailoring the process variables to produce particles of desired sizes and shapes. Although a great deal of information exists in the literature on mechanisms of formation of specific material particles, a general practical guide for the production of solid particles of specific sizes and shapes is lacking. This document attempts to remedy this situation by presenting an overview, as assessed from current literature, of solid particle formation phenomenology. Future work will focus on the prediction of the processing parameters required to produce particles of specified materials, sizes, and morphologies.

GENERAL PHENOMENOLOGY OF CRYSTAL GROWTH

Rate Phenomena

The sizes and shapes of crystals formed from a fluid phase is determined by the interplay of three basic processes: nucleation, crystal growth, and transport of heat and mass. The following is a general overall description of the interplays in the case of crystal growth from the melt.

To initiate the formation of a solid phase from a liquid phase, solid nuclei must form of large enough size (critical size) that further growth decreases the free energy of the system. The rate at which such nuclei form is a function of supercooling, generally as shown by curve A in Fig. 1. The rate of crystal growth subsequent to nucleation is generally as shown by curve B in Fig. 1.

The initial increase in rates as the supercooling increases is the result of an increased thermodynamic driving force for phase change. The subsequent decrease in rates at extreme supercooling is the result of increased activation energies as made manifest by increased viscosity.

Depending on the particular degree of supercooling, a variety of outcomes can occur. If the rate of nucleation is relatively high and the crystal growth rate low, a shower of minute crystals can result. On the other hand, if the rate of nucleation is relatively low and the rate of crystal growth high, a few large crystals can be the result.

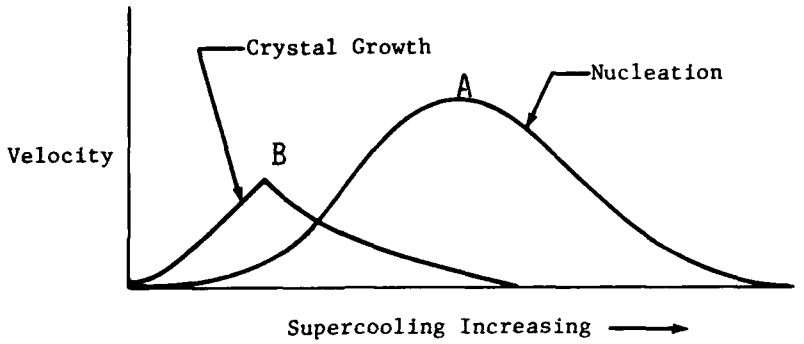

Fig. 1 Crystal Growth and Nucleation Rates as a Function of Supercooling

The overall rate of crystal growth, once nucleation occurs, is determined by the relative rates of the atomic attachment processes or interface kinetics and the rate of heat or mass transport. For example, consider a crystal growing from a melt. As the crystal grows, latent heat of fusion is liberated which has to be removed if the crystal is to grow further. If the rate of heat removal is slower than the rate at which the atomic attachment processes can occur, the interface temperature remains just a little below the equilibrium phase change temperature because latent heat is being liberated fast enough to replace that lost by transport. The overall rate of phase change can be said to be heat controlled. If, on the other hand, the rate of the atomic attachment processes is low while that of heat or mass transport is high, the interface temperature falls considerably below the equilibrium phase change temperature. The overall rate of phase change in such a case can be said to be kinetically controlled.

Material Factors

Shapes or morphologies of crystalline particles are determined both by the rate controlling process and by the nature of the material itself. The statistical mechanical treatment of Jackson (Ref. 1) of the atomic attachment processes gives an insight into the role of the material in determining crystalline morphology. According to Jackson, when additional molecules are added randomly to an initially plane surface at its equilibrium temperature T_e, the change in free energy is given by:

$$\frac{\Delta F}{NkT_e} = \alpha x(1 - x) + x \ell n\, x + (1 - x) \ell n\, (1-x)$$

where

$$\alpha = \frac{\Delta L}{RT_e} = \frac{\Delta S}{\xi R}$$

The terms in the above expressions are identified as:

- x = fraction of the N possible sites on an initially plane face
- k = Boltzmann constant
- ΔL = latent heat of transformation
- R = gas constant
- ΔS = entropy of transformation
- ξ = fraction of the total binding energy which binds a molecule in a layer parallel to the plane face to other molecules in the layer. The factor ξ is always less than unity and is largest for the most closely packed planes. For these it is invariably greater than or equal to 0.5.

A plot of $\Delta F/NkT_e$ vs x for different values of α is shown in Fig. 2.

For $\alpha<2$, the lowest free energy configuration corresponds to half the available sites filled and thus may be taken as a rough interface on an atomic or microscopic scale. For $\alpha>2$, few molecules are missing from the completed layer, and thus, this case may be taken as a smooth interface.

The effect of undercooling is to change the curves so that faces which are smooth at equilibrium may become rough at some large undercooling. For most materials, however, the effect of undercooling is to shift the maxima slightly.

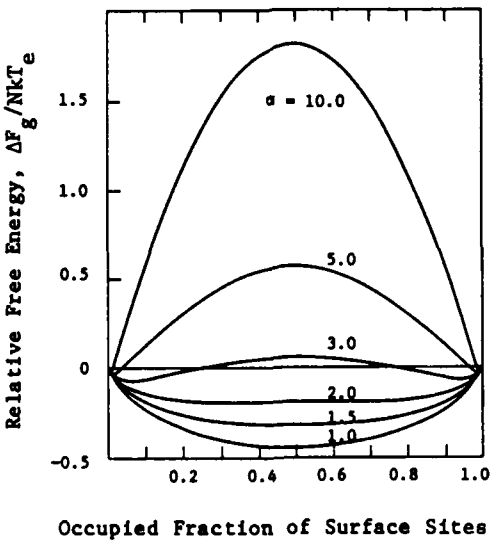

Fig. 2 Free Energy of an Interface vs Occupied Fraction of Surface Sites (after Jackson)

For materials with $\Delta S/R < 2$, even the most closely packed planes should be rough, and the initiation of new layers relatively easy. On an atomic scale, the interface will be rough. Rough interfaces, exhibiting as they do, low energetic barriers to growth, tend generally to have transport controlled growth rates. Low $\Delta S/R$ materials will thus tend to exhibit non-faceted morphologies and little growth rate anisotropy. For $\Delta S/R > 4$, the most closely packed faces should be smooth, and the initiation of new layers difficult. Less closely packed faces are expected to be rough. Materials with high $\Delta S/R$ will tend to show faceted morphologies, sizable growth rate anisotropy, and kinetically controlled growth rates.

Materials of intermediate $\Delta S/R$ values would be expected to show either non-faceted and faceted morphology depending on the actual conditions of growth.

Particle Morphologies and Conditions of Growth

The question of crystal morphology as a function of the rate controlling process is rather complicated because the growth mechanisms and growth rates of the separate crystal faces as a function of undercooling are generally not known. Rather elaborate rate studies are required to specify a particular sequence for a particular material. However, the following generalization can serve to indicate general tendencies.

For growth from the melt, the following sequence of morphologies as a function of undercooling occurs for materials of low $\Delta S/R$ and under condition of heat control (Ref. 2).

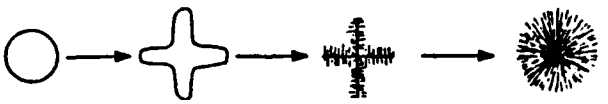

Dendrite Spherulite

Undercooling Increasing ⟶

The spherulite morphology is generally thought to be the result of the large undercooling producing such a high density of needles that the thermal fields of each overlap suppressing side branching.

Materials of high $\Delta S/R$ generally show anisotropic growth. In such cases the fastest growing face will soon be grown out leaving a crystal boundec by the slowest growing faces. The differences in growth rates of the various faces may be the result of: (1) intrinsic differences because of different molecular forces in different crystal plane; or (2) the occurrence of a screw dislocation on certain faces which makes growth on those faces much easier than on other faces; or (3) the occurrence of a twin crystal; or (4) preferential absorption of impurities on certain crystal faces, retarding or enhancing growth on those faces. For high entropy materials and heat control conditions the following sequences of morphologies as a function of undercooling can be projected:

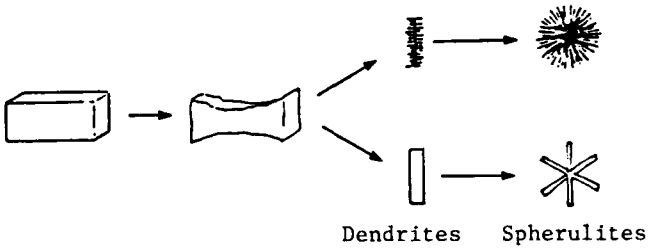

Undercooling Increasing ⟶

Under kinetically controlled conditions high entropy materials would be expected to show the following sequences:

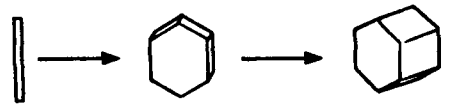

Undercooling Increasing ⟶

In this case the needle or whisker, morphology is generated as the result of a screw dislocation mechanism on one face of the crystal causing a faster growth in one direction. As the undercooling increases two-dimensional nucleation increases, causing the other faces to increase their growth rates.

Recently two works (Refs. 3 and 4) have expanded the concept of a controlling entropy term to include the cases of crystal growth from solution, from vapor, and from solid media. In the treatment of Bourne and Davey (Ref. 3), a surface entropy factor, α, is taken as the cefinitive parameter. The surface entropy factor, α, is defined by these authors as follows:

$$\alpha = 4\gamma/kT$$

where γ is the edge energy or the energy gain upon the creation of a solid-fluid bond. For qualitative purposes α can be taken as:

$$\alpha = \frac{n_s}{n_t} \frac{\Delta S}{R}$$

where ΔS is the entropy of phase transition and n_s and n_t the number of nearest neighbors parallel to the crystal surface and in the bulk crystal respectively. The appropriate entropy terms for the cases of crystal growth from solution and vapor are as follows:

Case	Entropy Term
Growth from Solution	Entropy of Solution
	$\Delta S = \Delta S_F + \Delta S_M$
Growth from Vapor	$\Delta S = \Delta S_{Sub}$

where the entropy terms ΔS_F, ΔS_M and ΔS_{Sub} are for the processes of fusion, mixing and sublimation.

In this treatment rough interfaces are characterized by α values of 2.2 or less and smooth interfaces by α values of greater than 4. Furthermore, because the energy gain upon the creation of a solid-fluid bond at the interface is a function of solvent-solute interactions, the value of γ may have different values for different solvents. Thus, a given face of a crystal may grow by different growth mechanisms from different solvents.

In another study, B. Lewis (Ref. 4) defines an edge energy coefficient β for crystal growth from solution as:

$$\beta = \Delta H_S - 2\rho \simeq T\Delta S_s - 2\rho$$

where ΔH_S is the enthalpy of solution, ΔS_S the entropy of solution, and ρ is the surface energy. Lewis' analysis leads to the conclusion that β is the primary material parameter for two-dimensional nucleation (2DN) and also for screw dislocation (SDG). When $\beta/kT>10$ which is typical of growth from the vapor on low energy planes, 2DN is slower than SDG. When $\beta/kT<8$, which is typical of melt growth,

2DN is faster than SDG at moderate supercooling and slower at low supercooling. When $\beta/kT \gtrsim 2$, growth by either mechanism is unimpeded at all supersaturations.

In earlier studies of whisker formation (Refs. 5 through 8) Sears found that whisker growth occurs only when the supersaturation ratio remains below a critical value, which is determined by the supersaturation at which two-dimensional nucleation occurs. Sears postulates that a nucleus with a built-in screw dislocation grows axially at low supersaturation by the action of the dislocation with absorbed atoms feeding the growth. Radial growth, however, cannot occur because the supersaturation is below the critical value for two-dimensional nucleation.

Lewis' work indicates that materials of $\beta/kT<10$, i.e., materials with high entropy of phase transition, readily form whisker and platelets over a wide range of processing parameters. Materials of lower β/kT will require careful adjustment of processing parameters such as the supersaturation to effect whisker or platelet formation.

The cited studies described in the preceding discussion have prompted the use of model materials to verify or to illuminate some points of crystal growth either for theoretical or practical purposes. For example, organic materials of low melting points, low entropies of fusion, and transparent melts have been taken as models for crystallization of metals from the melt (Ref. 8). Solutions of ammonium chlorice in water have been studied as models for crystallization phenomena in alloy castings (Ref. 9). The model materials work has been exceptionally fruitful in explaining and elucidating many processes involved metal crystallization.

The entropy of phase transition also plays a role in nucleation kinetics. For purposes of the present paper it is sufficient to note that materials with high entropies of phase transition are generally difficult to nucleate and will require either extreme supercooling, supersaturation, seeding, or catalysts.

Convection Effects on Crystal Growth

Natural convection has the effect of increasing the temperature or concentration gradients near growing crystal interfaces. It thus has the effect of increasing heat or mass transfer to growing

crystal surfaces. This increased mass or heat transport can affect crystal growth in a variety of ways. The increased gradients can not only increase crystal growth rate, but also, in certain cases, change the controlling process from heat or mass transfer to that of kinetic control. The crystal morphologies will thus change from dendrite to more three-dimensional, particle-like structures. In the case of the kinetically controlled process of whisker growth, convection currents can increase the mass flow to the side of the crystal, encouraging a thickening of the crystal by 2-D nucleation. In the absence of convection, i.e., the pure diffusion case, less mass would reach the sides and more the ends of the whiskers, thus encouraging growth lengthwise.

Natural convection can also introduce areas of nonuniform temperatures or concentrations along the growing crystal surface and can thus lead to a number of crystalline defects.

Conclusions

On the basis of the preceding discussion, the following generalization for growing micron-size particles of specified shapes are drawn. Materials with high entropy of phase transition can be expected to be easily grown in the specified morphologies, particularly from the vapor or solution phases. Materials with lower entropies of phase transition possibly can be grown to the specified shapes by carefully controlling the processing parameters.

ACKNOWLEDGMENT

This study was funded by CRDC through Battelle at Research Triangle Park, N.C. The author is grateful to Glen O. Rubel for stimulating consultation and discussion.

REFERENCES

1. Jackson, K. A., D.R. Uhlmann, and J.D. Hunt, "On the Nature of Growth from the Melt," J. Crystal Growth, Vol. 1, 1967, pp. 1-36.

2. Ovsienko, D. E., C. A. Alfintsev, and V. V. Noslov, "Kinetics and Shape of Crystals Growth from the Melt for Substances with Low L/kT Values," J. Crystal Growth, Vol. 26, 1974, pp. 233-238.

3. Bourne, J. R., and R. J. Davey, "The Role of Solvent-Solute Interactions in Determining Crystal Growth Mechanisms from Solution I and II," J. Crystal Growth, Vol. 36, 1976, pp. 278-286, 287-296.

4. Lewis, B., "The Growth of Crystals of Low Supersaturation, I and II," J. Crystal Growth, Vol. 21, 1979, pp. 29-39, pp. 40-50.

5. Sears, G. W., "A Growth Mechanism for Mercury Whiskers," Acta Metallurgcia, Vol. 3, 1955, pp. 361-366.

6. Sears, G. W., "Mercury Whiskers," Acta Metallurgcia, Vol. 1, 1953, pp. 457-459.

7. Sears, G. W., "A Mechanism of Whisker Growth," Acta Metallurgica, Vol. 3, 1955, pp. 367-369.

8. "Transparent Model Simulates Metal Solidification Mechanism," Metals and Materials, May 1967, pp. 153-154.

9. Cisse, J., G. S. Cole, and C. F. Bolling, "A Transparent Model for Simulation of Ingot Front Solidification," Metallurgical Transactions, Vol. 2, 1971, pp. 3243-3245.

10. Uyeda, R., "Growth of Polyhedral Metal Crystallites in Inactive Gas," J. Crystal Growth, Vol. 45, 1978, pp. 485-489.

11. Saito, Y., S. Yatsuga, K. Mihama, and R. Uyeda, "Crystal Structure and Habit of Fine Metal Particles Formed by Gas-Evaporation Technique; bcc Metals (V, Fe, Cr, C, and W)," J. Crystal Growth, Vol. 45, 1978, pp. 501-505.

GENERATION OF NONSPHERICAL AEROSOL PARTICLES

K. H. Leong
University of Illinois
Urbana, IL 61801

RECENT PUBLICATIONS, SUBMITTALS FOR PUBLICATION AND PRESENTATIONS:

A) K. H. Leong, "Generation of Nonspherical Aerosol Particles," presentation at the 1985 CRDC Conference on Obscuration and Aerosol Research, June 1985.

B) K. H. Leong, "Control of Particle Morphology in Aerosol Generation," presentation at the 17th Aerosol Technology Meeting, Battelle's Columbus Laboratories, August 1985, and at General Motors Research Laboratories, Warren, Michigan, September 1985.

C) M. Ramamurthi and K. H. Leong, "Generation of Monodisperse Nonspherical Aerosols," to be presented at the 1985 meeting of the American Association for Aerosol Research, Albuquerque, New Mexico, November 1985.

ABSTRACT

This paper reports ongoing research to determine the capability of using temperature, evaporation rate, and different chemical compounds to control particle morphology in the generation of monodisperse aerosol particles from the evaporation of solution droplets. Research accomplished shows the effects of evaporation rates on compounds of different solubilities and crystal habit. Future work will be on mixtures of compounds and the use of thermal decomposition and reducing gases for the formation of monodisperse particles with a metallic surface.

INTRODUCTION

The capability of the controlled generation of an aerosol is much sought after for experimental aerosol research. Past research has resulted in the production of monodisperse particles of a controllable size for performance of experiments where effects are sensitive to particle size. Recent research has focused on the aerodynamic and optical properties of nonspherical aerosol particles (e.g., Kasper, 1982; Barber and Massoudi, 1982). Although substantial advances have been made in the comprehension of the torques, aerodynamic size and orientations and the scattering properties of nonspherical particles, experimental confirmation has been often prohibited by the difficulty or inability to produce a monodisperse aerosol of uniformly nonspherical particles generally required to discern a particular particle shape effect. However, recent observations in aerosol generation indicates that a variety of particle shapes can be generated from the evaporation of solution droplets (see Leong, 1981). In fact, monodisperse aerosols consisting of nonspherical particles of uniform size and shape have been produced. Cubic crystals of sodium chloride and polycrystalline spheroids have been obtained by several investigators as noted by Leong (1981). Particle shapes were affected by the evaporation rate and the crystal habit and solubility of the compound used. These observations strongly indicate that control of particle shape is possible using the appropriate generation conditions and chemical compound.

PARTICLE FORMATION FROM SOLUTION DROPLETS

The extensive experiments by Duffie and Marshall (1953), Charlesworth and Marshall (1960) and others have shown that in the drying of solution droplets, the solute initially crystallizes or precipitates at the surface of the drop because of the low diffusivity of the solute compared to that of the gaseous solvent. Computations by Schlunder (1964) and Gardner (1965) showed that the concentration of an evaporating solution droplet is a maximum at the surface and could be twice that at the center of the drop. Hence, particles formed from the drying of solution drops will tend to be hollow. However, solid particles have been observed and this phenomenon has been attributed to the collapse of the initial shell (Charlesworth and Marshall, 1960).

Observations by Leong (1981) indicated that substantial supersaturation of the solution droplet occurred before the onset of crystal growth. This phenomenon has also been observed by others (e.g., Tang and Munkelwitz, 1983; Kurtz and Richardson, 1984; and Richardson and Spann, 1984). Substantial supersaturation is possible through the absence of foreign nuclei in solution droplets. The evaporation of the solvent leads to increasing supersaturation to the point of homogeneous nucleation and crystal growth. Nucleation theory predicts a higher critical supersaturation (for nucleation to proceed) for higher values of the interfacial energy between solid and liquid. Since the interfacial energy decreases with solubility (Walter, 1967), higher supersaturation is necessary for lower solubility compounds. The size of the resulting particle is then determined to some degree by the size of the solution droplet at the onset of crystallization. The maximum supersaturation ratio, S (defined as the ratio of the concentration of the solution to the concentration at saturation), averaged over the droplet volume at the onset of crystallization can be related to the density of the solid particle, ρ_p, and the saturated solution concentration, c_s, as follows:

The volume, V_m, of a solid particle resulting from a solution drop of initial radius, R, and concentration c_o is given by the equation,

$$V_m = 4\pi R^3 c_o / 3\rho_p \tag{1}$$

Similarly the volume, V_s, of the droplet at supersaturation S is given by

$$V_s = 4\pi R^3 c_o / 3 c_s S \tag{2}$$

Since V_m is always smaller than V_s, Eqs. (1) and (2) result in

$$S < \rho_p / c_s \tag{3}$$

Equation (3) indicates that higher supersaturation ratio is possible for lower solubility compounds. For example, the maximum value of S computed from Eq. (3) for lithium carbonate is 164 using a density of 2.11 g cm^{-3} and a saturation concentration of 0.0129 g cm^{-3}. Since it is not probable

that such a high value of S can be reached, a hollow or porous particle is expected. Experiments using lithium carbonate have indicated a value of S around 20 (Leong, 1981). Hence, compounds having low solubility would tend to produce hollow particles with the tendency to more solid particles for increasing solubility. If nominal values of $S = 4$ and $\rho_p = 2$ g cm^{-3} are used then, for the formation of a solid particle, the concentration of the solution at saturation would have to be larger than 0.5 g cm^{-3}. This value tends to be an overestimate since solid particles have been obtained with compounds that have lower values of c_s (see Leong, 1981). An example is manganese hypophosphite having a c_s value of 0.12 g cm^{-3}. This can be attributed to the collapse of the initial shell leading to a wrinkled particle. Hence, the solubility of the compound and the supersaturation ratio (S) achieved influences the density of the particle.

The time needed for a saturated solution droplet to evaporate to the point of crystallization is given by

$$\Delta t = K(r_s^2 - r_c^2) \tag{4}$$

where r_s and r_c are the radii corresponding to when the droplet was saturated and when crystallization was initiated and K is a function of the diffusivity of the solvent in vapor form and the differences in vapor densities. Expressing the radii in terms of the total mass of solute present, M_s, yields

$$\Delta t = K\left(\frac{3M_s}{4\pi}\right)^{2/3}[c_s^{-2/3} - (c_s S)^{-2/3}] \ . \tag{5}$$

If it is assumed that K and S are constant for any droplet size, then Δt will be longer for larger droplets with larger values of M_s. With longer nucleation times, the supersaturation ratio is expected to be lower. Hence, greater solute mass would tend to produce less compact particles if no shrinkage of the initial shell occurs. The more common occurrence of shells and hollow particles at supermicron sizes compared to micron or submicron sizes is then consistent with the trend discussed above.

The limited data of Leong (1981) for lithium carbonate, at 24% and 90% relative humidities, are also consistent with this trend. A higher value of $S = 23$ was indicated at a relative humidity of 24% for the smaller particle ($V_m = 2.99$ μm^3) compared to a value of 20 at a relative humidity of 90% for the larger particle ($V_m = 4.19$ μm^3). The higher evaporation rates at the lower humidity resulted in a porous wall particle compared to the smooth wall of the particle at 90% relative humidity. Lower supersaturation values for lithium carbonate droplets of hundreds of micrometers in size has been obtained by Gavin (1983). Similarly, even lower supersaturation was present in the larger droplets of different compounds used by Charlesworth and Marshall (1960). However, crystal

habit and growth rates may have a more significant influence on particle morphology. This was indicated by the lithium particles (obtained at 60% relative humidity) having a range of shapes and sizes (Leong, 1981) and the collapse of the initial shell that was observed for some compounds (Charlesworth and Marshall, 1960).

The shapes of crystals (particles) are affected by the rate of growth and interactions with the solvent and other compounds or impurities present (Wells, 1946; Walton, 1967). In the generation of aerosol particles, solution droplets are usually dried at a rapid rate. Consequently, crystal growth that is controlled by the supersaturation and evaporation rate is rapid and the equilibrium crystal habit of the compound used may not result. Another factor that may inhibit the crystal habit is the initiation of crystal growth at the droplet surface, caused by the higher supersaturation. Dendritic growth on the surface and into the droplet may be common for maximum heat dissipation and growth rates (Walton, 1967).

EXPERIMENT

An experimental study was conducted to determine the effects of temperature, evaporation rate and chemical properties of the solute on the morphology of particles generated from the evaporation of monodisperse solution droplets. The aerosol generation and drying system used is shown in Fig. 1. A vibrating orifice generator (modified TSI 3050) was used to generate monodisperse solution droplets. The solution was fed to the generator by a pressure feed system using a 500 cm^2 0.2 μm capsule filter (Gelman 12022). This method of solution feed together with a special start-up procedure enabled continuous operation of the generator with no clogging of the orifice (Leong, 1985). The generator is operated inverted so that the solution droplets produced will not dry prior to exiting the acrylic column. The wet aerosol then flowed through a metallic tube with a heated wall. The evaporation rate of the solution droplets before drying was controlled by the temperature and the amount of dilution air (humidity) used. This evaporation rate was determined indirectly by measuring the temperature and dew point of the carrier air. The purpose of the silica gel bed after the heated tube was to reduce the humidity of the air to prevent the possibility of water absorption by the dry particles. The aerosol particles were sampled by impaction above the silica gel bed.

RESULTS AND DISCUSSIONS

A series of electron micrographs of particles generated from different compounds under controlled conditions of temperature, dew point and solute mass are presented below. The micrographs are arranged to illustrate the effects of the variation of a particular parameter on the morphology

of the particles generated. Particle sizes given in the figure captions are the volume-equivalent solid-sphere diameters. The scale at the bottom of each micrograph (may not be visible for some) is 1 μm for one dot and 10 μm for two dots.

The first set of micrographs (Figs. 2a-2d) for sodium chloride (solubility = 36 g/100 g H_2O) show the effect of increasing solute mass. The maximum dimension for the particles in each micrograph is 1.2 μm, 4.2 μm, 4.6 μm, 7.6 μm, 5.9 μm, and 7.0 μm, respectively. The micrographs show the transition from a single crystal to a multicrystal particle. The transition to a multicrystal particle is evident in Fig. 2c where the particle exhibit a twinning habit. The individual crystals have sharp edges and tend to be tetragonal instead of cubic, with the crystals in Fig. 2a having higher energy surfaces. This formation of multiple crystals for a larger mass of solute is expected since the nucleation rate at the surface increases with the size (solute mass) of the droplet. Figures 2d-2f illustrate the effect of a lower dew point on the morphology of the particle resulting from the same size and concentration droplet. The higher evaporation rate results in a higher supersaturation and a more compact particle. The particle of multiple single crystals changes to a solid polycrystalline mass to a single crystal. The crystal habit is also modified from simple tetragonal to the appearance of octahedral faces. Since higher supersaturation with consequent larger growth rates are expected for smaller particle size or higher evaporation rates, the appearance of higher energy faces for the crystals in Figs. 2a-2f is consistent with the observations of Kern (1933). These micrographs for sodium chloride do not indicate that higher evaporation rates necessarily result in a more compact particle but that evaporation rates or crystal growth rates and habit affect the morphology of the particles formed.

If the maximum dimension of a particle is assumed to be the radius of the droplet at the onset of crystallization the maximum concentration of sodium chloride achieved decreases monotonically from 1.3 g cm^{-3} to 0.62 g cm^{-3} for the particles in Figs. 2a-2d. Hence, a decrease of the maximum supersaturation with increasing solute mass is indicated. However, this assumption, used for these particles that are not shells or spheroids, is not necessarily an absolute indication of supersaturation since a value of 0.79 g cm^{-3} was obtained for the case of Fig. 2f compared to 1.1 g cm^{-3} for Fig. 2e at a smaller evaporation rate. Nevertheless, the range of solute densities so obtained are the same order of magnitude as that observed by Tang and Munkelwitz (1978) for a sodium chloride droplet evaporating in a quadrapole trap.

The next set of micrographs in Fig. 3 is for potassium sulfate. The slightly elongated particles in Figs. 3a, b, f, and g are an artifact of the microscope. The maximum size for the particles in each micrograph is 1.8 μm, 3.2 μm, 7.1 μm, 6.6 μm, 9 μm, 3.5 μm, and 1.5 μm, respectively. Supersaturated concentrations calculated assuming that the maximum dimension of

the particle is the diameter of the droplet at the onset of crystallization are (a) 1.4, (b) 1.0, (c) 0.55, (d) 0.68, (e) 0.27 and 0.45 (f) 1.6 and (g) 2.4 g cm^{-3}. The trend is consistent with increasing supersaturation with increasing evaporation rate and decreasing solute mass considering the approximate method of deducing supersaturation. For the same generation conditions of temperature and dew point (Figs. (a)-(d)) the smaller particles have a rougher surface with a larger number of smaller crystal structures. Figures (c)-(f) show the effect of increasing temperature on droplets of the same size and concentration. At 30°C (Fig. 3e) a shell of crystals was formed. Higher temperatures (Figs. 3c, d, f) led to a more compact particle with a solid particle in Fig. 3f. Higher temperatures imply a higher evaporation rate and these results are similar to those obtained for sodium chloride. The particle in Fig. 3g is also consistent with the above trend, being solid at 80°C compared to the nonsolid particle formed at 40°C in Fig. 3a. In addition to increasing the evaporation rates, higher temperatures increases the solubility of potassium sulphate. Solubility values are 13.0 g/100 g H_2O, 14.8 g/100 g, 18.2 g/100 g and 21.4 g/100 g at temperatures of 30°, 40°, 60°, and 80°C, respectively. Consequently, a more compact particle would be expected at higher temperatures. The third set of micrographs is for lithium fluoride, a low solubility compound (0.27 g/100 g H_2O at 18°C). The particles in Figs. 4a-4e are slightly elongated in the vertical direction by the microscope. The micrographs in Figs. 4a-4d have the same magnification and the maximum horizontal dimensions measured for the particles are 1.7 μm, 1.4 μm, 1.2 μm and 0.95 μm, respectively. The particles were generated from the same size and concentration droplets for decreasing evaporation rates. The slower crystal growth rate resulted in more compact particles with larger crystals. This increase in crystal size with slower growth rates is commonly observed (Wells, 1946). At the highest humidity or slowest evaporation rate used a variety of polycrystalline shapes is evident in Figs. 4e and 4f with particles having an approximate maximum dimension of 1.3 μm. Lithium carbonate, another low solubility compound (1.2 g/100 g H_2O), has also been found to produce a range of particle shapes at a relatively high humidity (Leong, 1981). Crystal growth rates and habits tend to have a dominant influence on the particle morphology for these low solubility compounds.

Figures 5a-5e show lithium sulphate particles of the same mass that were generated at two different evaporation rates. The particle in Fig. 5a is slightly elongated by the microscope. The solubility of lithium sulfate is approximately 33 g/100 g H_2O from 40°C to 60°C. All the particles are hollow and approximately 3.4 μm in diameter. Smaller crystals are expected from higher evaporation rates and the particles produced (Figs. 5c and 5d) have a relatively smooth surface. The slower evaporation rates led to the formation of larger crystals evident in Figs. 5a and 5b. An interesting micrograph is presented in Fig. 5e. It shows the absorption of water and initial

deliquescence of the particles. Preparation of the sample for sputter coating in vacuum dried the particles and the mass of lithium sulfate that had deliquesced and later dried formed thin outgrowths that appear to anchor the particle to the surface.

Particles of rhodamine-B generated from solution droplets of initial diameter of 24 μm and concentration of 0.0364 g/100 g H_2O are shown in Figs. 6a and 6b. The effects of a change in solubility is illustrated. The higher solubility at the higher temperature resulted in a smaller particle of 1.8 μm with a smooth but dimpled surface. The particle generated at the lower temperature is a hollow 2.4 μm diameter sphere with numerous holes on its surface. The larger number of holes is probably the result of the initial shell formation at a larger size with the subsequent requirement for evaporating a larger amount of water.

Figures 7a-7c are for sodium sulfite particles generated from the same initial size and concentration droplet at different ambient conditions. The particles in Fig. 7a are probably solid. At 60°C, the hydrate ($Na_2SO_3 \cdot 7H_2O$) is expected but the particle size produced (3.47 μm) is smaller than the predicted solid size of 3.82 μm for the hydrate. This indicates that either the compound used may be partly hydrated or that the particle generated is composed of the hydrated and anhydrous compound. The particles in Figs. 7b and 7c were produced when particles that had not dried completely impacted on the electron microscope stub. Tnese particles in Fig. 7b do not have the typical shapes of particles produced as described above (Leong, 1981). The water content of this wet particle was probably very small and on impaction and drying produced the interesting shape. The maximum dimension of this "particle" is 5.2 μm compared to 6.2 μm in Fig. 6c.

ACKNOWLEDGEMENT

This work was funded by the Chemical Research and Development Center, U.S. Army, through Battelle Columbus Laboratories, the U.S. Environmental Protection Agency through the Advanced Environmental Control Technology Research Center and the Research Board of the University of Illinois at Urbana-Champaign. The particles and electron micrographs were obtained by M. Ramamurthi.

REFERENCES

Charlesworth, D. H. and Marshall, W. R., Jr. (1966). A.I.Ch.E. Journal, 6, 9.

Duffie, J. A. and Marshall, W. R., Jr. (1953). Chem. Engr. Progr., 49, 481.

Gardner, G. C. (1965). Int. J. Heat Mass Transfer, 8, 667.

Gavin, P. M. (1983). Ph.D. Tnesis, University of Illinois at Urbana-Champaign.

Kern, R. (1953). Compt. Rend., 236, 830.

Kurtz, C. A. and Richardson, C. B. (1984). Chem. Phys. Lett., 109,190.

Leong, K. H. (1981). J. Aerosol Sci., 12, 417.

Mullin, J. W. (1972). Crystallisation. CRC Press.

Richardson, C. B. and Spann, J. F. (1984). J. Aerosol Sci., 15, 563.

Schlunder, E. U. (1964). Int. J. Heat Mass Transfer, 7, 49.

Tang, I. N. and Munkelwitz, H. R. (1983). J. Colloid Interface Sci., 98, 430.

Walton, A. G. (1967). The Formation and Properties of Precipitates. Interscience Publishers.

Wells, A. F. (1946). Phil. Mag., 37, 184.

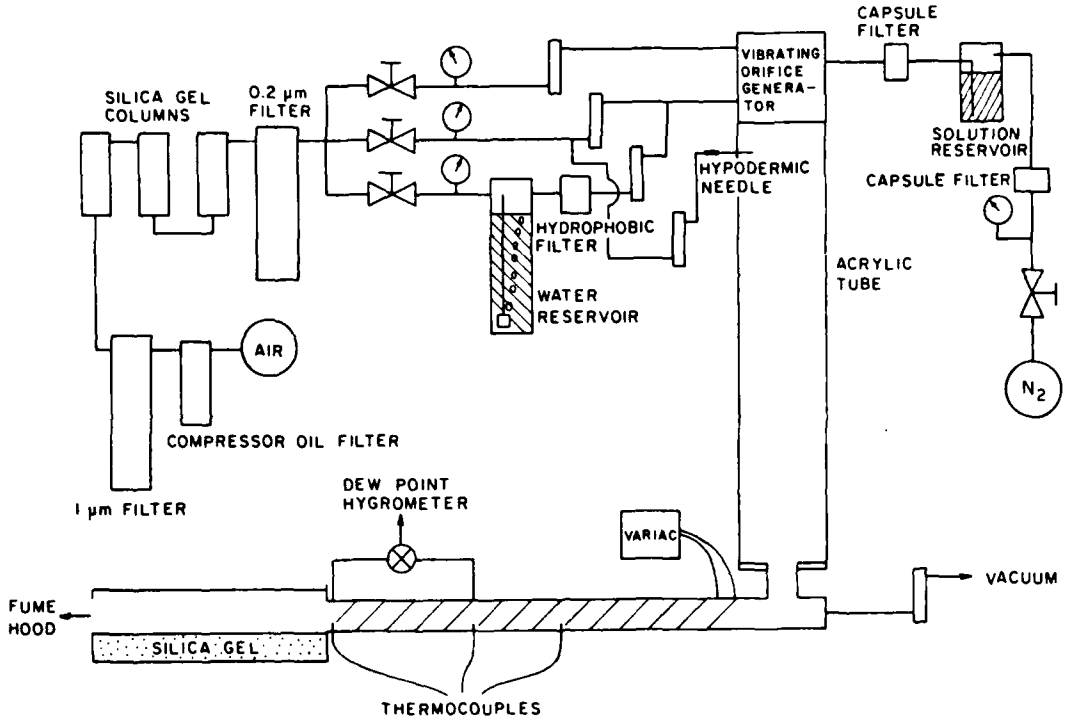

Fig. 1: Experimental system for the controlled generation of monodisperse aerosol.

0105
0108
0105
0133
0131
0104
0110
0100
0120
0120
0121
0121

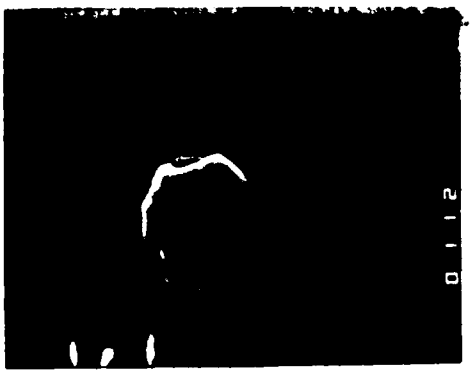

Fig. 3: Electronmicrographs of potassium sulfate particles generated at a dew point of -6.5°C. Equivalent solid sphere diameters were (a) 1.45 μm at 40°C, (b) 2.32 μm at 40°C, (c) 4.2 μm at 40°C, (d) 4.2 μm at 40°C, (e) 4.2 μm at 30°C, (f) 4.2 μm at 60°C and (g) 1.45 μm at 80°C.

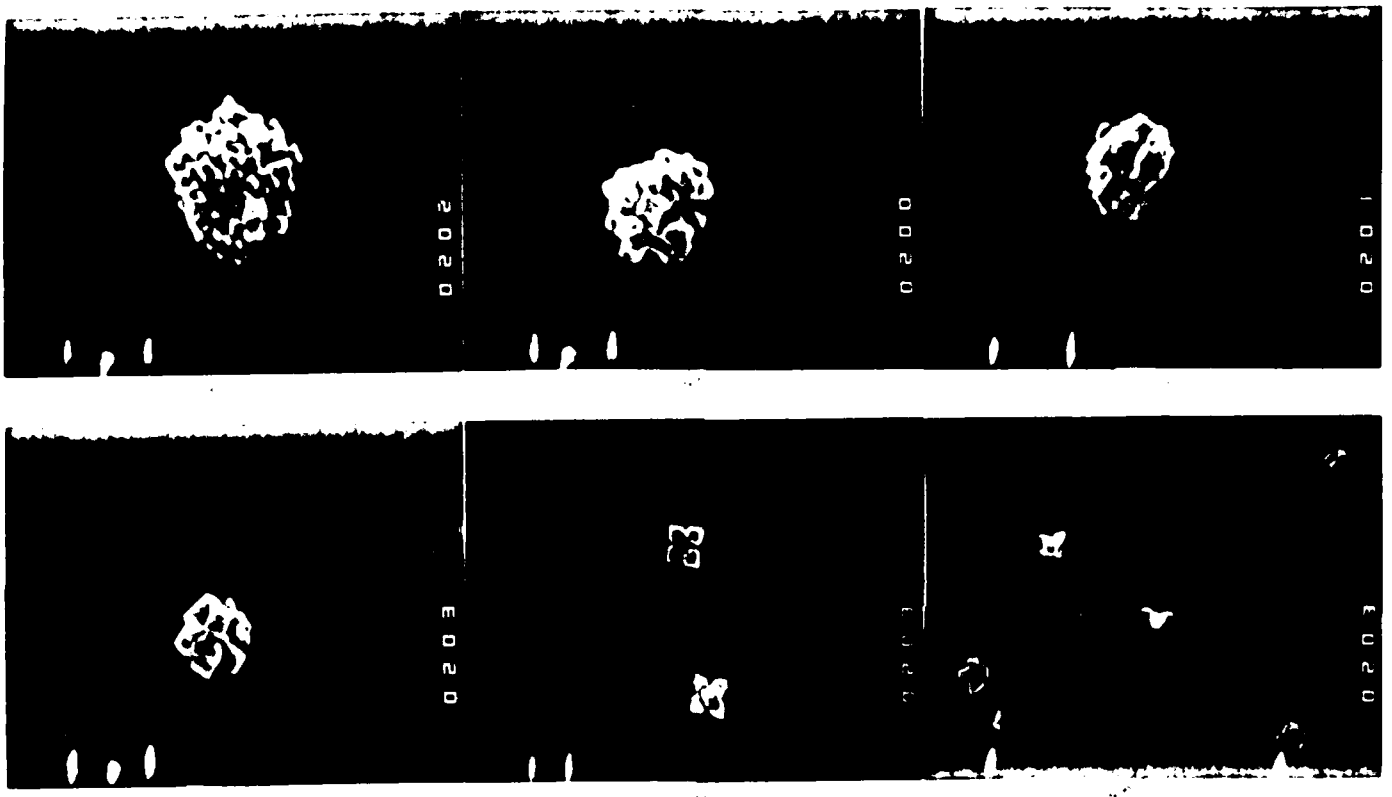

Fig. 4: Electronmicrographs of lithium fluoride particles generated at an ambient temperature of 40°C (except as noted). All the particles have the same equivalent solid sphere diameter of 0.9 μm (a) DP = -11.0°C, T = 60°C, (b) DP = -10.4°C, (c) 2.5°C, (d) 7.0°C, (e) and (f) 16.4°C. (a)-(d) have the same magnification.

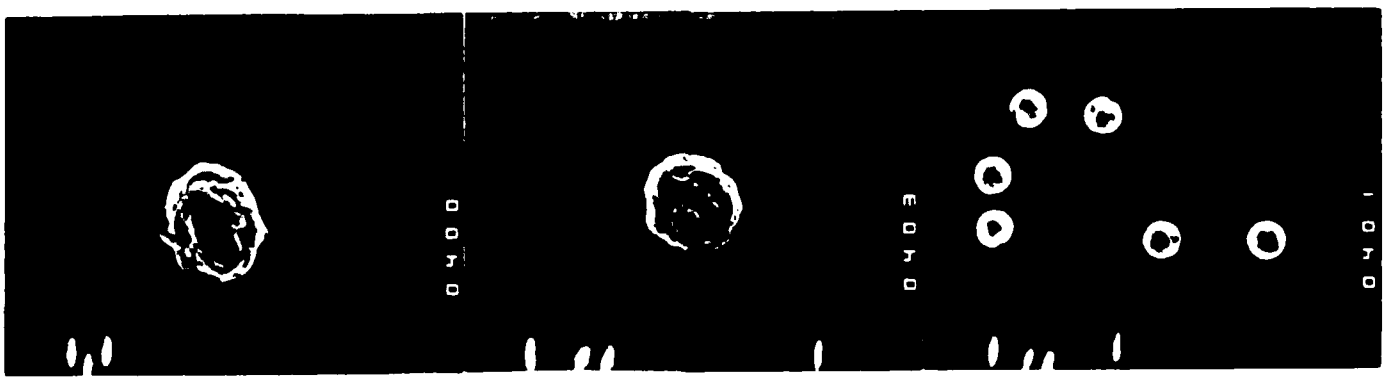

(continued)

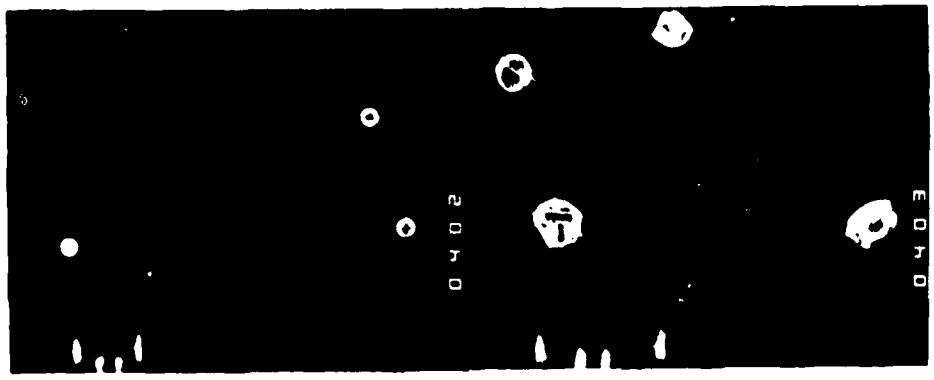

Fig. 5: Electronmicrographs of lithium sulfate particles of equivalent solid sphere diameter of 2.4 μm produced at (a) T = 50°C, DP = -6.0°C, (b) T = 60°C, DP = -6.0°C (c) T = 50°C, DP = -10.0°C (d) T = 60°C, DP = -6.0°C, and (e) T = 60°C, DP = -6.4°C but exposed to room air.

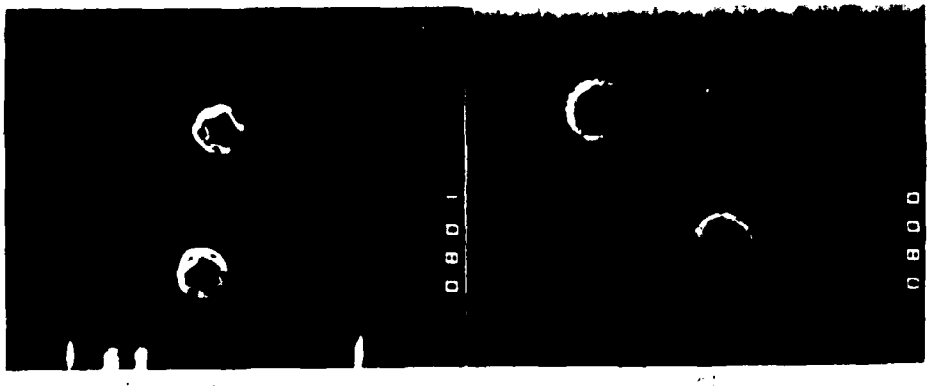

Fig. 6: Electronmicrographs of rhodamine-B particles of equivalent solid sphere diameter of 1.5 μm assuming a density of 1.5 g cm^{-3} produced at (a) T = 60°C, DP = -13.2°C and (b) T = 25°C, DP = -16.2°C.

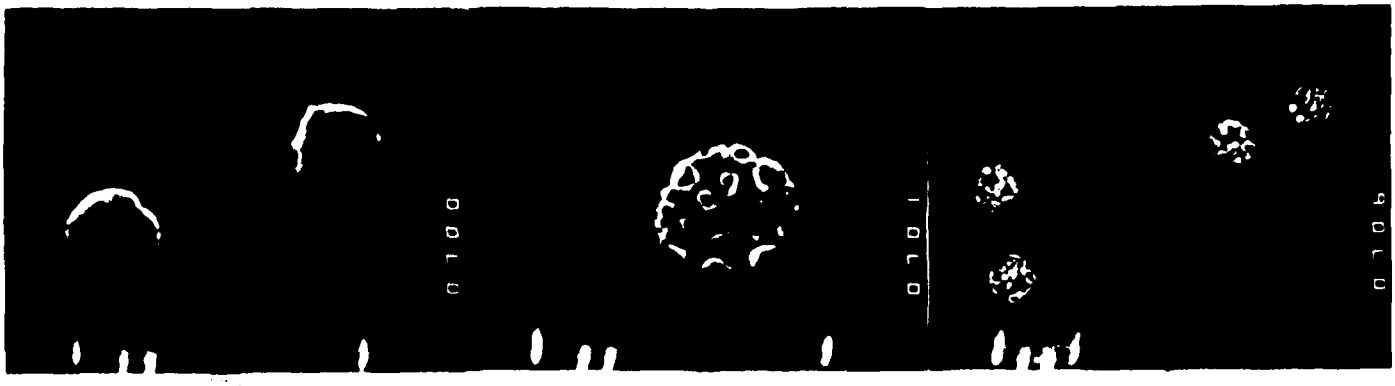

Fig. 7: Electronmicrographs of sodium sulfite particles produced from 23.5 μm diameter solution droplets at an initial concentration of 0.3 g/100 g H_2O of the anhydrous compound at (a) T = 60°C, DP = -12.0°C, (b) T = 60°C, DP = -7.9°C and (c) T = 40°C, DP = -14.0°C.

I. PHYSICAL AND CHEMICAL PROPERTIES OF AEROSOLS (CONTINUED)

IB. Plume Mechanics (and Particle Fluidization)

CHANNELING IN BEDS OF MICRON SIZE PARTICLES

H. Littman and M. H. Morgan, III
Department of Chemical Engineering
and Environmental Engineering
Rensselaer Polytechnic Institute
Troy, New York 12180-3590

ABSTRACT

A theory is developed which connects channeling in beds of micron size particles with their cohesive behavior. It shows that once a channel forms, the cohesive nature of the particles prevents significant flow of fluid from the channel into the dense phase surrounding the channel. The low axial pressure drop which results is shown by stability considerations to maintain the channel.

Future work will focus on understanding the cohesive behavior of micron sized powders and their pneumatic transport to produce deagglomerated aerosol sprays.

INTRODUCTION

The best known method of dispersing fine powder composed of micron sized particles to produce a deagglomerated aerosol spray is by the use of an air ejector.[1] Two general methods of dispersal of interest at CRDC are shown in Figures 1a and 1b. In Figure 1a, the powder is fluidized in the material storage container and fed through the transfer line to the air ejector. In Figure 1b, an eductor sucks powder from the storage container into the transfer line. In both methods, the cohesive nature of the particles affects both the quality of the deagglomeration and the particle concentration in the spray from the ejector.

The practical difficulties in producing deagglomerated aerosol sprays exposes the weakness in our understanding of phenomena involving the transport of fine particles that are cohesive. If practical devices are to be built which have a high degree of reliability and predictable performance, research into the fluidization, spouting and transport of micron size particles is necessary. The fact that such research is not far advanced provides an excellent research opportunity in the framework of a real engineering need.

FLUID-PARTICLE BEHAVIOR OF MICRON SIZED POWDERS

A. Channeling

Guichard (1) and Geldart and Wong (2) have observed that channels form in beds of fine cohesive particles when one tries to fluidize them. Such beds do not bubble or expand significantly. The channels, which are plainly visible at the top of the bed, have little or no particle throughflow and

[1] The fluidized beds have also been used to disperse fine powders (1). In that case, elutriation of the fine particles from a fluidized bed of larger ones is the mechanism for dispersion.

enlarge as the gas velocity increases. At sufficiently high gas velocities in small diameter beds, the whole bed can be ejected in a single clump leaving an amazed and unnerved investigator face to face with an empty column.

B. Classification of particles

Geldart (3) has classified particles for fluidization purposes as falling into one of four groups and Table I gives some of the important features of each group. We are concerned in this paper with particles in Group C whose behavior is dominated by strong interparticle forces.

Table I Some Features of Geldart's Four Groups of Particles (3)

Feature	Group C	Group A	Group B	Group D
Distinguishing word or phase	Cohesive	Aeratable	Bubble readily	Spoutable
Example	Flour	Fluid cracking catalyst	Sand	Wheat
Particle size for $\rho_p = 2500 kg/m^3$	$< 20\mu m$	$20 < d_p < 90\mu m$	$90 < d_p < 650\mu m$	$> 650\mu m$

Recently, Geldart and Wong (2,4) have published work aimed at developing criteria for predicting the boundary between cohesive Group C and slightly cohesive but aeratable Group A powders. They studied bed expansion and rates of deaeration of beds of particles and found that 1) dry cohesive powders have no clearly measurable minimum fluidization or bubbling velocity 2) the Hausner ratio (5) (ratio of the tapped to loosely packed bulk density) is large 3) increasing the relative humidity of the fluidizing gas promotes cohesive behavior and 4) the bed expansion is small. They also found that Group C powders deaerate exponentially rather than linearly. These papers make an important start on the classification of fine particles.

C. Mechanical theory of channeling

Channeling is basically a form of spouting rather than a mode of fluidization. For this reason, we will focus our discussion on a theory of particle circulation in spouted beds developed by the authors (6). A schematic diagram of a spouted bed is given in Fig. 2. The relevant part of that theory to the discussion of channeling lies in its prediction of the axial voidage distribution in a spout at minimum spouting (the choking condition).

In our model, the axial voidage distribution at minimum spouting is calculated from an Euler-Lagrange variational form as follows:

The momentum equation for gas and particle flow through an element of the spout assuming constant spout diameter axially and radially averaged velocities, pressure and voidage is [see Nomenclature below]

$$\rho_f \frac{d}{dz}(\varepsilon_S u_S^2) + \rho_p \frac{d}{dz}[(1 - \varepsilon_S) v_S^2] = -\frac{dp_S}{dz} - (1 - \varepsilon_S)(\rho_p - \rho_f)g \quad . \qquad (1)$$

Integrating over the height of the bed yields

$$\rho_f \varepsilon_S(H)\, u_{SH}^2 - \rho_f\, \varepsilon_S(0)\, u_{S0}^2 + \rho_p(1 - \varepsilon_S(H))v_{SH}^2 - \rho_p(1 - \varepsilon_S(0))\, v_{S0}^2$$

$$= p_S(0) - p_S(H) - \int_0^H (1 - \varepsilon_S(z))(\rho_p - \rho_f)\, g\, dz \qquad (2)$$

At minimum spouting, $v_{SH} = 0$, $\varepsilon_S(0) = 1$, $\varepsilon_S(H) = \varepsilon_{mF}$ and $p_S(0) - p_S(H) = \Delta P_{mS}$. Thus eq. (2) becomes

$$\rho_f \varepsilon_{mF} u_{SH}^2 - \rho_f\, u_{S0}^2 = \Delta P_{mS} - \int_0^H (1 - \varepsilon_S(z))(\rho_p - \rho_f)\, g\, dz \qquad (3)$$

Normalizing the pressure with ΔP_{mF} and the axial distance with H, and replacing u_{S0} by $[D_c/(d_S)_{mS}]^2\, u_{mS}$, we obtain

$$\int_0^1 \frac{[1 - \varepsilon_S(\zeta)]_{mS}}{(1 - \varepsilon_{mF})}\, d\zeta \equiv C_0 = \frac{\Delta P_{mS}}{\Delta P_{mF}} + \frac{\rho_f\{[D_c/(d_S)_{mS}]^4\, u_{mS}^2 - \varepsilon_{mF}\, u_{SH}^2\}}{[(1 - \varepsilon_{mF})(\rho_p - \rho_f)\, gH]} \qquad (4)$$

with $[\varepsilon_S(0)]_{mS} = 1$ and $[\varepsilon_S(1)]_{mS} = \varepsilon_{mF}$. (5)

This simple Euler-Lagrange variational problem has the solution (7)

$$\frac{[1 - \varepsilon_S(\zeta)]_{mS}}{1 - \varepsilon_{mF}} = C_2 - \frac{1}{\lambda}[1 - (\lambda\zeta + C_1)^2]^{1/2} \qquad (6)$$

where $\lambda = (1 - C_1^2)^{1/2} - C_1$ (7)

$$C_2 = (1 - C_1^2)^{1/2}/[(1 - C_1^2)^{1/2} - C_1] \qquad (8)$$

$$C_0 = C_2 - (1/2\lambda^2)[(1 - C_1^2)^{1/2}(|C_1| - C_1)$$

$$+ \sin^{-1}[(1 - C_1^2)^{1/2}] - \sin^{-1} C_1] \qquad (9)$$

C_1, C_2 and λ are obtained by solving eqs. (7), (8) and (9) simultaneously. A plot of $[\varepsilon_S(z)]_{mS}$ vs z/H for various values of C_0 and $\varepsilon_{mF} = 0.406$ is given in Fig. 3. The calculations show that only for

values of C_0 between 0.215 and 0.785 does $[\varepsilon_S(z)]_{mS}$ decrease monotonically. Values of C_0 outside this range require that the end conditions change if $[\varepsilon_S(z)]_{mS}$ is to decrease monotonically. Experimental data [8,9] show that $\varepsilon_S(z)$ does indeed decrease monotonically and this is certainly reasonable physically since particles feed into the spout from the annulus. The convex and concave shapes predicted in Fig. 3 have been reported in the literature [8,9].

Morgan et al. (6) have shown that the case for which $C_0 = 0.785$ represents the axial voidage distribution in a bed of coarse particles at its maximum spoutable height in the condition of minimum spouting. The curve $C_0 = 0.215$ in Fig. 3 is relevant to channeling.

If the gas cannot get into the annulus due to the cohesive nature of the particles, there will be no pressure drop there. Thus ΔP_{mS}, which is caused by the flow of fluid through in the annulus, decreases to the point where $C_0 < 0.215$. When this occurs stability considerations demand that the boundary condition, $\varepsilon_S[(z/H) = 1] = \varepsilon_{mF}$, release since $d\,\varepsilon_S(1)/dz = \infty$ when $C_0 = 0.215$. $\varepsilon_S(1)$ then rises toward unity which physically describes the hole with no particle transport observed by Geldart and Wong (2). The cause of channeling is now apparent. It is a result of the cohesive nature of the particles which prevents their aeration in the annulus (the dense phase surrounding the channel). When the gas flowrate is raised above minimum spouting, the channels enlarge and conditions in the annulus are unchanged.

NOMENCLATURE

C_0	$\equiv \int_0^1 \frac{1 - \varepsilon_S(\zeta)}{1 - \varepsilon_{mF}} d\zeta$ in a spouted bed (see equation 4)
C_1, C_2	constants
d_p	particle diameter
d_S	average spout diameter
D_c	column diameter
g	gravitational acceleration
H	bed height
p_S	fluid pressure in the spout (or channel)
$p_S(H)$	p_S at $z = H$
$p_S(0)$	p_S at $z = 0$
ΔP_{mF}	pressure drop at minimum fluidization in a bed of height, H $\Delta P_{mF} = (1-\varepsilon_{mF})(\rho_p - \rho_f)gH$
ΔP_{mS}	overall spout pressure drop at minimum spouting
u_{mS}	minimum spouting velocity

u_S interstitial fluid velocity in spout

u_{SH} u_S at $z = H$

u_{SO} u_S at $z = 0$

v_S interstitial particle velocity in the spout

v_{SH} v_S at $z = H$

v_{SO} v_S at $z = 0$

z vertical coordinate measured from spout inlet

Greek symbols

ε_{mF} voidage at minimum fluidization

ε_S spout voidage

$\varepsilon_S(H)$ ε_S at $z = H$

ζ z/H

λ constant in equation 6

ρ_f fluid density

ρ_p particle density

REFERENCES

1. Guichard, J. C., "Fine Particles: Aerosol Generation, Measurement, Sampling and Analysis" Liu, B.H.Y., Ed., Academic Press, New York, 1976.

2. Geldart, D. and Wong, A. C. Y., Chem. Eng. Sci., 39, 1481 (1984).

3. Geldart, D., Powder Tech., 7, 285 (1973).

4. Geldart, D. and Wong, A. C. Y., Chem. Eng. Sci, 40, 653 (1985).

5. Hausner, H. H., Int. J. of Powder Metal, 3, 7 (1967).

6. Morgan, M. H. III, Day, J. Y., Littman, H., Chem. Eng. Sci., 40, 1367 (1985).

7. Hildebrand, F. B., "Methods of Applied Mathematics," Prentice-Hall, New Jersey 1965.

8. Mathur, K. B. and Epstein, N., "Spouted Beds," Academic Press, New York, 1974.

9. Grbavcic, Z. B., Vukovic, D. V., Zdanski, F. K. and Littman, H., Can. J. Chem. Eng., 54 33 (1976).

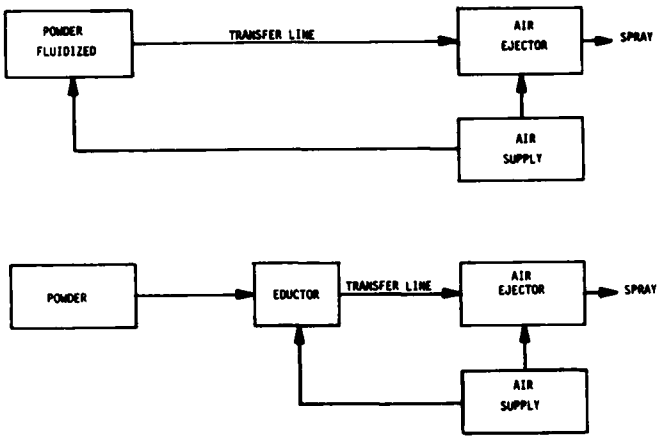

FIGURE 1. Schematic diagrams for producing deagglomerated aerosol sprays
a) fluidized material, storage-container feed to transfer line
b) eductor feed to transfer line

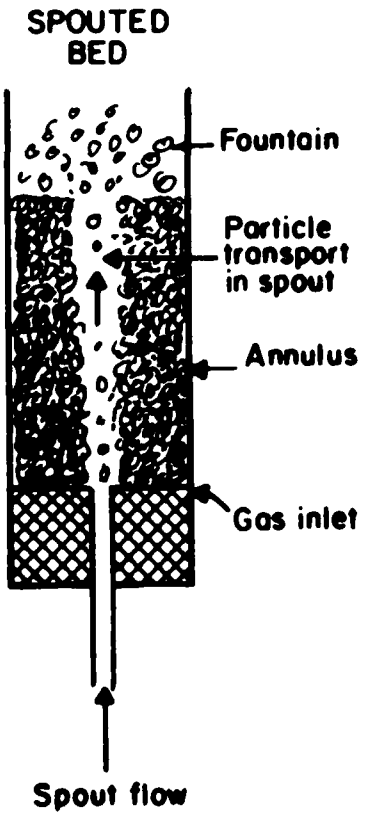

FIGURE 2. Schematic diagram of a spouted bed with a flat bottom. (Commercial columns have conical bottoms).

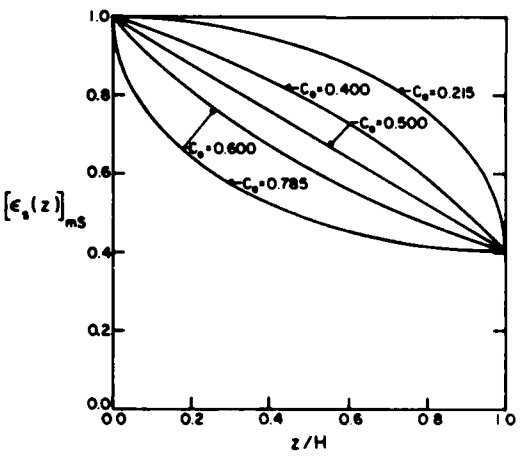

FIGURE 3. Predicted axial voidage distributions in the spout at minimum spouting by variational technique. ϵ_{mF} = 0.406.

JET PENETRATION AND PRESSURE DROPS IN SPOUTED BEDS OF FINE PARTICLES

M.H. Morgan, III, H. Littman, and B. Sastri

Department of Chemical Engineering and Environmental Engineering
Rensselaer Polytechnic Institute
Troy, NY 12180-3590

Introduction

To effectively design a pneumatic transport system one must know precisely the entrance condition to the delivery system. Although these systems have been in common use for decades, an accurate characterization of their inlet condition still evades researchers. What is needed is a standard feeder whose feed conditions can be precisely determined. One such system that offers promise is the spout-fluid bed with draft tube (see Figure 1). In this design the feeder is the spouted bed annulus surrounding the draft tube (pneumatic transport tube). Morgan, et al. (1) have shown recently that a complete characterization of the spout region of these systems allows them to predict both the radially averaged axial voidage distribution and solid circulation rate in spouted beds. Since the inlet conditions to the draft tube are represented by the spout outlet conditions one has in essence a standard feeder.

One of the key design variables that may be used to vary the solid circulation rate is the draft tube spacing (ℓ) or separation distance above the inlet orifice. An exceedingly large solid turndown range is possible with such a design since this spacing can be varied between ℓ^* and H_m.[#] It is immediately apparent to the designer that a knowledge of these two operating limits (ℓ^* and H_m) is important. If this device is operated outside these limits solids transport is not possible. At draft tube spacings above H_m, the jet formed by the spout will not penetrate the bed and only bubbling or choking within the draft tube occurs. When $\ell<\ell^*$, the pressure drop across the surrounding spout annulus is not large enough to support solid transport and only fluid will flow through the tube. This latter effect has been reported by Yang (2) and discussed in some detail by Morgan, et al. (1).

In this paper new models are developed for predicting the maximum jet penetration, H_m, in spouted beds using either a liquid or gas as the spouting fluid. Relationships are also developed for predicting the spout pressure drop (maximum feeder pressure drop) under such flow conditions ($\ell=H_m$).

Maximum Jet Penetration (H_m)

In a spouted bed there is an upper spoutable height, H_m above which all bed heights will be partitioned into an internal spouting zone and an upper level fluidized region. This upper region in gas-spouted systems appears as an aggregatively fluidized zone while with liquids this region will be particulately fluidized. The majority of the empirical and semi-empirical models for

[#][See Nomenclature below.]

predicting this quantity are founded in Reference(1). The most recent semi-empirical models are the two Littman, et al. (4,5) models of Equations (1) and (2). Both of these models were developed using monodispersed spherical particles:

$$m = 0.215 + \frac{0.005}{A} \qquad \text{for} \qquad A > 0.02 \tag{1}$$

and

$$\frac{H_m D_s}{D_c^2 - D_s^2} = 0.345 \left(\frac{D_s}{D_c}\right)^{-0.384} \tag{2}$$

The first of these models was derived from momentum considerations. It was shown that the A-parameter linked the maximum jet penetration to the momentum exiting the inlet orifice. The latter model (H_m-D_s relationship) followed from continuity considerations. It was assumed that a vectorial form of Ergun's equation could be used to solve for the annular flow field. A boundary-value problem was posed for this region and solved assuming McNab's relationship (6) held for the spout and that the Lefroy and Davidson pressure profile (7) was applicable at the spout-annular interface.

New models are developed here for H_m that are valid for both the small and large A regions. These models require only a knowledge of the basic geometric properties of the bed (d_i and D_c) and the physical properties of the fluid and particles (d_p, μ, ρ_f and ρ_p). Furthermore, this information when combined with an overall spout momentum balance can be used to predict the pressure drop ratio, $(\Delta P_{mS}/\Delta P_{mF})$, in these systems.

Development of an H_m Relationship

The authors have shown in other work (4) that the fluid-particle, inlet orifice and particle shape effects can be conveniently characterized by the following dimensionless grouping,

$$A = \frac{\rho_f u_{mF} u_T}{(\rho_p - \rho_f) g d_i} \tag{3}$$

Using this grouping they developed a correlation relating $m = H_m d_i/D_c^2$ to A via consideration of the momentum. That correlation is given above in Equation 1 for spherical particles. Littman et al. (4) found for $A < 0.02$ that Equation (1) predicts experimental data poorly. Here a new correlation for m is sought based on new correlating variables deduced from the original A parameter. Our objective is to develop a more general equation that is valid for both large and small A-values.

It follows that as $d_p \to 0$ the A-parameter will take the following asymptotic form:

$$A(d_p \to 0) = \left(\frac{d_p}{D_c}\right)(Ar)\left(\frac{u_T/u_{mF}}{d_i/D_c}\right) a_o \qquad (4)$$

Noting that the Archimedes Number, Ar, may be expressed in terms of the ratio, $\beta = (u_T/u_{mF})^{-1/2}$, Equation (1) reduces to

$$m = \left[f\left(\frac{u_T}{u_{mF}}\right)\right]\left[\frac{u_{mF}/u_T}{d_i/D_c}\right] \quad . \qquad (5)$$

Thus a new correlation for m was sought using the dimensionless groups suggested by Equation (5).

In Figure 2, a plot of m, the dimensionless jet-penetration height versus the dimensionless group $(d_i/D_c)/(u_{mF}/u_T) = A_{Lim}$ is shown for spherical particles spouted in both air and water. Two salient features of the data are readily apparent. First, it reveals there is a family of jet penetration curves (β-curves) and second, that jet penetration increases with A_{Lim}. In addition, there are both upper and lower bound curves ($\beta=\beta_{max}$ and $\beta=\beta_{min}$ curves in Figure 2) that would encompass the data.

For a fixed A_{Lim}, one finds that decreasing β reduces the dimensionless jet penetration. Such behavior is normally not observed in gas-spouted systems, since β values for these gases fall between $0.28 < \beta < 0.35$. Thus one would expect experimental error to mask this effect in systems where $\beta > 0.28$. Only with liquid-spouted systems is such an effect clearly apparent (see Figures 2 and 3).

The following correlation for m, was obtained for the data provided in Figure 2:

$$m = a_o(\beta)\left[\frac{d_i}{D_c\left(\frac{u_{mF}}{u_T}\right)}\right] \quad \text{for } 0.10 < \beta < 0.35 \qquad (6)$$

where

$$a_o(\beta) = 0.066 \text{ for } 0.10 < \beta < 0.20$$

$$a_o(\beta) = 0.135 \text{ for } 0.20 < \beta < 0.30$$

and

$$a_o(\beta) = 0.200 \text{ for } \beta > 0.30$$

This correlation shows that jet penetration becomes independent of d_i as A becomes small and inertia effects become less important. In this region, H_m varies as D_c.[1] When A is large, however, the Littman, et al. (6) correlation shows that m should approach 0.218 and vary with d_i^{-1} and D_c^{+2}. With large A, the inertia effects are obviously dominant and a different result is obtained. The experimental data was found to fit Equation (6) to within with 11 percent (see Figures 4 and 5).

Dimensionless Pressure Drop Ratio in a Small-A System (Maximum Feeder Pressure)

Starting with the combined, fluid and solid momentum equation, assuming a constant spout diameter axially and using radially-averaged velocity, pressure and voidage one obtains

$$\rho_f \frac{d}{dz}(\varepsilon_S u_S^2) + \rho_p \frac{d}{dz}((1 - \varepsilon_S)v_S^2) = -\frac{dp_s}{dz} - (1 - \varepsilon_S)\rho_p g - \varepsilon_S \rho_f g \tag{7}$$

Furthermore, noting that the inertia in small-A spouting systems is negligible,Equation (7) reduces to

$$\frac{-dp}{dz} = (1 - \varepsilon_S)(\rho_p - \rho_f)g \tag{8}$$

where

$$p = (p_S - \rho_f gz).$$

Thus,one major difference between small and large A systemsis the fact that in the latter systems the inertia terms are substantial in size and must be incorporated in the analysis. With liquid systems for example, the inertia term is typically much less than 10% of the pressure and gravitational contributions. Integrating Equation (8) one obtains

$$p_S = \int_0^{H_m}(1 - \varepsilon_S(z))(\rho_p - \rho_f)g\, dz \tag{9}$$

Now normalizing the pressure with ΔP_{mF} and the axial distance with H_m, Equation (9) becomes

$$\left.\frac{\Delta P_{mS}}{\Delta P_{mF}}\right|_{H_m} = \int_0^1 \frac{(1 - \varepsilon(\zeta))}{1 - \varepsilon_{mF}}\, d\zeta \tag{10}$$

Previously, Morgan et al. (1) have shown that a variational formulation can be posed for the spout voidage. Here a similar problem is formulated for the pressure. The Euler-Lagrange statement for the pressure in a small-A spouting system becomes

$$J = \int_0^1 \sqrt{1 + (f'(\zeta))^2}\, d\zeta \tag{11}$$

$$\zeta = 0: -\frac{dp^*}{d\zeta} = \frac{1 - \varepsilon(0)}{1 - \varepsilon_{mF}} = f(0) \tag{12}$$

with $p^* = p/\Delta P_{mF}$ and

$$\zeta = 1: -\frac{dp^*}{d\zeta} = 1 = f(1). \tag{13}$$

The pressure drop ratio $\Delta P_{mS}/\Delta P_{mF}$ is calculated from Equation (14)

$$\left.\frac{\Delta P_{mS}}{\Delta P_{mF}}\right|_{\zeta=1} = \int_0^1 f(\zeta)\, d\zeta \tag{14}$$

This approach obviously requires explicit information about the system boundary conditions. The pressure gradient at the inlet, $dp^*/d\zeta\,|_{\zeta=0}$ is estimated following Richardson-Zaki (8) by noting,

$$\frac{u_i}{u_T} = \varepsilon_i^n \quad , \tag{15}$$

noting that $u_i = u_{mF}(D_c/D_s)^2$ for a bed at $H = H_m$, and substituting this result into Equation (15) to obtain

$$\varepsilon_i = \left(\frac{u_i}{u_T}\right)^{1/n} = \left(\frac{u_{mF}}{u_T}\right)^{1/n} \left(\frac{D_c}{D_s}\right)^{2/n} \tag{16}$$

and

$$-\left.\frac{dp^*}{d\zeta}\right|_{\zeta=0} = \frac{1 - \left(\frac{u_{mF}}{u_T}\right)^{1/n} \left(\frac{D_c}{D_s}\right)^{2/n}}{1 - \varepsilon_{mF}} \tag{17}$$

Unlike the coarse particle systems, the voidage at the spout inlet in such systems may be less than 1.0. Morgan et al. (1) have suggested that the release of the boundary condition $\varepsilon_s(0) = 1$ to produce stable spouting is probably associated with a spouting regime change. They also suggested that a precise definition of the terms coarse and fine for particles in spouted beds may also be related to $C_o > 0.785$. In small-A systems, since the inertia terms are negligible, $C_0 \simeq \Delta P_{mS}/\Delta P_{mF}$.

So the complete variational problem in terms of the pressure takes the form

$$J = \int_0^1 \sqrt{1 + \left(\frac{d^2p^{*2}}{d\zeta^2}\right)}\, d\zeta \tag{18}$$

$$\zeta = 0; \quad \frac{-dp^*}{d\zeta} = \frac{1-\varepsilon_i}{1-\varepsilon_{mF}} = \frac{1 - \left(\frac{u_{mF}}{u_T}\right)^{1/n} \left(\frac{D_c}{D_s}\right)^{2/n}}{1 - \varepsilon_{mF}} \tag{19}$$

$$\zeta = 1; \quad \frac{-dp^*}{d\zeta} = 1 \tag{20}$$

and

$$\zeta = 1; \quad \frac{-d^2p^*}{d\zeta^2} = 0 \tag{21}$$

Or in terms of the voidage function $f(\zeta)$ one obtains

$$J = \int_0^1 \sqrt{1+(f'(\zeta))^2}\, d\zeta \tag{22}$$

$$\zeta = 0; \quad f(\zeta) = \frac{1-\varepsilon_i}{1-\varepsilon_{mF}} \tag{23}$$

$$\zeta = 1; \quad f(\zeta) = 1 \tag{24}$$

and

$$\zeta = 1; \quad f'(\zeta) = 0 \tag{25}$$

This variational problem is similar to the original one posed in Morgan, et al. (1). However, the boundary condition at $\zeta = 0$ is no longer homogeneous. If the following transformation is employed

$$y_i = \frac{\varepsilon_i - \varepsilon(\zeta)}{\varepsilon_i - \varepsilon_{mF}} . \tag{26}$$

This inhomogenity may be removed and the system of Equations (22) through (25) transforms as follows:

$$J = \int_0^1 \sqrt{1 + (y_i')^2}\, d\zeta \tag{27}$$

$$\zeta = 0; \quad y_i = 0 \tag{28}$$

$$\zeta = 1; \quad y_i = 1.0 \tag{29}$$

$$\int_0^1 y_i \, d\zeta = C_o'(max) \tag{30}$$

At $\zeta = 1$, the boundary $d\varepsilon/d\zeta = 0$ is equivalent to the integral condition given by Equation (30). From Morgan et al. we note that $C_o'(max) = 0.785$.

Thus, the pressure drop ratio, $\Delta P_{ms}/\Delta P_{mF}$ for systems where $\varepsilon_i < 1.0$ is given by

$$C_o \simeq \frac{\Delta P_{ms}}{\Delta P_{mF}} = \int_0^1 \frac{(1-\varepsilon(\zeta))}{1-\varepsilon_{mF}}\, d\zeta \tag{31}$$

or

$$\frac{\Delta P_{ms}}{\Delta P_{mF}} = \frac{1-\varepsilon_i}{1-\varepsilon_{mF}} + \frac{\varepsilon_i - \varepsilon_{mF}}{1-\varepsilon_{mF}} \int_0^1 \frac{\varepsilon_i - \varepsilon(\zeta)}{\varepsilon_i - \varepsilon_{mF}}\, d\zeta \tag{32}$$

The maximum pressure drop ratio, $(\Delta P_{ms}/\Delta P_{mF})_{max}$ occurs at $H = H_m$ and since $C_o'(max) = 0.785$ Equation (32) above reduces to

$$\left(\frac{\Delta P_{ms}}{\Delta P_{mF}}\right)_{max} = \left(\frac{1-\varepsilon_i}{1-\varepsilon_{mF}}\right) 0.215 + 0.785 \tag{33}$$

Note that $(\frac{\Delta P_{mS}}{\Delta P_{mF}})_{max}$ = 0.785 is the Morgan et al result when ε_i = 1.0. This result is observed in many coarse and fine particle systems spouted with air.

In Table I a comparison between $\Delta P_{mS}/\Delta P_{mF}$(expt) and $\Delta P_{mS}/\Delta P_{mF}$ (analytical solution) is provided for various water-spouted systems. In such systemsthe boundary condition at ζ = 0 is known to release and $\varepsilon(\zeta=0)<1$. The agreement with experimental data is within 2.6 percent on average. For beds less than H_m, the pressure drop ratio, $\Delta P_{mS}/\Delta P_{mF}$ is calculated by simply integrating the function y_i to the specific height of interest. This result follows directly from the application of the Grabavčić (9) condition. Previously, Morgan and Littman (10) derived a general pressure profile for a spouted bed based on that condition. That model required pressure drop versus bed height data, while the model developed here determines the bed pressure gradient, y_i, explicitly.

Conclusions

1) New empirical models are developed for predicting, H_m in both liquid and gas spouted beds of fine particles.

2) Jet penetration in liquid and gas systems is strongly affected by β. There are upper and lower asymptotes that bound the jet penetration data.

3) Jet penetration is described by Equation (6).

4) Pressure drop in small-A systems can be successfully predicted from a variational principle given adequate estimates of the inlet boundary condition.

5) The dimensionless pressure drop ratio, $(\Delta P_{mS}/\Delta P_{mF})_{max}$ is given by Equation (33).

Nomenclature

a_o = constant in Eqn. 4

$a_o(\beta)$ = coefficient in Eqn. 6

A = $[\rho_f/(\rho_p-\rho_f)]\,[u_T u_{mF}/g d_i]$

A_{Lim} = $[(d_i/D_c)/(u_{mF}/u_T)]$

Ar = Archimedes number = $d_p^2\,(\rho_p-\rho_f)g/\nu^2\rho_f$

C_o = $(\Delta p_{mS}/\Delta p_{mF}) + [\rho_f u_{mF}^2\,(\frac{D_c}{D_s})^4/\Delta p_{mF}]$

d_i = inlet tube diameter

d_p = particle diameter

D_s = spout diameter in a bed of height, H_m

D_c = column diameter

g = gravitational acceleration

H = bed height

H_m = maximum spoutable height

ℓ = distance between inlet orifice and draft tube entrance

ℓ^* = separation distance where solid circulation stops

m = $H_m d_i / D_c^2$

m^* = $m/a_o(\beta)$

n = Richardson-Zaki exponent

p = $[p_s - \rho_f gz]$, the dynamic pressure

p^* = $p/\Delta p_{mF}$

p_a = fluid pressure in the annulus

p_s = fluid pressure in the spout

ΔP_{mS} = overall spout pressure drop at minimum spouting

ΔP_{mF} = overall fluidization pressure drop at minimum fluidization = $(1-\epsilon_{mF})(\rho_b - \rho_f)gH_m$

ΔP_{mF^S} = overall fluidization pressure drop at minimum fluidization = $(1^{-\epsilon}mF)\ (P_b - P_f)gH_m$

u_i = fluid velocity at inlet tube

u_{mF} = minimum fluidizing velocity

u_T = terminal fall velocity of a single particle

v_s = interstitial particle velocity in spout

z = vertical coordinate measured from spout inlet

Greek Symbols

β = $(u_{mF}/u_T)^{1/2}$

ϵ_i = inlet tube voidage

ϵ_{mF} = voidage at minimum fluidization

ϵ_s = spout voidage

ρ_f = fluid density

ρ_p = particle density

μ, ν = fluid viscosity; kinematic viscosity

ζ = dimensionless vertical coordinate

References

1. Morgan, M.H., III, Day, J.Y., and Littman, H., Chemical Engineering Science, 40, 1369 (1985).

2. Yang, W.C. and Keairns, D.L., Can. J. of Ch.E., 61, 349 (1983).

3. Mamuro, T. and Hattori, H., J. Chem. Eng., Japan, 1, 1 (1968).

4. Littman, H., Morgan, M.H., III, Vuković, D.V., Zdanski, F.K., and Grbavcić, Z.B., Can. J. Chem. Engng. 57, 684 (1979).

5. Littman, H., Morgan, M.H., III, Vuković, D.V., Zdanski, F.K., and Grbavcić, Z.B., Can. J. Chem. Eng., 55, 497 (1977).

6. McNab, G.S., Brit. Chem. Eng. and Proc. Technol., 17, 532 (1972).

7. Lefroy, G.A. and Davidson, J.F., Trans. Instn. Chem. Engrs., 47, T120 (1969).

8. Richardson, J.F. and Zaki, W.N., Tran. Inst. Chem. Engrs., 32, 35 (1954).

9. Littman, H., Vukovic, D.V., Zdansk, F.K., and Grabavčić, Z.B., Can. J. Chem. Eng., 54, 33 (1976).

10. Morgan, M.H., III, and Littman, H., "General Relationships for the Minimum Spouting Pressure Drop Ratio, $\Delta P_{mS}/\Delta P_{mF}$, and the Spout-Annular Interfacial Condition in a Spouted Bed," Fluidization, Ed., Grace, J.R. and Matsen, J.M., pp. 387-396, Plenum Press, New York (1980).

11. Kim, S.J., "The Characteristics of Beds of Small Glass Particles Spouted in Water", Ph.D. Thesis, Rensselaer Polytechnic Institute, Troy, NY (1982).

Table I

Comparison of Predicted and Actual Pressure Drop Ratios

d_p mm	d_i mm	ε_i (Calculated)	$\Delta P_{mS}/\Delta P_{mF}$ [11] (Actual)	$(\Delta P_{mS}/\Delta P_{mF})_{Max}$ = $0.785 + 0.215\left(\frac{1-\varepsilon_i}{1-\varepsilon_{mF}}\right)$ (Theory)	Absolute Percent Error
0.275	6.35	0.803	0.847	0.853	0.71
	12.70	0.776	0.865	0.864	0.12
	19.05	0.730	0.878	0.880	0.23
0.460	6.35	0.818	0.856	0.850	0.7
	12.70	0.753	0.860	0.874	0.9
	19.05	0.726	0.880	0.883	0.34
0.774	6.35	0.760	0.830	0.872	5.1
	12.70	0.709	0.820	0.890	8.5
	19.05	0.678	0.830	0.902	8.7
0.995	6.35	0.893	0.850	0.824	3.1
	12.70	0.854	0.840	0.839	0.12
	19.05	0.799	0.841	0.856	1.8

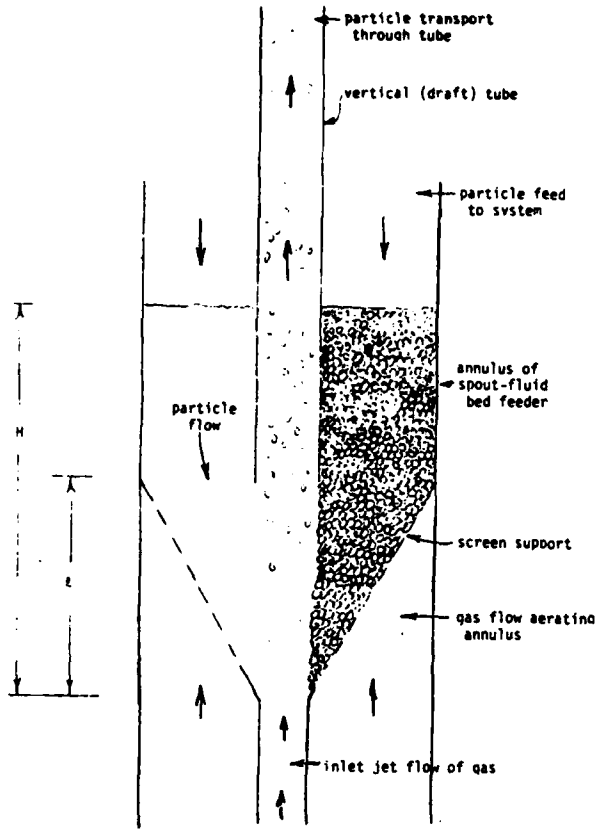

FIGURE 1. Schematic diagram of vertical (draft) tube with a spout-fluid bed feeder.

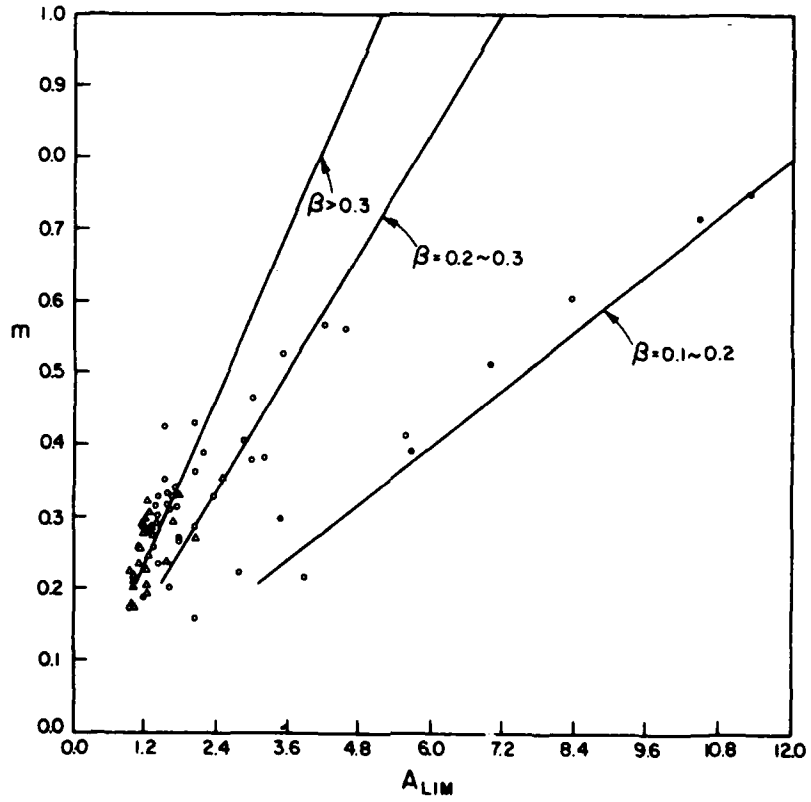

FIGURE 2. Dimensionless jet penetration versus A_{Lim} for air and water systems.

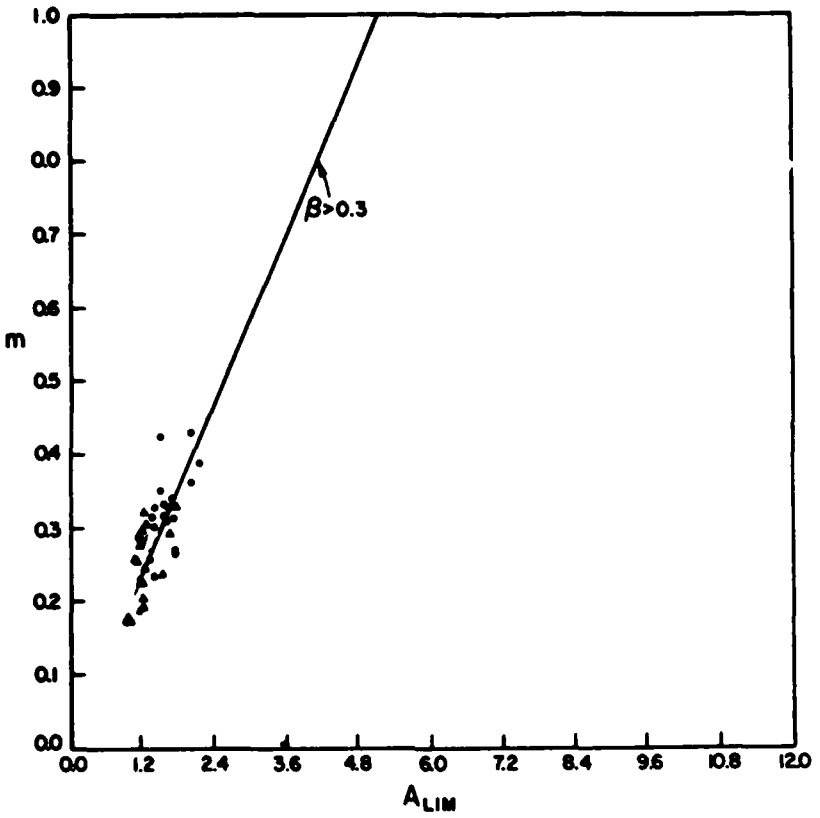

FIGURE 3. Dimensionless jet penetration versus A_{Lim} for air systems.

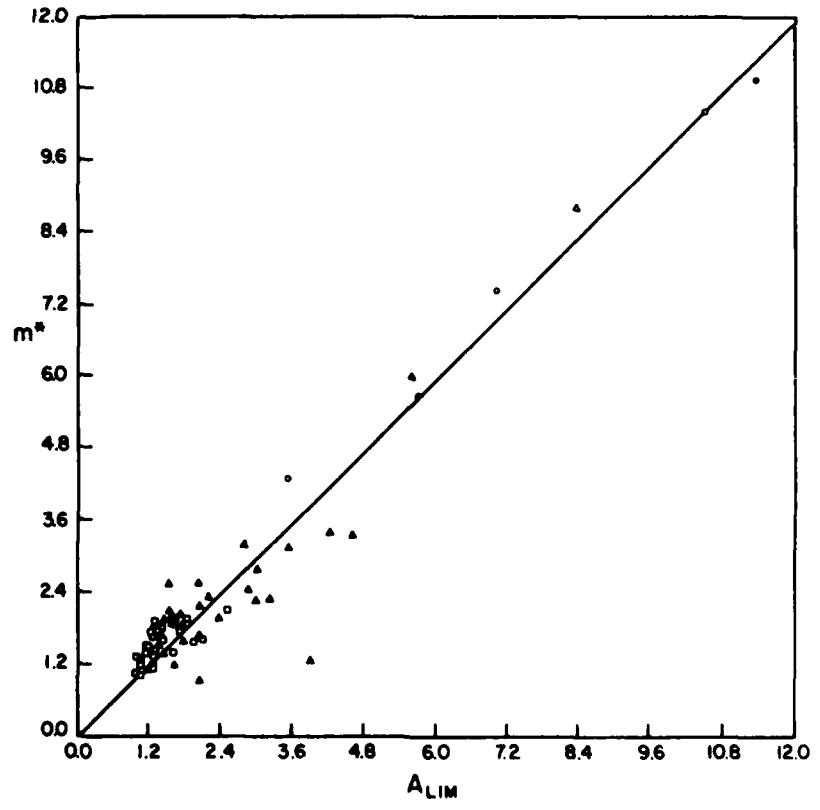

FIGURE 4. Normalized jet penetration versus A_{Lim} for air and water systems.

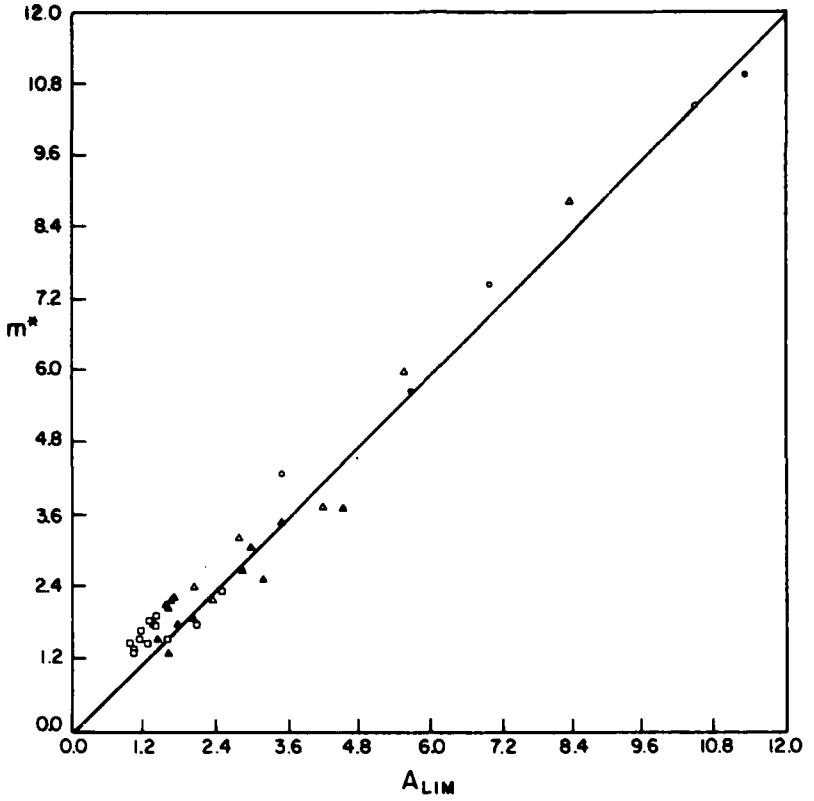

FIGURE 5. Normalized jet penetration versus A_{Lim} for water systems.

MIXING/PHASE-CHANGE PROCESSES IN WET-AEROSOL CLOUDS

J. Latham
Physics Department, U.M.I.S.T.,
Manchester M60 1QD, England

ABSTRACT

On 27 July 1981, as part of the CCOPE experiment, the University of Wyoming King Air research aeroplane made penetrations at six levels ranging from 590mb (-4.9°C) to 770mb (7.2°C) through a non-precipitating, unglaciated cumulus cloud whose top was at about 560mb (-7°C) and base at about 780mb (8°C). The entire flight sequence - from the top downwards - took about 6 minutes. Principal measurements were of droplet size distribution N(d), number concentration N and liquid-water-content L, measured at 10Hz (~10m spatial resolution); drop-count N' (50Hz, ~2m); temperature T. Also we calculated the fraction F of cloud-base air in the mixture sampled (1Hz, ~100m). The cloud was substantially sub-adiabatic throughout the volume studied. Paluch analyses, the observed air-motions near cloud-top, buoyancy profiles and the observed distribution of L and F with altitude demonstrated that the cloud was diluted principally by entrainment from cloud-top. Considerable scatter was found in all microphysical and thermodynamic variables on all spatial scales. Large variations in L were primarily attributable to fluctuations in N and N'. Bimodal spectra were sometimes found at the interface between statistically smooth and highly variable regions. The breadth of the droplet spectra and the size of the largest droplets in the condensate spectrum were not systematically related to the degree of dilution. Calculations showed that a small fraction of the droplets ($\sim 100l^{-1}$) exhibited super-adiabatic growth of up to 4μm diameter at the intermediate levels (in good agreement with the predictions of Baker et al, 1980), but not near cloud-base or cloud-top. Support for the idea that droplets in lower concentrations ($\sim 10l^{-1}$) grew even faster was provided by 1-D probe measurements of droplets of up to 75μm diameter in the central and upper regions of the cloud.

1. INTRODUCTION

This article is adapted from a longer one by A.M.Blyth and the author, entitled 'An airborne study of vertical structure and microphysical variability within a small cumulus' (Quart. J. Roy. Met.Soc., 111, 1985, 773-792). Attention is concentrated herein upon those aspects of the reported airborne study considered most relevant to the CRDC meeting and interests.

2. THE MIXING/PHASE-CHANGE STUDIES

The principal measurements with which this study was concerned are of droplet size distribution and liquid water content, obtained with a Particle Measuring Systems Forward Scattering Spectrometer Probe (FSSP) mounted on the aeroplane. This device measured the concentrations N(d) of droplets of diameter d between 2 and 32μm, the spectrum being divided into 15 channels each of width 2μm. The sampling rate was 15 $cm^3 s^{-1}$, and since the droplet concentrations in the cloud were around $200cm^{-3}$ the

number of droplets sampled in 0.1s (the shortest period over which spectra were produced) was characteristically about 300. Integration over this size range permitted determination of the total droplet concentration, N, and the liquid-water-content L. These measurements were made at a frequency of 10Hz, and, since the King Air flew at a speed around 100m s^{-1}, spatial variability in N(d), N and L could be examined on scales down to about 10m. In addition, the FSSP recorded at 50Hz the total number N' of droplets in the laser beam; not all of which contribute to N. Thus this measurement provided information on fluctuations in droplet concentration on scales down to about 2m. Measurements of L were also made with a Johnson-Williams (JW) hot-wire device, whose frequency response was nominally 10Hz but in reality, from observations made when the FSSP was indicating high-frequency variations in L, was closer to 1Hz. Its absolute values were in good agreement with those of the FSSP device. The JW value of L was used in all thermodynamic analysis. A PMS 1-D probe with a sampling rate of about 0.5 l s^{-1} (5 l km^{-1}) was used to measure the concentrations of drops in twelve equal size-bands covering the approximate diameter range 38 to 190μm. We are grateful to Dr. W. A. Cooper of the University of Wyoming for advice on the elimination of spurious signals from this device. Measurements of vertical velocity W were made at 10Hz using a vertically stabilized accelerometer combined with the aircraft motions. Long-term drift caused an uncertainty of $\pm$2m s^{-1} in the measurement of W at frequencies below 0.1Hz (Rodi and Lawson, 1983). The measurements of W during and 20 seconds after a turn had to be disregarded in this study due to problems with the gyroscope erection mechanism. Since the King Air descended through 2km in about 6 minutes many sharp turns were required, and only penetration 1 provided acceptable velocity data. Horizontal air motions were measured via an on-board Doppler radar. The in-cloud temperatures reported in this paper were made with a reverse-flow thermometer with a platinum resistance sensor, whose resolution was $\pm$0.1C and frequency response in the range 0.5 to 1s.

Table 1 presents information, for all six penetrations, of the average values and standard deviation S of cloud temperature (T_C), droplet concentration (N), liquid water content (L), droplet diameter (d), spectral dispersion ($\sigma = S/\bar{d}$, the ratio of the standard deviation to the mean size), the wet equivalent potential temperature (θ_q),

and the fraction (F) of cloud-base air in the cloudy mixture; the values of F (estimated to be accurate to within 5%) were determined from the Paluch diagrams using the technique described by Jensen, Austin, Baker and Blyth (1984). T_C is seen to be more variable in the upper regions than the lower, possibly because of fluctuations produced by cloud-top entrainment. N is highly variable but shows no systematic tendency to change with altitude. $\bar{d}$ increases steadily with height, while L is highly variable and peaks at an intermediate level, presumably because the tendency to increase with height above cloud-base is offset by dilution from cloud-top. θ_q exhibits a tendency to decrease with altitude, while σ, though variable, reveals no clear dependence upon height above cloud-base. F, for the four levels at which reliable measurements could be made, decreases with increasing altitude. The observations from the study are consistent with the hypothesis of air entrainment at cloud-top propagating downwards to all lower levels of the cloud, and producing a high degree of spatial variability in the microphysical and thermodynamical parameters.

Supporting evidence for this interpretation is provided by scatter-plots (with mean values), for all six penetrations, of F(1Hz), N(10Hz), $\bar{d}$(10Hz) and the ratio, L/L_A (10Hz), of the measured liquid water content to the adiabatic value. Considerable spread in all these parameters is found at all levels. The cloud was found to be substantially sub-adiabatic in L, the average value of L/L_A increasing from about 0.2 at the lowest level to a maximum of about 0.3 half-way up the cloud and dropping to about 0.1 at the highest level. Only at the lowest level (6) is evidence found for approximately adiabatic values of L; and these are rare. It is seen that there is considerable scatter in $\bar{d}$ at all levels, and that the scatter in L/L_A is significantly greater than that in N, indicating that variability in $\bar{d}$ is contributing significantly to liquid water content fluctuations; and therefore that evaporation - as well as dilution - is producing spatial variability in L. The $\bar{d}$ values are always substantially below the adiabatic ones, except for one or two points in the lowest regions of the cloud. No adiabatic (F=1) regions were found, and the lowest values of F found at each level were close to the critical values F_s which were shown by Jensen et al to correspond to an exactly saturated droplet-free region.

It is implicit in the foregoing discussion that vertical coherence exists between

the measurements made at each level. The flight-tracks suggest that this assumption is not strictly valid. The cloud did not consist of a simple cell, although the Paluch analysis and the limited duration of the entire experiment suggest that no significant variations in the location of cloud-top and cloud-base occurred in the course of it.

Spectra were measured for each of the six levels of penetration, obtained by averaging over all 10Hz spectra for which the liquid water content exceeded 10% of the adiabatic value; this qualification being designed to eliminate spectra from essentially droplet-free spaces between sections of the cloud. The general form of the spectral evolution is similar to that found by Warner (1969): a peak size increasing with altitude, with a relatively flat tail towards the smaller sizes, which extend down to the lowest limit of measurement. The slight tendency towards bimodality exhibited in the spectra is probably largely a consequence of the fact that they were produced by averaging over ones of very different shapes. In all cases L varies considerably throughout a passage, fluctuations occurring on all scales down to the smallest detectable (~10m). Comparison of the variations of L in the six passages with those of (T_C-T_E) for the same penetrations, reveals that minima in L are associated with strong negative buoyancy. In all six penetrations the fluctuations in L are due much more to those in N' than in the volume mean diameter d', although significant changes in d' are perceived, from time to time. This suggests that inhomogeneities in L are a consequence of mixing between cloudy and entrained air, the primary mechanism for reducing L probably being dilution, as argued by Telford and Chai. The regions of varying, sub-adiabatic L can be sub-divided, as shown by Austin et al, into 'smooth' regions in which N' is approximately constant and $R \sim 1$, and 'variable' ones in which N' varies rapidly and widely, and $R \gg 1$, R being the coefficient of variability. The droplet size distributions in the variable regions are generally broad and often bimodal, while those in the smooth regions are often but not always narrow, with well-defined single peaks. The microphysical structure of the cloud was found to be highly variable, particularly lower down, where evidence is found, particularly in penetrations 4 and 5, for two distinct regions, of horizontal extent around 1km, separated by an essentially cloud-free region of width around 0.5km .

Analysis was conducted of consecutive droplet size distributions separated by 0.1s. Thus they contain information on fluctuations in N(d) over about 500m of penetration, with a spatial resolution of about 10m. It reveals evidence for significant variability on scales down to a few tens of metres. As we descend lower into the cloud we find that the general spectral shape changes progressively from a skew distribution, with a small-droplet tail, to an approximately Gaussian distribution, the peak size diminishing at lower levels. A feature found at all levels in the cloud is the existence of regions, a few tens of metres in extent, in which N is markedly reduced. They are all ones defined as 'variable' ($R \gg 1$). In these regions the spectra are broader than elsewhere, and are sometimes bimodal. The bimodality, which was clearly delineated only in penetration 4, occurred at the boundary between smooth and variable regions.

ACKNOWLEDGEMENTS

The research described herein was supported by the Natural Environment Research Council under grant GR3/4458. The major contribution of data analysis was performed by Dr. A. M. Blyth, presently at N.M.I.M.T., Soccorro. We are appreciative of the considerable help provided by staff of the Convective Storms Division, N.C.A.R., Boulder, under the direction of Dr Patrick Squires. The advice and assistance of Dr. W. A. Cooper, University of Wyoming, has been of great value.

REFERENCES

Austin P, Baker M B, Blyth A M and Jensen J B 1985 Small-scale variability in warm continental cumulus clouds. J Atmos Sci.

Jensen J B, Austin P H, Baker M B and Blyth A M 1985 Turbulent mixing, spectral evolution and dynamics in a warm cumulus cloud. J Atmos Sci.

Paluch I R 1979 The entrainment mechanism in Colorado cumuli. J Atmos Sci, 36, 2467-2478

Rodi A R and Lawson R P 1983 Comparison of vertical air velocity measurements from INS and vertical gyroscope systems. AMS Vth Symp Met Observations & Instrumentation, Toronto, Canada

Telford J W and Chai S K 1980 A new aspect of condensation theory. Pageoph, 118, 720-742

Telford J W and Chai S K 1983 Comment on "Entrainment and the droplet spectrum in cumulus cloud" (Jonas & Mason) Quart J Roy Met Soc, 109, 896-899

Warner J 1969 The microstructure of cumulus cloud. Pt I. General features of the droplet spectrum. J Atmos Sci, 26, 1049-1059

TABLE 1.

Penetration	p (mb)	T_C(°C)	N(cm^{-3})	L($g\ m^{-3}$)	$\bar{d}$(μm)	σ	θ_q (K)	F
1	589	-4.9 ± 1.27	195 ± 98	0.37 ± 0.51	18.3 ± 1.3	0.34 ± 0.04	322 ± 0.7	-
2	631	-2.9 ± 1.78	168 ± 108	0.45 ± 0.46	16.5 ± 1.8	0.33 ± 0.03	321 ± 0.5	0.67 ± 0.06
3	655	-1.4 ± 2.07	173 ± 125	0.42 ± 0.35	15.4 ± 2.1	0.35 ± 0.05	322 ± 0.7	0.69 ± 0.06
4	683	0.9 ± 0.61	255 ± 135	0.52 ± 0.45	14.8 ± 2.4	0.32 ± 0.06	323 ± 1.0	0.78 ± 0.08
5	732	4.5 ± 0.25	184 ± 117	0.23 ± 0.25	12.0 ± 2.4	0.32 ± 0.04	324 ± 0.3	0.88 ± 0.03
6	769	7.2 ± 0.47	158 ± 100	0.09 ± 0.10	6.9 ± 1.6	0.34 ± 0.08	-	-

Table 1. The mean values and standard deviations of temperature T, droplet concentration N, liquid-water-content L (with the Johnson-Williams device), mean droplet diameter $\bar{d}$, spectral dispersion σ, wet equivalent potential temperature θ_q, and fraction F of cloud-base air in the mixture for each of the cloud penetrations, at the pressure-levels p.

NUMERICAL TECHNIQUES IN AEROSOL PLUME SIMULATION

T.H. Tsang and N. Korgaonkar
Department of Chemical Engineering
University of Kentucky
Lexington, Kentucky 40506-0046

RECENT PUBLICATIONS, SUBMITTALS FOR PUBLICATION AND PRESENTATIONS:

A) J.R. Brock, T.H. Tsang and S.G. Kim, "Aerosol Plume Mechanics and Particle Growth Processes," Proceedings of the Chemical Research and Development Center's 1984 Scientific Conference on Obscuration and Aerosol Research.

B) T.H. Tsang and J.R. Brock, "On Ostwald Ripening," Aerosol Science and Technology, 3, 283 (1985).

C) T.H. Tsang and J.R. Brock, "Dynamics of Ostwald Ripening with Coalescence for Aerosols with Continuum Diffusive Growth Laws," Aerosol Science and Technology (To be published in 1986).

D) T.H. Tsang and J.R. Brock, "Ostwald Ripening," presentation at the First International Aerosol Conference, University of Minnesota, Minneapolis, Minnesota, September 1984.

E) T.H. Tsang, "Simulation of Condensation Aerosol Growth by Condensation/Evaporation and Coagulation," presentation at the Atmospheric and Geophysical Sciences Division, Lawrence Livermore National Laboratory, October 1984.

F) T.H. Tsang, "Dynamics of Ostwald Ripening with Coalescence for Aerosols in Free Molecular Regime," presentation at the Annual Meeting of American Association for Aerosol Research, Albuquerque, New Mexico, November 1985.

G) J. Hippe and T.H. Tsang, "Simulation of Aerosol Growth Processes on a Vector Supercomputer," submitted to J. Aerosol Science, November 1985.

H) J. Hippe and T.H. Tsang, "Dynamics of Ostwald Ripening with Coalescence for Aerosols in Free Molecular Regime," submitted to Aerosol Science and Technology, December 1985.

ABSTRACT

This paper summarizes the numerical techniques used in aerosol plume simulation. Specifically, numerical techniques in the following areas are discussed: (1) advection, (2) diffusion, (3) condensation, (4) evaporation, (5) coagulation, and (6) simulation of aerosol dynamics on a vector supercomputer.

INTRODUCTION

Successful and reliable predictions of the effectiveness of aerosol obscurants require quantitative understanding on many physio-chemical processes. Such quantitative description presents a challenging problem to atmospheric scientists and aerosol scientists. Although significant progress has been made recently, much remains to be done. In the following sections, we will present some efficient and reliable numerical techniques which can be used in modeling advection, diffusion, condensation, evaporation and coagulation. A general model for the dispersion of an aerosol in the atmospheric surface layer is shown, in repeated indices form, as follows,

$$\frac{\partial U_i}{\partial X_i} = 0 \tag{1}$$

$$\rho_o \frac{\partial U_i}{\partial t} + \rho_o \frac{\partial}{\partial X_j}\left(U_j U_i + \overline{U_j' U_i'}\right) = \mu_o \frac{\partial^2 U_i}{\partial X_j \partial X_j} - \frac{\partial p}{\partial X_i} - \rho_o g_i \frac{T}{T_o} \tag{2}$$

$$\rho_o C_p \frac{\partial T}{\partial t} + \rho_o C_p \frac{\partial}{\partial X_j}\left(U_j T + \overline{U_j' T'}\right) = k_o \frac{\partial^2 T}{\partial X_j \partial X_j} \tag{3}$$

$$\frac{\partial n}{\partial t} + \frac{\partial}{\partial X_j}(U_j n + \overline{U_j' n'}) + \frac{\partial}{\partial m}[\psi(m,S)n] = D_o \frac{\partial^2 n}{\partial X_j \partial X_j}$$
$$+ G_1(m)\frac{\partial n}{\partial X_j} + \frac{1}{2}\int_{m*}^{m} b(m_1, m-m_1)n(m-m_1)n(m_1)\, dm_1$$
$$- n(m)\int_o^{\infty} b(m,m_1)n(m_1)\, dm_1$$
$$+ \frac{1}{2}\int_{m*}^{m} b(m_1, m-m_1)\overline{n'(m-m_1)n'(m_1)}\, dm_1$$

$$- \int_o^{\infty} b(m,m_1)\overline{n'(m)n'(m_1)}\, dm_1 \qquad (4)$$

$$\frac{\partial S}{\partial t} + \frac{\partial}{\partial X_j}(U_j S + \overline{U_j' S'}) = D_o \frac{\partial^2 S}{\partial X_j \partial X_j} - \frac{1}{C_v}\int_{m*}^{\infty} \psi n dm \qquad (5)$$

Equation (2) is the result of the Boussinesq approximation. Equations (1) to (5) are obtained by ensemble average of Reynolds decomposition. The terms with overbars are the covariances due to turbulent transport. To close the system of equations, it is necessary to approximate the covariances. First order closure leads to the K-theory model which is commonly used because of its simplicity. Second order and higher order closures require transport equations for the covariances and the parameterizations of higher correlation terms. Recent progress in second order closure models has been reported by Wyngaard (1980, 1982), Lumley et al. (1984) and Lumley (1985). Results by Lewellen et al. (1976, 1985) using Donaldson's second order closure model (1973) for the convective boundary layer are quite impressive. These successes are due to the fact that second order closure models retain more of the physics of turbulent diffusion.

Parallel to the development of second order closure models was the development of Large Eddy Simulation (LES). Deardorff (1972) and more recently, Moeng (1984) used LES, a volume average approach, to simulate unstable planetary boundary layers. Results from LES can be used for convective boundary layer parameterizations (Wyngaard et al. 1984a,b; Moeng and Wyngaard, 1984). The current state of the art for using LES is summarized by Wyngaard (1984). It is beyond doubt that second or higher order closure models and LES are superior to K-theory in describing atmospheric turbulence and turbulent diffusion. The disadvantage is that second order closure models and LES are computationally expensive. However, with the advent of supercomputers, these methods can be used to simulate the dispersion of aerosol obscurants in the atmospheric surface layer.

Our previous attempts for modeling aerosol plume dynamics were based on K-theory (Tsang and Brock, 1982a,b, 1983a). The mean wind profile (Panofsky, 1974) and eddy diffusivity profile (Smith, 1975) for neutrally stable atmospheric conditions were used for the simulations. Thus, only the solutions of Equations (4) and (5) were necessary. It is important to point out that, no matter what closure model we adopt, the transport equations [(2) to (5)] always contain advection terms (the second terms on the left hand side), diffusion terms (the first terms on the right hand side), a sedimentation term (the second

term on the right hand side of Equation (4)), coagulation terms (the integral terms on the right hand side of Equation (4)) and condensation/evaporation terms (the third term on the left hand side of Equation (4) and the integral term in Equation (5)). The molecular diffusion terms (the second order terms in Equations (2) to (5)) are orders of magnitude smaller than the turbulent fluxes (terms with overbar) and are usually neglected. In the following, we proceed to discuss the numerical techniques for these processes.

NUMERICAL TECHNIQUES FOR ADVECTION

The advection equation for a gaseous pollutant or aerosols is deceptively simple,

$$\frac{\partial C}{\partial t} + U_j \frac{\partial C}{\partial X_j} = 0 \qquad (6)$$

The low order finite difference (upwinding or donor cell) method and the finite element method (Petrov-Galerkin) give numerical diffusion manifested by lowering of the peak concentration or smearing of the front, whereas higher order methods give rise to numerical dispersion manifested by unphysical oscillations around the true solution. Because of its importance in air pollution modeling, numerous attempts have been made toward the numerical solution of Equation (6). In this paper, we do not attempt to review the current status of progress in this area. Instead, we will only mention recent tests of different numerical techniques for the advection problem.

Using the rotation of a cosine hill as a test problem, Chock and Dunker (1983) compared a flux correction method, a multidimensional flux-correction method, an orthogonal-collocation method, a second moment method, a pseudospectral method and the Chapeau-function method. They recommended the Chapeau method (finite element method with linear basis function) and multidimensional flux-correction methods. The same test problem was used by Long and Pepper (1981). They found after one revolution the Chapeau function could maintain the peak value of the cosine hill very well (99%) but the magnitude of the most negative value was about 10% of the peak concentration. In more recent tests by Chock (1985), the combination of the Forester method with the Chapeau function was recommended. For other test problems, Pepper and Cooper (1983) recommended the use of method of moments. In general, the pseudospectral method and the method of moments can give very accurate solutions, but they require longer computing time.

For modeling the dispersion of aerosols from a crosswind line source or a point source, we compared the finite-element method with the linear-basis function (Chapeau function), Petrov-Galerkin finite-element method, Fromm's method (1968), Van Leer's method (1974), McDonald's method (1984) and Smolarkiewicz's method (1984). The la t two methods are positive definite. Positive definite methods are attractive because they minimize the nonlinear instability problem which we may encounter if

condensation/evaporation and coagulation processes are included in the calculations. Figure 1 shows that the second order finite difference method and the Galerkin finite element method with linear basis function give severe numerical dispersion. Such dispersion can be greatly reduced by the Petrov-Galerkin method as shown in Figure 2. However, the front was smeared due to numerical diffusion. It is also obvious that Fromm's method, through greatly reducing numerical dispension, creates overshoot and undershoot which are about 4 to 6% of the peak value. Van Leer's method, which is a modification of Fromm's method, eliminates the overshoot and undershoot. Also, the dispersion level ahead of the front is orders of magnitude smaller than that from Fromm's method. This is very desirable property because it greatly reduces the possibility of a non-linear instability problem. Smolarkiewicz's method gives the same results as Van Leer's method. For the advection of a square wave, as shown in Figure 3, Fromm's method creates overshoots and undershoots whereas Smolarkiewicz's method creates an overshoot. McDonald's method distorts the shape of the distribution. Van Leer's method appears to give the most satisfactory result. Figure 4 shows the results for advection of a triangular wave. Most methods can maintain 93 to 96% of the peak value whereas Petrov-Galerkin method only retains 82% of the peak value. From these tests, we choose Smolarkiewicz's method and Van Leer's method for advection in the two dimensional crosswind-line-source problem and three-dimensional point-source problem. For simulation of a crosswind line source, Van Leer's method gives accurate steady state profiles for the test problem used in Tsang and Brock (1982a) but Smolarkiewicz's method fails because of the negative numbers created by vertical diffusion. These negative numbers usually appear at high altitudes, and the concentrations are several orders of magnitude smaller than those near the source height. (They can be removed if we use more grid points to model vertical diffusion.) However, the magnitude of these negative numbers increases drastically during the course of simulations using Smolarkiewicz's method, and the numerical results become meaningless. Furthermore, Smolarkiewicz's method can only give accurate results with small grid sizes. For the problem of the rotation of a cosine hill used by Long and Pepper (1981), Smolarkiewicz's method can give positive definite distributions with peak values of 97%, 82% and 43% of the initial distribution when grid systems of (97 × 97), (67 × 67) and (34 × 34) are used respectively. It must also be mentioned that Van Leer's method is 2 to 4 times faster than Smolarkiewicz's on the IBM 3081 for a variety of problems.

For dispersion of an aerosol from a point source, the transport equation is as follows,

$$\frac{\partial N}{\partial t} + U(Z)\,\frac{\partial N}{\partial X} = \frac{\partial}{\partial Z}\left[K_Z(Z)\,\frac{\partial N}{\partial Z}\right] + K_H\left[\frac{\partial^2 N}{\partial Y^2}\right] \tag{7}$$

$$N = \frac{q_p}{U}\,\delta\,(y - y_S)\,\delta\,(Z - Z_S) \qquad \text{at} \qquad x = 0 \tag{8}$$

AD-A173 878 PROCEEDINGS OF THE SCIENTIFIC CONFERENCE ON OBSCURATION 2/7
AND AEROSOL RESEA (U) KOHL (RONALD H) AND ASSOCIATES
TULLAHOMA TN R H KOHL JUL 86 CRDEC-SP-86019
UNCLASSIFIED DAAG29-81-D-0100 F/G 20/6 NL

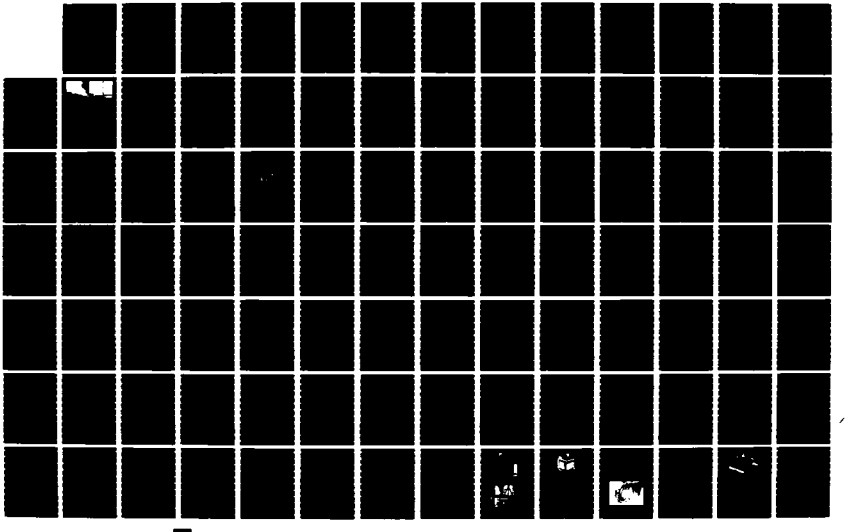

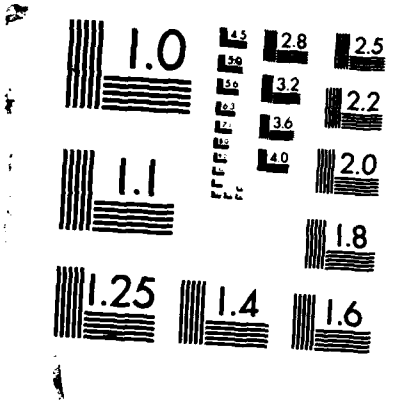

where N is the number concentration of aerosols. We use Van Leer's method for advection in the X direction, and orthogonal collocation on finite elements in the crosswind and vertical directions. To test the reliability of our algorithm, we assume constant wind speed and diffusivities and compare our numerical results with analytical solution. Figure 5 shows the transient solutions at downwind distances of 200, 500 and 1000 m. It also shows that our numerical results for the steady state concentration profile compare extremely well with the analytical solution. Figure 6 compares the results for the spread of the plume at different downwind distances. At this point, it is worthwhile to mention that it is a common practice to approximate a point source numerically as,

$$N_1 = \frac{q_p}{U\Delta Y\Delta Z} \tag{9}$$

where ΔY and ΔZ are grid sizes in Y and Z directions. Thus, the effective point source concentration N_1 depends on grid sizes. This approximation greatly affects the numerical results at downwind distances. The crucial question is what ΔY and ΔZ we should choose in order to give a reliable solution. We have a new method to approximate the point source which is independent of ΔY and ΔZ. The method will be reported elsewhere.

Having established the reliability of our computer model, we will proceed to use realistic wind and diffusivity profiles to simulate the dispersion of aerosols in the atmosphere. The results will be reported in the next CRDC conference.

NUMERICAL TECHNIQUES FOR DIFFUSION

Finite difference, finite element and orthogonal collocation methods are commonly used for the diffusion terms in Equation (6). In our work, we use orthogonal collocation on finite elements for horizontal and vertical diffusion. It has the flexibility of the finite element method and the accuracy of the orthogonal collocation method. The details of the method were described in Tsang and Brock (1982a) and will not be repeated here.

NUMERICAL TECHNIQUES FOR CONDENSATION/EVAPORATION

The dynamic behavior of the growth of Knudsen aerosols by condensation and evaporation has been a long-standing problem. Most existing works do not include evaporation and consider pure growth by condensation at constant vapor concentration. In practice, evaporation must be included because of the Kelvin effect which is especially important for submicrometer aerosol particles. Constant vapor concentration during condensational growth is hardly realized and must be considered as an exception, rather than a rule. For the case of variable vapor concentration, no theory is available except for a mass-conserved system. Recently, Tsang and Brock (1983b, 1984) developed a numerical scheme to solve

this problem. The details of the numerical scheme were reported in Tsang and Brock (1983b, 1984) and will not be repeated here. Figure 7 shows the effectiveness of this numerical scheme for ultrafine Knudsen aerosol growth by condensation/evaporation. The aerosol mass increased almost 170 times its initial value of 2×10^{-7} g/cc within 5×10^{-5} sec, while the supersaturation ratio decreased from 10 to 1.344. The total mass is conserved with only 0.0087% deviation from its initial value. The number density function is shown to approach a delta function during this transitional growth period. For such distributions with extremely steep gradients, Eulerian numerical schemes, such as the traditional finite element and finite difference methods with fixed grid points, will not do. The numerical scheme also has the capability of self-adapting the mesh locations to account for such steep gradients. This is a very desirable property for problems with variable condensation/evaporation rates which change many orders of magnitude between the smallest particle and the largest particle.

NUMERICAL TECHNIQUES FOR COAGULATION

The dynamic behavior of Brownian coagulation of Knudsen aerosols was simulated by Middleton and Brock (1976) and Suck and Brock (1979). More recent study (Seigneur et al., 1985) for comparison of different numerical schemes for Brownian coagulation proves that the J-space approach by Brock and his associates is accurate and fast. Gear's method (DGEAR in IMSL library) was used as the time integrator in Seigneur's study. The subroutine was written by Hindmarsh in 1973. A recent version of Gear's method, also written by Hindmarsh, is now available as Livermore's ODE solver. We now use this new version of Gear's method (LSODE) for time integration. For a variety of coagulation problems, it is three to five times faster than the Gear's method in the IMSL library. The J-space transformation technique for coagulation was reported in detail in Suck and Brock (1979) and will not be repeated here.

SIMULATION OF AEROSOL DYNAMICS ON A VECTOR SUPERCOMPUTER

From the discussion in previous sections, it is clear that aerosol plume dynamics presents itself as a large scale simulation problem. The availability of supercomputers such as Cyber 205, Cray-1, Cray XMP and Cray-2 will enhance our understanding of aerosol plume dynamics. Depending on the problems, these supercomputers, when executing a "vectorized" program, can be an order of magnitude faster than the common mainframe computers such as IBM 3081 and Cyber 175. To take advantage of the speed of these supercomputers, it is important to know the numerical algorithms used so as to "vectorize" all the inner DO loops in the program. A scalar computer program run on these supercomputers is only about two times faster, simply because the scalar speed of Cray-1 or Cyber 205 is about twice that of IBM 3081.

Currently, we have vectorized all the inner DO loops for subroutines used for condensation/ evaporation and coagulation. Significant savings in computing time results from "vectorization". For example, in the simulation of aerosol growth by simultaneous processes of coagulation, condensation and evaporation in a mass-conserved system, vectorization in the subroutine for calculating the integrals for coagulation (using a vectorized version of Runge-Kutta integration) results in a reduction of CPU time from 380 seconds to 80 seconds. Use of LSODE as the time integrator further reduces the CPU time to less than 30 seconds.

Details of vectorization techniques for aerosol growth processes will be reported in a future publication (Hippe and Tsang, 1985). Numerous case studies of the dynamics of aerosol growth in the free molecular regime will also be published elsewhere (Hippe and Tsang, 1986).

FUTURE WORK

We will continue the work on the dispersion of a volatile aerosol plume from a point source and on the vectorization of numerical methods used in the simulation.

REFERENCES

Chock, D.P., and Dunker, A.M. (1983). Atmos. Environ., 17, 11-24.

Chock, D.P. (1985). Atmos. Environ., 19, 571-586.

Deardorff, J.W. (1972). J. Atmos. Sci., 29, 91-115.

Donaldson, C. (1973). In "Workshop on Micrometeorology," (D.A. Haugen Ed.). Amer. Meteorological Soc., Boston.

Fromm, J.E. (1968). J. Comp. Phys., 3, 176-189.

Hippe, J., and Tsang, T.H. (1985). "Simulation of Aerosol Growth Processes on a Vector Supercomputer," (Submitted to J. Aerosol Sci.).

Hippe, J., and Tsang, T.H. (1986). "Dynamics of Ostwald Ripening with Coalescence for Aerosols in Free Molecular Regime," (Submitted to Aerosol Sci. and Technology).

Lewellen, W.S., and Teske, M.E. (1976). Boundary Layer Meteorology, 10, 69-90.

Lewellen, W.S., Sykes, R.I., and Parker, S.F. (1985). J. Atmos. Sci., 42, 1084-1085 (1985).

Long, P.E., and Pepper, D.W. (1981). J. Appl. Meteoro., 20, 146-156.

Lumley, J.L., and Mansfield, P. (1984). Boundary Layer Meteorology, 30, 109-142.

Lumley, J.L. (1985). In "Frontiers in Fluid Mechanics," (S.H. Davis and J.L. Lumley Eds.). Springer-Verlag, N.Y.

McDonald, B.E., and Ambrosiano, J. (1984). J. Comp. Phys., 56, 448-460.

Middleton, P., and Brock, J.R. (1976). J. Colloid and Interface Sci., 54, 249-264.

Moeng, C.H. (1984). J. Atmos. Sci., 41, 2052-2062.

Moeng, C.H., and Wyngaard, J.C. (1984). J. Atmos. Sci., 41, 3161-3169.

Panofsky, H.A. (1974). Annual Review of Fluid Mech., 6, 147-177.

Pepper, D.W., and Cooper, R.E. (1983). Atmos. Environ., 17, 1881-1895.

Seigneur, C., Seinfeld, J.H., Whitby, K.T., Whitby, E.R., Brock, J.R., and Barnes, H.M. (1986). Submitted to Aerosol Sci. and Technology.

Smith, F.B. (1975). Sci. Prog., Oxf., 62, 127-151.

Smolarkiewicz, P.K. (1984). J. Comp. Phys., 54, 325-362.

Suck, S.H., and Brock, J.R. (1979). J. Aerosol Sci., 10, 581-590.

Tsang, T.H., and Brock, J.R. (1982a). Atmos. Environ., 16, 2229-2235.

Tsang, T.H., and Brock, J.R. (1982b). Applied Optics, 21, 1588-1592.

Tsang, T.H., and Brock, J.R. (1983a). Aerosol Sci. Technology, 2, 429-436.

Tsang, T.H., and Brock, J.R. (1983b). Aerosol Sci. Technology, 2, 311-320.

Tsang, T.H., and Brock, J.R. (1984). Aerosol Sci. Technology, 3, 283-292.

Van Leer, B. (1974). J. Comp. Phys., 14, 361-370.

Wyngaard, J.C. (1980). In "Turbulent Shear Flows 2," (L.J.S. Bradbury et al., ed.). Springer-Verlag, N.Y.

Wyngaard, J.C. (1982). In "Atmospheric Turbulence and Air Pollution Modelling," (F.T.M. Nieuwstadt and H. Van Dop, ed.). Reidel Publishing Company, Boston.

Wyngaard, J.C. and Brost, R.A. (1984a). J. Atmos. Sci., 41, 102-112.

Wyngaard, J.C. (1984b). J. Atmos. Sci., 41, 1959-1969.

Wyngaard, J.C., Ed., (1984). DTIC, AD-A146381.

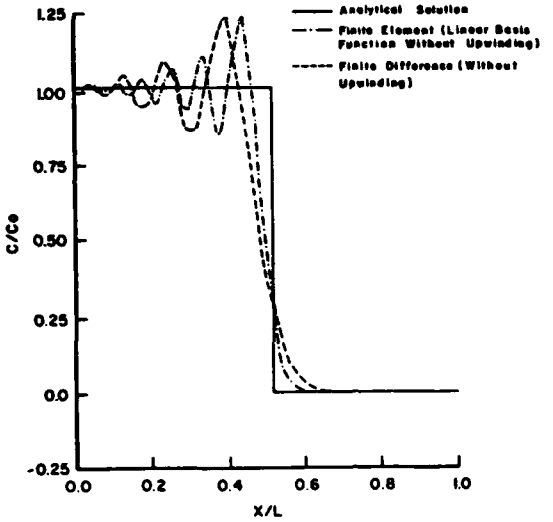

Figure 1. Numerical Results from Finite Difference and Finite Element Method for Advection of a Boundary Source.

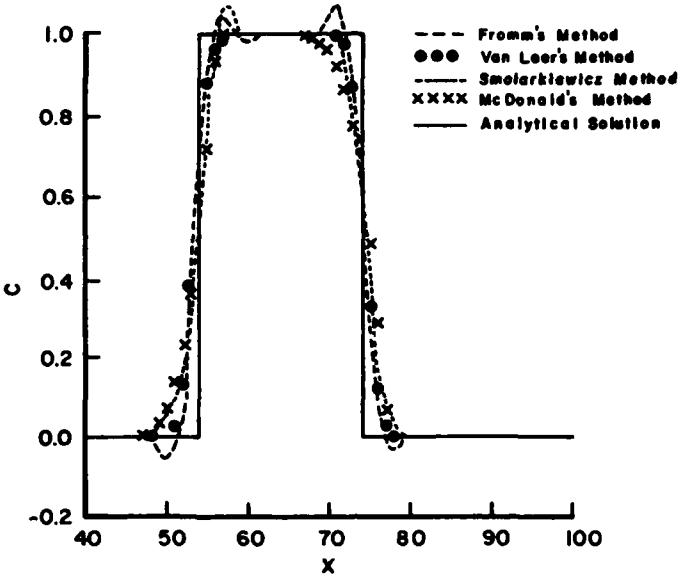

Figure 3. Comparison of Numerical Methods for Advection of a Square Wave.

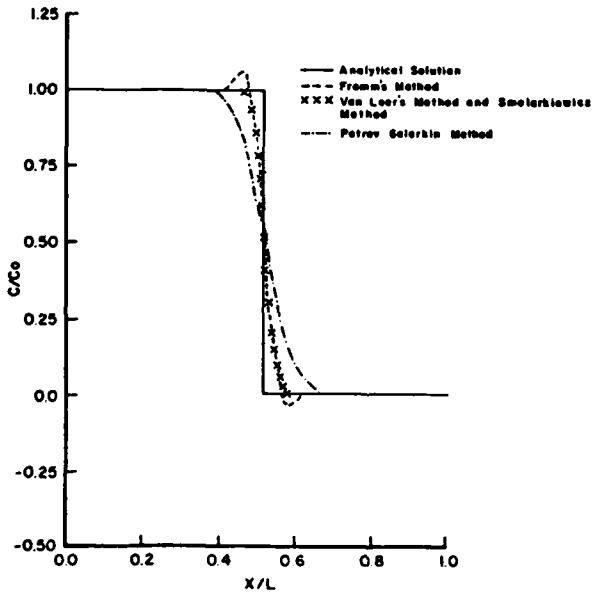

Figure 2. Comparison of Methods Which Reduce Numerical Dispersion.

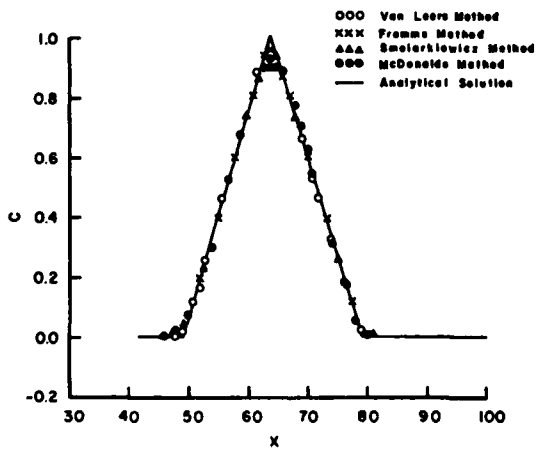

Figure 4. Comparison of Numerical Methods for Advection of a Triangular Wave.

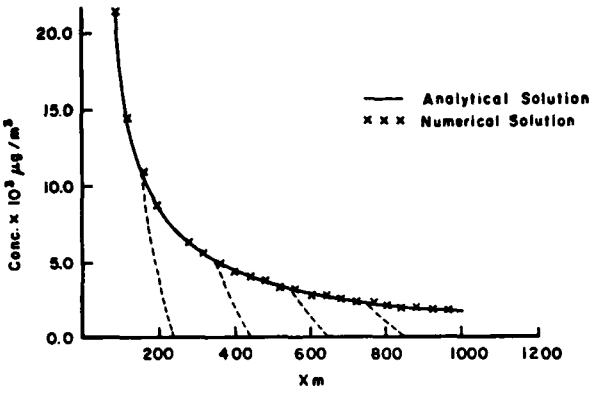

Figure 5. Transient and Steady State Concentration Profiles at Source Height for the Dispersion of Aerosols from a Point Source (Three-Dimensional Simulation).

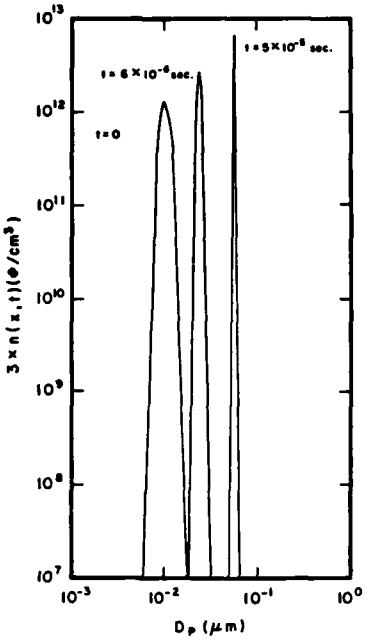

Figure 7. The Change of Number Density Function with Time of an Ultrafine Aerosol Undergoing Condensation of a Highly Supersaturated Vapor.

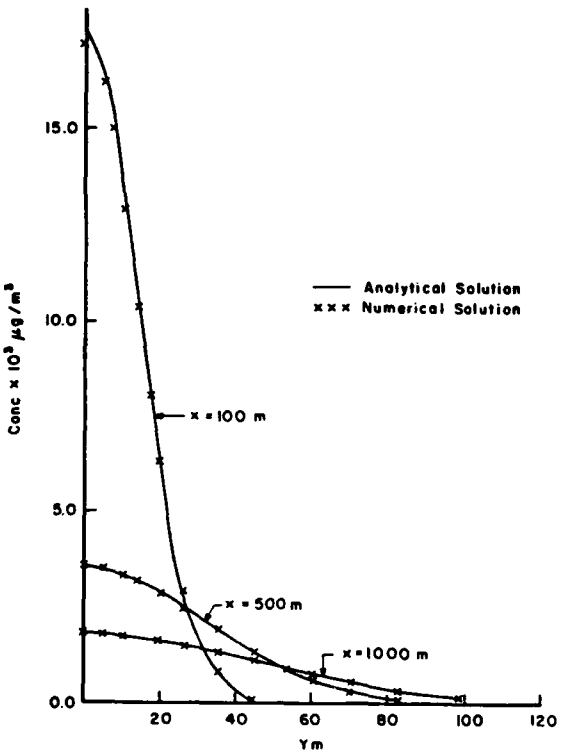

Figure 6. Crosswind Concentration Profiles at Different Downwind Distances

DISPERSION OF THERMAL AND CHEMILUMINESCENT AEROSOL PLUMES

J. R. Brock
Chemical Engineering Department
University of Texas
Austin, Texas. 78712

ABSTRACT

As part of work under Contract DAAK11-83-K-0006, a preliminary analysis has been made of thermal and chemiluminescent aerosol plumes propagating in the atmosphere. It is assumed that the particles in the plume are the sites for thermal or chemiluminescent chemical reactions. For thermal reactions, the plume is heated above ambient conditions. Chemiluminescent reactions may produce heating of the plume as well as emission of electromagnetic radiation. The coupled conservation equations for particles and energy are developed for atmospheric plumes from a crosswind line source. A few examples are given from numerical solution of these equations.

INTRODUCTION

Some interest has been expressed in the past (e.g. R. A. Mackay, CRDC Obscuration and Aerosol Research Conference Proceedings, 1981) in the production of infrared radiation above normal background levels by means of exothermic reactions occurring in particles. This concept, if feasible, could lead to smokes with improved screening efficiency in the infrared. In this concept, one recognizes two boundary cases. One, termed here thermal reactions (TR), results only in heating of the plume with attendant thermal radiation. The other, termed here chemiluminescent reactions (CR), results primarily in emission of em radiation from plume particles. CR are known with high quantum efficiency. For example it has been reported that the reaction of luciferin produces one photon for each molecule of luciferin reacted.

In this note the characteristics of smoke plumes dispersing in the atmosphere in the TR and CR cases are examined theoretically. First the theory for the dispersion of a plume in the TR and CR cases is developed. Then these equations are solved numerically and a result for each case is presented.

THEORY

The following definitions and assumptions are introduced in the development of a model for atmospheric dispersion of thermal and chemiluminescent plumes from a steady crosswind line source.

1. A particle in the plume contains c^* moles of reactant per unit volume of the particle. c^* is assumed to be independent of particle size but not of the dynamical processes operating in the plume.
2. The total moles of reactant, c, in unit volume of host gas is:

$$c = \int c^* v n(v) dv = c^* V$$

where v is the volume of a particle, V is the total volume concentration of particles in the plume, and $n(v)dv$ is the number of particles having volumes in the range v, dv at some point in space. Changes in V due to reaction are assumed to be negligible.

3. Inside a particle, reaction occurs by a pseudo-first order reaction:

$$dc^*/dt = -kc^*$$

4. First order closure is assumed for all conservation equations in simulation of atmospheric dispersion. Particles and gases have the same eddy diffusivities, K.

5. Particles have a deposition velocity at the surface given by the parameterization of Sehmel and Hodgson. A mean value is used for the particles determined from the particle size distribution. Gases have deposition velocities of zero.

With these restrictions, the reactant concentration, c, and particle volume concentration, V, obey the following conservation laws for dispersion in the atmosphere:

$$U(x,z)\partial c/\partial x = \partial/\partial z(K\partial c/\partial z) - kc/V \quad (1)$$

$$U(x,z)\partial V/\partial x = \partial/\partial z(K\partial V/\partial z) \quad (2)$$

where $U(x,z)$ is the mean wind speed at height z above the surface at downwind distance x from the source. Eqs. (1) and (2) are subject to the usual boundary conditions:

$$\partial c/\partial z = \partial V/\partial z = 0 \quad , \quad z = H \quad (3)$$

and

$$\begin{aligned} K\partial c/\partial z &= -wc \quad , \quad z = 0 \\ K\partial V/\partial z &= -wV \quad , \quad z = 0 \end{aligned} \quad (4)$$

where H is the mixing height and w is an average deposition velocity for the distribution of particles.

In the general case, chemical reaction in a particle results in emission of radiation as well as thermal heating of the particle. The thermal energy from the reaction is transferred by thermal radiation and conduction to the host gas. From the energy conservation equation, the following relation may be derived for the temperature of the host gas:

$$\rho \hat{C}_p U(x,z)\,\partial T/\partial x = \partial/\partial z(K_H\,\partial T/\partial z) + kc\,H_{RXN} \quad (5)$$

where ρ is the density and $\hat{C}_p$ the specific heat capacity of the host gas. K_H is the thermal eddy diffusivity. H_{RXN} is the heat of reaction per mole of reactant. The boundary conditions for eq. (5) are:

$$\partial T/\partial z = 0 \quad , \quad z = H$$

$$K_H\,\partial T/\partial z = g(T - T_s) \quad , \quad z = 0$$

where g is a heat transfer coefficient between the host gas at temperature $T(z=0)$ and the surface at temperature T_s.

With the usual assumption of quasi-stationarity and the mean field approximation, the temperature distribution in a particle, $T_p(r)$, is given in terms of the temperature of the host gas:

$$T_p(r) = -\hat{Q}\, r^2/6\, k_p + (\hat{Q}\, R_p^2/6)(2/k_g + 1/k_p) + T$$

where $\hat{Q} \equiv k\, c^*\, H_{RXN}$. The radial position inside a particle is r and R_p is the radius of the particle. The thermal conductivities of the particle and host gas are k_p and k_g, respectively.

In these equations for c, V and T, wind speed is given in terms of the power law:

$$U(z) = U_s(z/h_s)^{\alpha}$$

where U_s, h_s and α are parameters for a particular meteorological condition. Eddy diffusivity is given by the parameterization:

$$K(z) = K_s(z/h_s)\exp(-b\,(z-h_s)/H)$$

K_s and b are additional parameters.

For a crosswind line source, the source strengths for c and V are:

$$c(0,h) = (q_c/U(h))\,\delta(z-h)$$
$$V(0,h) = (q_v/U(h))\,\delta(z-h)$$

where h is the source height and q_c and q_v are the source strengths.

It is convenient to introduce dimensionless variables:

$$\tilde{x} = x/H \quad , \quad \tilde{z} = z/H \quad , \quad \tilde{c} = c\,U(h)/q_c \quad , \quad \tilde{V} = V\,U(h)/q_v$$

$$\tilde{T} = (T - T_o)/T_o \quad , \quad \tilde{U} = U/U_s \quad , \quad \tilde{K} = K/K_s$$

where T_o is a reference temperature (that outside the plume, for example). With these definitions eqs. (1), (2), and (5) become:

$$\tilde{U}\,\partial\tilde{c}/\partial\tilde{x} = \kappa(\partial/\partial\tilde{z})(\tilde{K}\,\partial\tilde{c}/\partial\tilde{z}) - E\,\tilde{c}/\tilde{V} \qquad (6)$$

$$\tilde{U}\,\partial\tilde{V}/\partial\tilde{x} = \kappa(\partial/\partial\tilde{z})(\tilde{K}\,\partial\tilde{V}/\partial\tilde{z}) \qquad (7)$$

$$\tilde{U}\,\partial\tilde{T}/\partial\tilde{x} = \kappa(\partial/\partial\tilde{z})(\tilde{K}\,\partial\tilde{T}/\partial\tilde{z}) + Q\,\tilde{c} \qquad (8)$$

with corresponding dimensionless boundary conditions. Here:

$$E = k\,U(h)\,H/q_v U_s \qquad (9)$$

$$Q = k\,H_{RXN} q_c H/U_s \rho\, \hat{C}_p\, U(h)\, T_o \qquad (10)$$

A dimensionless deposition velocity is also used: $\tilde{w} = H\,w/K_s$

DISCUSSION

Eqs (6), (7) and (8) are a coupled set of nonlinear equations. Analytical solution does not appear to be convenient. Numerical solutions are, however, readily obtained. Accuracy of the numerical solutions can be partially verified through assumption of constant U and K with a perturbation solution.

Two limiting cases are considered here. In one (TR) the chemical reaction in the particle only produces thermal energy. In the other, (CR) the reaction only results in emission of em radiation with no thermal energy. In the case of TR the reaction tends to heat the entire plume to temperatures above ambient. For CR, the temperature of the plume is constant (neglecting heating by the source generator).

For chemiluminescent reactions, one can define a radiation emission term: $R = \phi\, k\, c^*$ where ϕ is the quantum efficiency. For the CR limit, $\phi = 1$. In dimensionless form :

$$\tilde{R} = \ln(R /(\kappa \nu \phi \; N k q_c / U(h)))$$

Figs 1 and 2 show examples of the two limiting cases, TR and CR . In both figures, with reference to eqs.(6)-(8), parameter values have been set as: $\kappa = 0.002$, $E = 1$, $\tilde{w} = 0.033$. Parameters for wind speed and eddy diffusivity have been set from measurements taken at Cape Canaveral , Florida.

In these figures, the values shown as $\tilde{T}$ are the dimensionless temperatures $\tilde{T} = (T-T_o)/T_o$, where T_o is the ambient temperature. $\tilde{T}$ therefore represents net heating of the plume by the chemical reaction. The values $Q = 1$ and $E = 1$ in Figs. 1 and 2 represent relatively large source strengths for their practical realization, as can be noted from eqs.(9) and (10). There is a marked (and expected) contrast between Figs. 1 and 2. Since $\tilde{R}$ is defined as a logarithm of the emission term, it is clear from Fig. 2 that emission from the CR plume rapidly decreases with downwind distance . Since the thermal energy is, however, conserved by the plume, except for exchange with the surface, the plume remains "hot" in the TR case for relatively large downwind distances.

For certain obscuration purposes, the TR and CR plumes may have utility. While it is relatively simple to develop the theory, practical realization of such plumes will require considerable work.

ACKNOWLEDGMENT

Work performed here was supported under Contract DAAK11-83-K-0006 from Chemical Research & Development Center, U. S. Army. The advice and assistance of Dr. Edward W. Stuebing and Dr. Glenn O. Rubel of the Chemical Research & Development Center are gratefully acknowledged.

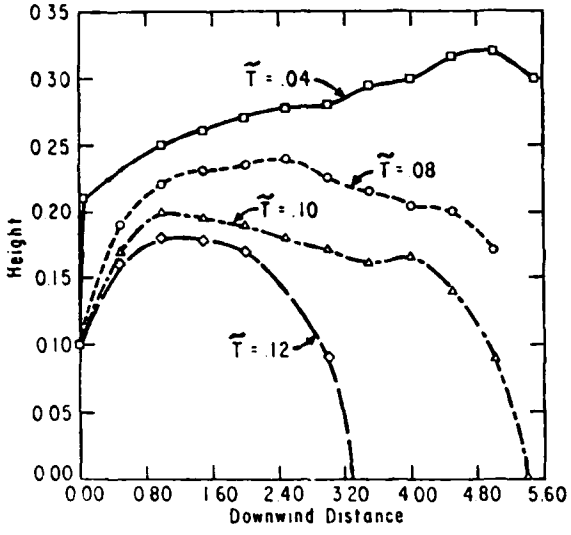

Figure 1. TR plume showing dimensionless height above surface versus dimensionless downwind distance with dimensionless temperature as parameter. Parameters: κ =0.002, Q=E= 1.0 , $\tilde{w}$ = 0.033

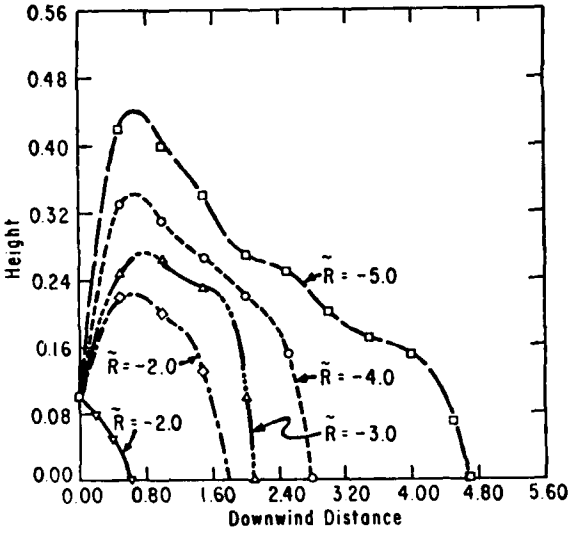

Figure 2. CR plume showing dimensionless height above surface versus dimensionless downwind distance with dimensionless em radiation energy emission as parameter. Parameters: κ = 0.002 , Q=0 , E=1.0 , $\tilde{w}$ = 0.033

DIFFUSION IN AN ATMOSPHERIC LAYER WITH AN ELEVATED INVERSION

M. Poreh and J. E. Cermak
Fluid Dynamics and Diffusion Laboratory
Colorado State University
Fort Collins, CO 80523

RECENT PUBLICATIONS AND PRESENTATIONS:

A. M. Poreh and J. E. Cermak (1985), Wind Tunnel Research on the Mechanics of Plumes in the Atmospheric Surface Layer (Part II). Fluid Dynamics and Diffusion Laboratory, Department of Civil Engineering, Colorado State University, Fort Collins, CO 80523, Report CER84-85MP-JEC47.

B. M. Poreh and J. E. Cermak (1985), Study of Neutrally Buoyant Plumes in a Convective Boundary Layer with Mean Velocity and Shear. AMS, Seventh Symposium on Turbulence and Diffusion, Nov. 1985, Boulder, CO, Report CEP85-86MP-JEC3.

ABSTRACT

This paper describes a simulation of neutrally buoyant gas diffusion from ground level and elevated sources within a convective boundary layer (CBL) below an elevated inversion. Future work includes simulation of negatively and positively buoyant plumes in neutrally stratified atmospheric surface layers.

DESCRIPTION OF THE WIND-TUNNEL SIMULATION

The experiments were made in the Meteorological Wind Tunnel at Colorado State University. A new wind-tunnel configuration was used which made it possible to produce a temperature gradient in the stable region above the CBL of 60°C/m, much larger than the gradient in the previous study in the same tunnel by Poreh and Cermak [1984]. The average height of the inversion base was 0.40 m and the average heat flux was $\overline{\omega'\theta'}$ = 0.3 C° m/sec.

EXPERIMENTAL RESULTS

The study, like previous laboratory and numerical simulations, revealed the unique nature of diffusion of neutrally buoyant plumes in a CBL. Figure 1 shows the cross wind integrated concentrations of plumes from sources at different heights. The dimensionless distance is $x^* = xw^*/(hU)$, where h is the thickness of the CBL, $w^* = (hg\overline{w'\theta'}/\theta)^{1/3}$ is the characteristic convective velocity, and U is the average mean velocity within the layer. The results seem rather surprising, as the "average trajectories" of plumes from ground-level sources appear to cross the average trajectories from elevated sources. Moreover, the ground-level concentrations at $1.0 < x^* < 1.5$ from elevated sources were found to be many times larger than ground-level concentrations from similar ground-level sources, as can be seen from this figure.

The cause for this unique diffusion pattern is the thermal-dominated structure of the CBL. Heat flux from the warm ground is mostly in the form of hot thermals which rise at relatively high velocities. To balance this mass flux, the cool air around the thermals descends toward the ground at a relatively low speed. This is manifested in the measured skewed probability-density distribution (pdd) of both the velocity fluctuations and the temperature fluctuations measured at z/h = 0.2. The negative mode of the pdd indicates that most of the time the air at a given point flows downward. Flow visualization of a developing strong CBL in a neutral atmosphere is shown in Fig. 2(a). Figure 2(b) shows a smoke filament emitted from a source outside the layer. The photographs show clearly that the smoke filament is carried by the cool air toward the hot floor, while the air heated by the floor rises in the form of thermals.

Recent field experiments compiled by Briggs [1984] are shown in Figs. 3 and 4 together with the results of the present simulation, using dimensionless representation. The field and laboratory data are generally in good agreement, except at larger values of x^* where the wind-tunnel inversion became weak.

REFERENCES

Briggs, G. A.: 1984, Diffusion Modeling with Convective Scaling and Effects of Surface Inhomogeneities, AMS Specialty Conference on Air Quality Modeling of the Urban Boundary Layer, Baltimore, MD.

Cermak, J. E.: 1981, Wind Tunnel Design for Modeling of Atmospheric Boundary Layer, J. of Eng. Mech. Div., ASCE 107, No. EM3, pp. 623-642.

Deardorff, J. W. and G. E. Willis: 1975, A Parameterization of Diffusion into the Mixed Layer, J. Appl. Meteo. 14, pp. 1451-1458.

Poreh, M. and J. E. Cermak: 1984, Wind Tunnel Simulation of Diffusion in a Convective Boundary Layer, 29th OHOLO Biological Conference, Zichron Ya'Acov, Israel. Boundary Layer Meteorology, Vol. 30, pp. 431-455.

Poreh, M. and J. E. Cermak: 1985, Wind Tunnel Research on the Mechanics of Plumes in the Atmospheric Surface Layer (Part II), Fluid Dynamics and Diffusion Laboratory, Department of Civil Engineering, Colorado State University, Fort Collins, CO 80523, CER84-85MP-JEC47

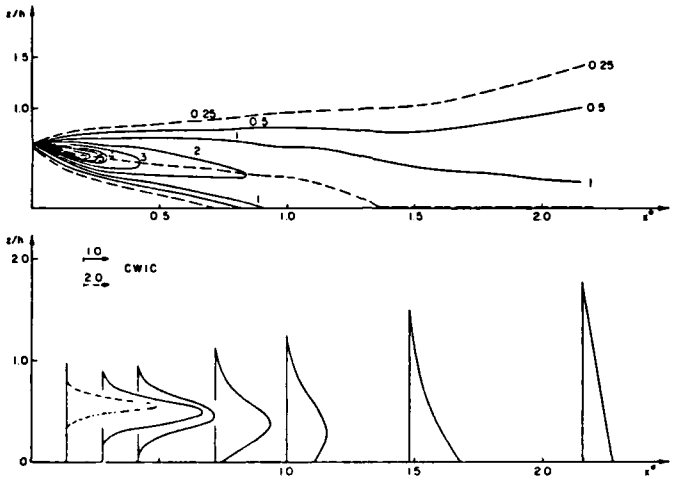

(a) Elevated source ($z^S/h = 0.61$)

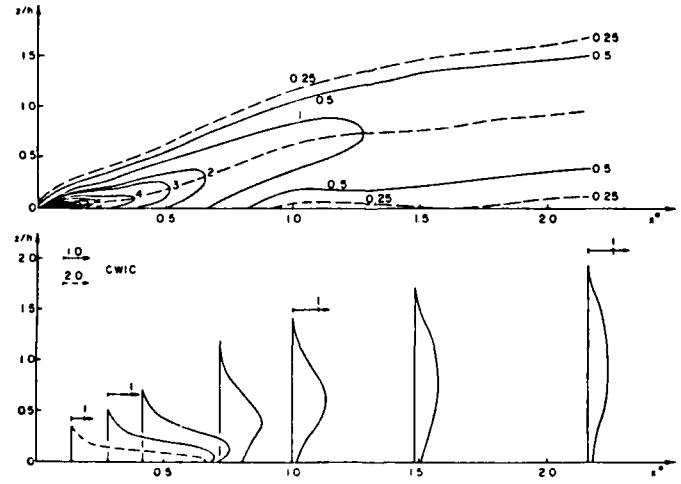

(b) Ground-level source ($z^S/h = 0.0175$)

FIGURE 1. Measured dimensionless cross-wind integrated concentrations for (a) an elevated source and (b) a ground-level source.

WIND TUNNEL SIMULATION OF A PARTICLE PLUME WITH APPRECIABLE SETTLING VELOCITIES IN A NEUTRALLY STRATIFIED ATMOSPHERIC SURFACE LAYER

M. Poreh and J. E. Cermak
Fluid Dynamics and Diffusion Laboratory
Colorado State University
Fort Collins, CO 80523

RECENT PUBLICATIONS:

M. Poreh, J. E. Cermak: Wind Tunnel Research on the Mechanics of Plumes in the Atmospheric Surface Layer (Part III). Fluid Dynamics and Diffusion Laboratory, Dept. of Civil Engineering, Colorado State University, Fort Collins, CO 80523, Report CER84-85MP-JEC48, May 1985.

ABSTRACT

This paper summarizes a study of diffusion and deposition of particles with appreciable settling velocities, V_g, and small Froude numbers $V_g^2/(gh)$, where h is the height of the source from the ground, in a neutrally stratified boundary layer.

Future work on aerosol plume dynamics includes: simultaneous measurements of particle and tracer plumes, measurements of instantaneous characteristics of plumes such as obscuration intermittency.

INTRODUCTION

The motion, diffusion in the atmospheric surface layer and deposition on the ground of particles are complex phenomena governed by numerous factors. See, for example, Csanady [1955], Godson [1958], and Overcamp [1976]. This work is a preliminary attempt to simulate these phenomena in a Meteorological Wind Tunnel, as has been successfully accomplished for simulation of atmospheric dispersion of passive plumes (Cermak, 1971; Poreh and Cermak, 1984). The study has focused on monodispersed particles with appreciable relative fall velocity to mean wind velocity, $0.04 < V_g/U < 0.1$, and small Froude number, $V_g^2/(gh) < 0.03$. Such particles are expected to have a sufficiently small response time constant and to respond to most turbulent eddies that determine the diffusion process. In addition their deposition velocity V_d is V_g. This eliminates many factors from the analysis, which otherwise affect the above phenomena, and makes it easier to evaluate the effect of other factors.

THEORETICAL CONSIDERATIONS

The longitudinal deposition of monodisperse particle plumes with a given V_g, has been estimated theoretically using the Gaussian prediction for a passive plume,

$$C^y(x,z) = \frac{Q}{\sqrt{2\pi}\,\sigma_z U} \exp\left[-\frac{(h-z)^2}{2\sigma_z^2}\right] , \qquad (1)$$

where C^y is the cross-wind integrated concentration. It is assumed that for the considered range of relative fall velocities and Froude numbers, the probability $P(x)dx$, that a particle with V_g will be deposited in a uniform velocity field $u = U$ between x and $x+dx$ is equal to the probability that a passive particle at the same distance passes between $z = V_g x/U$ and $z+dz$, where $dz = V_g\, dx/U$. Taking into consideration that in a mean horizontal velocity field, where $u(z)/U(h) = (z/h)^m$, plumes with $\sigma_z \to 0$ should converge at $x = hU/[(1+m)V_g]$, it is proposed that:

$$P(x^*) = \frac{(1+m)\,V_g h}{\sqrt{2\pi}\,U\,\sigma_z} \exp\left[-\frac{(1-\frac{(1+m)\,V_g\,x^*}{U})^2}{2(\sigma_z/h)^2}\right] \qquad (2)$$

where $x^* = x/h$ and $\int P(x^*)dx^* = 1$. Typical dimensionless distributions of $P(x^*)$ are plotted in Figs. 1 and 2 for different h/δ and V_g/U, where δ is the boundary layer thickness.

THE EXPERIMENTAL PROGRAM

Expanded polystyrene particles supplied by the Arco Chemical Co. at Newport, PA, with fall velocities of the order of 0.3 m/sec, were used in the study. The particles were classified by aerodynamic separation into groups with equal fall velocities ±10 percent. At each run a few thousand particles were emitted from sources at either h = 0.5 m or 0.375 m in a wind-tunnel turbulent boundary layer with a boundary layer thickness δ = 1.0 m. The wind-tunnel floor was smooth, and covered with oil, so that particles adhered to it upon touching. The longitudinal distribution and lateral distribution (σ_y) were measured for 16 runs.

COMPARISON WITH THE THEORETICAL ESTIMATES

The value of the vertical and lateral characteristic length scales $\sigma_z(x)$ and $\sigma_y(x)$ for passive plumes in the wind tunnel were estimated, using Briggs [1973] atmospheric diffusion estimates, which were transformed to the wind tunnel scale, assuming that $\sigma/x = f(x/\delta)$ for neutral boundary layers. Good agreement between the predicted and measured longitudinal distributions was found in most runs, as evident from the examples shown in Fig. 3. However, the lateral dispersion of the particles was found to be much smaller than the predicted one, as shown in Fig. 4 (the upper power law is the predicted one).

The differences between the theoretical and experimental results could be due to one or more of the following factors: (1) the approximate nature of the theoretical model, (2) Froude numbers which are not sufficiently small to secure a full response to all eddies and in particular to horizontal fluctuations, (it has been shown in the analysis that the response time to horizontal fluctuations of such particles can be larger than the response time to vertical fluctuations), (3) incorrect estimates of σ_z and/or particularly σ_y for the wind tunnel, due to incorrect simulation of the horizontal wind fluctuations, (4) classification of particles into groups with a wide distribution of V_g and (5) experimental errors.

PLANNED CONTINUED STUDY

It is planned to extend the study to particles with smaller settling velocities and smaller Froude numbers, to refine the particle classification, to examine the effect of boundary roughness (the present experiments were made over a very smooth floor, which resulted in a small value of m) and to measure simultaneously the diffusion of particle plumes and passive plumes. The result of such an investigation would make it possible to better understand the effect of the factors mentioned above, eliminate many uncertainties and extend the applicability of the results to a wider range of variables, so that they may be more applicable to practical problems.

It is also planned to study instantaneous plume characteristics, such as obscuration intermittency and fluctuations.

REFERENCES

Briggs, G. A. 1973. In Handbook on Atmospheric Diffusion, by Hanna, S. R., Briggs, G. A., and Hosker, R. P., Jr. Technical Information Center, U.S. Dept. of Energy (1982).

Cermak, J. E. 1971. "Laboratory Simulation of the Atmospheric Boundary Layer." AIAA, Vol. 9, No. 9, pp. 1746-1749.

Csanady, G. T. 1955. "Dispersal of Dust Particles from Elevated Sources." Aust. J. Physics, Vol. 8, pp. 545-550.

Godson, W. L. 1958. "The Diffusion of Particulate Matter from an Elevated Source." Arch. Meteor. Geophys. Bioklim., Vol. 10, pp. 305-327.

Overcamp, T. J. 1976. "A General Gaussian Diffusion-Deposition Model for Elevated Point Sources." Journal of Applied Meteorology, Vol. 15, pp. 1167-1171.

Poreh, M. and J. E. Cermak. 1984. "Criteria for Wind-Tunnel Simulation of Particle Plumes in the Atmospheric Surface Layer." Proceedings of the 1984 CRDC Conference on Obscuration and Aerosol Research, Aberdeen Proving Ground, MD, 25-29 June, CEP84-85MP-JEC5.

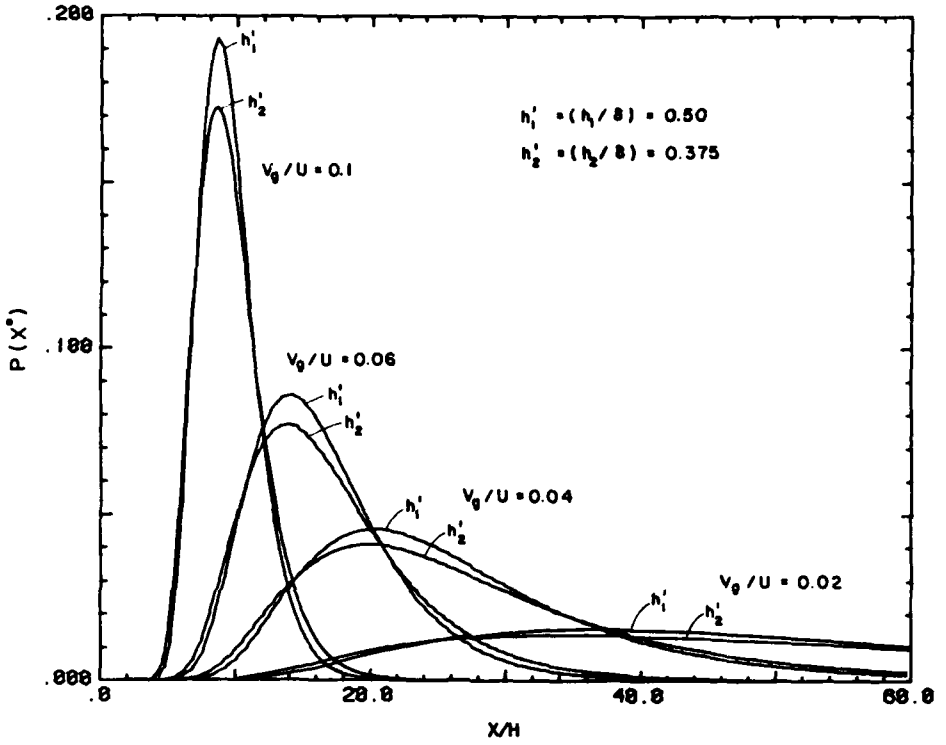

FIGURE 1. The dimensionless distribution P(x*) for different velocity ratios and different source heights.

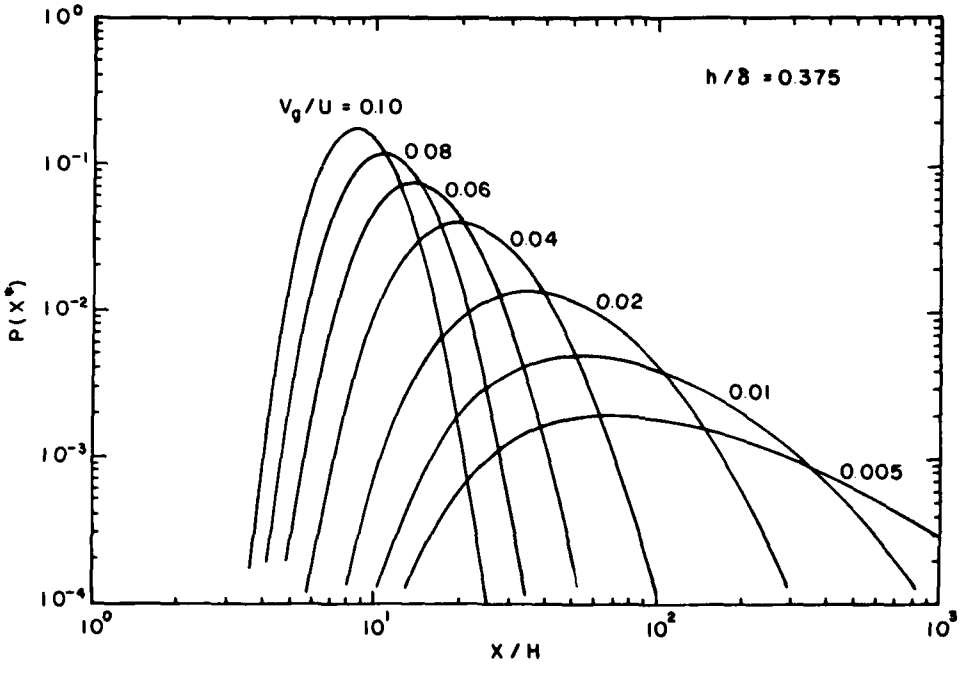

FIGURE 2. The effect of V_g/U on the longitudinal deposition of particles (Eq. 2).

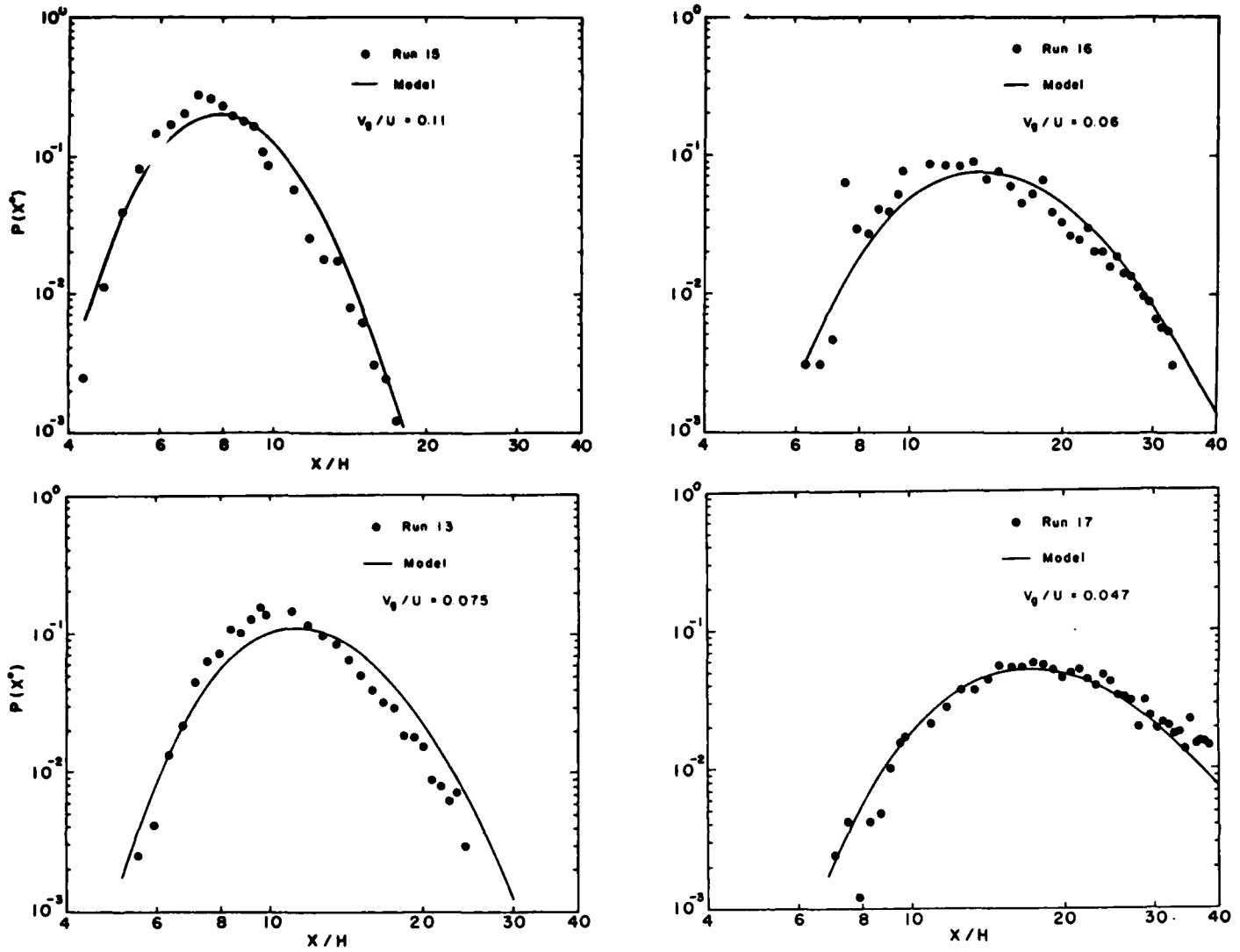

FIGURE 3. The longitudinal deposition of particles P(x*).

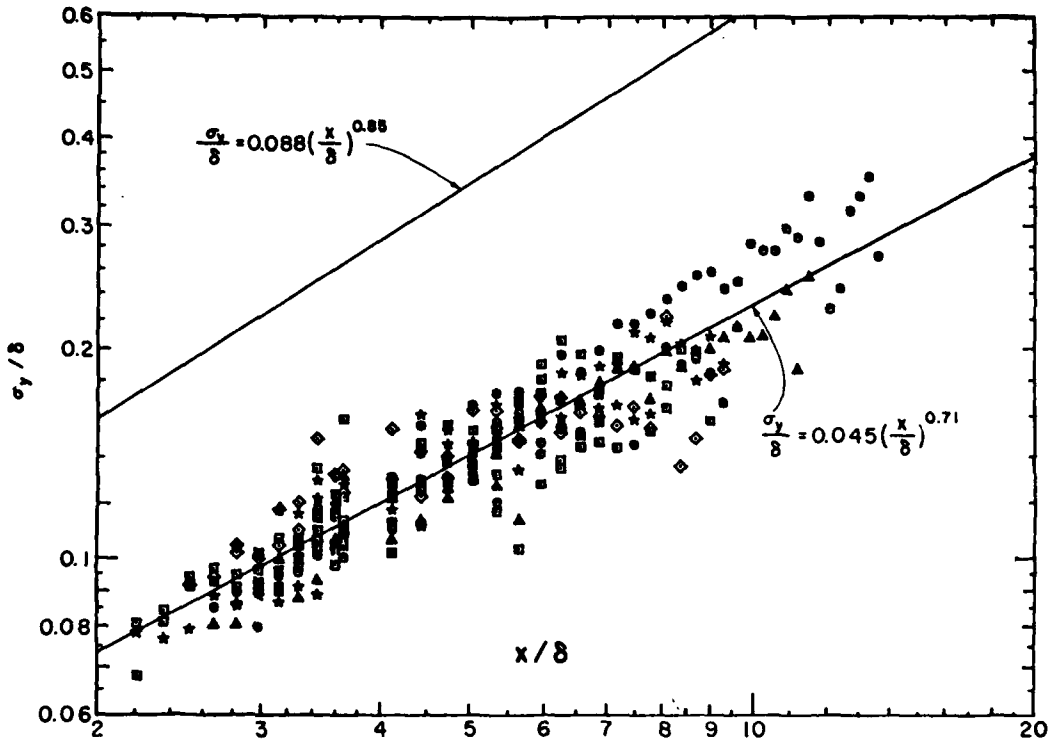

FIGURE 4. The lateral deposition of particles (runs 1-17).

I. PHYSICAL AND CHEMICAL PROPERTIES OF AEROSOLS (continued)

IC. Particle Dynamics: Orientation Effects, Concentration Sampling and Size-Shape Analysis

USE OF CONDITION NUMBERS IN INTERPRETING ATMOSPHERIC AEROSOL SIZE DISTRIBUTIONS

Carolyn R. Kaplan
Combustion Section
Naval Research Laboratory
Washington, DC 20375-5000

and

James W. Gentry
Department of Chemical and Nuclear Engineering
Univeristy of Maryland
College Park, MD 20742

RECENT PUBLICATIONS, SUBMITTALS FOR PUBLICATION AND PRESENTATIONS:

A) F. Farzanah, C. Kaplan, P. Yu, J. Hong, J. Gentry, "Condition Numbers As Criteria for Evaluation of Atmospheric Aerosols," Environ. Sci. Tech., 19, 121 (1985).

B) C. R. Kaplan, "Systematic Use of Condition Numbers in Experimental Design," M.S. Paper, University of Maryland (1985).

C) C. R. Kaplan and J. W. Gentry, "Use of Condition Numbers for Short-Cut Experimental Design," submitted to AIChE J., September 1985.

D) C. R. Kaplan, J. Wang and J. W. Gentry, "Condition Numbers, Monte Carlo Simulations, and Filter Clogging," presented at meeting of Aerosols in Science, Medicine, and Technology, Gesellschaft Fuer Aerosolforschung, Garmisch-Partenkirchen, Federal Republic of Germany.

E) C. R. Kaplan, R. V. Calabrese, and J. W. Gentry, "Condition Numbers: Application to Correlations, Distribution Analysis, and Experiment Location," presented at 1985 meeting of the American Association for Aerosol Research, Nov. 18-22, 1985, Albuquerque, NM.

ABSTRACT

Condition numbers are a quantitative measure of how the solutions of linear equations are perturbed by small changes in the measurements of the forcing function. They depend on experiment location but are independent of experimental error. We examine the effect of condition numbers for three cases: the type of correlation, the procedure used to obtain parameters for multi-modal distributions, and the location of experiments in power law correlations. In each case we use two parameters: the condition number and the bound on the relative error to characterize the equations. Non-linear equations must be linearized before measurements can be made. It was found that the number of parameters and the form of the parameters strongly affect the condition number for single variable correlations. We found that for tri-modal distributions (atmospheric aerosols) the choice of analysis procedure can reduce the relative error bound by three orders of magnitude. We found that experiment location is the critical factor in evaluating power law correlations.

CONDITION NUMBERS

Several mathematical criteria were developed in the mid forties to estimate round-off error in the solution of large sets of linear algebraic equations. The criterion most widely used today is the condition number defined by the relation

$$C_q = |A|_q \cdot |A^{-1}|_q \qquad (1)$$

where $|A|_q$ is the qth norm of the matrix [A]. The condition number provides an upper bound to the solutions X_i to the linear equations [A][X] = [B].

Specifically one has the inequalities

$$\frac{|\Delta X|_q}{|X|_q} \leq C_q \frac{|\Delta B|_q}{|B|_q} \qquad (2)$$

The right hand side of equation 2 can be regarded as the product of the condition number and the relative error in the measurement. The left hand side can be regarded as the relative error in the solution.

Since condition numbers depend only on the coefficients of [A] they serve as criteria for experimental design or for selecting the form of the correlation. Moreover since the condition numbers are the product of the q-norms of [A] and the inverse, one has, from the norm equivalence theorem, with $a_1 \sim 1/3$, $a_2 \sim 3$

$$a_1 C_q < C_{q'} < a_2 C_q \qquad (3)$$

which implies that regardless of the choice of norm, q, the condition number corresponding to another choice, q', will be of similar magnitude.

Previously we have (Farzaneh et al (1985)(A)) reported that condition numbers can explain, 1) the choice of indicator elements in source identification, 2) why inversion of measurements from inertial impactors yield more detail than those from diffusion batteries, and 3) why differential fractions yield better results than cumulative fractions. In this paper we consider the application of condition numbers in selecting correlations and in selecting objective functions for non-linear parameter searches. Specifically, we examine the application of the method to finding the parameters for the Whitby atmospheric aerosol distribution as well as for generalized power law correlations.

GENERALIZED POWER LAW CORRELATIONS

We present the condition number as a criterion for choosing experimental conditions such that the data may be fit most accurately to a power law type correlation

$$g = a x^b y^c \; . \qquad (4)$$

The correlation is linearized and the following set of equations is solved to determine the unknown coefficients, a, b, c.

$$[A'] \qquad [X] \quad = \quad [B']$$

$$\begin{bmatrix} 1 & \ln x_1 & \ln y_1 \\ 1 & \ln x_2 & \ln y_2 \\ & \cdot & \cdot \\ & \cdot & \cdot \\ & \cdot & \cdot \\ 1 & \ln x_n & \ln y_n \end{bmatrix} \bullet \begin{bmatrix} \ln a \\ b \\ c \end{bmatrix} = \begin{bmatrix} \ln g_1 \\ \ln g_2 \\ \cdot \\ \cdot \\ \ln g_n \end{bmatrix} \tag{5}$$

If n, the number of data points, is greater than the number of unknown coefficients (three in this case), we use a least squares regression technique to solve for the coefficients. The least squares regression solution is:

$$[A']^T[A'][X] = [A']^T[B'] \tag{6}$$

The condition number for the least squares regression is

$$C_q = |A'^T A'|_q \cdot |(A'^T A')^{-1}|_q \tag{7}$$

Figure 1 shows the relative difference in the values of the condition number for different distributions of the x, y data. The significance of this result is that the condition number is minimized as the data are more broadly distributed; hence, the broader the distribution, the more accurately the data will fit the power law correlation. It is important to minimize both the condition number and the product of the condition number and the relative error in the measurements, as expressed in equation (2).

In Reference C, this concept is generalized and the approach is extended for an n-parameter power-law correlation. A procedure is presented by which one can completely predetermine experimental conditions such that the condition number is minimized and the data will accurately fit the correlation, or to determine the applicability of fitting existing data to a correlation. In Reference C, we also present a procedure by which one can determine the optimal number of dimensionless groups to be included in the correlation such that the data will fit most accurately.

CONDITION NUMBERS: ANALYSIS OF SIZE DISTRIBUTIONS

In this section we consider the use of moments to evaluate parameters for multiple modal distributions of atmospheric aerosols. Atmospheric size distributions are frequently described as the sum of two or three log normal distributions, with number, area, and mass distributions measured using different instruments. In our investigation we assume that moments of the distribution can be either measured or

calculated from the measurements. The distribution parameters that fit the distribution are then selected. Minimization of the condition numbers is used as the criteria for the selection of the moments.

Specifically, for multiple log normal distributions the pth moment is given by

$$M_p = \int_o^\infty x^p F(x)\, \delta x = \sum_i C_i X_i^p \exp\left[\frac{p^2 \sigma_i^2}{2}\right] \qquad (8)$$

where C_i, X_i, and σ_i are the relative weight, the log mean size and the standard deviation for each of the constituent distributions. For three log normal distributions there are nine parameters and, at least, nine moments are required. Our procedure is to choose the moments so that both condition number and the product of condition numbers and relative error are a minimum.

The calculational procedure was as follows: The function was linearized about a set of parameters $\bar{C}_i$, $\bar{X}_i$, and $\bar{\sigma}_i$. The parameters for a typical atmospheric aerosol given by Whitby et al (1975)(1) were used for the trimodal distribution. The coefficients were G_i, $p_j G_i$, $p_j^2 G_i$ where G_i is equal to $\bar{C}_i \bar{X}_i^{p_j} \text{Exp}\left[\frac{p_j^2 \bar{\sigma}_i^2}{2}\right]$. The condition numbers were calculated for different sets of p_j, j = 1 to 9. Repeated iterations were used to calculate the values of the parameters C_i, σ_i, X_i which match the measured moments. Convergence was usually obtained provided the values of σ_i were initially small (i.e. a narrow distribution).

Results are shown in Figure 2 for the moment sets centered around moments p_o such that $p_j = p_o \pm k\Delta$ (k=0,1,2,3,4). The equations are normalized and the p_o's have a uniform spacing. This was one of a number of different cases studied. The important feature of the curve is that the condition number changes over several orders of magnitude depending on the choice of p_o. This implies that a poor choice of moments will lead to an ambiguous and useless result. The best results are obtained when some of the moments are negative. Normally the wider the spectra of moments the smaller the condition number. However, the spread of the moments is less important than the inclusion of negative moments. Moreover the greater the spread, the more substantial the experimental error.

In conclusion, we have presented the use of condition numbers as a criterion for determination of experimental location in evaluating power law correlations, and in choosing the proper set of moments when solving moment equations to determine the parameters of a multiple modal log normal distribution. We believe that condition numbers have a much wider range of application than discussed here, and some of this may be presented in future work.

REFERENCE

1) Whitby, K. T., and B. Cantrell, "Proceedings of the 1975 International Conference on Environmental Sensing and Assessment, Sept. 1975, Las Vegas, Nevada.

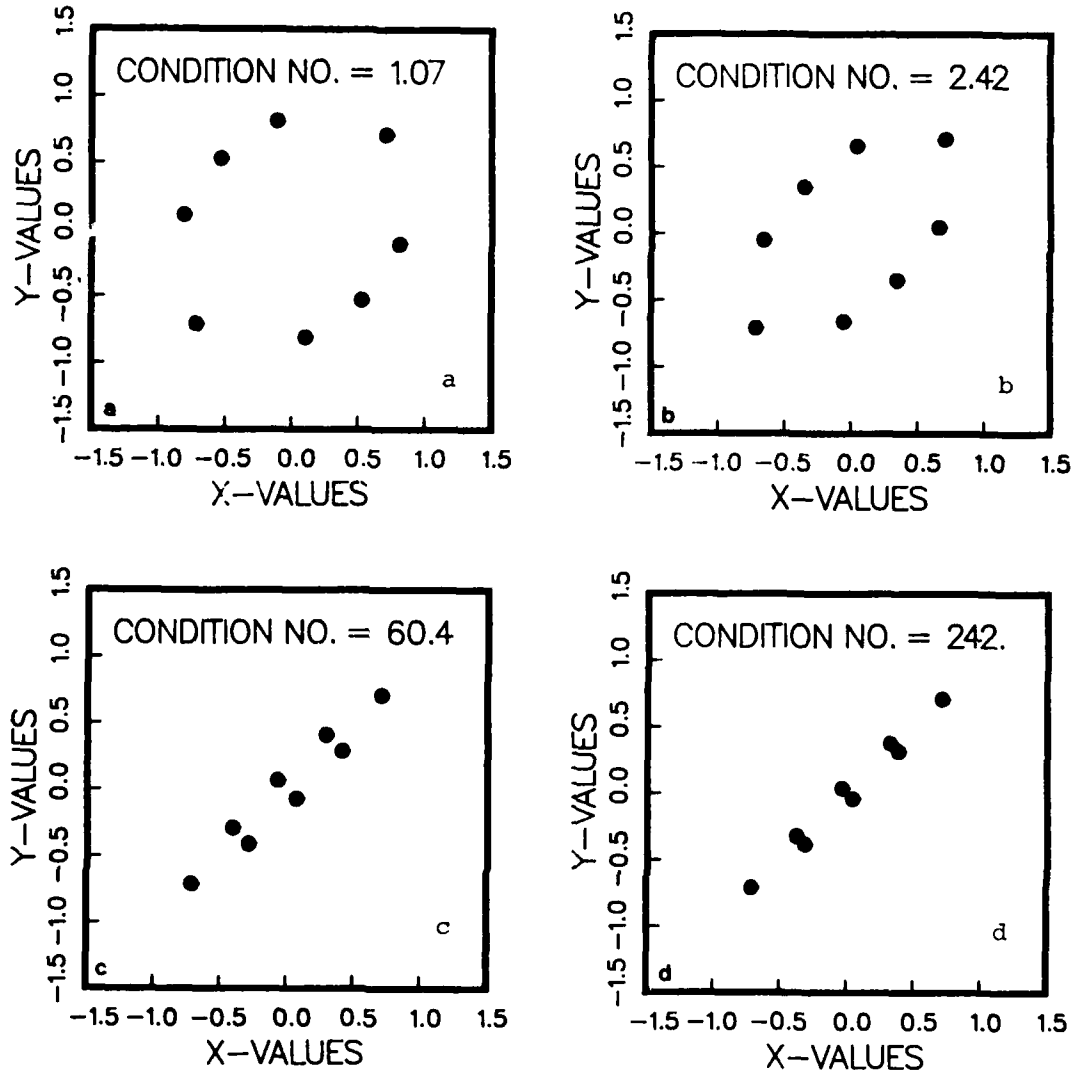

FIGURE 1. DEPENDENCE OF CONDITION NUMBERS ON DISTRIBUTION OF DATA POINTS. Condition numbers for least squares regression solution to a two-dimensional power-law correlation for data distributed on $x^2 + \frac{y^2}{g^2} = 1$, 8 data points.

a) g = 0.75, b) g = 0.5, c) g = 0.1, d) g = 0.05.
Condition number is minimized as data are more broadly distributed.
(Here x and y are lnx and lny in the text.)

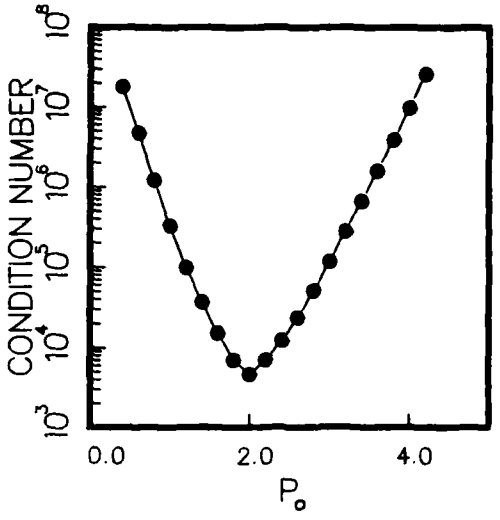

FIGURE 2. DEPENDENCE OF CONDITION NUMBERS ON CHOICE OF MOMENTS. Condition number is minimized for the set of moments P_j = -2, -1, 0, 1, 2, 3, 4, 5, 6.

DETERMINATION OF THE ORIENTATION OF NONSPHERICAL PARTICLES IN A TURBULENT FIELD: EXPERIMENTAL

Isaiah Gallily and Moshe Goldenberg
Department of Atmospheric Sciences
The Hebrew University of Jerusalem
Jerusalem, Israel

RELATED PUBLICATIONS:

Krushkal E.M. and Gallily, I., "On the Orientation Distribution Function of Nonspherical Aerosol Particles in a General Shear Flow. I."the Laminar Case" , J. Colloid Interface Sci. 99, 141 (1984), and

Isaiah Gallily and E.M. Krushkal, "The Orientation Distribution Function of Nonspherical Aerosol Particles in a General Shear Flow: The Turbulent Case,"
Proceedings of the 1984 CRDC Conference on Obscuration and Aerosol Research, p. 57,1984.

ABSTRACT

The aim of this stage of the orientation studies was to conduct under "meaningful" conditions model experiments by which our developed theory will be checked. We hope to reach a position from which intelligent estimates of particle orientation in real situations can be made.

I. THEORETICAL BASIS

Assuming the realization picture of turbulence, the governing Fokker-Planck equation for the orientation density function (o.d.f.) $F^{(j)}$ in realization j (1),

$$\partial F^{(j)}/\partial t + \nabla\cdot(\omega^{(j)} F^{(j)} - \alpha_e^{-1} \nabla F^{(j)}) = 0 \quad , \qquad (1)$$

is characterized by an effective Peclet number α_e defined by

$$\alpha_e = W_o / {}^{r}D_e \qquad (2)$$

where ${}^{r}De$, the combined effective (rotational) diffusion coefficient is

$${}^{r}D_e = {}^{r}D_B + {}^{r}D_t \quad , \qquad (3)$$

${}^{r}D_B$ being the (rotational) Brownian diffusion coefficient and ${}^{r}D_t$ the (rotational) turbulent diffusion coefficient. The last parameter, which can be formally defined by

$${}^{r}D_t \nabla\overline{F} = -\overline{\omega' F'} \quad , \qquad (4)$$

is given for particles smaller than the Kolmogoroff's length scale η ($\eta = \nu^{3/4}/\epsilon^{1/4}$,0.1-1 cm in the atmosphere) in

$$^{r}D_t \approx (\epsilon/\nu)^{1/2} \tag{5}$$

where ϵ, the energy dissipation rate per unit mass, is

$$\epsilon = \nu \sum_i \sum_k \overline{\left(\frac{\partial u_i'}{\partial x_k'}\right)^2} \tag{6}$$

Out of this theoretical model, it has been found that:

i. For a "weak turbulence" ($W_o' \ll W_o$, ϵ small) the average o.d.f. is stuctured (i.e. preferred orientation),

ii. For a "strong turbulence" ($W_o' \gg W_o$, ϵ large), the average o.d.f. is essentially random, while its dispersion (measured by F_m for $\overline{W_{ik}} \pm \Delta W_{ik}, W_{ik} = \frac{\partial u_i}{\partial x_k}, \Delta W_{ik} = \left(\overline{\partial u_i'/\partial x_k}\right)^2$) is noticeable.

II. EXPERIMENTAL METHOD

According to theory, the particle average and spread of orientation depend on the above characteristic of the turbulence, which has to be known.

In principle, the o.d.f can be experimentally determined directly or through some effect. Here we chose the second line of approach, though concurrently we are starting now to persue the first line too.

Adopting the light scattering effect as a gauge for orientation, we have for the case of cylindrical particles, as an example,

$$\bar{I} = \int_0^{\pi}\int_0^{2\pi}\int_l\int_r I(n,\lambda,r,l,\varphi,\theta,\beta)\, f(r)\, g(l)\, F(\theta,\varphi)\, dr\, dl\, d\varphi \sin\theta\, d\theta \tag{7}$$

and

$$\overline{I_o^2} = \int_0^{\pi}\int_0^{2\pi}\int_l\int_r (I-\bar{I})^2 f(r) g(l) F(\theta,\varphi)\, dr\, dl\, d\varphi \sin\theta\, d\theta \tag{8}$$

where $\bar{I}$ is the average (scattered)light signal; $\overline{I_o^2}$ is the(central) second moment); n and λ are the index of refraction and wavelength of light, respectively , β is the observation

angle, and l and r are the length and radius of a cylindrical particle, respectively.

Apparatus

General

Experiments are conducted in the fully developed turbulent region of a straight round pipe, where quite a bulk of characterizing information exists (2). Thus for that (round)pipe geometry, one has that in a fully developed flow (2),

$$\left.\begin{aligned} &\bar{u}_r \,,\, \bar{u}_\varphi = 0 \\ &\frac{\partial}{\partial \varphi} = 0 \\ &(u_x, u_r, u_\varphi) \neq f(x) \end{aligned}\right\} \qquad (9)$$

Also,

$$\overline{u'_r u'_\varphi} = 0 \quad \text{for all } r \,. \qquad (10)$$

Specific

A schematic diagram of apparatus is shown in Fig. 1 in which;

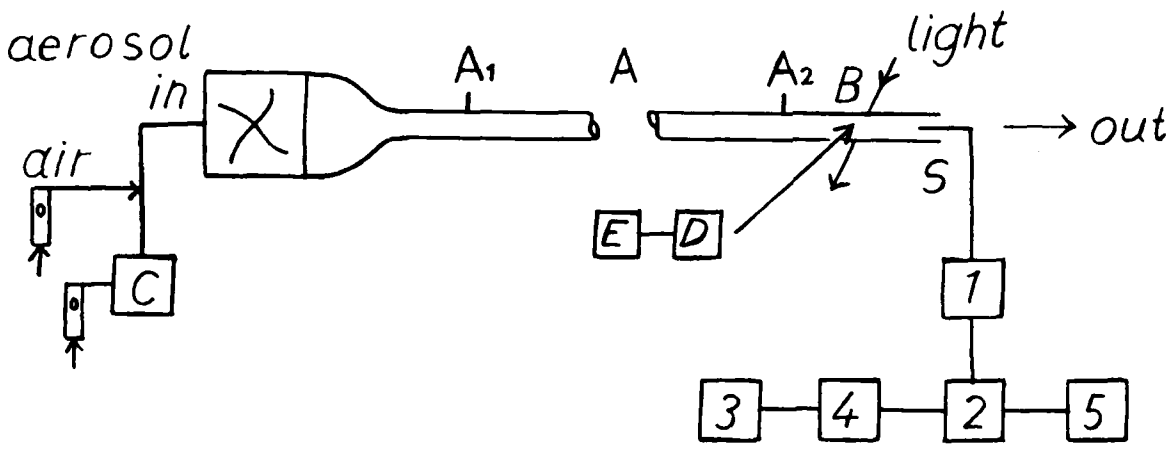

Fig. 1: A schematic diagram of the apparatus

A- is a 5 m long, 5 cm i.d. cylindrical tunnel (A_1, A_2 -aerosol sampling portholes

B- is an aerosol observation section,

C- is Spurny's fiber aerosol generator

D- is a He-Ne 15 mW light source

E- scattered light detector (EMI Photomultiplier, Type 9558) and readout

S - is a 3D (TSI, Model 1295-T1.5) or, a 2D X-wire hot-wire sensor

1- a CTA supplier and linearizer (Disa, 56N21 with 56 C16 Bridges)

2- A mini-computer (Digital, LSI/11/23+, 300 K samples/sec)

3,4,5 - Diskette drive (FWT Series) printer (FACIT), monitor (Visual 102)

The Spurny's aerosol generator (3) and a typical production sample (4) are shown in Fig. 2 .

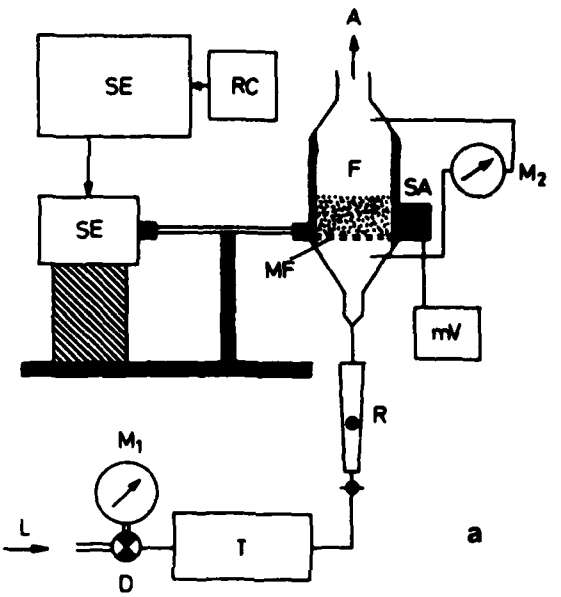

(a)

F- container of fiber mass; SE, RC - electromechanical device

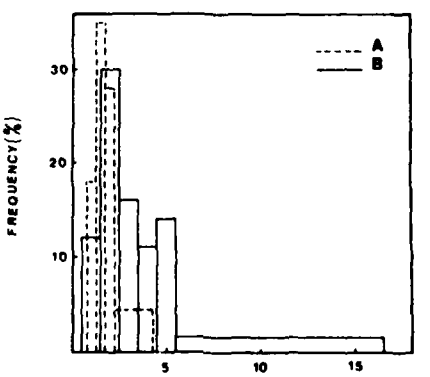

A: Diameter x 10^{-5} cm, B: Length x 10^{-4} cm

Fig. 2: (a) Spurny's aerosol generator and (b) a typical production sample.

Procedure

Setting the average air flow through the tunnel at a certain value befitting, say, an (average) Reynolds number $Re \approx 10^4 - 5 \times 10^5$ the (turbulent) component velocities along the x (flow direction), u'_x, and the r (pipes radial distance), u'_r, coordinates are sampled at a prescribed rate by the (computerized) system (1-4, Fig. 1) and the data processed for $\overline{u'^2_x}$, $\overline{u'^2_r}$, $\overline{u'_x u'_r}$. The necessary gradients, say $\left(\overline{\frac{\partial u'^2}{\partial x}}\right)^{1/2}$, can be deduced from the Taylor hypothesis (1),

$$\partial u'_x / \partial t = - \bar{u}_x \frac{\partial u'_x}{\partial x} \qquad (11)$$

The incompressibility demand, supplementary values taken from Laufer (2) for the dissipation terms, and the isotropic conditions assumed to hold far from pipes walls (2). Then, the aerosol generator is operated, and samples taken through the portholes A_1, A_2 for concentration and size determination by scanning electron microscopy (on a wetted surface to obviate the need for photogrametry). Scattered light signals are also taken.

III FUTURE PLANS

While results are accumulated now with the aid of the above apparatus, a new study, on which the o.d.f will be directly determined, has been started.

Some of the inherent drawbacks of the hereby described adopted method, namely, experimental noise in the determination of the F(r), g(1) functions of Eqs. (8 and 9), and (possible) ill-conditioning effects, are expected to be overcome in the new study.

REFERENCES

1. Isaiah Gallily and E.M. Krushkal, Proc.1984 CRDC Conference on Obscuration and Aerosol Research, p. 57,1984.

2. J. Laufer, "The Structure of Turbulence in Fully Developed Pipe Flow", NACA Report 1174, 1954.

3. Spurney, K.R et al. Staub Reinhalt Luft 35, 440 (1975).

4. A.D. Eisner and Isaiah Gallily, J. Colloid Interface Sci. 101, 356 (1984).

ON THE NONSTEADY MOTION OF AN ARBITRARY PARTICLE IN A STOKES FLOW

Ehud Gavze and Isaiah Gallily
Department of Atmospheric Sciences
The Hebrew University of Jerusalem
Jerusalem, Israel

RELATED PUBLICATIONS:

Ehud Gavze, "The Accelerated Motion of Rigid Bodies in Nonsteady Stokes Flows", submitted to J. Fluid Mech.,1985.

I. THE PROBLEM

Actually, every motion of a particle in a fluid near a rigid (or liquid) surface is accelerated (Fig. 1).

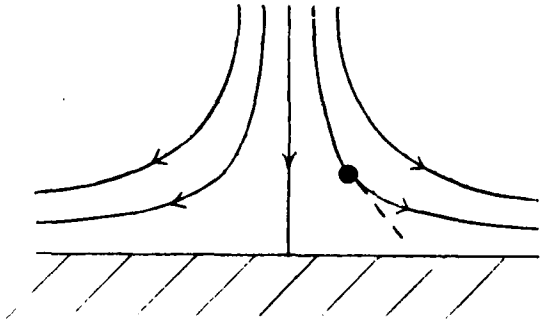

FIGURE 1. (Schematic) trajectory of an aerosol particle near a plane.

Thus, in the equations of the deterministic motion of such a particle

$$m\,dU/dt = \sum_n E_n + F \qquad (1)$$

and

$$I_1\dot{\omega}_1 - (I_2 - I_3)\,\omega_2\,\omega_3 = \sum_n L_n + M \quad \text{etc. (Euler)} \qquad (2)$$

where m is its mass, U is its linear velocity, ω is its rotational velocity, I is its moment of inertia, E_n and L_n are respectively an external force and torque, and F and M are respectively a fluid-dynamic force and torque, the values of F and M must be time-dependent. However, in essentially all situations considered up to now, the quasi-stationary assumption has been evoked, namely, it has

been assumed that

$$F(t) = F_{stationary} \quad \text{at } t \quad . \qquad (3)$$

and

$$M(t) = M_{stationary} \quad \text{at } t \quad . \qquad (4)$$

The case of a rigid spherical particle moving in a creeping motion (Re, Kn $<<$ 1) within a viscous fluid was solved to give

$$F_K(t) = -\frac{2}{3}\rho\pi a^3 \dot{V}_K(t) - 6\pi\mu a V_K(t) - 6a^2\sqrt{\pi\mu\rho}\int_0^t \frac{\dot{V}_K(\tau)}{\sqrt{t-\tau}}\,d\tau \qquad (5)$$

in which the first term on the r.h.s. is the "Added Mass" term (a solution of a potential flow around the particle) the second term is the quasi-stationary term, and the third term is the "memory" Basset term; ρ and μ are respectively the density and viscosity of the medium and a is the radius of the sphere.

Here, the inclusion of the first and third term in the equation of linear particle motion (1) was found in most cases to be insignificant though it is yet not clear whether this is so in situations of strong particle accelerations, say within very strong jets and turbulent fields.

The reported study intends to find general relationships for F(t) and M(t) for an arbitrary particle.

II. THE THEORETICAL APPROACH

In a continuous fluid,

$$\left.\begin{aligned} F_i &= \int_S \sigma_{ij} n_j \, ds \\ \text{and} \qquad M_i &= \int_S \epsilon_{ijk} \sigma_{kl} x_j n_l \, ds \end{aligned}\right\} \qquad (6)$$

where the stress tensor σ_{ij} is

$$\sigma_{ij}(u) = \mu(\partial u_j/\partial x_i + \partial u_i/\partial x_j) - \delta_{ij} p$$

and S indicates integration over the surface of the particle. For a creeping motion, σ_{ij} can be obtained from the solution of the Stokes' equation for a nonsteady flow

$$\rho \partial u_i / \partial t = \mu \Delta u_i - \partial p / \partial x_i \qquad (7)$$

or, for a steady flow

$$\mu \Delta u_i - \partial p / \partial x_i = 0 \qquad (8)$$

and the equation of continuity

$$\partial u_i / \partial x_i = 0 \ . \qquad (9)$$

Formally, for a steady particle motion, one has, see Ref. (1),

$$F_i = K_{ij} V_j + C_{ij} \omega_j \qquad (10)$$

and

$$M_i = C_{ji} V_j + \Omega_{ij} \omega_j \qquad (11)$$

where K, Ω are symmetric tensors.

The main features of our approach are essentially:

i. The deduction of a Generalized Reciprocal Theorem (G.R.T.) for the nonsteady flow,

ii. The use of a "Basic (particular) Solution."

The G.R.T deduced is

$$\rho \int_\Omega [u_i(o) V_i(t) - u_i(t) V_i(o)] d\Omega$$
$$= \int_o^t d\tau \int_S [u_i(t-\tau) \sigma_{ij}(V(\tau)) - V_i(\tau) \sigma_{ij}(u(t-\tau)] n_j ds \qquad (12)$$

where Ω indicates integration over the (external) space.

III. ANALYTICAL (FORMAL) RESULTS

The (physical) situations treated by us were:

a. Force in pure translation and torque in pure rotation, quiet medium at infinity; motion starts from rest.

b. Force and torque for coupling between translation and rotation, same b.c. and i.c. as for a; an explicit solution for a sphere.

c. Force and torque on a particle within an arbitrary Stokes flow at infinity; sphere. Here we bring as an example the above case a in part. Thus, if $W_i(x,t)$ is the flow resulting from the(pure) body translation $U_i(t)$ $(U_i(o)=o)$ satisfying:

1. Stokes equation; 2. $W_i|_S = U_i(t)$; 3. $W_i|_\infty = 0$, 4. $W_i|_{t=o} = 0$,

and

if V_i^κ is the "basic Solution" for pure translation satisfying:

1. Stokes equation; 2. $V_i^\kappa|_S = e_i^\kappa$, $t>o$; 3. $V_i^\kappa|_\infty = o$, $t>o$ $(e_i^\kappa = \delta_{i\kappa})$;

4. $V_i^\kappa|_{t=o} = \frac{\partial \phi^\kappa}{\partial x_i}$ where ϕ^κ is the solution for the potential flow

$\Delta\phi^\kappa = o$ $\left(\frac{\partial \phi^\kappa}{\partial x_i} n_i|_S = e_i^\kappa n_i = n_\kappa ; \quad \phi^\kappa|_\infty = o \right)$,

then,

introducing $W(t)$, $V^k(t)$ in the G.R.T. and performing time differentiation, we finally get

$$F_\kappa(t) = \rho \dot{U}_i(t) \int_S \phi^\kappa n_i \, ds + \int_o^t \dot{U}_i(\tau) \int_S \sigma_{ij}(V^\kappa(t-\tau))\, n_j \, ds \, d\tau \ . \tag{13}$$

Defining

$A_{\kappa i} = \int_S \sigma_{ij}(V^\kappa(t)) n_j \, ds$, which depends on the "Basic Solution" and is common to all $U_i(t)$ and which can be shown to be symmetric, and

$Q_{\kappa i} = \int_S \phi^\kappa n_i \, ds$,which depends on ϕ^κ and which can be shown to be symmetric too, we have

$$F_\kappa(t) = Q_{\kappa i} \dot{U}_i(t) + \int_o^t A_{\kappa i}(t-\tau) \dot{U}_i(\tau) \, d\tau \ . \tag{14}$$

It is reasonable to assume that

$$V_i^\kappa = \bar{V}_i^\kappa + \hat{V}_i^\kappa \tag{15}$$

where $\bar{V}_i^\kappa$ satisfys the steady Stokes equation (8), $\bar{V}_i^\kappa|_S = \delta_{i\kappa}$, $\bar{V}_i^\kappa|_\infty = o$,

and where $\hat{V}_i^\kappa|_S = o$, $\hat{V}_i^\kappa|_\infty = o$, $\hat{V}_i^\kappa|_{t=o} = \frac{\partial \phi^\kappa}{\partial x_i} - \bar{V}_i^\kappa$ and $\hat{V}_i^\kappa \to o$ as $t \to \infty$.

So, we can decompose the tensor $A_{\kappa i}$ into two parts

$$A_{\kappa i} = \int_S \sigma_{ij}(\bar{V}_i^{\kappa}) n_j \, ds + \int_S \sigma_{ij}(\hat{V}_i^{\kappa}) n_j \, ds \qquad (16)$$

where the second term on the r.h.s. tends to zero as $t \to \infty$. Thus, we obtain

$$F_{\kappa}(t) = Q_{\kappa i} \dot{U}_i(t) + K_{\kappa i} U_i(t) + \int_0^t B_{\kappa i}(t-\tau) \dot{U}_i(\tau) \, d\tau \, . \qquad (17)$$

$Q_{\kappa i}$ may be called the "Added Mass" tensor, $K_{\kappa i}$ may be called the quasi-stationary tensor, and $B_{\kappa i}$ may be called the "Basset" tensor. Eq. (17) compares nicely in form with the equation for a sphere (5). The equations deduced for the above (physical) situations have a similar form.

REFERENCES

1. J. Happel and H. Brenner,"Low Reynolds Number Hydrodynamics", Prentice-Hall,1965, p.173.

I. PHYSICAL AND CHEMICAL PROPERTIES OF AEROSOLS (CONTINUED)

ID. Aerosol Elimination

A REALISTIC ASSESSMENT OF CLEARING SMOKE CLOUD BY SCAVENGING TECHNIQUE

Josef Podzimek
Department of Mechanical and Aerospace Engineering
and Graduate Center for Cloud Physics Research
University of Missouri-Rolla, MO 65401

RECENT PUBLICATIONS, SUBMITTALS FOR PUBLICATION AND PRESENTATIONS:

A) J. Podzimek and J. Martin, "Results of Past and Current Investigation of the Smoke Particle Scavenging by Nonspherical Collectors", Proceedings of the 1984 CRDC Scientific Conference on Obscuration and Aerosol Research, p. 73 in the Draft of Proceedings, submitted September 1984.

B) J. Podzimek, "Overview of Mechanical and Other Methods for Visibility Reduction", Proceedings of the Workshop on Microphysics of Visibility, October 1984, El Paso, TX, R.H. Kohl and D. Stroud Editors, Tullahoma, Tennessee, Dec. 1984, p. 27-41.

ABSTRACT

This contribution describes mainly the investigations performed in 1984 and 1985. They concentrated on the determination of the collection efficiency of grid and electret fiber scavengers, and on the behavior of settling collectors in a "falling scavenger zone".

COLLECTION EFFICIENCY OF ELECTRET TYPE SCAVENGERS

For a polydisperse aerosol prepared by the reaction of titanium chloride ($TiCl_4$) with water vapor (typical particle size distribution from the electrostatic precipitator is plotted in Fig. 1) the wind tunnel and free fall experiments described earlier (Podzimek, 1981 and 1983) led to the following conclusions:

The nonspherical and planar scavengers are more efficient in removing smoke particles than spherical drops. The most effective uncharged planar scavengers will have the maximal collection efficiency of about one or two percent. This might slightly increase by an oscillatory motion of the scavenger. A considerable increase in collection efficiency was reached by the electric charge imparted to conductive cylindrical models (up to 10%), however, the difficult maintaining of a high electric charge on scavengers in a dense smoke cloud limits strongly the practical applicability of this technique.

Electret fiber and grid-type scavengers showed high collection efficiency during the wind tunnel experiments with charged and uncharged scavengers (Fig. 2), especially for particles with diameters smaller than 1.0 μm at low airflow velocity. This indicates an important role played by the diffusion, phoretic and electrostatic

forces. On the other hand, coarse electret fibers (200-300 μm in diameter and settling velocities 1.0 m/s and larger) cause an increase in deposition of particles with diameter larger than 1.0 μm due to the inertial forces. This prompted a new series of systematic measurements with grid and fiber-type scavengers in a settling chamber provided with instrumentation for light extinction measurement in a dense smoke cloud (first described by Podzimek et al, 1980).

Most of the experiments have been done by the fibers denoted as "Dust Magnet" Poly-Mag 80 and 90 (Polyester Plastic), a product of Bruhow Industries, Collierville, TN. Two different types of scavengers were used in 1984 and 1985 for a systematic investigation: coarse fiber scavengers with a grid-type structure of scavenger mean size 2.5 cm x 2.5 cm and mean fiber diameter around 250 μm. The mean scavenger mass was 0.105 g and the mean scavenger settling velocity was 176.9 cm/s. Another type of scavenger had the dimensions of 2.5 cm x 2.5 cm x 1.3 cm and the mean mass 0.101 g and was formed of randomly oriented dense packed fine electret fibers of approximately 40 μm diameter. The mean settling velocity was 176.3 cm/s. The main aim of these experiments, performed in a settling chamber 1.60 m high and 0.80 m in diameter, was to find a relationship between the collection efficiencies calculated from wind tunnel experiments and those deduced from the light extinction measurements by assuming specified smoke particle-size distribution and the validity of the general formula for visual range in a fog (Podzimek, 1981),

$$L = \frac{\ln (1/\varepsilon)}{\frac{\pi}{4} n \int_0^{\infty} n_p(d_p)\, d_p^2\, K_{ext}(x,m)\, d(d_p)} \qquad (1)$$

In Eq. (1), $\varepsilon \cong 0.02$; $K_{ext} \cong 2.0$; n and $n_p(d_p)$ are total droplet (particle) concentration and relative droplet concentration at the diameter d_p. $x = (\pi \cdot d_p)/\lambda$; λ is the wavelength used for the experiments, and m is the index of refraction of the particles. Another important goal of these studies was to find the optimal groups of scavengers with the highest scavenging efficiency and to find the most suitable time intervals between the dropping of scavengers.

All data are plotted in Fig. 3 which shows clearly that, in spite of a large spread of points, which is caused probably by the induced fluctuating velocities in the settling chamber, there is a significant improvement of visibility in a dense smoke after dropping a specific number of scavengers. The number of scavengers

dropped during 5 minute intervals varied between 10 and 150 scavengers. There is a strong indication that the highest scavenger dropping rate (30 scavengers/min) did not cause the most significant improvement in visibility. Dropping in smaller scavenger groups with long intermission was more effective. This stresses the importance of the induced velocity study in a falling scavenger zone. Irrespective of the scavenger groups and the type of scavenger, the mean value of the change of extinction in 1 minute was plotted in Fig. 3 as a function of time (or drop times for the scavenger groups, usually at 5 minute intervals). In mean, 30 mV/min - which corresponds to the improvement of visibility for a monodisperse aerosol with d_p = 0.4 μm in Eq. (1) - was measured after each 5 minute interval of scavenger dropping. This significant collection efficiency of electret fiber scavengers lasts for more than half an hour. The efficiency is usually smaller during the first half an hour after the dense smoke cloud was introduced into the settling chamber and also drops down after one hour (due to the clearing period of a smoke cloud). At this time it is not possible to describe the nature of the particle deposition on coarse fiber (d = 240 μm), mesh-type scavengers or on randomly oriented, dense packed, fine fiber (d = 40 μm) scavengers. There is, however, some indication that fine fibers collect mainly particles smaller than 0.5 μm by diffusion and phoretical forces, whereas coarse fibers also capture micron size particles due to their inertia. The dual character of particle deposition on coarse fibers is clearly demonstrated in Fig. 4, where a cumulative particle size distribution features the particles found on coarse fibers (sampled in a settling chamber) in a scanning electron microscope. It was also observed that $TiCl_4$ smoke found on both sides of the stagnation point (line) of a fiber tended to form chain-like aggregates due to the combined effect of electrostatic and inertial forces.

EXPERIMENTS WITH A LARGE POPULATION OF FALLING SCAVENGERS

The experiments in a cylindrical settling chamber revealed the importance of the velocities induced by falling scavengers, which might influence the collection efficiency in a smoke cloud, and also the shape of the scavenger dispersion cone (assuming that scavengers were dropped from a point in the space). Comparative measurements with specific scavengers (paper disks and rectangles, "dust magnet" mesh and filter type scavengers of different size) have been done simultaneously in the cylindrical settling chamber--described above--and in the UMR gymnasium where

hundreds of scavengers were dropped at a height of 10 m and their positions evaluated on the floor.

The main results summarized in Table I can be described as follows: there is a permanent difference between the scavenger fall velocities and "dispersion cone" found in laboratory (along a settling pa[illegible] approximately 1.6 m or 2.0 m) and in the gymnasium where scavengers were dr[illegible]ped at 10 m above the floor. Settling velocities for the same type of scavenge[illegible]s are higher in the tank than in the gymnasium. The induced velocities by a population of simultaneously falling scavengers also affect the scavenger dispersion area on the floor of the gymnasium. This is described by a mean dispersion radius, $\bar{r}$, (the radius of the circle around the vertical where 50% of all released scavengers were found) and by a coefficient of dispersion, D_S. Both are related to the height of the dropping point above the ground, H, and the scavenger settling velocity V_S, by the equation

$$\bar{r} = (2\ D_S\ t)^{1/2} \sqrt{\frac{2H\ D_S}{V_S}} \quad . \tag{2}$$

The dispersion coefficient was found to be very large in cases where the shape of the scavengers supported their sliding, swinging or rotation along their settling path (e.g. paper disks and rectangles - Fig. 5). Grid and mesh type scavengers are featured by their quiet settling and small dispersion in calm air (Fig. 6). (In Figs. 5 and 6 - the "distance zone" is the multiple of 27.4 cm).

DYNAMICS OF THE FALLING SCAVENGER ZONE

The main motive of these investigations was to obtain some information on the downdrafts induced by the population of falling scavengers. These downdrafts and the induced horizontal air motion affect the scavenger collection efficiency, scavenger dispersion, nature of motion and, potentially, the transport of smoke particles towards the ground.

The two-dimensional dynamic model--which in the first stage does not include the thermal instability and sophisticated models of turbulent exchange in the boundary layer--is mainly based on several articles dealing with the dynamics of falling precipitation elements (e.g. Clark and List, 1971). It includes also several improvements of the computation technique which, in our opinion, contribute considerably to higher accuracy of the results. The basic set of equations is as follows:

$$\frac{\partial w}{\partial t} + \frac{\partial (uw)}{\partial x} + \frac{\partial (ww)}{\partial z} = - \frac{\partial \phi}{\partial z} - gq + K_\ell \nabla^2 w \qquad (3)$$

$$\frac{\partial u}{\partial t} + \frac{\partial (uu)}{\partial x} + \frac{\partial (uw)}{\partial z} = - \frac{\partial \phi}{\partial x} + K_\ell \nabla^2 u \qquad (4)$$

$$\frac{\partial u}{\partial x} + \frac{\partial w}{\partial z} = 0 \qquad (5)$$

$$\frac{\partial q}{\partial t} + \frac{\partial (qu)}{\partial x} + \frac{\partial}{\partial z} [q (w - V_T] = 0 \qquad (6)$$

$$\frac{\partial}{\partial t} \int\int [1/2 (u^2 + w^2) + gqz] \, dx \, dz = - \int\int gq V_T \, dx \, dz -$$

$$- K_\ell \int\int [(\frac{\partial u}{\partial x})^2 + (\frac{\partial u}{\partial z})^2 + (\frac{\partial w}{\partial x})^2 + (\frac{\partial w}{\partial z})^2] \, dx \, dz \qquad (7)$$

With boundary conditions

$$\frac{\partial w}{\partial x} = u = \frac{\partial \phi}{\partial x} = 0 \qquad \text{at } x = 0 \text{ and } 3000 \text{ m}$$

$$\frac{\partial u}{\partial z} = w = \frac{\partial \phi}{\partial z} = 0 \qquad \text{at } z = 0 \text{ and } 3000 \text{ m}$$

Scavengers are released at 1000 m in an 800 x 200 m layer; $\phi = \frac{p}{\rho} + gz$; w, u = vertical and horizontal velocity; K_ℓ = eddy viscosity (e.g. 1000 $m^2 s^{-1}$); g = gravity acceleration; p, ρ = air pressure and density; q = scavenger mixing ratio (0.01; 0.03; 0.07; 0.15 g/g air); V_T = terminal velocity of scavengers (1.21, 1.50, 1.73 m/s).

The current 2-D model depicts the hemispace around the center of the scavenger zone. The mesh area is 3,000 m x 3,000 m containing 31 x 31 nodes. A mesh area of this size is required in order to meet the still air criteria along the upper and right side boundary if the scavengers are released in a 800 m x 200 m layer at the 1000 m level. The scavenger zone is composed of, e.g., 400 cells with each of them containing 25 scavengers similar to circular paper disks 0.6 cm in diameter.

In order to meet initial memory constraints of the microcomputer, a 31 x 31 node mesh was also used for the velocity fields (u,w). This approximation generated a significant error in determining the induced air motion and therefore scavenger motion. With an expansion of the usuable memory, a 61 x 61 node mesh was used for the velocity fields. These are shown in Figs. 7 and 8. These figures show clearly how the same number of scavengers induces different downdrafts and the flow pattern dependence on the original shape of the scavenger zone. Different height-to-width ratios of the scavenger zone are used (e.g., in Fig. 7, 1:1.56 and in Fig. 8, 1:4). The thicker layer shows clearly a markable effect on increasing the

downdraft velocity and stimulating the air circulation around the scavenger zone. This supports the transport of small particulates to the ground. On the other hand, a thin scavenger zone does not affect much the overall downward transport of particulates. However, it enhances the more effective inertial deposition of smoke particles on scavengers due to the larger relative velocity (scavenger-air with smoke particles).

Further, scavengers settling in a scavenger zone experience some spreading along their path which is demonstrated in Figs. 7 and 8. The largest spreading (15.55% of the original scavenger zone) was obtained for the height to width ratio 1:1, 12.73% for 1:1.56 and 6.75% for 1:4. This spreading will be increased by the aerodynamic dispersion of scavengers described in the previous section.

CONCLUSION

From all types of nonspherical scavengers (paper disks, rectangles, hexagonal plates, cylinders, grids) investigated in a laboratory wind tunnel and in a cylindrical settling chamber filled with smoke particles, the grid and fiber mesh type collectors were the most effective. Their collection efficiencies, estimated from the smoke particle deposition rate on a single fiber, were higher than the measured deposition on a disk or on a simple cylinder. For the latter scavengers an analytical-numerical model based on creeping flow equations (done in cooperation with Dr. J. Martin) now exists. The uncharged, dense packed, electret fiber scavengers have a collection efficiency of up to 13% for particles with radii, $r_p \cong 0.4$ µm, and 39% for $r_p \cong 4.0$ µm. Thick, uncharged, fiber grid scavengers showed efficiencies up to 5.3% for $r_p \cong 0.4$ µm and 26.5% for $r_p \cong 4.0$ µm. In spite of the large spread of data from the cylindrical smoke chamber, there was a definite clearing effect of scavengers, especially of the "dust magnet" (electret) type collectors. Preliminary calculations reveal that an improvement of visibility of 30% and more can be reached with mesh-type scavengers in a micron-sized smoke cloud. The estimated total mass of scavengers is about 100 kg for the 30% improvement in visibility in still air to be attained over an area of 100 m x 100 m .

The investigation of scavenger dispersion in still air enabled us to estimate the effect of nonspherical particle motion and the hydrodynamic interaction of a population of scavengers. Symmetrical models with internal ventilation (grid type models) show the smallest dispersion characterized by a dispersion coefficient around

one hundred (in c.g.s. units) whereas coefficients of unsymmetrical models and disks amount to several thousands. For practical application of the laboratory tests on scavenger dispersion only large scale experiments are suitable.

Numerical modeling of the dynamics of the falling scavenger zone stressed the importance of the induced downdrafts by falling scavengers (which might amount to several tens of cm/s). The shape of the scavenger zone, mainly its depth, strongly affects the induced velocities. In the case of "dust magnet" (electret) fibers the models of the evolution of the falling scavenger zone offer a unique means for combining the scavenger shape, mass and fall velocity, stressing more or less the transport of small smoke particulates to the ground. On the other hand, using a thin scavenger layer and heavier mesh-type scavengers, higher collection efficiency can be reached due to the electric charge effect and inertial deposition. In the future the model will include thermal stratification and a more realistic description of the turbulent exchange in the atmospheric boundary layer.

ACKNOWLEDGEMENT

The author is indebted to Dr. J. Martin for cooperation in calculating the collection efficiency of oblate spheroids (disks) and to Mr. Y.-J. Liu, W.-H. Shyu, G. Stowell, V. Wojnar, graduate students of UMR, and Mr. W. Rottman, T. Smith and G. Teste who ably assisted during laboratory experiments and evolution of numerical models. Mrs. V. Maples effectively helped in the manuscript preparation for printing. The financial and technical assistance of the Department of the Army, USAARRADCOM-DRDAR under the DAAK 11-83-K-0007 project is appreciated.

REFERENCES

Clark, T.L., and R. List, 1971: Dynamics of Falling Particle Zone, J. Atmos. Sci. 28, p. 718-727.

Podzimek, J., 1981: Clearing of Military Smoke Cloud with Scavenging Technique, Final Report DAAG-79-C-0073, submitted to USAARRADCOM-DRDAR by UMR, June 1, pp. 121.

Podzimek, J., 1983: Investigation of a Technique Clearing/Modifying a Military Smoke Cloud, Final Report DAAK-11-81-C-0075, submitted to USAARRADCOM-DRDAR by UMR, September 19, pp. 89.

Podzimek, J., P.C. Yue, D.E. Reed, and M.S. Schenewerk, 1980: Fog Dispersion with Artificial Scavengers, Proc. of the 3rd WMO Sci. Conf. on Weather Modification, Clermont-Ferrand, July, WMO-Geneva, Vol. 1, p. 341-347.

TABLE I. COMPARISON OF SCAVENGER DISPERSION

Scaven. Type	Fall Velocity cm/s Tank	Gymn.	Stand Dev. σ_r Tank	Gymn.	50% Radius [cm] Tank	Gymn.	Coeff. Dispersion Tank	Gymn.
Coarse rect. "dust magn."	191.81	163.66	15.59	4.79	12.122	43.293	68.92	159.63
Small coarse rect. "dust magnet"	192.81	166.35	15.89	4.79	12.293	33.790	70.87	98.84
Coarse fine fiber "dust magnet"	176.35	173.40	8.79	10.78	33.000			
Small fine fiber "dust magnet"	146.05 146.05 146.05	120.90	18.29 18.29 18.29	10.78	19.308 14.529 15.52	45.755	133.13 75.38	129.15
Paper disk r=0.6 cm	150.76	143.35	9.40	10.17	33.840	197.28	516.10	2892.80
Paper rect. 0.13x0.3 cm	177.31 177.31 177.31	175.70	15.96 15.96 15.96	11.95	34.837 36.542 33.626	130.545	526.11 578.87 490.191	1559.36
Paper square 0.13x0.14 cm		173.93		14.976		47.843		207.34

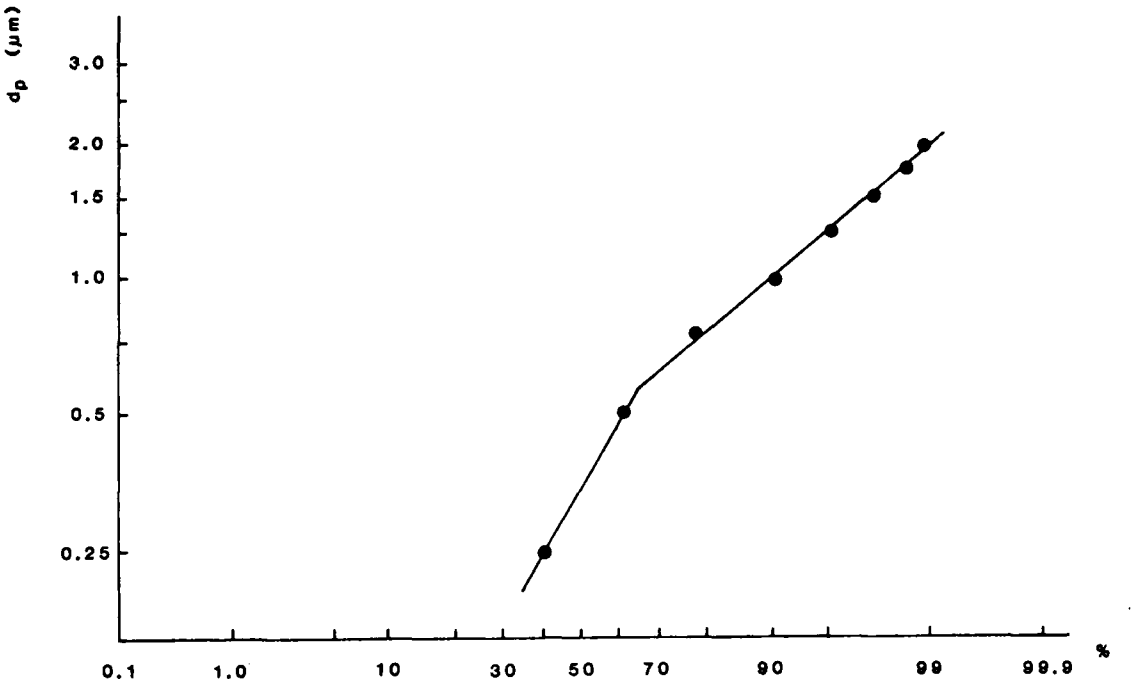

FIGURE 1. ELECTROSTATIC PRECIPITATOR (TSI) SAMPLE OF SMOKE PARTICLES. Particles are generated by the reaction of $TiCl_4$ with water vapor. Cumulative size distribution covers particle diameters from 0.2 to 2.5 μm.

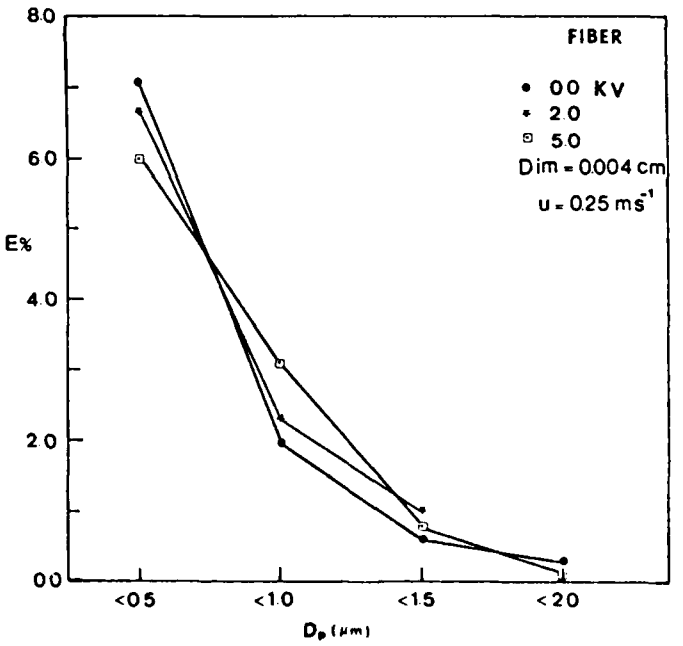

FIGURE 2. COLLECTION EFFICIENCY OF "DUST MAGNET" (ELECTRET) FINE FIBER, (d = 0.004 cm) - which was uncharged or connected with a generator of an electrostatic charge - was exposed to polydisperse aerosol of size D_p in a wind tunnel. Air (aerosol) flow velocity was 0.25 m s^{-1}. (Proc. CRDC Scientific Conf. on Obscuration and Aerosol Research, 1984, Ed. R.H. Kohl, p. 83.)

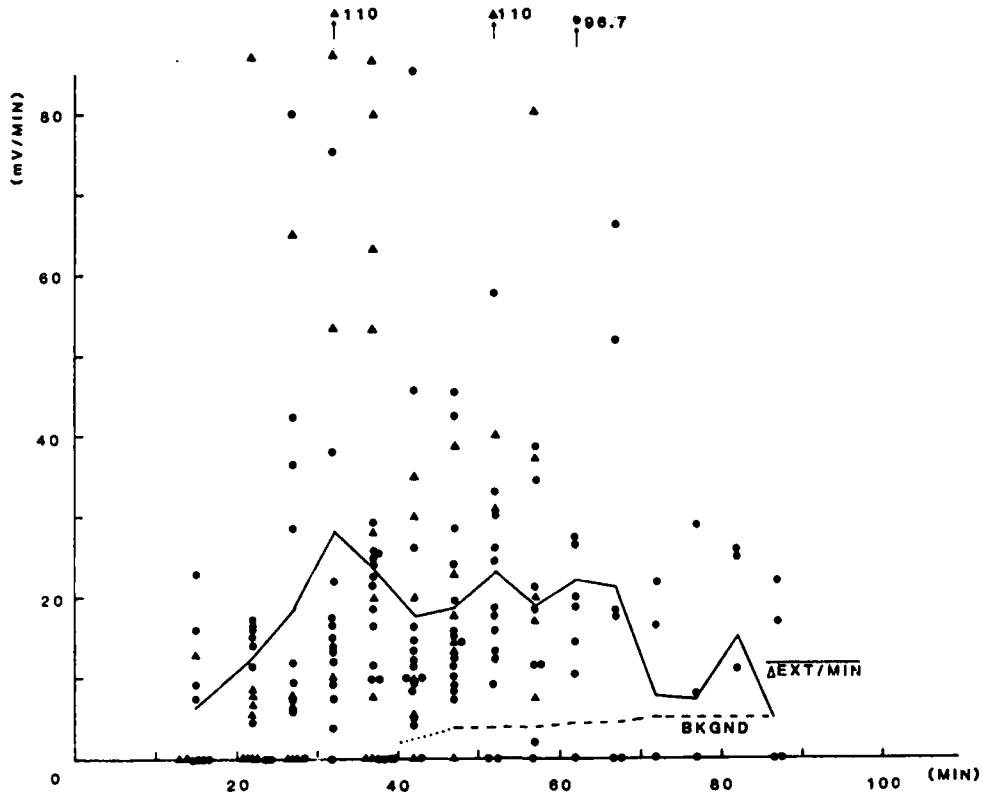

FIGURE 3. CHANGE IN LIGHT EXTINCTION IN A SMOKE CLOUD. Extinction change in one minute (ΔEXT/MIN ≡ mV/MIN) was caused by dropping a specific number of scavengers in 5 minute intervals. Triangles correspond to fine fiber "Dust Magnet" scavengers, dots to the coarse fibers.

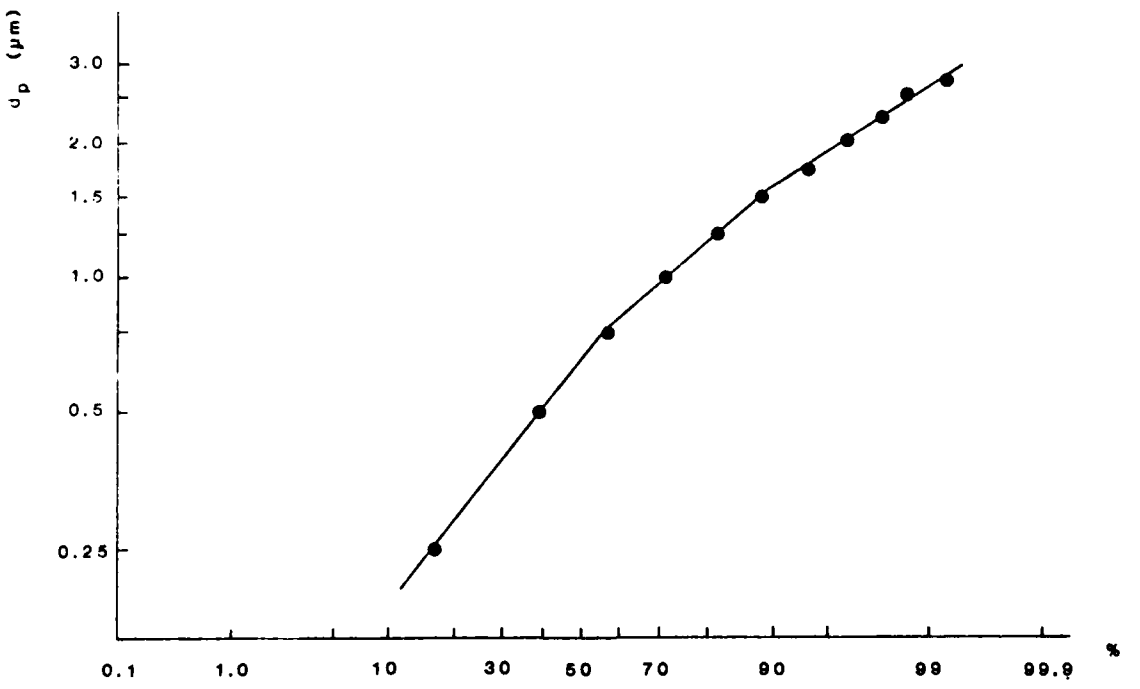

FIGURE 4. CUMULATIVE SIZE DISTRIBUTION OF SMOKE PARTICLES. Particles are deposited on coarse "Dust Magnet" and evaluated in electron microscope.

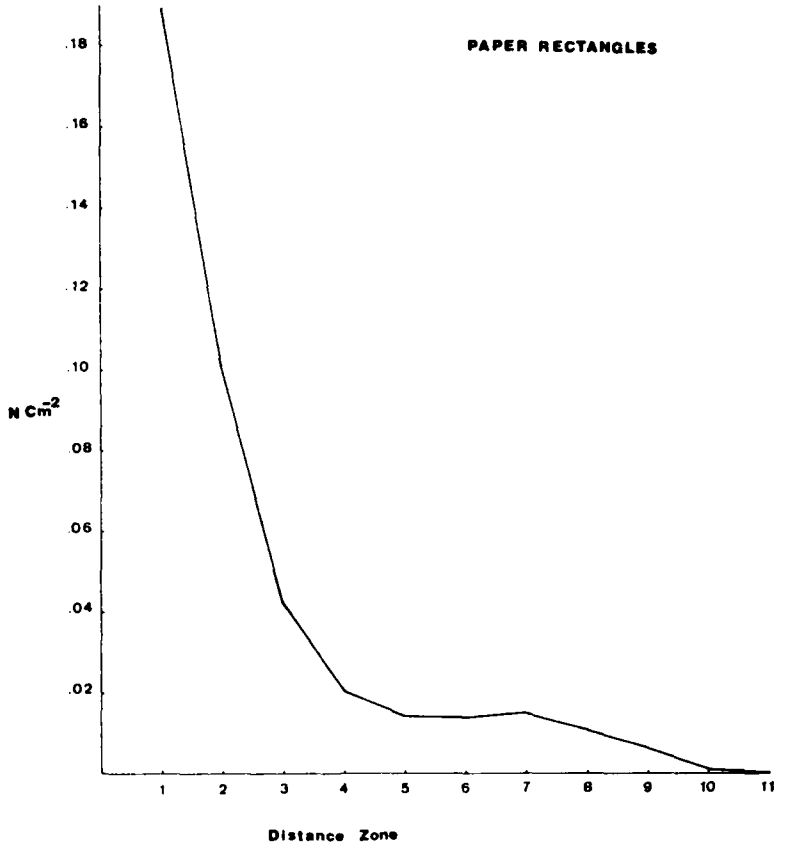

FIGURE 5. SCAVENGER DISPERSION. Measured on the floor of gymnasium where 3888 punch card paper rectangles 0.13 cm x 0.30 cm were dropped from the height of 10 m. The number of deposited scavengers in a specific distance zone (multiples of 27.4 cm) is divided by the ring's area and evaluated in N cm^{-2}.

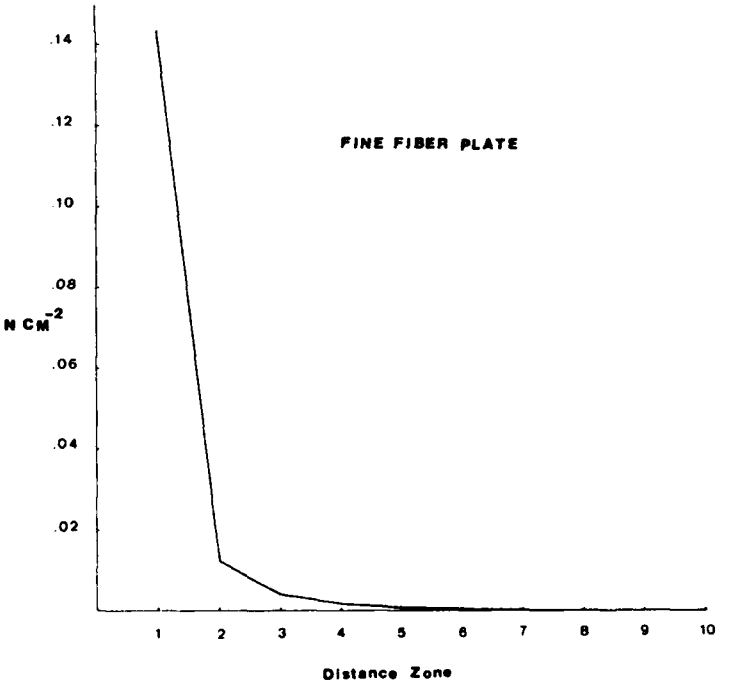

FIGURE 6. VARIATION OF THE SURFACE CONCENTRATION OF "DUST MAGNET" FINE FIBER SCAVENGERS. Scavengers had a mean size of 1.92 cm x 1.74 cm x 0.72 cm and mean settling velocity of 146 cm s^{-1}. Scavenger concentration is plotted in the same way as in Fig. 5.

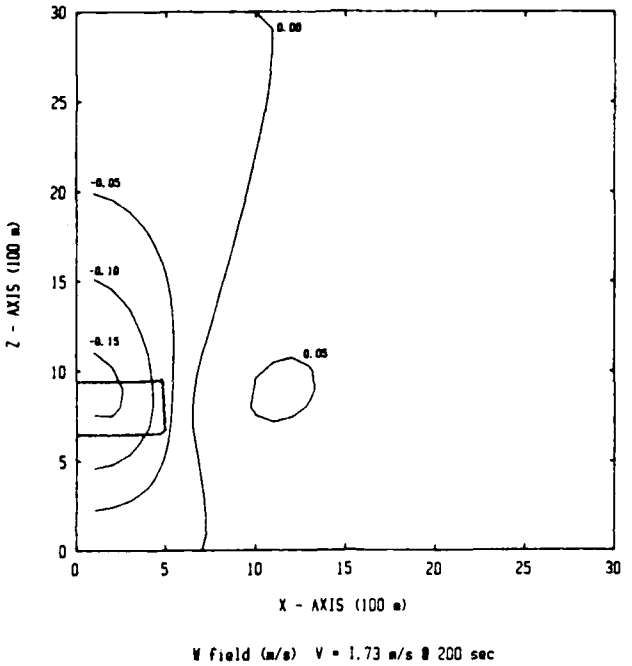

FIGURE 7a. DOWNDRAFT VELOCITY FIELD INDUCED BY FALLING SCAVENGERS. Scavengers of mean settling velocity of 1.73 m/s were dropped in a zone 500 m x 320 m at the height of 1000 m. The Fig. 7a represents the field after 200 sec, 7b after 400 sec, and 7c after 600 sec.

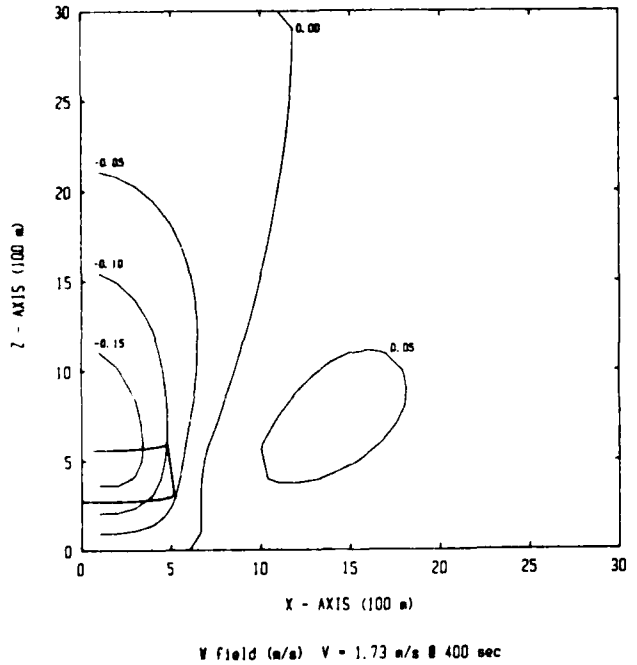

FIGURE 7b

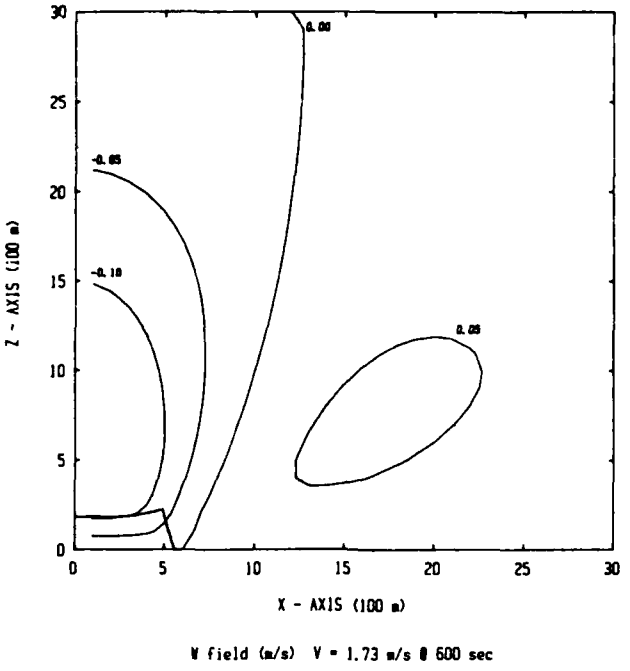

FIGURE 7c

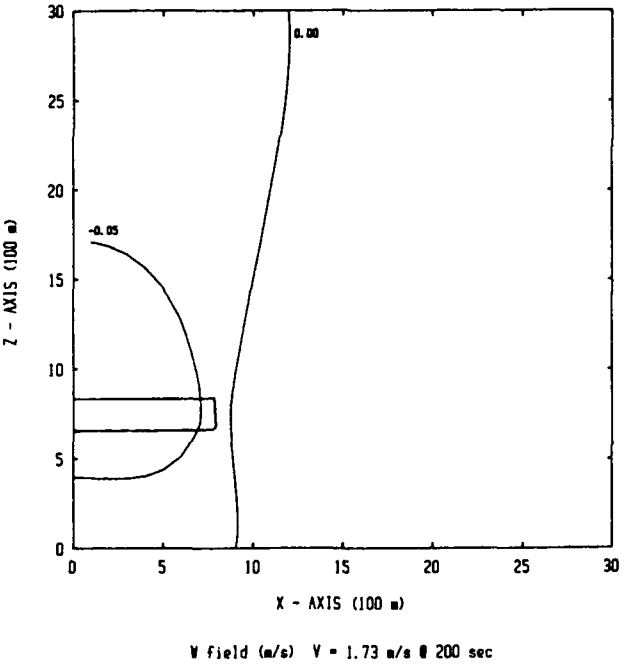

FIGURE 8a. DOWNDRAFT VELOCITY FIELD INDUCED BY A FALLING SCAVENGER ZONE 800 m x 200 m. All other parameters are the same as in Fig. 7a, b, c.

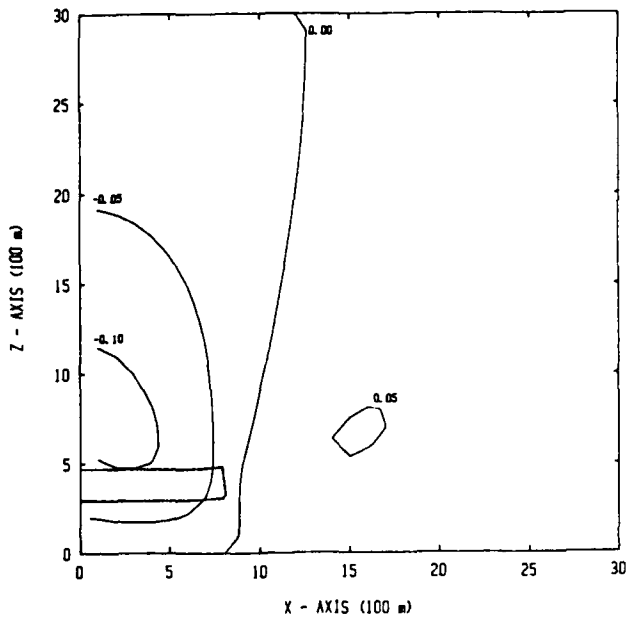

W field (m/s) V = 1.73 m/s @ 400 sec

FIGURE 8b

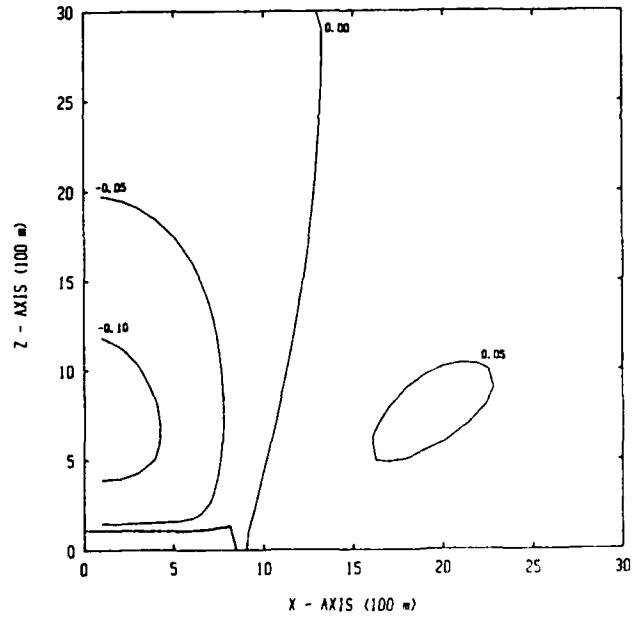

W field (m/s) V = 1.73 m/s @ 600 sec

FIGURE 8c

II. AEROSOL CHARACTERIZATION METHODS

(OTHER THAN AERODYNAMIC METHODS - SEE IC)

IIA. Optical Inversion Methods for Size, Size Distribution and Other Particle Properties

DETERMINATION OF THE PARTICLE SIZE DISTRIBUTION FROM BLIND INVERSION OF SYNTHETIC DATA
(This paper is from the 1984 Conference)

B. P. Curry and E. L. Kiech
Calspan Field Services, Inc.
Arnold Air Force Station, TN 37389

ABSTRACT

This paper reports the inversion of four computer-generated sets of noisy,synthetic Mie scattering data by use of two previously reported size distribution inversion procedures. The data were supplied by Chemical Research and Development Center (CRDC), and the particle size distribution functions (PSDF's) were inverted by the authors without advance knowledge of the PSDF's.

INTRODUCTION

Since 1980, a research program at AEDC has been sponsored by the Army Chemical Research and Development Center (CRDC) to develop and test computational procedures which can invert light scattering measurement data to obtain the particle size distribution function (PSDF). The PSDF is defined such that the integral of the PSDF between any two sizes represents the probability of finding a particle in that size range. Any combination of measurements of the angular intensity distribution, polarization distribution (as a function of scattering angle), and spectral distribution of light scattered by a polydispersion of small spherical particles is suitable as input for these techniques. This report presents the results of calculating the PSDF from four sets of noisy, synthetic scattering data which were sent to the authors by Dr. Jerry Bottiger of CRDC. Two computer programs developed at AEDC were used to invert the data. The first program (PARTSIZ) uses a nonlinear regression technique to determine the parameters of an assumed PSDF, while the second program (FRED-HIL) uses a constrained eigenfunction expansion approach.

SELECTION OF INPUTS

The data received from CRDC contained multiwavelength, polarized angular scattering data, representing 2160 scattering inputs for each of four cases. The totality of inputs included both linearly polarized scattering states and elliptically polarized states; however, only linear polarization was considered. Using selection procedures to be described below, the chosen scattering data were further reduced to sets corresponding to 30 inputs. The four PSDF inversions were then performed using computational procedures which have been previously reported (Ref. 1-3). For all the results quoted herein the scattering inputs were normalized by their mean, and both inversion codes accounted iteratively for the variation of the normalization denominator with the parameters of the PSDF.

Although many scattering inputs were available for PSDF inversion, it can be readily shown by the methods of Ref. 4 that the majority of the information needed for the inversions is concentrated in a small subset of the original inputs. Inclusion of other inputs often introduces more error than additional information. A final set of 15 wavelengths was chosen with the following restrictions: (1) for

each wavelength a single, different scattering angle was chosen and (2) for each scattering angle both orthogonal linear polarization states were retained, resulting in 30 total inputs. The actual selection of inputs was made by examining computed plots of the ratio of the linearly polarized, Mie scattering intensities (kernels) versus particle diameter, and selecting those inputs whose corresponding polarization ratios exhibited essentially monotonic dependence on particle diameters. The wavelengths selected in this fashion are listed in Table I.

All 30 inputs were used to obtain the PSDF's by the nonlinear regression code (PARTISIZ). Program memory limits of the constrained eigenfunction code (FRED-HIL) prevented use of more than 26 inputs for PSDF deconvolutions obtained by this method. However, use of substantially more inputs than a minimal number required for a given PSDF actually degraded the accuracy of the FRED-HIL deconvolutions, though such was not the case for the PARTSIZ regressions. Specifically, use of more than 16 inputs (optimally chosen) for single mode deconvolutions gave worse results (on the basis of closeness of computed residual error to "experimental" error) than those obtained from 12-16 optimal inputs. In contrast, good bimodal deconvolutions required the use of at least 22 inputs. For the purpose of determining optimal inputs for the code FRED-HIL, input channels were ranked by the degree of their redundancy with all other input channels. Table II shows the ranking of inputs (least redundant to most redundant) obtained by this method, subject to the added restriction that perpendicular/parallel polarization pairs were kept intact. This ranking proved to be suitable for the determination of optimal input sets for FRED-HIL, but not for PARTSIZ. In the case of PARTSIZ, best results were obtained by using all 30 inputs, but rather good results were also obtained (for both bimodal and unimodal PSDF's) using only the minimal set of 12 inputs shown in Table III. Significantly, the optimal set of 12 inputs for PARTSIZ where chosen on the basis of the steepness of their associated kernels as functions of particle diameter, but a complete algorithm for optimizing inputs for this nonlinear regression procedure has yet to be devised.

The 12 least redundant inputs (including both linear polarization states) in Table II form the optimal input set for use with FRED-HIL, except that the input pair with wavelength 4.14 μm occurs in the chosen optimal set (Table IV) instead of the 4.91 μm input pair. These two input pairs have very nearly the same redundancy level, but the relative information content (determined as described in Ref. 1) of the 4.14 μm input pair is twice that of the 4.91 μm input pair. Deconvolutions were performed using both the set of inputs in Table IV and the set obtained by substituting the 4.91 μm input pair for the 4.14 μm input pair. The set of inputs in Table IV gave decidedly better deconvolutions than the alternate set.

INVERSION RESULTS

As was mentioned in the preceding section, the PSDF inversion procedures used in this paper are of two types: (1) a nonlinear regression technique (PARTSIZ) and (2) a constrained eigenfunction expansion technique (FRED-HIL) which incorporates a trial function in a doubly-iterative fashion. Both procedures have been thoroughly described in Refs. 1-3, and both require an initial guess of the parameters which characterize the PSDF. It has been found that the use of a residual error, contour plotting routine is quite helpful (though, emphatically, it is not required) in establishing the initial PSDF parameters as indicated by the logic flow path shown in Fig. 1. Figure 2 is a residual-error contour plot for the inputs of Case G. The abscissa of Fig. 2 is the modal diameter, and the ordinate is analogous to the full-width-at-half-maximum (FWHM) of a family of single mode PSDF's. Actually, the width parameter shown in Fig. 2 is the PSDF width measured from the peak value of the PSDF to the diameter on the right side of the peak at which the PSDF value has decreased to 1/e of the peak value. Contours of constant residual error are plotted in Fig. 2 for various pairs of the PSDF modal diameter and PSDF width parameter. It can be seen from Fig. 2 that the smallest residual error obtainable with a two parameter regression is about 5 percent - only slightly larger than the stated "experimental" imprecision of 4 percent. Hence, Fig. 2 indicates that the final recovered PSDF should likely be unimodal.

The result of using the pair of starting parameters which correspond to contour A in Fig. 2 in conjunction with the scattering data of Case G as inputs for the nonlinear regression code (PARTSIZ) is shown in Fig. 3. The final regressed PSDF is a three parameter, single mode PSDF, and the computed residual error of 3.6 percent agrees well with the stated imprecision of 4 percent. Figure 3 also shows the original PSDF (provided by Dr. Jerry Bottiger of CRDC after his examination of our results) from which the scattering data were computed. The agreement between the original and regressed PSDF's is excellent. The upper and lower, one-standard-deviation imprecision limits shown in Fig. 3 were obtained by perturbing the scattering inputs corresponding to the regressed PSDF with ten sets of Gaussian errors and carrying out ten additional regressions. An algorithm is currently being installed in PARTSIZ to accomplish this calculation analytically using the curvature matrix which corresponds to PSDF parameters near the values of the final regression. Figure 4 shows the mass normalized PSDF (where each ordinate is multiplied by the diameter cubed and renormalized to unit area under the curve) which corresponds to Fig. 3.

The data of Case G have also been deconvolved using code FRED-HIL. The deconvolution was carried out using optimal sets of 12, 16, 20, 22, 24 and 26 inputs chosen from Table II. The deconvolutions using 12 (Table IV) and 16 inputs were very similar, but the associated residual errors were 4.5 percent and 4.1 percent respectively. Consequently, the 16 input results were chose for inclusion here. Figure

5 shows the resulting deconvolution before the application of a final numerical filter, and Fig. 6 shows the recovered PSDF after 6 passes through an arithmetic mean filter. Substantially worse results were obtained when more than 16 inputs were used. The kernels used here were computed to a maximum diameter of only 10 μm. Had a more extensive set of kernels been used for this deconvolution, the agreement between recovered and original PSDF's would have been better (as was found to be true of PARTSIZ regressions using sets of kernels computed to 10 μm and 20 μm, respectively).

The residual error contours for Case H are shown in Fig. 7. Note that contour A denotes a residual error of 8 percent, well above the stated imprecision of 4 percent. This observation suggests that the recovered PSDF should be at least bimodal in complexity. The results of the regression are shown in Fig. 8, and the regressed PSDF is obviously bimodal. The residual error in this case is 3.99 percent, showing by agreement with the stated imprecision that no higher structural complexity need be considered. The mass-normalized PSDF obtained from these results is shown in Fig. 9.

Similar results were obtained from the deconvolution procedure when the initial trial PSDF was taken to be the sum of two lognormal PSDF's having equal geometric standard deviations of 1.14, but unequal number median diameters of 2.54 and 5.0 μm, respectively. The relative number fractions of these modes were varied to give approximate agreement between the computed residual error and the stated imprecision of 4 percent. Figure 10 shows the recovered PSDF for Case H (after 4 passes through the final filter). This deconvolution used the 22 least redundant inputs from Table II. More inputs produced significantly worse results.

For the remaining PSDF inversions, the PSDF recovery procedure was the same as in the two previous cases; however, the residual error curves are not shown. The PSDF regressed from the scattering data for Case I is shown in Fig. 11. The corresponding mass normalized PSDF is shown in Fig. 12.

Case I was very difficult to deconvolve. The result shown in Fig. 13 was obtained using a trial bimode composed of PSDF's whose geometric standard deviations were 1.27 and whose number median diameters were 2.1 μm and 4.3 μm. Relative heights of each mode were varied to give best agreement between computed residual error and the stated imprecision of 4 percent. Using 22 optimized inputs, the deconvolution yielded 6.2 percent residual error. With 24 optimized inputs, the residual error was 4.2 percent, and with 26 inputs it was 4.3 percent. The deconvolution shown in Fig. 13 was obtained from the 24 least redundant inputs in Table II. The recovered PSDF was passed 6 times through the final filter to smooth variations in the large particle tail of the PSDF.

The final PSDF inversion was another single mode distribution. Figure 14 shows the regression results of Case J, and Fig. 15 shows the corresponding mass normalized PSDF. The residual error of this regression was 3.6 percent.

Figure 16 shows the deconvolution results of Case J using 16 optimized inputs. This deconvolution had a residual error of 4 percent. The corresponding deconvolution with the optimal 12 inputs had a residual error of 4.5 percent. Use of more than 16 inputs produced significantly worse results.

In all cases considered, the use of more inputs than was necessary for good deconvolutions degraded the results from FRED-HIL. Both the single mode PSDF's (Cases G and J) were best rendered by use of 16 optimized inputs. In contrast, the bimodal features of Cases H and I were not apparent when less than 20 inputs were used, and best results were obtained with 22 optimized inputs for Case H and 24 optimized inputs for Case I. These results demonstrate dramatically the necessity to consider the expected nature of the recovered PSDF's when optimizing the design of a scattering experiment whose result will be interpreted by use of an orthogonal decomposition procedure for solution of the integral scattering equation.

The nonlinear regression method, however, is much less susceptible to the choice of inputs for the regression analysis. Clearly, one can determine a minimal, optimal subset of a larger set of inputs and obtain better regressions than with any other subset of equal size, but the rules for defining such an optimal subset of inputs have not yet been determined. Further, increasing the number of inputs for the regression procedure always improves the accuracy of the regression, as indicated by the calculated recovered PSDF imprecision limits.

CONCLUSIONS

All four cases of simulated particle scattering data supplied by CRDC were successfully inverted using both the nonlinear regression procedure (PARTSIZ) and the constrained eigenfunction expansion deconvolution procedure (FRED-HIL) reported in Refs. 1-3. The recovered PSDF imprecision levels obtained by PARTSIZ were generally smaller than those of FRED-HIL. In addition, PARTSIZ yielded equally good, number normalized and mass normalized results, whereas FRED-HIL always included sufficient oscillations to invalidate the mass-normalized results.

Optimization of the scattering inputs for PSDF deconvolution by FRED-HIL (or any other orthogonal decomposition solution procedure) is a matter of some criticality, and the number and choice of optimum inputs depend on the nature of the recovered PSDF. Regression of the PSDF is much less sensitive to the choice of inputs than is the deconvolution procedure. Further work should address the problem of determining the optimal experimental configuration for each measurement.

REFERENCES

1. Curry, B. P. and Kiech, E. L. "Two Particle Size Inversion Procedures for Interpretation of Mie Scattering Measurements," AEDC-TR-83-32, November 1983.

2. Curry, B. P., and Kiech, E. L. "A Constrained Eigenfunction Expansion Method and a Nonlinear Regression Procedure for the Inversion of Mie Scattering Data," in Proceedings of the 1983 Chemical

Research and Development Center Scientific Conference on Observation and Aerosol Research, ed. by R. H. Kohl, Aberdeen Proving Ground, Md.

3. Curry, B. P., and Kiech, E. L. "Improved Methods to Invert the Particle Size Distribution Function from Mie Scattering Measurements," AEDC-TR-83-52, February 1984.

4. Capps, C. D., Henning, R. L., and Hess, G. M. "Analytic Inversion of Remote Sensing Data," Applied Optics, Vol. 21, No. 19, 1 Oct. 1982, pp. 3581-3587.

TABLE I. SELECTED INPUTS FOR PARTICLE SIZE INVERSION
(BOTH LINEAR POLARIZATIONS)

WAVELENGTH (MICRONS)	ANGLE (DEGREES)
0.222	95
0.266	100
0.524	130
0.782	135
1.040	140
1.550	145
2.330	160
2.590	130
2.850	130
3.630	45
3.880	150
4.140	140
4.910	135
6.200	80
8.990	85

TABLE II. RANKING OF INPUTS BY LEAST REDUNDANCY
(PERPENDICULAR/PARALLEL POLARIZATION PAIRS ARE KEPT INTACT)

RANK	INPUT	
	$\lambda(\mu m)$	θ(deg)
1	2.33	160
2	1.55	145
3	3.88	150
4	0.524	130
5	1.04	140
6	4.91	135
7	4.14	140
8	0.782	135
9	2.85	130
10	8.99	85
11	6.2	80
12	3.63	45
13	2.59	130
14	0.266	100
15	0.222	95

TABLE III. OPTIMAL INPUTS FOR NONLINEAR REGRESSION
(BOTH LINEAR POLARIZATION STATES)

WAVELENGTH (MICRONS)	ANGLE (DEGREES)
.524	130
2.59	130
2.85	130
4.91	135
6.20	80
8.99	85

TABLE IV. OPTIMAL INPUTS FOR CONSTRAINED EIGENFUNCTION DECONVOLUTION
(BOTH LINEAR POLARIZATION STATES)

WAVELENGTH(μm)/ANGLE(DEG)	
0.524/130	2.33/160
1.04/140	3.88/150
1.55/145	4.14/140

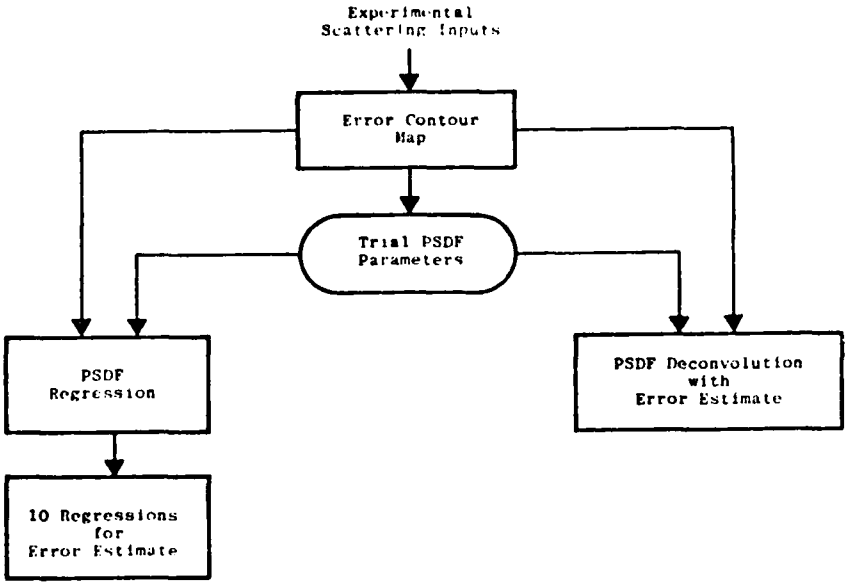

FIGURE 1. PROCEDURE FOR PARTICLE SIZE INVERSION.

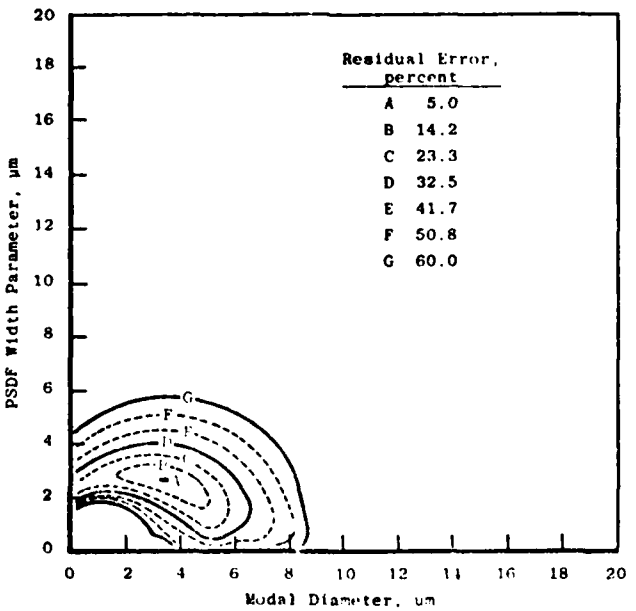

FIGURE 2. RESIDUAL ERROR CONTOUR MAP SHOWING OPTIMUM SINGLE MODE PSDF PARAMETERS FOR CASE G.

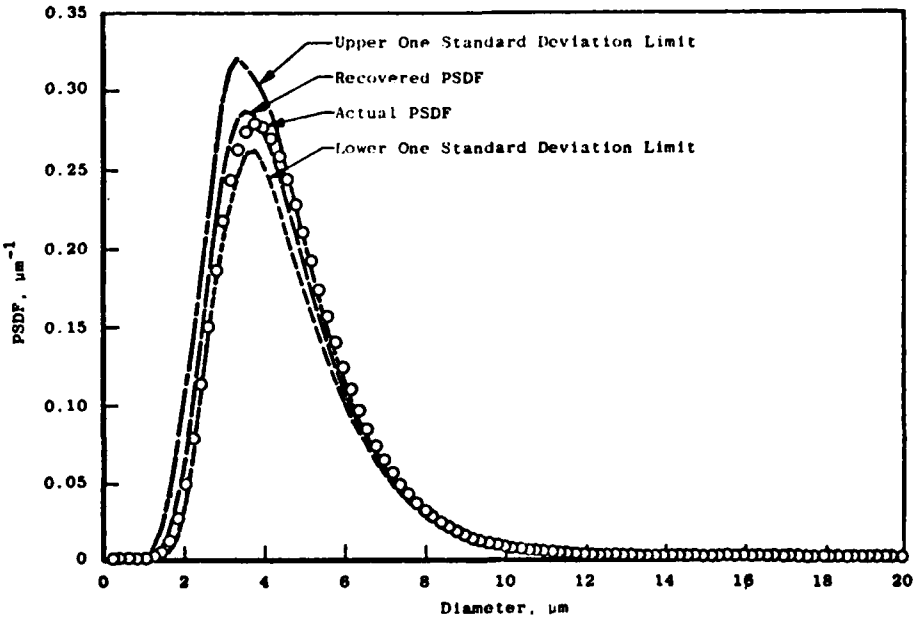

FIGURE 3. REGRESSION OF CASE G.

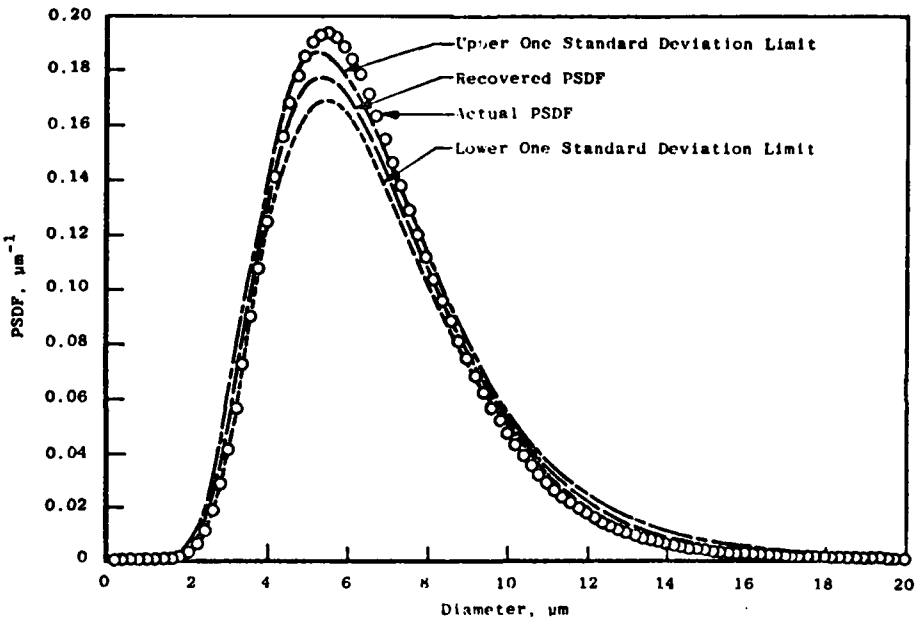

FIGURE 4. MASS NORMALIZED PSDF CORRESPONDING TO FIG. 3.

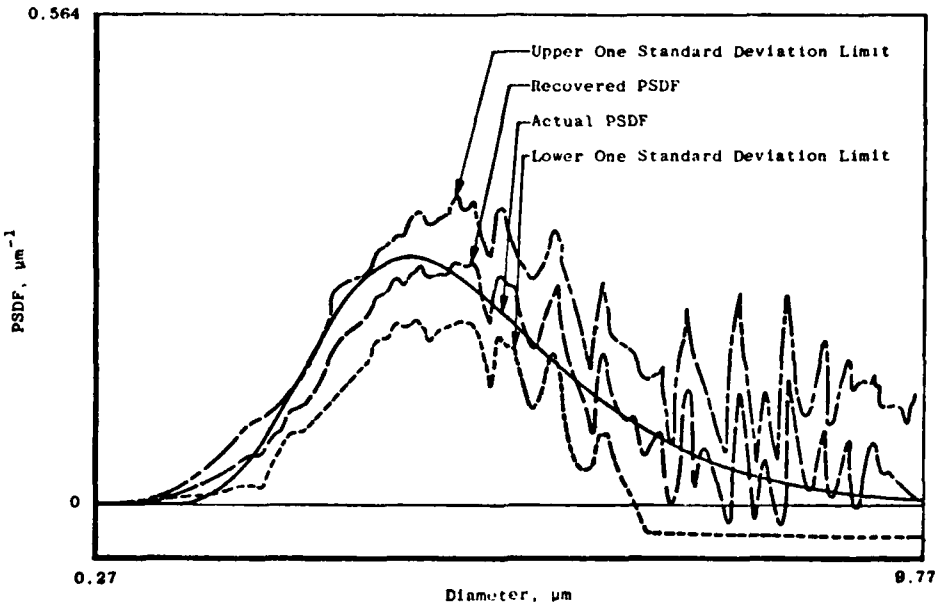

FIGURE 5. CASE G DECONVOLUTION

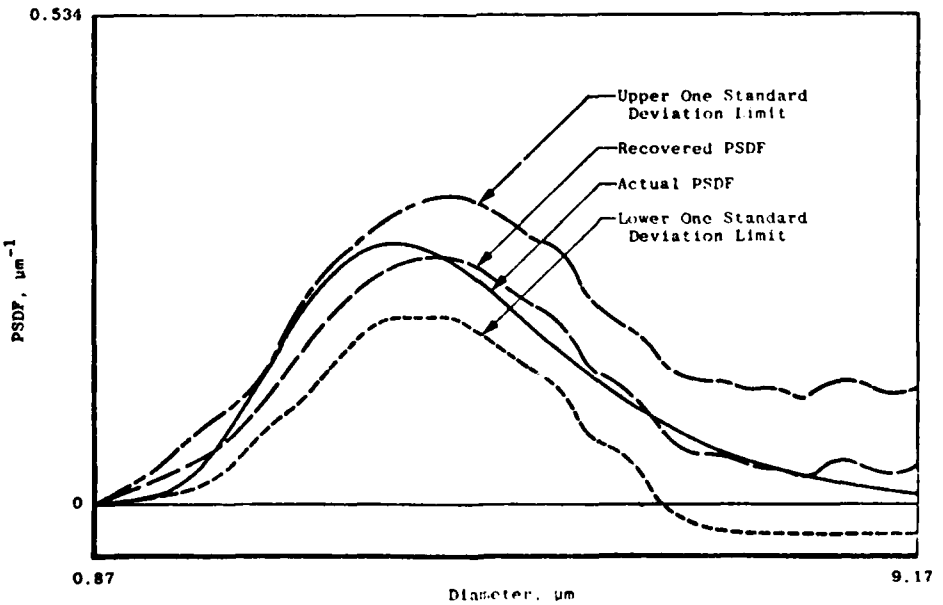

FIGURE 6. DECONVOLUTION OF CASE G (including smoothing by arithmetic-mean filter).

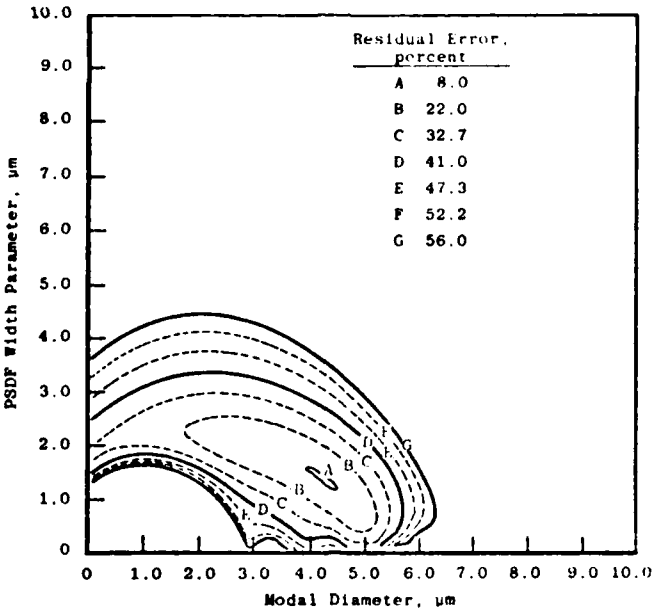

FIGURE 7. RESIDUAL ERROR CONTOUR MAP SHOWING OPTIMUM SINGLE MODE PSDF PARAMETERS FOR CASE H.

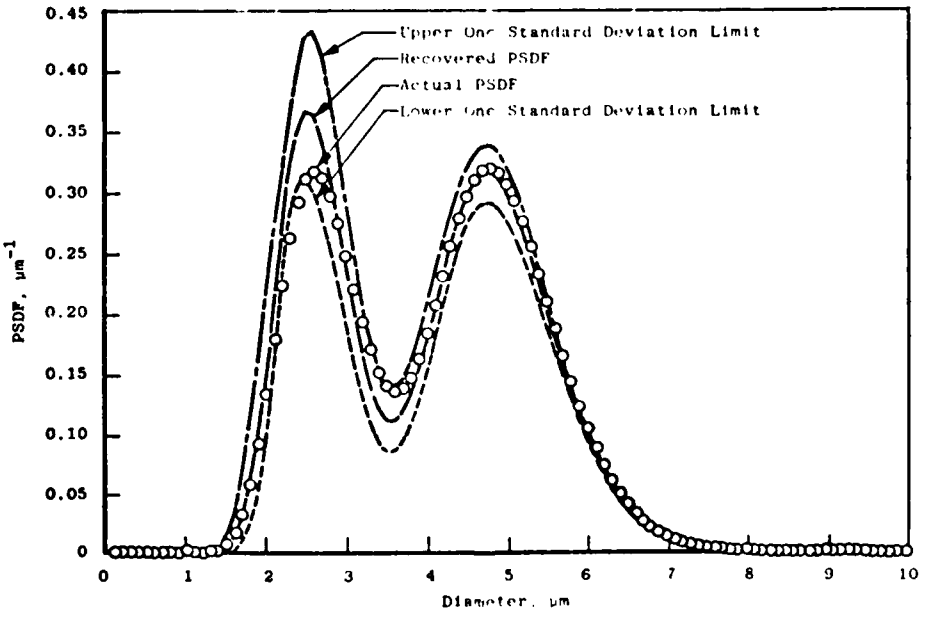

FIGURE 8. REGRESSION OF CASE H.

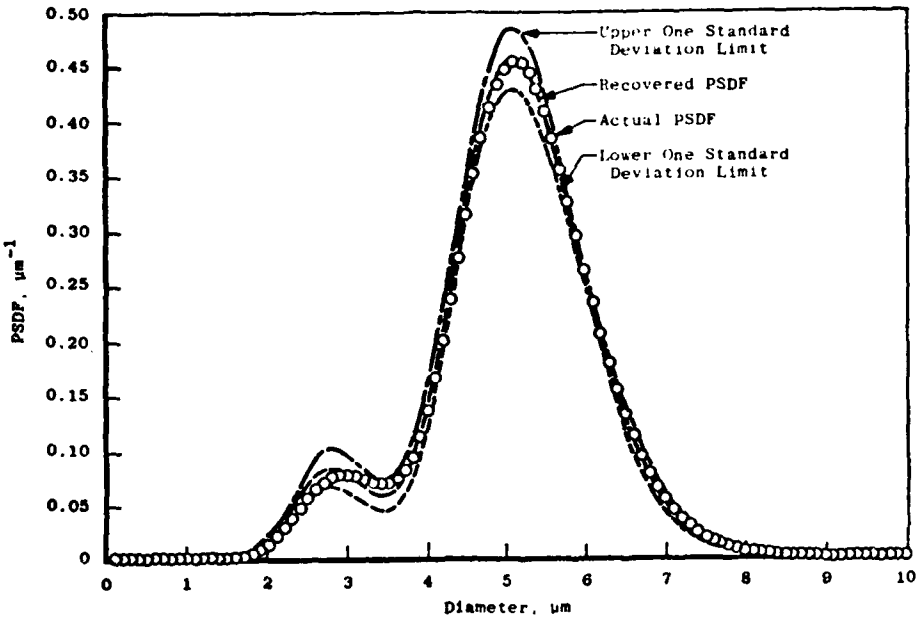

FIGURE 9. MASS NORMALIZED PSDF CORRESPONDING TO FIG. 8.

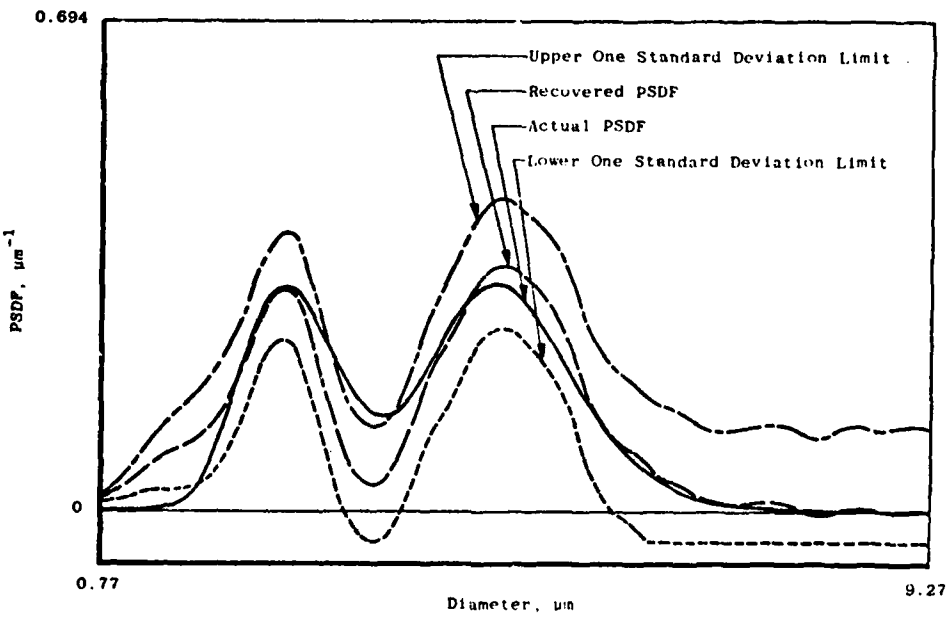

FIGURE 10. DECONVOLUTION OF CASE H.

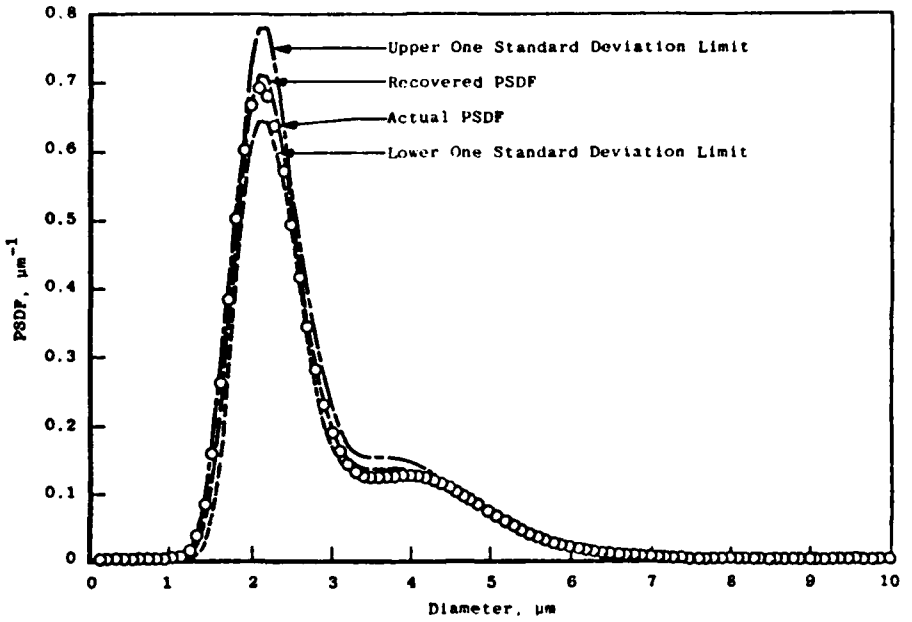

FIGURE 11. REGRESSION OF CASE I.

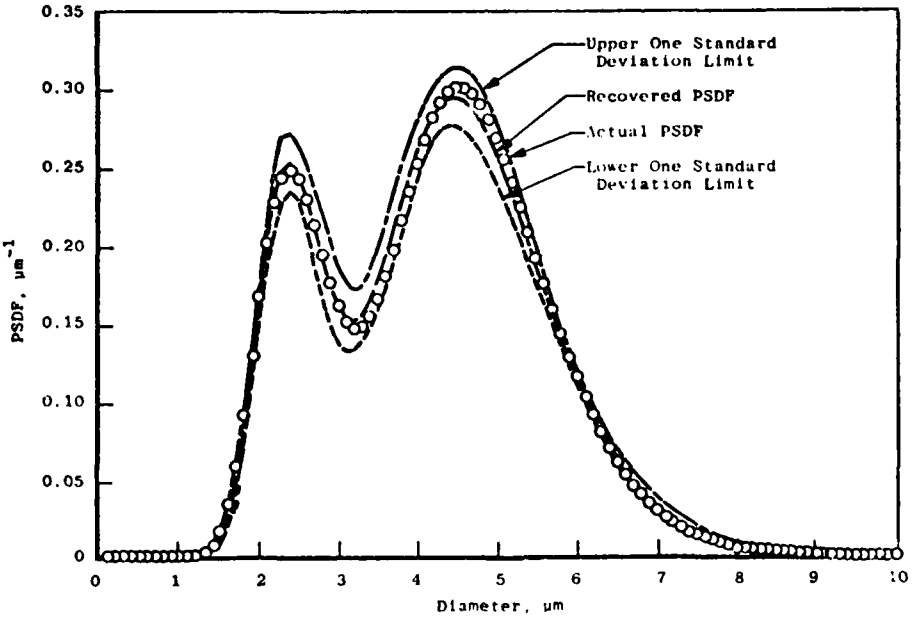

FIGURE 12. MASS NORMALIZED PSDF CORRESPONDING TO FIG. 11.

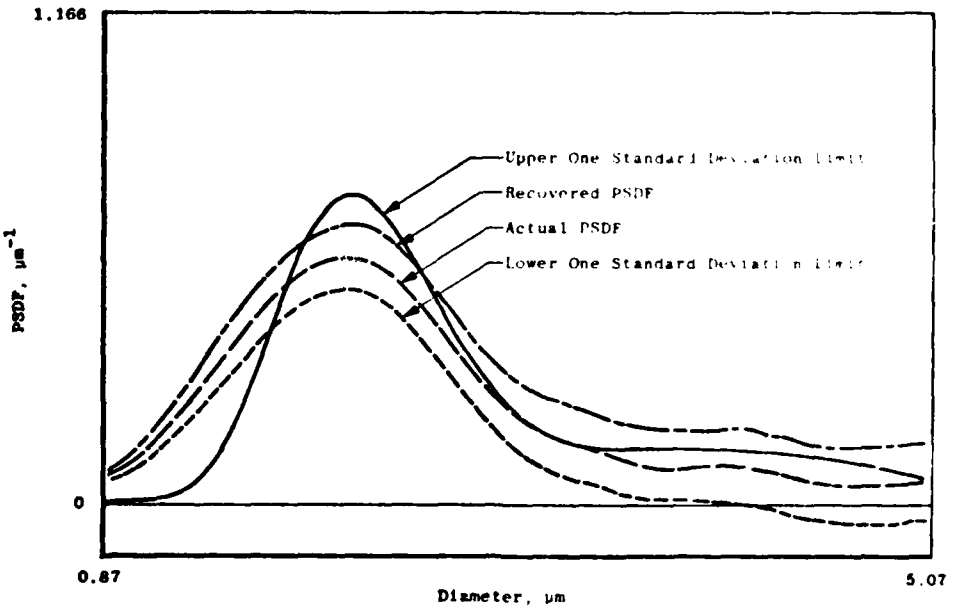

FIGURE 13. DECONVOLUTION OF CASE I.

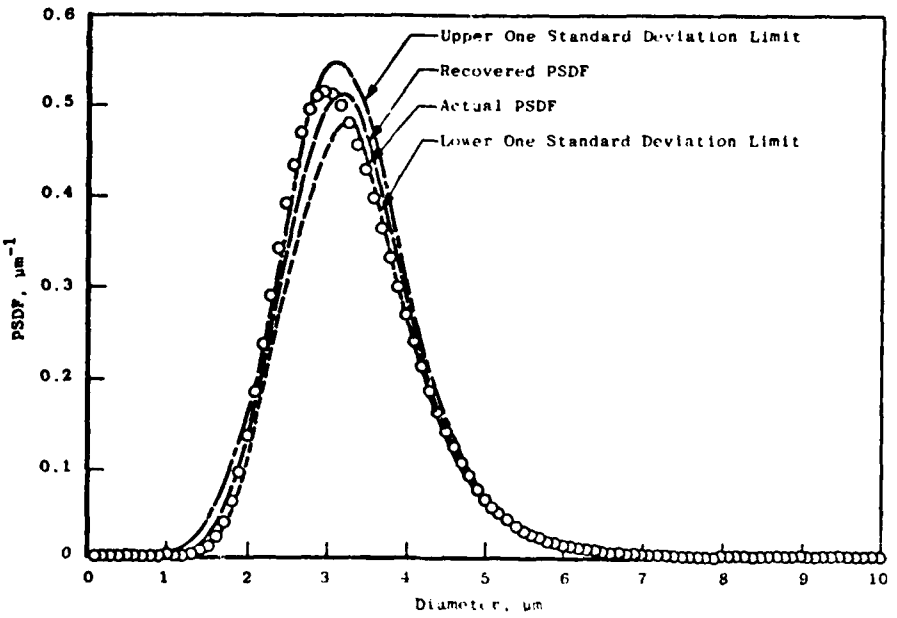

FIGURE 14. REGRESSION OF CASE J.

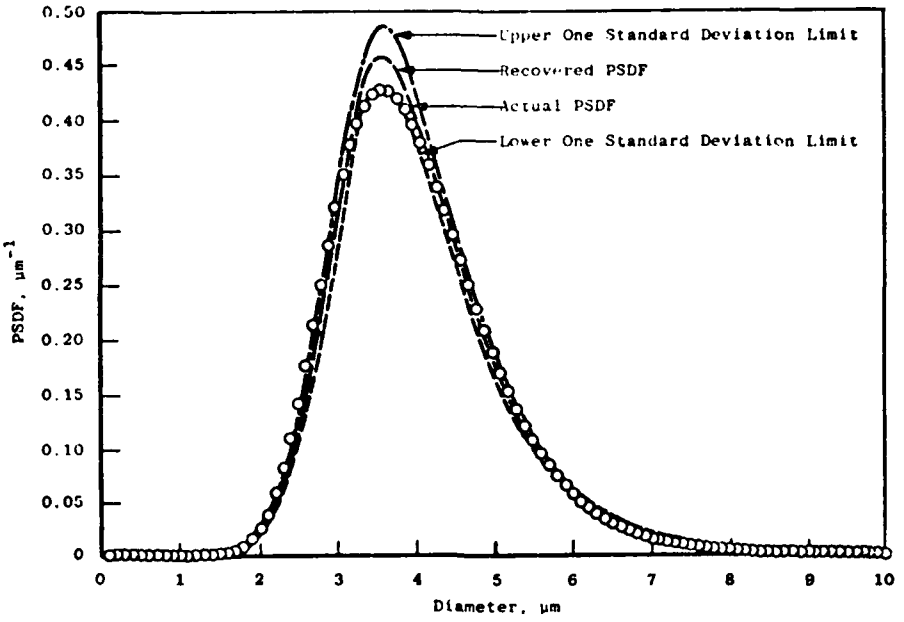

FIGURE 15. MASS NORMALIZED PSDF CORRESPONDING TO FIG. 14.

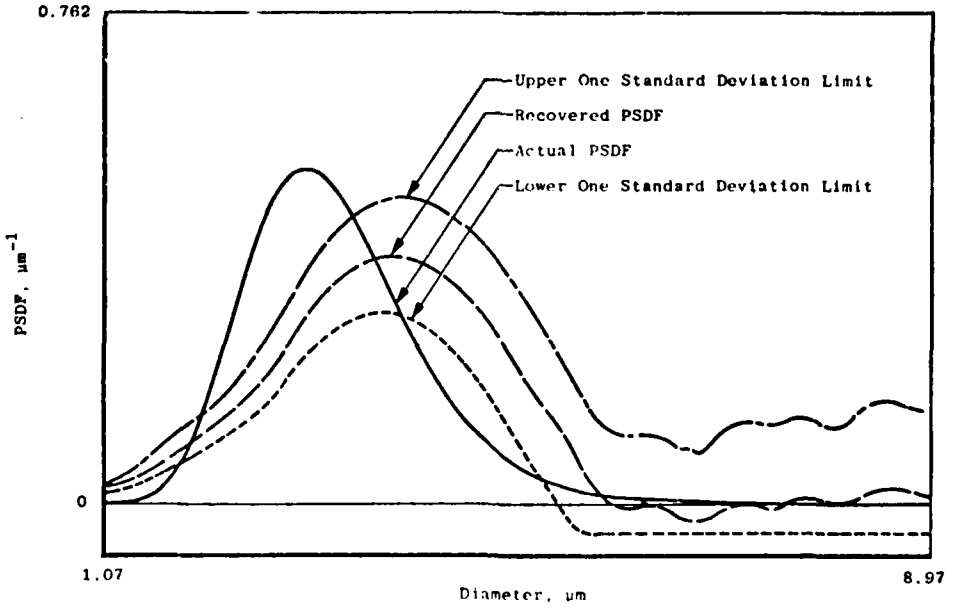

FIGURE 16. DECONVOLUTION OF CASE J.

OPTIMIZATION OF MIE SCATTERING WAVELENGTHS AND ANGLES FOR PARTICLE SIZING

Earl L. Kiech
Calspan, Inc.
Arnold Air Force Station, Tennessee 37389

ABSTRACT

This paper reports the development of a technique to optimize the design of particle sizing experiments which use light scattering information to determine size distributions. The technique determines, from an overall set of possible wavelengths and angles, the best subset to use in a sizing experiment under specified conditions. Several test cases are used to compare results using optimized configurations with backscattering.

INTRODUCTION

Over the past three years, several techniques for determining the particle size distribution function (PSDF) from optical (Mie) scattering measurements have been developed at AEDC (Ref. 1-3). Extensive studies of these techniques have indicated that a nonlinear regression approach is superior for data which contain random errors. The nonlinear regression technique developed at AEDC uses a linear combination of modified lognormal basis functions to represent the actual PSDF. Each mode in the PSDF is modeled as a pseudo-lognormal whose modal position and three basic shape factors (width, skewness and kurtosis) are variable. A companion program has been developed which will determine the optimum wavelengths and angles to use in designing a particle sizing experiment. Two test cases are used to show the advantages and limitations of the optimized configurations over a reference backscattering configuration.

DEFINITION OF FIGURE OF ERROR

Since this optimization procedure minimizes a quantity related to the recovered PSDF imprecision, a figure of error was used instead of the more usual figure of merit. The error figure represents the uncertainty associated with recovering some characteristic of the PSDF. The optimization procedure minimizes the error figure by the selection of appropriate wavelength and angle inputs. For this study, the error figure was defined as the sum of the variances of all the parameters describing the PSDF. The parameter variances are easily obtained from a nonlinear regression procedure by inverting the curvature matrix as described by Bevington (Ref. 4). Nonlinear regression has the added advantage of easily incorporating a priori information into the procedure through the definition of appropriate basis functions. A priori information or assumptions have been found to be necessary to prevent the noise in actual measurements from causing recovered PSDF's to exhibit unrealistic characteristics such as negative values. Constraints such as positivity and smoothness can be used in many cases to stabilize the regression and assure physically realistic recovered PSDF's.

The flexibility in the definition of the error figure allows the experiment designer to optimize the measurements for the recovery of particular features of the size distribution. For example, determining the average particle size with greater precision might be more desirable than completely characterizing the distribution with somewhat less precision. This could be done by defining the error figure as the variance of the recovered average particle size.

REQUIRED INPUTS

The information which is necessary for the optimization procedure includes: an estimate of the actual PSDF, the overall or global set of wavelengths and angles from which to select an optimum subset, the number of inputs in the optimum subset, the refractive indices of both particles and medium, and the polarization components to be measured. The global set of possibilities is usually determined by experimental constraints such as a limited number of source wavelengths or detector locations. Although increasing the size of the measurement subset will always improve the recovery capability, a tradeoff is involved between the increase in information and the increased cost and complexity of the experiment. All particles are assumed to have the same known refractive index and to be immersed in a medium of constant refractive index. At the cost of some increase in experimental complexity, additional polarization terms may be included to provide more sizing information. Any of these quantities can be varied to investigate the resulting changes in the optimum subset and accuracy of the recovered distribution. For example, the designer could determine whether measuring a different polarization component would improve his results.

OPTIMIZATION ALGORITHM

The procedure for determining an optimum subset of N inputs begins by selecting N-1 starting inputs from the global set. The global set is then searched for the Nth input which yields the smallest error figure. This Nth input then replaces one of the original starting inputs forming a new N-1 subset. The sequence is repeated until the error figure is minimized. Experience has indicated that the final optimum subset is very insensitive to the selection of the starting inputs, implying a high probability that the true optimum subset has been found. Although the actual starting inputs selected do not affect the final computed optimum inputs, the time required for the computation is reduced by selecting a starting set which is close to the final set. For this reason, the preferred procedure is to first calculate the optimum subset containing the minimum number of inputs (equal to the number of parameters to be used in the regression). This subset is then used as starting inputs for the calculation of the next higher order optimum subset and the process repeated until the desired number of inputs is attained.

TEST CASES

In order to determine how accurate the original estimate of the actual PSDF must be, test cases were devised which involved finding optimum, 15-input subsets for single (shown as the dashed

line in Fig. 1) and bimodal (shown as the solid line in Fig. 1) estimates for a distribution of latex spheres in water. These two optimized input subsets were then used to recover actual PSDF's which varied in some way from the estimates. A third input set was needed as a reference to represent the results to be expected from a non-optimized experiment. Backscattering was selected for the reference because of its widespread use and the fact that it included an input from each wavelength in the global set.

Table I shows the optimum input subsets (assuming unpolarized measurements) determined for the single and bimodal PSDF estimates, and the reference backscatter inputs. The global set consisted of the 15 wavelengths used for the backscatter inputs with associated angles ranging from 50 to 180 degrees in 5 degree steps. Table II shows the indices of refraction for latex and water which were used. The optimum input subsets are quite different for the two distributions due probably to the fact that although they have the same median particle size, the bimode contains proportionally more large particles. In particular, the optimum bimode inputs tend to concentrate at the long wavelengths while the optimum single mode inputs tend to represent both long and short wavelengths. Experience with other distributions has confirmed a logical tendency to prefer longer wavelengths as distributions include more large particles.

RESULTS

Figure 2 shows the effectiveness of each of the three input subsets at recovering actual single model PSDF's which differed by translation from the single mode estimate. On this and the following plots, the circle represents the point at which the actual PSDF was identical to the estimated PSDF. The ordinate represents the square root of the error figure which roughly corresponds to the overall standard deviation of the recovered PSDF. The inputs optimized for the single mode estimate (shown as the dashed line) show an improvement over backscattering of up to 200% over a range of relative peak locations from 0.2 to 1.2. This indicates that optimization is effective for original estimates of the single mode peak ranging from 0.8 to 5 times the actual value. The inputs optimized for the bimode estimate (shown as the solid line) are also somewhat better than backscattering especially at smaller sizes. The results which would be obtained with a backscattering configuration (indicated by the dot/dash line) are presented here for reference because of the widespread use of backscattering in actual sizing experiments and the fact that each of the wavelengths in the global set is represented. It is interesting to note that this plot graphically illustrates the increase in recovery uncertainty as the particle size decreases and begins to enter the Rayleigh scattering domain.

Figure 3 shows the effectiveness of each of the input subsets at recovering actual single mode PSDF's which differed in width from the single mode estimate. The optimized single mode inputs are much better than backscattering over a range of relative widths from 0.6 to 1.6, indicating that the original estimates for the single mode width could range from 0.6 to 1.7 times the actual value. The optimized bimode inputs are equal to or better than backscattering over almost the entire range of relative widths. These curves graphically illustrate the general tendency toward increasing parameter uncertainty as the distribution becomes broader.

Figure 4 shows the effectiveness of each of the input subsets at recovering actual bimodal PSDF's which differed by translation from the bimode estimate. The optimized bimode inputs show an improvement of up to 100% over backscattering for the entire range of relative positions from 0.2 to 2, indicating that the original estimates for the bimode peak locations could range from 0.5 to 5 times the actual value. The optimized single mode inputs are generally worse than backscattering for recovering these bimodes, and the transition to Rayleigh scattering is again accompanied by a marked increase in parameter uncertainty.

Figure 5 shows the effectiveness of each of the input subsets at recovering actual bimodal PSDF's which differed in width from the bimodal estimates. The optimized bimode inputs are superior to backscattering over a range of relative widths from 0.5 to 1.8, indicating the original estimate for the width of the bimode distribution could range from 0.6 to 2 times the actual value. The optimized single mode inputs are again much worse than backscattering for recovering these bimodes, and all the curves show the characteristic tendency toward increasing uncertainty for very broad distributions.

SUMMARY

This optimization procedure can aid in the design of a Mie scattering experiment in several ways. The designer can determine the best combination of wavelengths and angles to use within the particular experimental constraints; the effects of changing the constraints can be investigated; and the experiment can be designed to enhance the recovery of specified features of the PSDF. Although good estimates of the actual PSDF (particularly the number of modes) are desirable, significant improvement can be realized with poor initial estimates. As a general rule, if the number of modes in the actual distribution is unknown, the optimization should be run for the maximum number of modes to be used in the regression. For the test cases presented here, optimization improved by up to 200% the results obtained with backscattering. Although the actual improvement will vary for other cases and different basis functions, these results demonstrate the value of the procedure. Further work is needed to extend these conclusions to other particle/medium combinations, wavelength ranges, and more complicated PSDF's.

REFERENCES

1. Curry, B. P., and Kiech, E. L., "Two Particle Size Inversion Procedures for Interpretations of Mie Scattering Measurements," AEDC-TR-83-32, November 1983.

2. Curry, B. P., and Kiech, E. L., "A Constrained Eigenfunction Expansion Method and a Nonlinear Regression Procedure for the Inversion of Mie Scattering Data," in Proceedings of the 1983 Scientific Conference on Obscuration and Aerosol Research, July 1984.

3. Curry, B. P., and Kiech, E. L., "Improved Methods to Invert the Particle Size Distribution Function from Mie Scattering Measurements," AEDC-TR-83-52, February 1984.

4. Bevington, P. R., Data Reduction and Error Analysis for the Physical Sciences, McGraw-Hill, New York, 1969.

TABLE I
INPUT SUBSETS USED IN COMPARISONS
(UNPOLARIZED)

WAVELENGTH (MICRONS)	OPTIMUM FOR SINGLE MODE ANGLE, Deg	OPTIMUM FOR BIMODE ANGLE, Deg	BACKSCATTER ANGLE, Deg
0.300	175		180
0.357	175	100, 105, 175	180
0.697	5		180
1.038	10		180
1.374			180
2.023	5, 10, 170		180
2.727			180
3.580	45	75	180
3.873		120	180
4.828		165	180
5.125			180
5.403		135, 145, 150	180
6.560		130, 135	180
8.000	110, 115, 120, 125	105, 110, 135	180
10.600	5, 10, 110	115	180

TABLE II

REFRACTIVE INDICES FOR LATEX PARTICLES IN WATER

(Both particles and medium assumed transparent)

Wavelength (Microns)	Refractive Index	
	Particle	Medium
.300	1.6948	1.349
.357	1.6485	1.343
.697	1.5839	1.331
1.038	1.5739	1.327
1.374	1.5706	1.321
2.023	1.5682	1.305
2.727	1.5674	1.170
3.580	1.5669	1.383
3.873	1.5668	1.359
4.828	1.5666	1.330
5.125	1.5666	1.321
5.403	1.5666	1.305
6.560	1.5665	1.336
8.000	1.5664	1.291
10.600	1.5664	1.179

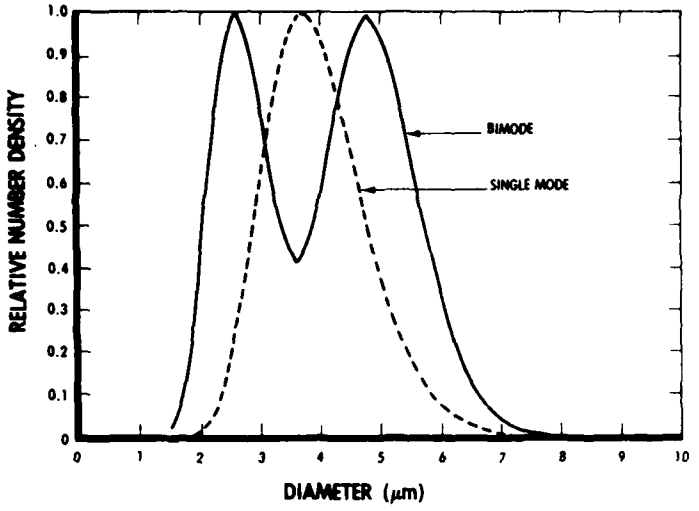

Fig. 1 Estimated PSDF's Used to Test Optimization Procedure

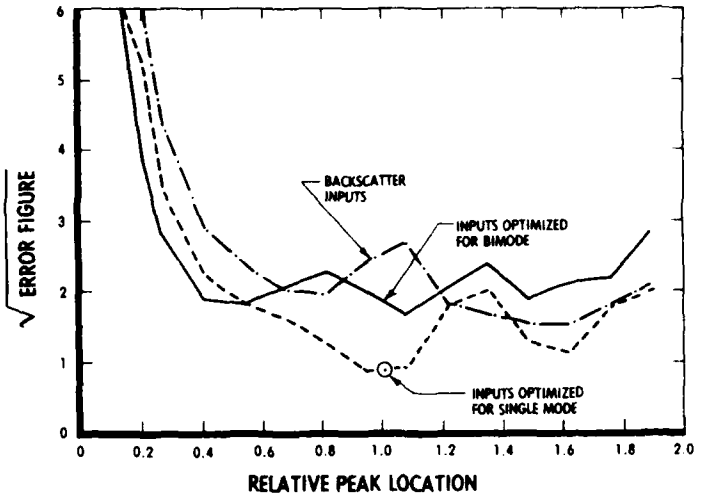

Fig. 2 Single-Mode Recovery Uncertainty Versus Peak Location

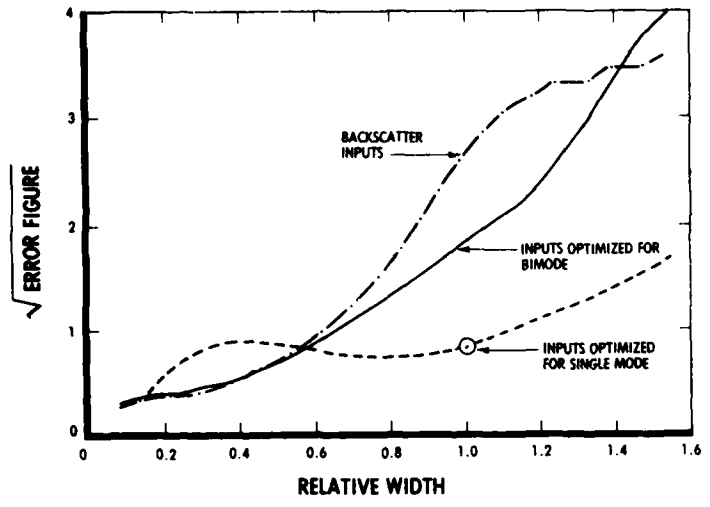

Fig. 3 Single-Mode Recovery Uncertainty Versus Width

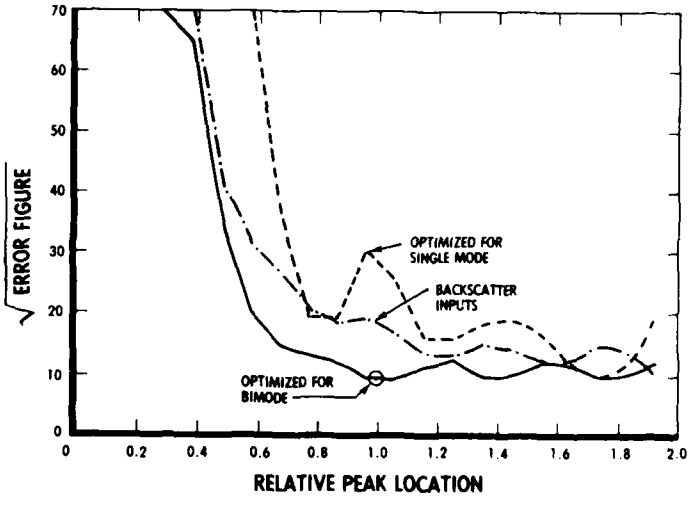

Fig. 4 Bimode Recovery Uncertainty Versus Peak Location

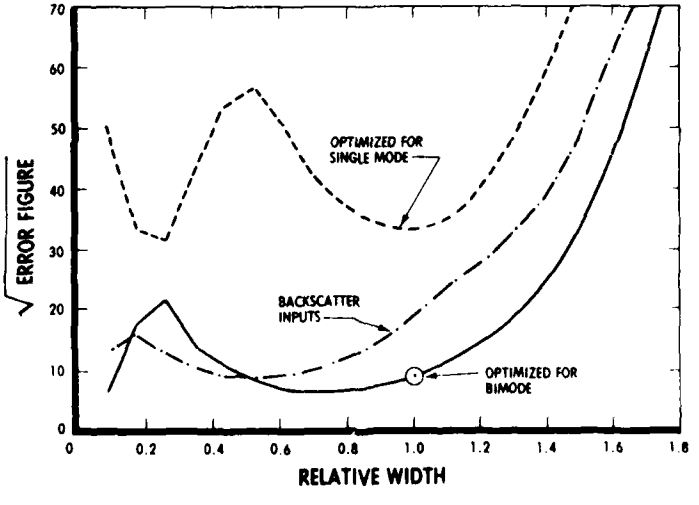

Fig. 5 Bimode Recovery Uncertainty Versus Width

ORTHOGONAL FUNCTION APPROACH TO THE INVERSION OF BACKSCATTERED DATA

Avishai Ben-David and Benjamin M. Herman
Institute of Atmospheric Physics
and
John A. Reagan
Electrical and Computer Engineering
The University of Arizona, Tucson, AZ 85721

RECENT PUBLICATIONS, SUBMITTALS FOR PUBLICATION AND PRESENTATIONS:

A) J. D. Spinhirne, J. A. Reagan, and B. M. Herman, "Vertical Distribution of Aerosol Extinction Cross Section and Inference of Aerosol Imaginary Index in the Troposphere by Lidar Technique." J. Appl. Meteorol., 19, 426-438, April 1980.

B) J. A. Reagan, Dale M. Byrne, and B. M. Herman, "Bistatic Lidar: A Tool for Characterizing Atmospheric Particles: Part I - The Remote Sensing Problem." IEEE Transactions on Geoscience & Remote Sensing, GE-20, 236-243, July 1982.

C) Avishai Ben-David and B. M. Herman, "Method for Determining Particle Size Distribution by Non-Linear Inversion of Backscattered Radiation." Applied Optics, 24, 1037, April 1985.

ABSTRACT

A library of aerosol size distributions based upon reasonable analytic functions, is used to form a set of orthogonal basis functions. It is assumed that any unknown aerosol size distribution may be constructed from a linear sum of these basis functions. The problem then becomes one of solving for the unknown coefficients of the basis functions. A solution with a smoothing constraint and a positivity constraint is developed, and results of the method are presented.

INTRODUCTION

Many schemes have been developed to solve the so-called "inverse problem." However, it remains a fact, regardless of the scheme, that normally the information content in a given set of measurements is severely limited. Therefore, our recoverable knowledge of the unknown, if deduced solely from the measurements, is also going to be severely limited. The difference between the various inversion schemes is primarily due to the additional information that the set of equations is given. This additional information is normally in the form of physically plausible constraints. The well-known second derivative smoothing constraint is one such method. Minimizing differences from an *a priori* trial solution is another. The list of methods is too large to repeat here, but it follows that, in any method employing a constraint, the final solution will depend to some degree on the validity of the constraint for the particular problem.

For those inverse problems for which there exists a large body of observed solutions, *e.g.*, temperature soundings, ozone vertical distributions, etc., one can make use of this large reservoir of observed "solutions" by the method of empirical orthogonal functions. In this method, the observed information is put into the form of a matrix from which the eigenvectors are determined. A set of orthogonal basis functions may be constructed from these eigenvectors which are the best set of orthogonal vectors to use to reconstruct the original observed distributions. If one now assumes that any other distribution can be composed of a linear combination of one or more of the observed distributions, then the set of basis functions will be able to reproduce these distributions also.

Any distribution that has components orthogonal to the original distribution set from which the basis functions were constructed will not be perfectly reproduced. It is exactly equivalent to attempting to describe an arbitrary three-dimensional vector in terms of unit vectors along the x and y axes only. So long as the arbitrary vector lies completely in the x - y plane, this can be done. However, any vector with a component along the z-axis can only be partially reproduced, the z-component being non-recoverable.

In the case of aerosols, we do not have any reliable catalogue of observed size distributions from which to construct basis functions. However, we may analytically construct size distribution functions based on our knowledge of the types of functions these distributions normally follow. Thus, in the present method, a large library of log-normal distribution functions with various widths, σ, and mean radii, $\bar{r}$, as well as a large range of Junge and gamma distribution functions, was assumed to make up the "observed" distributions. Calling the vector of these "observations" $\tilde{n}(r)$, each distribution making up one component of the vector, and calling its transpose, $\tilde{n}^T(r)$, the eigenvectors of $\tilde{n}(r)\tilde{n}^T(r)$ were computed. The eigenvectors were then used to construct a new set of orthogonal functions, $\phi_1(r)$, $\phi_2(r)$, $\cdots$, $\phi_n(r)$, the set of which we will denote as a vector $\tilde{\phi}(r)$, and refer to as our basis functions. The unknown size distribution, f(r), is now assumed to be expressible as a linear combination of these basis functions, i.e.,

$$f(r) = \tilde{a}^T\tilde{\phi}(r) = \sum_j a_j\phi_j(r) \ , \tag{1}$$

where the coefficients, a_j, are now the unknowns to be solved for. It should be noted here that, if our original library of size distribution functions were a complete set, then any f(r) could be expressible as the linear combination of basis functions from Eq. (1). Since the set is obviously not complete, then any unknown size distribution, f(r), will have, in general, some component orthogonal to the basis functions, which will be unrecoverable from Eq. (1). Furthermore, since one is generally limited as to the number of measurements available, the number of coefficients, a_j, directly recoverable will be limited. Additional constraints are required to increase the number of coefficients which may be recovered. In the present problem, as described below, two constraints have been applied.

METHOD OF SOLUTION

As described above, from the library of log-normal, Junge and gamma distributions, each distribution function being considered as 1 component $n_j(r)$ of a vector $\tilde{n}(r)$, the real, symmetric matrix $\tilde{n}(r)\tilde{n}^T(r)$ was constructed. The eigenvectors of this matrix, $\tilde{u}(r)$, were then computed and basis functions determined from the equation (see Twomey, p. 141),

$$\phi_n(r) = \lambda_n^{-1/2} \sum_k u_{kn}n_k(r) \tag{2}$$

where λ_n is the nth eigenvalue corresponding to the nth eigenvector, the kth component of which is u_{kn},

and $n_k(r)$ is the kth "library" size distribution, as previously described. From the basis functions, we want to determine the set of coefficients, a_j, such that the unknown size distribution, f(r), is given by Eq. (1).

The governing equation for the backscatter problem may be put into the form

$$\tilde{g} = \int \tilde{k}(r)\ f(r)\ dr \tag{3}$$

where $\tilde{g}$ is the observation vector, each component of which is the measured backscatter at some wavelength, λ, $\tilde{k}(r)$ is the kernel vector composed of the backscatter cross sections at radius r and wavelength λ, and f(r) is, of course, the unknown size distribution function.

Substituting for f(r) from Eq. (1) yields

$$\tilde{g} = \int \tilde{k}(r)\ \tilde{a}^T\tilde{\phi}(r)\ dr \tag{4}$$

or

$$g_i = \int k_i(r) \sum_j a_j\phi_j(r)\ dr = \sum_j \left\{ \int k_i(r)\phi_j(r)\ dr \right\}\ a_j\ . \tag{5}$$

Writing the integral in Eq. (5) above as a matrix, A_{ij}, we have

$$g_i = A_{ij}a_j$$

or

$$\tilde{g} = \tilde{A}\ \tilde{a}\ , \tag{6}$$

where the unknown is the expansion coefficient vector, $\tilde{a}$.

In cases where f(r) is known (i.e., in the "forward" problem), due to the orthogonal properties of the basis functions, $\tilde{\phi}(r)$, the expansion coefficients may be determined from the expression

$$a_j = \int f(r)\phi_j(r)dr \tag{7}$$

In the present, inverse problem, since f(r) is unknown, the coefficients may be determined from the inverse of Eq. (6). Thus,

$$\tilde{a} = \tilde{A}^{-1}\tilde{g} = (\tilde{A}^T\tilde{A})^{-1}\ \tilde{A}^T\tilde{g}\ , \tag{8}$$

a direct inversion which is almost always unstable.

In order to stabilize Eq. (8), we have employed the following two constraints:

1. A *smoothing constraint* such that $\sum_i \dfrac{\partial^2 f(r_i)}{\partial r_i^2} = \min$.

2. A "positivity" constraint, such that $f(r_i) > 0$ for any r_i.

The smoothing constraint yields a result identical in form to the normal second derivative smoothing as first derived by Twomey (1963).

The positivity constraint is employed in an iterative manner. An initial, first-guess distribution, y(r), which is positive for all r, is used to start the procedure. The expression

$$q \equiv f^{2(1)}(r) - y(r)f^{(1)}(r) \ , \tag{9}$$

where $f^{(1)}(r)$ is the first iterative solution, is then minimized as the positivity constraint. Figure 1 shows a graph of q vs. f(r).

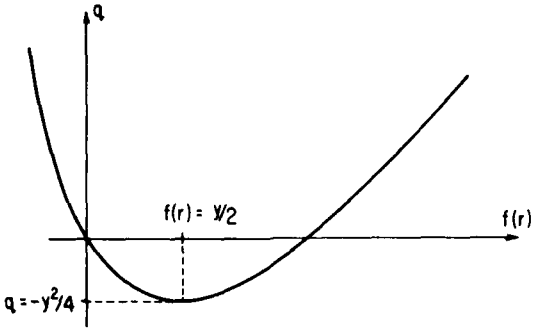

FIGURE 1. POSITIVITY CONSTRAINT as demonstrated by graph of q vs. f(r).

For any value of y(r), the minimum value of q is $- y^2/4$, for which f(r) = y/2, a positive number. This constraint will tend to force the solution towards y/2 for the first iteration. The degree of forcing depends upon the strength given to the constraint. For the next iteration, $f^{(1)}(r)$ is set = y(r), and the process repeated. Any negative values of f(r) which may appear are "encouraged" to become positive in successive iterations by this constraint.

Using the method of Lagrangian multipliers, the final solution employing both constraints is given by

$$\tilde{a} = \left[\tilde{A}^T\tilde{A} + \gamma_s\tilde{H}_s + \gamma_p\tilde{H}_p\right]^{-1}\left[\tilde{A}^T\tilde{g} + \gamma_p\tilde{\Phi}\tilde{y}\right] \ , \tag{10}$$

where $\tilde{H}_p$ and $\tilde{H}_s$ are constraint matrices arising from the minimization criteria, and γ_s and γ_p the Lagrangian multipliers which determine the strength of the smoothing and positivity constraints.

With the coefficient vector, $\tilde{a}$, given by Eq. (10), the solution is

$$f(r) = \tilde{\Phi}^T(r)\tilde{a} \ . \tag{11}$$

Expressing r at finite points as opposed to a continuous variable, the $\tilde{\Phi}(r)$ vector becomes a matrix, whose rows are the values of Φ at discrete of values of r and whose columns are the various basis functions, and yields

$$\tilde{f} = \tilde{\Phi}^T\tilde{a} \ ,$$

where $\tilde{f}$ is now a column vector, each component of which is the value of f at a discrete value of r. For each iteration, the solution vector, $\tilde{f}$, becomes $\tilde{y}$ for the next iteration. Iterations are continued until a predetermined convergence criterion is met.

RESULTS

Simulated measurements of backscattered radiation were calculated by Dr. Jerald Bottiger for fifteen wavelengths (between 0.2 μm and 9.0 μm) and for four aerosol size distributions (denoted by data sets "G", "H", "I" and "J"). These measurements were then perturbed with various random errors up to 10% and served as the measurement vector, $\tilde{g}$, which was provided to the authors.

For solving Eq. (10), the $\tilde{A}$ matrix was calculated assuming spherical particles with known refractive indices, single scattering only, and negligible attenuation by the medium. The radii limits of the unknown solution were assumed to be between 0.2 μm and 10.0 μm.

Equation (10) was solved by the iterative process described in the previous section with the initial guess $\tilde{y}$ chosen to be a uniform size distribution. With this initial guess, a first solution vector $\tilde{a}$ and $\tilde{f}^{(1)}$ ($\tilde{f}=\tilde{\Phi}^{T}\tilde{a}$) were computed. This first solution $\tilde{f}^{(1)}$ was used to construct a new vector, $\tilde{y}$, such that $\tilde{f}^{(1)}$ replaces $\tilde{y}$ in Eq. (10). This process is repeated until the final solution, $\tilde{f}$, can reproduce the measurements within the measurement accuracy and has an "acceptably small" number of negative solution points. In the iteration process, the numerical values of the Lagrange multipliers, γ_s and γ_p, were chosen such that the condition number of the matrix $(\tilde{A}^{T}\tilde{A} + \gamma_s\tilde{H}_s + \gamma_p\tilde{H}_p)$ was the smallest subject to the condition that $\tilde{A}^{T}\tilde{A} > \gamma_p\tilde{H}_s + \gamma_p\tilde{H}_p$.

Figures 2-5 show results of inversions for data sets "G", "H", "I", and "J". In these figures, the empirical orthogonal function solutions (denoted by square boxes) are compared with results obtained by applying an iterative smoothing constraint method (Ben-David and Herman, 1985) denoted by a solid line. The true solution (from which the measurements were simulated) is denoted by a dashed line.

Figure 6 shows the simulated measurements for data "G" as a function of wavelength (solid line) and the computed measurements (denoted by triangles) from the empirical orthogonal function solution of Figure 2. The other solutions shown in Figures 3, 4 and 5 reproduce the simulated measurements equally well and are not shown here.

Figure 7 shows the iterative process in solving Eq. (10) for data set "I". The residual error (difference between the simulated measurements and the computed measurements from the solution vector $\tilde{f}$) and the number of negative solution points converge toward some small values consistent with the constraints and the values of γ_p and γ_s.

In order to check the ability of the basis functions to reproduce small-scale features in the size distribution, measurement vectors $\tilde{g}$ were computed for 4 delta functions with peaks at r = 1 μm, 3 μm, 5 μm, and 8 μm. Figure 8 shows the resulting inverted size distributions. The basis functions produce narrow curves at the correct locations but with a spread of about 0.5 μm in radius.

Figure 9 shows that portion of the function space spanned by the backscattered kernels that is parallel to the function space spanned by the basis functions, and so can be recovered by the basis

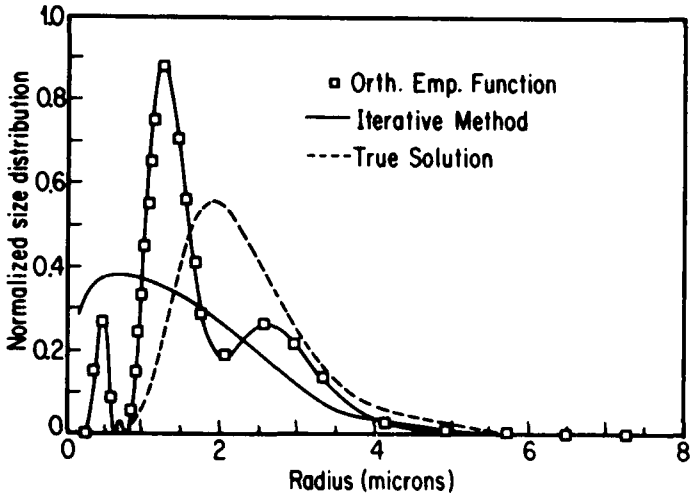

FIGURE 2. NORMALIZED PARTICLE-SIZE DISTRIBUTION of the correct size distribution for data set "G". Also shown are the empirical orthogonal function solution and the iterative method solution. All curves are as a function of particle radius.

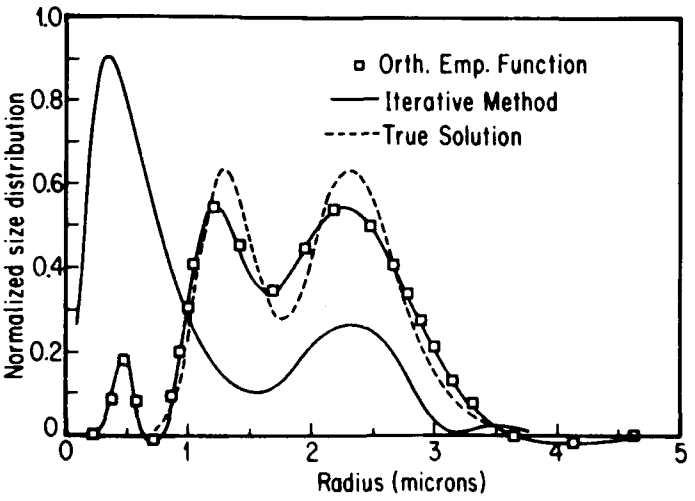

FIGURE 3. Same as Fig. 2 but for data set "H".

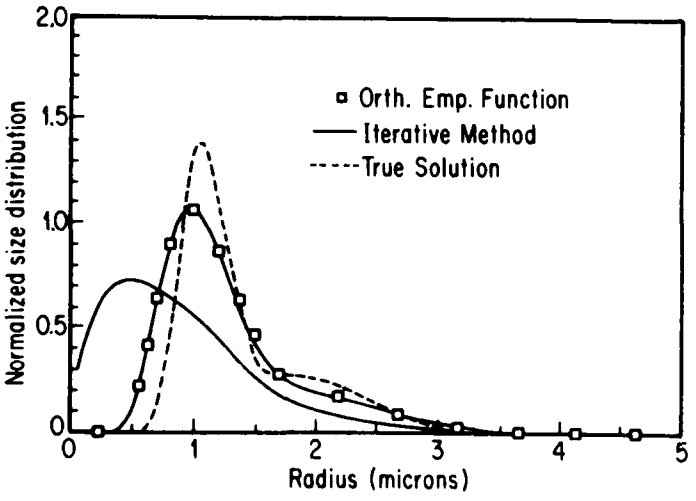

FIGURE 4. Same as Fig. 2 but for data set "I".

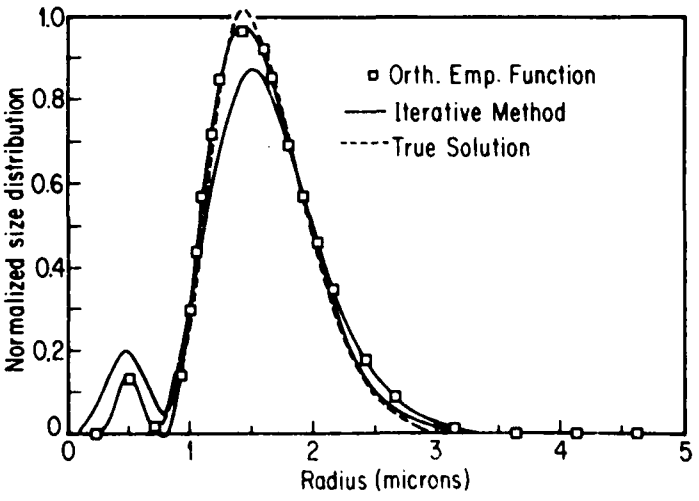

FIGURE 5. Same as Fig. 2 but for data set "J".

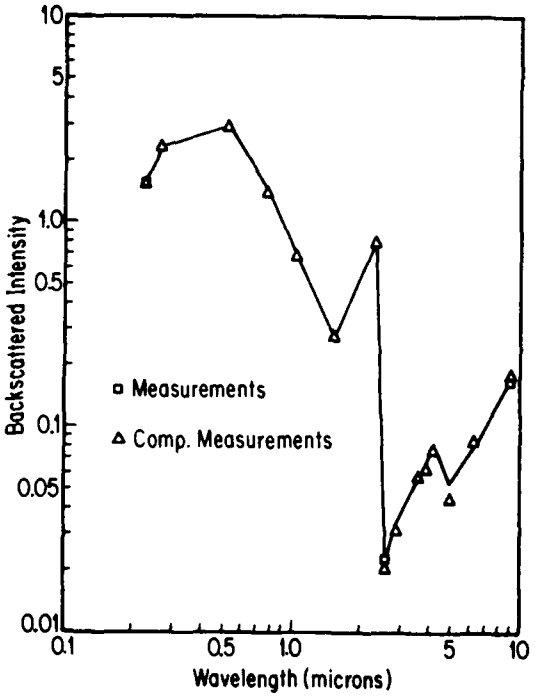

FIGURE 6. BACKSCATTERED INTENSITY as function of wavelength for the simulated measurements of data set "G" and the computed measurements from the empirical orthogonal function solution shown in Fig. 2.

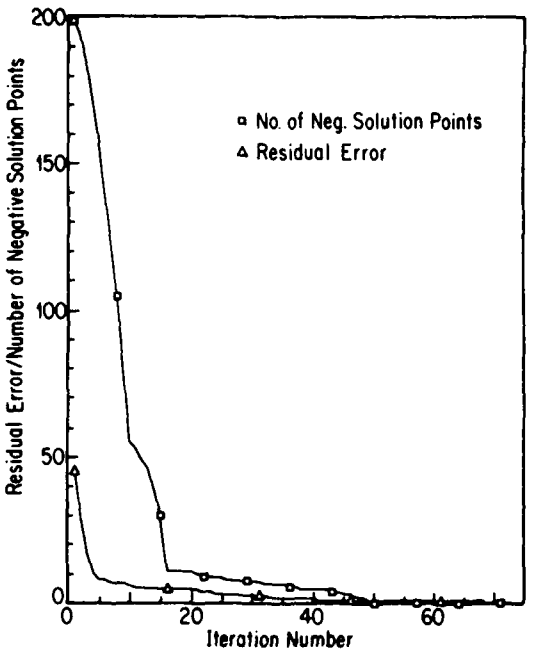

FIGURE 7. THE RESIDUAL ERROR and the number of negative solution points as function of increased iteration number, for data sets "I".

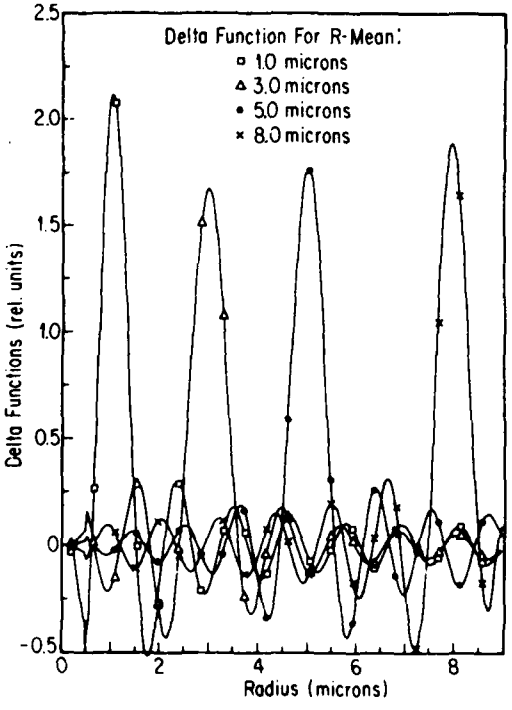

FIGURE 8. PARTICLE SIZE DISTRIBUTION as function of particle radius for four simulated Dirac delta functions constructed from the basis functions.

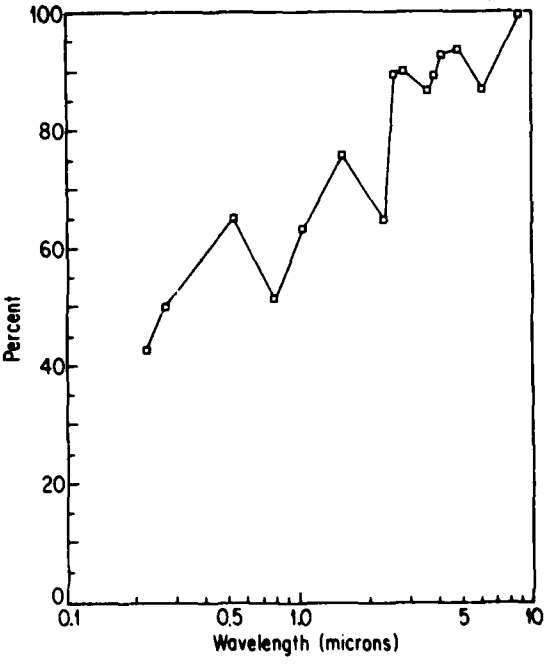

FIGURE 9. THE PORTION OF THE FUNCTION SPACE (in percent) of the backscattered kernels that can be accounted for by the basis functions for 15 wavelengths.

functions. In this figure, it can be seen that, for short wavelengths ($\lambda < 1$ μm), a large portion of the backscattered kernels is orthogonal to the basis functions. For long wavelengths ($\lambda > 1$ μm) more than 80% of the information in the backscattered kernels is parallel to the basis functions, and therefore the measurements, g_i, contain considerable information at these wavelengths.

SUMMARY

The figures presented here indicate that very good results can be obtained by using the empirical orthogonal function method for situations where the solution is in the function space spanned by the basis functions. For atmospheric aerosols where the aerosol size distribution is expected to take a form composed of combinations of Junge type, log-normal, and gamma distributions, this method gives good results. However, this method can account only for as much as 80% of the information contained in the backscattered kernels (for the wavelengths employed here) and cannot resolve features of the solution with width smaller than about 0.5 μm in radius. In cases where it is suspected that the unknown distribution is very narrow, or otherwise considerably different from the distributions employed for the current "library" set, a new library set may be employed to compute the basis functions.

REFERENCES

A. Ben-David and B. M. Herman, "Method for Determining Particle Size Distributions by Nonlinear Inversion of Backscattered Radiation," Applied Optics, 24, 1037, 1985.

S. Twomey, "Introduction to the Mathematics of Inversion in Remote Sensing and Indirect Measurements." Elsevier Scientific Publishing Company, New York, 1977.

———, "On the numerical solution of Fredholm integral equations of the first kind by the inversion of the linear system produced by quadrature," J. Ass. Comput. Mach., 10, 97-101, 1963.

MULTICHANNEL NEPHELOMETER

S. R. Beck, C. D. Capps, N. E. Carroll, T. R. Majoch, and A. R. Tokuda
Boeing Aerospace Company
P.O. Box 3999, Seattle, WA 98124

RECENT PUBLICATIONS, SUBMITTALS FOR PUBLICATION AND PRESENTATIONS:

A) A. R. Tokuda, G. M. Hess, T. R. Majoch, S. R. Beck, C. D. Capps, and N. E. Carroll, "Multichannel Nephelometer Design," Proceedings of the 1984 CRDC Conference on Obscuration and Aerosol Research, p. 119, submitted September 1984.

ABSTRACT

This paper reports on the development of a multichannel nephelometer that samples an aerosol, measures the light scattering pattern of single aerosol particles illuminated by a CW laser, and records scattering data for future analysis. The nephelometer has been designed, built, tested, and delivered to and demonstrated at CRDC. The nephelometer is operational for particles 2 - 10 micron in size. Work to reduce laser 'noise' will extend this range of operation down to 0.3 micron.

INTRODUCTION

The Boeing Aerospace Company developed a multichannel nephelometer capable of measuring and recording the far-field light-scattering pattern from individual particles in an aerosol. The nephelometer will enable extensive research into the scattering pattern characteristics of nonspherical particles. In operation, test particles in an aerosol cloud are input to the nephelometer. The nephelometer then dilutes the aerosol and serially guides single particles, in a coaxial jet, through a laser beam. The scattering pattern for each of the target particles is monitored by 108 photomultiplier tubes (PMTs) whose signal levels are then digitized and stored for future analysis. The instrument can measure and record data for 1,000 separate particles in a single test run, thus providing the capability for developing a good statistical data base for future nonspherical particle scattering pattern studies.

The multichannel nephelometer comprises an aerosol sampling system, light scattering chamber, and data acquisition system. The nephelometer consists of two separate units mounted on casters and connected by an umbilical cord. The main unit contains the aerosol sampling system, the light scattering chamber and part of the data acquisition system. It is mounted on a 3 by 6 foot optical table and stands 8 feet tall. Figure 1 shows the diluter stack which constitutes the upper portion of the main unit. Figure 2 shows the lower portion of the main unit which constitutes the heart of the multichannel nephelometer. The second unit is a roll-around computer cart and is shown in figure 3.

The aerosol sampling system includes the diluters and the aerosol jet. The diluters are mounted above the scattering chamber so vertical motion of the sample aerosol through the system minimizes

bias. The diluters are a self-contained, readily demountable unit to allow transport of the main unit through doorways. The light scattering chamber is mounted on the main table surface and is centered on the point where the laser beam intercepts the particle stream. The aerosol jet, laser, and front-end electronics for the data acquisition system are all integrated with the light scattering chamber on the same table to maintain both mechanical and optical alignment after initial setup. The computer and its peripherals plus the power supplies for the PMTs and nephelometer electronics are located on the computer cart.

Each of the basic nephelometer systems is discussed in greater detail in the sections which follow.

AEROSOL SAMPLING SYSTEM

The aerosol sampling system is designed to 1) sample test aerosols with particle densities of up to 10^6 particles/cc, 2) dilute the test sample to produce a stream of single particles, and 3) entrain the sampled particles in the center of a coaxial jet directed through the laser beam. The particles traverse the beam, one at a time, at a velocity of less than 10 meters/second, and at a nominal particle rate of 10/second. A schematic of the overall aerosol system operation is shown in figure 4. The aerosol sampling system is conceptually divided into the diluters and the aerosol jet.

The most visible part of the diluter subsystem is the serial combination of the two ATEC 303-LF diluters mounted in a 19 inch rack on a shelf above the light-scattering chamber. Filters, flow controllers, air pumps, and plumbing needed to drive the system are mounted between the two bottom shelves of the main unit. The diluters operate on a capillary and filtered by-pass principle where only a portion of the concentrated aerosol is allowed to pass through the capillary and the remainder of the flow is first filtered then recombined with the concentrated capillary flow to dilute the aerosol density. The diluters used were selected for their flexibility. They allow operation at a number of different aerosol flow rates by adjusting the pressure drop across the capillary using valves in the bypass flow. There is also a shuttle in each of the diluters which allows the selection of either one of two installed capillaries, an input from an auxiliary port, or a by-pass through a straight through tube -- all with the simple pull of a knob. By putting two diluters in series, very high dilution ratios can be obtained by using both stages simultaneously. Greater flexibility can be achieved by outfitting each diluter with a different set of capillaries and using the combination best suited to the task at hand.

A capillary, similar to those used in the diluters, draws off a sample of the aerosol flow from the diluter stack and injects the particles into the aerosol jet system. The aerosol jet system, shown conceptually in figure 4, is diagramed in greater detail in figure 5. This system forms the low velocity (<10 meters/sec) coaxial jet used to pass the aerosol particles through the laser beam in the center of the light-scattering chamber. This is a closed loop system in which most of the flow is filtered and constantly recycled. A controlled leak introduced by the flow controller draws the sample flow through the sample capillary to replace the air being leaked. The entire system must be well sealed to maintain proper control over the sample flow. To pump the air and maintain good sealing, it is necessary to use diaphragm pumps which introduce pulsations in the air flow capable of disrupting the aerosol jet. Pulse suppression units, each consisting of a small filter and a Quincke tube are installed before, between, and after the pumps to minimize the pulses. The Quincke tube is a set of two tubes, one short and one long, in parallel which divide the flow and cause a partial pulse cancellation when the flows are recombined because the pulses transmitted through the tubes have a path-length difference of one half cycle. Two pumps are used in the system to provide the necessary pumping capacity while maintaining pulses small enough to mute out. Further pulse suppression is performed by the orifice constrictions in the flow controllers, additional small filters and the large air mass in the light-scattering chamber. Operating the two pumps in series rather than in parallel proved critical in maintaining the proper balance of pressures and flows needed for a stable jet.

The final result is shown in figure 6. This aerosol sampling system has been operated stably and reliably with no particle loss to the test chamber with nozzle separations as wide as 3.6 inches. The aerosol sampling system can be adjusted or disassembled for cleaning without having to remove either of the chamber hemispheres. All the air which is exhausted from the system is filtered and therefore constitutes no hazard to personnel or equipment.

LIGHT SCATTERING CHAMBER

The light scattering chamber is a 10.4 inch I.D. spherical shell with 76 individual photodetector assemblies and four high-angular-resolution array assemblies. A class IV argon-ion laser emitting at 488nm illuminates the aerosol particles. The optically sealed chamber shields users from the laser beam and allows compliance with TB MED279, "Control of Hazards to Health from Laser Radiation." Six inches of access space are provided in front of the scattering chamber for auxilliary optical components, supplied by the user.

The laser head is situated on the upper of two shelves which are mounted beneath the optics table, figure 2. The laser beam is directed up through the table and into the chamber by two beam steering mirrors. The beam then passes through an AR-coated window and a light baffle before entering the scattering chamber. The laser beam diverges to a $1/e^2$ diameter of two millimeters at the chamber center where it intercepts the aerosol particle stream. Due to losses at the steering mirrors and entrance window, the maximum available TEM_{oo} power from the laser is 700mW, at the chamber center. After intercepting the aerosol stream, the unscattered laser beam passes through the chamber and directly into a curved, polished-copper beam dump.

The scattering chamber, consists of two near-hemispherical shells bolted to a 1" thick support plate which is itself mounted on the upper surface of the optics table. The forward scatter hemisphere is shown in figure 7 prior to the installation of detector assemblies. Four large, array-assembly mounting areas surround the beam dump mounting point. The inner chamber walls were anodized black and then painted ultra-flat black to decrease surface reflections. The chamber is designed for easy access and disassembly. Numerous o-rings are used to seal the chamber, both mechanically and optically.

The light scattered from aerosol particles is received by individual and arrayed photodetector assemblies surrounding the aerosol-laser intercept point. The detectors are arranged in an unsymmetric fashion along four great circles of the spherical chamber, separated by 45^o. Detection begins 9^o from forward-scatter and extends to within 11^o of the back-scatter direction. Angles from 76^o of forward-scatter to 78^o of back-scatter have no coverage since detector assemblies must be positioned away from the support plate which occupies the 90^o scatter plane. Four high-angular-resolution array detector assemblies, each containing eight Hamamatsu R1770 photomultiplier tubes, detect the scatter in the forward 9^o to 21^o region. Seventy-six individual detector assemblies, each employing one Hamamatsu R647 photomultiplier tube, cover the remainder of the scatter region from 28^o forward to 11^o from backward.

A simple optical system is employed for the array assemblies consisting of a rotatable dichroic linear polarizer and an aperture plate, immediately in front of the PMT array, figure 8. Each detector element in an array subtends 1.5^o.

The individual detector PMTs are mounted in molded, black plastic assemblies, figure 9, which

contain removable sheet-type dichroic linear polarizers. A second molded unit is threaded to fit the detector mounting holes in the scatter hemisphere. It contains a lens and an aperture to limit the detector field of view. This system reduces detection of reflections from the far chamber wall and the unsymmetric detector spacing prevents specular reflections off optics in the near-forward, higher scatter directions from reaching detectors in the near-backward, lower scatter directions. Each individual detector element subtends 6^{o}.

DATA ACQUISITION SYSTEM

The data acquisition system consists of signal discrimination and timing circuits, front-end electronics for all PMTs, A/D converters and signal multiplexers, and a Micro PDP-11 computer. This system monitors light scattering in real-time to determine which signals correspond to valid particle scatter and when to store these signals. It converts wide dynamic range particle light scatter into compressed analog voltage representations and then digitizes these voltages. It then places the results on a computer mass-storage device for subsequent retrieval and analysis. The system digitizes 128 available analog channels at rates in excess of 80 times per second. Of these analog channels, 117 are used directly by the Multichannel Nephelometer System and 11 are free for use by the operator.

The discrimination circuit, figure 10, determines when valid particles are transitting the laser beam by monitoring signals from two of the 32 forward-scatter arrayed detectors, in real-time. Analog signal processing performed on these two signals produces velocity and position dependent waveforms. A particle's scatter, and its subsequent PMT generated current signal, are 'gaussian' in time as the particle passes through the beam. This signal is converted to a 'quadratic' form by a log-amp and then to a 'linear' form by differentiating the 'quadratic'. The 'linear' signal is proportional to the particle's position in the laser beam. This signal is also differentiated, resulting in a 'constant' signal that is proportional to the velocity of the particle through the laser beam. These signals are used jointly to decide if and when the A/D converters, under control of the computer, acquire scatter data from the detector assemblies. When a particle travels through the beam at the proper velocity and arrives very near the beam center, all T/H amps are placed in a 'hold' mode and a 'DATA READY' signal is sent to the computer. After all signals are digitized by the computer a 'DATA TAKEN' signal is sent to the discriminator circuit and T/H amps are placed in a 'track' mode. Further 'DATA READY' signals are suppressed for about a millisecond to allow analog switch transients (not shown) to settle. This delay does not measurably affect particle signal throughput. Two

wave-shaping circuits are used in parallel to cover the 0.3 - 10 micron particle size range. Currently, the low signal level, wave-shaping circuit has been disabled due to false triggering from excessive laser 'noise'. This 'noise' puts the smallest effective particle size range for discriminant operation near two microns.

Light scattered from a particle is converted by a PMT to current which, in turn, is introduced to a switchable band-pass load arrangement, figure 11. This prevents high frequency 'noise' and d.c. 'molecular' induced signals from reaching the remaining electronics. A low-noise op-amp then increases the PMT signal enough to drive a log-amp over a 5 decade dynamic range. Logarithmic signal compression reduces susceptibility to noise degradation when sending low-level signals over long lines to the computer where the A/D converters are installed. Finally, a track/hold amp 'tracks' all scatter signals until ordered by the discrimination circuits to 'hold' a valid one. Though proper operation of the discrimination circuits is possible over the 2 - 10 micron range, the laser 'noise' suppresses valid scatter data from most of the detection channels. With the removal of this 'noise', valid data will be available from all channels over the full 0.3 - 10 micron range.

Analog signals from the track/hold amplifiers are transferred in a 12 foot long cable bundle from a distribution box mounted on the optics table to another distribution box inside the computer rack. Within the computer rack-mounted distribution box, all analog signals are terminated with low-pass filters to further reduce externally generated noise. Signal-ground sense lines are also employed to allow psuedo-differential operation of the A/D converters. Computer-type ribbon connections transfer these filtered signals to the A/D converters. Since the A/D converters are plugged into the computer bus, they are under immediate control of the computer. This reduces the amount of ancilliary hardware and shortens the computer's access time to the digitized data. To take advantage of this configuration, assembly language programs perform asynchronous data transfer to the hard disk drive, and all other programs are written in compiled Fortran IV. An aerosol 'sample' can represent data for up to 1000 particles; by compressing the data, the computer can store enough information to characterize six aerosols (six Mueller matrices), on the internal hard disk drive, before it is necessary to transfer data to floppy disks for long-term storage.

The computer 'rack' is a 30 inch tall, RETMA specification, roll-around cart with a wood desk-top, upon which is a medium resolution VT-240 graphics terminal and an LA-50 dot matrix printer, figure 3. A Micro PDP-11 computer occupies the upper area of the 'rack', while a bipolar power supply

from Acopian and a high voltage power supply from Bertan occupy the lower area. Software manuals for DEC's RT-11 operating system occupy the remaining rack space, for user convenience.

INSTALLATION

The Multichannel Nephelometer is now resident at the U.S. Army CRDC, Aberdeen Proving Grounds, Maryland. Two intensive weeks were spent teaching operations to local personnel.

CONTINUING RESEARCH

Laser beam 'noise' limits the particle size range over which the Nephelometer operates effectively to 2 - 10 microns. However, working with an A-O or E-O laser beam power-leveler, that range will be extended to 0.3 micron. Coordinated engineering efforts between CRDC and Boeing personnel will continue along these lines.

ACKNOWLEDGEMENT

This work was supported by the U.S. Army Chemical Research Development Center, Aberdeen Proving Ground, Maryland, under contract DAAK11-83-C-0089.

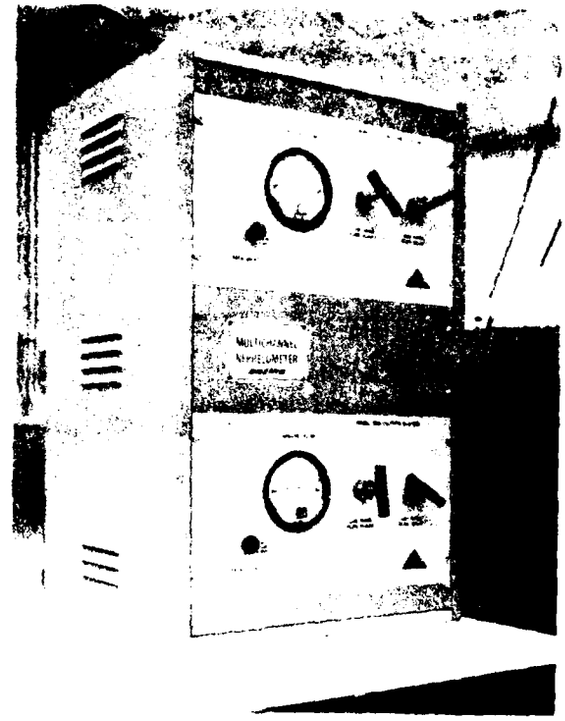

FIGURE 1. DILUTER STACK. This constitutes the upper portion of the main nephelometer unit.

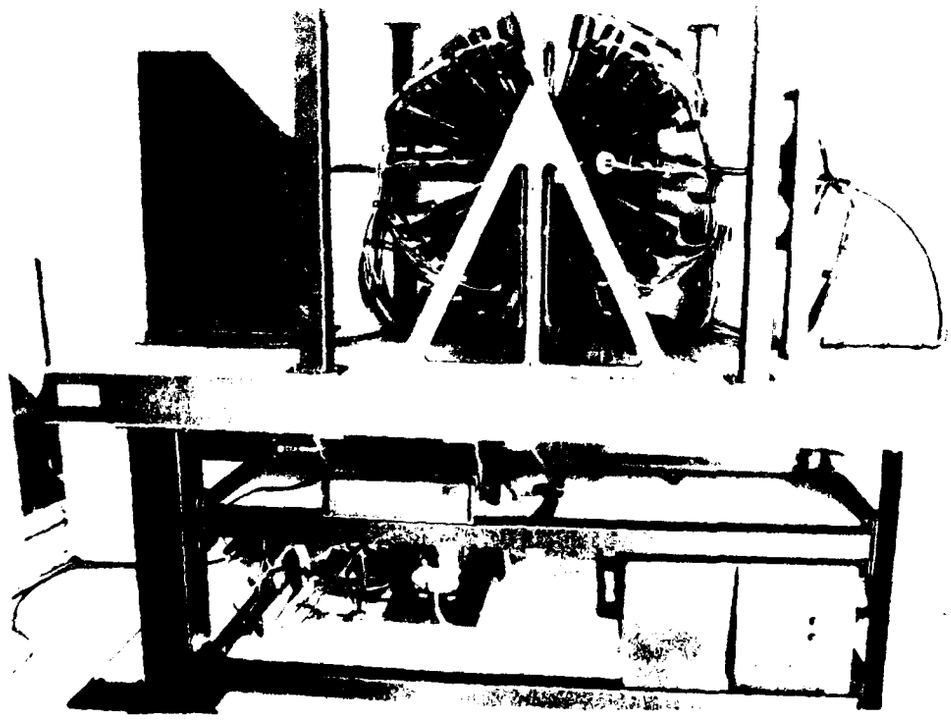

FIGURE 2. LOWER MAIN NEPHELOMETER UNIT. This includes the aerosol jet system, scattering chamber, laser and detector assemblies and forms the heart of the Multichannel Nephelometer.

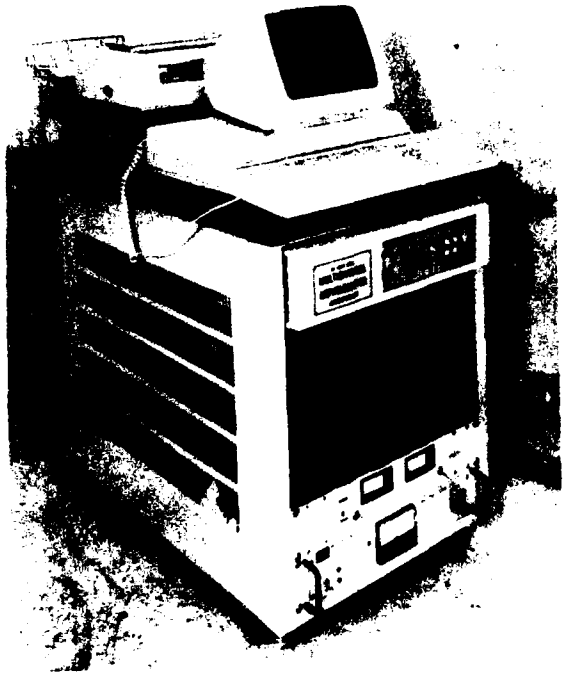

FIGURE 3. NEPHELOMETER COMPUTER UNIT. This unit contains a uPDP-11 uC, a VT-240 graphics terminal and an LA-50 graphics printer. Two lower rack mounted items are low voltage electronics and high voltage PMT power supplies. RT-11 operating system software manuals occupy the middle rack space.

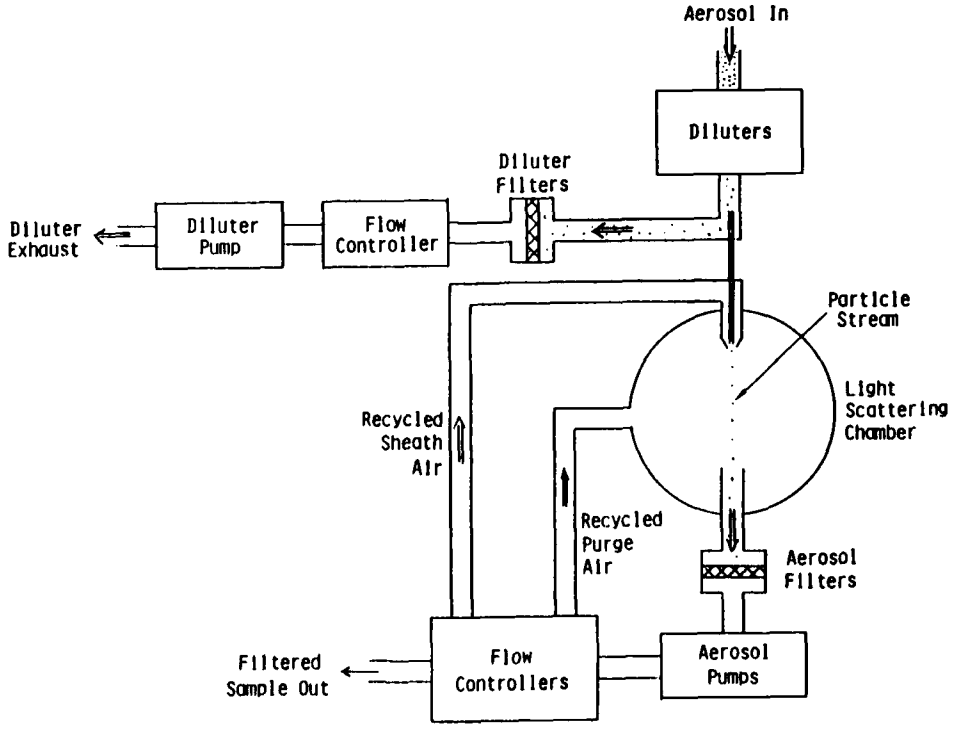

FIGURE 4. AEROSOL SYSTEM SCHEMATIC.

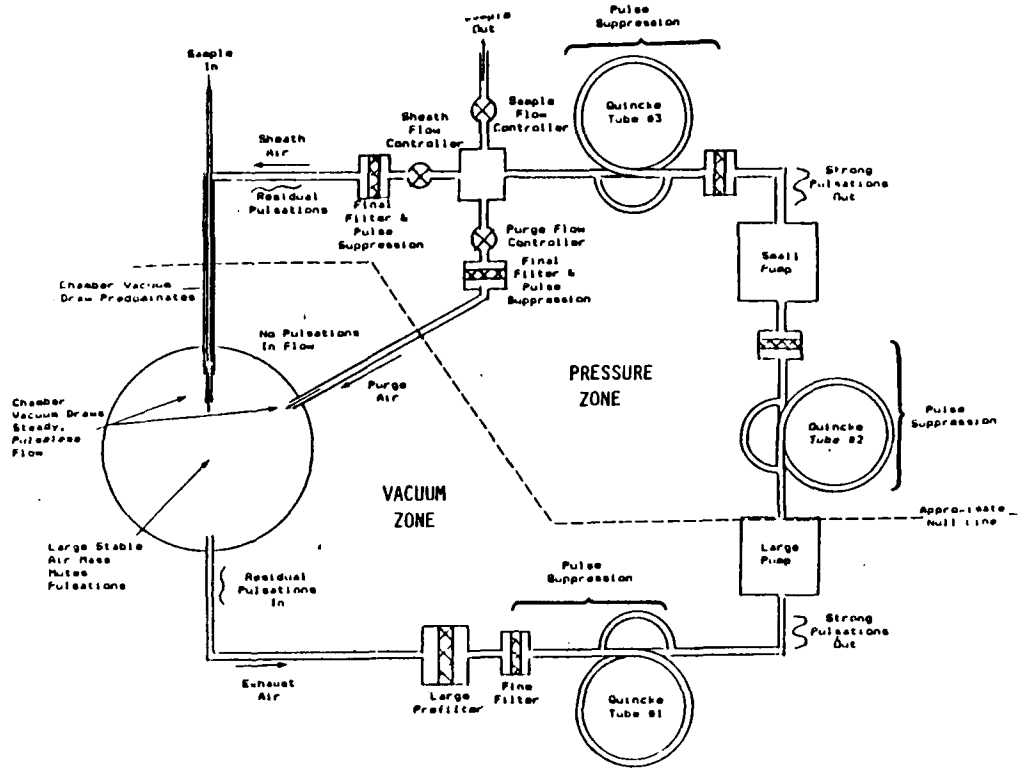

FIGURE 5. AEROSOL JET SYSTEM, DETAILED SCHEMATIC.

FIGURE 6. COAXIAL AEROSOL JET JUMPING GREATER THAN TWO INCH GAP. The aerosol is a dense sugar crystal aerosol from a TSI Tri-Jet Aerosol Generator to allow easy visualization of the aerosol stream. The stream is highlighted by a microscope illuminator, located behind the mounting plate and pointed at the center of the jet.

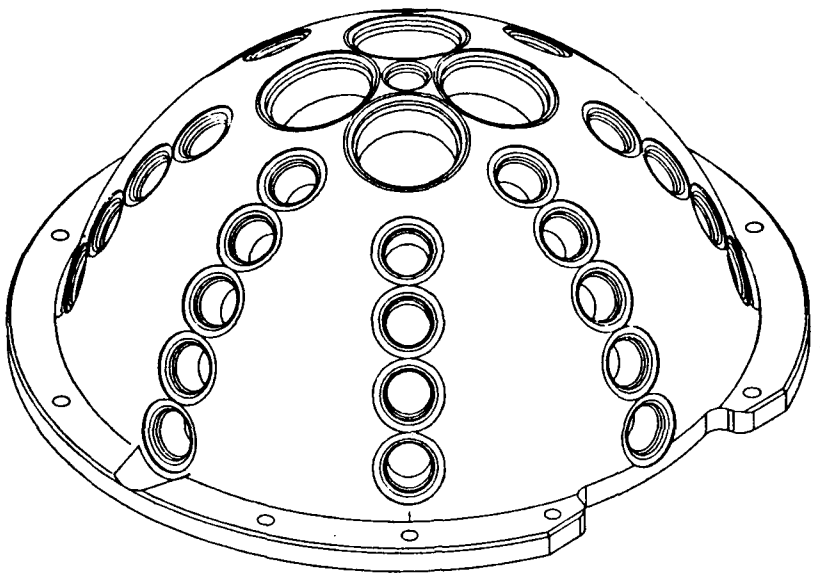

FIGURE 7. SCATTERING CHAMBER HEMISPHERE. This drawing shows four large mounting locations for the array detector assemblies and illustrates the four great circles of mounting for the individual detector assemblies. At the center of the large mounting locations is the beam dump outlet and mount.

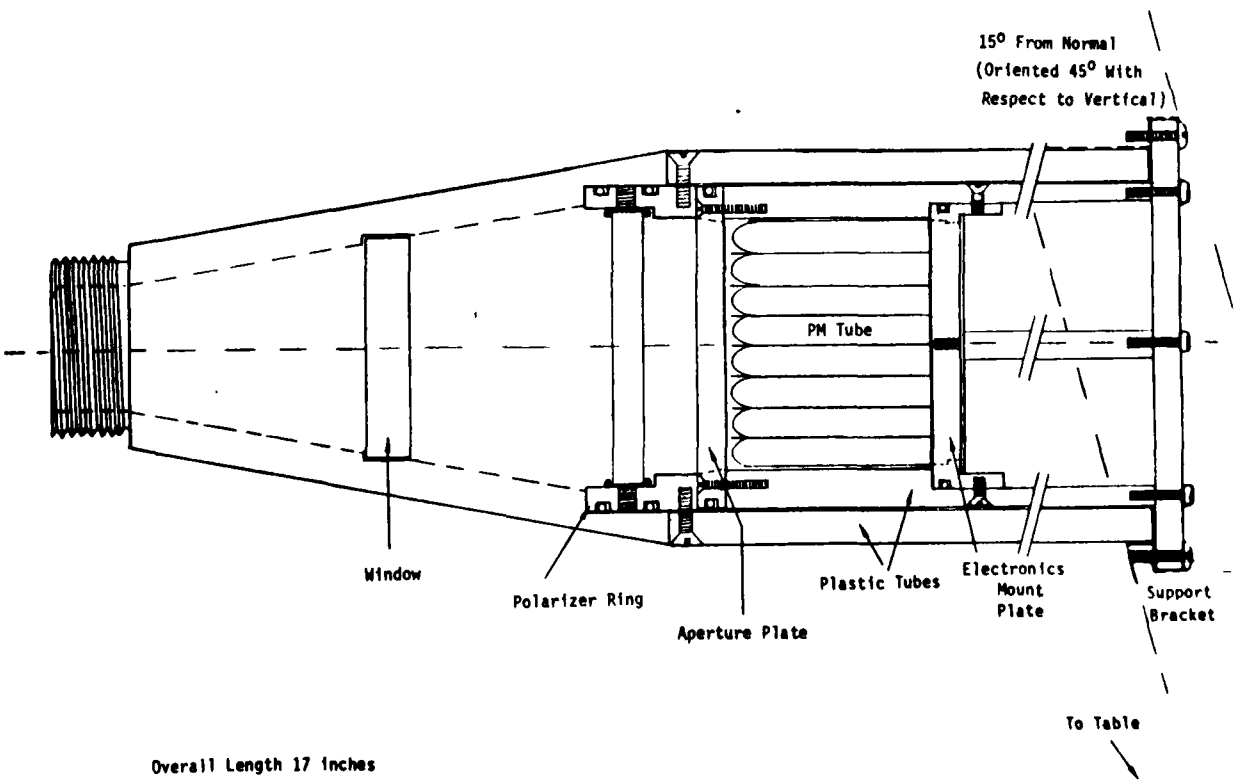

FIGURE 8. ARRAY DETECTOR ASSEMBLY OUTLINE DRAWING. Inner plastic tube is held fixed by the support bracket. Polarizer ring is mounted to outer plastic tube and rotates with it, relative to the PMT array.

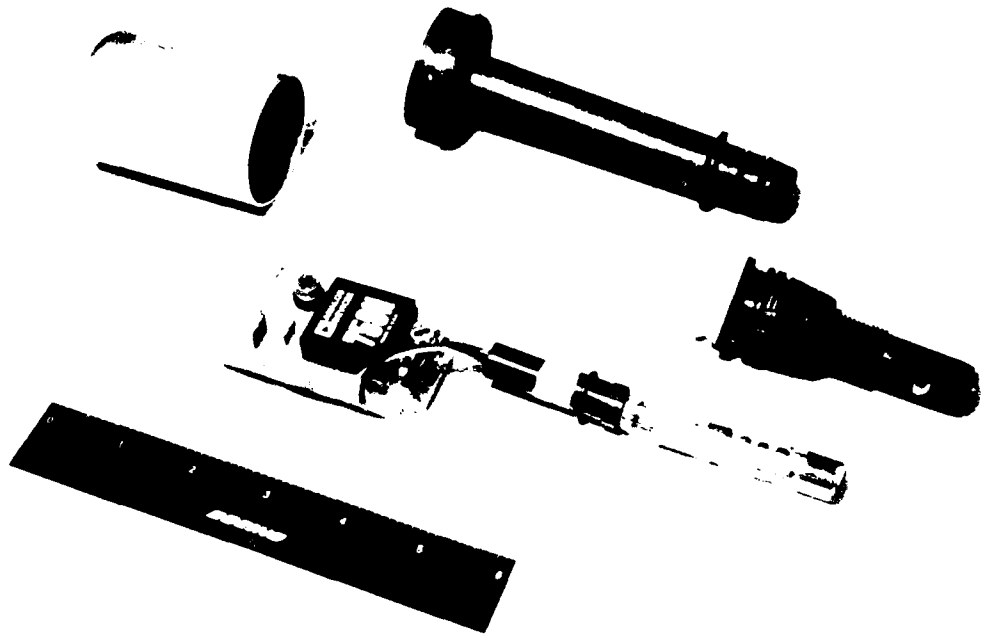

FIGURE 9. INDIVIDUAL DETECTOR ASSEMBLY BREAK-DOWN. PMT and printed circuit board in center are loaded into plastic molded unit at top of photo. Input-output cables (not shown) feed through the metal cannister (upper left) which then fits around the installed PC board/holder assembly. This final unit then plugs into the molded optics unit (far right) which itself is threaded into the scattering chamber.

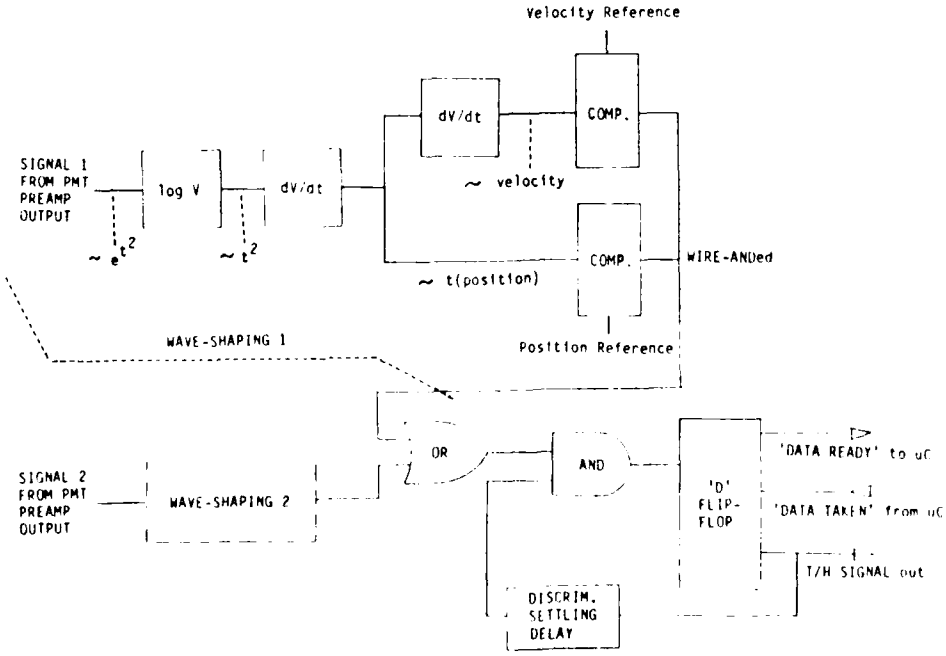

FIGURE 10. SIGNAL DISCRIMINATION AND TIMING CIRCUIT BLOCK DIAGRAM.

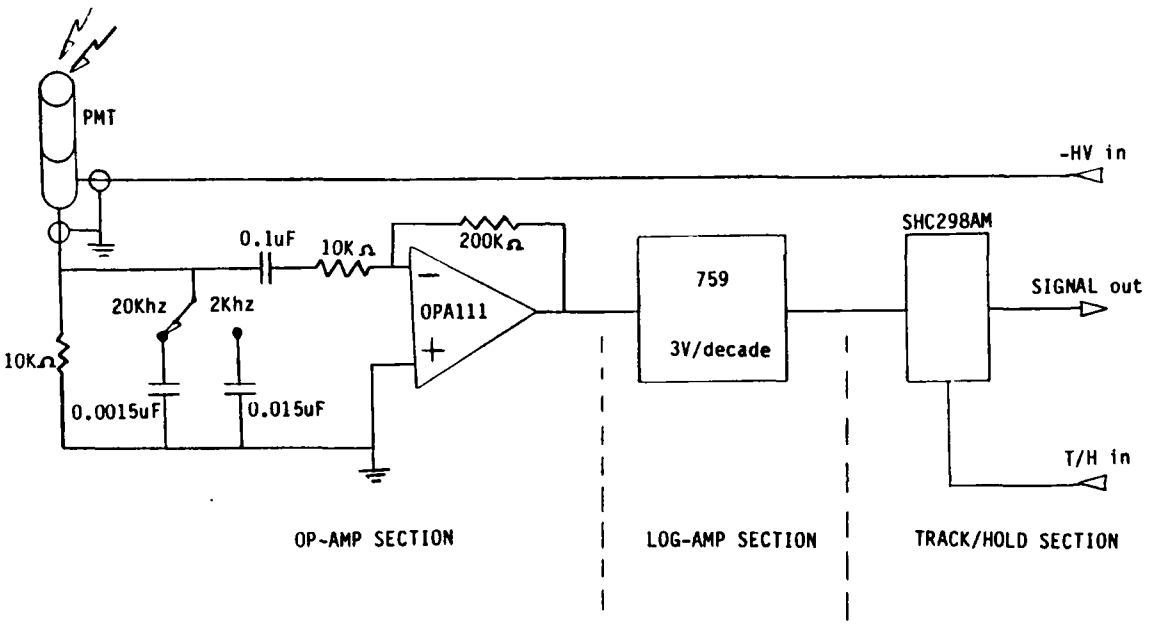

FIGURE 11. FRONT-END ELECTRONICS. PMT is biased by calibrated -HV to obtain a target responsivity, depending upon chamber placement. An R-C load does double duty as a low-pass filter and the op-amp input serves as a hi-pass filter. The lo-pass cut-off is set by a PC board mounted switch at either 2Khz or 20Khz. The op-amp magnifies the PMT signal current to drive the log-amp for large signals.

AD-A173 878 PROCEEDINGS OF THE SCIENTIFIC CONFERENCE ON OBSCURATION 1/7
AND AEROSOL RESEA (U) KOHL (RONALD H) AND ASSOCIATES
TULLAHOMA TN R H KOHL JUL 86 CRDEC-SP-86019
UNCLASSIFIED DAAG29-81-D-0100 F/G 20/6 NL

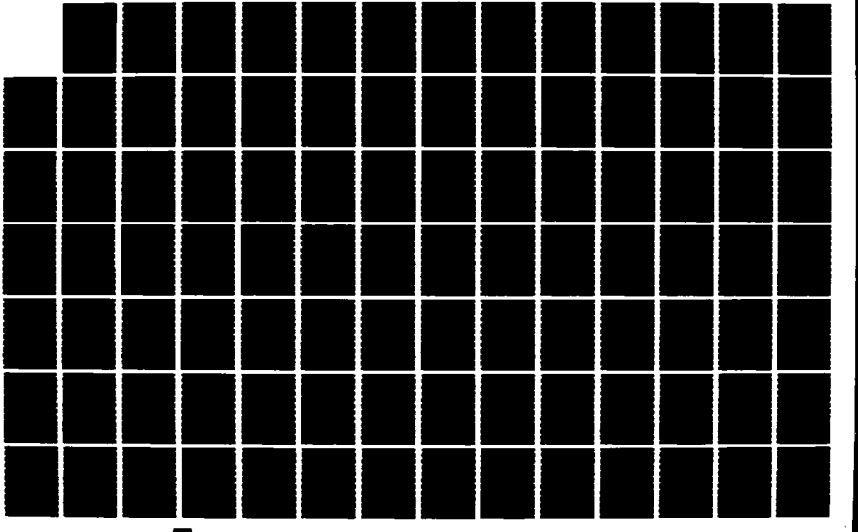

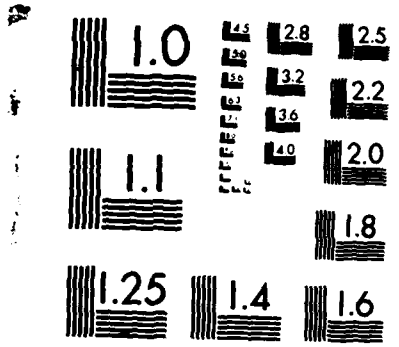

LASER TROLLING FOR MICROPARTICLES

Philip J. Wyatt and Steven D. Phillips
Wyatt Technology Corporation
Santa Barbara, California 93130-3003

RECENT PUBLICATIONS, SUBMITTALS FOR PUBLICATION AND PRESENTATIONS:

A) This paper is based on an article submitted to Limnology and Oceanography.

ABSTRACT

The light scattering properties of individual microparticles in a liquid medium are recorded as they fall through a laser beam having a Gaussian profile. Means by which this may be accomplished are described together with various features of particle size and shape that may be deduced from the recorded data.

Measurement of the light scattering properties of individual microparticles provide an exceptional basis for their optical characterization.[1-4] Although often oversimplified, application of such light scattering techniques can result in determination of particle size, shape, internal structure, anisotropy, and eventually, identification. Generally, the more detail of the scattered flux intensity that may be recorded as a function of solid angle, the more likely will such a characterization be possible.

A variety of scientific instruments have been developed to measure such light scattering properties of individual aerosol particles, and others are under development. Most are relatively expensive and require elaborate optical and detection electronics to capture the appropriate scattered signals arising during the usually brief passage of each particle through the illuminating beam. For the case of particles in liquids at very low concentrations, a relatively simple measurement technique has been devised whereby their light scattering properties may be recorded in a plane.

By means of some simple modifications to a classical light scattering photometer (DAWN-B), the light scattering patterns of liquid-borne particles may be recorded and studied. The DAWN system consists of a vertically polarized He-Ne laser (5mW @ 632.8nm -- Melles Griot) incident on a sample-containing glass cuvette (typically, a standard 25 mm diameter scintillation vial) placed at the center of a stage. Equidistantly placed about the center of the cuvette is a set of 15 collimated, high gain, transimpedence photodiodes

fixed at angles θ_i, where

$$0.20 \leq \sin(\theta_i/2) \leq 0.90, \quad i = 1 \text{ to } 15. \tag{1}$$

The $\sin(\theta/2)$ increment is 0.05. The laser beam is of nominal $(1/e^2)$ diameter $\underline{D}$ = 0.8 mm. In the conventional instrument, the detectors subtend an illuminated volume of about 2.5 μl (2 mm of the laser beam at 90°).

By inserting restricting apertures into the collimators, the scattering volume detected is reduced to about 0.60 μl. Thus at a particle concentration of 10^3 per ml, on average only one particle will be in the scattering volume at any time. Typically for water, a spherical particle of radius R and specific gravity ρ will reach a terminal velocity under the influence of gravity according to Stokes' law

$$\begin{aligned} mg &= 6\pi\eta Rv, \text{ or} \\ v &= mg/(6\pi\eta R) \\ &= 2R^2(\rho-1)g/(9\eta), \end{aligned} \tag{2}$$

where η is the viscosity, g the acceleration of gravity, and ρ the particle specific gravity. The transit time, τ, through the beam diameter D, is therefore given by

$$D/v = \tau = 9\eta D/[2R^2(\rho-1)g], \tag{3}$$

where we have assumed that the beam is horizontal, i.e., perpendicular to the gravitational field.

Consider a sea urchin egg of diameter 80 μm and specific gravity of 2.0. The corresponding transit time through the 0.8 mm beam at room temperature (η = 0.89cp) would be given (in c.g.s. units) by

$$\begin{aligned} \tau &= \frac{9 \times 8.9 \times 10^{-3} \times 8.0 \times 10^{-2}}{2 \times 16 \times 10^{-6} \times 9.80 \times 10^{2}} \\ &= 2 \times 10^{-1} \text{sec} \\ &= 200 \text{ ms} . \end{aligned} \tag{4}$$

Interfacing the DAWN-B to a personal computer containing a Data Translation DT 2801A analog-to-digital multiplexer permits the conversion (to 12 bit accuracy) of up to 27.5 thousand channels per second. Since the photometer has a 16 channel output (15 detectors plus 1 laser monitor), approximately 27500/16 scans may be collected per second, corresponding to about 0.6 msec/scan. Thus even for so large and dense an object as a sea urchin egg, scattering data from more than 300 complete scans could be collected during the particle's transit time through the beam.

We present now some simple examples of collected scattering data for the modified DAWN instrument. Since the profile of the beam is Gaussian, the intensity of light incident upon the particle will vary as the particle's distance from the center of the beam ("impact parameter"). Similarly, the scattered light intensity at any angle will also vary. If the particle is spherically symmetric[5,6], the relative scattered intensity at any angle will remain constant, independent of the level of incident flux, subject, of course, to the sensitivity limit of the detectors and A/D converter. This "relative" intensity may be generated easily by collecting the digitally converted scattered intensities at all angles and dividing these results by the non-zero value at one particular angle. If the particle is non-spherical, then the relative scattered intensities will not remain constant during the transit through the beam, but will vary as the particle tumbles. If the particle is motile, there will be no straight trajectory through the beam.

The procedure by which the scattering pattern of a single particle passing through the laser beam may be captured is straightforward. A threshold signal voltage for a particular channel is selected together with a scan rate and the number of scans, N, to be saved. These parameters are entered into the controlling program (GRABEM) which also contains the normalized detector gains and offset values. The program begins a continuous scan of the 16 channels and saves up to 500 distinct scans before overwriting the saved data array. As the data are stored via direct memory access (DMA), the program follows by examining the data collected at the threshold channel. As soon as the threshold value exceeds the preset value, the subsequent N scans are saved and the scanning is stopped. Control then returns to the program which permits printing of the results. Until a particle is "caught", the computer screen remains in a standby status. Upon finding a particle, the screen presents the catch information such as the number of the scan after which the threshold was detected. At very low particle concentrations, the system resembles conventional trolling as experienced by a fisherman. A sufficiently high threshold value will be found to correspond to a sufficiently small impact parameter. Appropriate ranges for each type of suspended particle ensemble may be obtained by watching the output voltage signals for the selected channel on the instrument channel monitor display.

Table I presents the scattered intensities as a function of sin $\theta/2$ per Eq. (1) for

Table I. Raw scattering data recorded during 100 successive scans from a 4060 nm latex particle (313 scans per second).

1	2	3	4	5	6	7	8	9	10	11	12	13	14	15	1	2	3	4	5	6	7	8	9	10	11	12	13	14	15
358	216	117	163	57	40	7	21	14	15	6	1	4	11	1	355	214	119	163	55	40	6	22	15	15	9	5	2	4	5
365	225	125	167	61	40	5	21	12	9	6	-3	4	7	2	367	227	118	174	55	46	8	26	14	13	4	4	2	12	-3
379	230	128	174	57	44	6	23	16	15	3	1	7	7	2	391	234	119	176	60	47	4	20	17	15	3	2	2	8	2
408	240	132	175	59	46	9	19	17	16	11	4	4	11	4	401	251	141	181	58	45	8	23	13	17	6	7	7	10	-5
410	251	142	183	62	48	6	21	17	12	6	0	9	9	6	415	256	143	186	66	41	9	23	18	15	5	2	4	6	2
423	265	151	190	67	48	10	21	19	15	10	3	0	11	7	443	277	153	204	65	46	13	22	22	19	4	3	0	8	4
431	272	151	196	63	48	8	24	18	19	-8	4	3	8	3	463	294	159	213	74	49	11	21	26	16	5	2	5	8	7
436	279	154	190	65	55	11	30	24	15	6	2	0	11	6	468	302	169	220	71	56	15	27	22	17	1	11	8	7	5
467	297	163	211	71	53	14	25	27	15	8	5	8	14	2	484	309	168	220	74	56	13	25	31	17	3	6	2	10	3
483	315	170	230	79	61	12	26	27	20	7	1	7	11	2	503	316	178	228	78	62	11	28	21	18	3	-2	7	11	6
500	325	177	239	83	61	15	29	25	21	4	7	7	16	7	524	332	183	243	78	62	15	31	24	13	8	9	7	14	1
530	337	183	246	82	66	12	28	26	21	4	7	9	12	3	538	344	173	250	88	65	9	30	27	20	7	7	4	13	3
561	354	192	263	90	66	14	33	26	22	6	1	11	11	5	556	349	186	257	92	65	15	30	27	23	10	3	14	11	1
570	368	203	274	95	71	16	26	29	22	8	3	6	12	-13	579	363	198	274	91	74	14	31	32	22	6	6	8	14	4
618	388	207	290	97	78	19	32	31	22	5	6	4	10	5	611	384	208	287	102	78	14	33	33	24	9	8	14	14	-14
635	393	205	296	99	77	16	35	29	22	6	3	11	12	2	645	400	212	301	101	83	16	32	34	29	12	6	10	13	2
656	406	215	308	106	81	16	33	32	22	3	9	12	15	1	671	418	221	314	110	88	25	34	34	21	12	8	11	8	6
699	425	228	315	109	85	20	33	37	25	7	9	13	12	4	696	435	237	320	110	86	20	35	38	24	7	7	10	14	4
711	440	235	318	109	87	20	38	37	29	7	4	7	9	4	724	442	243	321	113	89	20	28	38	24	6	7	9	16	5
740	453	252	335	122	89	28	34	35	29	10	10	8	21	5	771	469	252	338	118	87	25	33	39	23	10	3	10	18	2
759	459	252	341	122	94	17	36	40	28	7	11	10	16	3	797	473	262	349	127	92	22	37	41	25	8	10	10	17	4
815	481	267	345	133	98	28	33	43	34	7	12	12	14	0	819	482	267	345	126	97	25	37	46	26	7	9	13	20	5
851	498	277	363	135	101	28	40	44	32	10	7	13	17	7	863	499	283	368	138	100	29	38	44	38	13	9	10	15	6
857	494	281	366	137	101	26	41	49	28	9	8	11	18	5	898	514	289	373	142	100	26	43	49	27	9	10	4	16	2
878	508	290	381	143	102	30	42	48	30	12	9	11	20	3	906	526	303	371	147	104	30	42	47	32	14	5	10	16	7
916	541	308	400	153	109	26	46	47	30	17	13	12	16	-3	905	522	310	388	143	108	28	43	40	31	11	8	14	21	4
949	544	325	417	162	110	25	51	49	32	9	9	11	15	1	911	525	308	392	152	103	29	44	46	32	5	11	11	20	7
944	547	331	408	167	114	29	47	46	37	9	12	13	20	8	962	550	330	400	163	105	37	45	51	36	13	10	13	24	6
982	565	344	421	171	121	33	49	53	41	8	7	11	28	6	976	553	337	413	164	110	28	45	53	37	3	10	18	16	10
1030	576	351	425	172	115	26	53	53	36	10	10	14	18	5	1017	564	346	422	173	117	32	49	54	38	12	14	13	22	10
1052	584	356	429	175	115	35	49	61	35	9	12	17	20	5	1061	592	362	426	174	121	34	46	64	39	12	13	16	19	4
1105	609	374	442	192	123	35	47	60	39	12	20	14	21	14	1121	610	366	435	185	123	34	46	60	38	12	16	11	19	6
1096	601	371	437	185	121	37	49	59	39	10	13	14	18	8	1144	626	392	456	193	126	42	48	63	35	12	15	14	21	9
1137	618	386	453	195	128	39	51	74	40	16	12	16	26	7	1202	640	402	461	198	123	40	47	70	50	14	13	12	20	11
1186	627	391	454	193	130	37	53	67	38	17	13	16	23	10	1234	655	412	467	199	130	43	50	68	38	12	13	11	17	5
1237	655	416	470	203	133	42	52	69	38	16	15	21	20	5	1267	674	418	474	206	134	42	57	71	38	13	14	18	24	7
1286	670	422	477	213	131	39	50	69	46	13	16	18	23	-1	1319	684	436	482	219	135	49	55	69	43	12	12	27	23	11
1300	677	430	474	213	134	49	49	75	47	11	10	16	22	6	1338	696	448	481	215	129	50	55	74	49	13	12	11	22	2
1359	702	450	491	220	135	47	48	76	43	11	14	18	24	12	1351	703	451	498	225	137	48	56	76	47	13	15	17	17	12
1397	721	464	504	234	140	49	56	76	46	10	15	23	23	9	1395	714	460	475	223	133	48	50	76	45	11	13	17	20	7
1428	724	472	502	226	139	55	55	82	52	19	16	17	20	7	1448	729	469	501	225	132	56	49	78	47	16	11	19	21	8
1455	734	481	503	224	138	61	54	84	48	16	12	18	15	7	1488	746	489	513	226	137	60	54	81	52	12	12	19	22	10
1506	747	490	510	229	132	60	52	79	51	9	13	19	20	6	1509	733	485	503	230	127	62	52	81	53	3	14	12	18	11
1574	757	511	519	233	127	62	51	83	51	15	11	18	21	8	1540	737	495	510	228	126	66	39	83	44	14	18	17	28	-9
1588	754	518	512	233	127	65	53	88	51	14	11	15	20	12	1572	759	512	509	228	129	66	51	88	52	18	15	6	19	9
1612	766	524	514	241	131	68	53	84	46	16	14	17	21	7	1594	760	521	520	245	134	63	54	86	56	18	12	20	20	6
1640	765	529	518	242	124	69	50	81	51	15	15	19	23	13	1620	749	527	518	247	130	71	54	88	53	16	10	29	19	7
1668	765	533	517	246	128	69	55	83	52	23	10	16	26	2	1658	765	540	522	251	132	72	52	85	51	18	14	17	20	10
1686	767	540	517	248	131	70	55	88	52	18	15	23	18	7	1697	760	547	530	247	128	72	53	85	52	17	13	20	23	6
1664	749	539	511	251	128	72	53	89	54	15	6	15	18	9	1723	772	548	521	252	129	72	50	91	55	20	17	22	21	3

100 successive scans of a "captured" polystyrene latex particle of nominal diameter 4060 nm (Dow Chemical Company). The data at $\lambda = 632.8$ nm are unnormalized and represented digitally; each bit corresponding to a signal of 0.610 mV. The trigger channel is channel #5 at a threshold of 30 mV. Thus the 57 bit value of the first scan for channel 5 corresponds to 57 x 0.61 = 34.8 mV. The scan frequency is 5000 channels/sec or about 313 scans per second. The odd numbered scans (following the triggering event) are on the left (columns 1 through 15) and the even numbered scans on the right. The time between subsequent odd or subsequent even scans is approximately 2/313 = 6.4 m sec. The negative values that ocassionally show up generally arise from a negative noise spike, usually from the line supply. As is evident from an examination of these data, the particle is seen to enter the beam and has not yet reached its maximum value during the 100 scan period examined.

Table II presents the data of Table I normalized to correct for gain differences of the photodiodes. All values for a given scan have been further referred to Channel #3, i.e., divided by the corresponding value at that channel.

Tables III and IV correspond, respectively, to data generated similar to those of Tables I and II, but for a sea urchin (Strongylocentrotus purpuratus) egg ($2R \sim 80$ μm). Here the trigger channel is again channel #5, but the detection threshold is 140 mV. Each bit, in this example, corresponds to 1.22 mV and there are 250 scans per second. The consistency of normalized values (Table IV) confirms the near sphericity of the particle or its lack of appreciable tumbling as it falls through the beam.

Tables V and VI correspond to data collected from a non-flaggelated alga particle at 250 scans per second, detection threshold of 80 mV, and 1.22 mV/bit resolution. We see a large variation of scattered intensity with time corresponding to a non-spherical structure. During the 50 scans presented, note the almost 10-fold variation of channels #5 and #6.

The above data have not, for the most part, been analyzed. Much information remains in them, such as mean velocities, sizes (from Stokes' law), aspect ratios, etc. The most important element of these results is that this measurement technique permits us a slow

Table II. Data of Table I normalized and relative to the scattered intensity of channel #3 (sin $\theta/2 = 0.30$).

2.232	2.795	1.000	1.789	0.896	0.595	0.155	0.409	0.292	0.340	0.162	0.050	0.106	0.277	0.040
2.176	2.723	1.000	1.759	0.850	0.585	0.130	0.422	0.308	0.335	0.239	0.244	0.052	0.099	0.196
2.130	2.725	1.000	1.716	0.897	0.557	0.104	0.383	0.234	0.191	0.152	-0.139	0.099	0.165	0.074
2.268	2.912	1.000	1.894	0.857	0.679	0.175	0.502	0.290	0.292	0.107	0.196	0.052	0.300	-0.118
2.159	2.720	1.000	1.746	0.819	0.599	0.121	0.410	0.305	0.311	0.074	0.045	0.169	0.161	0.073
2.396	2.977	1.000	1.899	0.927	0.688	0.087	0.383	0.349	0.335	0.080	0.097	0.052	0.198	0.078
2.254	2.753	1.000	1.703	0.822	0.607	0.176	0.328	0.314	0.322	0.264	0.176	0.094	0.246	0.141
2.074	2.695	1.000	1.649	0.756	0.556	0.147	0.372	0.225	0.320	0.135	0.288	0.153	0.209	-0.165
2.106	2.676	1.000	1.655	0.803	0.589	0.109	0.337	0.292	0.224	0.134	0.000	0.196	0.187	0.197
2.117	2.710	1.000	1.671	0.848	0.499	0.163	0.367	0.307	0.278	0.111	0.081	0.086	0.124	0.065
2.043	2.657	1.000	1.616	0.816	0.554	0.171	0.317	0.307	0.264	0.209	0.115	0.000	0.215	0.216
2.112	2.741	1.000	1.712	0.781	0.524	0.220	0.328	0.351	0.330	0.083	0.114	0.000	0.154	0.122
2.082	2.727	1.000	1.667	0.767	0.554	0.137	0.362	0.291	0.334	-0.168	0.154	0.061	0.156	0.092
2.124	2.799	1.000	1.720	0.856	0.537	0.179	0.301	0.399	0.267	0.099	0.073	0.097	0.148	0.205
2.065	2.743	1.000	1.585	0.776	0.622	0.185	0.444	0.380	0.259	0.123	0.075	0.000	0.210	0.181
2.020	2.705	1.000	1.672	0.772	0.577	0.230	0.364	0.318	0.267	0.019	0.377	0.146	0.122	0.138
2.089	2.759	1.000	1.663	0.801	0.566	0.222	0.350	0.404	0.244	0.155	0.178	0.152	0.253	0.057
2.101	2.785	1.000	1.682	0.810	0.581	0.200	0.339	0.450	0.269	0.056	0.207	0.037	0.175	0.083
2.072	2.805	1.000	1.738	0.854	0.625	0.183	0.349	0.388	0.312	0.130	0.034	0.127	0.191	0.055
2.061	2.688	1.000	1.645	0.806	0.607	0.160	0.359	0.288	0.268	0.053	-0.065	0.122	0.182	0.157
2.060	2.780	1.000	1.734	0.862	0.600	0.219	0.374	0.345	0.315	0.071	0.229	0.122	0.266	0.184
2.088	2.747	1.000	1.705	0.784	0.590	0.212	0.386	0.320	0.189	0.138	0.285	0.118	0.225	0.025
2.112	2.788	1.000	1.726	0.824	0.628	0.170	0.349	0.347	0.305	0.069	0.222	0.152	0.193	0.076
2.268	3.010	1.000	1.856	0.935	0.654	0.135	0.395	0.381	0.307	0.128	0.235	0.071	0.221	0.081
2.131	2.791	1.000	1.759	0.862	0.599	0.189	0.392	0.330	0.304	0.099	0.030	0.177	0.169	0.121
2.180	2.841	1.000	1.775	0.909	0.609	0.209	0.368	0.354	0.328	0.170	0.093	0.233	0.174	0.025
2.048	2.745	1.000	1.734	0.860	0.609	0.204	0.292	0.349	0.288	0.125	0.086	0.091	0.174	-0.298
2.133	2.776	1.000	1.777	0.845	0.651	0.183	0.357	0.394	0.295	0.096	0.176	0.125	0.208	0.094
2.177	2.838	1.000	1.799	0.861	0.656	0.238	0.353	0.365	0.282	0.076	0.168	0.060	0.142	0.112
2.142	2.795	1.000	1.772	0.901	0.653	0.174	0.362	0.387	0.306	0.137	0.223	0.208	0.198	-0.313
2.259	2.902	1.000	1.854	0.888	0.654	0.202	0.389	0.345	0.285	0.093	0.085	0.166	0.172	0.045
2.219	2.857	1.000	1.823	0.876	0.682	0.195	0.344	0.391	0.363	0.179	0.164	0.146	0.181	0.044
2.225	2.859	1.000	1.840	0.906	0.656	0.193	0.350	0.363	0.272	0.044	0.243	0.173	0.206	0.022
2.214	2.864	1.000	1.825	0.915	0.693	0.293	0.351	0.375	0.252	0.172	0.210	0.154	0.107	0.126
2.236	2.822	1.000	1.774	0.879	0.649	0.227	0.330	0.396	0.291	0.097	0.229	0.176	0.155	0.082
2.142	2.779	1.000	1.734	0.853	0.632	0.218	0.337	0.391	0.269	0.093	0.171	0.130	0.174	0.079
2.207	2.835	1.000	1.738	0.853	0.645	0.220	0.369	0.384	0.328	0.094	0.099	0.092	0.113	0.079
2.173	2.754	1.000	1.697	0.855	0.638	0.213	0.263	0.382	0.262	0.078	0.167	0.114	0.194	0.096
2.142	2.722	1.000	1.707	0.890	0.615	0.288	0.308	0.339	0.305	0.126	0.230	0.098	0.246	0.092
2.231	2.818	1.000	1.723	0.861	0.601	0.257	0.299	0.378	0.242	0.126	0.069	0.123	0.210	0.037
2.197	2.758	1.000	1.738	0.890	0.650	0.175	0.326	0.387	0.295	0.088	0.253	0.123	0.187	0.055
2.219	2.733	1.000	1.711	0.891	0.612	0.217	0.322	0.382	0.253	0.097	0.221	0.118	0.191	0.071
2.226	2.727	1.000	1.660	0.916	0.639	0.271	0.282	0.393	0.338	0.083	0.261	0.139	0.154	0.000
2.237	2.733	1.000	1.660	0.867	0.633	0.242	0.316	0.420	0.258	0.083	0.195	0.150	0.221	0.105
2.241	2.722	1.000	1.683	0.896	0.635	0.262	0.329	0.388	0.307	0.114	0.146	0.145	0.181	0.118
2.224	2.670	1.000	1.670	0.896	0.615	0.265	0.306	0.379	0.356	0.145	0.184	0.109	0.156	0.099
2.224	2.662	1.000	1.673	0.896	0.626	0.239	0.333	0.426	0.264	0.101	0.165	0.121	0.189	0.083
2.266	2.693	1.000	1.658	0.903	0.603	0.233	0.339	0.414	0.248	0.099	0.201	0.043	0.163	0.032
2.208	2.652	1.000	1.687	0.906	0.613	0.268	0.330	0.404	0.275	0.131	0.180	0.117	0.203	0.048
2.181	2.628	1.000	1.573	0.892	0.598	0.256	0.316	0.379	0.280	0.146	0.096	0.102	0.156	0.107
2.169	2.659	1.000	1.668	0.913	0.616	0.218	0.341	0.372	0.259	0.175	0.245	0.120	0.153	-0.045

(Continued)

Table II. (continued)

2.129	2.549	1.000	1.607	0.848	0.607	0.234	0.316	0.315	0.265	0.112	0.150	0.140	0.200	0.060
2.130	2.534	1.000	1.648	0.916	0.589	0.199	0.358	0.368	0.261	0.088	0.161	0.105	0.136	0.014
2.157	2.581	1.000	1.635	0.907	0.582	0.244	0.326	0.364	0.276	0.051	0.207	0.110	0.191	0.106
2.080	2.502	1.000	1.583	0.927	0.600	0.227	0.324	0.339	0.297	0.086	0.210	0.121	0.178	0.112
2.126	2.523	1.000	1.557	0.908	0.554	0.290	0.311	0.377	0.290	0.125	0.176	0.122	0.214	0.085
2.082	2.487	1.000	1.572	0.914	0.613	0.248	0.325	0.376	0.316	0.074	0.118	0.099	0.240	0.081
2.112	2.484	1.000	1.574	0.895	0.568	0.215	0.305	0.384	0.291	0.028	0.172	0.165	0.140	0.138
2.140	2.484	1.000	1.555	0.901	0.571	0.192	0.344	0.368	0.272	0.090	0.165	0.123	0.151	0.066
2.144	2.468	1.000	1.566	0.919	0.589	0.239	0.323	0.381	0.292	0.110	0.235	0.116	0.187	0.134
2.155	2.484	1.000	1.548	0.904	0.563	0.254	0.314	0.418	0.261	0.080	0.195	0.148	0.166	0.065
2.138	2.476	1.000	1.511	0.884	0.582	0.243	0.290	0.431	0.286	0.105	0.208	0.137	0.155	0.051
2.155	2.465	1.000	1.518	0.944	0.573	0.242	0.287	0.391	0.277	0.101	0.310	0.116	0.165	0.174
2.234	2.523	1.000	1.526	0.929	0.585	0.240	0.287	0.400	0.276	0.104	0.253	0.093	0.153	0.076
2.155	2.453	1.000	1.513	0.917	0.568	0.258	0.301	0.388	0.279	0.085	0.203	0.117	0.143	0.100
2.128	2.418	1.000	1.494	0.905	0.560	0.277	0.279	0.392	0.237	0.097	0.222	0.110	0.158	0.107
2.148	2.424	1.000	1.507	0.929	0.577	0.261	0.301	0.468	0.275	0.131	0.180	0.128	0.198	0.084
2.181	2.410	1.000	1.473	0.905	0.533	0.258	0.267	0.425	0.330	0.110	0.187	0.092	0.147	0.127
2.212	2.428	1.000	1.491	0.907	0.579	0.245	0.309	0.418	0.258	0.138	0.193	0.126	0.173	0.119
2.184	2.407	1.000	1.456	0.888	0.550	0.270	0.277	0.403	0.245	0.092	0.183	0.083	0.122	0.056
2.169	2.384	1.000	1.451	0.897	0.557	0.261	0.285	0.405	0.242	0.122	0.209	0.156	0.142	0.056
2.211	2.441	1.000	1.456	0.906	0.558	0.260	0.311	0.415	0.241	0.098	0.194	0.133	0.169	0.078
2.222	2.404	1.000	1.452	0.928	0.541	0.239	0.270	0.399	0.289	0.097	0.220	0.132	0.161	-0.011
2.206	2.375	1.000	1.420	0.923	0.539	0.291	0.288	0.386	0.262	0.087	0.160	0.191	0.155	0.117
2.205	2.384	1.000	1.416	0.911	0.543	0.295	0.260	0.426	0.290	0.081	0.135	0.115	0.151	0.065
2.178	2.352	1.000	1.379	0.882	0.501	0.289	0.280	0.403	0.290	0.092	0.155	0.076	0.145	0.021
2.203	2.362	1.000	1.401	0.899	0.522	0.270	0.243	0.412	0.254	0.077	0.180	0.124	0.157	0.124
2.185	2.360	1.000	1.418	0.917	0.529	0.275	0.283	0.411	0.277	0.091	0.193	0.117	0.111	0.124
2.196	2.353	1.000	1.395	0.927	0.525	0.273	0.275	0.400	0.263	0.068	0.187	0.153	0.146	0.090
2.212	2.350	1.000	1.326	0.891	0.504	0.270	0.248	0.403	0.260	0.076	0.164	0.114	0.128	0.071
2.206	2.322	1.000	1.366	0.880	0.513	0.302	0.266	0.424	0.292	0.127	0.196	0.111	0.125	0.069
2.252	2.353	1.000	1.372	0.882	0.490	0.309	0.238	0.406	0.266	0.108	0.136	0.125	0.132	0.079
2.206	2.310	1.000	1.343	0.856	0.500	0.328	0.256	0.426	0.265	0.105	0.145	0.116	0.092	0.068
2.219	2.310	1.000	1.347	0.850	0.488	0.318	0.252	0.404	0.282	0.078	0.142	0.120	0.133	0.095
2.241	2.309	1.000	1.337	0.859	0.469	0.317	0.242	0.393	0.276	0.058	0.154	0.120	0.120	0.057
2.269	2.288	1.000	1.332	0.872	0.456	0.331	0.245	0.408	0.290	0.020	0.167	0.076	0.109	0.106
2.246	2.243	1.000	1.304	0.838	0.433	0.314	0.228	0.396	0.265	0.093	0.125	0.109	0.121	0.073
2.269	2.254	1.000	1.323	0.847	0.443	0.345	0.180	0.409	0.236	0.089	0.211	0.106	0.167	0.085
2.236	2.204	1.000	1.269	0.827	0.427	0.325	0.233	0.415	0.261	0.085	0.123	0.090	0.114	0.108
2.239	2.244	1.000	1.277	0.819	0.439	0.334	0.227	0.419	0.270	0.111	0.170	0.036	0.109	0.082
2.244	2.213	1.000	1.260	0.845	0.435	0.336	0.231	0.391	0.233	0.097	0.155	0.100	0.118	0.062
2.231	2.208	1.000	1.282	0.864	0.448	0.313	0.236	0.403	0.285	0.109	0.134	0.119	0.113	0.054
2.261	2.189	1.000	1.258	0.841	0.408	0.338	0.216	0.374	0.256	0.090	0.164	0.111	0.128	0.114
2.242	2.152	1.000	1.262	0.862	0.430	0.349	0.234	0.407	0.267	0.096	0.110	0.170	0.106	0.062
2.282	2.173	1.000	1.246	0.848	0.418	0.335	0.235	0.380	0.259	0.136	0.109	0.093	0.144	0.017
2.239	2.145	1.000	1.242	0.854	0.426	0.345	0.220	0.384	0.251	0.105	0.150	0.097	0.109	0.086
2.277	2.150	1.000	1.230	0.844	0.422	0.336	0.232	0.398	0.256	0.105	0.161	0.132	0.098	0.060
2.263	2.104	1.000	1.244	0.830	0.408	0.341	0.221	0.379	0.252	0.098	0.138	0.113	0.124	0.051
2.252	2.104	1.000	1.218	0.856	0.414	0.346	0.224	0.403	0.265	0.088	0.065	0.086	0.098	0.078
2.293	2.133	1.000	1.221	0.845	0.410	0.340	0.209	0.405	0.266	0.115	0.180	0.124	0.113	0.025

Table III. Raw scattering data recorded during 50 successive scans from a sea urchin egg (2R ~ 80 μm) (250 scans per second).

1	2	3	4	5	6	7	8	9	10	11	12	13	14	15	1	2	3	4	5	6	7	8	9	10	11	12	13	14	15
193	97	124	44	116	52	68	20	75	17	14	4	2	4	2	198	102	129	44	122	59	68	20	89	17	16	4	4	3	0
211	100	135	33	127	50	78	21	92	21	16	3	5	5	0	234	113	149	49	144	60	82	24	96	22	20	5	3	5	4
258	125	165	54	159	74	91	26	98	25	20	3	4	3	2	266	132	172	55	164	71	91	24	107	26	26	5	5	4	1
288	140	182	58	171	72	95	27	114	26	21	2	5	3	2	300	141	202	65	186	73	104	27	121	28	25	4	7	4	1
320	157	209	64	198	83	113	35	136	33	26	4	4	3	1	340	177	227	74	222	91	125	36	151	33	29	6	5	7	3
354	175	229	69	227	91	126	36	149	34	32	7	7	5	5	363	171	245	72	240	94	131	39	157	36	31	6	11	5	5
398	190	265	81	257	102	145	39	172	40	35	9	11	8	5	450	218	303	92	288	121	159	49	187	45	39	12	10	10	4
473	209	310	89	293	110	163	46	192	39	41	8	5	7	1	457	205	303	80	293	110	160	44	189	39	37	8	9	8	5
471	211	313	85	309	115	175	48	209	38	40	8	13	5	5	527	242	349	102	342	132	190	54	229	54	44	10	11	7	6
577	280	377	108	370	147	204	55	242	51	46	9	12	9	13	569	259	380	116	378	147	208	59	254	51	47	11	12	8	6
562	247	372	101	369	134	203	57	247	51	48	13	14	8	3	602	273	407	121	413	159	229	65	277	62	54	10	13	10	6
676	311	449	129	446	175	248	72	297	62	58	13	16	11	7	687	311	447	132	444	172	244	66	296	64	57	11	12	10	7
691	304	463	129	447	169	242	71	288	58	57	10	13	8	5	680	316	465	132	473	182	263	73	316	69	55	13	15	14	9
753	348	514	145	501	203	275	79	336	75	66	17	17	14	10	810	373	538	153	528	209	287	81	342	72	67	14	14	12	9
792	362	529	149	527	202	288	81	339	64	65	16	18	14	7	740	341	506	137	498	191	277	82	340	72	71	15	15	13	6
821	392	562	164	559	222	309	89	376	84	74	17	15	15	7	912	428	625	178	606	250	337	98	398	92	78	15	18	13	11
905	406	601	173	594	237	322	96	383	89	74	16	16	15	8	872	404	588	164	579	223	314	90	374	80	76	30	15	15	7
893	422	603	179	605	236	334	92	395	87	79	18	18	17	10	965	449	657	192	654	266	360	107	437	105	85	22	22	23	11
1018	484	679	203	662	269	345	105	432	96	83	20	20	17	9	978	470	656	193	639	261	341	98	413	97	81	16	18	1	5
954	445	642	187	637	260	347	104	416	103	80	19	10	16	11	991	470	665	192	664	272	367	116	442	107	88	21	20	17	11
1095	539	731	225	723	312	392	124	474	118	89	21	22	20	12	1107	533	722	216	712	304	383	114	456	107	90	17	21	19	11
1027	500	684	201	669	281	371	112	440	103	84	20	20	20	-3	1051	506	689	202	698	281	373	114	454	107	87	21	24	22	10
1128	549	744	227	752	321	420	125	510	125	97	25	23	22	14	1192	588	782	234	766	333	417	129	498	121	95	22	29	21	10
1129	539	756	219	740	314	407	123	490	111	89	21	23	21	8	1079	521	716	204	716	295	401	117	483	112	92	19	21	20	10
1144	552	770	223	774	328	423	131	511	119	95	23	23	22	12	1246	611	819	246	801	354	442	136	529	128	100	26	22	23	12

Table IV. Data of Table III normalized relative to the scattered intensity of channel #3 (sin $\theta/2 = 0.30$).

1.135	1.184	1.000	0.456	1.720	0.730	1.419	0.368	1.476	0.364	0.357	0.187	0.050	0.095	0.075
1.119	1.197	1.000	0.438	1.739	0.797	1.364	0.354	1.684	0.350	0.392	0.180	0.096	0.069	0.000
1.140	1.121	1.000	0.314	1.729	0.645	1.495	0.355	1.663	0.413	0.375	0.129	0.114	0.109	0.000
1.145	1.148	1.000	0.422	1.777	0.701	1.424	0.367	1.572	0.392	0.425	0.195	0.062	0.099	0.125
1.140	1.147	1.000	0.420	1.771	0.781	1.427	0.359	1.449	0.402	0.383	0.105	0.075	0.054	0.056
1.128	1.162	1.000	0.411	1.753	0.719	1.369	0.318	1.518	0.401	0.478	0.169	0.090	0.069	0.027
1.154	1.165	1.000	0.409	1.727	0.689	1.351	0.338	1.529	0.379	0.365	0.064	0.085	0.049	0.051
1.083	1.057	1.000	0.413	1.693	0.629	1.333	0.305	1.462	0.368	0.391	0.115	0.107	0.058	0.023
1.117	1.137	1.000	0.393	1.742	0.692	1.399	0.382	1.588	0.419	0.393	0.111	0.059	0.042	0.022
1.092	1.181	1.000	0.419	1.798	0.698	1.425	0.362	1.623	0.386	0.404	0.153	0.068	0.091	0.061
1.127	1.157	1.000	0.387	1.822	0.692	1.424	0.358	1.588	0.394	0.442	0.177	0.094	0.064	0.102
1.081	1.057	1.000	0.377	1.801	0.668	1.384	0.363	1.564	0.390	0.400	0.142	0.139	0.060	0.095
1.095	1.085	1.000	0.393	1.783	0.670	1.416	0.336	1.584	0.401	0.418	0.197	0.128	0.089	0.088
1.083	1.089	1.000	0.390	1.747	0.695	1.358	0.369	1.506	0.394	0.407	0.230	0.102	0.097	0.061
1.113	1.021	1.000	0.369	1.737	0.618	1.361	0.338	1.511	0.334	0.418	0.150	0.050	0.067	0.015
1.100	1.024	1.000	0.339	1.778	0.632	1.367	0.331	1.522	0.342	0.386	0.153	0.092	0.078	0.077
1.097	1.021	1.000	0.349	1.815	0.640	1.447	0.350	1.629	0.322	0.404	0.148	0.128	0.047	0.074
1.101	1.050	1.000	0.375	1.801	0.659	1.409	0.353	1.601	0.411	0.399	0.166	0.097	0.059	0.080
1.116	1.124	1.000	0.368	1.804	0.679	1.400	0.333	1.566	0.359	0.386	0.138	0.098	0.070	0.160
1.092	1.032	1.000	0.392	1.829	0.674	1.417	0.354	1.631	0.356	0.391	0.168	0.098	0.062	0.073
1.102	1.005	1.000	0.349	1.823	0.627	1.412	0.349	1.620	0.364	0.408	0.203	0.116	0.063	0.038
1.079	1.016	1.000	0.382	1.865	0.680	1.456	0.364	1.661	0.404	0.420	0.142	0.099	0.072	0.069
1.098	1.049	1.000	0.369	1.826	0.679	1.430	0.366	1.614	0.367	0.409	0.168	0.110	0.072	0.073
1.121	1.053	1.000	0.379	1.826	0.670	1.413	0.337	1.616	0.380	0.403	0.143	0.083	0.066	0.073
1.088	0.994	1.000	0.358	1.775	0.636	1.353	0.350	1.518	0.332	0.389	0.125	0.087	0.051	0.050
1.067	1.029	1.000	0.365	1.870	0.682	1.464	0.358	1.658	0.394	0.374	0.162	0.100	0.089	0.090
1.068	1.025	1.000	0.362	1.792	0.688	1.385	0.350	1.595	0.387	0.406	0.192	0.102	0.080	0.091
1.098	1.050	1.000	0.365	1.804	0.677	1.381	0.343	1.551	0.355	0.394	0.151	0.080	0.066	0.078
1.092	1.036	1.000	0.362	1.831	0.665	1.409	0.349	1.564	0.321	0.389	0.175	0.105	0.078	0.062
1.067	1.020	1.000	0.348	1.809	0.657	1.417	0.370	1.640	0.378	0.444	0.172	0.092	0.076	0.055
1.065	1.056	1.000	0.375	1.828	0.688	1.423	0.361	1.633	0.397	0.416	0.175	0.082	0.079	0.058
1.064	1.037	1.000	0.366	1.782	0.697	1.396	0.358	1.554	0.391	0.395	0.139	0.089	0.061	0.082
1.098	1.023	1.000	0.370	1.817	0.687	1.387	0.364	1.555	0.393	0.389	0.154	0.082	0.074	0.062
1.082	1.040	1.000	0.358	1.810	0.660	1.382	0.349	1.552	0.361	0.409	0.296	0.079	0.075	0.055
1.080	1.060	1.000	0.381	1.844	0.682	1.434	0.348	1.599	0.383	0.414	0.173	0.092	0.083	0.077
1.071	1.035	1.000	0.375	1.830	0.705	1.418	0.371	1.623	0.424	0.409	0.194	0.104	0.103	0.078
1.093	1.079	1.000	0.384	1.792	0.690	1.315	0.353	1.553	0.375	0.387	0.171	0.091	0.074	0.062
1.087	1.085	1.000	0.378	1.791	0.693	1.345	0.341	1.536	0.392	0.391	0.141	0.085	0.004	0.035
1.084	1.049	1.000	0.374	1.824	0.705	1.399	0.369	1.581	0.426	0.394	0.172	0.048	0.073	0.080
1.087	1.070	1.000	0.371	1.836	0.712	1.428	0.398	1.622	0.427	0.419	0.183	0.093	0.075	0.077
1.092	1.116	1.000	0.395	1.818	0.743	1.388	0.387	1.582	0.428	0.385	0.167	0.093	0.081	0.076
1.118	1.118	1.000	0.384	1.813	0.733	1.373	0.360	1.541	0.393	0.394	0.136	0.090	0.078	0.071
1.095	1.107	1.000	0.377	1.798	0.715	1.404	0.373	1.570	0.400	0.388	0.169	0.090	0.086	-0.020
1.112	1.112	1.000	0.377	1.862	0.710	1.401	0.377	1.608	0.412	0.399	0.177	0.108	0.094	0.068
1.106	1.117	1.000	0.392	1.858	0.751	1.461	0.383	1.673	0.446	0.412	0.195	0.096	0.087	0.088
1.112	1.138	1.000	0.384	1.801	0.742	1.380	0.376	1.554	0.411	0.384	0.163	0.115	0.079	0.060
1.089	1.079	1.000	0.372	1.799	0.723	1.393	0.371	1.582	0.390	0.372	0.161	0.094	0.082	0.049
1.099	1.102	1.000	0.366	1.838	0.718	1.450	0.373	1.646	0.415	0.406	0.154	0.091	0.082	0.065
1.084	1.085	1.000	0.372	1.848	0.742	1.422	0.388	1.619	0.410	0.390	0.173	0.092	0.094	0.077

Table V. Raw scattering data recorded during 60 successive scans from an alga (250 scans per second).

1	2	3	4	5	6	7	8	9	10	11	12	13	14	15	1	2	3	4	5	6	7	8	9	10	11	12	13	14	15
193	112	38	33	72	9	10	12	18	8	9	5	6	7	8	196	117	38	32	67	9	14	11	17	12	10	9	1	11	7
194	114	43	32	77	8	13	10	19	11	10	8	4	9	6	181	130	43	44	79	11	16	29	17	15	10	13	4	7	7
194	136	41	55	78	10	15	31	17	16	9	13	4	8	8	194	143	38	51	75	9	17	25	14	19	11	15	2	4	10
196	148	38	55	82	8	15	33	20	25	12	21	2	3	10	190	153	43	50	82	10	17	17	22	22	12	26	4	6	10
223	158	45	43	83	11	12	31	21	29	14	15	6	5	12	221	168	40	50	87	12	13	29	20	25	11	9	9	10	9
219	160	40	50	92	15	16	32	19	25	7	11	6	13	12	217	169	40	62	94	12	18	34	31	26	11	12	8	-7	10
218	165	42	42	93	14	11	21	18	18	13	9	7	15	10	226	142	40	37	97	12	19	18	18	12	10	8	7	18	7
233	143	46	36	90	10	19	14	14	18	13	6	8	16	8	237	144	45	35	87	14	15	13	15	10	11	7	14	20	8
247	119	47	27	83	14	15	9	16	8	13	5	11	22	7	250	118	47	25	82	13	15	8	15	8	14	3	16	19	6
247	101	46	32	84	20	18	8	15	3	12	2	18	23	1	242	102	48	29	87	26	15	5	14	4	8	12	19	22	1
237	78	48	32	76	34	9	5	12	14	12	1	22	24	2	221	64	51	28	59	37	16	7	11	7	9	-2	16	14	0
217	69	64	29	59	36	12	3	10	8	8	-1	21	21	-1	228	77	47	25	69	24	11	4	12	9	11	0	21	18	0
226	59	49	26	59	25	16	6	11	19	11	8	20	18	0	223	52	48	25	53	25	11	5	14	12	9	7	6	14	2
215	47	46	22	68	11	10	6	23	10	9	1	9	8	1	203	64	46	22	74	8	9	7	21	18	9	4	16	7	2
193	54	46	22	74	7	12	7	21	13	9	1	14	10	0	203	59	45	24	69	11	9	3	16	8	7	2	15	15	-1
201	57	45	26	66	18	8	4	15	3	9	-1	18	9	1	209	60	45	25	58	20	6	-7	11	8	19	1	14	18	0
188	53	46	30	46	30	6	5	13	6	1	3	15	17	0	183	53	44	32	45	33	12	5	10	6	7	-1	10	17	-2
169	46	45	28	42	31	9	6	12	6	8	-1	5	15	2	178	48	45	24	44	28	6	4	9	7	4	0	13	15	-1
183	52	38	26	45	22	7	2	7	5	6	0	16	12	-2	184	53	39	26	46	25	5	3	10	7	6	-7	9	13	-6
172	49	41	25	38	28	3	4	7	5	6	-2	14	12	2	183	51	40	26	42	20	4	2	6	4	6	0	10	14	-1
186	52	40	25	40	18	-1	2	7	4	4	2	8	10	-1	176	52	39	11	39	19	6	2	5	2	6	-2	7	8	3
175	52	40	23	39	17	4	4	7	1	5	1	6	9	2	181	52	39	25	36	17	4	2	8	4	1	0	9	10	2
181	47	38	27	36	12	4	1	10	2	3	0	5	19	-1	176	59	30	25	33	10	5	2	8	2	3	-1	5	8	-3
174	60	36	26	32	8	6	-2	9	0	4	2	1	6	-1	170	51	36	25	31	2	6	2	10	1	1	-2	1	6	0
169	43	37	24	29	5	4	0	8	2	2	-1	3	2	0	172	41	35	24	24	4	1	0	7	2	0	-1	4	0	-1
168	41	38	22	25	1	6	2	4	1	2	-1	-3	2	1	167	40	37	20	24	3	7	1	0	-2	1	-3	0	1	-3
173	44	36	24	23	6	5	2	4	2	0	0	0	3	2	174	42	41	27	21	6	7	-3	5	1	3	-2	0	1	0
181	39	38	25	19	3	6	-13	5	1	2	-3	0	1	3	183	40	42	25	19	2	6	2	2	0	-1	-1	1	0	1
182	38	38	28	13	0	3	-1	3	-6	0	-2	10	0	-1	191	40	38	28	15	2	2	0	2	1	-1	-3	0	3	-3
197	41	40	30	11	3	4	2	-1	-1	0	-2	2	0	0	197	40	40	33	10	3	1	1	2	1	-1	-2	0	1	-1

Table VI. Data of Table V normalized and relative to the scattered intensity of channel #3 (sin $\theta/2 = 0.30$).

3.258	1.918	1.000	0.742	2.696	0.697	0.460	0.203	0.813	0.177	0.633	-0.129	1.236	0.589	0.103
3.387	2.019	1.000	0.714	2.369	0.774	0.345	-0.355	0.597	0.472	1.336	0.129	0.962	1.178	0.000
2.981	1.744	1.000	0.838	1.838	1.136	0.338	0.248	0.690	0.346	0.069	0.378	1.008	1.089	0.000
3.033	1.824	1.000	0.934	1.880	1.306	0.706	0.259	0.555	0.362	0.503	-0.132	0.702	1.138	-0.212
2.739	1.548	1.000	0.799	1.716	1.200	0.518	0.304	0.651	0.354	0.562	-0.129	0.343	0.982	0.207
2.885	1.615	1.000	0.685	1.797	1.084	0.345	0.203	0.488	0.413	0.281	0.000	0.893	0.982	-0.103
3.512	2.072	1.000	0.879	2.177	1.008	0.477	0.120	0.450	0.349	0.499	0.000	1.301	0.930	-0.245
3.441	2.057	1.000	0.856	2.168	1.116	0.332	0.175	0.626	0.476	0.487	-1.040	0.713	0.982	-0.716
3.060	1.809	1.000	0.783	1.704	1.189	0.189	0.222	0.417	0.324	0.463	-0.283	1.055	0.862	0.227
3.337	1.930	1.000	0.835	1.930	0.871	0.259	0.114	0.366	0.265	0.474	0.000	0.773	1.031	-0.116
3.391	1.968	1.000	0.803	1.838	0.784	-0.065	0.114	0.427	0.265	0.316	0.290	0.618	0.737	-0.116
3.291	2.019	1.000	0.362	1.838	0.848	0.398	0.117	0.313	0.136	0.487	-0.297	0.555	0.604	0.358
3.191	1.968	1.000	0.738	1.792	0.740	0.259	0.228	0.427	0.066	0.395	0.145	0.464	0.663	0.233
3.385	2.019	1.000	0.823	1.697	0.759	0.265	0.117	0.501	0.272	0.081	0.000	0.713	0.755	0.239
3.474	1.873	1.000	0.913	1.742	0.550	0.272	0.060	0.642	0.140	0.250	0.000	0.407	1.473	-0.122
4.279	2.977	1.000	1.070	2.022	0.581	0.431	0.152	0.651	0.177	0.316	-0.193	0.515	0.786	-0.465
3.525	2.523	1.000	0.928	1.634	0.387	0.431	-0.127	0.610	0.000	0.351	0.322	0.086	0.491	-0.129
3.444	2.145	1.000	0.892	1.583	0.097	0.431	0.127	0.678	0.074	0.088	-0.322	0.086	0.491	0.000
3.331	1.759	1.000	0.833	1.441	0.235	0.280	0.000	0.528	0.143	0.171	-0.157	0.251	0.159	0.000
3.584	1.774	1.000	0.881	1.261	0.199	0.074	0.000	0.488	0.152	0.000	-0.166	0.353	0.000	-0.133
3.224	1.634	1.000	0.744	1.209	0.046	0.409	0.120	0.257	0.070	0.166	-0.153	-0.244	0.155	0.122
3.292	1.637	1.000	0.694	1.192	0.141	0.490	0.062	0.000	-0.143	0.085	-0.470	0.000	0.080	-0.377
3.505	1.850	1.000	0.856	1.174	0.290	0.359	0.127	0.271	0.147	0.000	0.000	0.000	0.246	0.259
3.095	1.551	1.000	0.846	0.942	0.255	0.442	-0.167	0.298	0.065	0.231	-0.283	0.000	0.072	0.000
3.474	1.554	1.000	0.845	0.919	0.137	0.409	-0.780	0.321	0.070	0.166	-0.458	0.000	0.078	0.367
3.178	1.442	1.000	0.764	0.832	0.083	0.370	0.109	0.116	0.000	-0.075	-0.138	0.074	0.000	0.111
3.493	1.514	1.000	0.946	0.629	0.000	0.204	-0.060	0.193	-0.419	0.000	-0.305	0.813	0.000	-0.122
3.666	1.594	1.000	0.946	0.726	0.092	0.136	0.000	0.128	0.070	-0.083	-0.458	0.000	0.233	-0.367
3.592	1.552	1.000	0.963	0.506	0.131	0.259	0.114	-0.061	-0.066	0.000	-0.290	0.155	0.000	0.000
3.592	1.514	1.000	1.060	0.460	0.131	0.065	0.057	0.122	0.066	0.079	-0.290	0.000	0.074	-0.116
3.704	4.462	1.000	1.115	3.483	0.412	0.681	0.720	1.156	0.559	0.749	0.763	0.488	0.543	0.980
3.762	4.661	1.000	1.082	3.241	0.412	0.954	0.660	1.092	0.838	0.832	1.373	0.081	0.853	0.857
3.290	4.014	1.000	0.956	3.292	0.324	0.782	0.530	1.078	0.679	0.736	1.078	0.288	0.617	0.649
3.070	4.577	1.000	1.314	3.377	0.446	0.963	1.538	0.965	0.926	0.736	1.752	0.288	0.480	0.757
3.451	5.022	1.000	1.723	3.497	0.425	0.947	1.724	1.012	1.036	0.694	1.838	0.302	0.575	0.908
3.723	5.697	1.000	1.724	3.628	0.412	1.158	1.500	0.899	1.327	0.916	2.288	0.163	0.310	1.225
3.762	5.897	1.000	1.859	3.967	0.367	1.022	1.980	1.284	1.746	0.999	3.203	0.163	0.233	1.225
3.223	5.387	1.000	1.493	3.506	0.405	1.023	0.902	1.249	1.358	0.883	3.505	0.288	0.411	1.082
3.614	5.316	1.000	1.227	3.391	0.426	0.690	1.571	1.139	1.710	0.984	1.932	0.412	0.327	1.241
4.029	6.359	1.000	1.605	3.998	0.522	0.841	1.653	1.220	1.659	0.870	1.304	0.695	0.737	1.047
3.993	6.056	1.000	1.605	4.228	0.653	1.035	1.824	1.159	1.659	0.554	1.594	0.464	0.958	1.396
3.956	6.397	1.000	1.991	4.320	0.522	1.165	1.938	1.891	1.725	0.870	1.739	0.618	-0.516	1.163
3.785	5.948	1.000	1.284	4.070	0.581	0.678	1.140	1.046	1.138	0.979	1.242	0.515	1.052	1.108
4.121	5.375	1.000	1.188	4.458	0.522	1.229	1.026	1.098	0.796	0.791	1.159	0.541	1.326	0.814
3.694	4.707	1.000	1.005	3.597	0.379	1.069	0.694	0.743	1.039	0.894	0.756	0.538	1.025	0.809
3.841	4.845	1.000	0.999	3.554	0.542	0.863	0.659	0.813	0.590	0.773	0.902	0.962	1.309	0.827
3.833	3.833	1.000	0.738	3.246	0.519	0.826	0.437	0.831	0.452	0.875	0.617	0.723	1.379	0.693
3.879	3.801	1.000	0.683	3.207	0.482	0.826	0.388	0.779	0.452	0.942	0.370	1.052	1.191	0.594
3.916	3.324	1.000	0.893	3.357	0.757	1.013	0.397	0.796	0.173	0.825	0.252	1.210	1.473	0.101
3.677	3.217	1.000	0.776	3.332	0.943	0.809	0.238	0.712	0.221	0.527	1.449	1.224	1.350	0.097
3.601	2.460	1.000	0.856	2.911	1.234	0.485	0.238	0.610	0.774	0.791	0.121	1.417	1.473	0.194
3.160	1.900	1.000	0.705	2.127	1.263	0.812	0.313	0.526	0.364	0.558	-0.227	0.970	0.809	0.000

(continued)

Table VI. (continued)

2.473	1.632	1.000	0.582	1.695	0.980	0.485	0.107	0.381	0.332	0.395	-0.091	1.014	0.967	-0.073
3.538	2.480	1.000	0.683	2.699	0.889	0.606	0.194	0.623	0.508	0.740	0.000	1.381	1.128	0.000
3.364	1.823	1.000	0.681	2.213	0.889	0.845	0.279	0.548	1.029	0.710	0.946	1.262	1.082	0.000
3.388	1.640	1.000	0.669	2.030	0.907	0.593	0.238	0.712	0.664	0.593	0.845	0.386	0.859	0.194
3.409	1.547	1.000	0.614	2.717	0.416	0.563	0.297	1.220	0.577	0.619	0.126	0.605	0.512	0.101
3.218	2.106	1.000	0.614	2.957	0.303	0.506	0.347	1.114	1.039	0.619	0.504	1.075	0.448	0.202
3.060	1.777	1.000	0.614	2.957	0.265	0.675	0.347	1.114	0.750	0.619	0.126	0.941	0.640	0.000

motion look at a microscopic particle moving through an inhomogeneous illumination source. It forms the basis for new instrumentation to be used for the real time classification and identification of such particles.

The laboratory assistance and advice of Jeffrey M. Reece, Joseph B. Estrada, and Professor Robert S. Jacobs of UC Santa Barbara is gratefully acknowledged. The work was supported by the Office of Naval Research, Contract #N00014-85-C-0067.

References

1. D.T. Phillips, P.J. Wyatt, and R.M. Berkman, J. Colloid and Interface Sci. **34**, 159 (1970).
2. H.M. Blau, D.J. McCleese, and D. Watson, Appl. Optics **9**, 2522 (1970).
3. P.J. Wyatt, J. Appl. Bact. **38**, 47 (1975).
4. P.J. Wyatt and G.M. Quist, J. Opt. Soc. Amer. **2** (1985 -- in press).
5. P.J. Wyatt, Phys. Rev. **127**, 1837 (1962); Ibid., errata **134**, AB1 (1964).
6. M. Kerker, The Scattering of Light and Other Electromagnetic Radiation (Academic Press, New York, 1969).

NONLINEAR METHODS FOR THE INVERSION OF REFRACTIVE INDEX PROFILES

D.L. Jaggard, P.V. Frangos and Y. Kim
Moore School of Electrical Engineering
University of Pennsylvania
Philadelphia, PA 19104

RECENT PUBLICATIONS, SUBMITTALS FOR PUBLICATION AND PRESENTATIONS:

A) P.V. Frangos and D.L. Jaggard, "Inverse Scattering for One-Dimensional Dielectrics," presented at the 1984 Benjamin Franklin Symposium on Advances in Antennas and Microwave Technology, Philadelphia (May 5, 1984).

B) D.L. Jaggard, K.E. Olson and P.V. Frangos, "Inverse Scattering for One-Dimensional Dispersionless Dielectrics," presented at the 1985 IEEE/AP Symposium and National Radio Science Meeting, Boston (June 25-28, 1985).

C) D.L. Jaggard, N.H. Farhat, K. Schultz and T.H. Chu, "Three-Dimensional Tomographic Microwave Imaging," presented at the XXI General Assembly of URSI, Florence, Italy (Aug. 28-Sept. 5, 1984).

D) D.L. Jaggard, "Microwave Imaging of Dielectric Bodies," invited talk, SOHIO, Dallas Texas (April 18, 1985).

E) Y. Kim and D.L. Jaggard, "Inverse Blackbody Radiation: An Exact Closed-Form Solution," 1985 Benjamin Franklin Symposium on Advances in Antennas and Microwave Technology, Philadelphia (May 4, 1985).

F) D.L. Jaggard, P. Frangos and Y. Kim, "Some Nonlinear Methods for Inverse Scattering," 1985 Benjamin Franklin Symposium on Advances in Antennas and Microwave Technology, Philadelphia (May 4, 1985).

G) D.L. Jaggard and Y. Kim, "Inverse Blackbody Radiation," US-France Conference on Near Field Microwave Imaging, Georgia Tech., Atlanta, Georgia (June 10-11, 1985).

H) D.L. Jaggard, P.V. Frangos and Y. Kim, "Nonlinear Inversion Techniques for One-Dimensional Inhomogeneous Dielectrics," US-France Conference on Near Field Microwave Imaging, Georgia Tech., Atlanta, Georgia (June 10-11, 1985).

I) D.L. Jaggard and K. Schultz, "Imaging of Multiply Connected Dielectrics for Nondestructive Evaluation," US-France Conference on Near Field Microwave Imaging, Georgia Tech., Atlanta, Georgia (June 10-11, 1985).

J) D.L. Jaggard, K. Schultz, Y. Kim and P.V. Frangos, "Inverse Scattering for Dielectric Media," to be presented at the Annual Meeting of the Optical Society of America, Washington, D.C. (October 14-18, 1985).

K) D.L. Jaggard and A.K. Jordan, "Inversion Theory for Almost Periodic Media," Radio Science 19 1333-1341 (1984).

L) Y. Kim and D.L. Jaggard, "Inverse Black Body Radiation: An Exact Closed-Form Solution," IEEE Trans. Ant. AP-33, 797-800 (1985).

M) D.L. Jaggard and K.E. Olson, "Numerical Reconstruction for Dispersionless Refractive Profiles," to appear in the special issue on Inverse Problems, J. Opt. Soc. Am. (Nov. 1985).

N) D.L. Jaggard and Y. Kim, "Accurate One-Dimensional Inverse Scattering Using a Nonlinear Renormalization Technique," to appear in special issue on Inverse Problems, J. Opt. Soc. Am. (Nov. 1985).

O) D.L. Jaggard and P. Frangos, "Numerical Profile Reconstructions for Incomplete and Noisy Data," submitted for publication.

ABSTRACT

The problem of reconstructing one-dimensional dispersionless refractive index profiles from reflection data is considered in this report. Here the available data consist of reflection coefficient measurements at many wavenumbers due to an electromagnetic plane wave that is normally incident on a dielectric half-space or, equivalently, the data consist of the sampled impulse response of the unknown dielectric half-space.

Two fundamentally different nonlinear inversion approaches are used. The first is an approximate nonlinear renormalization technique that is based on a nonlinear approximation to the Riccati equation for the reflection coefficient. The second approach is exact and based on the Balanis integral equation. This equation is solved both analytically and numerically.

Work is continuing on efficiently applying these results to new materials and discovering new inversion methods.

I. INTRODUCTION

Inversion theory for waves is concerned with extracting the characteristic parameters of a medium from remote scattering data as opposed to the use of *in situ* measurements. Here the emphasis will be on electromagnetic or optical wave interactions with media such as inhomogeneous aerosols where the density of the aerosol is desired as a function of distance. It is assumed that the aerosol particles are small so that an effective refractive index can be defined.

Much of the original work in inversion theory was concerned with approximate *linear* relations between the characteristics of weak scatterers and their scattered fields so that inversion of the scattering data to obtain the desired characteristics was relatively straightforward. In these relations, the scattered field was typically expressed as a Fourier transform of an appropriate characteristic quantity such as the refractive index or potential function. Although this scheme was esthetically pleasing it incorrectly implied a linear relationship which did not exist between these quantities. This led to several problems in the electromagnetic case. First, in the forward problem, as the refractive index or the optical size of the scatterer became large, the magnitude of the reflection coefficient violated fundamental physical principles by becoming greater than unity. In the inverse problem this phenomena manifested itself by underestimating the contrast of the desired refractive index as compared to that of the host median. Second, in the inverse problem, a significant phase error accumulated as the reconstruction proceeded due to the incorrect use of the background or average refractive index. This evidenced itself by longitudinal errors in the reconstructed profiles. Any accurate reconstruction method for dense aerosols must overcome these obstacles which are due to the assumption of *linearity* between the characteristics function and the scattered field.

Here we examine two *nonlinear* inversion techniques which address the problems noted previously. The first technique, a *non-linear approximation method*, uses as its starting point the Riccati differential equation. This equation exactly relates the reflection coefficient to the refractive index of the medium under consideration. The Riccati equation is then approximated in a nonlinear manner which tends to preserve the amplitude information as a function of optical distance and allows a solution to be constructed using transform techniques. Subsequent coordinate stretching removes the phase accumulation error and accurately reproduces most refractive indices as a function of physical distance. The second technique, *an exact non-linear method*, is based on the efficient and accurate solution of the Balanis integral equation for an unknown kernel function when the reflection data is known. The refractive index profile is then calculated directly from the kernel function in a manner reminiscent of Gel'fand-Levitan-Marchenko theory.

II. APPROXIMATE TECHNIQUE

The exact relation between a refractive medium defined by a refractive index n(z) and the local reflection coeffient r(z,k) is

$$\frac{d\, r(z,k)}{dz} = \frac{1}{2}\left[1 - r^2(z,k)\right] \frac{d}{dz}\left\{\ln[n(z)]\right\} - 2i\, k\, n(z)\, r(z,k) \tag{1}$$

with the boundary condition

$$r(d,k) = r_o \qquad (d > 0) \tag{2}$$

This expression can be inverted approximately but accurately to find the effective refractive index profile n(z). Here k is the vacuum wavenumber and the measured reflection coefficient values at z=0 are

$$r(k) = r(z,k)\Big|_{z=0} . \tag{3}$$

The result of the inversion procedure is the relation [1]

$$\tilde{n}(z) = \exp\left[-2L^{-1}\left\{\frac{1}{p}\,\hat{r}(p)\right\}\right]\Bigg|_{x = \int_0^z \tilde{n}(z')\, dz'} \tag{4}$$

where the carat on the reflection data denotes the nonlinear function of the reflection data

$$\hat{r}(k) \equiv \tanh^{-1}\left[r(k)\right], \tag{5}$$

the new transform variable is defined by $p \equiv -2ik$, L^{-1} is the inverse Laplace transform and x is the variable corresponding to p but in the space reached by L^{-1}.

The linear perturbational or Born approximation is given by expanding (4) in the limit for diaphanous dielectrics and is found from (4) to be

$$n(z) = 1 - 2\, L^{-1}\left\{\frac{1}{p}\, r(p)\right\} \tag{6}$$

This is consistent with the results derived from a variety of other techniques.

In Figs. 1 and 2 reconstructions are shown for discontinuous and continuous profiles, respectively. In each case the solid line represents the exact profile found by analytical methods from the reflection coefficient. In the left plot the dashed line indicates the linear reconstruction obtained from (6) while in the right plot the dashed line indicates the approximate nonlinear reconstruction obtained from (4). Note that here the nonlinear reconstructions are almost indistinguishable from the exact results while the linear reconstructions exhibit considerable error.

III. EXACT RECONSTRUCTION

Balanis [2] has shown that an exact expression for the refractive index profile can be found in terms of an unknown kernel function K(x,y) by the expression

$$n[z(x)] = [1+K(x,x)]^{-2} \tag{7}$$

where the coordinates z and x are related by the coordinate stretching relation

$$z(x) = \int_0^x [n(x')]^{-1}\, dx' \tag{8}$$

and the kernel function K(x,y) satisfies an integral equation

$$\kappa(x,y) = \int_{-y}^{x} [1 + K(x,y')]\, R(y+y')\, dy' = 0 \tag{9}$$

where R(y) is the impulse response given by

$$R(y) = \frac{1}{2} \int_{-\infty}^{\infty} r(k) e^{iky}\, dk \tag{10}$$

The kernel also satisfies the differential equation

$$\frac{\partial^2 K(x,y)}{\partial x^2} - \frac{\partial^2 K(x,y)}{\partial y^2} - \frac{2}{[1+K(x,x)]} \frac{\partial K(x,y)}{\partial x} \frac{dK(x,x)}{dx} = 0 \tag{11}$$

Auxiliary conditions on the kernel function,

$$K(x,y) = 0 \qquad (y > x,\ y < -x) \tag{12}$$

$$K(x,-x) = 0, \tag{13}$$

allow solutions to be constructed both analytically and numerically as detailed in [3]. The procedure is to find the kernel function K(x,y) by use of (9), (10) and (11), subject to (12) and (13), and to use the result in (7) and (8) to find the desired index n(z).

For a restricted class of reflection coefficients the above set of equations can be solved analytically with closed-form solutions while for arbitrary reflection data an accurate and economical numerical technique has been developed [3,4]. This latter technique is demonstrated for imprecise and bandlimited data in Figs. 3 and 4.

In Fig. 3 the ideal impulse response of (10) is contaminated by noise with various values of amplitude signal to noise ratios (S/N) varying from 4 to 1/2. Here the dotted line corresponds to the reconstruction with an ideal impulse response ($S/N \to \infty$) while the solid line represents the profile reconstructions that are degraded by noise. It can be shown that the techniques developed here are relatively robust with respect to noise and this is evidenced in the plots.

In Fig. 4, the reflection coefficient r(k) is lowpass filtered with various values of bandwidths denoted by Δk. The dotted lines again correspond to reconstructions with complete data ($\Delta k \to \infty$) while the solid lines represent the bandlimited profile reconstructions. As expected, loss of detail is evident as the bandwidth decreases.

IV. CONCLUSIONS

In this report the shortcomings of linear inversion theory have been noted and demonstrated. For optically large scatterers and/or those with large contrast, linear perturbation methods or Born type expansions will eventually fail. For problems which are inherently one-dimensional and nondispersive, one can replace the linear inversion technique with one of two nonlinear techniques described here. The first technique is approximate while the second is exact.

Experimental results (not shown) using microwaves confirm the theories presented here. In the last analysis this is of utmost importance since experimental data is always both imprecise and bandlimited in nature. It is gratifying to realize that the techniques presented represent not only well-constructed theories but are also useful in practice. This is a pleasant surprise to find in a field where ill-posedness is (almost) always lurking.

ACKNOWLEDGEMENTS

The support of the Air Force Office of Scientific Research under Grant AFOSR-81-0240 and the Army Research Office under Grant DAAG29-83-K-0120 is gratefully acknowledged.

V. REFERENCES

[1] D.L. Jaggard and Y. Kim, "Accurate One-Dimensional Inverse Scattering Using a Nonlinear Renormalization Technique", J. Opt. Soc. Am. A2, Special Issue on Inverse Problems (Nov. 1985).

[2] G.N. Balanis, "Inverse Scattering: Determination of Inhomogeneities in Sound Speed", J. Math. Phy. 23, 2562-2568 (1982).

[3] D.L. Jaggard and K.E. Olson, "Numerical Reconstruction for Dispersionless Refractive Profiles", J. Opt. Soc. Am. A2, Special Issue on Inverse Problems (Nov. 1985).

[4] D.L. Jaggard and P.V. Frangos, "The Electromagnetic Inverse Scattering Problem for Layered Dispersionless Dielectrics", submitted for publication.

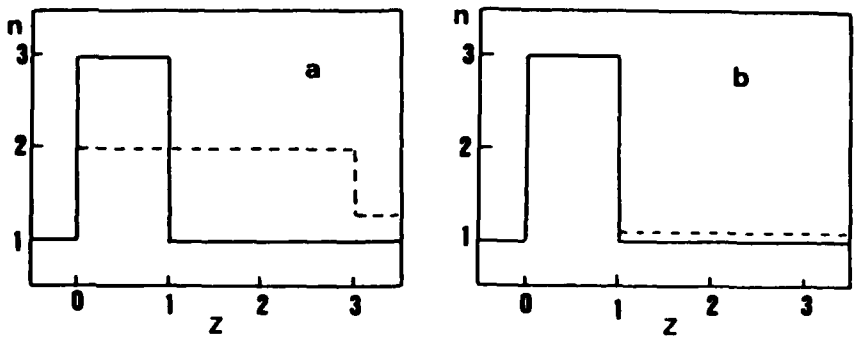

FIGURE 1. Refractive profile reconstruction of a finite homogeneous slab with a refractive index of three. a) Exact (solid line) and linear perturbational (dashed line) reconstructions. b) Exact (solid line) and approximate nonlinear (dashed line) reconstructions.

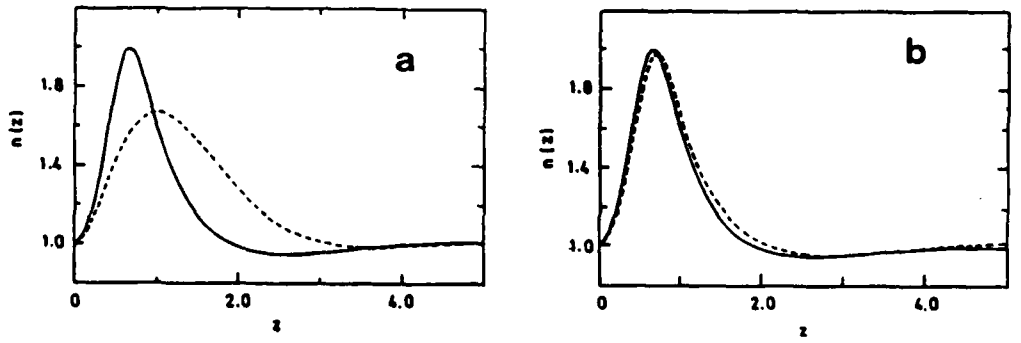

FIGURE 2. Refractive profile reconstruction of a continuous dielectric profile. a) Exact (solid line) and linear perturbational (dashed line) reconstructions. b) Exact (solid line) and nonlinear approximate (dashed line) reconstructions.

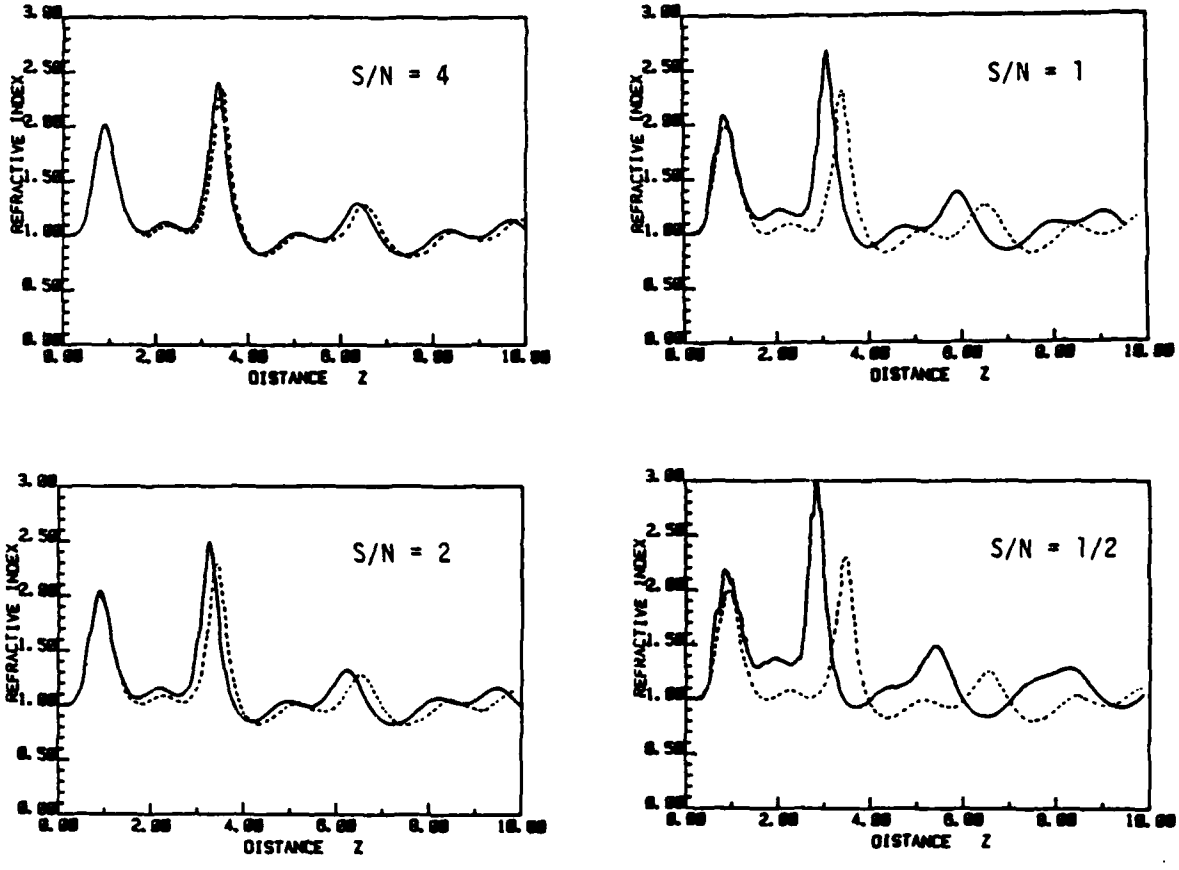

FIGURE 3. Refractive profile reconstructions using a numerical implementation of the exact nonlinear method for decreasing S/N. The dashed lines indicate reconstructions with no noise ($S/N \to \infty$) while the solid lines indicate S/N = 4,2,1,1/2 as noted.

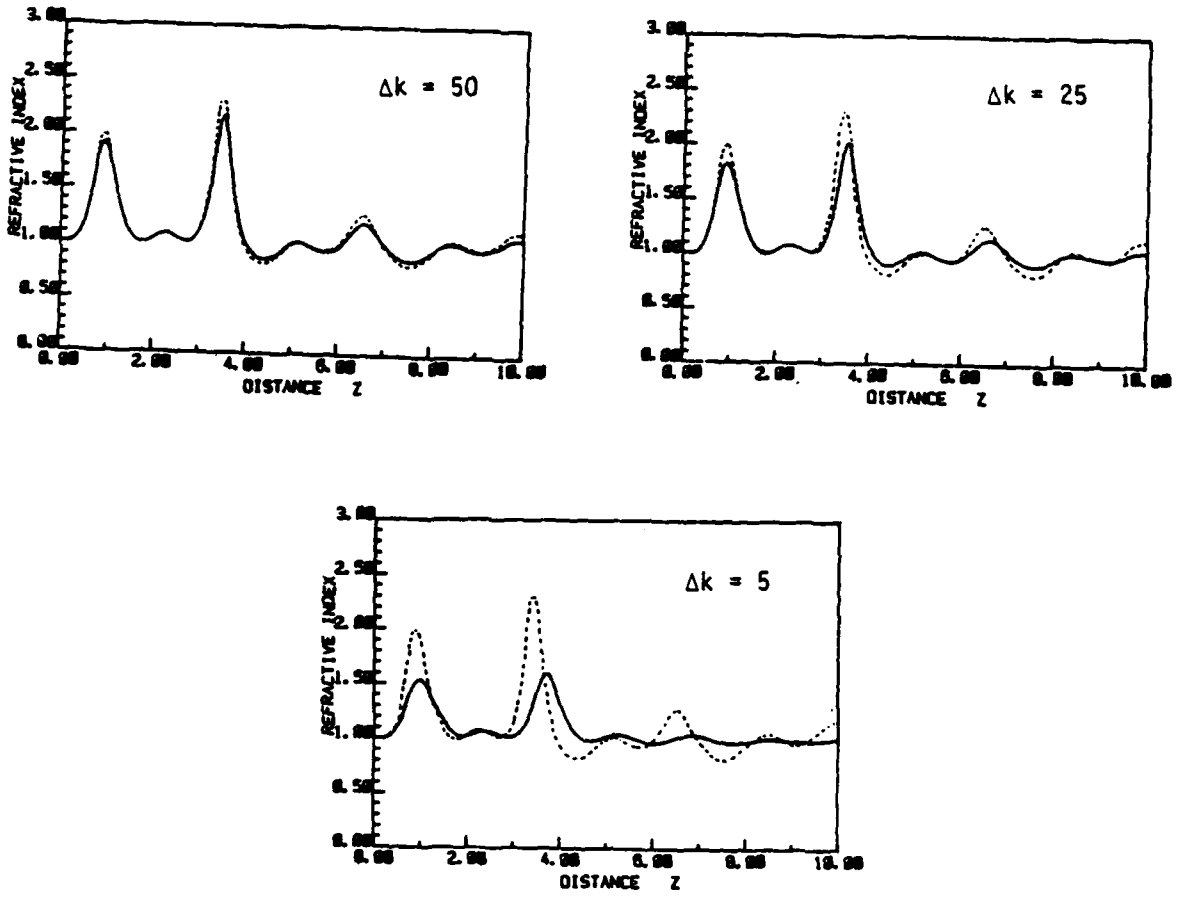

FIGURE 4. Refractive profile reconstructions using a numerical implementation of the exact nonlinear method for decreasing bandwidth Δk. The dashed lines indicate the infinite bandwidth case ($\Delta k \to \infty$) while the solid lines indicate lowpass values of $\Delta k = 50, 25, 5$ as noted.

II. AEROSOL CHARACTERIZATION METHODS (continued)

(OTHER THAN AERODYNAMIC METHODS - SEE IC)

IIB. Optical Constants of Liquids and Powders

X-BAND MULTIPLE-POSITION CAVITY METHOD[1] FOR DETERMINING COMPLEX PERMEABILITY AND PERMITTIVITY

H. H. Chung, G. A. Pfaff, and S. Y. Peng
Teledyne Micronetics
San Diego, California 92120

ABSTRACT

A multiple-position cavity method presented in this paper is a generalized solution which can be used to determine complex values of both μ and ϵ for any kind of material which has anisotropic magnetic and isotropic electric properties. It requires measuring the resonant frequency and unloaded Q of a resonant cavity, first, without and then with a test sample located at each of three different positions. A closed form solution and test procedure were obtained for practical application in determining both $\tilde{\mu}$ and $\tilde{\epsilon}$ of a material. To implement the test method, an X-band waveguide cavity test fixture was designed and built. An extensive laboratory measurement program was conducted to insure data quality. Measurement of known dielectric materials yielded good agreement between computed results and published data.

1. INTRODUCTION

The cavity method used to determine the complex permittivity ($\tilde{\epsilon}$) of non-magnetic material has been thoroughly studied by many authors. However, less attention has been given to the determination of the complex permeability ($\tilde{\mu}$) for anisotropic magnetic material by using the cavity method. The multiple-position cavity method presented in this paper is a generalized solution which can be used to determine both $\tilde{\mu}$ and $\tilde{\epsilon}$ for any kind of material which has anisotropic magnetic and isotropic electric properties. It requires measuring the resonant frequency and unloaded Q of a resonant cavity first without and then with a test sample located at three different positions. An analytical model for a TE_{011} rectangular waveguide cavity was developed and a set of equations was derived that relates both $\tilde{\mu}$ and $\tilde{\epsilon}$ to the change in resonant frequency and unloaded Q caused by the insertion of a thin material sample into the cavity. A closed form solution was obtained for practical application in computing both $\tilde{\mu}$ and $\tilde{\epsilon}$ of a material. The theoretical formulation of this test method is presented in section 2.

---

[1]This paper is based on work performed at Teledyne Micronetics under the Contract No. DAAK11-83-C-0011 for the Chemical/Ballistics Procurement Division, Aberdeen Proving Ground, Maryland.

A set of samples, including one made from a thin Mylar sheet, another composed of a thin epoxy layer on a Mylar sheet and the last composed of a thin layer of an iron/epoxy composition on a Mylar sheet, was tested to determine the magnetic and electric properties of the iron material. Based on the samples provided, a test procedure was developed to measure the resonant frequency and unloaded Q of the cavity for each of the required sample test positions. A summary of the test procedure is given in section 3.

To implement the test method, an X-band rectangular waveguide cavity test fixture was designed and built. An extensive laboratory measurement program was conducted to insure data quality. In addition to the samples mentioned above, Teflon and Rexolite samples were also tested to provide baseline data for known materials as a measure of confidence in the final test results. Six sample positions inside the cavity were selected for taking the measurement of resonant frequency and unloaded Q of the cavity. For usual non-magnetic materials, only one position is sufficient to determine $\tilde{\varepsilon}$ of a material. However, for anisotropic magnetic materials, three positions are required to determine both $\tilde{\mu}$ and $\tilde{\varepsilon}$. Six positions were selected to provide redundant data for cross-checking the final results. The experimental results of $\tilde{\mu}$ and $\tilde{\varepsilon}$ for the tested samples are summarized in section 5. Finally, the conclusions are discussed in section 6.

2. THEORETICAL FORMULATION

Let $\tilde{\omega}$, $\vec{E}$ and $\vec{H}$ represent the complex resonant frequency, electric field and magnetic field, respectively, of the original cavity filled with a very low density foam (μ_0 and ε_1) where $\tilde{\varepsilon}_1 = \varepsilon_0 \tilde{\varepsilon}_{r1}$ and $\tilde{\varepsilon}_{r1}$ is the relative complex dielectric constant. Maxwell's field equations must be satisfied, that is

$$\begin{cases} \nabla \times \vec{E} = -j\tilde{\omega}\mu_0 \vec{H} & (1) \\ \nabla \times \vec{H} = j\tilde{\omega}\varepsilon_0 \tilde{\varepsilon}_{r1} \vec{E} & (2) \end{cases}$$

Again, let $\tilde{\omega}'$, $\vec{E}'$ and $\vec{H}'$ represent the corresponding quantities of the perturbed cavity which contains a composite sample held by a very low density foam. It is assumed that the sample can be composed of several thin layers. The complex permeability and permittivity of each layer can be represented by $\tilde{\mu}_n$ and $\tilde{\varepsilon}_n$, respectively, for n = 2, 3, ... N. All layers, except for n = N, are assumed to be non-magnetic material. The N-th layer of volume ΔV_N is an anisotropic material with magnetic and electric properties of $\overleftrightarrow{\tilde{\mu}}_N$ and $\tilde{\varepsilon}_N$, respectively. The permeability dyadic of

the sample is given by Collin (1960),

$$\overline{\overline{\mu}}_N = \mu_0(\overline{\overline{I}} + \overline{\overline{\chi}}_m) \quad , \tag{3}$$

where $\overline{\overline{I}}$ is the unit dyadic and $\overline{\overline{\chi}}_m$ is the dyadic magnetic susceptibility of the medium. Maxwell's field equation must also be satisfied and is

$$\begin{cases} \nabla \times \vec{E}' = -j\bar{\omega}'(\mu_0 + \Delta\overline{\overline{\mu}})\,\vec{H}' & (4) \\ \nabla \times \vec{H}' = j\bar{\omega}'\epsilon_0(\bar{\epsilon}_{r1} + \Delta\bar{\epsilon}_r)\,\vec{E}' & (5) \end{cases}$$

where

$$\Delta\overline{\overline{\mu}} = \overline{\overline{\mu}}_N - \mu_0 = \mu_0\overline{\overline{\chi}}_m, \text{ occupied in } \Delta V_N$$

$$\Delta\bar{\epsilon}_r = \sum_{n=2}^{N} \Delta\bar{\epsilon}_{rn}$$

$$\Delta\bar{\epsilon}_{rn} = \bar{\epsilon}_{rn} - \bar{\epsilon}_{r1}, \text{ occupied in } \Delta V_n$$

$\bar{\epsilon}_{rn}$ = denotes the relative complex permittivity of the n-th material

ΔV_n = denotes the volume of the n-th material

By manipulating Equations (1), (2), (4) and (5), applying perturbation techniques and boundary conditions to the fields, $\vec{E}'$ and $\vec{H}'$, one obtains

$$\frac{\bar{\omega}' - \bar{\omega}}{\bar{\omega}} = \frac{-\left\{\sum_{n=2}^{N} \Delta\bar{\epsilon}_{rn} \iiint_{\Delta V_n} \vec{E}_{int} \cdot \vec{E}^* dv + \eta_0^2 \iiint_{\Delta V_N} \overline{\overline{\chi}}_m \vec{H}_{int} \cdot \vec{H}^* dv\right\}}{\iiint_{V_c} \left[\eta_0^2 |\vec{H}|^2 + \bar{\epsilon}_{r1} |\vec{E}|^2\right] dv} \tag{6}$$

where the superscript "*" means complex conjugate, η_0 is the intrinsic characteristic impedance of air and V_c denotes the volume of the cavity. $\vec{E}_{int}$ and $\vec{H}_{int}$ represent the internal electric and magnetic fields of the corresponding sample. It should be noted that the above equation is based on the following assumptions:

a. The cavity wall is a good conductor.

b. The field internal to ΔV_n is related to the field external to ΔV_n in the same manner as for static fields.

c. The perturbation of the cavity is small.

The complex resonant frequency of a high Q cavity can be approximated as (Van Valkenberg (1955)),

$$\tilde{\omega} = \omega_r\left(1 + j\,\frac{1}{2Q}\right) , \tag{7}$$

where ω_r is the real resonant angular frequency and Q is the unloaded-cavity quality factor. Hence, the left-hand side of Eq. (6) can be approximated by

$$\frac{\tilde{\omega}' - \tilde{\omega}}{\tilde{\omega}} = \Delta f + j\Delta q \tag{8}$$

where

$$\Delta f = \frac{\Delta\omega_r}{\omega_r} \tag{8a}$$

$$\Delta q = \Delta\left(\frac{1}{2Q}\right) + \frac{1}{2Q'}\left(\frac{\Delta\omega_r}{\omega_r}\right) \tag{8b}$$

are the change in the real resonant frequency and unloaded Q, respectively. From Eqs. (6 and 8) one can obtain the following

$$\Delta f + j\Delta q = \frac{-\left\{\sum_{n=2}^{N} \Delta\tilde{\epsilon}_{rn} \iiint_{\Delta V_n} \vec{E}_{int} \cdot \vec{E}^{*} dv + n_0^2 \iiint_{\Delta V_N} \tilde{\tilde{\chi}}_m \vec{H}_{int} \cdot \vec{H}^{*} dv\right\}}{\iiint_{V_c} \left[n_0^2 |\vec{H}|^2 + \tilde{\epsilon}_{r1} |\vec{E}|^2\right] dv} \tag{9}$$

The above equation shows that any increase in $\tilde{\mu}$ and $\tilde{\epsilon}$ within a cavity can only decrease the resonant frequency and unloaded Q of the cavity. It is also observed that the change of the cavity resonant frequency will be mainly related to the real part of the complex permeability and permittivity of the sample, and the change in Q will be mainly related to the imaginary part of the complex permeability and permittivity. Therefore, if one can properly design the test sample, the $\tilde{\mu}$ and $\tilde{\epsilon}$ of the sample can

be computed from the measured resonant frequency and unloaded Q change.

From the observation mentioned above, a TE_{011} mode rectangular cavity and rectangular shape test sample configuration, as shown in Figure 1, were used in the analysis. All of the samples were assumed to have flat, parallel surfaces. As shown in Figure 2, six positions were selected for taking the measurement of resonant frequency and unloaded Q of the cavity. For usual non-magnetic materials, only one position is sufficient to determine $\tilde{\varepsilon}$ of a material. However, for anisotropic magnetic materials, three positions are required to determine both $\tilde{\mu}$ and $\tilde{\varepsilon}$. Six positions were selected to provide redundant data for cross-checking the final results. By observing the field distributions inside the TE_{011} mode cavity, closed form solutions were obtained to compute both $\tilde{\mu}$ and $\tilde{\varepsilon}$ of a material.

For the convenience of future application, the derived formulas at the indicated test positions are summarized in Table 1. Note that the test position selected for non-magnetic isotropic materials is either position 3 or 4 where the electric field is maximum. For the anisotropic magnetic materials, the preferred test positions are positions 1, 3, and 4.

3. TEST PROCEDURES

A set of samples, including one made from a thin Mylar sheet, another composed of a thin epoxy layer on a Mylar sheet and the last composed of a thin layer of an iron/epoxy composition on a Mylar sheet, was tested to determine the magnetic and electric properties of the iron material. Based on the samples provided, a test procedure was developed to measure the resonant frequency and unloaded Q of the cavity for each of the selected sample test positions. The $\tilde{\mu}$ and $\tilde{\varepsilon}$ of each sample was then determined. The test procedures are summarized in Table 2.

4. EXPERIMENTAL INVESTIGATION

To compute complex permeability and permittivity using the formulas, given in section 2, measured values of Δf and ΔQ are required. Δf and ΔQ are the change of resonant frequency and unloaded quality factor, respectively, due to the insertion of a test sample into the test cavity. The impedance method for measuring quality factor outlined in Chapter 9 of Ginzton (1957) was selected. A network analyzer system is used for measuring the complex input impedance of the cavity as a function of frequency.

To implement a test method based upon the analytic solution, the X-band test fixture shown in Figure 3 was designed and fabricated. The test fixture is made up

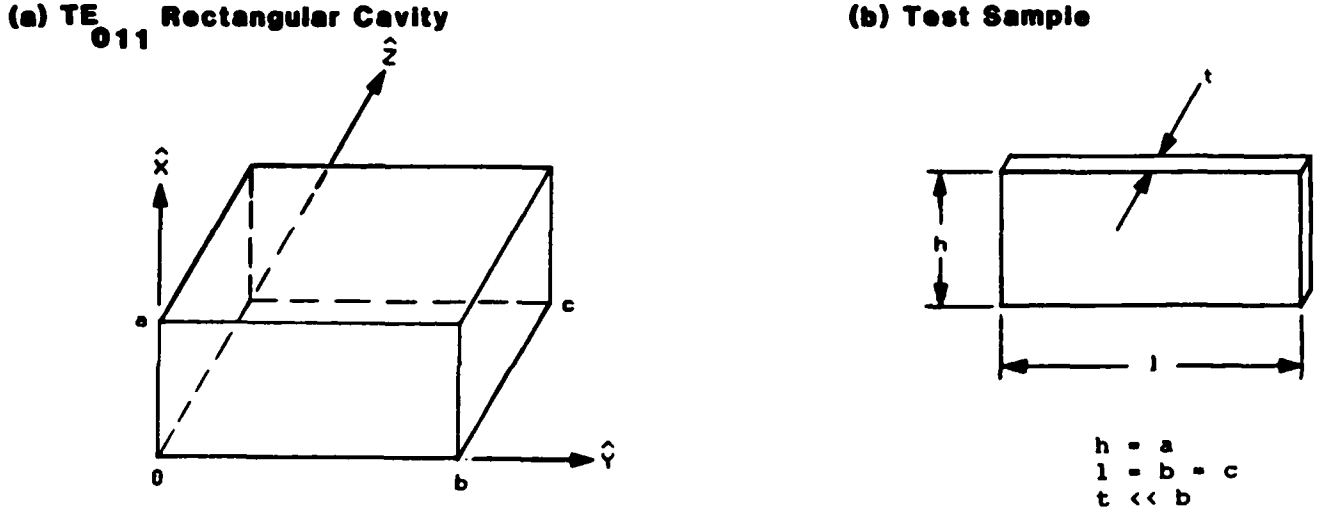

FIGURE 1. Dimensions of cavity and test sample used in analysis

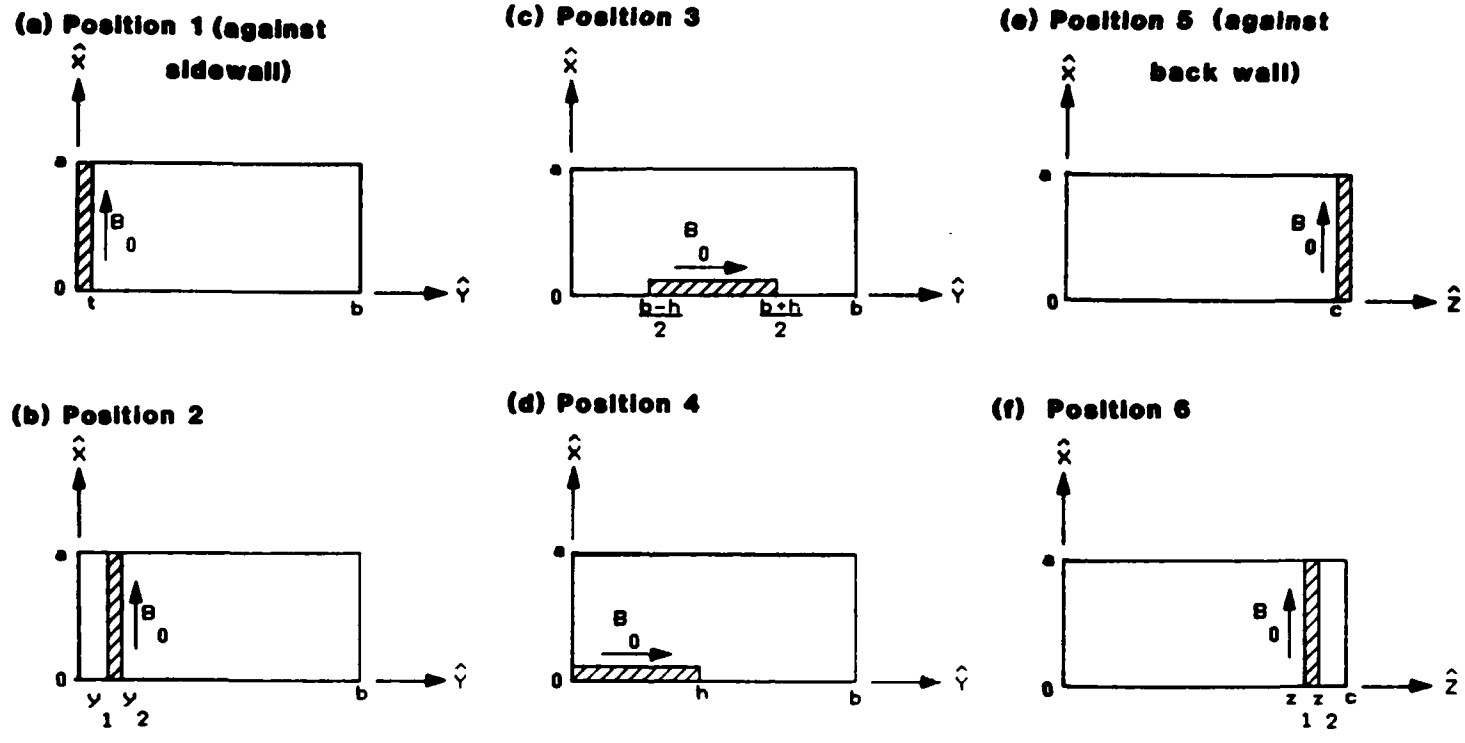

FIGURE 2. Sample locations used in the analysis.

TABLE 1 SUMMARY OF FORMULAS

A. For foam filled cavity (p = 0):

$$\tilde{\epsilon}_{r1} = \frac{1}{1 + 2(\Delta f^p + j\Delta q^p)} \qquad (T.1)$$

B. For non-magnetic materials (at position p = 3 or 4):

$$\tilde{\epsilon}_{rN} = \frac{\tilde{\epsilon}_{r1}}{1 + \dfrac{0.5\tilde{\epsilon}_{r1}U_c\,(\Delta f^p + j\Delta q^p)}{g^p_{5N}} + I_N \sum_{n=2}^{N-1} I_n \left(\dfrac{g^p_{5n}}{g^p_{5N}}\right)\left(\dfrac{\Delta\tilde{\epsilon}_{rn}}{\tilde{\epsilon}_{rn}}\right)} \qquad (T.2)$$

C. For anisotropic materials:

$$\tilde{\epsilon}_{rN} = \frac{\tilde{\epsilon}_{r1}}{1 - \dfrac{g^4_{44}\,A - g^3_{44}\,B}{g^4_{44}\,g^3_{54} - g^3_{44}\,g^4_{54}}} \qquad (T.3)$$

$$\tilde{\mu}_{rN} = 1 + \tilde{\chi}_N \quad \text{, principal permeability} \qquad (T.4a)$$

$$\tilde{\chi}_N = \frac{g^4_{54}\,A - g^3_{54}\,B}{\tilde{\epsilon}_{r1}(\,g^3_{44}\,g^4_{54} - g^4_{44}\,g^3_{54}\,)} \quad \text{, magnetic susceptibility} \qquad (T.4b)$$

$$j\tilde{\mu}_{crN} = \sqrt{(1 + \tilde{\chi}_N)\left[\frac{C}{\tilde{\epsilon}_{r1}\,g^1_{24}} - \tilde{\chi}_N\right]} \quad \text{, cross-coupling permeability} \qquad (T.5)$$

where,

$$A = -\left[(\Delta f^3 + j\Delta q^3)(0.5\tilde{\epsilon}_{r1}U_c) + I_N \sum_{n=2}^{N-1} I_n\, g^3_{5n}\, \frac{\Delta\tilde{\epsilon}_{rn}}{\tilde{\epsilon}_{rn}}\right]$$

$$B = -\left[(\Delta f^4 + j\Delta q^4)(0.5\tilde{\epsilon}_{r1}U_c) + I_N \sum_{n=2}^{N-1} I_n\, g^4_{5n}\, \frac{\Delta\tilde{\epsilon}_{rn}}{\tilde{\epsilon}_{rn}}\right]$$

$$C = -\left[(\Delta f' + j\Delta q')(0.5\tilde{\epsilon}_{r1}U_c) + \tilde{\epsilon}_{r1}\, g^1_{14}\, \frac{\tilde{\chi}_N}{1 + \tilde{\chi}_N} + \sum_{n=2}^{N} \Delta\tilde{\epsilon}_{rn}\, g^1_{3n}\right]$$

TABLE 1 (Continued)

---

n= 1, 2, 3, ..., N denotes the n-th material
(n = 1 is reserved for the sample holder)

$$I_n = \begin{cases} 1, & \text{if the corresponding n-th material present} \\ 0, & \text{otherwise} \end{cases}$$

$$I_N = \begin{cases} 1, & \text{if } N > 2 \\ 0, & \text{otherwise} \end{cases}$$

$$\Delta\tilde{\epsilon}_{rn} = \tilde{\epsilon}_{rn} - \tilde{\epsilon}_{r1}$$

$\tilde{\epsilon}_{rn}$ = denotes the n-th sample relative complex permittivity

$$g^p_{1n} = \frac{b^2}{b^2 + c^2} h_n \left[\frac{t_n}{2} - \frac{b}{4\pi} S(y^p_n)\right]\left[\frac{l_n}{2} + \frac{c}{4\pi} S(z^p_n)\right]$$

$$g^p_{2n} = \frac{c^2}{b^2 + c^2} h_n \left[\frac{t_n}{2} + \frac{b}{4\pi} S(y^p_n)\right]\left[\frac{l_n}{2} - \frac{c}{4\pi} S(z^p_n)\right]$$

$$g^p_{3n} = h_n \left[\frac{t_n}{2} - \frac{b}{4\pi} S(y^p_n)\right]\left[\frac{l_n}{2} - \frac{c}{4\pi} S(z^p_n)\right]$$

$$g^p_{4n} = \frac{c^2}{b^2 + c^2} t_n \left[\frac{h_n}{2} + \frac{b}{4\pi} S(y^p_n)\right]\left[\frac{l_n}{2} - \frac{c}{4\pi} S(z^p_n)\right]$$

$$g^p_{5n} = t_n \left[\frac{h_n}{2} - \frac{b}{4\pi} S(y^p_n)\right]\left[\frac{l_n}{2} - \frac{c}{4\pi} S(z^p_n)\right]$$

$$S(y^p_n) = \text{SIN}\left[\frac{2\pi}{b} y^p_{2n}\right] - \text{SIN}\left[\frac{2\pi}{b} y^p_{1n}\right]$$

$$S(z^p_n) = \text{SIN}\left[\frac{2\pi}{b} z^p_{2n}\right] - \text{SIN}\left[\frac{2\pi}{b} z^p_{1n}\right]$$

a, b, and c = denotes the width, height and length, respectivly, of the cavity

t_n, h_n and l_n = denotes the thickness, height and length, respectivly, of the n-th sample

TABLE 1 (Concluded)

$$\Delta f^p = \frac{\omega_{new} - \omega_{old}}{\omega_{old}}$$

$$\Delta q^p = \frac{1}{2Q_{new}} \left[\frac{\omega_{new}}{\omega_{old}} \right] - \frac{1}{2Q_{old}}$$

ω_{old} and Q_{old} = measured resonant frequency and unloaded Q, respectivly, of a cavity filled with a foam sample holder

ω_{new} and Q_{new} = measured resonant frequency and unloaded Q, respectivly, of a cavity which contains a sample and the foam sample holder

V_c = abc = volume of the cavity

NOTE: All superscripts, including p, denote test position. p = 0 denotes foam-filled cavity (with no test sample present).

TABLE 2 SUMMARY OF PROCEDURES

Procedures	Description
1 - a	Measure the resonant frequency and unloaded Q for the empty cavity and foam (sample holder) filled cavity.
1 - b	Compute $\tilde{\epsilon}_{r1}$ by Eq.(T.1).
2 - a	Measure ω_{new} and Q_{new} at position 3 for the Mylar sample.
2 - b	Compute $\tilde{\epsilon}_{r2}$ by Eq.(T.2).
3 - a	Measure ω_{new} and Q_{new} at position 3 for the epoxy on Mylar sample.
3 - b	Compute $\tilde{\epsilon}_{r3}$ by Eq. (T.2).
4 - a	Measure ω_{new} and Q_{new} at position 3 and 4 for the mixture of multispectral material and epoxy on Mylar sample.
4 - b	Compute $\tilde{\mu}_{r4}$ and $\tilde{\epsilon}_{r4}$ by Eqs. (T.4) and (T.3), respectively.
5 - a	Measure ω_{new} and Q_{new} at position 1 for the mixture of multispectral material and epoxy on Mylar sample.
5 - b	Compute $j\tilde{\mu}_{cr4}$ by Eq. (T.5).

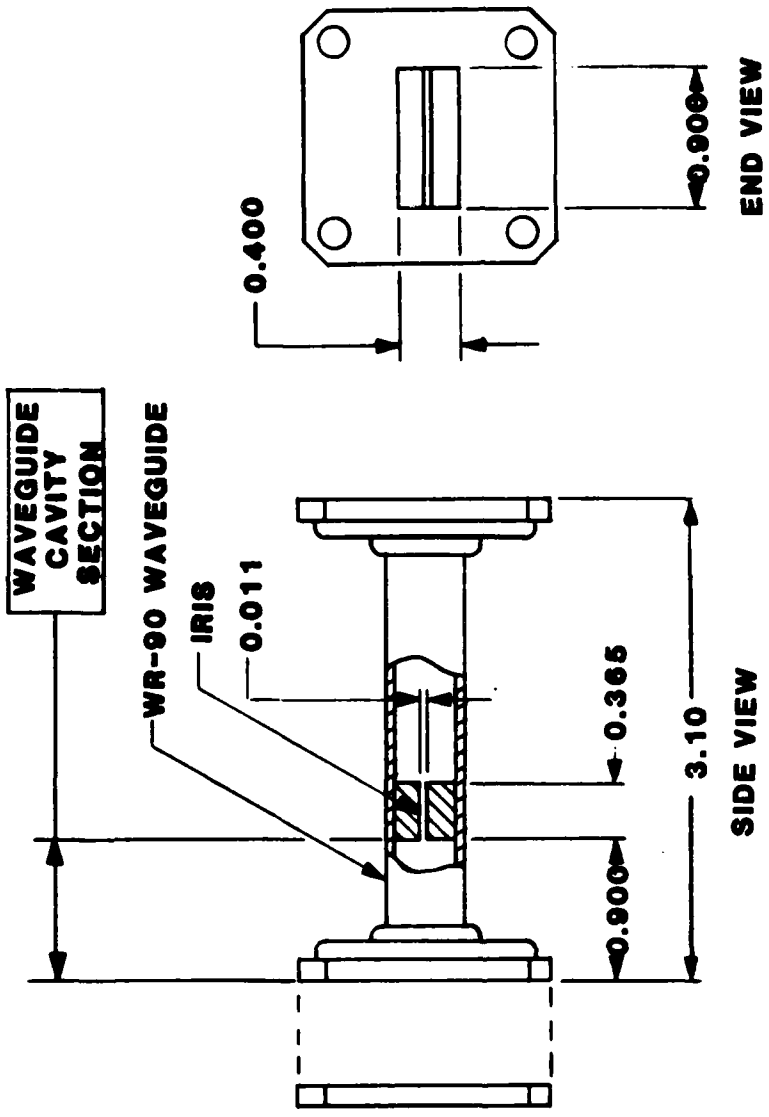

FIGURE 3. X-band waveguide cavity test fixture.

of two pieces, the waveguide cavity section and a shorting plate. One narrow slotted waveguide iris is built into the waveguide cavity section. This iris is positioned into the waveguide to form a cavity at one end of the waveguide section with dimensions of 0.400 in. high x 0.900 in. wide x 0.900 in. long. A cavity is formed when the shorting plate is attached to the waveguide flange at the cavity end.

The test equipment setup used for making the waveguide cavity measurements is shown in Figure 4. It employs an HP8410 Network Analyzer system with an HP8743B Reflection-Transmission Test Unit, a frequency counter and an X-Y recorder. Input impedance was recorded on a specially prepared Smith Chart data sheet and frequencies for the resonant frequency and half-power points were carefully measured and recorded. The network analyzer and X-Y recorder were carefully calibrated before and during the measurements.

An important consideration in developing the cavity test method was the question of how to accurately position and hold the test samples in the test fixture cavity without introducing a source of error that could not be accounted for. It was decided to use a low density foam material to position and hold the samples in place while making the cavity measurements.

Two groups of test samples were used during the program. The first group, designated "known samples" includes two Teflon samples, and one Rexolite sample. Test results from the known samples is used to help evaluate the test method. The second set of samples designated "unknown samples" includes the set of three pieces, described in the previous section. The principal objective of this program was to measure the value of $\tilde{\mu}$ for the iron/epoxy on Mylar film sample.

All of the samples tested were trimmed to match the cross-section of the X-band waveguide dimensions (0.400 in. high x 0.900 in. wide). The samples were inserted into the waveguide and supported in position with low density foam blocks. The foam blocks were made by carefully cutting foam pieces to match the inside dimensions of the waveguide cavity using specially designed trimming tools. Cavity measurements were made on each full-sized foam block; it was then trimmed to hold the sample in the desired test position. Cavity measurements were then repeated with the sample in the desired test position. Each of the six samples were tested in all six test positions. The measured data was used to compute values for $\tilde{\mu}$ and $\tilde{\varepsilon}$ of the tested samples. The results are presented in the next section.

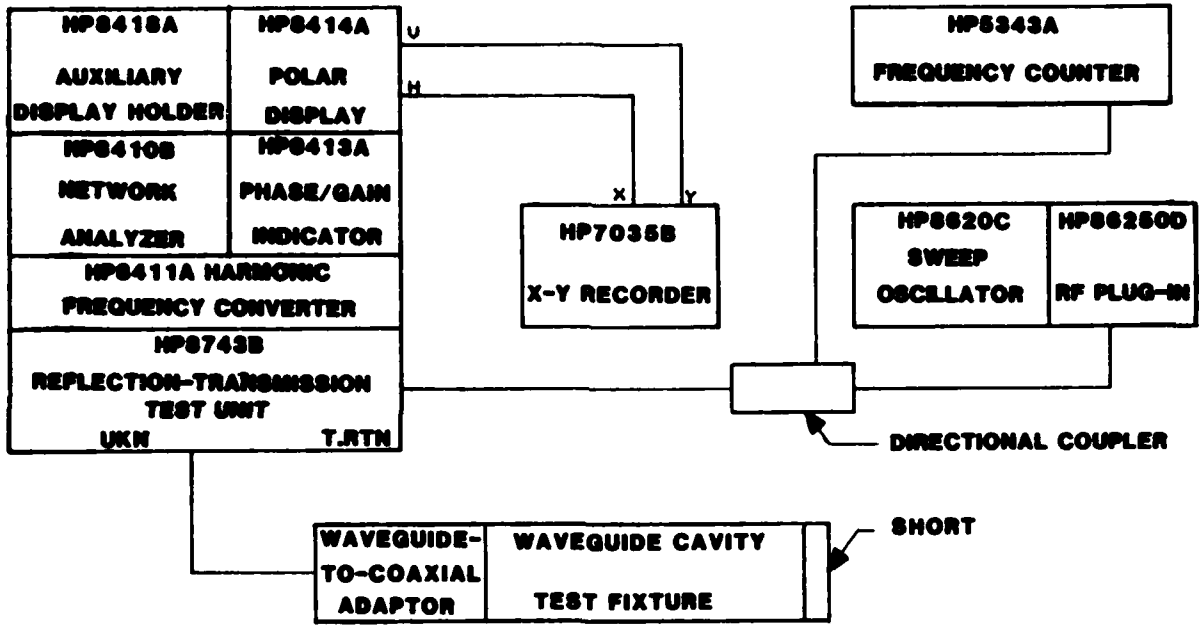

FIGURE 4. Test equipment setup for waveguide cavity complex input impedance measurements. (block diagram)

5. RESULTS

Based on the formulas derived in section 2 and the measured data, the complex permittivity ($\tilde{\varepsilon}$) of known samples was calculated for foam, Teflon, and Rexolite. Results are summarized in Table 3. It is noted that these computed results agree very well with the published reference data which are also included in Table 3.

Similarly, the complex permittivity ($\tilde{\varepsilon}$) and permeability ($\tilde{\mu}$) of unknown samples was also calculated for Mylar, epoxy, and iron. Results are summarized in Table 4. Again, the computed results of $\tilde{\varepsilon}$ agree well with the published data. For the $\tilde{\mu}$, however, published data was not available. Therefore, no comparison was made.

It should be mentioned that from the analysis of the measured data the following uncertainties were identified:

a. measured frequency uncertainty is $\pm$0.5 MHz

b. measured unloaded Q error is $\pm$50

c. measured sample size error is $\pm$0.001 in.

d. sample position error is $\pm$0.005 in.

These measurement uncertainties were used in the computation to determine the tolerances of $\tilde{\mu}$ and $\tilde{\varepsilon}$ listed in Tables 3 and 4. It is felt that the above error could be minimized by refining the measurement technique and improving sample surface conditions.

6. CONCLUSIONS

An extensive theoretical and experimental study has been conducted to determine the complex permittivity ($\tilde{\varepsilon}$) and permeability ($\tilde{\mu}$) properties of a material. The following is a summary of the main conclusions:

a. a multiple position waveguide cavity method has been formulated to determine $\tilde{\mu}$ and $\tilde{\varepsilon}$ for any material which has anisotropic magnetic and isotropic electric properties,

b. a laboratory test fixture was designed and fabricated,

c. both magnetic and non-magnetic materials were measured,

d. computer software was generated to analyze the measured data and to compute $\tilde{\mu}$ and $\tilde{\varepsilon}$,

e. the measured values of $\tilde{\varepsilon}$ for both magnetic and non-magnetic materials agreed well with the published reference data,

f. the test sample surface conditions (smoothness) of the magnetic material and measurement errors need to be improved and minimized.

TABLE 3 SUMMARY OF RESULTS FOR THE KNOWN SAMPLES AT X-BAND

Sample	Size (in.) (t,h,l)	Computed Results @ 9.26 GHz (ϵ_r' , tanδ)[2]	Reference Value[1] @ 9.26 GHz (ϵ_r' , tanδ)[2]
Foam	(0.9,0.4,0.9)	(1.017±0.001,0.0000845±0.000015)	(1.03,0.0001)
Teflon	(0.023,0.4,0.9)	(2.077±0.15,0.000492±0.00015)	(2.08,0.00037)
Rexolite	(0.023,0.4,0.9)	(2.582±0.17,0.000321±0.00017)	(2.54,0.00048)

NOTE: (1) From Jasik's "Antenna Engineering Handbook," pp. 35-12 to 35-15, 1961 ed.

(2) ϵ_r' denotes relative dielectric constant and tanδ denotes loss tangent.

TABLE 4 SUMMARY OF THE RESULTS FOR THE UNKNOWN SAMPLES AT X-BAND

Sample	Size[2] (in.) (t,h,l)	Computed Value @ 9.26 GHz (μ_r' , μ_r'')[3]	Computed Value @ 9.26 GHz (ϵ_r' , tanδ)[4]	Reference[1] Value (ϵ_r' , tanδ)
Mylar	(0.0022, 0.385, 0.896)	(1.0,0)	(2.809±0.2, 0.0095±0.008)	(2.98, 0.016) @1 MHz
Epoxy	(0.011, 0.385, 0.883)	(1.0,0)	(3.063±0.2, 0.04±0.003)	(3.1,0.0263) @10 GHz
Iron	(0.0254, 0.388, 0.892)	μ_r: (94.6±10,7.5±1.2) $j\mu_{cr}$:(13.5±0.8,19.5±5.8)	(29.5±5, 0.0862±0.0117)	NOT AVAILABLE

NOTE: (1) From Jasik's "Antenna Engineering Handbook," pp. 35-12 to 35-15,1961 ed.

(2) The thickness "t" for the epoxy and iron samples are the average values of the irregular surface.

(3) $\mu_r' = \mu_r' - j\mu_r''$ denotes the complex principal permeability

$j\mu_{cr} = j(\mu'_{cr} - j\mu''_{cr})$ denotes the complex coupling permeability.

(4) ϵ_r' denotes the relative dielectric constant and tanδ denotes loss tangent.

ACKNOWLEDGMENTS

The authors are grateful to Mr. Les Lemke, President, and Mr. Thomas Witkowski, Director of Engineering at Teledyne Micronetics, for their support and encouragement. Thanks are also due to Ms. Laura Peck for her help in preparing this paper.

We would also like to express our appreciation to the Chemical/Ballistics Procurement Division, Aberdeen Proving Ground for sponsoring this program.

REFERENCES

Collin, R. E., 1960: Field Theory of Guided Waves, McGraw-Hill Book Co., New York.

Ginzton, E. L., 1957: Microwave Measurements, McGraw-Hill Book Co., New York.

Van Valkenberg, M. E., 1955: Network Analysis, Prentice-Hall, Inc., Englewood Cliffs, New Jersey.

NOISE TUBE SPECTRUM IN THE MILLIMETER REGION

K. D. Moeller, R. G. Zoeller and N. G. Ugras
Physics Research Laboratory
Fairleigh Dickinson University
Hackensack, NJ 07601

ABSTRACT

A comparison is presented of a mercury lamp and a noise tube as the source in a lamellar grating spectrometer in the millimeter wave region.

INTRODUCTION

Spectrometers in the far infrared and millimeter wave region use mercury lamps or black body radiation as sources. The decrease of the emission to longer wavelength is proportional to $1/\lambda^3$. Noise tubes are available as broad band sources in the millimeter wave region. Noise tubes use gas discharges for the generation of the electromagnetic waves, and their wavelength range depends on the mechanical dimensions of the waveguides.

We have compared the emission of a noise tube with mercury lamps. The noise tube was Model TN-167 made by C. P. Clare & Co. with an advertised frequency range of 90 to 140 GHz. It was operated with 225 volts and 75 mA from a regulated power supply also manufactured by Clare. The mercury lamps were G. E. ac-lamps of 100 watts and 250 watts. They were operated with a SOLA transformer and a ballast.

SPECTROMETER

Figure 1 shows schematically the spectroscopic set-up. The noise tube was attached to an antenna horn and placed at the focal point of a collimator mirror having 8" diameter and 16" focal length. The mercury lamps were used with a spherical mirror of short focal length. The image of the burning arc was focused at an aperture placed at the focal plane of the collimating mirror.

In the spectroscopic arrangement of Figure 1, the lamellar grating produces an interferogram which was digitized by a digital voltmeter and transformed to the final spectrum by a HP9845A computer using a Fast Fourier Transformation. Figures 2 to 4 show the spectra of a mercury lamp, a noise tube and a mercury lamp in conjunction with a Fabry Perot filter. Several highly sensitive, pumped, He-cooled bolometers, made by Infrared Laboratories, Inc., were used as detectors. These detectors have a NEP of 10^{-14}.

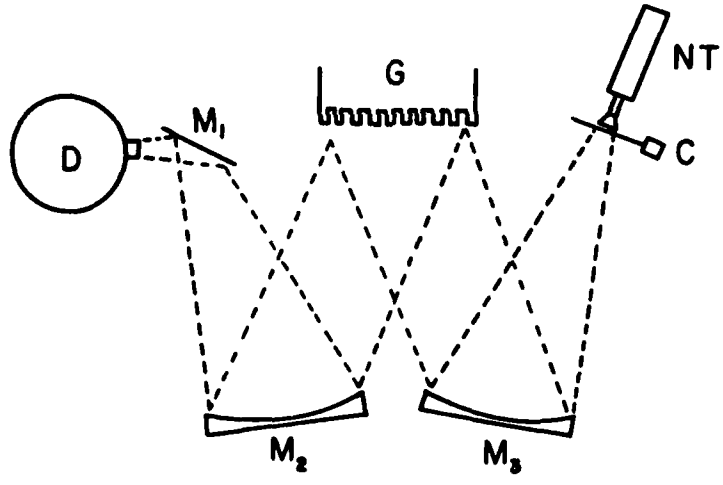

FIGURE 1. SPECTROMETER ARRANGEMENT. NT-noise tube, C-chopper, M_1 to M_3-mirrors, G-lamellar grating, D-He cooled detector.

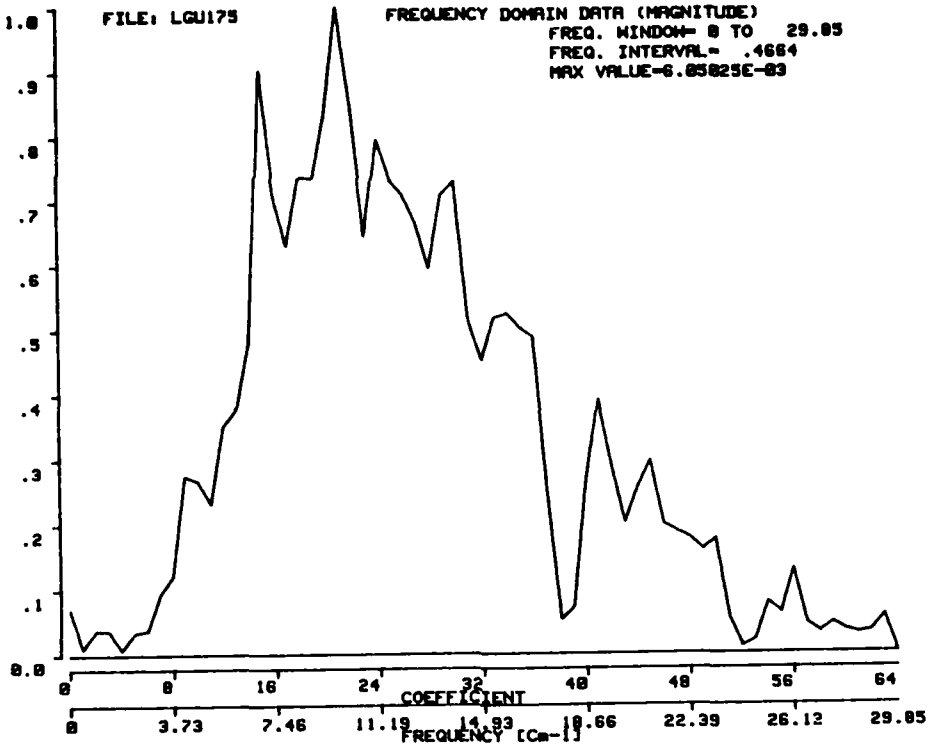

FIGURE 2. SPECTRUM USING A 250 WATT MERCURY LAMP SOURCE.

DISCUSSION

The spectrum of the 250 watt mercury lamp is shown in Figure 2. The strong dips at 18 cm^{-1} and 25 cm^{-1} are water vapor lines. Other dips are due to interference from the fused quartz envelope of the lamp. The noise tube spectrum is shown in Figure 3. The structure in the spectrum has its origin in the noise tube. This has been confirmed by taking the noise tube spectrum with two different pumped He-cooled detectors having approximately the same sensitivity but different concentration optics. One has a conical light pipe with an exit opening of 3.5mm, the other a parabolic light pipe with a 5mm exit opening. The long wavelength cutoff for the noise tube has been observed at about 2.3 cm^{-1} with both of these detectors. However, with a third detector of approximately the same sensitivity, a cutoff at much shorter wavelength has been observed for the same noise tube by J. Heaney [1]. This detector had a conical light pipe with an exit opening of .75mm.

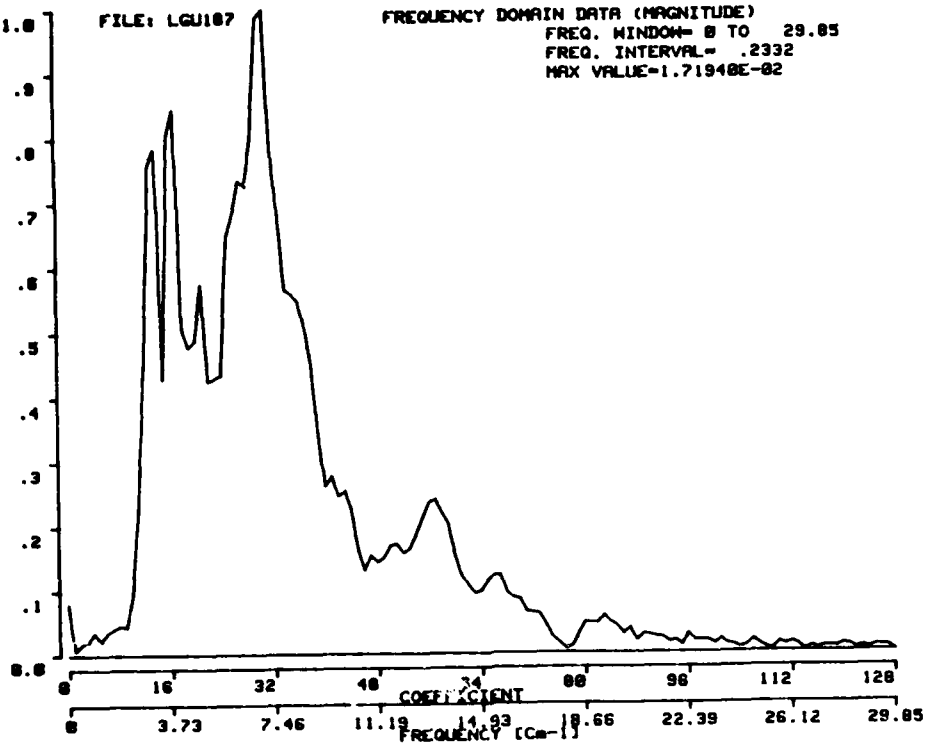

FIGURE 3. SPECTRUM USING A 90-140 GHz NOISE TUBE.

Comparing the peak power of the noise tube spectrum and the spectrum of the mercury lamp, we found that the peak at 10 cm^{-1} (300 GHz) of the mercury lamp is about 10 times higher than the peak at 7 cm^{-1} (140 GHz) of the noise tube. The noise tube output is higher than the output of the mercury lamp for wave numbers smaller than 3.3 cm^{-1}. The noise of the noise tube appeared lower even after using much higher sensitivities for amplification. We attribute this to the use of a regulated power supply in contrast to a ballast transformer and SOLA transformer used with the mercury lamp. A dc mercury lamp with regulated power supply may result in less noise.

The noise tube was placed at the focal point of an 8" diameter mirror with 16" focal length. The solid angle used is roughly the same as the antenna opening. However, a study of the divergence of the noise tube is planned.

NOISE TUBE AS BROAD BAND SOURCE

The emission of the noise tube has a narrower bandwidth compared to the mercury lamp, but may be used as a broad band source in comparison with oscillator type sources. If one wants to do Fourier transform spectroscopy in the 1-3mm region, a certain time is necessary to obtain an interferogram with a certain signal to noise ratio. If the spectrum of a cloud chamber is to be taken, the distribution of the material in the cloud chamber may change during the time the interferogram is taken. One can use noise tubes in conjunction with filters to obtain directly the transmission of the cloud chamber. The width of the band of the noise tube may be made more narrow by the use of a Fabry Perot type of band pass filter, see Figure 4, or a low pass filter [2]. A Fabry Perot filter can be designed to suppress the peak around 3.73 cm^{-1} resulting in a peak transmission at 7.5 cm^{-1} and an estimated width at half height of 2.3 cm^{-1}.

Noise tubes are available in the millimeter region in the following bands:

26-40 GHz, 40-60 GHz, 60-90 GHz

90-140 GHz (the one of this paper), 140-220 GHz

A set of these noise tubes with appropriate filters could be used for direct measurements on cloud chambers and would be considerably less expensive than a set of klystrons. A noise tube with power supply and antenna is about 1/10 the cost of an oscillator.

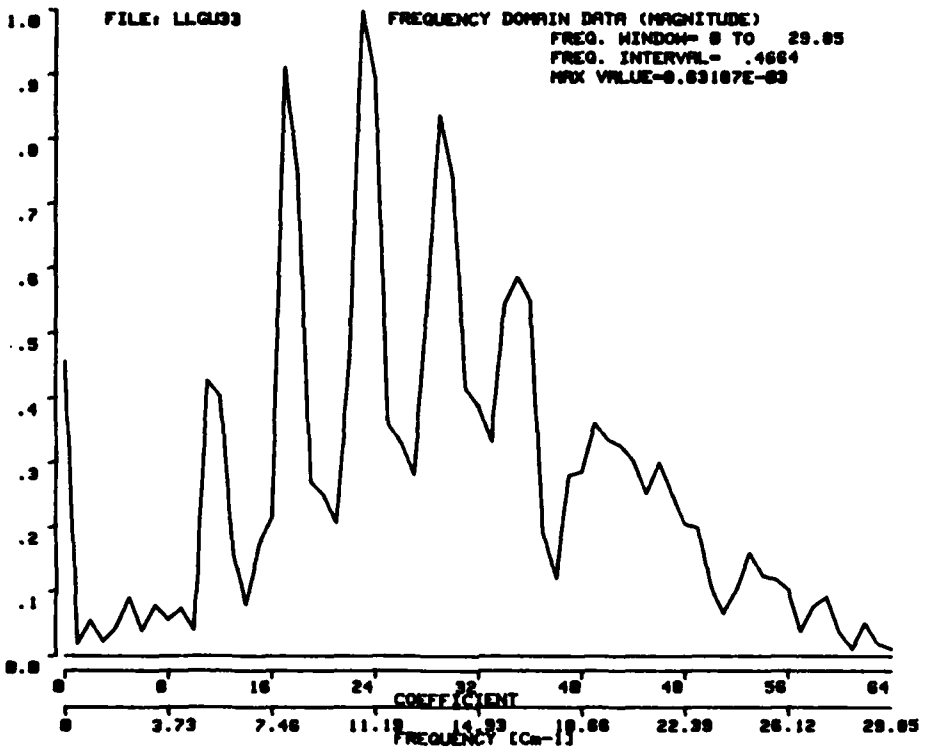

FIGURE 4. SPECTRUM USING A 250 WATT MERCURY LAMP SOURCE AND AN 80 MESH FABRY PEROT FILTER.

Ref. 1. J. Heaney, NASA Goddard Space Flight Center, private communication.

Ref. 2. K. K. Mon and A. J. Sievers, Appl. Opt. 14, 1054 (1975).

OPTICAL PROPERTIES OF NATURAL MINERALS IN THE FAR INFRARED AND SUBMILLIMETER WAVELENGTH REGIONS

L. L. Long, R. J. Bell, M. A. Ordal, and R. W. Alexander, Jr.
Physics Department
University of Missouri-Rolla
Rolla, MO 65401

and

M. Querry
Physics Department
University of Missouri-Kansas City
Kansas City, MO 64110

RECENT PUBLICATIONS, SUBMITTALS FOR PUBLICATION AND PRESENTATIONS:

A) L. L. Long, M. A. Ordal, R. J. Bell, and R. W. Alexander, Jr., "The Optical Constants of Smoke Materials in the Submillimeter and Millimeter," Proceedings of the 1984 CRDC Conference on Obscuration and Aerosol Research, p. 167, submitted September 1984.

B) M.A. Ordal, L. L. Long, R. A. Paul, R. W. Alexander, Jr., and R. J. Bell, "Metals and Graphite: Predicting Optical Properties in the Submillimeter and Millimeter Wavelength Ranges," Proceedings of the 1984 CRDC Conference on Obscuration and Aerosol Research, p. 179, submitted September 1984.

C) M. A. Ordal, R. J. Bell, R. W. Alexander, Jr., and R. A. Paul, "Absorption Coefficient of DuPont Teflon FEP in the 20-130 Wavenumber Range," to appear Appl. Opt. (September 1985.)

D) M. A. Ordal, R. J. Bell, R. W. Alexander, Jr., and M. R. Querry, "Optical Properties of 14 Metals in the Infrared and Far Infrared: Al, Co, Cu, Au, Fe, Pb, Mo, Ni, Pd, Pt, Ag, Ti, V and W," to be published in Applied Optics.

E) R. J. Bell, M. A. Ordal and R. W. Alexander, "Equations Linking Different Sets of Optical Properties for Nonmagnetic Materials," submitted to Applied Optics.

ABSTRACT

Optical constants of natural minerals measured during the period June 1985 to August 1985 under the U. S. Army grant DAAA-15-85-K-0004 (M. Milham) are reported. Included are the minerals anhydrite, colemanite, fluorapatite, illite, kaolinite, kernite, limonite, montmorillonite, pyrolusite, olivine, and single crystal gypsum.

I. INTRODUCTION

Studies of the optical properties of natural minerals have been conducted in the near and middle infrared spectral regions,[1-5] but little experimental data exists in the longer wavelength regions, i.e. the far infrared. This spectral region has often been neglected because of the lack of commercial instruments and the difficulties involved in working in this low signal region.

Knowledge obtained from the measurements of the optical properties have several interesting and useful applications. First, particulate matter of natural minerals exists in the atmosphere[6] where it serves to scatter and absorb both sunlight and terrestrial thermal radiation. To properly determine the effect these particles have on the earth, it is essential to know their optical constants at wavelengths ranging from the ultraviolet to the far infrared,[7] since scattering theories require extensive knowledge of the optical and physical properties of the particles involved.[8] The optical properties consist of the complex refractive index or the complex dielectric function. Second, remote sensing of terrestrial and extraterrestrial environments require detailed knowledge of the optical properties of natural minerals in order to determine surface composition. These surfaces are composed of mixtures of several minerals, so knowledge of the optical properties of individual minerals is necessary to correctly ascertain the surface composition. This information is necessary not only to determine composition but also to understand the background spectra that must be eliminated from the target signatures.[9] Third, much of the spectrum of the lattice vibrations of these minerals lies in the infrared spectral region, resulting in large variations in the refractive index. Finally, the optical properties of atmospheric particulate matter must be known to properly determine the usefulness of these minerals in obscuration.

This work complements the efforts of other researchers working in the shorter wavelength spectral regions. Since one of the major analysis tools requires knowledge of the reflectance over a wide spectral range, this work also aids in determining the optical constants with higher precision by providing long wavelength data. It is important to emphasize that the combined wavelength range from the UV to the submillimeter provided by data from the University of Missouri-Rolla group and the University of Missouri-Kansas City greatly improves

the accuracy of the optical constants obtained.

The term optical properties refers to the real part, n, and the imaginary part, k, of the index of refraction, N. The relationships between the index of refraction and the dielectric constant, $N = n + ik$ and $\epsilon = \epsilon_1 + i\epsilon_2$, are $\epsilon_1 = n^2 - k^2$ and $\epsilon_2 = 2nk$. Each sample is presented with an introduction and two graphs, one for the reflectance and one for n and k.

II. EXPERIMENTAL PROCEDURE

A. APPARATUS

The far-infrared (20-400 cm^{-1}) reflectivity measurements were done using a RIIC FTS-720. Three attachments were constructed for these studies. They are used to perform transmission, pellet reflectance and crystal reflectance measurements. The shorter wavelength measurements were made using a Perkin-Elmer 580B (200 cm^{-1}) and a Varian model 14 (4000-50,000 cm^{-1}.)

An aluminum mirror was used as a reflectance standard. The absolute reflectance of this mirror was measured by us.

B. SAMPLE PREPARATION

The reflectance samples were either powdered samples pressed into pellets, oriented crystal samples, or polished amorphous samples. The pellets were made by pressing a fine powder in a piston-cylinder arrangement with a hydraulic press. There were two dies available for producing samples, one with a diameter of 13 mm, the other with a diameter of 1 1/8 inches; each die could be placed under a maximum of 24000 lbs. force. The die of larger area was used for samples with very low reflectance. The smaller die was used for the majority of the sample preparation, since higher pressure could be obtained. Single crystal samples were oriented by X-ray diffraction and the amorphous samples were cut and polished from the sample's naturally occurring solid form whenever the sample material could be obtained in a large enough section.

C. ATTACHMENTS

1. Reflection. There were two types of reflection attachments constructed for the far infrared work, each having advantages and disadvantages. The first reflection attachment, basically, consisted of four mirrors and a sample or reference. The radiation from the combined beams of the interferometer was directed toward a parabolic mirror which focused the beam onto the sample with

an angle of incidence of 15° to 20°, as shown in figure 1. The samples and reference mirror were mounted on a square post, which could be rotated from outside the sample compartment. The sample compartment had to be kept under a vacuum to eliminate absorption lines due to atmospheric water vapor. The square post allowed data to be taken on a maximum of three samples, with the fourth used for the reference mirror, without bringing the interferometer up to atmospheric pressure, thereby, eliminating the time necessary to evacuate the instrument between data runs. Of greater importance the sample and background runs were taken under as nearly identical conditions as possible.

The second reflection attachment, shown in figure 2, was constructed especially to study irregularly shaped samples such as crystals. The optical path of the radiation was similar to that of the first reflection attachment, with the angle of incidence equivalent between the two attachments. The main difference was that a vertical plate with a 1 1/8 inch hole replaced the sample post. Special sample holders were constructed with a beveled front to reflect unwanted radiation, or radiation that did not impinge upon the sample. These sample holders have a 10 mm hole to allow

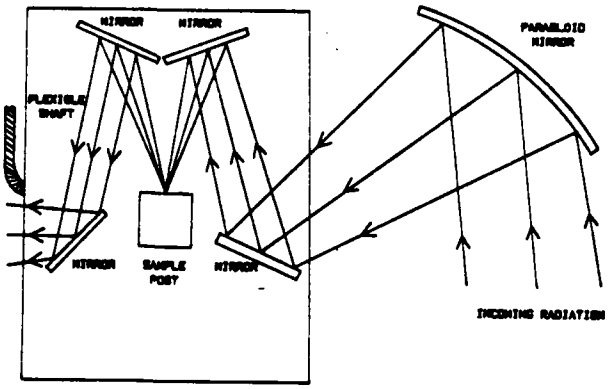

FIGURE 1. PELLET REFLECTANCE ATTACHMENT.

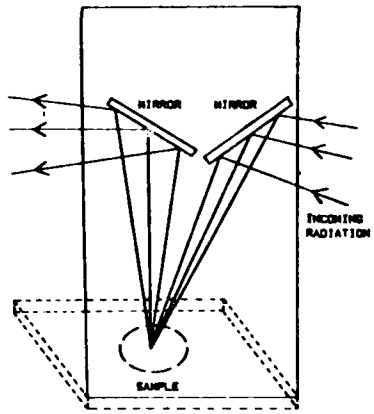

FIGURE 2. CRYSTAL REFLECTANCE ATTACHMENT.

exposure of the sample material to the radiation. With this reflection attachment the ability to change samples from outside the sample compartment was lost. It was determined that the venting and evacuating of the instrument between the sample and reference had minimal effects on the spectrum after the interferometer had been evacuated to less than 40 millitorr. An additional

benefit of this attachment was that it allowed easy insertion of a polarizer after the sample, thereby, allowing orientation dependent studies. The polarizer used for this work was a gold wire grid polarizer with a polyethylene substrate made by Perkin-Elmer Corporation.

III. RESULTS

A. PRESSED PELLET SAMPLES

The minerals studied in this section were ground in a mortar and pestle by hand until the sample material consisted of a very fine and uniform powder. This powder was then pressed into a pellet using either a Perkin-Elmer model 186-0025 die, producing 13mm pellets, or a homemade die, producing 1 1/8" pellets. These dies consisted of a metal cylinder with a polished metal anvil and plunger. The sample material was placed between the anvil and plunger where a maximum force of 20000 lbs. could be applied. All the pressed pellet samples were produced in this fashion.

The twelve samples in this section will be presented in alphabetical order with an introduction and description of each sample followed by two plots. The first displays the reflectance and the second the optical properties, n and k. If a dispersive analysis is done, the reflectance plot will present two sets of data, one set will be the experimental data and the other will be the fit.

The mineralogical information is taken from refs. 10-15.

1. Anhydrite. Anhydrite, $CaSO_4$, or calcium sulfate, crystallizes in the orthorhombic system. It is less abundant than gypsum, $CaSO_4 \cdot 2H_2O$, because it easily takes up water and converts to gypsum. The material is biaxial positive, meaning there are two optical axes forming the optic plane and a normal to the plane, the optic normal, each having a particular index of refraction. The optic normal is labeled Y, the maximum index is labeled Z, and the minimum index is labeled X. With these designations a mineral is referred to as positive whenever $(n_y-n_x) < (n_z-n_y)$ and negative whenever $(n_y-n_x) > (n_z-n_y)$. The indices of refraction, determined at the sodium line corresponding to 5893 A are $n_x=1.571$, $n_y=1.576$, and $n_z=1.614$. Anhydrite has a space group of D_{2h}^{17}; the primitive unit cell has lengths a=6.991, b=6.996, and c=6.238 A.[16,17] On the Mohs hardness scale anhydrite is rated at 3.5, which makes it slightly harder than calcite, and it has a specific gravity of 2.98.

The sample was pressed in a 13mm diameter die at 16000 lbs. force, producing a very glossy white pellet. This material was more difficult to press into a pellet than comparable materials of the same hardness. It had a tendency to stick to the inside cylinder of the die causing it to fracture when being removed. The reflectance spectrum for a pressed pellet of anhydrite is shown in figure 3. The optical properties, n and k, are shown in figure 4, where n and k are determined from a dispersive analysis of the reflectance.

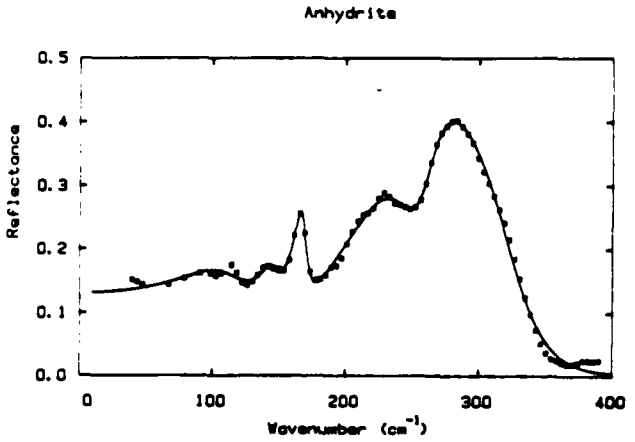

FIGURE 3. REFLECTANCE OF ANHYDRITE. The solid line is the dispersive analysis fit. The squares represent the data.

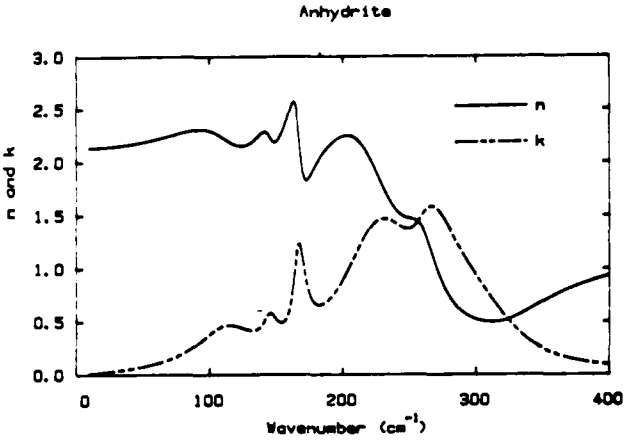

FIGURE 4. REFRACTIVE INDEX OF ANHYDRITE. The solid line is n and the dashed is k.

2. Colemanite. Colemanite, $Ca_2B_6O_{11}\cdot 5H_2O$, or hydrous calcium borate, crystallizes in the monoclinic system. The unit cell has lengths of a=8.74, b=11.26, and c=6.10 A, where the angle between the plane formed by the a and b axes and the c axis is $\beta=110^{o}\ 7'$. The indices of refraction, determined at the sodium line, 5893A, are $n_x=1.586$, $n_y=1.592$, and $n_z=1.614$. making the sample biaxial positive. The space group of colemanite is 2/m. On the Mohs hardness scale colemanite is rated at 4.5 with a specific gravity of 2.42.

The sample was pressed in a 1 1/8" diameter die at a force greater than 24000 lbs., producing a dull light gray pellet. Even though the hardness was 4.5, the material pressed easily into a pellet, while other materials of like hardness were much harder to press. This was assumed to be due to the water, which makes up 21.9% of the composition of colemanite. Due to the large amount of H_2O, the data was taken while the interferometer was purged with dry nitrogen to eliminate water loss that might have occurred under vacuum. The dry nitrogen

purge was necessary to eliminate atmospheric water vapor absorption lines.

The reflectance spectrum for a pressed pellet of colemanite is shown in figure 5. The optical properties, n and k, are shown in figure 6, where n and k are determined from a dispersive analysis of the reflectance.

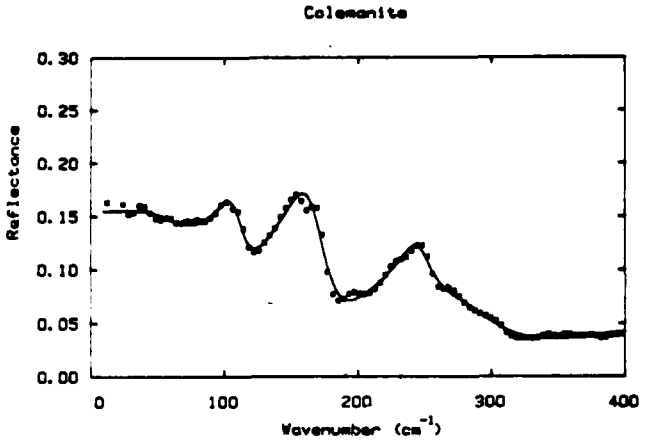

FIGURE 5. REFLECTANCE OF COLEMANITE. The solid line is the dispersive analysis fit. The squares represent the data.

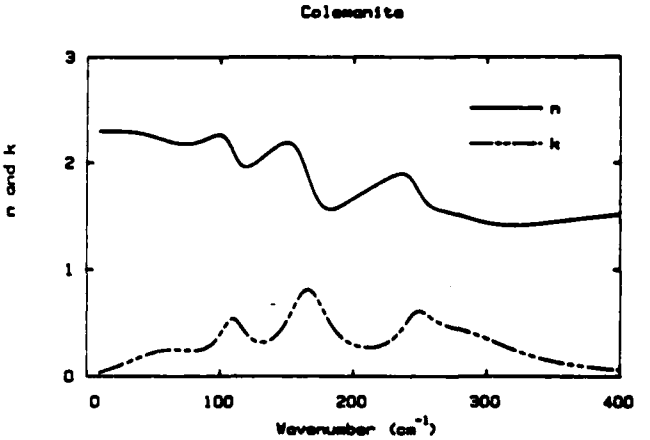

FIGURE 6. REFRACTIVE INDEX OF COLEMANITE. The solid line is n and the dashed is k.

3. Fluorapatite. Fluorapatite, $Ca_5(PO_4)_3F$, or calcium phosphate with fluorine, one of the most common phosphates, crystallizes in the hexagonal system, C_{6h}^2. The length of the a and c axes are 9.39 and 6.89 A, respectively. This mineral is uniaxial negative with the index of refraction for the ordinary ray, n_o=1.633, and extraordinary ray, n_e=1.630, measured at the sodium line 5893 A giving it a low birefringence of 0.003. On the Mohs hardness scale fluorapatite is rated at 5 and can, therefore, be scratched by a knife blade. It has a specific gravity of 3.1-3.4.

The sample was pressed into a 13mm diameter pellet by applying 16000 lbs. force, producing a whitish green pellet. When pressing the pellet the best method seemed to be to apply pressure, then immediately release. If the pressure was applied for longer than a few minutes, it caused cracks in the pellet when removed from the die. This was attributed to the hardness of the pellet causing the powder to gather better at the surface than at the center.

The reflectance spectrum for a pressed pellet of fluorapatite is shown in figure 7. The optical properties, n and k, are shown in figure 8, where n and k are determined from a dispersive analysis of the reflectance.

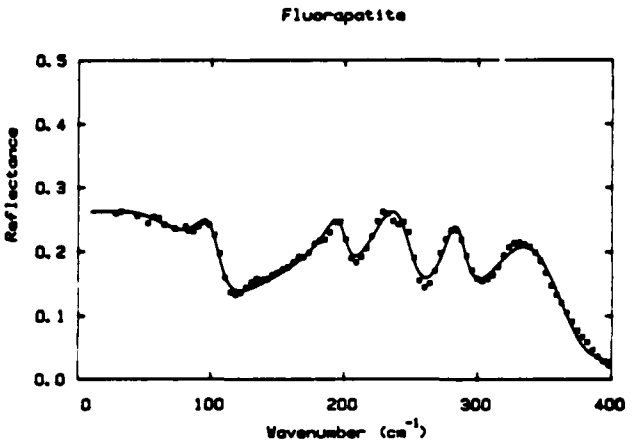

FIGURE 7. REFLECTANCE OF FLUORAPATITE. The solid line is the dispersive analysis fit. The squares represent the data.

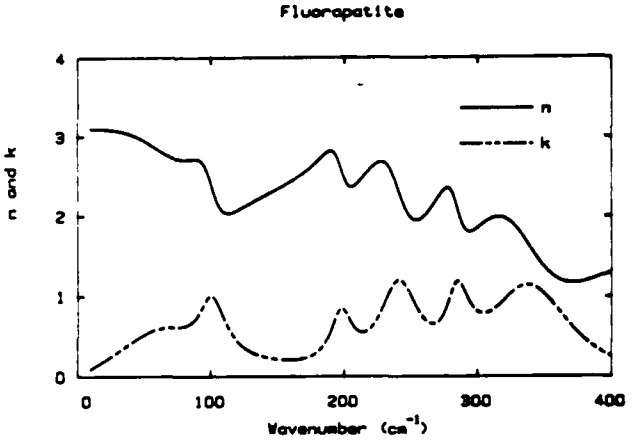

FIGURE 8. REFRACTIVE INDEX OF FLUORAPATITE. The solid line is n, and the dashed is k.

4. Illite. Illite, $K_{1-1.5}Al_4Si_{7-6.5}Al_{1-1.5}O_{20}(OH)_4$, is a general term for mica-like clay and is the chief constituent in many shales. It crystallizes in the monoclinic system with indices of refraction n_X=1.54-1.57, n_Y=1.57-1.61, and n_Z=1.57-1.61 measured at 5893 A. Illite is biaxial negative with a birefringence of 0.03 to 0.05, a specific gravity of 2.6 to 2.9, and a hardness of 1 to 2, making it the softest mineral studied.

The sample material was pressed at 16000 lbs. force, producing a dull light green pellet. The original solid sample, illite-bearing shale, was darker in color and the decrease in color darkness was assumed to be due to a decrease in density of the pressed pellet. Producing a pellet was not difficult, but not as easy as the specific gravity would indicate. This may be due to the small amount of shale present in the sample.

The reflectance spectrum for an 8 ton pressed pellet of illite-bearing shale is shown in figure 9. The optical properties, n and k, determined by a dispersive analysis of the reflectance, are shown in figure 10.

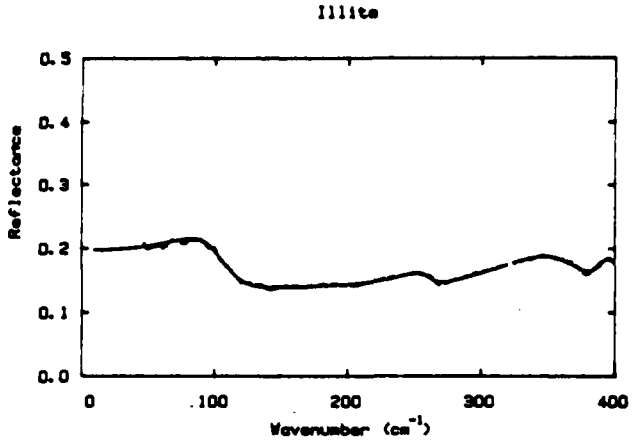

FIGURE 9. REFLECTANCE OF ILLITE. The solid line is the dispersive analysis fit. The dashed line represents the data.

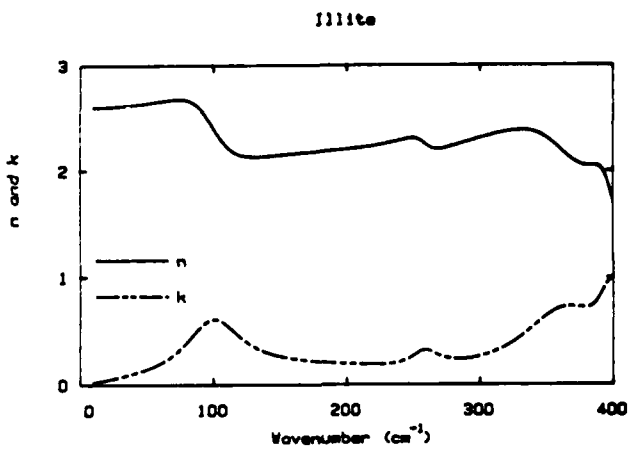

FIGURE 10. REFRACTIVE INDEX OF ILLITE. The solid line is n, and the dashed is k.

5. Kaolinite. Kaolinite, $Al_2Si_2O_5(OH)_4$, or hydrous aluminum silicate, crystallizes in the triclinic system. Kaolinite's plasticity and its ability to withstand high temperatures when dried makes it useful for firebricks and other refractory materials. Additional uses are as whitening agents, whitewares, china, and as a filler in paper. The unit cell lengths are a=5.14, b=8.93, and c=7.37 A with an angle between the b and c axes of α=91° 48', between the c and a axes of β=104° 30', and between the a and b axes of γ=90°. The indices of refraction for clays are not as precisely known as for other materials, therefore, for a wavelength of 5893 A n_X=1.553-1.563, n_Y=1.559-1.569, and n_Z=1.560-1.570 making the sample biaxial negative. Kaolinite has a Mohs hardness of 2-2.5 and a specific gravity of 2.6.

The sample was pressed in a 13mm die, producing a dull white pellet. Due to the soft nature of this material, it easily pressed into a pellet.

A specular reflectance spectrum of a kaolinite pellet is shown in figure 11. The optical properties, n and k, are shown in figure 12 and are obtained from a dispersive analysis of the reflectance.

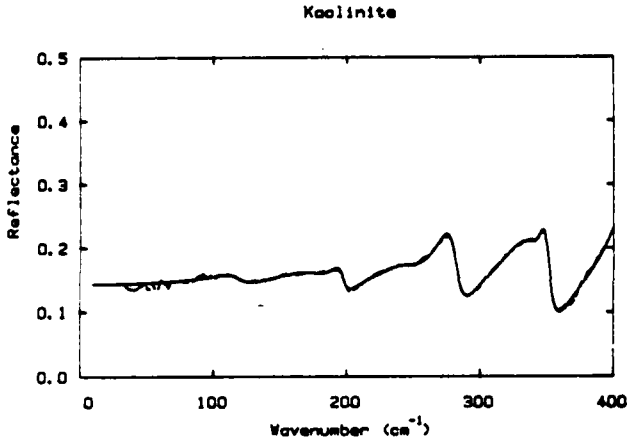

FIGURE 11. REFLECTANCE OF KAOLINITE. The solid line is the dispersive analysis fit. The dashed line represents the data.

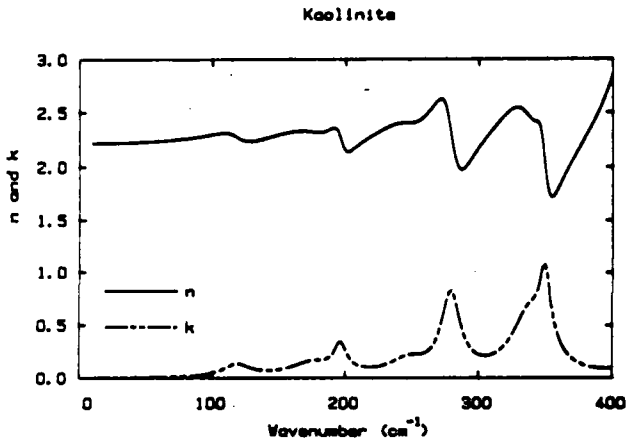

FIGURE 12. REFRACTIVE INDEX OF KAOLINITE. The solid line is n and the dashed is k.

6. Kernite. Kernite, $Na_2B_4O_7 \cdot 4H_2O$, or hydrous sodium borate, crystallizes in the monoclinic system. This material rarely occurs in crystals, but is usually found in coarse cleavable aggregates and is named for Kern County, California where the mineral was originally found. The unit cell lengths are a=15.68, b=9.09, and c=7.02 A with an angle of β=108° 52' between the ab plane and c axis. The indices of refraction at 5893 A are n_x=1.454, n_y=1.472, and n_z=1.488, therefore, the sample is biaxial negative. Kernite has a hardness of 2.5, placing it between gypsum, 2, and calcite, 3, and its specific gravity is 1.908.

The sample was pressed in a 1 1/8" die, producing a slightly glossy white pellet. The samples were easily pressed due to the softness of the material. Because of the composition of kernite, Na_2O: 22.7%, B_2O_3: 51.0%, and H_2O: 26.3%, the data were acquired under a dry nitrogen purge to eliminate the possibility of dehydrating the sample.

The reflectance spectrum for a pressed pellet of kernite is shown in figure 13. The optical properties, n and k, are shown in figure 14, where n and k are determined from a dispersive analysis of the reflectance.

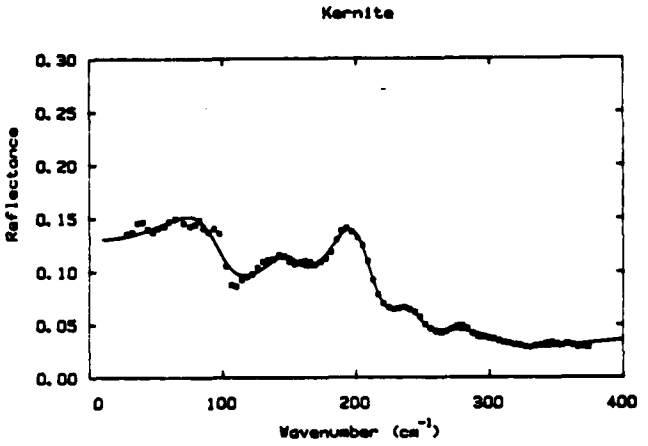

FIGURE 13. REFLECTANCE OF KERNITE. The solid line is the dispersive analysis fit. The squares represent the data.

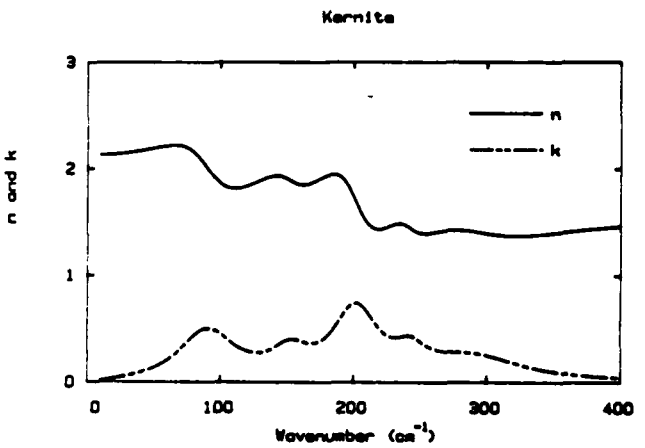

FIGURE 14. REFRACTIVE INDEX OF KERNITE. The solid line is n, and the dashed is k.

7. Limonite. Limonite is a hydrated ferric oxide consisting largely of goethite, $Fe_2O_3 \cdot H_2O$. The term goethite is used when the material shows definite evidence of crystallinity. Goethite crystallizes in the orthorhombic system and the unit cell has lengths a=4.65, b=10.02, and c=3.04 A. The indices of refraction are n_x=2.26, n_y=2.39, and n_z=2.40 at 5893 A, resulting in goethite being biaxial negative. Goethite has a Mohs hardness of 5 to 5.5 and a specific gravity of 3.3 to 4.3.

The sample was pressed in a 13mm diameter die, producing a dull reddish brown pellet with no gloss. When pressing this sample material only one useable side was usually produced, but there was generally little problem with the pellet fracturing during removal from the die. There were two 13mm dies used to produce pellets, one homemade and the other commercial. Pellets were pressed at 5 tons and 8 tons force. The 8 ton pellet exhibited a higher reflectance, thus, that result will be presented.

The reflectance spectrum of the the 8 ton limonite pellet is presented in figure 15 and the optical properties in figure 16. Figure 16 is obtained by a dispersive analysis of the data in figure 15.

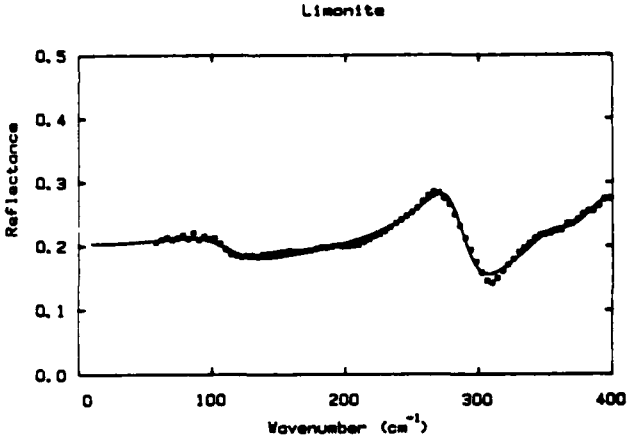

FIGURE 15. REFLECTANCE OF LIMONITE. The solid line is the dispersive analysis fit. The squares represent the data.

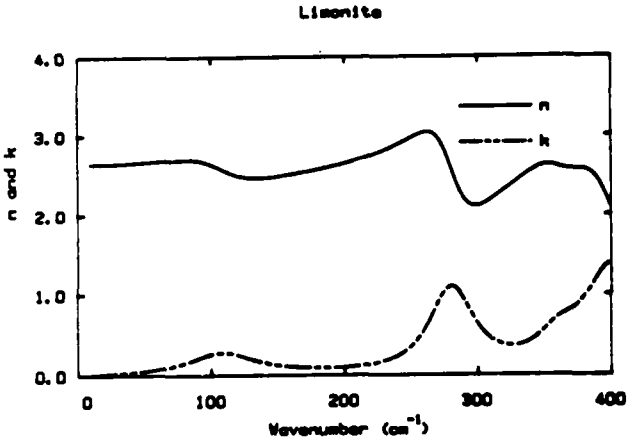

FIGURE 16. REFRACTIVE INDEX OF LIMONITE. The solid line is n and the dashed is k.

8. Montmorillonite. Montmorillonite, $(Ca, Na)_{0.35-0.7}(Al, Mg, Fe)_2(Si,Al)_4O_{10}(OH)_2 \cdot nH_2O$, or hydrous calcium-sodium aluminum-magnesium-iron silicate, crystallizes in the monoclinic system and is a biaxial negative clay with indices of refraction n_x=1.48-1.59, n_y=1.51-1.60, and n_z=1.51-1.63 measured at the sodium line 5893 A. Montmorillonite has a hardness of 1-2 and a specific gravity of 2-3.

This sample material was used to prepare samples for both surface roughness and pressure dependent studies presented in later sections. Some of these samples were prepared with the homemade die resulting in a lower reflectance due to the lower pressure at which this die could be operated.

The reflectance spectrum of a montmorillonite pellet pressed with a force of 10 tons is presented in figure 17 and the optical properties are shown in figure 18. The spectral values of n and k are obtained from a dispersive analysis.

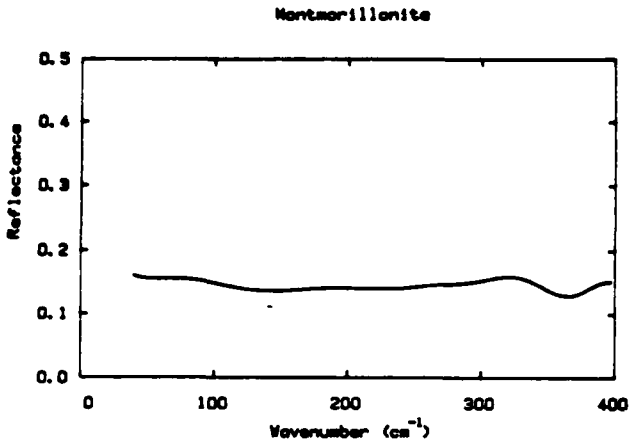

FIGURE 17. REFLECTANCE OF MONTMORILLONITE.

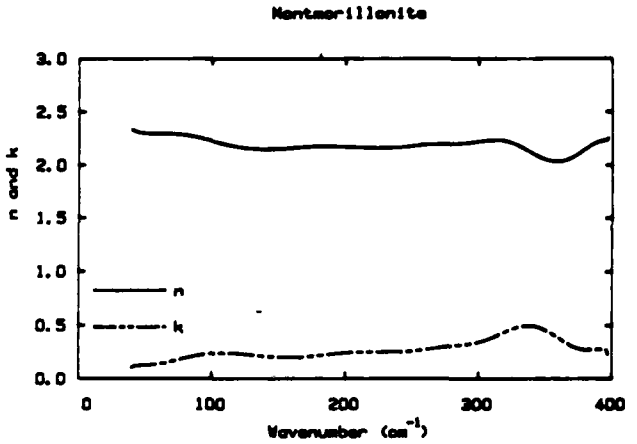

FIGURE 18. REFRACTIVE INDEX OF MONTMORILLONITE. The solid line is n and the dashed is k obtained from a Kramers-Kronig analysis of the reflectance.

9. Pyrolusite. Pyrolusite, or manganese dioxide, crystallizes in the tetragonal system. It is uniaxial with the a and c axes of the unit cell having lengths of 4.39 and 2.86 A, respectively. Usually found in powdery or granular crystals, single crystals are rare. The Mohs hardness is 6 to 6.5, making it only slightly softer than quartz, which is rated at 7 by definition. A high specific gravity of 5.04 to 5.08 makes it one of the denser samples measured.

The sample material was pressed at 24000 lbs. force into a 13mm diameter pellet. Due to the extreme hardness of this material, it was very difficult to press. The method which produced useable pellets was to apply the 24000 lbs. force to the sample material for, approximately, one half hour. The pellet produced was dull black in color and very fragile.

Figure 19 presents the reflectance for a 12 ton pellet of pyrolusite and figure 20 represents the optical properties, n and k. The optical properties are determined from a Kramers-Kronig analysis of the reflectance spectrum, since the majority of the features were at wavelengths shorter than 25 micrometers, a dispersive analysis was difficult. The upper wing was taken from a final report of Dr. M. Querry.[18]

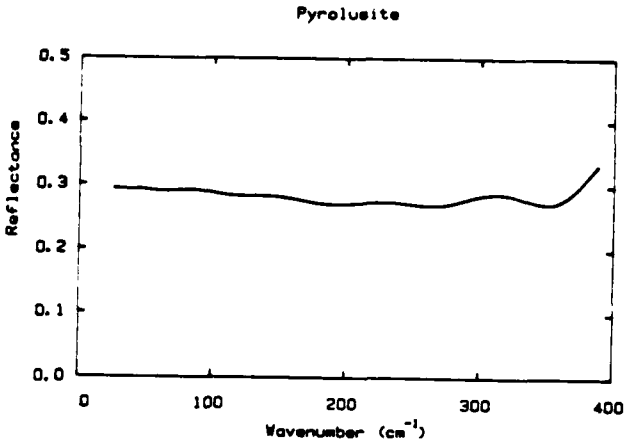

FIGURE 19. REFLECTANCE OF PYROLUSITE.

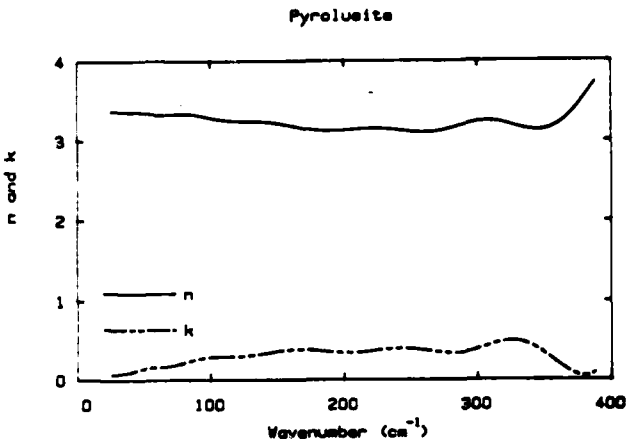

FIGURE 20. REFRACTIVE INDEX OF PYROLUSITE. The solid line is n n and the dashed is k.

B. NON-POWDERED SAMPLES

1. Gypsum, Crystal. Gypsum crystallizes in the monoclinic system, meaning there are three optical axes X, Y, Z, with Y being parallel to the b crystallographic axis. Figures 21 and 22, 23 and 24, and 25 and 26 represent the reflectance and optical properties of the X, Y, and Z axes, respectively.

The gypsum samples were obtained from Dr. M.R. Querry of U.M.K.C. Two samples of gypsum were needed to provide all three orientations.

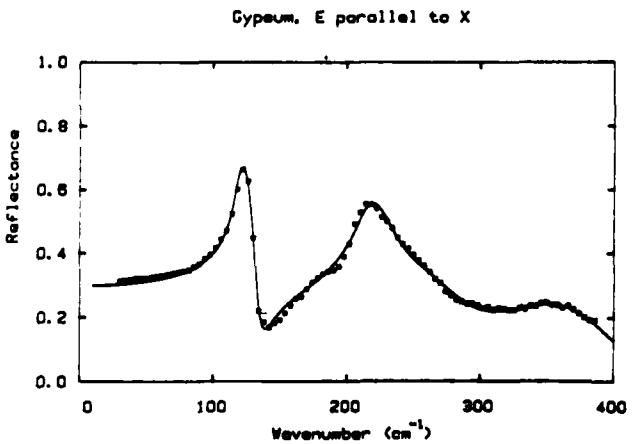

FIGURE 21. REFLECTANCE OF GYPSUM PARALLEL TO THE X AXIS. The solid line is the dispersive analysis fit. The squares represent the data.

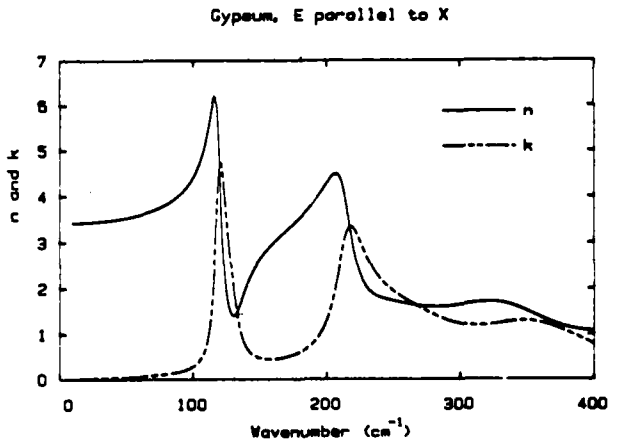

FIGURE 22. REFRACTIVE INDEX OF GYPSUM PARALLEL TO THE X AXIS. The solid line is n and the dashed is k.

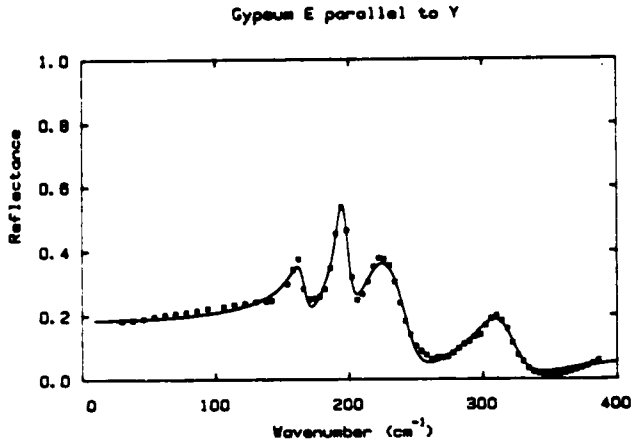

FIGURE 23. RELECTANCE OF GYPSUM PARALLEL TO THE Y AXIS. The solid line is the dispersive analysis fit. The squares are the data.

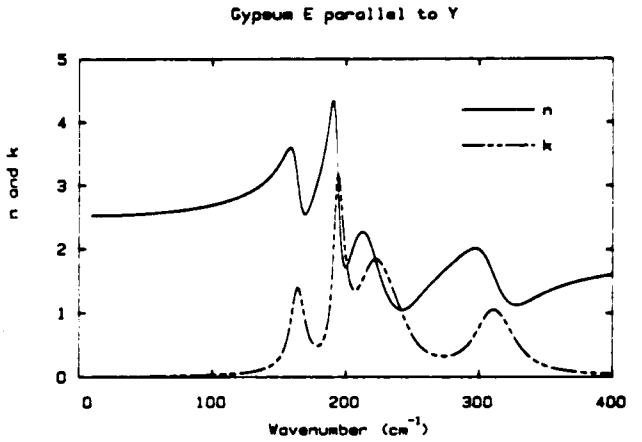

FIGURE 24. REFRACTIVE INDEX OF GYPSUM PARALLEL TO THE Y AXIS. The solid line is n and the dashed is k.

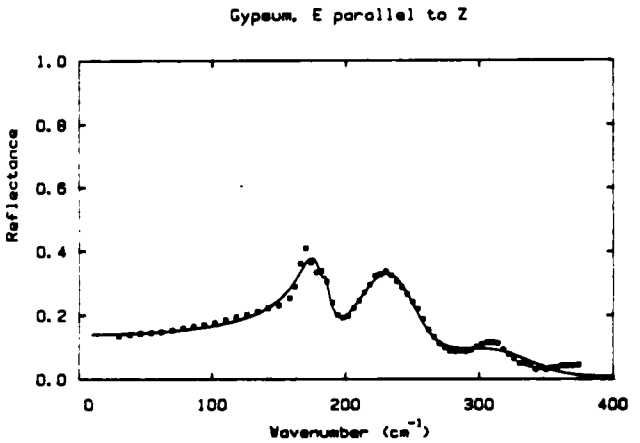

FIGURE 25. REFLECTANCE OF GYPSUM PARALLEL TO THE Z AXIS. The solid line is the dispersive analysis fit. The squares are the data.

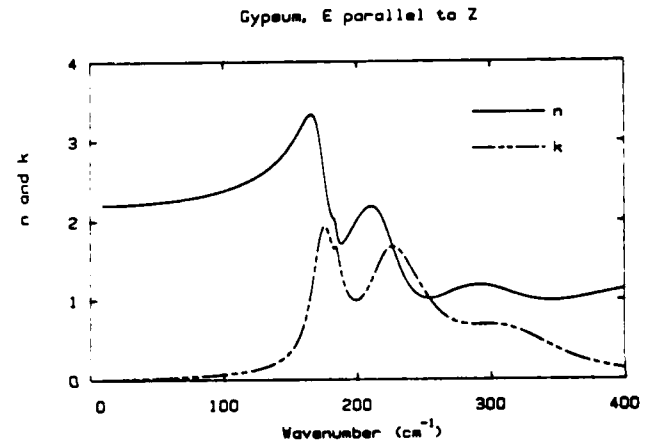

FIGURE 26. REFRACTIVE INDEX OF GYPSUM PARALLEL TO THE Z AXIS. The solid line is n and the dashed is k.

2. Gypsum, Solid. Since gypsum is a hydrous calcium sulfate, removing the water will change the reflectance spectrum as shown in figure 27. This form of gypsum is alabaster and is noted for its lack of an apparent crystalline structure as is common with other forms of gypsum. Figures 27 and 28 represent the reflectance and optical properties for this form of gypsum.

An interesting feature is the large difference between the reflectance of the pressed pellet of gypsum and this solid amorphous gypsum. In fact, the spectrum actually resembles the anhydrite spectrum. To determine if the absence of water causes this change, a freshly pressed pellet of gypsum was left under a

vacuum for several days and the resulting spectrum is very similar to the reflectance in figure 27. The sample produced due to the vacuum is hemihydrate, plaster of paris, which corresponds to $CaSO_4 \cdot 1/2H_2O$. Hence the surface of the solid gypsum sample appears to be partially dehydrated and resembles calcium hemihydrate.

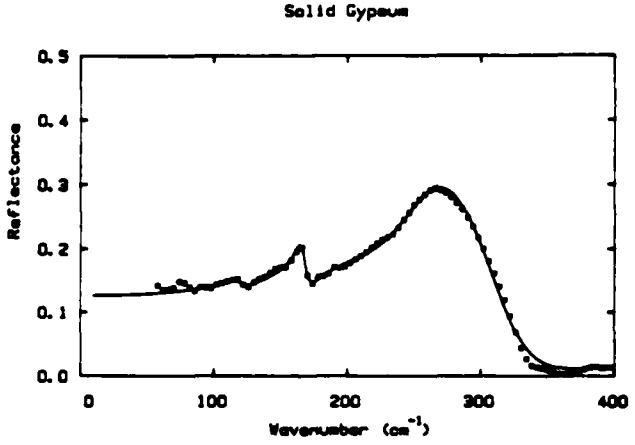

FIGURE 27. REFLECTANCE OF SOLID GYPSUM. The solid line is the dispersive analysis fit. The squares represent the data.

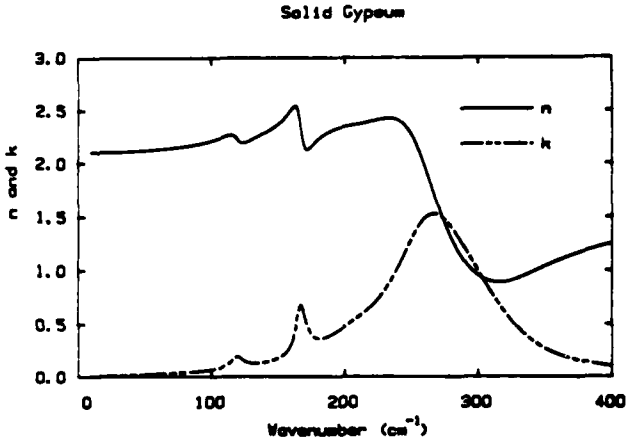

FIGURE 28. REFRACTIVE INDEX OF SOLID GYPSUM. The solid line is n and the dashed is k.

3. Limonite, Solid. Limonite as a pressed pellet was examined in an earlier section. This sample of limonite was obtained by cutting and then polishing the naturally occurring solid form. There appeared to be no definite crystalline structure.

Figures 29 and 30 represent the reflectance and optical properties of solid limonite. The main difference between the powdered and solid limonite is the level of the reflectance, although the general shape is still maintained. This generally higher reflectance, of course, results in a larger n and k.

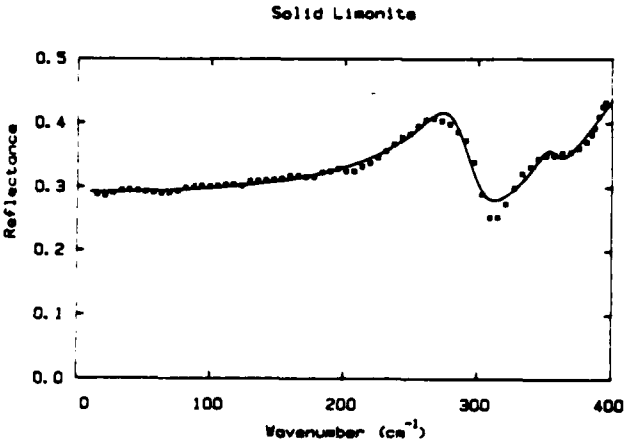

FIGURE 29. REFLECTANCE OF SOLID LIMONITE. The solid line is the dispersive analysis fit. The squares represent the data.

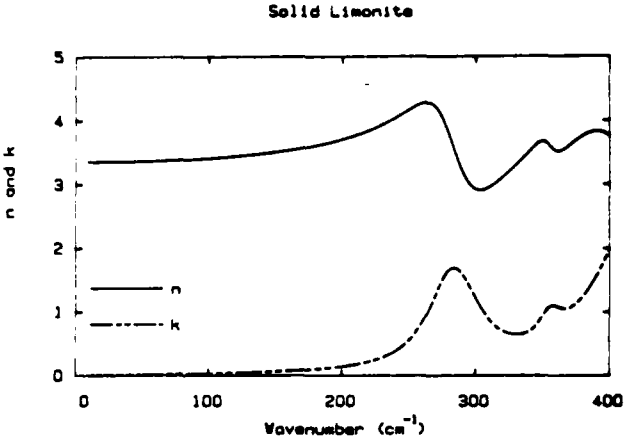

FIGURE 30. REFRACTIVE INDEX OF SOLID LIMONITE. The solid line is n and the dashed is k.

4. Olivine. This particular sample was green in color, which identified it as the forsterite member of the olivine group. Forsterite, Mg_2SiO_4, or magnesium silicate, crystallizes in the orthorhombic system. The size of the unit cell is a=4.76, b=10.20, and c=5.98 A and is biaxial positive. The specific gravity of forsterite is 3.27, while the hardness is 6.5-7, slightly less than that of quartz.

Due to the extreme hardness of the sample, a pellet could not be produced, therefore, a section was polished for spectroscopic analysis. This particular sample was granular massive and appeared as numerous small crystals cemented together resulting in the reflectance spectrum containing all orientations.

Figure 31 represents the reflectance for a polished sample of forsterite and figure 32 presents the optical properties, n and k, obtained from a dispersive analysis of the reflectance.

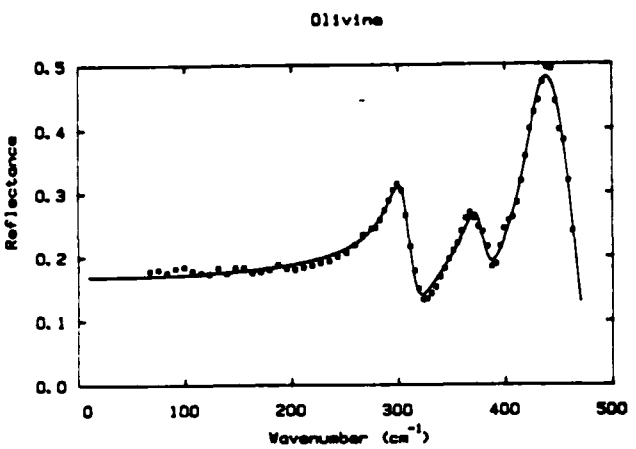

FIGURE 31. REFLECTANCE OF OLIVINE. The solid line is the dispersive analysis fit. The squares represent the data.

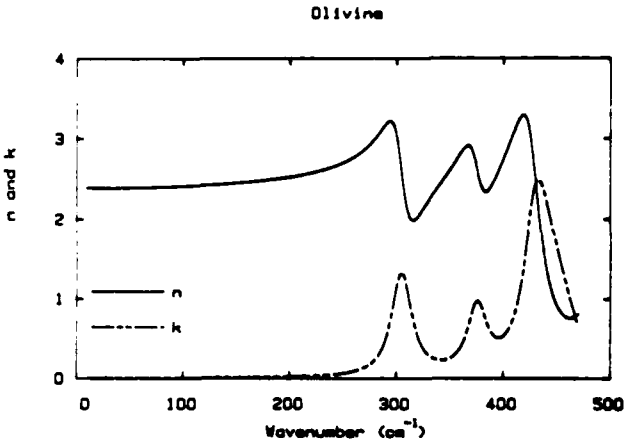

FIGURE 32. REFRACTIVE INDEX OF OLIVINE. The solid line is n and the dashed is k.

IV. CONCLUSION

The complex refractive indices, n and k, are presented for a number of natural minerals. An important feature of the results is the very wide frequency range covered (from 20 cm^{-1} to 400 cm^{-1}.) This allows an excellent determination of the refractive index from the reflectance using either a Kramers-Kronig analysis or a dispersion analysis.

REFERENCES

1. Gillespie, James B., Lindberg, James D., and Smith, Michael S. "Visible and Near-Infrared Absorption Coefficients of Montmorillonite and Related Clays," American Mineralogist, 59, 113-116 (1974).
2. Lindberg, James D. and Smith, Michael S. "Visible and Near-Infrared Absorption Coefficients of Kaolinite and Related Clays," American Mineralogist,59, 274-279 (1974).
3. Hovis, W.A., Jr. "Infrared Spectral Reflectance of Some Common Minerals," Applied Optics 5, 245-248 (1966).
4. Lindberg, James D. and Snyder, David G. "Diffuse Reflectance Spectra of Several Clay Minerals," American Mineralogist, 57, 485-493 (1972).
5. Lindberg, James D. and Laude, Larry S. "Measurements of the Absorption Coefficient of Atmospheric Dust," Applied Optics, 13, 1923-1927 (1974).
6. Hoidale, Glenn B. and Blanev, Abel J. "Infrared Absorption Spectra of Atmospheric Dust over an Interior Desert Basin," Pure and Applied Geophysics, 74, 151-164 (1969).
7. Toon, Owen B., Pollack, James B., and Khare, Bishun N. "The Optical Constants of Several Atmospheric Aerosol Species: Ammonium Sulfate, Aluminum Oxide, and Sodium Cloride," Journal of Geophysical Research, 81, 5733-5747 (1976).
8. Lindberg, James D. "The Composition and Optical Absorption Coefficient of Atmospheric Particulate Matter," Optical and Quantum Electronics, 7, 131-139 (1975).
9. Hunt, Graham R. and Salisbury, John W. "Visible and Near-Infrared Spectra of Minerals and Rocks: I Silicate Minerals," Modern Geology, 1, 283-300 (1970).
10. Sorrell, Charles A. Rocks and Minerals. New York: Western Publishing Company, Inc., 1973.
11. Moorhouse, W.W. The Study of Rocks in Thin Sections. New York: Harper & Row Publishers, 1959.
12. Hurlbut, Cornelius S., Jr. Dana's Manual of Mineralogy 18th edition. New York: John Wiley & Sons, Inc., 1971.
13. Carmichael, Robert S. Handbook of Physical Properties of Rocks, I. Florida: CRC Press, Inc., 1982.

14. Van der Marel, H.W. and Beutelspacher, H. Atlas of Infrared Spectroscopy of Clay Minerals and their Admixtures. Amsterdam: Elsevier Scientific Publishing Company, 1976.

15. Simpson, Brian. Rocks and Minerals. Oxford: Pergamon Press, 1966.

16. Berenblut, B.J., Dawson, P. and Wilkinson, G.R., "A Comparison of the Raman Spectra of Anhydrite ($CaSO_4$) and Gypsum ($CaSO_4 \cdot 2H_2O$)," Spectrochimica Acta 29A,29-36 (1973).

17. Cheng, G.C.H. and Zussman, J., "The Crystal Structure of Anhydrite ($CaSO_4$)," Acta Cryst. 16, 767-769 (1963).

18. Querry, Marvin R. "Optical Properties of Natural Minerals and Other Materials in the 350-50,000 cm^{-1} Spectral Region," Final Report of Contract Number DAAG-29-79-C0131 (August 1983).

OPTICAL PROPERTIES OF Ni; CAVITY MEASUREMENTS AT FIR AND SUBMM λ RANGES; RESISTIVITY RATIOS, AND LINKAGE EQUATIONS*

R.J. Bell, R.W. Alexander, M.A. Ordal, and L.L. Long
Physics Department
University of Missouri-Rolla
Rolla, MO 65401

and

M. Querry
Physics Department
University of Missouri-Kansas City
Kansas City, MO 64110

*U.S. Army Grant: DAAA-15-85-K-0004 (M. Milham)

RECENT PUBLICATIONS:

A) M.A. Ordal, L.L. Long, R.A. Paul, R.W. Alexander, Jr., and R.J. Bell, "Metals and Graphite: Predicting Optical Properties in the Submm λ and mm λ Ranges"; Proceedings of the 1984 CRDC Scientific Conference on Obscuration and Aerosol Research, R.H. Kohl, ed., p.179.

B) L.L. Long, M.A. Ordal, R.J. Bell and R.W. Alexander, Jr., "The Optical Constants of Smoke Materials in the Submm λ and mm λ"; Proceedings of the 1984 CRDC Scientific Conference on Obscuration and Aerosol Research, R.H. Kohl, ed., p.167.

C) M.A. Ordal, R.J. Bell, R.W. Alexander, Jr., and R.A. Paul, "Absorption Coefficient of DuPont Teflon FEP in the 20-130 Wavenumber Range", Appl. Opt. (Sept. 1985).

D) M.A. Ordal, R.J. Bell, R.W. Alexander, Jr., and M.R. Querry, "Optical Properties of 14 Metals in the Infrared and Far Infrared: Al, Co, Cu, Au, Fe, Pb, Mo, Ni, Pd, Pt, Ag, Ti, V and W," accepted by Appl. Opt.

ABSTRACT

The nonresonant cavity technique (Pinkerton and Sievers) has been extended in computation approaches eliminating needless approximations and improving data inversion to obtain the normalized surface resistance and reactance. New optical data for Ni at low frequencies are introduced and show that the data obtained from the nonresonant cavity technique fit well with data obtained differently with the Drude model. The scattering frequency, ω_τ, the plasma frequency, ω_p, and the optical resistivities, ρ_{opt}, for 14 elemental metals are tabulated using our and open literature data. We provide three tables of equations linking the complex dielectric function, the complex index of refraction, the complex normalized surface impedance, and the complex conductivity with and without the Drude model. Also included are the reflectance at normal incidence (nonmagnetic materials; no overlayer) and the absorption coefficient in all of the different parameter sets.

I. INTRODUCTION

Far infrared, submm λ, and mm λ studies of metals are being made. We are using Ni as a standard in these wavelength ranges to study many other metals[1,2] and in this paper we introduce new experimental data for Ni. For these experiments on metals the non-resonant cavity technique initiated by Pinkerton and Sievers[3] to measure the normalized surface resistance has been reexamined by us resulting in approximate relations replaced by exact equations. Along with these experimental developments we have also developed computer techniques for easy, careful data analysis. The nonresonant cavity technique has some low frequency difficulties on which we're still working.

In our studies on metals from the literature[1,2], we have fit the experimental dielectric functions of fourteen metals with the free electron Drude model parameters: the scattering frequency ω_τ and the plasma frequency ω_p. The Drude model should be valid for $\omega \lesssim 10^3$ cm^{-1} since most interband effects occur at the higher frequencies. However, the criteria that the dc resistivity ρ_o, should equal the high frequency resistivity $\rho_{opt} = 60\omega_\tau/\omega_p^2$, is not always found as we'll discuss with Table I.

In our studies we have found any of four different parameters are often used in describing the optical properties of metals. These are the complex dielectric function $\varepsilon_c = \varepsilon_1+i\varepsilon_2$, the complex indices of refraction $n_c = n+ik$, the normalized surface impedance $z_c = r+ix$, and the conductivity $\sigma_c = \sigma_1+i\sigma_2$. In these equations n is the index of refraction; k is the extinction coefficient; $z_c = z/(4\pi/c)$ is given in terms of the complex surface impedance z; r is the normalized surface resistance; and x is the normalized surface reactance. We present an exhaustive table linking these parameters in all combinations to help ease the transition from one set of parameters to another. Also we include the Drude model parameters ω_τ and ω_p in these linkage equations.

Often enough, one is simply interested in the reflectance and the absorption coefficient for a metal; so, we present those relations in terms of n_c, z_c, σ_c, ε_c, ε_∞, ω_τ, and ω_p where ε_∞ is the high frequency dielectric constant of the metals.

TABLE I. RESULTS OF A DRUDE MODEL FIT TO THE DIELECTRIC FUNCTION OF 14 METALS IN THE FAR IR

Metal	$10^{-2}\omega_\tau$ (cm^{-1})	$10^{-4}\omega_p$ (cm^{-1})	ρ_{opt} ($\mu\Omega$ cm)	ρ_o ($\mu\Omega$ cm)	$\frac{\rho_o}{\rho_{opt.}}$
Al	6.60	11.9	2.80	2.74	0.98
Co	2.95	3.20	17.3	5.80	0.34
Cu	0.732	5.96	1.24	1.70	1.3
Au	2.15	7.28	2.43	2.20	0.91
Fe	1.47	3.30	8.10	9.80	1.20
Pb	16.3	5.94	27.7	21.0	0.76
Mo	4.12	6.02	6.82	5.33	0.78
Ni	3.52	3.94	13.3	7.04	0.52
Pd	1.24	4.40	3.84	10.55	2.8
Pt	5.58	4.15	19.4	10.42	0.54
Ag	1.45	7.27	1.65	1.61	0.98
Ti	3.82	2.03	55.6	43.1	0.78
V	4.89	4.16	17.0	19.9	1.2
W	4.87	5.17	10.9	5.33	0.49

II. NON-RESONANT CAVITY TECHNIQUE

The basic idea of a non-resonant cavity is that it has no modes established in the cavity[3]. By distorting the geometry of the cavity, by keeping the input and output ports away from each other, by making the cavity large, and by optimizing the size of the input and output orifices, nonresonance is achieved as long as the radiation wavelength is not too large. Fig. 1 is a drawing of our cavity made of Aℓ.

For the details we refer the reader to Pinkerton and Siever's paper[3]. We replace their approximations involved with Eqs. (22), (25), and (26) with

$$\underset{J}{P}(\omega) \equiv \int_0^1 \left[A_p(\eta)+A_s(\eta)\right]\eta \, d\eta \tag{1}$$

which for the sample is

$$P_s(\omega)=\left(\frac{I_r(\omega)}{I_s(\omega)}\right)\left[\frac{2S_1+(S_2+S_3+S_4)P_r(\omega)}{S_4}\right] - \left[\frac{2S_1+(S_2+S_3)P_r(\omega)}{S_4}\right] \tag{2}$$

and which for the reference plate is

$$\begin{aligned} P(\omega) \equiv 4r\Bigg\{&\left[1+\frac{1}{r^2(1+g^2)}\right] - \left[r+\frac{1}{r^3(1+g^2)^2}\right]\ln\left(1+2r+r^2(1+g^2)\right) \\ &+ r\ln\left(r^2(1+g^2)\right) \\ &+ \frac{(1-g^2)}{g}\left[r\tan^{-1}\left(\frac{g}{1+r(1+g^2)}\right) + \frac{1}{r^3(1+g^2)^2}\tan^{-1}\left(\frac{rg}{1+r}\right)\right]\Bigg\} \end{aligned} \tag{3}$$

where $A_p(\eta)$ and $A_s(\eta)$ are (1-R) for each state of polarization with $\eta=\cos\theta$ in

terms of the angle of incidence, θ. In these Eqs. $I_r(\omega)$ is the signal intensity transmitted through the cavity with the reference end plate in position; $I_s(\omega)$ is the intensity when the reference end plate is replaced with the sample. The areas are defined in the figure caption of Fig. 1. The definition of ξ is that

$$\xi \equiv k/n = -\frac{x}{r} \tag{4}$$

for the reference metal plate. Our reference metal is the same Aℓ from which the cavity itself was made.

For several metals, j, of known optical constants we empirically found in the FIR that the integrals can be replaced with

$$P_s(\omega) = \frac{1}{D + Er_s + F/r_s} \tag{5}$$

with D = 1.495, E = -10.56 and F = 0.1876 for $10^{-4} \leq r_s \leq 5\times10^{-2}$. D, E and F are the same for all metals. The procedure is that one knows r and x for the reference sample and therefore knows ξ and $P_R(\omega)$. One then measures $I_r(\omega)$ and $I_s(\omega)$ (knowing the areas) and obtains $P_s(\omega)$[or in general $P_j(\omega)$] for the sample. Then the normalized surface resistance $r_j(\omega)$ for the sample is obtained from

$$r_s = \frac{1}{2E}\left\{\frac{1}{P_s(\omega)} - D - \left[\left(D - \frac{1}{P_s(\omega)}\right)^2 - 4EF\right]^{1/2}\right\} \tag{6}$$

The advantage of this computational technique is that it gives r_j in a straight forward calculation without having to invest Eqs. (2)-(4) for r_j. Our inversion of $P_j(\omega)$ to obtain $r_j(\omega)$ is crudely

$$r_j(\omega) = \frac{3P_j(\omega)}{16}[1+P_j(\omega)] \tag{7}$$

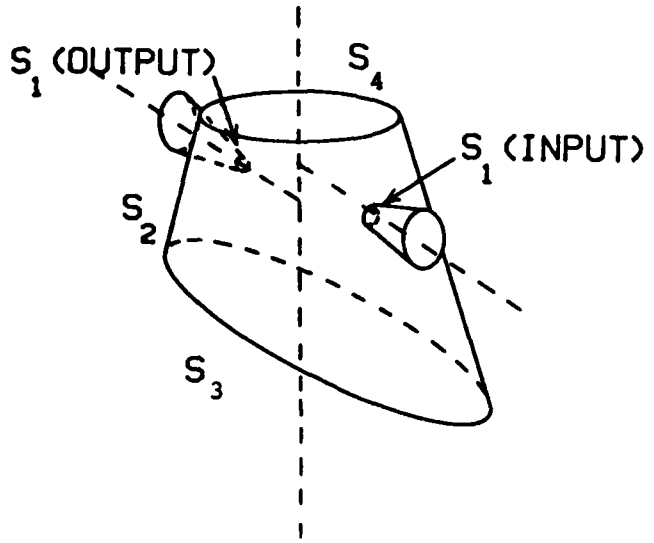

FIGURE 1. INTERIOR SURFACES OF OUR NON-RESONANT CAVITY. In use the top surface of area S_4 is horizontal as shown. The input/output holes of area S_1 lead to small input/output cones machined in the cavity body. A large brass light cone (not shown) attaches to the cavity body on the input side. The axes of the input and output cones lie in the same horizontal plane and are parallel and noncolinear (the axes lie about 2 cm apart). The sidewalls have an area S_2 (excluding the area of the input/output holes). The sidewalls of our cavity slope about one degree from vertical--the bottom opening of area S_3 being larger than the top opening of area S_4. The bottom of the cavity body slopes about four degrees from horizontal.

This equation is useful for quick and easy estimates and as a seed for data fitting techniques.

One only has r_j but also wants x_j for the jth sample; slopes can be used to obtain the x_j. Noting

$$r_j = n/(n^2+k^2) \tag{8}$$

and defining

$$0 \leq L_j \equiv \frac{\omega}{r_j}\frac{dr_j}{d\omega} \leq 1/2 \tag{9}$$

one has

$$n = L_j/r_j \tag{10}$$

and

$$k = [(n/r_j)-n^2]^{\frac{1}{2}} \tag{11}$$

In terms of the Drude model

$$\omega_\tau = \left[\left(\frac{2\omega\sqrt{L}}{1-2L}\right)\sqrt{1-L}\right] \tag{12}$$

and

$$\omega_p = \left[\frac{\omega}{r}\sqrt{\frac{L}{1-2L}}\right] \tag{13}$$

The main problem with the nonresonant cavity is that at low frequencies modes develop as seen in Fig. 2. The transmittance of the cavity with the reference Aℓ alloy plate in the sample plate position is not flat with respect to wavenumber. The gradual slope to about 70 cm^{-1} is tolerable when used in the ratio $I_S(\omega)/I_R(\omega)$ of Eq. (2). However, the slope at lower frequencies due to cavity modes is too great to be reliable. We're working on larger and more complex cavity designs to partially overcome these problems.

III. Ni AND OTHER METAL STUDIES

In Fig. 3 we bring together the dielectric data obtained by us employing different experimental techniques. We show that the nonresonant cavity produces good data using our experimental-computational procedures. At high frequencies we measured the Ni reflectance and used Kramers-Kronig analysis to obtain $-\varepsilon_1$ and ε_2. Interband effects subsided by about $\omega \simeq 700$ cm^{-1}. From 180 cm^{-1} to 700 cm^{-1} we fit the data with the Drude model obtaining $\omega_\tau = 352$ cm^{-1} and $\omega_p = 3.98 \times 10^4$ cm^{-1}. (For the Aℓ alloy we knew[1,2] $\omega_\tau = 4.0 \times 10^3$ cm^{-1} and $\omega_p = 1.1 \times 10^5$ cm^{-1}.) The Drude model extrapolation is close to the nonresonant cavity results as seen in Fig. 3. Agreement is within estimated errors for the cavity data and the Drude model extrapolation.

From the literature we fit $-\varepsilon_1$ and ε_2 data at low frequencies (below interband effects) for 14 metals[2]. Also we introduced new data for Cu, Fe, and Ni. In Table I we tabulate ω_τ, ω_p, ρ_{opt}, ρ_o, and ρ_o/ρ_{opt} for these metals. The last ratio would be equal unity if the Drude model were perfect.

IV. LINKAGE EQUATIONS

Often in our literature searches we encountered optical data given in different formats. To overcome these communication problems we fabricated the Tables II, III, and IV.

Table II is a collection of equations involving the model-free parameters ε_c, z_c, n_c, and σ_c. All parameter combinations are given.

In Table III all the combinations of equations are given in terms of the free electron Drude model. Also in Table III one has ρ_{opt} and ρ_o in terms of the other parameters.

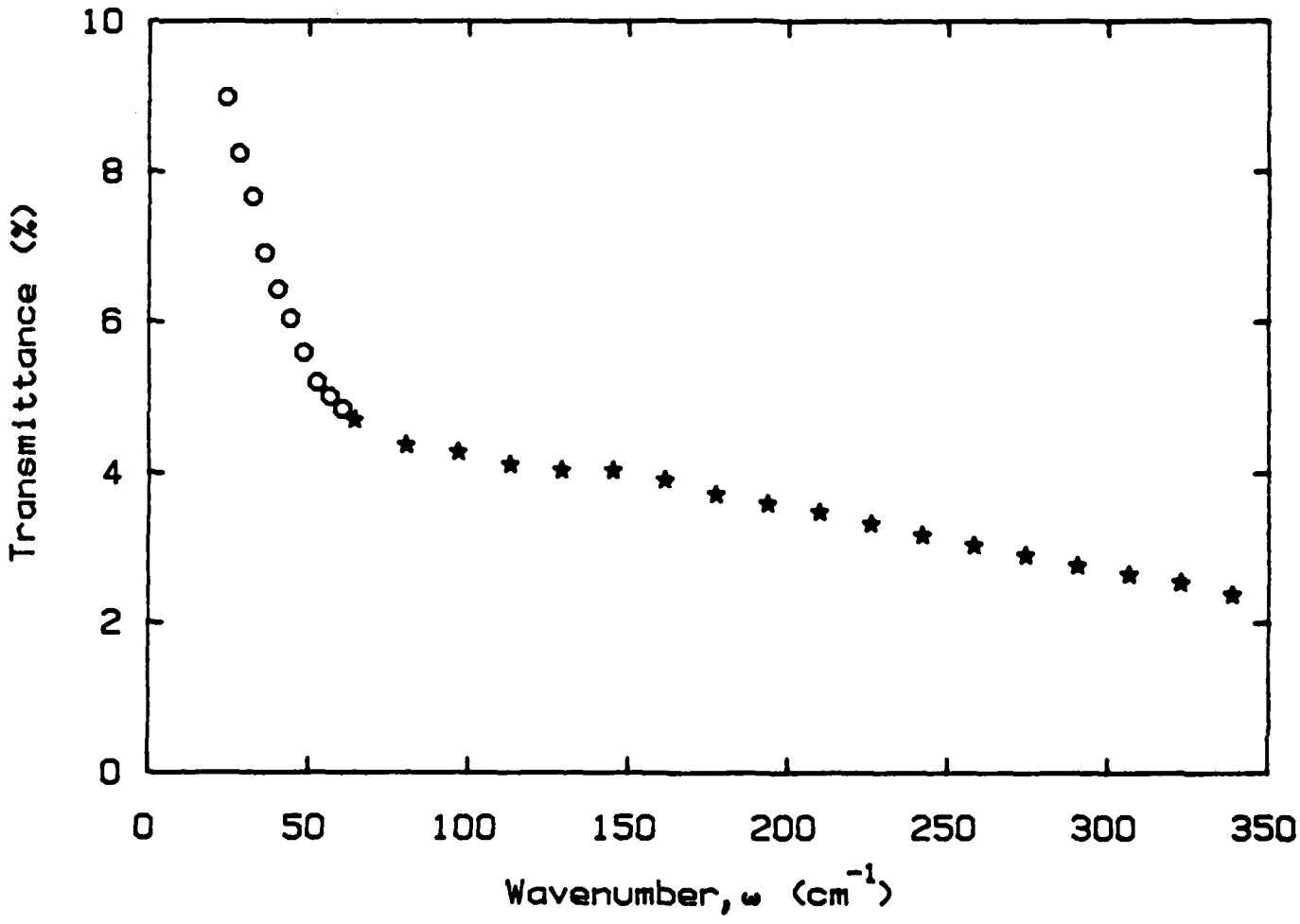

FIGURE 2. TRANSMITTANCE OF OUR NONRESONANT Aℓ ALLOY CAVITY VS FREQUENCY.

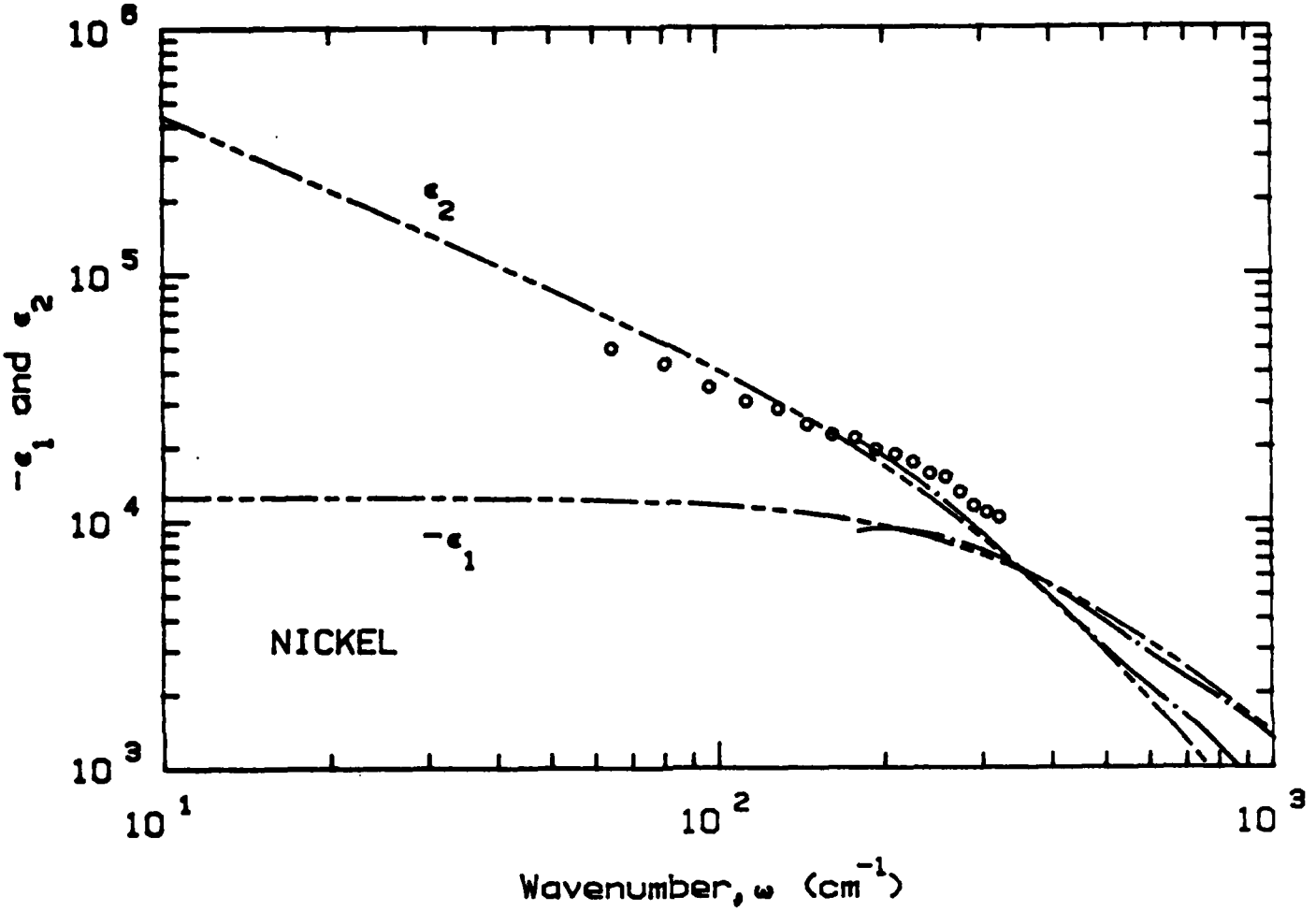

FIGURE 3. NICKEL: NONRESONANT CAVITY CALIBRATION RESULTS. The symbols are the nonresonant cavity results for ϵ_2 when ω_τ=4000 cm^{-1} and ω_p=110 000 cm^{-1} are used to calculate n and k of the Al alloy reference metal. The dashed-dot lines are $-\epsilon_1$ and ϵ_2 obtained from Kramers Kronig analysis of reflectance measurements made in the 180 to 50 000 cm^{-1} region. The dashed lines are the Drude model fit extrapolations for $-\epsilon_1$ and ϵ_2. The Drude model fit parameters are $\omega_\tau = 3.52 \times 10^2$ and $\omega_p = 3.98 \times 10^4$.

TABLE II. LINKAGE EQUATIONS

$$0 \geq \varepsilon_1 = (n^2-k^2) = \left[\frac{r^2-x^2}{(r^2+x^2)^2}\right] = \varepsilon_\infty - \frac{2\sigma_2}{c\omega}$$

$$0 \leq \varepsilon_2 = 2nk = \left[\frac{-2rx}{(r^2+x^2)^2}\right] = \frac{2\sigma_1}{c\omega}$$

$$0 \leq n = \sqrt{\frac{\varepsilon_1+\sqrt{\varepsilon_1^2+\varepsilon_2^2}}{2}} = \left[\frac{r}{r^2+x^2}\right] = \sqrt{\frac{2\sigma_2-c\omega\varepsilon_\infty}{2\omega c}}\left\{-1+\sqrt{1+\left[\frac{2\sigma_1}{c\omega\varepsilon_\infty-2\sigma_2}\right]^2}\right\}^{1/2}$$

$$0 \leq k = \sqrt{\frac{-\varepsilon_1+\sqrt{\varepsilon_1^2+\varepsilon_2^2}}{2}} = \left[\frac{-x}{r^2+x^2}\right] = \sqrt{\frac{2\sigma_2-c\omega\varepsilon_\infty}{2\omega c}}\left\{1+\sqrt{1+\left[\frac{2\sigma_1}{c\omega\varepsilon_\infty-2\sigma_2}\right]^2}\right\}^{1/2}$$

$$0 \leq r = \left[\frac{n}{n^2+k^2}\right] = \sqrt{\frac{\varepsilon_1+\sqrt{\varepsilon_1^2+\varepsilon_2^2}}{2(\varepsilon_1^2+\varepsilon_2^2)}} = \sqrt{\frac{c\omega}{2}}\left\{\frac{-(2\sigma_2-c\omega\varepsilon_\infty)+\sqrt{(2\sigma_2-c\varepsilon_\infty\omega)^2+4\sigma_1^2}}{(2\sigma_2-c\varepsilon_\infty\omega)^2+4\sigma_1^2}\right\}^{1/2}$$

$$0 \geq x = \left[\frac{-k}{n^2+k^2}\right] = -\sqrt{\frac{-\varepsilon_1+\sqrt{\varepsilon_1^2+\varepsilon_2^2}}{2(\varepsilon_1^2+\varepsilon_2^2)}} = -\sqrt{\frac{c\omega}{2}}\left\{\frac{(2\sigma_2-c\omega\varepsilon_\infty)+\sqrt{(2\sigma_2-c\varepsilon_\infty\omega)^2+4\sigma_1^2}}{(2\sigma_2-c\varepsilon_\infty\omega)^2+4\sigma_1^2}\right\}^{1/2}$$

$$0 \leq \sigma_1 = \frac{c\omega\varepsilon_2}{2} = c\omega nk = \frac{-c\omega rx}{(r^2+x^2)^2}$$

$$0 \leq \sigma_2 = \frac{c\omega}{2}(\varepsilon_\infty-\varepsilon_1) = \frac{c\omega}{2}(\varepsilon_\infty-n^2+k^2) = \frac{c\omega}{2}\left[\varepsilon_\infty+\frac{x^2-r^2}{(r^2+x^2)^2}\right]$$

TABLE III. In the Drude model the real and imaginary parts of n_c, ε_c, z_c and σ_c are presented in terms of ω, ω_τ, ω_p and ε_∞. The scattering, ω_τ, and plasma, ω_p, frequencies are given in terms of the real and imaginary parts of n_c, ε_c, z_c, and σ_c. The high frequency resistivity, the real part of the complex optical resistivity, is given in the four sets of parameters. Also the dc conductivity, σ_o (sec^{-1}), is related to the dc resistivity ρ_o (ohm-cm).

$$0 \le n = \left\{ \frac{[(\omega_\tau^2+\omega^2)\varepsilon_\infty-\omega_p^2] + \sqrt{[(\omega_\tau^2+\omega^2)\varepsilon_\infty-\omega_p^2]^2+\omega_p^4\omega_\tau^2/\omega^2}}{2(\omega_\tau^2+\omega^2)} \right\}^{\frac{1}{2}},$$

$$0 \le k = \left\{ \frac{-[(\omega_\tau^2+\omega^2)\varepsilon_\infty-\omega_p^2] + \sqrt{[(\omega_\tau^2+\omega^2)\varepsilon_\infty-\omega_p^2]^2+\omega_p^4\omega_\tau^2/\omega^2}}{2(\omega_\tau^2+\omega^2)} \right\}^{\frac{1}{2}},$$

$$\varepsilon_1 = \left(\varepsilon_\infty - \frac{\omega_p^2/\omega_\tau^2}{1+\omega^2/\omega_\tau^2} \right)$$

$$0 \le \varepsilon_2 = \left(\frac{\omega_p^2/(\omega_\tau\omega)}{1+\omega^2/\omega_\tau^2} \right),$$

$$0 \le r = \sqrt{\frac{\omega_\tau^2+\omega^2}{2}} \left\{ \frac{[(\omega_\tau^2+\omega^2)\varepsilon_\infty-\omega_p^2] + \sqrt{[(\omega_\tau^2+\omega^2)\varepsilon_\infty-\omega_p^2]^2+\omega_p^4\omega_\tau^2/\omega^2}}{[(\omega_\tau^2+\omega^2)\varepsilon_\infty-\omega_p^2]^2+\omega_p^4\omega_\tau^2/\omega^2} \right\}^{\frac{1}{2}},$$

$$0 \ge x = -\sqrt{\frac{\omega_\tau^2+\omega^2}{2}} \left\{ \frac{-[(\omega_\tau^2+\omega^2)\varepsilon_\infty-\omega_p^2] + \sqrt{[(\omega_\tau^2+\omega^2)\varepsilon_\infty-\omega_p^2]^2+\omega_p^4\omega_\tau^2/\omega^2}}{[(\omega_\tau^2+\omega^2)\varepsilon_\infty-\omega_p^2]^2+\omega_p^4\omega_\tau^2/\omega^2} \right\}^{\frac{1}{2}},$$

$$0 \le \sigma_1 \ (sec^{-1}) = \frac{c\omega_p^2}{2\omega_\tau(1+\omega^2/\omega_\tau^2)}$$

$$0 \le \sigma_2 \ (sec^{-1}) = \frac{c\omega_p^2\omega}{2\omega_\tau^2(1+\omega^2/\omega_\tau^2)}$$

$$0 \le \omega_\tau = \left(\frac{\omega\varepsilon_2}{\varepsilon_\infty-\varepsilon_1}\right) = \left(\frac{2nk\omega}{\varepsilon_\infty+k^2-n^2}\right) = \left(\frac{-2rx\omega}{(r^2+x^2)^2\varepsilon_\infty+x^2-r^2}\right) = \frac{\omega\sigma_1}{\sigma_2},$$

$$0 \le \omega_p = \omega\sqrt{\frac{(\varepsilon_\infty-\varepsilon_1)^2+\varepsilon_2^2}{\varepsilon_\infty-\varepsilon_1}} = \omega\left(\frac{(\varepsilon_\infty+k^2-n^2)^2+4n^2k^2}{\varepsilon_\infty+k^2-n^2}\right)^{\frac{1}{2}} = \omega\left(\frac{[(x^2+r^2)^2\varepsilon_\infty+x^2-r^2]^2+4x^2r^2}{(r^2+x^2)^2[(x^2+r^2)^2\varepsilon_\infty+x^2-r^2]}\right)^{\frac{1}{2}}$$

$$= \sqrt{\frac{2\omega(\sigma_1^2+\sigma_2^2)}{c\sigma_2}}$$

$$\rho_{opt.}(\Omega\text{-cm}) = \frac{2x10^{-9}c\omega_\tau}{\omega_p^2} = \frac{2x10^{-9}c\varepsilon_2}{\omega[(\varepsilon_\infty-\varepsilon_1)^2+\varepsilon_2^2]} = \frac{4x10^{-9}cnk}{\omega[(\varepsilon_\infty+k^2-n^2)^2+(2nk)^2]}$$

$$= \frac{-120\ rx(r^2+x^2)^2}{\omega([\varepsilon_\infty(r^2+x^2)^2+x^2-r^2]^2+4r^2x^2)}$$

$$\sigma_o(sec^{-1}) = \frac{10^{-9}c^2}{\rho_o(\Omega\text{-cm})} = 2\pi c\sigma_o(cm^{-1})$$

TABLE IV. Reflectances at normal incidence (vacuum overlayer) for any material. For $R(\omega, \omega_\tau, \omega_p)$ there is an approximation (as stated in the text).

$$R = \frac{(n-1)^2+k^2}{(n+1)^2+k^2} = \frac{(r^2+x^2-r)^2+x^2}{(r^2+x^2+r)^2+x^2} = \frac{1+\sqrt{\epsilon_1^2+\epsilon_2^2} - \sqrt{2}\sqrt{\epsilon_1+\sqrt{\epsilon_1^2+\epsilon_2^2}}}{1+\sqrt{\epsilon_1^2+\epsilon_2^2} + \sqrt{2}\sqrt{\epsilon_1+\sqrt{\epsilon_1^2+\epsilon_2^2}}}$$

$$= \left(\frac{c\omega+\sqrt{(c\omega\epsilon_\infty-2\sigma_2)^2+4\sigma_1^2} - \sqrt{2c\omega}\sqrt{(c\omega\epsilon_\infty-2\sigma_2) + \sqrt{(c\omega\epsilon_\infty-2\sigma_2)^2 + 4\sigma_1^2}}}{c\omega+\sqrt{(c\omega\epsilon_\infty-2\sigma_2)^2+4\sigma_1^2} + \sqrt{2c\omega}\sqrt{(c\omega\epsilon_\infty-2\sigma_2) + \sqrt{(c\omega\epsilon_\infty-2\sigma_2)^2 + 4\sigma_1^2}}}\right)$$

$$= \frac{\sqrt{1+\omega^2/\omega_\tau^2} + [\omega_p^2/(\omega_\tau\omega)] - \sqrt{2}\sqrt{\omega_p^2/(\omega_\tau\omega)}\sqrt{-(\omega/\omega_\tau)+\sqrt{1+\omega^2/\omega_\tau^2}}}{\sqrt{1+\omega^2/\omega_\tau^2} + [\omega_p^2/(\omega_\tau\omega)] + \sqrt{2}\sqrt{\omega_p^2/(\omega_\tau\omega)}\sqrt{-(\omega/\omega_\tau)+\sqrt{1+\omega^2/\omega_\tau^2}}}$$

The reflectance at normal incidence (nonmagnetic material, vac. overlayer) of any material is given in Table IV in terms of all of the parameters. The only approximation in any of the tables is that $\epsilon_\infty << (\omega_p^2/\omega_\tau^2)/(1+\omega^2/\omega_\tau^2)$ in the last R equation in terms of ω_p and ω_τ. The approximation should be good to better than 1% for metal with $\omega \lesssim 10^3$ cm^{-1}.

The absorption coefficient of any linear material, $\alpha(cm^{-1})$, is given by

$$\alpha = 4\pi k\omega \qquad (14)$$

and by using Tables II and III one can have α via k in any set of optical parameters.

V. FUTURE WORK

We will soon finish the calibration of new nonresonant cavities for metal studies at low ω. We plan to use the knowledge of metals to study graphite at low ω. Major efforts will be made to examine liquid samples at low ω.

VI. SUMMARY

We have further developed the nonresonant cavity technique[3] such that accurate measurements of the normalized surface resistance of many conductors can be made at low ω. We have introduced new data for Ni and shown that the results look reasonable[1,2]. See Fig. 2.

We have reported the ω_τ's and ω_p's for fourteen different metals[2] - part of the data such as for Cu, Fe, and Ni is new. See Table I. We gave the ratios of ρ_o/ρ_{opt} for each metal and find that the ratio is not always unity as it should be.

In working in different disciplines, one encounters different forms of the optical constants. We have presented Tables II-IV which give all the combinations of $\epsilon_c, n_c, z_c, \sigma_c$ and ω_τ and ω_p that exist. Also the normal incident reflectances, R, (vacuum overlayer) are given in all forms as is the absorption coefficients, α.

VII. REFERENCES

1. M.A. Ordal, L.L. Long, R.J. Bell, S.E. Bell, R.R. Bell, R.W. Alexander, Jr. and C.A. Ward, Appl. Opt. 22, 1099 (1983).

2. M.A. Ordal, R.J. Bell, R.W. Alexander, Jr., and M.R. Querry, accepted 8-8-85 by Appl. Opt.

3. F.E. Pinkerton and A.J. Sievers, Infrared Phys. 22, 377 (1982).

III. TUTORIAL REVIEW:

SMALL NEEDLE-SHAPED FILAMENTS BASED ON CARBON

SMALL, NEEDLE-SHAPED FILAMENTS BASED ON CARBON

-A Review-

Mildred S. Dresselhaus
Departments of Electrical Engineering and Computer Science,
and Physics
Massachusetts Institute of Technology
Cambridge, MA 02139

Harris A. Goldberg
Celanese Research Company
86, Morris Avenue
Summit, NJ 07901

Ian L. Spain
Department of Physics
Colorado State University
Fort Collins, CO 80523

ABSTRACT

A review is given of needle-shaped filaments of carbon which have potential applications as obscurants. Three main types of carbon filament are discussed: commercial fibers prepared by heat-treating an organic precursor, filaments grown by catalytic decomposition of a hydrocarbon onto a heated substrate, and those by the bombardment of a carbon surface by energetic Ar^+ ions. Modification of the physical properties by thermal annealing and metal coating, and a chemical modification called intercalation are described. It is shown that filament sizes and electrical conductivity, which control scattering and absorption cross-sections, can be varied over wide ranges of values.

ACKNOWLEDGEMENT

[On behalf of the participants and the aerosol research community, the editor would like to thank the authors and, particularly, Ian Spain who organized and put together this review.]

INTRODUCTION

The subject of Obscuration Science may be considered to consist of two major components: firstly, the physics of scattering by small particles; secondly, the science of the small particles themselves. The latter part has tended to be neglected in CRDC Conferences, but it is clear that optimization of scattering and absorption of radiation can only be achieved by carefully matching the specific needs of the problem to well defined properties of the scattering particles.

The objective of the present paper is to discuss the properties of a class of needle-shaped particles based on carbon. The properties of carbon filaments can be modified considerably by thermal annealing, metal coating, or by a chemical modification, called intercalation. As a result, these materials are very interesting candidates for various applications in Obscuration Science.

It is emphasized that much research needs to be done in bridging the gap between the two components mentioned above. This paper will describe the current status of materials availability, and mention areas of research. It will not include material on the interaction of radiation with carbon filaments, since this work is still in its infancy.

The organization of this review will be straightforward. First, the various types of carbon filaments will be introduced with their properties described. Then the process of intercalation will be defined, and the property modifications brought about by this process described. The electrical and structural properties of intercalated fibers will then be considered. The review is brief, and references are made to more extensive descriptions. Only those material properties of relevance to the application of obscuration will be included.

COMMERCIAL CARBON FIBERS

The most extensive source of carbon filaments is commercial carbon fibers. These fibers are continuous, and have diameters which are typically ~7-10 μm. A typical yarn consists of several hundred to several thousand filaments. The yarn can be chopped into sub-millimeter lengths without difficulty.

The two major commercial fibers are based on the continuous extrusion of polyacrylonitrile (PAN) or pitch into thin filaments, followed by thermal processing steps (Sittig, 1980). These are outlined for PAN fibers in Fig. 1 and have been reviewed recently by Olivé and Olivé (1983). The essential steps in the process are, first, the spinning process, forming the precursor materials

into a continuous filament; second , a preoxidation step makes the fibers more thermally stable; and third, a carbonization process, during which a major weight loss occurs due to evolution of H, O, and N. The chemistry of the preoxidation step is not fully understood, although it is clear that polymer cross-links are formed which result in the formation of extended ring structures. These structures grow in the carbonization process. Sometimes a fourth processing step is used, where the fiber is heat-treated in an inert atmosphere to temperatures in excess of 2000°C, resulting in the further growth of these extended carbon ribbons, and partial graphitization, in which the ribbons lock into a regular sequence with respect to their neighbors.

The resulting structure can be imagined as a set of interacting ribbons of defective hexagonal carbon layers, illustrated schematically in Fig 2. A simple model could be constructed by tearing a newspaper into ribbons, then arranging these ribbons into a loosely packed rope. Each page of the newspaper represents a carbon (hexagonal) layer, with neighboring pages stacked in a disordered (turbostratic) way.

As the heat treatment temperature (T_{HT}) of the carbonization step increases, a number of changes occur in the structure (see Reynolds (1973)).

1. Defects in the carbon hexagon layers (missing atoms, bond disorder, impurities. . .) are reduced.
2. The carbon ribbons increase in average width and length.
3. The average number of layers stacked together tends to increase, and at sufficiently high T_{HT} ($\gtrsim$2200°C) the layers begin to lock into an ordered sequence on an atomic scale (graphitization).
4. The density of voids tends to decrease, so that material density increases.

The layer planes tend to be randomly disordered within a plane perpendicular to the axis of PAN fibers, with a preferred orientation parallel to the external surface. The layer planes are arranged radially in pitch-precursor fibers. PAN fibers are made with circular or "dog-bone" shapes while pitch fibers can be circular or "PAC-man" shaped (see Fig. 3).

The layer planes are not perfectly aligned along the fiber axis, and the average misorientation angle tends to decrease with T_{HT}, but is also influenced strongly by the tension under which the fiber is held during processing.

The misorientation of the layer planes can be measured by looking at the orientation of the 002 (or any 00h) diffraction lines. The full width at half maximum of those diffraction lines lies in the range 7-30 degrees, with the best oriented fibers having the highest modulus.

Structural modifications are accompanied by changes in physical properties. An important property is the modulus of elasticity. $E \equiv \sigma \ell_0/\Delta\ell$) where σ is the stress applied to the filament, ℓ_0 the initial length, and $\Delta\ell$ the increase of length. The variations of E with T_{HT} is sketched in Fig. 4 for a PAN fiber. The highest values approach that of an ideal system of aligned hexagonal planes (graphite), E = 1020 GPa (1.5×10^8 psi) [Kelly (1981)].

The variation of E can be understood as arising from two main causes: first, the increase in the modulus with increasing orientation of the stiff layer planes; second, variability in the ease with which the layer planes can slide past one another (i.e. sheer) [Goldberg (1985) and references therein].

Since there is a close connection between the elastic modulus and structural perfection, it is conventional to characterize fibers by their Young's modulus. The units used in the USA are Mpsi (pounds force per square inch x 10^6), but SI units will also be used here.

The strain to failure ($\Delta\ell/\ell_0$) is lower for higher modulus fibers (Table I shows typical data for two commercial fibers) and also the stress to failure. Accordingly, lower modulus fibers have generally been used for critical applications, such as aircraft fiber--epoxy laminates. This is also partly due to cost considerations, since heat treatment to higher temperatures is expensive. For instance, Celion fibers (T_{HT} ~1200°C, E ~30 Msi) cost ~$40/kg, while GY-70 fibers (T_{HT}) ~2200C, E~75 Msi) cost ~$1300/kg.

The electronic properties of fibers depend sensitively on structural perfection [see Spain (1981)]. The longitudinal resistivity as a function of modulus is shown in Fig. 5 for PAN fibers. The rapid drop as modulus rises to ~35 Msi (240 GPa) is largely due to the closing of the gap between conduction and valence states as hydrogen is removed from the polymer. At the highest moduli, a further decrease is due to growth of ribbons and graphitization, but the resistivity still remains ~ twelve times that of pure graphite (~5×10^{-4} Ωcm) for PAN fibers [Spain et al. (1983)] and about five times higher for pitch fibers [Bright and Singer (1978)]. The transverse resistivity has not been measured on any fiber, but is probably higher than the longitudinal value, and dependent on the type of fiber.

Measurements of the resistivity must be carried out with care to ensure that the current does not heat the fiber appreciably [Spain et al. (1983)]. A technique for measuring fiber resistance at ~10GHz without applying contact has been described [Azzeer et al. (1985)]. The conductivity is the same at this frequency as at DC conditions, as would be expected theoretically.

A commercial process allows nickel to be plated onto carbon fibers [Beetz and Brinen (1983)] and several metals can be evaporated on easily (e.g., Pt, Au, Ni . . .). The thickness of such coatings can be varied readily between ~0.1-1 μm. Since metals have much higher electrical conductivities than the fibers, the net DC resistance per unit length is typically dominated by the metal, except for cases where the coating thickness is less than a few percent of the fiber diameter. The mechanical properties of the carbon fiber are retained. At very high frequency, the skin depth of the metal can become sufficiently small that the electric currents induced by the external fields are limited to the metal layer (e.g., for a typical metal, the skin depth is ~0.1 μm at 100 GHz). Thus, at very high frequencies, one may only need to know the conductivity of the metal coating in order to determine the electromagnetic properties. If the coating thickness becomes less than the mean-free-path of the conduction electrons in the metal, then a size-effect on the conductivity must be taken into account [see for example Ziman (1960)]. The mean free path of electrons in copper at room temperature is ~0.03 μm, so that size effects could reduce the conductivity of copper coatings of 0.01 μm thickness appreciably.

FILAMENTS PREPARED BY CHEMICAL VAPOUR DEPOSITION (CVD)

Carbon filaments can be prepared by passing a hydrocarbon/hydrogen mixture over a heated substrate with a catalyst such as Fe or Ni (Fig 6). Much of the earlier work was carried out on this process in order to understand growth of filaments in nuclear reactors [Baker et al. (1972, 1973)]. However, Koyama (1972) showed that long fibers could be grown (≥300 mm for example) with diameter ~3-100 μm from benzene/hydrogen mixtures. These are called benzene-derived fibers (BDF). These fibers have been studied extensively by Japanese workers [Koyama et al. (1972); Koyama and Endo (1974); Koyama, Endo and Hishiyama (1974); Oberlin et al. (1976), Endo et al. (1977); Endo et al. (1982)] and in the laboratory of one of the present authors (M.S.D.) (see later references). Similar fibers have also been prepared from natural gas, and studied at General Motors Research Labs [Tibbetts (1983)].

Although it has not been possible to produce continuous lengths, there are many polymer reinforcing applications which can use chopped fibers. The possibility of producing vapour grown fibers with superior properties at considerably reduced costs (e.g., ~$10/kg) compared to PAN or pitch fibers, make them attractive candidates for such applications.

The growth mechanism is interesting. The small particles of catalyst metal act as sites where the hydrocarbon decomposes to deposited carbon and hydrogen gas [Baker et al. (1972, 1973); Oberlin et al. (1976)]. The carbon particles then diffuse to the base of the catalyst particle,

allowing a hollow filament to grow underneath it (Fig. 6). The structure of larger diameter filaments is that of "tree rings" of carbon planes (Fig. 7).

Although the growth process occurs at a relatively low temperature (typically $\lesssim$1100°C), the carbon planes exhibit significant ordering [Koyama et al. (1974); Endo et al. (1977)]. It is this ordering which is responsible for the superior physical and mechanical properties of vapor-grown, compared to commercial PAN and pitch fibers. As shown in Fig 8 the resistivity as a function of temperature is similar to that of a commercial PAN fiber heat-treated to much higher temperatures.

As prepared, BDF exhibit considerable disorder compared to perfect graphite, which is reflected in the relatively high resistivity of the fibers. Heat treatment of the fibers greatly increases the degree of ordering of the graphite planes (see Fig. 9) while decreasing the resistivity by more than an order of magnitude (See Fig. 10) [Koyama and Endo (1974); Endo et al. (1983); Chieu et al. (1983)]. At a heat treatment temperature of 3000°C, the resistivity is within 30% of that of single crystal graphite [Chieu et al. (1983b)]. Of particular interest to applications of the BDF is the wide range of conductivities that can be achieved by heat treatment (see Fig. 10 and compare to Figure 5 for PAN fibers).

The temperature dependence of the resistivity of the BDF is highly unusual for conducting media, as shown in Fig 8 where it is seen that the resistivity is nearly independent of temperature over broad ranges of temperature [Endo et al. (1983)]. This near independence of temperature is due to the competition between the efficient thermal generation of carriers and the increase in electron-phonon scattering as the temperature is increased.

The size dependence of the fibers is also of interest. Typically, the larger diameter fibers exhibit a lower resistivity [Tahar et al (1985)] than the very thin fibers (see Fig. 11), due to the boundary scattering at the interface between the highly graphitic sectors forming the polygonal cross section of the BDF, heat treated to ~3000°C. For the very thin fibers (~1000 Å), large aspect ratios ($>10^2$) can be achieved [Endo and Shikata (1985)].

It is possible to grow CVD filaments with very small diameters (<1000 Å) [Tibbetts (1984)]. Tibbetts developed a simple model to explain the size of filaments in the initial growth stage, based on thermodynamic and mechanical strain concepts [see also Sears (1959)]. He proposed an equation for the change in chemical potential, $\Delta\mu$, driving the precipitation of carbon:

$$\Delta\mu = \Delta\mu_o - \frac{2\sigma\Omega}{r_o - r_i} - \frac{Ec^2\Omega}{12(r_o^2 - r_i^2)} \ln(r_o/r_i) \qquad (1)$$

where $\Delta\mu_o$ = chemical potential change when carbon precipitates from the Fe/C phase to the filament

r_o = outer radius

r_i = inner radius

σ = energy required to form unit area of (001) surface of graphite

E = Young's modulus

Ω = volume of a carbon atom in graphite

c = graphitic interplanar spacing

The first term on the right-hand side of this equation represents the change in chemical potential for precipitation of carbon, the second the surface energy contribution, and the third the elastic energy required to bend graphite planes into nested cylinders.

Growth occurs when $\Delta\mu < 0$. Using reasonable values for E, σ, c, and Ω, Tibbetts showed that r_i could be less than 50 Å. The smallest values of r_i and r_o observed by him were 35 and 50 Å respectively with values below r_o = 200 Å fitting Eq. (1) well.

A program of study was initiated in 1983 at Colorado State University to grow small diameter filaments. There is also some recent activity in this area by Endo and co-workers in Japan, and by Tibbetts at General Motors. Baker et al. (1973) suggested that r_o was controlled by the size of the catalyst particle. Accordingly, several methods of preparing carbon surfaces with small metal catalyst particles have been tested, including glassy carbon with embedded catalysts, and HOPG and nuclear-grade graphite with coated surfaces prepared either by painting on compounds, or vapour deposition. The aim of the work was to prepare, and if possible control, the growth of filaments with uniform diameters ~200-1000 Å. Although filaments have been grown successfully in this regime, the control of reasonable uniformity has not yet been obtained. Further work is underway.

A final reason for possible application of CVD carbon filaments to obscuration lies in the observation that carbon filaments have been produced continuously. Hatano et al. (1985) and Endo and Shikata (1985) have described a fluidized bed process in which very small catalyst particles float in the fluidizing chamber. Carbon filaments with diameters of the order of tenths of microns have been grown successfully by cracking hydrocarbons in a hydrogen atmosphere. This method could conceivably be the basis for large-scale production of smokes.

FILAMENTS DERIVED FROM ION BOMBARDMENT OF CARBON SURFACES

If a carbon surface is bombarded with energetic ions (e.g., 1000 eV Ar^+ ions), then carbon filaments grow from the surface towards the ion source, as illustrated in Fig. 12 [Floro et al.

1983)]. The mechanism of growth appears to be one in which the impinging ions create energetic C atoms on the substrate, which can diffuse to preferential sites, and cluster. The growth of the cluster is into a roughly conical shape with low included angle (e.g., $\leq 20°$) (see Fig. 13). Filaments then grow from the top of the cones. It is probable that electric-field-enhanced diffusion is associated with the filament growth.

There are certain similarities between these and CVD filaments discussed in the previous section. First, there is an initial growth phase of small diameter, followed by elongation and thickening. Second, the filaments are either hollow, or the core is of low density. Third, thickened filaments have a structure which is "tree-ring" like. However, no evidence has yet been found for a catalyst particle promoting growth.

Research into the properties and growth mechanisms(s) of these interesting filaments at Colorado State University and IBM, Thomas T. Watson Research Center is still at a preliminary stage. However, it is possible that there may be interesting applications for obscuration phenomena and also solid state devices.

SUMMARY OF FIBER PROPERTIES

Carbon filaments can be prepared in several ways with diameters ranging typically ~5-10 μm for commercial fibers to ~0.01-100 μm for those prepared by chemical vapour deposition. High aspect ratios (length/diameter $\geq$ 100-1000 for instance) can be obtained. The filaments have high strength, high thermal conductivity and resistance to vaporization, and relatively low density (~2 gm/cm^3). The resistivity of pristine filaments can be varied over large ranges. Typical commercial fiber resistivities at room temperature are ~10^{-3}-3.10^{-3} Ωcm, but can be increased easily by six orders of magnitude by using lower carbonization temperatures (such material is sometimes referred to as a partially pyrolyzed polymer). CVD filaments having higher structural perfection can be prepared with lower resistivities approaching that of graphite ($4x10^{-5}$ Ωcm at room temperature). The lowest value reported so far is $5.5x10^{-5}$ Ωcm [Chieu et al. (1983b)].

These filaments can be metal-coated to resistivities approaching metals such as Ni and Cu (~$2x10^{-6}$ Ωcm). However, if the coating is very thin (e.g., $\leq$0.1 μm), the effect of size on the conductivity needs to be taken into consideration. Another means of reducing resistivity is by a chemical treatment called intercalation, which will be discussed in the next section.

INTERCALATION

Intercalation is a chemical process by which atoms or molecules enter a graphite crystal, occupying positions between the hexagonal carbon planes. Two popular accounts have appeared in the last few years [Fisher and Thompson (1978) and Dresselhaus (1984)] while a review of physical properties has been given by Dresselhaus (1981) and of the chemistry by Ebert (1976).

The chemical reaction for intercalation is:

$$nC + I \rightarrow C_nI$$

(graphite) (intercalant) (intercalation compound)

The location of the intercalant between the layer planes causes the crystal to swell in the c-direction.

De-intercalation is the reverse process:

$$C_nI \rightarrow C_nI_\delta + (1-\delta)I.$$

The residue compound normally formed (C_nI_δ) has a small concentration of the intercalant ($\delta << 1$) at defect sites, which is very difficult to remove, except by heating to extremely high temperatures.

If an intercalation compound is heated rapidly, then the high vapour pressure of the intercalant may cause the sample to disintegrate in a special way, so that it appears to be like an accordian (Fig. 14). This special type of deintercalation is called exfoliation.

The structure of intercalation compounds is especially interesting, since a wide range of crystal structures of various compositions is possible. This results in many different types of phase transitions which are being explored vigorously.

The most important structural feature is called staging, illustrated in Fig. 15. Consider the compound C_8K, in which every layer of carbon is separated by a layer of potassium atoms. Other compounds of composition $C_{24}K$, $C_{36}K$, $C_{48}K$ . . . exist in which two, three, four . . . layers, respectively, of carbon atoms are separated by intercalant. These compounds are described as first, second, third and fourth . . . stage compounds, respectively. Note that the packing of K atoms between the layers changes between first and second stage compounds.

The many different (~500) types of intercalant fall into two main classes--donors and acceptors. Donor intercalants donate electrons to the host lattice ($C_n^{(-)}D_m^{(+)}$) and are metals, such as Li, K, Rb, Cs . . . Acceptors ($C_n^{(+)}A_m^{(-)}$) are of many different kinds, such as Br_2, ICl, H_2SO_4, $NiCl_2$, $FeCl_3$, AsF_5 . . .etc. Ternary compounds can also be formed, such as the donor compound KHg_xC_4.

Most intercalation compounds are not stable under atmospheric conditions, but a few are essentially so. Convenient stable intercalants are $FeCl_3$ and $CuCl_2$ which are inexpensive and non-toxic.

As mentioned above, intercalation is accompanied by swelling of the crystal normal to the planes. If disorder impedes this swelling process, then intercalation may not occur. Accordingly, it is found that certain types of carbon hosts will not intercalate, including isotropic carbon, low modulus carbon fibers [E $\lesssim$50 Msi (240 GPa)], glassy carbon . . . etc. Most physical and chemical studies have been carried out on highly oriented pyrolytic graphite (HOPG) [Moore (1981)] and the succeeding discussions of properties will be for this material. HOPG consists of small ($\lesssim$ 1 μm) crystallites which are oriented randomly about the c-axis but whose c-axes are very well aligned (<0.4°). For the purpose of most properties, identical results are obtained on intercalated HOPG and intercalated single crystals of graphite.

There are several preparation methods for intercalation compounds. First, a sample of graphite can be immersed directly in a fluid, such as Br_2. Second, the sample can be held in a vapour. (These two techniques are essentially identical from a thermodynamic point of view, since the condition for equilibrium is that the activity of the intercalant in the graphite be equal to that in the pure external phase.) Figure 16 illustrates a typical two-zone arrangement for $FeCl_3$ intercalation. Higher stage compounds would be formed by reducing the vapour pressure of $FeCl_3$. Third, compounds can be prepared by an electrolytic technique. The final stage prepared can be controlled through the applied voltage.

Ubbelohde was the first person to realize the potential of intercalated graphite as a highly electrically conducting material [see for example, Blackman et al. (1960)]. He coined the term "synthetic metal" to fit the case where two lesser conducting materials combine to form a highly conducting material. A large increase in research activity followed the report that compounds with strong Lewis acids, such as AsF_5, exhibited room temperature conductivities greater than copper [Vogel (1977); Vogel et al. (1977)]. These early reports have not been substantiated [Zeller et al. (1979)], and Fig. 17 illustrates the increase of conductivity that can be obtained with several intercalants as a function of concentration (or reciprocal stage). The maximum conductivity peaks typically at ~3rd or 4th stage and does not rise above ~2/3 that of copper, which represents about a sixteen-fold increase over that of graphite. (There have been recent reports that Japanese work-

ers have obtained conductivities higher than that of copper with intercalated BDF's, but no information has appeared in the written literature). Whether or not conductivities as high as copper can be obtained, the decrease in resistivity of intercalated filaments from ~6×10^{-5} Ωcm to ~3×10^{-6} Ωcm, and the ability to control the resistivity in this range, is of importance to obscuration phenomena.

The mechanism giving rise to high conductivity is unusual. Table II summarizes the conductivities, carrier densities and mobilities of graphite, copper, and second stage AsF_5 compound. The carrier density of graphite is very low (~1 carrier for 10^4 atoms compared to 1:1 for Cu) because it is a semimetal, but its mobility is extremely high (>300 times that of Cu), resulting in a conductivity 1/25 that of Cu at room temperature. Intercalation can increase the carrier density approximately 300 times, but it is still only less than 1% of that of Cu. The mobility decreases somewhat to ~1/3 that of graphite, resulting in a sixteen-fold increase in conductivity over that of graphite.

It is noteworthy that the large conductivity anisotropy of graphite, σ_a/σ_c, is increased to very high values for this acceptor compound (>10^6). σ_a is the conductivity with current parallel to the layer planes, and σ_c that with current perpendicular to them. The anisotropy of donor compounds such as C_nK is lower than that of graphite.

Another important property which is modified by intercalation is the optical reflectivity. Optical reflectance can occur from two different surfaces--basal and prism--in an anisotropic material such as graphite. Reflectivity is generally high from the basal surface, and low from the prism. Figure 18 illustrates the reflectivity as a function of photon energy (and wavelength) for several intercalation concentrations of RbC_n [Guerard et al. (1977)]. At low frequency, the basal reflectivity is high, but above a critical photon energy, the plasma energy, E_p falls to a low value. The plasma energy, in SI units, is

$$E_p = \hbar \left[\frac{n}{\varepsilon_o m^*} \right]^{1/2}$$

where $\hbar$ is $h/2\pi$ (h is Planck's constant), n is the density of carriers, ε_o the permittivity of the medium and m* the effective mass of the carriers. As intercalant concentration increases, n increases, so that E_p should increase in accord with the data in Fig. 18.

Reflectivity of intercalation compounds, such as that illustrated in Fig. 18, offers the possibility of "tailoring" this phenomenon to specific applications. However, caution needs to be exercised in

extending this idea to less perfect material in which misorientation of hexagon planes averages phenomena over prism edges and basal surfaces, since the reflectivity from prism surfaces is generally much smaller than that from basal [see Guerard et al. (1977)].

INTERCALATED FIBERS OR FILAMENTS

Commercial (PAN and pitch) and benzene derived fibers (BDF) have been intercalated and properties measured. As discussed in the previous section, only commercial fibers heat treated to ~2000°C can be intercalated successfully. BDF can be intercalated as grown, or after heat-treatment. No attempts to intercalate ion-prepared filaments have been reported.

Much of the early work on intercalated fibers has been directed at the problem of producing useful conductors with high electrical conductivity, high strength, and low density. A research program at Celanese Research Company produced a multi-filament cable with end contacts and a total cross sectional area near that of AWG 17 wire based on intercalated PAN fibers [Kalnin and Goldberg (1983)].

The achievable increase in conductivity depends on the degree of perfection of the filament. Highest conductivities obtained decrease in the sequence; intercalated BDF fiber, pitch fiber and PAN fiber. For instance, room temperature resistivities ~5×10^{-5} Ωcm have been reported for intercalated BDF [Chieu et al. (1983b)], 12×10^{-5} Ωcm for pitch fibers [Oshima et al. (1982)] and ~20×10^{-5} Ωcm for PAN fibers [Goldberg and Kalnin (1981)]. The resistivity found in each case can be correlated with the scattering length of the charge carriers from defects.

Oshima et al. (1982) showed that $CuCl_2$-intercalated pitch fibers were air stable to ~150°C. The favorable tree-ring geometry of the BDF tends to inhibit intercalate desorption [Gaier (1984); Endo and Ueno (1984)] which is prevalent in many of the highly reactive graphite intercalation compounds.

Figure 19 illustrates the temperature dependence of the resistivity of BDF and intercalated BDF fibers. Again the improvement in structural perfection obtained by heat-treating to higher temperatures can be seen in both neat and intercalated fibers. Room temperature resistivities of intercalated BDF which are closer to that of copper than the data in Fig. 19 have been reported recently [Endo and Ueno (1984)], and there are oral reports that this group may have obtained higher conductivity than copper. For obscuration purposes we again emphasize that it is the range of values which can be obtained which is of greatest importance, rather than the absolute values.

Since the crystalline a-axis is predominantly along the fiber axis, graphite fibers have unusually high thermal conductivities, among the highest found in solids [Piraux et al. (1984)]. Intercalation also modifies the thermal conductivity of graphite fibers, leading to a reduction in the

room temperature thermal conductivity, because of the increased electron-phonon and defect scattering, and an increase in the low temperature (<10K) thermal conductivity through the dominance of the electronic contribution at low T.

The fiber geometry is particularly favorable for the thermopower measurements, and in fact techniques have been developed to measure the thermal conductivity and thermopower of single fibers [Piraux et al. (1984, 1985)]. Intercalation greatly modifies the temperature dependence of the thermopower, yielding positive values for acceptor intercalants and negative values for donors.

The special tree-ring morphology of benzene-derived graphite fibers makes it possible to fabricate ribbons with a spongy texture by the process called exfoliation (see Fig. 20). The exfoliation process leads to an expansion in cross sectional area by several orders of magnitude [Jimenez-Gonzalez et al. (1985)] yielding a texture in many ways similar to that of exfoliated HOPG. Exfoliated filaments may have interesting applications for obscuration.

Raman scattering provides an important non-destructive characterization tool for both pristine and intercalated graphite fibers [Chieu et al. (1982, 1983b)]. For the pristine fibers, a comparison of the intensity of the disorder-induced line near 1360 cm^{-1} to that of the Raman-allowed line near 1580 cm^{-1} gives valuable information about the degrees of structural ordering. For the intercalated fibers, the frequencies and intensities of the graphite bounding-layer modes relative to those for the graphite interior layers gives valuable information about the stage of the intercalation compound. With the Raman microprobe, it is possible to characterize single fibers [McNeil et al. (1985)] and also to investigate the variation of the crystalline perfection and staging fidelity along the length of the fiber.

Vapor-grown fibers provide unique opportunities for high resolution transmission electron microscopy studies because of the small fiber diameters ($\lesssim 1$ μm) that can be achieved with these fibers. Of particular interest has been the study of the lattice damage introduced into anisotropic materials by ion implantation and its subsequent annealing and crystalline regrowth [Endo et al. (1984); Salamanca-Riba et al. (1985)]. Ion-implanted fibers may also have properties of interest for obscuration applications.

ACKNOWLEDGEMENTS

MSD gratefully acknowledges support from DARPA, administered through AFOSR contract F49-620-85-C-0147, and ILS from AFOSR Contract #F49-620-84-K-0006.

REFERENCES

A.M. Azzeer, L.M. Silber, I.L. Spain and C.E. Patton (1985), Applicability of the Microwave Cavity Perturbation Method for Conductivity Measurements on Carbon Fibers," J. Appl. Phys. 57, 2529.

R.T.K. Baker, P.S. Harris, R.B. Thomas, R.J. Waite (1973), "Formation of Filamentous Carbon from Iron, Cobalt, and Chromium Catalyzed Decomposition of Acetylene," J. Catalysis 30, 86.

R.T. Baker, M.A. Barber, P.S. Harris, F.S. Feates, R.J. Waite (1972), "Nucleation and Growth of Carbon Deposits from the Nickel Catalyzed Decomposition of Acetylene," J. Catalysis 26, 51.

C.P. Beetz and J.S. Brinen (1983), "The Effects of a Metal Overlayer on Carbon Fiber Properties," Proc. 16th Biennial Conf. Carbon, p. 535.

M.S. Dresselhaus (1984), "Modifying Materials by Intercalation," Physics Today, March, p. 60.

M.S. Dresselhaus (1984), "Intercalated Fibers and their Physical Properties," J. de Chimie Physique 81, 739.

M.S. Dresselhaus and G. Dresselhaus (1981), "Intercalation Compounds of Graphite," Advances in Physics 30, 139.

L. Ebert (1976), "Intercalation Compounds of Graphite," Annual Reviews of Materials Science 6, 181.

M. Endo, T. Koyama, Y. Hishiyama (1976), "Structural Improvement of Carbon Fibers Prepared from Benzene," Japn. J. Appl. Phys. 11, 2073.

M. Endo, A. Oberlin, T. Koyama (1977), "High Resolution Electron Microscopy of Graphitizable Carbon Fiber Prepared by Benzene Decomposition," Japan. J. Appl. Phys. 15 1519.

M. Endo, Y. Hishiyama, T. Koyama (1982), "Magnetoresistance Effect in Graphitizing Carbon Fibers Prepared by Benzene Decomposition," J. Phys. (Gt. Britain) D:Appl. Phys. 15, 353.

M. Endo, T.C. Chieu, G. Timp, M.S. Dresselhaus (1983), "Properties of Acceptor Intercalated Graphite Fibers," Synthetic Metals 8, 251.

M. Endo, L. Salamanca-Riba, G. Dresselhaus, and J.M. Gibson (1984), "Structure of Ion Implanted Graphite Fibers," J. de Chimie Physique 8, 803.

M. Endo and M. Shikata (1985), "Growth of Vapor-Grown Carbon Fibers using Fluid Ultrafine Particles of Metals," Ohyobutsuri 54, 507 (In Japanese).

M. Endo and H. Ueno (1984), "Growth and Applications of Vapor-Grown Carbon Fibers," Extended Abstracts, Symposium of Materials Research Society on Graphite Intercalation Compounds (ed. P.C. Eklund, M.S. Dresselhaus and G. Dresselhaus), p.177.

J.E. Fischer and T.E. Thompson (1978), "Graphite Intercalation Compounds," Physics Today, July p. 36.

J.A. Floro, S.M. Rossnagel, R.S. Robsinson (1983), "Ion-Bombardment Induced Wisker Formation on Graphite," J. Vac. Sci. Technol. A1, 1398.

J.R. Gaier (1984), "Stability of Bromine Intercalated Graphite Fibers," Extended Abstracts, Symposium of Materials Research Society on Graphite Intercalation Compounds (ed. P.C. Eklund, M.S. Dresselhaus and G. Dresselhaus), p. 205.

H.A. Goldberg (1985), "Electrical and Mechanical Properties of Intercalated Graphite Fibers; Final Report to the U.S. Army Research Office, contract DAAG29-81-C-0016," available NTIS AD-A155 560/6/WMS.

H.A. Goldberg and I.L. Kalnin (1981), "Electrical Resistance Measurements on Intercalated High Modulus Graphite Fiber Bundles," Synthetic Metals, 3, 169-176.

D. Guerard, G.M.T. Foley, M. Zanini and J.E. Fischer (1977), "Electronic Structure of Donor-Type Graphite Intercalation Compounds," Il Nuovo Cimento 38B, 410.

J. Heremans (1985), "Electrical Conductivity of Vapor-Grown Carbon Fibers," Carbon 23, 431.

M. Hatano, T. Ohasaki, K. Arakawa (1985), "Graphite Wiskers by a New Process, and their Composites," Proc. 30th National Society for the Advancement of Material and Process Engineering Vol. 30, p. 1467.

H. Jiménez-Gonzalez, G. Roth and M.S. Dresselhaus (1985), "Exfoliation of Benzene Derived Graphite Fibers," Extended Abstracts of the 17th Biennial Conference on Carbon, p.75.

I.L. Kalnin and H.A. Goldberg (1983), "Intercalation and Electrical Properties of Graphite Fibers," Synthetic Metals 8, 277.

B.T. Kelly (1981), "Physics of Graphite," Applied Science Publishers, Barking, UK.

T. Koyama (1972), "Formation of Carbon Fibers from Benzene," Carbon 10, 757.

T. Koyama, M. Endo, Y. Onuma (1972), "Carbon Fibers Prepared by Thermal Decomposition of Vaporized Hydrocarbon," Japan. J. Appl. Phys. 11, 445.

T. Koyama and M. Endo (1974), "Electrical Resistivity of Carbon Fiber Prepared from Benzene," Japan. J. Appl. Phys. 13, 1175.

T. Koyama, M. Endo, Y. Hishiyama (1974), "Structure and Properties of Graphitized Carbon Fiber Prepared from Benzene," Japan. J. Appl. Phys. 13, 1933.

E. McRae, D. Billaud, J.F. Marêche, A. Herold (1980), "Basal Plane Resistivity of Alkali Metal Graphite Compounds," Physica 99B, 489.

L. E. McNeil, J. Steinbeck, L. Salamanca-Riba and G. Dresselhaus (1985), "Raman Microscopy of Intercalated Graphite Fibers," Carbon (accepted).

A.W. Moore (1982), "Highly Oriented Pyrolytic Graphite and its Crystal Compounds," Chapter 4 in Chemistry and Physics of Carbon, Vol. 16, (ed. P.L. Walker and P.A. Thrower) Marcel Dekker, New York.

A. Oberlin, M. Endo, T. Koyama (1976), "Filamentous Growth of Carbon Through Benzene Decomposition," J. Cryst. Growth 32, 335.

G. Henrici Olivé and S. Olivé (1983), "The Chemistry of Carbon Fiber Formation from PAN," Adv. in Polymer Sci. 51, 1.

H. Oshima, J.A. Woollam, A. Yavrouian (1982), "Metallic Conductivity and Air Stability of Copper Chloride Intercalated Carbon Fibers," J. Appl. Phys. 53, 9220.

W.N. Reynolds (1973), "Structural and Physical Properties of Carbon Fibers," in "Chemistry and Physics of Carbon," Vol. 11 (P.L. Walker, Jr. and P.A. Thrower, eds.) Marcel Dekker, New York.

L. Piraux, B. Nysten, A. Haquenne, J.P. Issi, M.S. Dresselhaus, and M. Endo, (1984) "The Temperature Variation of the Thermal Conductivity of Benzene-Derived Carbon Fibers," Solid State Communications 50, 697.

L. Piraux, B. Nysten, J.P. Issi, L. Salamanca-Riba and M.S. Dresselhaus (1985), "Thermal Conductivity and Thermopower of $CuCl_2$ Intercalated Benzene-Derived Carbon Fibers," Carbon, submitted March.

G.W. Sears (1959), "Growth Mechanism for Graphite Wiskers," J. Appl. Phys. 31, 358.

M. Sittig (1980) (editor), "Carbon and Graphite Fibers," (Noyes Data Corporation, Park Ridge, NJ).

I.L. Spain (1981), "Electronic Transport Properties of Graphite, Carbons, and Related Materials," in "Chemistry and Physics of Carbon," Vol. 16, p. 119 [P.L. Walker, Jr., and P.A. Thrower, eds.] Marcel Dekker, New York.

I.L. Spain, K.J. Volin, H.A. Goldberg, and I. Kalnin (1983), "Electronic Properties of PAN-based Carbon Fibers," J. Phys. Chem. Solids 44, 839.

M.Z. Tahar, M.S. Dresselhaus and M. Endo (1985), "Size Effects in Electrical Properties of Benzene-Derived Graphite Fibers," Carbon (accepted).

G.G. Tibbets (1983), "Carbon Fibers Produced by Pyrolysis of Natural Gas in Stainless Steel Tubes," Appl. Phys. Lett. 42, 666.

G.G. Tibbets (1984), "Why are Carbon Filaments Tubular?" J. Cryst. Growth 66, 632.

F.L. Vogel, G.M.T. Foley, C. Zeller, E.R. Falardeau, J. Gan (1977), "High Electrical Conductivity in Graphite Intercalated with Acid Fluorides," Mater. Sci. and Eng. 31, 261.

B.J. Wicks (1975), "Microstructural Disorder and the Mechanical Properties of Carbon Fibers," J. Nucl. Mater. 56, 287.

C. Zeller, L.A. Pendrys, F.L. Vogel (1979), "Electrical Transport Properties of Low-Stage AsF_5-Intercalated Graphite," J. Mater. Sci. 14, 2241.

J.M. Ziman (1960), "Electrons and Phonons," Oxford University Press.

AD-A173 878 PROCEEDINGS OF THE SCIENTIFIC CONFERENCE ON OBSCURATION 4/7
AND AEROSOL RESEA (U) KOHL (RONALD H) AND ASSOCIATES
TULLAHOMA TN R H KOHL JUL 86 CRDEC-SP-86019
UNCLASSIFIED DAAG29-81-D-0100 F/G 20/6 NL

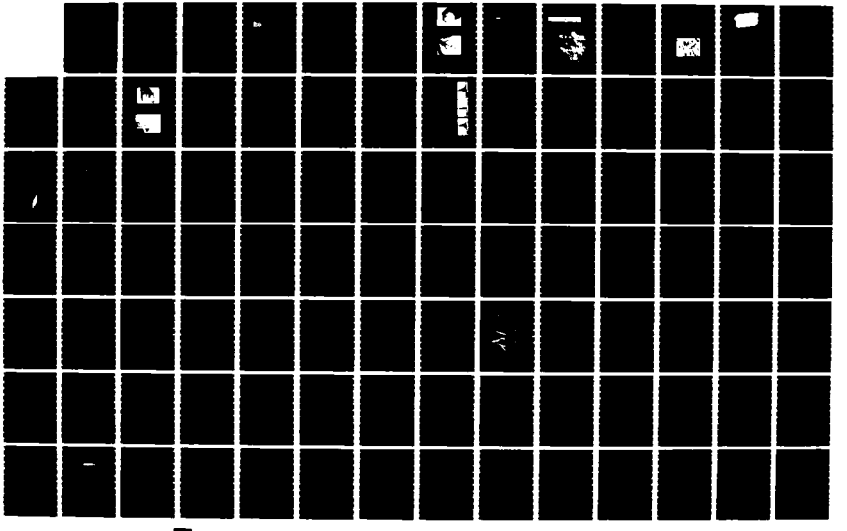

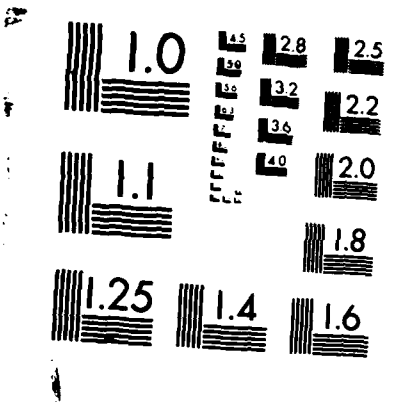

TABLE I. PROPERTIES OF COMMERCIAL CARBON AND GRAPHITE FIBERS

	STRENGTH		MODULUS		ELONGATION (%)	RESISTIVITY (micro-ohm-cm)	DENSITY (gm/cc)
	(Kpsi)	(GPa)	(Mpsi)	(GPA)			
CELION	600	4	35	240	1.7	1,500	1.72
GY-70	300	2	75	520	0.4	650	1.9
P-100	300	2	100	690	0.3	300	2.1

Celion and GY-70 are trademarks of Celanese (Fibers) and P-100 is a product of Union Carbide Corporation.

TABLE II. ELECTRONIC PROPERTY CHANGES

	Cu	Graphite	$C_{16}AsF_5$
Conductivity $(\Omega m)^{-1}$	58×10^6	2.5×10^6	$\sim 40 \times 10^6$
$\frac{\sigma_a}{\sigma_c}$	1	2.3×10^3	2.7×10^6
Carrier Concentration (m^{-3})	8.5×10^{28}	2.2×10^{25}	$\sim 1.2 \times 10^{27}$
Mobility $(m^2 V^{-1} s^{-1})$	4.3×10^{-3}	0.71	~ 0.3

PAN PRECURSOR	PREOXIDATION (STABILIZATION IN AIR AT 200-300 °C FOR 1-2 HOURS)	CARBONIZATION (TREATMENT IN N_2 AT 1200-2000 °C FOR 30-60 SECONDS)
67.9 %C	63.9 %C	95.5 %C
5.7 %H	3.9 %H	0.2 %H
26.4 %N	21.2 %N	5.0 %N
	11.0 %O	0.5 %O

MODULUS = 34 Mpsi (230 GPa)
STRENGTH = 550 k psi (3.7 GPa)
% ELONGATION = 1.5 %

FIGURE 1. CARBON FIBER PROCESS. Schematic showing the principal steps in the preparation of PAN fiber.

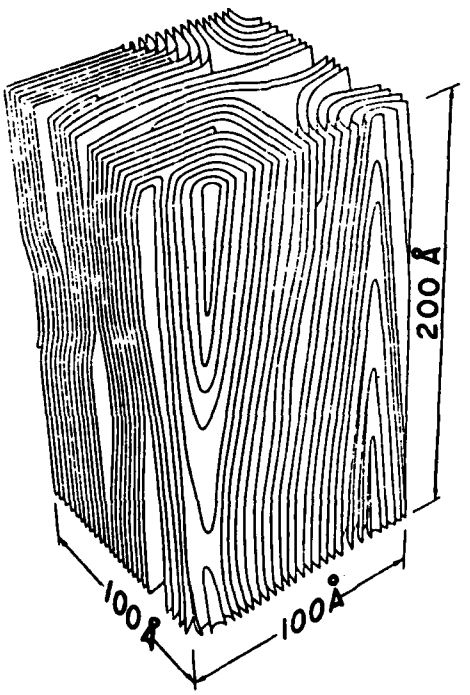

FIGURE 2. PAN FIBER STRUCTURE. Illustration of a small segment of PAN fiber, with axis vertical. [Figure reproduced from Wicks (1975).]

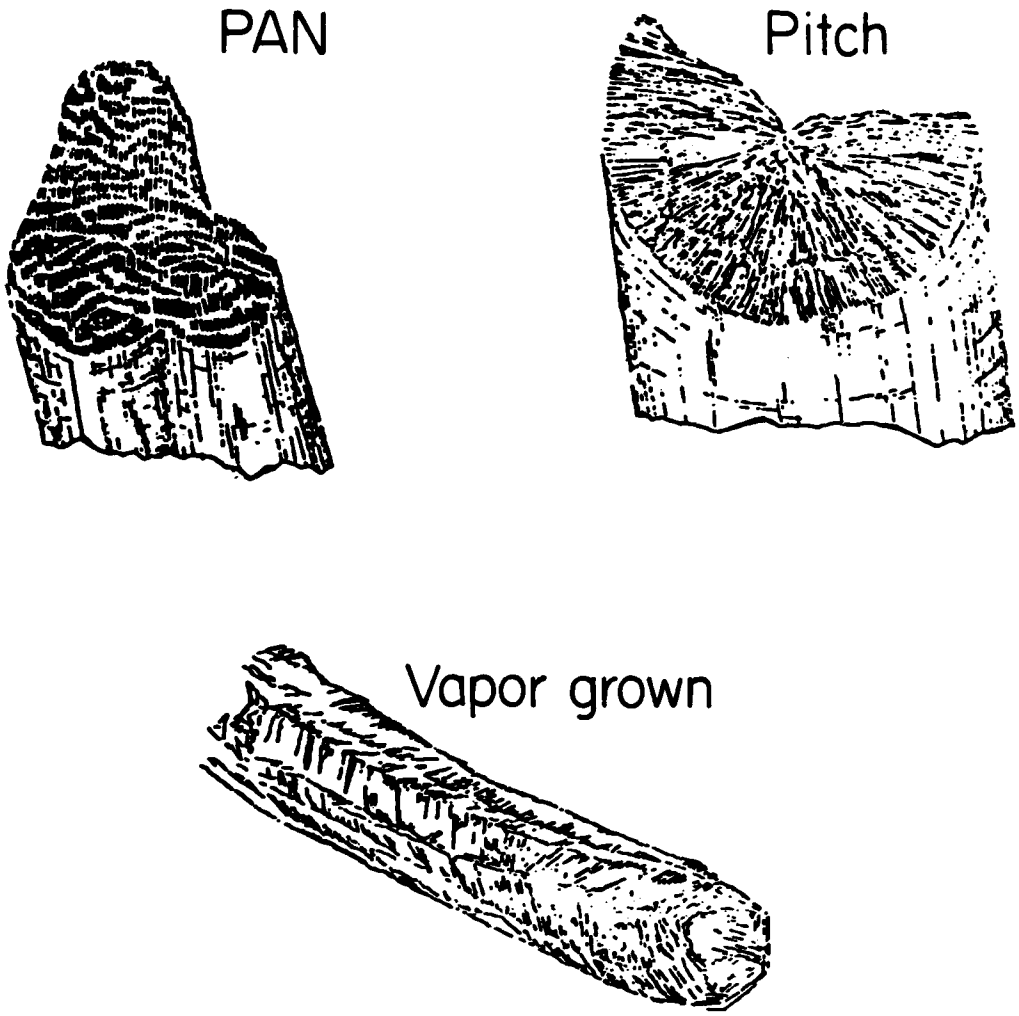

FIGURE 3. FIBER MORPHOLOGY. Schematic showing the arrangement of carbon hexagon planes in dog-bone PAN fiber, PAC-man pitch fiber and vapour grown fiber (see next section).

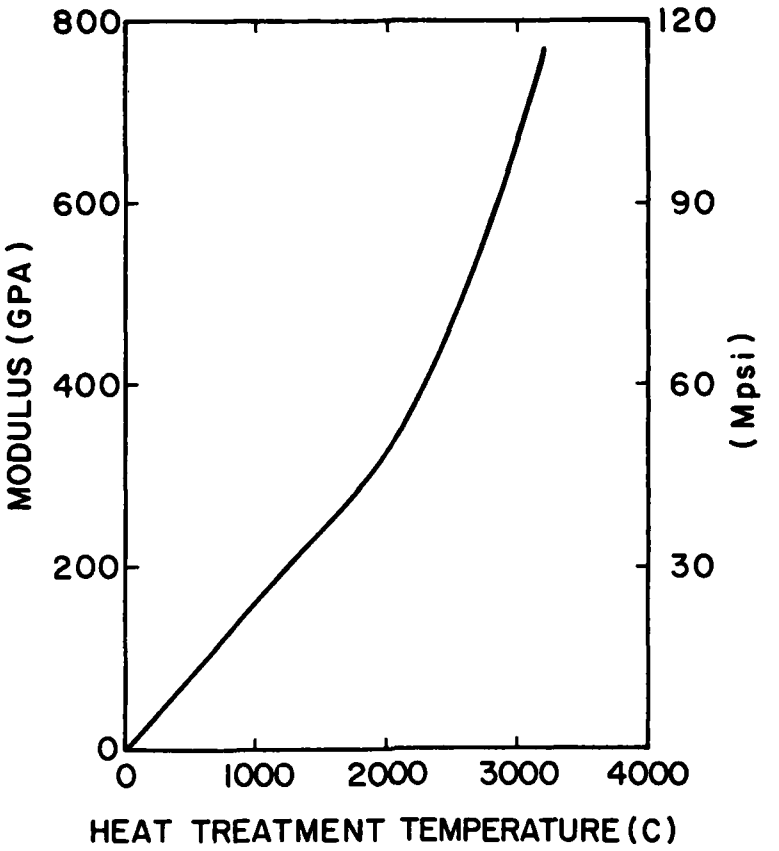

FIGURE 4. YOUNG'S MODULUS. Variation of Young's modulus for PAN fibers as a function of T_{HT} (5 minute residence time).

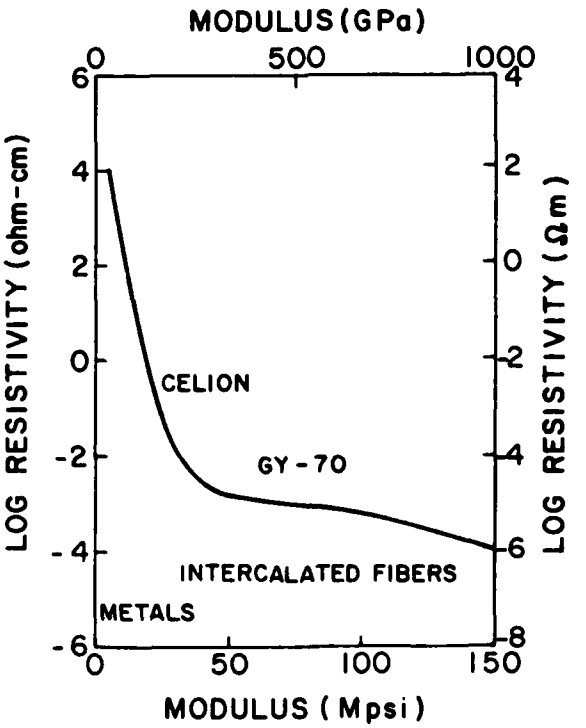

FIGURE 5. RESISTIVITY VERSUS MODULUS. The electrical resistivity of pyrolyzed PAN fibers as a function of elastic modulus.

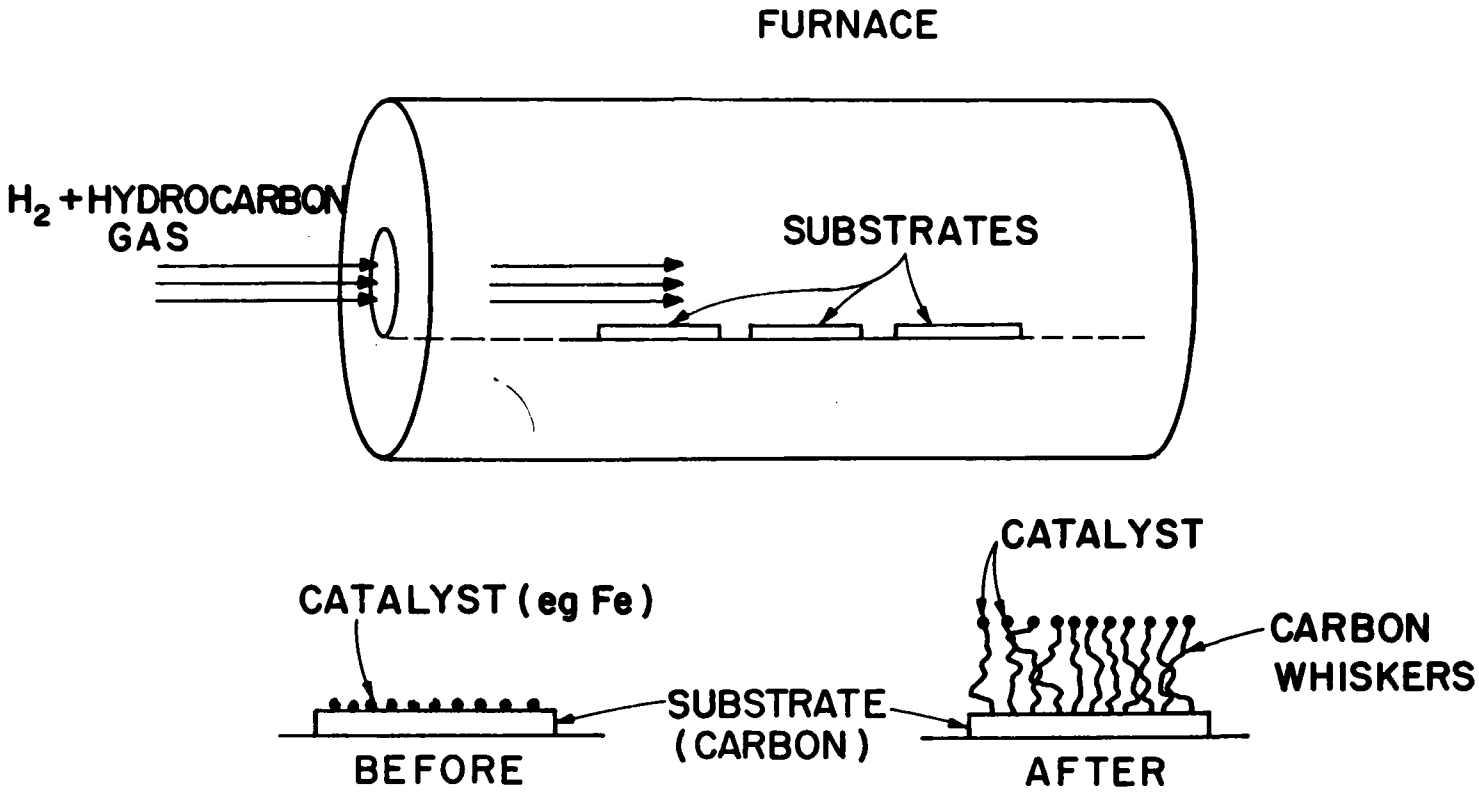

FIGURE 6. CVD FILAMENT PREPARATION. Schematic of a simple arrangement for preparing CVD filaments. The inset shows the action of the catalyst.

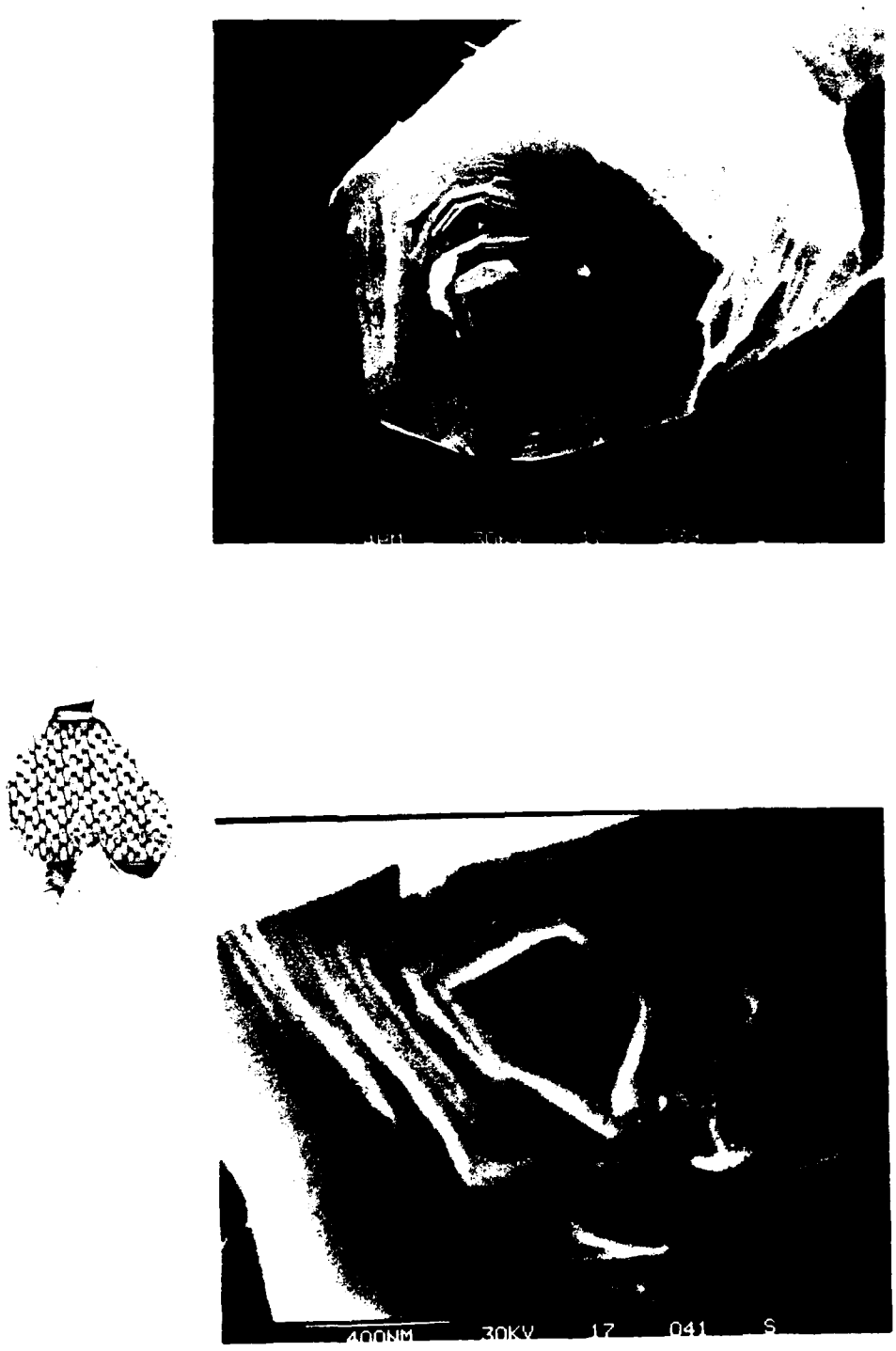

FIGURE 7. STRUCTURE OF BENZENE DERIVED FIBER. Electron microscope photograph of a broken BDF, showing the tree-ring structure.

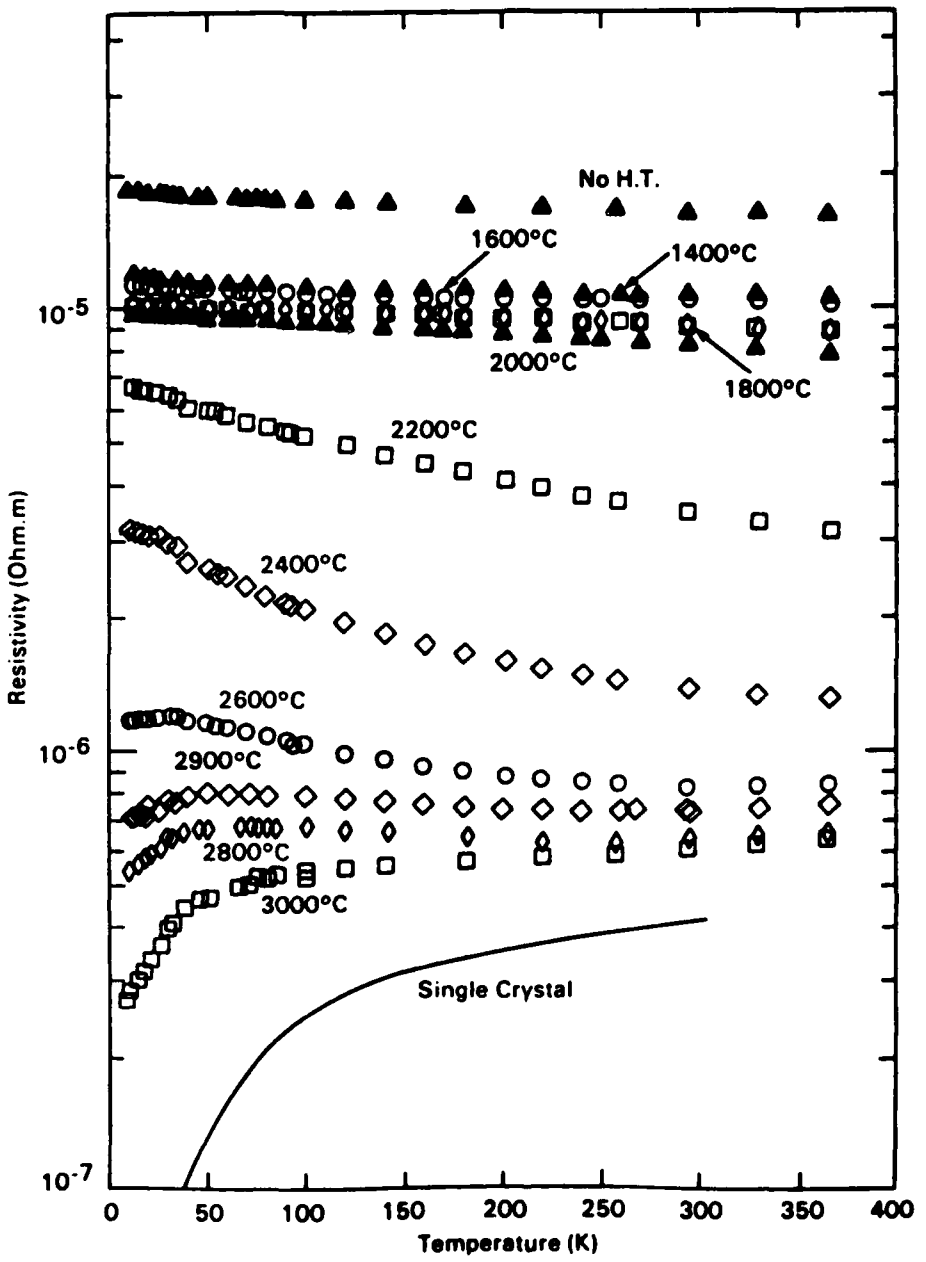

FIGURE 8. RESISTIVITY OF BENZENE-DERIVED FIBERS. The resistivity of benzene-derived fibers plotted as a function of temperature. Curves are drawn for several heat treatment temperatures, and compared to single crystal graphite.

FIGURE 9. STRUCTURE OF BDF. Lattice fringe images of BDF heat-treated to 2900°C.

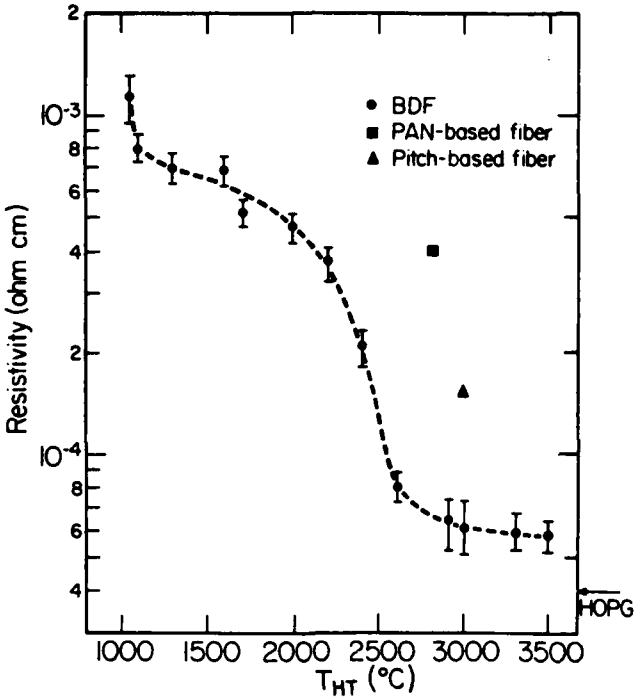

FIGURE 10. FIBER RESISTIVITY. Resistivity at room temperature for fibers as a function of heat-treatment temperature. [Figure from Heremans (1985)].

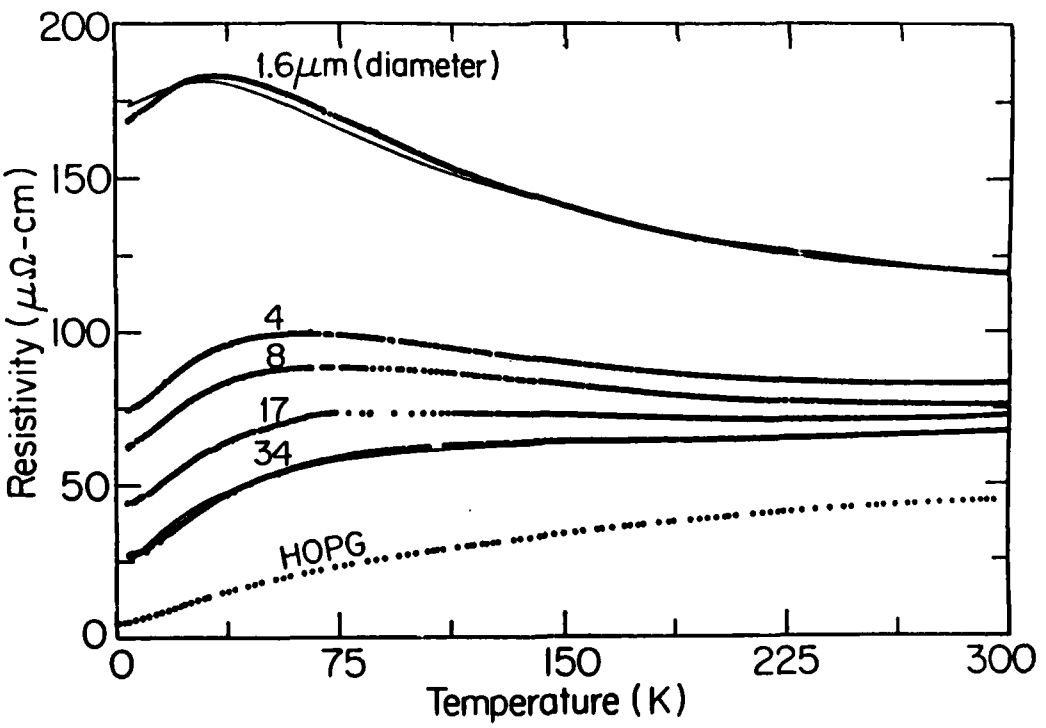

FIGURE 11. SIZE DEPENDENT RESISTIVITY. Resistivity as a function of temperature for several benzene-derived fibers with different diameters. Solid lines are results of calculations.

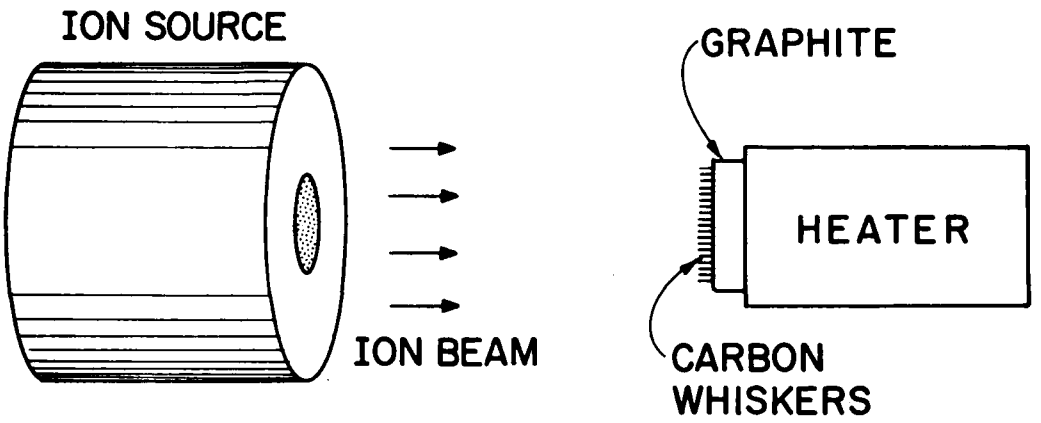

FIGURE 12. ION-BEAM GROWN FILAMENT PREPARATION. Schematic of the method for producing carbon filaments by the ion bombardment of a carbon surface.

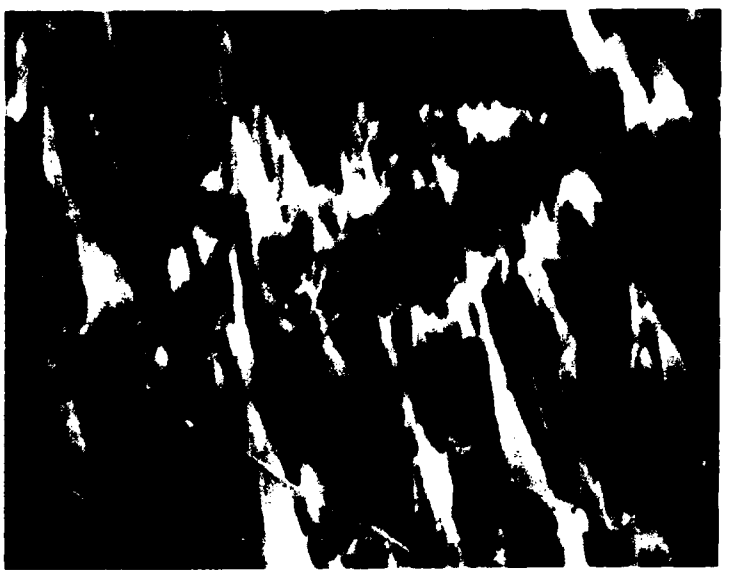

FIGURE 13. ION-BEAM GROWN FILAMENTS. Scanning electron microscope image of filaments (~0.5μm diameter) growing from conical bases.

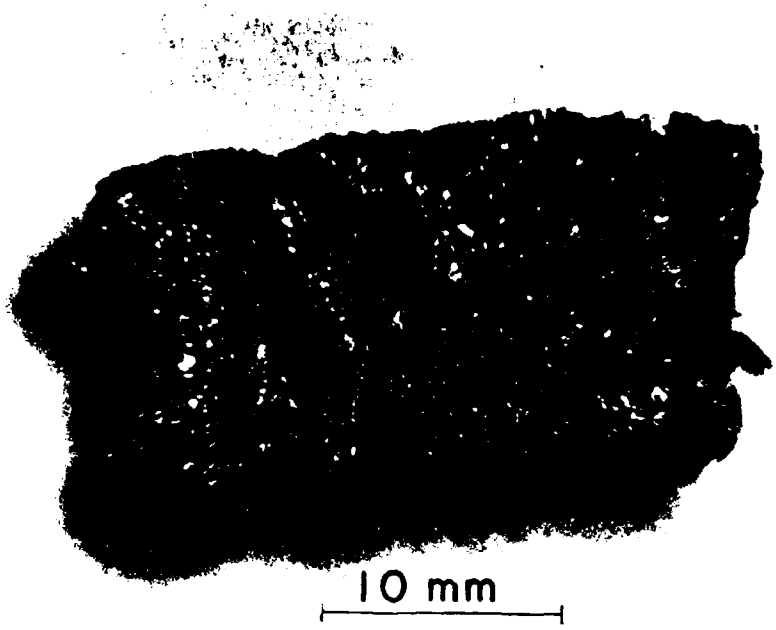

FIGURE 14. EXFOLIATION. Photograph of a sample of exfoliated highly oriented pyrolytic graphite. The original sample was ~0.5 mm thick.

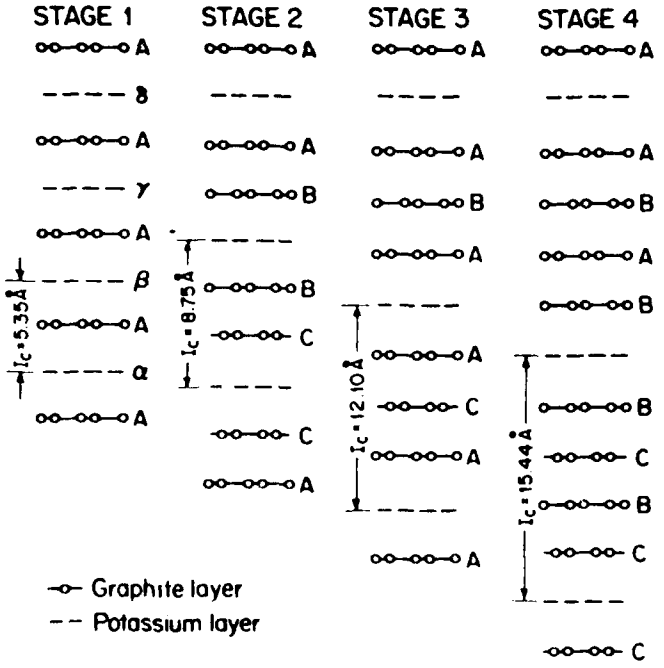

FIGURE 15. STAGING. Illustration of the concept of staging in intercalation compounds. The compound KC_n is used for illustration only.

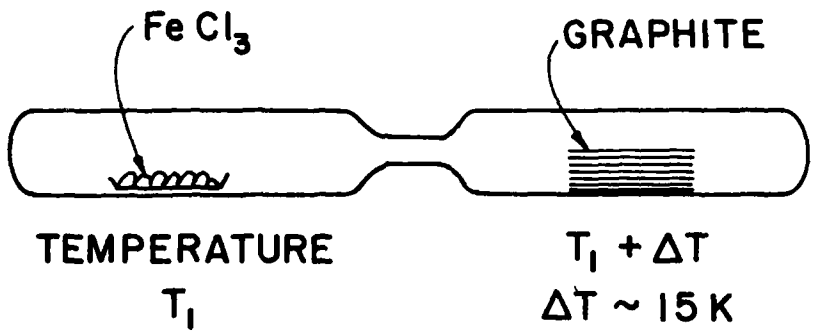

FIGURE 16. INTERCALATION OF $FeCl_3$ Schematic of a two-zone furnace for preparing intercalation compounds. $FeCl_3$ is chosen for convenience only.

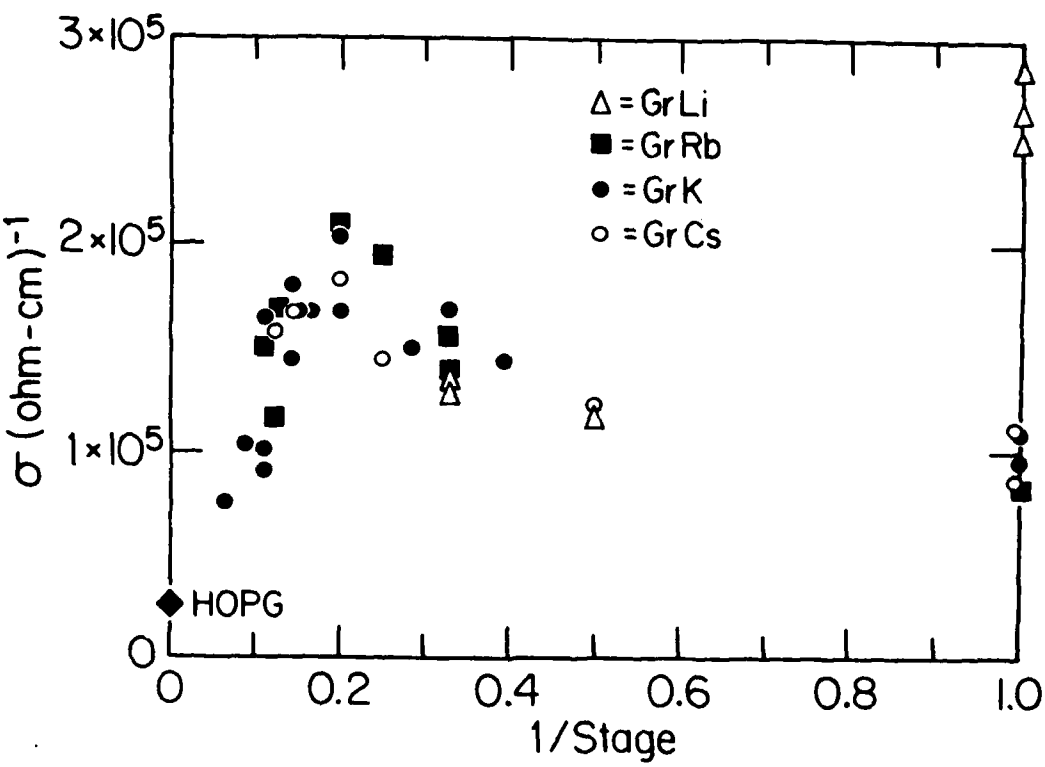

FIGURE 17. INTERCALANT CONDUCTIVITY. The electrical conductivity of several compounds as a function of intercalant concentration. Donor compounds of alkali metals are used for illustration purposes [Data from McCrae et al. (1980)].

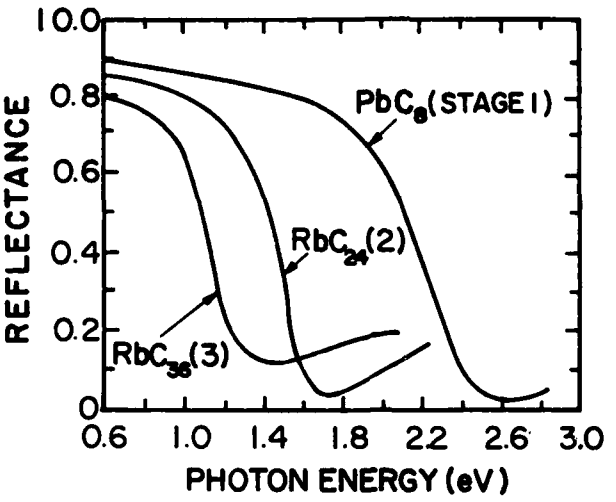

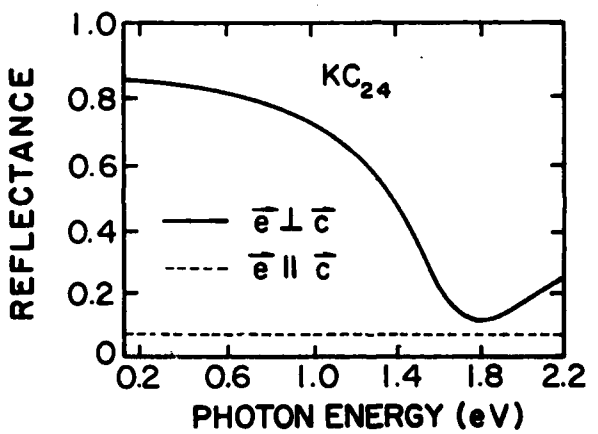

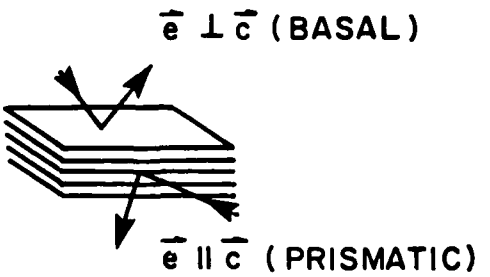

FIGURE 18. OPTICAL REFLECTIVITY OF INTERCALATION COMPOUNDS. (a) The basal optical reflectivity of a series of rubidium compounds; (b) Basal and prismatic reflectivity of KC_{24} [Figures from Guerard, Foley, Zanini and Fischer (1977)].

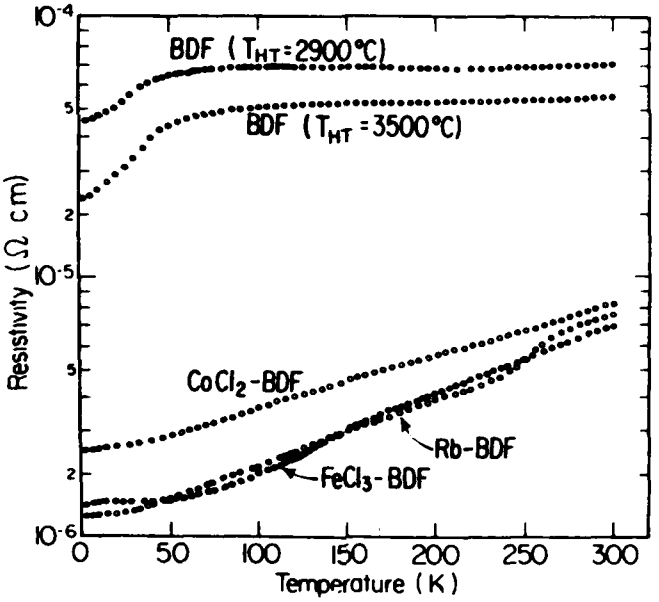

FIGURE 19. RESISTIVITY OF INTERCALATED BDF. Resistivity as a function of temperature for two BDF heat-treated to 2900°C and 3500°C, and three BDF after intercalation.

(a)

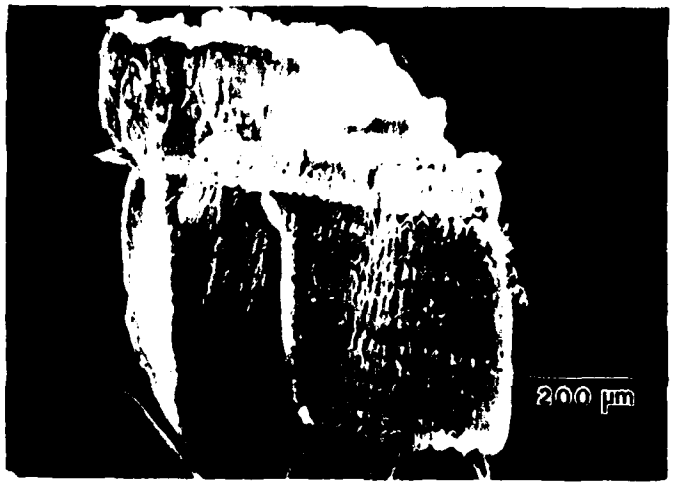

(b)

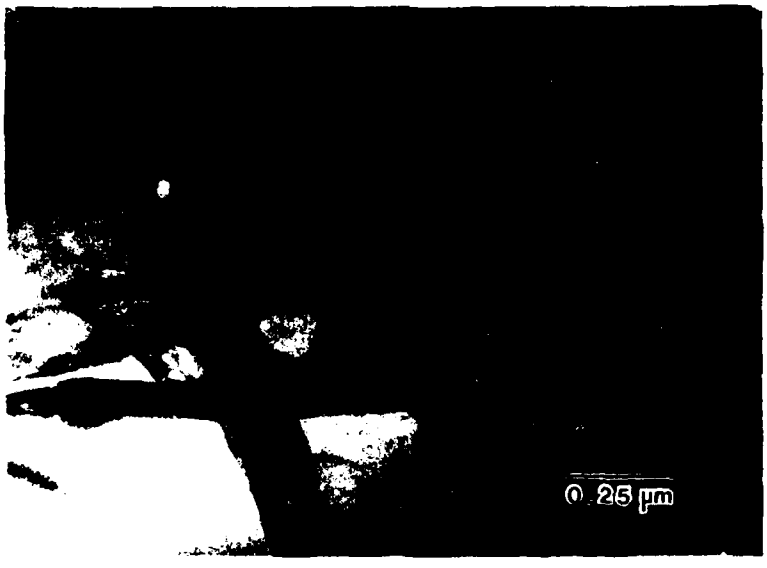

FIGURE 20. EXFOLIATED BDF. (a) SEM micrograph of BDF after exfoliation; (b) Overall structural appearance of an exfoliated BDF as seen by TEM.

IV. NONLINEAR EFFECTS AT HIGH ENERGY

INTERACTION OF AEROSOLS WITH LASER RADIATION

J. Carls and J. R. Brock
Chemical Engineering Department
University of Texas
Austin, Texas 78712

SUBMISSIONS FOR PUBLICATION
(Contract DAAK11-83-K-0006)

J. Carls and J. R. Brock, "Explosive vaporization of small particles by laser radiation", Journal of Aerosol Science, Submitted.

S. Davies and J. R. Brock, "Rapid vaporization of small liquid particles by laser radiation", Journal of Aerosol Science, Submitted.

ABSTRACT

Under Contract DAAK11-83-K-0006, studies have been initiated recently of interactions of aerosols with laser radiation. Theoretical and experimental work is described in two areas. In one, the nonlinear interaction of single particles with laser radiation is studied as an aid. In the second, the more general problem of laser transmission through an aerosol is investigated. The theory for single particle evaporation and explosion has been developed. Single particles are being investigated using an electrodynamic cell. Experiments of a preliminary nature are summarized in which laser transmission through an aerosol is investigated. A corresponding theoretical program is being initiated.

INTRODUCTION

Laser transmission through an aerosol involves complex interactions whose details are currently poorly understood. We are engaged in their experimental and theoretical investigation. These interactions range with increasing em radiation energy from evaporation of particles to particle explosion and plasma formation by breakdown. In an atmospheric-aerosol plume these interactions will be, in addition, influenced by the dynamical properties of the plume.

Current work and preliminary results are summarized here. First theoretical and experimental single particle studies are described. Then our preliminary work on aerosol - em radiation interaction is summarized.

SINGLE PARTICLE STUDIES

A model has been developed for the evaporation of a small liquid droplet in laser radiation in the approximation of uniform heating of the particle (radial symmetry). The model is believed to be an improvement over previous work in that all important terms in the conservation equations of the particle-gas system are accounted for, including surface capillary wave instabilities. Coupling between the particle and laser radiation is obtained by use of Mie theory in which constitutive properties are allowed to be functions of radius and time.

In a separate investigation, a model for explosive vaporization of small particles has been

developed. We have again assumed radial symmetry and include the coupling between the particle and em radiation using Mie theory. Of course, the principal difficulty in developing this model with these restrictions lies in an accurate computer code for the hydrodynamic equations. These are the conservation equations of mass, momentum, and energy:

$$\partial \rho / \partial t = - \nabla \cdot \rho \vec{v}$$

$$\partial \rho \vec{v} / \partial t = - \nabla \cdot \rho \vec{v}\vec{v} - \nabla p$$

$$\partial \rho E / \partial t = - \nabla \cdot \rho E v - \nabla \cdot p \vec{v}$$

From a numerical point of view, the solution of these equations poses the principal difficulty. This is because of the nonlinear nature of the equation of motion (which admits the possibility of shocks) and the fact that the conservation equations tend toward hyperbolic PDE's when molecular dissipation processes become negligible. Standard numerical techniques break down when applied to systems of equations such as these that manifest shocks or sharp fronts. This has led us to use the Flux Corrected Transport (FCT) method of Boris and Book. FCT is a medium accuracy method that is designed to remain stable near highly structured regions of flow. FCT does this by adding sufficient artificial diffusion locally to maintain monotonicity and positivity in the transport profile. We have carried out simulations using this method for small liquid spheres with initial densities near that of water. The aerosol is small compared to the incident wavelength from a laser with a pulse duration small compared to the times of propagation of acoustic waves in the particle. Fig 1 shows a result for expansion of the particle for various initial energies. We plan to extend this work to include two dimensions in the conservation equations to remove the restriction of radial symmetry.

In our laser laboratory we have constructed an electrodynamic balance to permit suspension of single particles in one or more laser beams. The laboratory is equipped with an Ar-Ion laser+dye laser, He-Ne lasers, an N_2-dye laser, and a CO_2 laser with a Q-switch option. Also, the usual laser accessories are available as well as spectrum analyzers , double monochromators with photodiode arrays and a TN rapid-scan spectrometer with computer. Studies in process include particle evaporation, induced reactions, particle explosion and plasma breakdown in the presence of particles.

AEROSOL STUDIES

We are currently developing models for laser radiation transmission through an aerosol . The single particle models are to be incorporated into a model for evolution of the particle size distribution during evaporation in the beam. This in turn will be used in a more comprehensive model for radiative transfer.

Preliminary experiments have been carried out for transmission of laser radiation through an aerosol. The experimental arrangement is shown schematically in Fig. 3. In our experiments we have used an aerosol consisting of methyl alcohol, ethylene glycol and the fluorescent dye Rhodamine 6G. With our rapid-scan spectrometer system, we are able to detect changes of particle size in the aerosol in the laser beam by following changes in the fluorescence spectrum of the R6G in the aerosol particles. Fig. 4 shows the shifts in the spectrum as evaporation proceeds in the aerosol. These shifts may be related to similar shifts in calibration bulk samples, thereby permitting

in-situ determination of R6G concentration , and, from knowledge of initial particle size distribution, the average particle size in the aerosol evaporating in the laser beam. Temperatures may also be measured similarly by calibration. These studies have been carried out using an Ar-Icn laser By further refining techniques such as these, it is our aim to develop experimental systems for detailed study of aerosol evolution in laser beams.

ACKNOWLEDGMENT

Work performed here was supported under Contract DAAK11-83-K-0006 from the Chemical Research & Development Center, U. S. Army. The advice and assistance of Dr. Edward W. Stuebing and Dr. Glenn O. Rubel of the Chemical Research & Development Center are gratefully acknowledged.

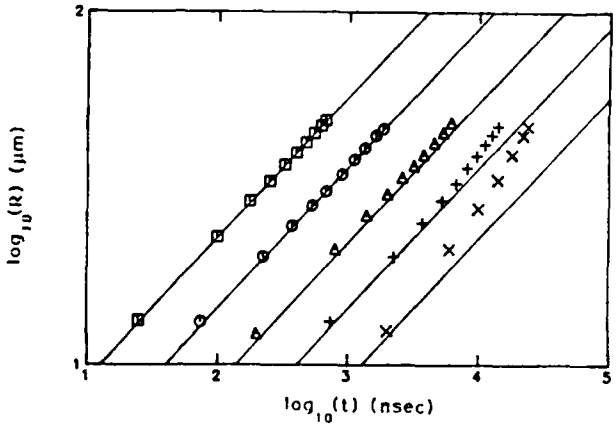

LEGEND	Initial Pressure (kPa)	Input energy (erg/gm)
□	4.0E+10	1.0E+12
○	4.0E+09	1.0E+11
△	4.0E+08	1.0E+10
+	4.0E+07	1.0E+09
×	4.0E+06	1.0E+08

Note Energy input is in addition to the energy required for vaporization (~ 1.0E+10 erg/gm)

Figure 1. Shock Position vs. Time: Computed, and Taylor Blast Wave Solutions for Various Energies.

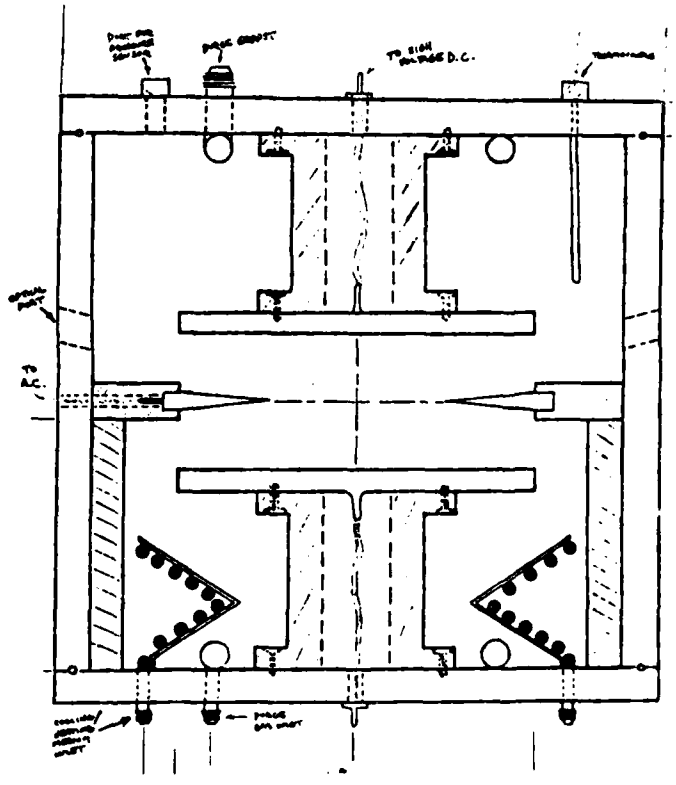

Figure 2. Schematic diagram of electrodynamic balance cell for single particle-laser radiation studies.

Figure 3.

Schematic Diagram of Laser/
Aerosol Dynamics System

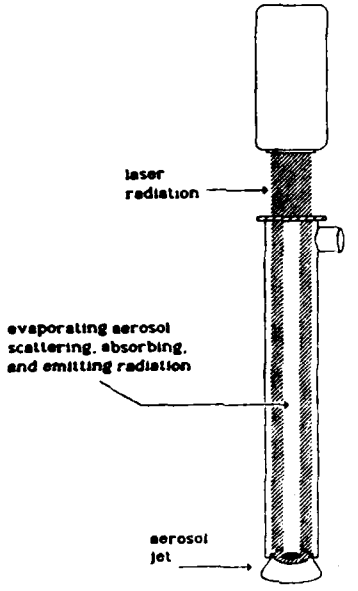

Figure 4. Fluorescence spectra from aerosol in laser/aerosol dynamics system shown in Fig. 3. Aerosol consists initially of 21 mmol/liter of R6G in methyl alcohol (0.9 volume fraction) and ethylene glycol (0.1 volume fraction). (b) represents aerosol with methyl alcohol evaporated in system and (c) represents continued eveporation of ethylene glycol. For initial particle size (a) of 9μm, mean particle sizes are: (b) 4.2 μm, (c) 2.1 μm .

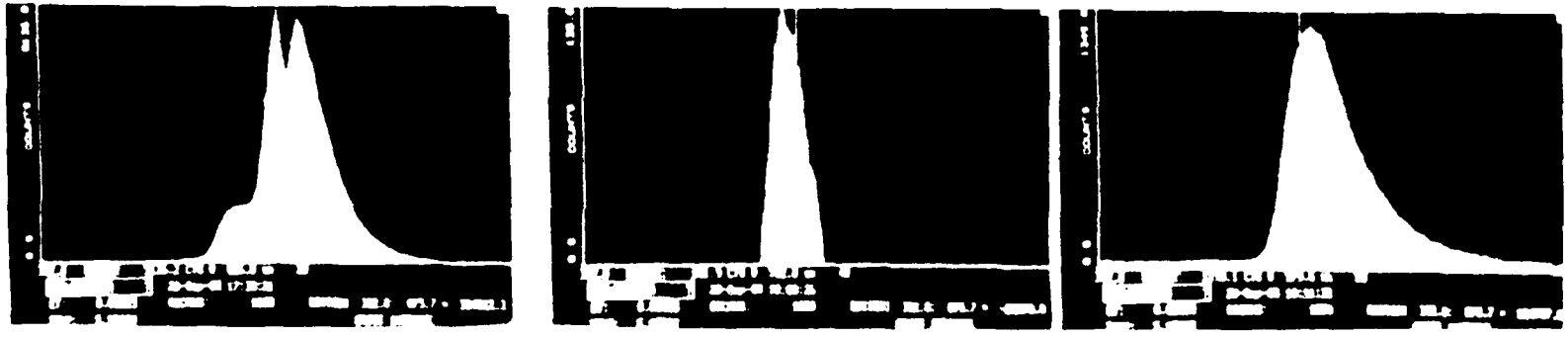

(a) (b) (c)

On the Propagation of Intense Optical Pulses through Vaporizing Aerosols

R. L. Armstrong
Physics Department, Applied Laser Optics Group
New Mexico State University
Las Cruces, NM 88003

A. Zardecki and S. A. W. Gerstl
Theoretical Division, MS P371
Los Alamos National Laboratory
Los Alamos, NM 87545

RECENT PUBLICATIONS, SUBMITTALS FOR PUBLICATION, AND PRESENTATIONS:

R. L. Armstrong, "Scattering and Absorption of Laser Radiation by Atmospheric Aerosols", International Symposium - Workshop on Particulate and Multi-Phase Processes", April 1985, Miami Beach, FL

R. L. Armstrong, S. A. W. Gerstl and A. Zardecki, "Nonlinear Pulse Propagation in the Presence of Evaporating Aerosols", J. Opt. Soc. Am. A2, 1739 (1985).

R. L. Armstrong, A. Zardecki and S. A. W. Gerstl, "On the Propagation of Intense Optical Pulses through Vaporizing Aerosols", 1985 CRDC Conference on Obscuration and Aerosol Research, June 1985.

ABSTRACT

A mathematical model has been developed describing the propagation of a pulsed, quasi-monochromatic beam of electromagnetic radiation in a medium containing vaporizing aerosols. Spatial and temporal distortions in the propagating beam result from radiation-induced changes in the absorption and scattering coefficients as well as in the angular spread of the scattering phase function. Numerical solutions to the equations are obtained for the case of pulse propagation through a cloud of vaporizing water droplets. These solutions demonstrate that significant pulse distortion accompanies enhanced aerosol vaporization.

DISCUSSION

The characteristics of laser beams propagating along an atmospheric path may be significantly altered by interactions with absorbing aerosols. For sufficiently intense beams, the aerosols may reach elevated temperatures, exhibit enhanced vaporization, and serve as the source of shock wave and plasma formation in the surrounding medium. The resulting, possibly substantial, perturbations on the propagating beam include beam wander or spread, partial or total attenuation in an absorbing plasma, and effective clearing of the aerosols along the propagation path with an attendant increase in the transmitted irradiance.

In a recent analysis[1] of the interactions of absorbing aerosols with pulsed light beams, approximate expressions have been obtained for the time-dependent aerosol temperature and vaporization rate. This analysis, in turn, permits the determination of the beam intensity and the droplet temperature along the beam path[2] when scattering and back reaction effects are neglected. The purpose of this paper is to extend this analysis for the case of a coupled system consisting of a dense aerosol medium and an intense laser pulse. As in Ref. 1, we maintain the assumption of low mass flux conditions which enables us to neglect the convective contribution to the mass flux. We also neglect the explicity time-dependent terms in the mass and energy conservation equations. The neglect of these unsteady terms restricts applications of this analysis to longer laser pulse lengths (e.g., greater than 10^{-7} sec for absorbing water droplets), and, generally, precludes a discussion of hydrodynamic effects. Finally, to the first approximation, we neglect the effect of non-uniform droplet heating and the localization of the beam at the droplet walls. These two effects are significant at short times, and for larger droplets whose radius exceeds 10 μm. On the other hand, the radiative transfer part of the problem is described correctly within the limits of the small-angle approximation to the equation of transport[3]. In this way, we are in a position to formulate the aerosol-beam interaction problem. The incoming beam heats the aerosol droplets, leading through evaporation to reduced values of the medium absorption and scattering coefficients; these changes in the coefficients of the medium, in turn, modify the shape of the pulse, producing pulse distortion.

The droplet-beam system is described by a set of coupled, non-linear differential equations expressing conservation of mass and energy in the irradiated droplet and the

radiative transport of the propagating beam[4]. We have obtained numerical solutions to these equations for the case of pulse propagation through a cloud of water droplets. At t=o, the leading edge of a pulse of monochromatic radiation propagating in the positive Z direction is incident on the Z=0 plane. The half-space Z>0 is filled with a uniform, monodisperse concentration of n water droplets per unit volume, each having an initial radius a . Note that the model calculations scale as the product (nZ) so that equivalent concentration-range regimes are easily generated. With the aid of the cited coupled equations, the droplet temperature rise and radius, and the beam irradiance are obtained on a three-dimensional (ρ,Z,τ) grid, where ρ is the transverse distance from the beam axis and τ is the retarded time. The step sizes on this grid, ($\Delta\rho$, ΔZ, $\Delta\tau$), are selected to achieve stability in the numerical integration scheme. For example, for intense beams, the medium characteristics change rapidly and a small time step must be used in the integration of the droplet temperature and radius equations.

Figures 1-3 illustrate the results of these calculations for the case of a weak beam. Each figure is a three-dimensional plot with the appropriate system variable (i.e., beam irradiance, droplet temperature rise or droplet radius) plotted against Z and τ, along the beam-axis, ρ=0. The incident beam, as illustrated in Fig. 1, is a rectangular pulse of 10.6μmradiation with a pulse length of 10^{-3} sec and an irradiance of 637 W/cm^2. The total energy in the pulse is 1J when the irradiance is integrated over the radial coordinate. The pulse is strongly attenuated for Z>0 as it advances into the aerosol medium which consists of a concentration of 2×10^5 droplets per cm^3, each having an initial radius of 5 μm. There is no observable distortion as the beam penetrates the aerosol cloud. The beam irradiance is simply uniformly reduced by the combined effects of aerosol absorption and scattering.

The reason for the lack of beam distortion is revealed by an examination of Figs. 2 and 3. Some droplet heating occurs which, as seen from Fig. 2, is sufficient to elevate the droplet temperature by about 40K at the Z=0 plane with progessively smaller elevations as Z advances into the medium. However, the increased vaporization produced by this elevated droplet temperature is insufficient to produce a substantial change in the droplet radius. This is seen from Fig. 3 where the droplet radius is virtually constant for all spatio-temporal points of interest. The scattering and

absorption characteristics of the medium then remain fixed with the result that the pulse propagates undistorted through the medium.

Figures 4-6 illustrate the results for the same aerosol-beam system as for the previous case, with the single distinction that the total beam energy is now 15J. The incident rectangular pulse is seen from Fig. 4 to undergo a marked distortion as it propagates into the aerosol cloud. The effect of pulse clearing is evident in Fig. 4 where the latter portion of the pulse is propagated with smaller attenuation. Figures 5-6 detail how the increased beam energy produces significant changes in the aerosol medium. The droplet temperature rise is seen from Fig. 5 to be nearly 80K at the entrance plane, and in contrast to Fig. 2 for the weak beam case, remains large as the beam propagates into the aerosol cloud. The marked increase in vaporization produced by this temperature increase is seen from Fig. 6 to result in a reduction in the droplet radius from 5 μm to about 2 μm at the entrance plane and to about 4 μm after the beam has penetrated 20 cm into the cloud. Since the scattering and absorption coefficients are proportional to a^{ν}, where the exponent ν typically lies between 2 and 3, the medium characteristics become strongly dependent on the spatio-temporal coordinates, and produce the distortion displayed in Fig. 4.

The results of this study suggest several areas where a more general treatment of aerosol-beam interactions is needed. First, the assumption of spherically symmetric aerosol heating becomes increasingly invalid for large, optically thick aerosols with the appearance of "hot spots" on the entrance and exit faces[5]. Internal thermal conductive processes, however, will tend to smooth out these heating inhomogeneities. It may be seen[6] that these processes occur with a characteristic time scale given by the thermal diffusion time, τ_σ, which is a function of the droplet radius. Therefore, for irradiation times shorter than τ_σ, heating inhomogeneities will be present in the irradiated droplet, whereas, for times longer than τ_σ, these inhomogeneities will be smoothed out and the droplet will approach a uniform temperature. Second, hydrodynamic effects, both within the heated aerosol and in the surrounding vapor should be investigated. They will become increasingly important at higher beam intensities and may be expected to modify the aerosol heating and vaporization scenarios sketched here. We are currently implementing a hydrodynamics computer code to begin to investigate hydrodynamic effects in intensely irradiated aerosols.

REFERENCES

1. R. L. Armstrong, Appl. Opt. 23. 148 (1984).

2. R. L. Armstrong, Appl. Opt. 23, 156 (1984).

3. R. L. Fante, Proc. IEEE, 68, 1424 (1980).

4. R. L. Armstrong, S. A. W. Gerstl and A. Zardecki, J. Opt. Soc. Am. A2, 1739 (1985).

5. P. W. Dusel, M. Kerker and D. D. Cooke. J. Opt. Soc. Am. 69, 55 (1979).

6. R. L. Armstrong, J. Appl. Phys. 56, 2142 (1984).

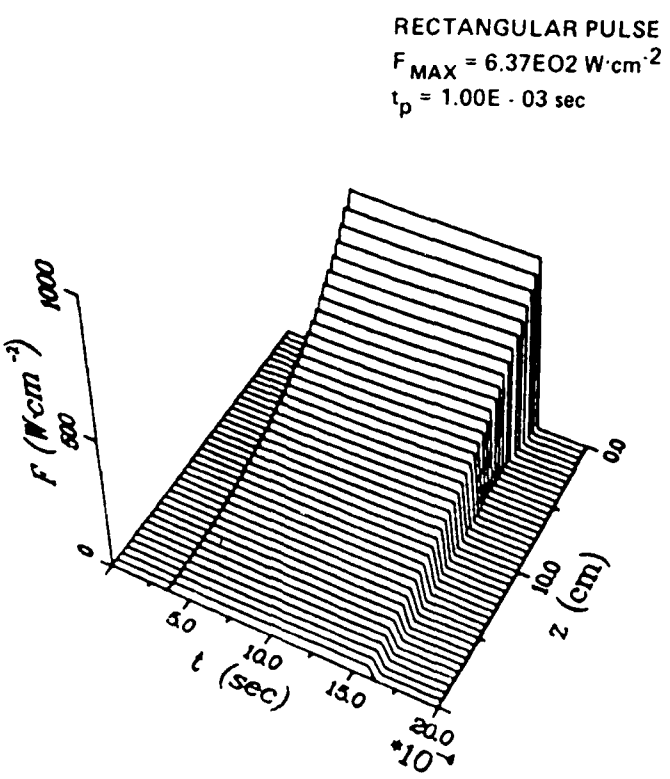

FIGURE 1. Space-time dependence of axial beam irradiance (W/cm^2) for 10.6 μm, 1 msec, 1 J rectangular pulse propagating in mono-disperse fog of 5 μm water droplets at a concentration of 2x10^5 cm^{-3} .

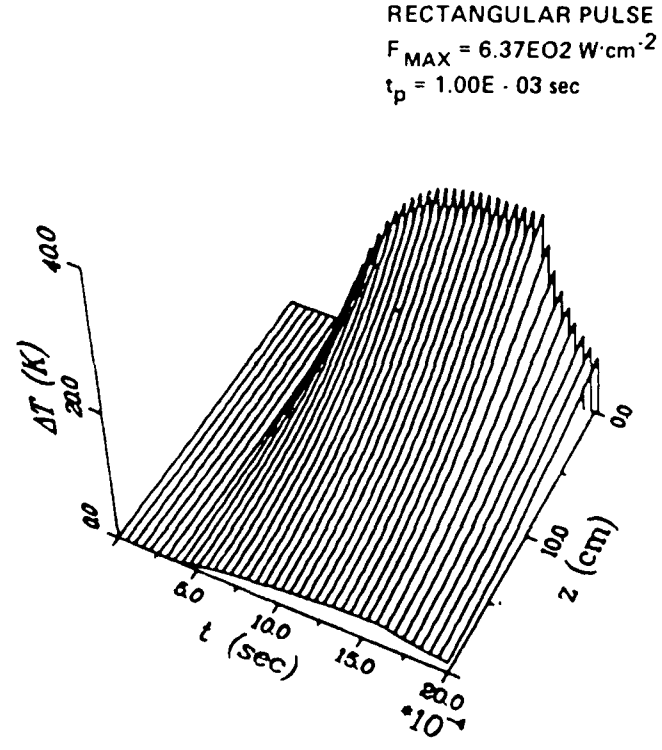

FIGURE 2. Space-time dependence of droplet temperature rise (K) for system of Fig. 1.

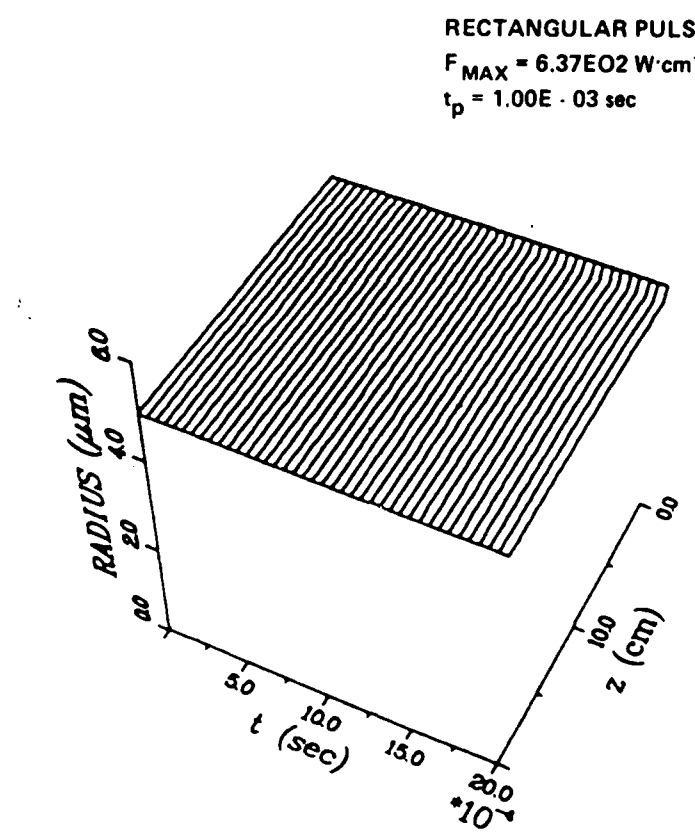

FIGURE 3. Space-time dependence of droplet radius (μ ≡ μm) for system of Fig. 1.

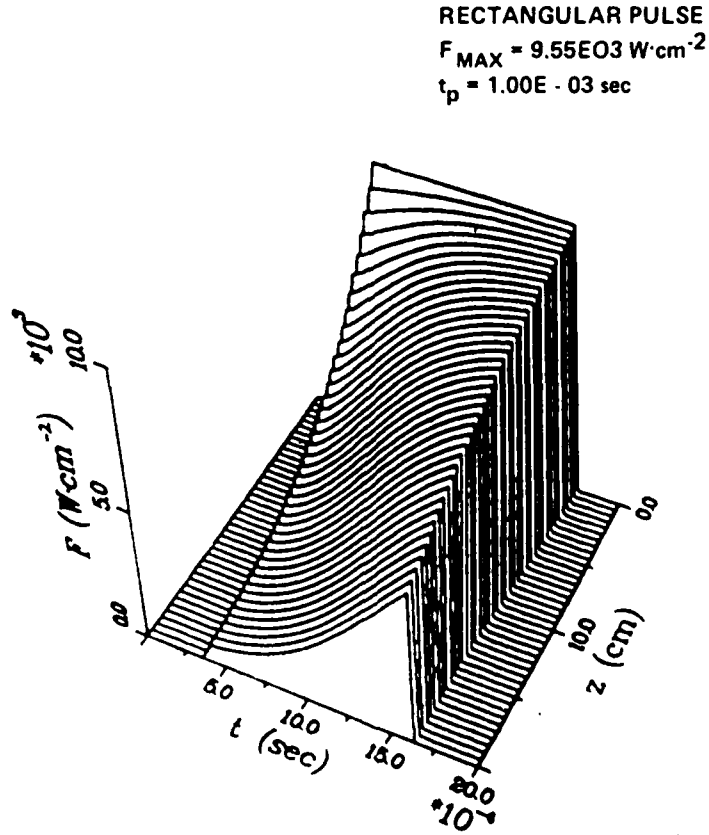

FIGURE 4. Space-time dependence of axial beam irradiance (W/cm^2) for system of Fig. 1 except beam energy is 15J.

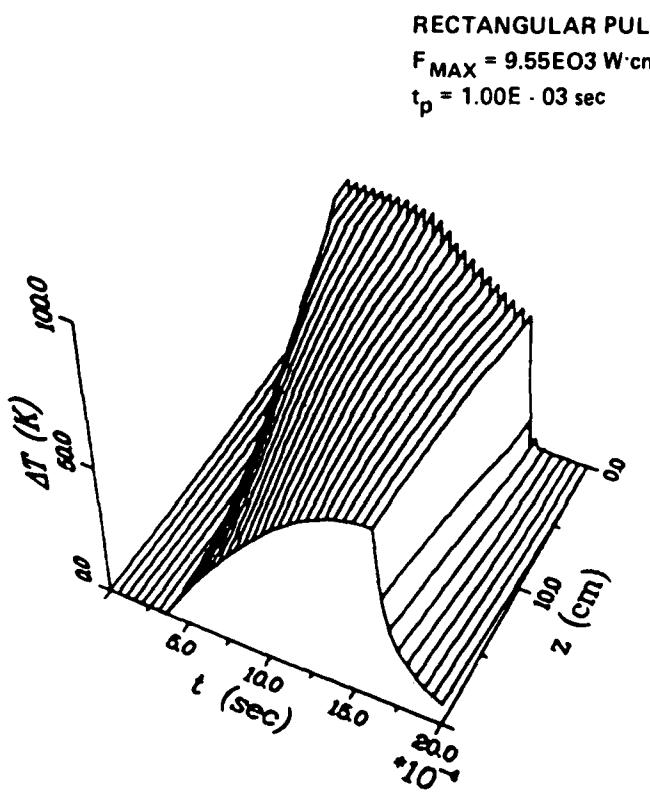

FIGURE 5. Space-time dependence of droplet temperature rise (K) for system of Fig. 1 except beam energy is 15J.

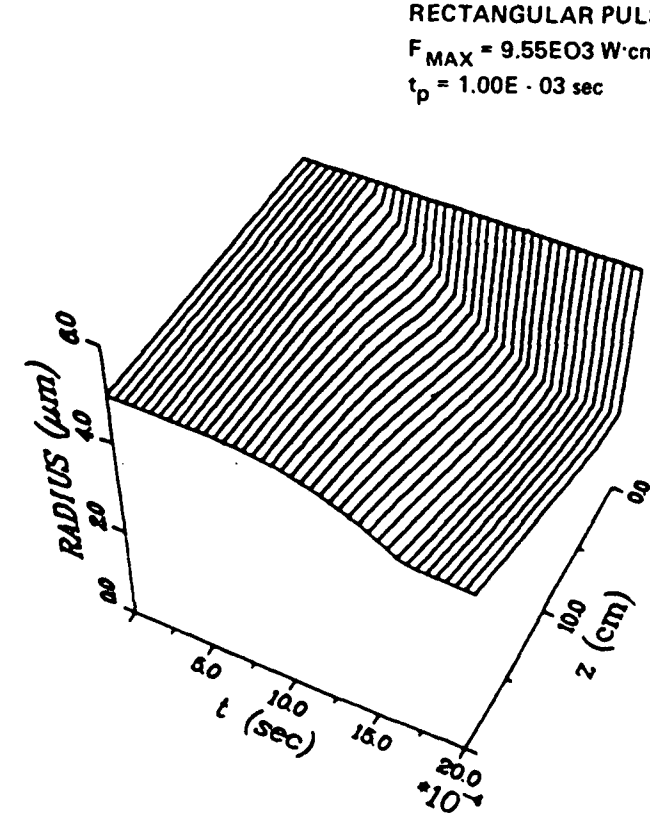

FIGURE 6. Space-time dependence of droplet radius (μ) for system of Fig. 1 except beam energy is 15J.

Hydrodynamic Response to Uniform Laser Absorption in a Droplet

B. Yudanin

Dept. of Physics, City College of CUNY
New York, N. Y. 10031

M. Lax

Dept. of Physics, City College of CUNY
New York, N. Y. 10031
AT & T Bell Laboratories
Murray Hill, New Jersey 07974

ABSTRACT

The hydrodynamical interaction of an aerosol with the ambient air requires the matching of boundary conditions at three points. The matching conditions will be discussed and approximate solution obtained.

Laser induced absorption in a spherical droplet will possess cylindrical symmetry (for circularly polarized input radiation) rather than spherical symmetry. Nevertheless, if the drop is small compared to the wave-length, the absorption will be approximately uniform. The response of the droplet is governed by several time scales, as pointed out by R. L. Armstrong [1]. At sufficiently short times, thermal conduction will be unimportant but a hydrodynamic response ensues in a time of the order of the droplet radius divided by the velocity of sound. The evaluation of this hydrodynamic response for the case of uniform absorption is a problem of interest in its own right. It will also, later, provide a test for two-dimensional hydrocode. The latter, needed when the absorption is non-uniform, can be tested for accuracy in the uniform case.

Our problem can be formulated in an idealized manner: at time $t<0$ a small water droplet (aerosol particle) starts in a hydrodynamical state with $V(r,t)=0$, $T(r,t)=T_w$, $\rho(r,t)=\rho_w$, $P(r,t)=P_w$; at the same time surrounding air starts in the state: $V(r,t)=0$, $T(r,t)=T_a$, $\rho(r,t)=\rho_a$, $P(r,t)=P_a$, where T_w, P_w, ρ_w, t_a, P_a, ρ_a - are given initial temperature, pressure and density of water droplet and air respectively (assumed uniform for simplicity). The above state can be understood to occur upon absorption of a short laser pulse, before any hydrodynamical response has occurred. At time $t = 0$ the surface separating the aerosol from surrounding atmosphere is withdrawn and acoustic interaction begins.

The full time-dependent solution to this problem in analytic form does not appear

[1] R. L. Armstrong, "Interaction of absorbing aerosols with intense light beams", J. Appl. Phys. 56, (7), 1984, (2142-2153).

feasible. Complexity arises because the boundary conditions on the surface of the droplet are unknown before the solution of the problem is found. As a result of an initial pressure difference inside and outside the droplet, the interface will gain velocity as soon as the interaction starts. This moving boundary will serve as a cause of waves in both water and air. On the other hand, boundary conditions at the surface couple changes in state of the water and air. If we neglect surface tension, then, at the interface, the pressure on both sides of the surface should be equal (the imaginary surface separating droplet from air does not have any mass), and furthermore the hydrodynamical velocity of water and air should be the same and equal the as yet unknown velocity of the surface $R(t)$.

In other words the boundary conditions for internal (droplet) and external (surrounding air) problems are:

$$V_{\text{water}}(r = R(t)) = V_{\text{air}}(r = R(t)) = \dot{R}(t) \tag{1}$$

$$P_{\text{water}}(r = R(t)) = P_{\text{air}}(r = R(t)) \tag{2}$$

where $\dot{R}(t)$ (rather $R(t)$) can be found from the mass conservation condition provided the solution for the water droplet is known, e.g.

$$\int_0^{R(t)} \rho_{\text{water}}(r, t) r^2 dr = \int_0^{R_0} \rho_w r^2 dr \tag{3}$$

where $R_0 \equiv R(0)$.

We must deal with two sets of hydrodynamic equations which describe waves in water and air respectively, (adiabatic type equations of state are used because no additional energy source is present).

$$\frac{2}{\gamma-1}\frac{\partial a}{\partial t} + a\frac{\partial V}{\partial r} + \frac{2}{\gamma-1}\frac{\partial a}{\partial r} + \frac{2Va}{r} = 0 \tag{4}$$

$$\frac{\partial V}{\partial t} + V\frac{\partial V}{\partial r} + \frac{2}{\gamma-1}a\frac{\partial a}{\partial r} = 0 \tag{5}$$

where $a^2(r, t) = (\partial P / \partial \rho)_s$ - local sound velocity; $\gamma = 1.4$ for air, $\gamma = 3.0$ for water; and additional condition (3), mass conservation, in integral form. We specialize to the case where the droplet has a gas-like equation of state, for illustrative purposes only.

Because of the unusual nature of this integral condition (3) we do not attempt to get a complete numerical solution for the stated problem, but rather try to get the interface velocity using a crude approximation for the waves inside and outside the droplet and then use this velocity to get a more correct numerical solution for these waves.

In this paper we present a rough calculation of the interface velocity (assuming it to be constant in time) as a function of a given initial pressure difference in water and in air due to interaction with laser irradiation.

Let us first consider a wave which propagates in air due to an expanding spherical surface near the origin. If the sphere expands with velocity greater than the sound velocity of the air then a shock wave will develop. For the case when the initial pressure of the water is several orders of magnitude greater than that of the air, the velocity of the interface will instantly become greater than the sound velocity of the air which means that a shock will start immediately from the boundary and propagate into undisturbed air with some yet unknown velocity U_{shock} satisfying the relations $U_{\text{shock}} \gg \dot{R}(t) > a_{\text{air}}$. After a short time $t > R_0 / a_0$ the shock in air will be at a distance R_{shock} much greater than initial radius of the sphere R_0 which means that motion of the shock will not be affected by the expanding sphere any longer so to a good

approximation it can be considered as self-similar. The solution of such a problem was found by G.I.Taylor [2].

For the wave propagating in the drop the situation is more complicated. A rarefaction wave starting from the outwards - moving surface will propagate toward the center. Even before this wave will reach the center and reflect as a compression wave, interfering with the initial rarefaction wave and producing a very complicated "standing - type" wave, it cannot be considered as a simple wave. This initial rarefaction wave has two points of weak discontinuity [3] separating regions in which different types of solution exist.

So the complete problem (drop and surrounding air) can be divided into 5 simpler ones in 5 different regions of radial variable r with matching conditions at the boundaries of these regions.

Region 1 ($0<r<r_1$) and 2 ($R_{shock}<r<\infty$) where disturbance has not yet arrived.

Region 3 ($r_1<r<r_2$) where the wave can be described as a simple one possessing

$$V_{water}+\frac{2}{\gamma-1}a_{water}\approx\frac{2}{\gamma-1}a_w \tag{6}$$

where a_w is the initial sound velocity of water.

Region 4 ($r_2<r<R(t)$) and 5 ($R(t)<r<R_{shock}$) where to a good approximation the wave is of self-similar type.

The boundary points r_1, r_2 and R_{shock} are given via equations:

$$r_1=R_0-a_w t \tag{7}$$

$$r_2=(R_0+Ut)(V_{water}-a_{water})/U \tag{8}$$

$$R_{shock}=U_{shock}t+R_0 \tag{9}$$

where V_{water} and a_{water} are time-dependent.

In order to get a solution in regions 4 and 5 we introduce a self-similarity variable z and use rescaling of velocity and sound velocity (self-similar behavior of $V(r,t)$ and $a(r,t)$ was assumed)

$$z=\frac{r}{R(t)}=\frac{r}{R_0+Ut}\qquad x=\frac{V(r,t)}{Uz}\qquad y=\frac{a^2(r,t)}{U^2z^2} \tag{10}$$

where the surface velocity was assumed constant ($\dot{R}(t)=U$). Equations (4), (5) after the substitution (10) can be reduced to the set of 4 equations for water and air (subscripts w and a are suppressed):

$$\frac{dy}{dx}=2\frac{y}{x}\frac{(1-x)(\gamma x-1)+y}{3y-(1-x)^2} \tag{11}$$

[2] G. I. Taylor, "The air wave surrounding an expanding sphere", Proc. R. Soc. London, **A 186**, 1946, (273-292).

[3] Y. B. Zeldovich and Y. P. Raizer, "Physics of Shock Waves and High-Temperature Hydrodynamics Phenomena", Academic Press, New-York, 1966.

$$\frac{dz}{dx} = \frac{z}{x}\frac{(x-1)^2 - y}{3y - (x-1)^2} \tag{12}$$

with boundary conditions

$$x_1 = 1 \quad z_1 = 1 \quad y_1 = ?$$
$$x_2 = ? \quad z_2 = ? \quad \begin{cases} y_2 = (1 + 0.5(\gamma - 1)\,x_2)(1 - x_2) & \text{for air } (\gamma = 1.4) \\ y_2 = (1 - x_2)^2 & \text{for water } (\gamma = 3.0) \end{cases} \tag{13}$$

Here Huqoniot conditions on the shock front at point R_{shock} and equations (6), (8) at point r_2 were used.

In the outer gaseous region 2, all variables remain at their initial value. This value is used to initiate a solution of equations (4) and (5) into region 2 from R_{shock} to $R(t)$. Also, the undisturbed solution in region 1 is used to initiate a solution in region 3 which is approximately given by Eq.(6). These solutions provide one boundary condition at r_2 and another at $R(t)$. Thus equations (10) and (11) in region 4 must be solved for a two-point boundary condition which requires an iterative procedure. Matching obtained solutions at the boundary from the outer and inner sides one can get the velocity of the surface of a droplet. The latter is presented in Fig.1.

ACKNOWLEDGMENTS

Work at City College was supported in part by the Army Research Office and the Department of Energy.

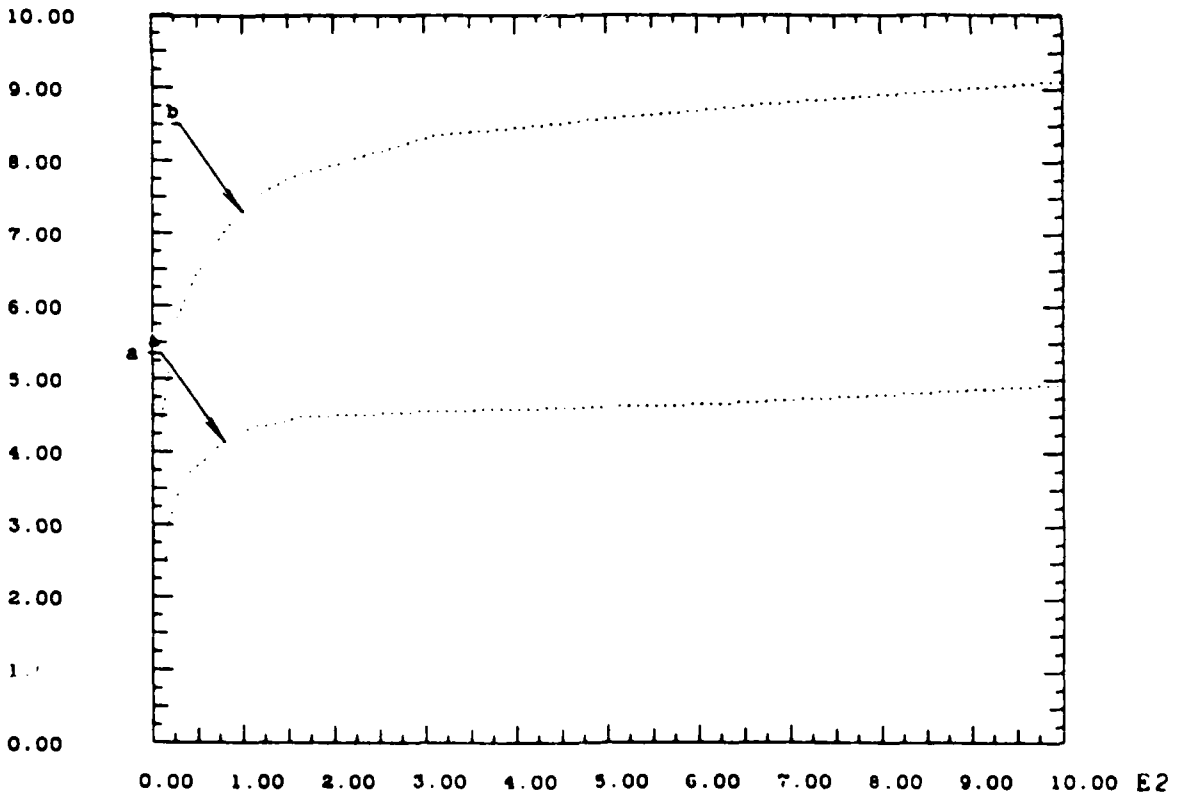

Figure 1. Velocity of the surface U / a_s as a function of initial pressure P_w / P_s for:
a) $a_w / a_s = 5$
b) $a_w / a_s = 10$

Editing Procedures for the Sandia TOODY Hydrodynamics Code.

Melvin Lax and Shirish M. Chitanvis[†]

Physics Department, City College of the City University of New York, New York, 10031

ABSTRACT

We describe some of the general procedures used to transform the non-portable TOODY hydrodynamical code so that it can run on any machine using a fortran 77 compiler.

(1) INTRODUCTION

The reason for making these changes is that this code was written for a CDC7600, in a non-portable dialect of fortran66, making it impossible to be run on a VAX which uses a fortran77 compiler, or indeed on any other computer except a CDC7600.

The files are large, one of them being one Mbyte long, with more than 25K lines. The UNIX utility fsplit can split a Fortran program into its separate subroutines. However, it was not useful here because many "MAIN" files resulted, because this file contained eight overlays. These overlays were located by using the command

fgrep -n OVERLAY f2

where f2, the second of four files read from the tape was the only one containing overlays. The eight overlay files were then separated with the command

extract m n f2 g10

which extracts the lines from m to n from f2 and places them into g10. In this way, the eight files g00, g10, g20, g21, g22, g23, g24, and g30 corresponding to the eight overlays were constructed. The **extract** command was constructed using a small C program extract.c written for

[†]Present address: Los Alamos National Laboratory, T.DOT, MS-P371 Los Alamos, NM 87545

the purpose. Since the individual overlay files were themselves as large as 300,000 characters, ordinary editors are inadequate for processing these files.

To cope with these enormous files, as well as to handle the complex editing required, we found several UNIX[1] tools to be especially convenient. Our most frequently used tool was the programable stream editor **sed**.[2] Our second most useful tool was the field oriented programable editor **awk**.[3] We also made use of the **m4**[4] macro processor, and the most powerful tool of all, the lexical analyzer, **lex**.[5] Occasionally, it was necessary to write a small C program[6] to perform a particular function, or as a support file for **lex**.

Without such tools, it would be much harder, if not impossible to make the required changes in the code except by writing a special purpose program for each required change. Incidentally, this underscores the point that it is not always wise to write non-portable code. It would have saved a lot of labor at no cost in efficiency to have written the TOODY code in a portable manner to begin with.

We have provided below a selection of the programs we wrote to effect some of the required changes in the TOODY code. We hope it will give the reader a taste of the kinds of problems we encountered and solved.

---

[1]UNIX is a trademark of A.T.T. Bell Laboratories A general description of UNIX is given in *The UNIX Programming Environment*, by Brian W. Kernighan and Rob Pike, Prentice Hall 1984 and in two special issues of the Bell System Journal: July, 1978 and October 1984.

[2]Lee E. McMahon, SED — A Non-interactive Text Editor Bell Laboratories Technical Memorandum August 1978 See Vol. 2 of the UNIX Programmer's Manual, Holt Rinehart, and Winston. References to a Bell Laboratories Memorandum and Volume 2 of the UNIX Programmers Manual will hereafter referred to by ibid.

[3]Alfred V. Aho, Brian W. Kernighan, and Peter J. Weinberger, AWK# — A Pattern Scanning and Processing Language Software — Practice and Experience, July 1978. Also ibid.

[4]Brian W. Kernighan and Dennis M. Ritchie, The M4 Macro Processor, July 1977. ibid.

[5]Michael E. Lesk and E. Schmidt, Lex — A Lexical Analyzer Generator ibid.

[6]Brian W. Kernighan and Dennis M. Ritchie, The C Programming Language, Prentice-Hall 1978

(2) IF(X) 123 , 456

This is a fortran66/CDC idiosyncrasy. This must be translated into:

```
IF(X) GO TO 123
GO TO 456
```

This is accomplished by the shell file **logicalif** which invokes the stream editor **sed** and applies it to a set of files:

```
for i
{
sed '
s/\(IF *(\)\(.*\)) *\([1234567890][1234567890]*\) *,
 *\([1234567890][1234567890]\) *$/IF(\2) GO TO \3\
      GO TO \4/
' $i > if.$i
}
echo $0 done
```

The line following the comma in the substitution command is actually part of the previous line in logicalif. It is broken up here for readability.

(3) DECODE STATEMENTS.

Fortran 77 does not accept decode statements. Fortran 66 does (did). The **decode** file translates

DECODE(13,15,AA) G , T etc.

into

READ(AA,15) G , T etc.

which is acceptable by fortran 77. The stream editor command **decode** is given by:

```
sed '
s/DECODE *(\(.*\) *, *\(.*\) *, *\(.*\) *)\(.*\)$/READ(\2,\3)\4/'
```

(4) ARRAY(N).

Fortran 66 is clever/stupid enough to know that if you declare an array to be two-dimensional, and later in the program call it as a one-dimensional array, e.g.

```
DIMENSION ARRAY(N,M)

ARRAY(N) = 1.0
```

then, you really mean

```
ARRAY(N,1) = 1.0
```

The **fixequiv** file does that job for you. The **fixequiv** file has the form:

```
sed '
s/ARRAY *(\([0123456789][0-9]*\))/ARRAY(\1,1)/g' <$1 >$1.eq
```

(5) COMMON STATEMENT.

Fortran 77 does not like the statement

```
COMMON/number/...
```

Instead, it likes

```
COMMON/characters/...
```

The **sed** file called **common** takes care of this fact. The **common** file takes the form:

```
sed '
s/COMMON\(.*\)\([1234567890]\)\(\/\)/COMMON\1C\2\3/'
```

(6) MULTIPLE EQUAL SIGNS

More complicated than the preceding examples of non-portability is the frequent use of multiple equal signs on one line as in

A = B = C = D = SUM

Because the number of equal signs on a line is unknown, the usual editing programs, **ed** and **sed** are difficult to use. However, the field oriented editor **awk** is particularly appropriate because the = can be adopted as the field delimiter. The 11 lines of the awk code **equal**, shown in Table 1, sets each field equal to the last:

The problem lies with all the exceptional cases to which **equal** should *not* be applied. For example, multiple = signs can appear in PROGRAM, COMMENT, FORMAT, READ, WRITE and PRINT statements. For such lines, the transformation should not be applied. There is a simple scheme to accomplish this: place a % symbol at the beginning of each such line with **putpercent** (an **sed** program). The code shown for **equal** will only correct lines that do not start with a %.

Now the plot thickens. We must not only protect these lines with a percent symbol, we must also find any continuation lines associated with these statements and guard the latter as well. This can be done, but only by making rather sophisticated use of **sed** in putpercent. The correct code for **putpercent**, found only after some "experimentation", is shown in Table 2.

The next stage consisted in recognizing that the multiple equal signs themselves are sometimes continued beyond one line. (In one megabyte of code, all the bad things that could happen did.) It was not too difficult to modify putpercent to detect such continuations and put all the equal signs on one long line. The length of the line is no problem since it will be split later by **equal**.

The **putpercent** program that recognizes an arbitrary number of continuation lines must absorb at least one extra line while doing so. This caused failure when any two statements (FORMAT, WRITE etc.) are adjacent to each other. So we wrote a precursor program **protect** that put two extra comment lines containing only CC before each case to be protected. (One such line should have been enough!) Finally, all comment lines themselves should be protected. Thus our complete procedure can be executed by the command:

runtoody g??

where the shell file **runtoody** is given by:

SHELL FILE RUNTOODY

```
for i
{
protect <$i | putpercent | yy | equal |
        rmpercent | rmdol | ffold >$i.out
}
echo $0 done
```

The command **runtoody** g?? will cause runtoody to act on g00, g10, g20, g21, g22, g23, g23, g30, the overlay files produced by extract.

The file **rmpercent** removes the now extraneous percents and the extra comment lines. The **sed** file rmdol replaces the $ as a statement separator by newline plus six blanks, so that multiple statements are now on separate lines. The command ffold comes from a C file ffold.c that we have written to perform a Fortran fold at column 80 in case some lines have been made too long by a previous transformation. The folding takes place at column 80 and appropriately formatted continuation lines are automatically produced.

(7) CONDITIONAL MULTIPLE EQUAL STATEMENTS

So far, we have done only the easy part! In addition to the above complications, we discovered that there were lines containing an IF statement, followed by multiple equal signs. Clearly, the first field, containing the IF, should not be set equal to the last field. In addition, such IF statements also occurred with continuation lines! These lines must be combined into a single line by **putpercent**. Then we follow a strategy suggested by B.W. Kernighan: Replace

```
      IF (CONDITION) STATEMENT
```

by

```
      IF (.NOT.CONDITION) GOTO N
      STATEMENT
N     CONTINUE
```

This is to done, of course only if STATEMENT contains multiple signs. The integer N is chosen to start at 10,000 and incremented by 10 for each case to avoid collision with existing

statement labels. The computational ability of awk is used to compute these statement numbers. The remaining difficulty is that there is no simple procedure with **ed**, **sed** or **awk** to recognize the CONDITION. The reason is that CONDITION can contain arrays and subconditions such as

```
IF ((A(1) .EQ.B) .AND. (C(2,1).EQ D(7))) X=YZ=WAB
```

The most likely tool to recognize a CONDITION is the lexical analyzer **lex**. The program lexif.l shown in Table 3 is converted by lex to lex.yy.c and compiled by C to give the binary file yy used in runtoody above. With the experience gained in **lex** it might be possible to make all the changes needed using a large lex file.

(7) CONCLUSIONS.

We have presented here a selection of the some of the problems we ran into in trying to port the TOODY code written in a nonportable version of fortran 66 to a VAX running a fortran 77 compiler.

A problem that we ran into, but have not yet been able to solve is one in which integers are compared with character strings (in some input/output routines). Such a comparison poses no problems on the 7600 when the character strings are 10 bytes long. This is because one word occupies 10 bytes on the 7600. On the other hand on a VAX, where one word occupies 4 bytes, this definitely poses a problem, as the comparison involves an integer and a character string, both of different lengths. Equivalencing the appropriate integer and string does not solve the problem, since we would still be comparing two entirely different entities.

We continue to work on this problem of porting the TOODY code to a VAX. And we hope to bring the project to a successful completion.

ACKNOWLEDGEMENTS

Work at City College was supported in part by the Army Research Office, and the Department of Energy.

Table 1. THE AWK PROGRAM EQUAL

```
awk '
BEGIN { FS = "=" }
!/^ %/  {
      if (NF == 1) print $0
      else {
            for (i = 1; i < NF; i++)
            if (i<NF-1) printf "%s=%s\ n      ", $i, $NF
            else printf "%s=%s\ n", $i, $NF
            }
      }
/^ %/ { print $0
}'
```

Table 2. THE **sed** PROGRAM **putpercent**

```
sed '
:back
/^  *[0-9]*  *[Ff][Oo][Rr][Mm][Aa][Tt]/{
s/^ /\ %\ %/
t reset0
: reset0
:start0
s/\ *\ "/g
n
s/^      \([^  ]\ )/\ %\ %     \ 1/
tstart0
b back
}
/[Ww][Rr][Ii][Tt][Ee] *(/{
s/^ /\ %/
t reset2
: reset2
```

```
:start2
n
s/^     \([^ ]\)/\%     \1/
tstart2
b back
}
/[Rr][Ee][Aa][Dd] *(/{
s/^ /\%/
t reset7
: reset7
:start7
n
s/^     \([^ ]\)/\%     \1/
tstart7
b back
}
s/[Pp][Rr][Ii][Nn][Tt] *\([0-9][0-9]*\),\(.*\)/write(6,\1)\2/
s/[Pp][Rr][Ii][Nn][Tt] *\([0-9][0-9]*\) *$/write(6,\1)/
/^C/s/^ /\%/
/[Pp][Rr][Oo][Gg][Rr][Aa][Mm]/{
s/^ /\%/
t reset4
:reset4
:start4
n
s/^     \([^ ]\)/\%     \1/
tstart4
b back
}
/[Ii][Ff] *(.*).*=.*=/{
t reset5
:reset5
:start5
N
s/\n     \([^ ]\)//
tstart5
```

```
P
D
b back
}
/^ [^ %#].*=.*=/{
t reset6
:reset6
:start6
N
s/\n     \([^  ]\)//
tstart6
P
D
b back
}
/^ [cC]/s/^ /\ %/
s/common *\ / *\ ([0-9]\ )/common \ /cmn\ 1/
 ' $1
```

Table 3. THE LEX PROGRAM **lexif.l**

```
%%
IF[ ]*"(".*")".*=.*=.*${ fix(yytext);}
%%
int n = 1000;
fix(ss)
char *ss;
{
      int npar;
      char c;
      char t[81], *tmp;
      printf("if(.not.");
      while(*ss++ != '(');
      *t = '(' ;
      tmp=t+1;
      for(npar = 1 ;npar > 0;) {
```

```
            *tmp++ = c = *ss++;
            if(c == '(') npar++;
            if(c == ')') npar--;
            if( c == ' ') break;
        }
        if( *ss == ' ') {
        }
        *tmp=' ';
        printf("%s) GO TO %d\n",t,10*++n);
        printf("      %s\n",ss);
        printf("%d   continue",10*n);
}
yywrap()
{
        fprintf(stderr,"end of yy processing\n");
        return 1 ;
}
```

A COMPARISON SOFTWARE FOR A SET OF NONLINEAR SIMULATIONS WITH AN EXAMPLE: CW PROPAGATION OF HIGH POWER LASER IN SATURABLE TWO-LEVEL ABSORBERS*

Farrès P. Mattar[1,2] and Alain W. Matos[1]
[2]Department of Physics, New York University, New York, NY 10003 and
[2]George R. Harrison Spectroscopy Laboratory, Massachusetts Institute of Technology, Cambridge, MA 02139

in collaboration with

Jiri Teichmann*, Yves Claude, Michel Cormier, Pierre Cadieux and Ramsay Zahar; and Claude Goutier**
Department of Physics*, Departement d'Informatique et de Recherche Operationelle; and Centre de Calcul**
Departement d'Informatique et de Recherche Operationelle; and Centre de Calcul*
Université de Montreal, Montreal, P.Q., Canada

RECENT PUBLICATIONS, SUBMITTALS FOR PUBLICATION AND PRESENTATIONS:

A) K. Tai, H.M. Gibbs, M.C. Rushford, N. Peyghambarian, J.S. Satchell, M.G. Boshier, R.J. Ballagh, W.J. Sandle, M. LeBerre, E. Ressayre, A. Tallet, J. Teichmann, Y. Claude, F.P. Mattar and P.D. Drummond, "Observation of Continuous-Wave On-Resonance Self-Focusing", Opt. Lett. 9, 243-245 (1984).

B) F.P. Mattar and C.M. Bowden, "Coherent Pump Dynamics and Pulse Evolution in Three-Level Superfluorescence and Control of Light by Light", in the Section on Laser Propagation and Laser Matter Interaction in Gas Flow and Chemical Lasers IV ed. M. Onorato, p. 739-747, Plenum Press, 1984).

C) M. LeBerre, E. Ressayre, A. Tallet and F.P. Mattar, "Quasi-Trapping of Gaussian Beams in Two-Level Systems", J. Opt. Soc. Am. B2, 956-967 (1985).

D) J. Teichmann, Y. Claude and F.P. Mattar, "On the Perturbative Theory of the Onset of the Self-Focusing in the Purely Absorptive CW Optical Beam Propagation", Opt. Commun. 54, 33-38 (1985).

E) J. Teichmann, Y. Claude, F.P. Mattar, C. Bardin, J.P. Babuel-Peyrissiac and J.P. Marinier, "Physical Insights on the CW On-Resonance On-Axis Focusing in the Purely Absorptive CW Optical Beam Propagation of Intense Laser Beams in Absorbers", Abstract Digest 1984 DEAP Meeting of the Am. Phys. Soc., Univ. Connecticut, Storrs, CT, (May 1984) and submitted to J. Opt. Soc. B. (Sept. 1985)

F) P.R. Berman, E.J. Robinson and F.P. Mattar, "Transverse and Dispersion Effects in the Strong Pump Weak Probe Interaction", Abstract Digest of the Southwest Conference on Optics, Albuquerque (4-8 March 1985).

G) F.P. Mattar, "Fresnel Dependence of Quantum Fluctuations in Two-Color Superfluorescence from Three-Level Systems", Abstract Digest of the Southwest Conference on Optics, Albuquerque (4-8 March 1985), and submitted to Phys. Rev. A. (Fall 1985)

H) J. Teichman, Y. Claude, F.P. Mattar, C. Bardin, J.-P. Babuel-Peyrissac and J.P. Marinier, "Physical Insights on the CW On-Resonance On-Axis Focusing in the Purely Absorptive CW Optical Beam Propagation of Intense Laser Beams in Absorbers," Abstract Digest of the Southwest Conference on Optics, Albuquerque (4-8 March 1985), and submitted to publication in Optical Engineering by SPIE. (Sept. 1985)

I) J.P. Babuel-Peyrissac, J.P. Marinier, C. Bardin, F.P. Mattar, J. Teichmann, Y. Claude and B.R. Suydam, "Small-Scale Whole-Beam Self-Focusing of very Intense Laser Beams in Saturable Absorbers", Abstract Digest of the Southwest Conference on Optics, Albuquerque (4-8 March 1985), and in Conference Proceedings, ed. R.S. McDowell and S.C. Stotlar, to be published by SPIE, vol. 540, 569-580 (1985).

J) C. Bardin, J.P. Babuel-Peyrissac, J.P. Marinier and F.P. Mattar, "A Finite Hankel Algorithm for Intense Optical Beam Propagation in Saturable Medium", Abstract Digest of the Southwest Conference on Optics, Albuquerque (4-8 March 1985), and in Conference Proceedings ed. R.S. McDowell and S.C. Stotlar, published by SPIE, vol. 540, p. 581-587 (1985).

K) F.P. Mattar, J.P. Babuel-Peyrissac, J.P. Marinier, and C. Bardin "Transverse Effects in the Simultaneous Propagation of Coherent Different-Wavelength Pulses in Three-Level Absorbers", Abstract Digest of the Southwest Conference on Optics, Albuquerque (4-8 March 1985), and to be published as invited paper in J. Opt. Soc. B. as well as in Multiple Photon Dissociation of Poly-Atomic Molecules, ed. C.D. Cantrell (to be publ. Springer-Verlag 1985).

L) F.P. Mattar and C.M. Bowden, "Quantum Fluctuations in Light Control by Light: Coherent Pump Depletion Effects and Spectral Variations on the Evolution of Superfluorescence", Abstract Digest Southwest Conference on Optics, Albuquerque (4-8 March 1985).

M) F.P. Mattar, "Transverse and Dispersion Effets in the Strong Pump Weak Probe Coherent Interaction", (invited paper) Proceedings of the Seventh International Conference of Laser Spectroscopy, Maui, Hawaii (June 1985) ed. by T.W. Hänsch and Y.R. Shen, pub. by Springer-Verlag, p. 218-219; and in Proceedings of the Southwest Conference, Albuquerque, ed. R.S. McDowell and S.C. Stotlar to be published by SPIE, vol. 540, p. 588-603 (1985).

N) F.P. Mattar, Y. Claude, C. Goutier and C.M. Bowden, "Coherent Pump Dynamics, Propagation, Transverse, Diffraction and Dispersion Effects in Three-Level Superfluorescence Evolving from Either Deterministic or Quantum Initiation: Control of Light by Light", in Multiple Photon Dissociation of Poly-Atomic Molecules, ed. C.D. Cantrell (to be publ. Springer-Verlag 1985).

*[The original contribution of 200 pages has been severely edited to fit the constraints of these Proceedings. The original forms the basis of a final report to CRDC which may be obtained through the usual channels or from the first author.]

O) F.P. Mattar, J.P. Babuel-Peyrissac, J.P. Marinier and C. Bardin, "Self-Action Phenomena Associated with the Simultaneous Propagation of Coherent Different-Wavelength in Three-Level Absorbers", appearing in the Abstract Digest of the Instabilities and Dynamics of Lasers and Nonlinear Optical Systems Conference, Univ. of Rochester, Rochester, NY (18-21 June 1985) and appearing in Conference Proceeding published by Cambridge University Press, UK (1986) ed. by R.W. Boyd, M.G. Raymer and L.M. Narducci (Studies in Modern Optics, No. 4, pgs. 341-345).

ABSTRACT

A novel two-dimensional projection graphics feature PROJRES (Projection Graphical Comparison of Results) was built up in the DESRES Package to allow the comparison of recently defined or pre-existing diagnostic two- and three-dimensional functions for a set of nonlinear simulations versus an auxiliary axis. PROJRES represents the pivoting module to the SYNTH (the Synthesis of Results) package. A second package FUNCEVAL (FUNCtion EVALuation) has also been developed to allow further (additional) diagnostic functions to be evaluated in a post-treatment process, (that is, after the calculation is carried out). This software allows us to remove from our Laser programs the diagnostics output subroutines and reduce the memory required to store the simulation results. These universal single and double parametric-dependence contexts provide additional physical insight which can be considered a computer-aided design-tool 'inverse-problem' for projected "Gedanken" experiments.

A. MOTIVATION

This article describes a data base management software system developed to support the numerical laser modeling project by organizing the storage of the results in a canonical fashion and by post-processing of the results. Organized around files we have called SIMRES and DATSIM, this system encompasses software packages which control file access, application programs and the laser programs themselves. That is to say, the system manages the data generation, the data storage, and the data retrieval for inter-comparisons and multi-dimensional graphic displays to enable an efficient synthesis of the role of physical processes from the generated results. The SIMRES files, which contain self-descriptive information, permit the user to store all the information relative to a simulation in the same direct access file. The SIMRES package is used to generate a SIMRES file while the XTRACT package permits the reading of the information stored in a SIMRES file. The DATSIM files, permanently located on a disk, form a summary of the SIMRES files which are on magnetic tape. The DATSIM package permits the reading and writing of the DATSIM files. This software encompasses three additional application programs: 1) the DEFPARM* program which helps the user to manipulate the parameters for the simulation program, 2) the DESRES program which plots the simulation results, and 3) the SYNTH program which performs the comparisons. (An intermediate software PROJRES has been developed to allow some of the features of SYNTH to be temporarily carried out within DESRES.) The aim of this system is to offer a reliable, powerful and adaptable tool which efficiently organizes and coordinates the results storage for the laser simulations and for subsequently studying the results of the simulations through the drawing and comparison of functions.

B. BACKGROUND

The project for the numerical modeling of light-matter interaction, i.e., nonlinear laser propagation was started several years ago. The various numerical algorithms and graphical post-treatment of the results for physical analysis were carried out in collaboration with experimentalists. It soon appeared necessary to produce a system which could handle the large quantity of data to be generated, stored, and transformed.

*DEFPARM is the interactive form of DEFSIM.

A first production system was created in 1979/1980. This system allowed the simulation of one laser represented by a cylindrical model (at that time, the only simulation program) and its graphical results. This first system was based on a fixed structure of the output files; these being generated according to an implicit order of calculations done in the simulation programs. Consequently, the programs using this structure were not very flexible; they were totally dependent on the structure. Eventually the need for new features appeared (catalogues of input data and comparisons of output results), and their implementation made the system more complex and less efficient because these new possibilities could not be adequately integrated. Finally, we introduced new models (i.e., different independent variables and additional physical variables and diagnostics) to the system for which the fixed format was not adequate, for they required the evaluation of functions in spaces that differed from the original model.

A second system, more structured and thus more flexible and powerful was undertaken in 1982/1983. The object of the present article is to present this new system as well as further enhancements recently introduced 1984/1985. The new system consists of a nucleus composed of general packages which permit the creation and manipulation of output files consisting of functions of one or several dimensions and also consists of a set of programs adopted to carry out precise tasks such as graphic representation of results and comparisons. It is important to note that the current system is applicable not only to laser-simulation problems but also to other contexts where models of numerical integration are used to determine a set of functions evolving (marching) in a given space and time domain.

C. SUMMARY OF THE DESIRED CHARACTERISTICS

This present software is a second generation data base management program that enables physicists (i.e., non-computer scientists) to readily carry out a family of complex numerical laser simulations, plot the results and extract, from their inter-parametric comparison, a physical understanding. Through the various disgnostics, one can appreciate the interplay of the nonlinear physical processes in multi-dimensional space.

SIMRES† (it stands for SIMulation RESults) replaces the manual bookkeeping of results and permits further data manipulation and reduction under the direct control of the user. The mechanical work of manipulating the data files and complex functions, such as temporal and spatial correlation functions, can be performed automatically subsequent to the simulation itself. For instance, one would be able to evaluate the Fast Fourier or Quasi-Fast-Hankel Transforms to study the spectrum contents and the far field structures of the field.

SIMRES also provides the capability to evaluate additional functional expressions (such as the

† In section C, SIMRES is the overall system name. SIMRES was originally conceived as a single package, but later broken into several, one of which is also called SIMRES.

effective beam radius, the energy moments, the variable width detector output power functions...) and can generate graphical representations in two dimensions and three-dimensional perspective.

SIMRES enables physicists to use the computer at a higher, far more productive level in the problem-solving cycle. It not only provides savings in time and effort, but allows the user to achieve better solutions. In many cases, SIMRES enables the user to solve problems for which the manpower requirements would have otherwise been prohibitive.

SIMRES is a program designed for physicists, with emphasis on speed, user-friendly interfaces, high capacity via sophisticated memory management, efficient numerical evaluation, and extensibility. The physical, functional diagnostics repertoire can be easily extended by direct addition of procedures after the XTRACT package and before the DESRES graphical program and without the need to access its underlying laser simulation program environment.

SIMRES is involved in assessing new physical dependencies; it could thus help in conceptualizing the experimental problem, formulating the physical parameters which interplay, manipulating the processes by studying a series of limiting cases where few processes clearly prevail in the nonlinear interaction, obtaining symbolic solutions through curve fitting of the numerical results for a given dependence, and maintaining a data base of the results obtained from numerical solutions of complex programs,

SIMRES thus increases productivity, increases user efficiency, produces more useful and accurate results, solves previously intractable problems and is designed for end-users.

SIMRES handles laser, nonlinear propagation, aerodynamic shock-formation, molecular dynamics, underwater acoustics, and heat transfer calculations.

D. INTRODUCTION

A software system of adequate sophistication was developed to coordinate the various laser studies such as self-induced-transparency, superfluorescence, swept-gain superradiance, two-color superfluorescence, optically pumped three-level superfluorescence, far- and mid-infrared optically Raman pumped Stokes build-up, CW on-resonance self-enhancement, optical bi-stability and fluid approach to light propagation. These can be of different dimensionality both in dependent and independent variables.

The wealth of information that will ensue from this computer output will be tremendous. One must dissect these results to decide upon the proper method of summarizing them. Similar to a jigsaw puzzle, we have the pieces, but must be able to put them together in the correct manner, filling in any gaps along the way. Only in this way, can we deepen and strengthen our physical understanding. We cannot over-emphasize how vital this conceptualization is to the absolute value of our program.

It is important to note that the acquisition of numerical data and isolated results is only the beginning. The results must be fully understood if the program of study is to achieve its purpose.

An extensive software must be developed to organize and coordinate effectively the flow of data generation. It is necessary that the software simplifies the digestion of the computed data. This would enable one to extract universal intrinsic dependencies.

SIMRES would allow for interpretation of conclusions to refine the physical picture. The rigorous three-dimensional calculation results stored in SIMRES refine the approximate picture obtained by perturbation.

SYNTH, which is in the process of development, is a generalization of the comparison code of the fixed output structure of the first system. It would enable comparison with experimental results in order to extract a unified conclusion to establish the connection between such experimental results and the ones predicted by the previous one-dimensional analysis.

An interim software, PROJRES, has been developed in FY85 to realize comparisons within the same family of simulations in which one physical parameter varies. This variation parameter can be a product of several parameters such as the gain Fresnel number $F = \pi r^2/\lambda\tilde{\alpha}^{-1}$ with $\tilde{\alpha} = \alpha[1+\{(\Delta\omega)\tau_p\}^2]^{-1}$ and $\alpha = \mu^2\omega N/\hbar c$. This characteristic parameter which varies from one element simulation to the other is accounted for through an additional axis.

The availability of the data-base results permits us to identify experiments that can now be attempted to generalize the theory. This in turn can suggest possible further exploration, experiments and analytical work.

The design objective of this software is (1) to efficiently organize and coordinate the simulation generation (by insuring the validity of the parameters); (2) to construct structured results in the data base for storing and (3) to extract physical conclusions by comparing and drawing the various characteristic functions.

This software represents a reliable, adaptable and easy tool for the production and comparative studies of laser simulations which insure practical parametric assessment of real-life experiments in Quantum Electronics.

The software system is characterized by (a) its simplicity for readability, (b) its flexibility and extensibility in accommodating the constant evolution of the research requirements by exploring new dependencies (which add to the dimensionality of the problem, such as degeneracies of the atomic medium), and (c) portability to maintain close collaboration with experimentalists at multiple sites to enhance the conformity of simulation with actual data acquisitions.

The system is organized around SIMRES and DATSIM type files and encompasses software packages and procedures which control file access, application programs and the various laser propagation programs.

The SIMRES package is used to generate SIMRES files which store in the same direct access file all the information relative to a simulation. The XTRACT package permits the reading of this (SIMRES file) stored information. The DATSIM files, permanently located on disk, contain summaries (namelists of parameters and functions monitored) of the SIMRES files which are on magnetic tapes. The DATSIM package permits the reading and the writing of canonical procedures of the DATSIM files.

This software also encompasses three additional application programs: 1) the DEFPARM* program which helps the user to construct ensembles of parameters for the simulation programs, 2) the DESRES program which plots the simulation results, and 3) the SYNTH program (in process of development) which makes the comparisons.

This software enables one to manage the data bank, the retrieval of the simulation results for inter-comparison within the same calculation (e.g., time evolution, spatial reshaping of a given phenomenon) or for different parameter families, and the generation of multi-dimensional graphic displays and a cost effective, correct synthesis of the complex results.

E. DESCRIPTION OF THE SOFTWARE

1. OVERVIEW

[In this section a comprehensive view of the system is given (subsection 2) followed by an assessment of the software of the system (subsection 3). A more detailed description of the software packages and applications programs is made in the final report. See the footnote on the first page.]

2. A COMPREHENSIVE VIEW OF THE SYSTEM

The system supporting the laser modeling project has been developed on a CDC CYBER 173 computer at the Centre de Calcul at the Universite de Montreal. It consists of programs and packages written in FORTRAN IV and more recently in FORTRAN 77, ANSI Standard. The three main tasks accomplished by the system are: 1) managing the generation of simulations results; 2) drawing of simulations results; 3) comparisons of simulations results. Moreover, some peripheral functions, not dealt with here formally, are included in the system, and these are: 1) generation of catalogue of the physical parameters characterising the simulations; 2) generation of catalogue-directory of comparison

---

* DEFPARM is the interactive form of DEFSIM.

and higher order comparison; 3) archiving on magnetic tapes of the simulations results; 4) reloading on disk of the simulations results; 5) generation of histograms and probability functions.

2.1 Generation of Results

The study of lasers is done with programs simulating the spatial and temporal evolution of a laser beam, according to a specific numerical model. Initially, there was only one program which used a single laser in a cylindrical geometry. Eventually, with developments in the physical theory, the initial model was improved (it now takes into account Doppler effects, initial quantum fluctuations, ...) and new models were developed (the 2 (two) laser,three-level model; the Cartesian single laser interacting with two-levels and the counter-beam ,2 (two) laser in a two-level atomic system). There are now many laser simulation programs, each corresponding to a specific model.

Each simulation is controlled by a set of parameters defining the field and the material through which the laser beams propagate. These parameters are given to the laser programs as FORTRAN NAMELISTS.

Each simulation is identified by the model used and a number unique among the simulations done with that model. This number is a kind of special parameter which identifies the simulation more succinctly than does the complete list of parameters.

The results of a simulation are written on SIMRES type files (SIMulation RESults). Each file is identified through a root to which a suffix is added: the root corresponds to the identifier of the program which produced the simulation, and the suffix is the simulation number. The SIMRES files contain general information (name of the operating program: for eg., single or double laser, version number, creation date of the file, ...), the list of the simulation parameters, the rate of sampling and the simulation results. The handling of the simulation results can be summarized as follows: 1) the programs evaluate functions of varying dimensions,and the parameters of the simulations determine the points at which the functions are to be evaluated; 2) the values of the functions as well as the points at which the different functions have been evaluated are kept on SIMRES files.

This data, points of evaluation and value of functions, form the major part of the SIMRES files. Thus only one entity, the SIMRES file will be sufficient to store all the data of one simulation.

Added to this basic scheme (NAMELISTS, simulation programs, SIMRES files) are the DEFSIM program and the DATSIM files.

The DEFSIM (DEF for definition and SIM for simulation) is used to assist the user in writing NAMELISTS. It is an interactive program which allows the user to describe a simulation or a family of simulations by using a compact syntax, and in return produces the corresponding NAMELISTS. Although this program may not be essential, its advantage is to relieve the user of the need of writing often

repetitive NAMELISTS and thus to avoid some trivial errors in the simulation specification, i.e., errors of syntax of the NAMELISTS, errors in the names of the parameters, ... Furthermore, it enables one to submit a family of calculations where only one physical variable is altered. More importantly, the program DEFSIM checks whether the suggested calculations were not already realized.

The purpose of the DATSIM (DATa SIMulation) program is linked to the context of extensive production. To be efficient at the production level, it is necessary that any information concerning any given, produced simulation be available. Because the SIMRES files are too large and too numerous to be kept on disk, a mechanism has been devised to transfer data between disk and tape. This archival system, though essential, slows considerably the access to information. To be efficient, it was necessary therefore to make a compromise and keep on disk some high priority information concerning all produced simulations.

The data is gathered in a data bank made up of as many DATSIM files as there are types of simulation models and thus of simulation programs. These different files are called DT(model) where DT is the link to the DATSIM type and "(model)" is the value of the simulation under study. A DT (model) file contains the general data in the SIMRES files and the values of the different parameters of the simulations for all the simulations generated by a given program. The programs of the IC(model) group (IC for Installation Catalogues and "(model)" to mark the link with the model) extract from a SIMRES file the needed data and posts them in the corresponding DT(model) file. Thus, the DEFSIM program uses data of the DATSIM file to get the numbers to be given to the new simulations.

The configuration of the system with regard to the production of simulations is given in Figure 2.1 for the 1-laser, cylindrical, frequency, statistics model: 1CFS. This abbreviation is used as a suffix. The same can be applied to other models whether they are 2CFS (double laser in a cylindrical configuration with Doppler broadening and quantum initiation encompassed), 1CP (single laser cylindrical with plasma nonlinearity), 2PS (double laser in a cartesian geometry where statistics associated with an ensemble of quantum fluctuations are included), or 1P4S (single laser in a Cartesian geometry, the four quadrant included to calculate the short-scale length, phase and magnitude fluctuations in the initiation process for large Fresnel numbers).

As shown in the chart, the DEFSIM program takes the user's specifications, validates them, and then writes the information needed to generate the requested simulation in the SX1CFS file (SX, simulation to be executed). Then, the program LR1CFS (LR for Laser R) reads the appropriate data from the SX1CFS file, generates the simulation and produces a SIMRES file whose identifier is LR1CFS (no) [(no): simulation number]. Finally, the LR1CFS(no) file gives to the LR1CFS program the data needed to record the results in the SIMRES files using the DATSIM and XTRACT packages. The DATSIM file

contains a summary of the different simulations carried out with the 1CFS model.

2.2 Drawings of a Simulation

The study of the simulation results requires graphical support in order to visualize the profiles of the functions evaluated by the simulation programs. The DESRES program (DES for DESsins/Drawings and RES for RESults) has been designed for this purpose. This program can be used either in batches or in interactive mode.

The needed drawings are specified by using a syntax similar in structure to that of a program and allows inner loops on simulations, functions, selection criteria, etc. .... The DESRES program analyzes the user's commands and, through the XTRACT package, breaks them down into simple drawings. The SIMRES files thus provide all the data needed to identify and produce the drawings. There are four types of drawings available: 1) 2-dimensional representation of a function; 2) 3-dimensional representation of a function; 3) level curves; (contour, eg., iso-fluency graphs); and more recently 4) projection of a 3-dimensional representation. The 3-D projections and the level curves are performed by the TRSURF package (CACM, Sept. 74).

Figure 2.2 shows the portion of the program that carries out the drawing production.

2.3 Comparisons of Simulations

The SYNTH (SYNTHesis) has been designed to allow comparisons between simulations. A comparison is done by superimposing on one drawing 2-dimensional representations of functions (eg., the output power) coming either from different simulations or of functions of characteristic features of the output power for which each point comes from a different simulation. The SYNTH program is a powerful tool which encompasses the following applications: (i) comparisons between simulations of the same model, thus bringing out the role of certain parameters and their interplay in the nonlinear interaction; (ii) comparisons between the different lasers for the models with several lasers, thus showing the role of each of the lasers, for example, pump 'Lasera' versus driven superfluorescence 'Laserb'; (iii) comparisons between different models to demonstrate their impact, i.e., the two-level superfluorescence with the superfluorescence emission emitted in a three-level atom driven coherently by an optical pump which can get depleted. Another example displays the effect of each of the various refinements (such as including Doppler Broadening, quantum initiation in a cylindrical geometry, and general fluctuations at the initiation where azimuthal symmetry is assumed) on the evolution of the two-level superfluorescence; (iv) double comparisons* that study, for example, the dependence of specific features of the output power pulses (such as the pulse delay, the pulse maxima, the pulse width, spectral width, etc.) on Fresnel number for a family of atomic densities or for different families of profiles of the atomic density (Gaussian, superGaussian, and hyperGaussian for example). This specific double

* [further comparisons.]

comparison feature is presently limited to a specific type of laser simulation (e.g., same family of single laser). It is yet to be integrated in the new format with this second generation data management system. A structured program whose features have been specified is presently being developed.

For current comparison, an auxiliary axis characterising the physical parameter under study (or the product of parameters) has been added to the laser program and a projection PROJRES program was constructed enabling both simple comparisons, of functions such as the output power, and double comparisons*, of quantities such as the effective temporal width of the output power, to be carried out.

The user specifies the work to be done by indicating the objects to be compared and the comparison parameters.

After validating the request, the SYNTH program (in the process of development) produces the necessary headings identifying the comparison (by isolating the fixed parameters from the variable ones) then produces the graphics corresponding to the comparison.

The running of a comparison requires all the information needed at the same time in one disk. It is at this level that the DATSIM files are useful as they give access to the parameter list of all the simulations already produced. However, if the data on the DATSIM files are not sufficient, the user request reverts to the archival procedures and the reloading of the needed SIMRES files.

The structure of the system of comparison is shown in Figure 2.3.

2.4 *Practical Aspects of the System*

By keeping the fixed format of the old system, each simulation program would have generated a parallel system. But with a system based on auto-descriptive files, the DEFSIM, DESRES, and SYNTH (as well as all the other application programs such as PROJRES, FUNCEVAL and HISTO) can adapt by themselves to different environments (i.e., different computer sites) and do not have to be split up; thus a proliferation of parallel versions differing only by the number and the arrangement of the information to be treated is avoided.

It follows that each simulation program becomes the starting point, not of a parallel system, but of a subsystem, including with the simulation program a data bank associated with the model. Finally, each of these subsystems shares with the rest of the data base the unique copy of each of the production tools [DEFSIM, DESRES, and SYNTH (in process of development)].

3. SOFTWARE ASSESSMENT

At this point the system contains the functioning packages SIMRES, XTRACT, and DATSIM, and the application programs DEFSIM and DESRES, which are in use. While the application program SYNTH is still

---

* [further comparisons.]

being developed, it would be of value to review our objectives and to examine how the software developed so far for the laser-model-building project answered our expectations. (A partial realization of SYNTH involved the addition of an auxiliary axis in the laser program, (for example, the probe detuning in the Double Laser Three-Level propagation code), and the design of PROJRES which allows a projection comparison, e.g., the output power, and double comparison, e.g., τ_{peak} versus the auxiliary axis $\Delta\omega_b$, compatible with DESRES.)

With respect to modularity, it is evident at this stage that a considerable effort has been extended to divide the work into concrete jobs and to limit these different jobs into procedures or groups of procedures. By their very definition and by their conception, these packages constitute evident examples of modularity. This modularity can also be found in the step by step division of the application programs.

As to flexibility, there was an effort, all along the conception of the new system, to identify the problems of general concern by liberating us of the specific constraints of the laser project in order to concentrate on the fundamental aspects of the tasks at hand. It follows that the softwares thus developed have enough flexibility to be adapted to the different situations arising within the same laser modeling project or even to be adapted to other projects where the results are functions and where there is a sufficient quantity of results to justify a data bank.

The question of validity and reliability is more difficult to evaluate. Nevertheless, the use of techniques such as data validation, exhaustive tests during the set-up period, etc., increase the accuracy aspects of the programs. Moreover, splitting up the work into modules facilitates the inception and set up of the programs and contributes to their strength. Finally, the fact of using these programs in the context of production (i.e., parametric studies) makes it easier to test them and to find their loopholes.

As to efficiency, it is clear that the development of more complex laser models has forced us to take into consideration execution time and memory requirements. For instance, the direct access to the SIMRES and DATSIM files has increased the efficiency of the application programs and made them more amenable to interactive use. Moreover, the use of pagination in the laser modeling programs has cut down the size of the programs, and facilitates their use on academic computers with limited memory.

Much attention was given to transportability in order, on the one hand, to execute certain laser programs on computers more powerful than those at our disposal, and on the other, to use our auxiliary software in other projects. To make the software more transportable, we have chosen to write it in

FORTRAN IV and FORTRAN 77 and to respect the ANSI standard. Moreover, we have isolated, in procedures with enhanced local characteristics, such as the input/output buffer, access to the instructions or portions of code that are particular to a given environment (like the files direct access subroutines) thus making it easy to locate what is to be modified in order to transfer the software to another system.

With respect to documentation, finally, we have established and tried to follow a strict standard for the program comments. We expect to publish (internal publication) a technical report and a user's manual for the different packages and the programs dealt with in this article.

F. APPLICATION OF DESRES AND PROJRES

To illustrate the importance of the interactive graphic packages DESRES and PROJRES†, we present two nonlinear studies [in the report submitted to CRDC]. The first study is the illustration of an edge-stripping process during the propagation of a CW, very intense laser beam in a saturable absorber. The computation involves three axes Rho, Eta and the number of modes of the perturbation treatment for the diffraction. Whereas the second case analyzes the concomitant longitudinal reshaping of a strong on-resonance pump and an off-resonance weak probe, and the calculation involves four axes: Rho, Eta, Tau and the detuning of the probe. That is, the second physical problem deals with the temporal (Tau) and spatial (Rho and Eta) reshaping of the coherent transients of a double laser study in a three-level atomic system in conjunction with dispersion.

The first study, or Case 1, displays the surprising prediction of the CW on-resonance enhancement (i.e., self-focusing) of a laser beam more intense than the saturation intensity I_s in two-level systems. The CWORSF evolves by the interplay of the radially distributed absorption (defined in UPW* analysis by the Beer length α^{-1}), and the forward free-space diffraction (characterized by the Rayleigh length z_d), towards the beam center. A Fresnel number defined in terms of α, namely $F = \alpha z_d$, perfectly characterizes the competitive effects of the nonlinear medium and the beam geometry. The saturable absorption decreases with increasing intensity and attenuates the low-intensity 'wings' of the beam more than the high-intensity 'center', thus abruptly stripping the beam as described analytically using a mode analysis perturbatively. The perturbation must be followed by a free-space propagation so that the same on-axis self-focusing, obtained by rigorous calculations, occurs. The stripped beam can be approximated by a beam with a parabolic profile. The free-space propagation of a parabolic beam is expressed analytically as an equivalence to the aperture model. However, the on-axis intensity enhancement of the free space beam is larger than what it would have been had the absorbing medium effect been maintained. A small corrective nonlinear field can be obtained as a perturbation driven solely by the free-space parabolic beam.

In collaboration with Teichmann et al., a soft shrinking aperture model has been developed in which the stripping is elucidated over the propagation distance by expanding the field profile at the

† The PROJRES software was developed under CRDC sponsorship solely, as was the inclusion of an auxiliary axis in the laser programs.

* UPW: Uniform Plane Wave

edges into power series in terms of decaying exponentials. The beam-edge clipping process is followed (beyond the range of validity of the perturbation of the diffraction coupling) by free space propagation where diffraction is the dominant mechanism leading to Fresnel rings resulting in on-axis minima and maxima.* Mathematically one could consider the equivalent free space propagation of a parabolic beam instead of a Gaussian beam. The edges of the parabolic beam are stripped, compared to those of the Gaussian beam. Indeed, one can solve analytically the free space propagation of such parabolic beams and obtain the CW, on-resonance, on-axis intensity enhancement. A refinement which encompasses a corrective absorptive term due to the free space parabolic source has also been developed.

The stripping mechanism is substantiated in Fig. F.1 by intensity isometric plots of the numerically computed zero, e_0, and first correction, e_1, modes due to diffraction in ρ and z.

Figure F.2 demonstrates using the PROJRES software the transverse profile of the first three modes e_0, e_1 and e_2 intensities as well as z-derivatives as a function of z.

Figure F.3 illustrates the analytical stripping process through the radial profile of the intensity, the transverse Poynting vector, the phase evolving due to the diffraction coupling and the associate wavefront curvature.

[The capabilities of the software are truly shown by the many results and intercomparisons of the second study or Case 2. However, these require 95 pages for presentation and may be found in the final report. (See the footnote on the first page of this article.)]

G. ASSESSMENT OF WORK REALIZED AND DEFINITION OF NEW TASKS

In the first version of the system, we had a sole simulator (single laser in an r,z,t configuration) which writes the physical results functions in a preset fixed file structure. The graphics and comparison programs relied on this fixed structure to extract data files of results. The number of functions, the number of axes, the number of stored points, the types of graphics, everything was preset, thus fixed.

The old comparison program handled automatically only one type of simulation at a time (either the single laser, or the double laser but not outputs from the two types concurrently).

Therefore, it was not possible to compare the two-level superfluorescence (SF), (obtained from the single laserz LR1CFS simulator), and the coherently optically pumped three-level superfluorescence, (Laserb calculation from the double laser LR2CFS simulator). Neither could it have been possible to compare the longitudinal and transverse coherent-pump reshaping (Lasera in the 3-level SF calculation) with that of the two-level Self-Induced-Transparency, SIT. In both situations, it is desirable to compare 'one' element (of a single element laserz module) with 'one out of two' elements constituting the double

*[The beam-edge clipping process generates warefront curvature which leads to this result.]

laser ensemble in a systematic "non-ad hoc" manner.

As the research progresses, the need to include new functions and parametize the modeling has become mandatory. New functions need to be calculated as well as new refinements introduced onto the modeling modifying the number of dependent and independent variables. The (pre-selected) fixed, now rigid, structure of the software must be modified and enhanced to handle our new requirements (needs).

In realizing the software support that the laser modeling and simulation effort requires, we have set up the foundations of a second version of the SIMRES (simulation results software) system. Adopting the data base concept, we design a data base management system that handles a family of (record types) files. Each file is thoroughly described by a heading that summarizes its contents, such as the sequential order in which the various functions resulting from the simulations are stored, the axes and the (associated) sampling rates for which the functions were calculated (and thus stored).

The (preset) fixed structure has now been replaced by a self-adjusted dynamic (flexible) format that enables each simulation to have its most appropriate sampling format which defines the way in which the simulation results are stored (thus, how they might be read). The graphics and comparison programs are being modified and adapted to interface with the data base management system.

The data base interface software package has been written. The various laser programs have been adapted to the new structure. All the old results files have been re-formatted. The graphics package was rewritten to be operated interactively. The projection comparison program, PROJRES, has been written enabling simple and double comparison to be performed within a family set of simulations carried out, e.g., with the double laser program with the augmented dimension being the parameter under study. A canonical, post-simulation function-evaluation program FUNCEVAL has been constructed to unify all simulation diagnostics for the sake of comparison with newer observations. However, the full, new comparison program SYNTH is yet to be finalized.

The new version of the comparison in progress will be able to handle almost any logical comparison as long as the data format in the SIMRES files is not a constraint. The elements that can vary in a comparison between families of simulations are the following: physical functions (energy, output power,...) to be compared, the simulation types (single, double laser,...), the independent variables axis (ρ, τ, r, $\Delta\omega$, trajectories of a statistical ensemble,...), and the domain of extraction dependence (whether it is a single point, a full curve or a family of trajectories). The program checks the validity of the comparison request. SYNTH also generates the identfying header as precisely as possible. One can extract through SYNTH the required information from the data base as well as generate the graphics.

The main desired feature of the SYNTH program to be introduced is the interactive mode. Contrary to the old version which operated only in a batch mode, SYNTH is being written as a questioning

program which allows the user to interactively select the desired comparison and provides diagnostic error messages that arise as a result of the mistakes the user might experience when specifying his choice of comparisons. This feature has been built into PROJRES.

The necessity for an additional feature in the SYNTH package has recently emerged. It deals with comparing statistical quantities resulting from histogram calculations of ensembles of trajectories (each ensemble is evolving from quantum fluctuations as an initiation process) for a family of simulations: (a) an automatic, nonlinear multi-dimensional curve-fitting of an array, both discrete and continuous (i.e., functional) of statistical quantities with error-bars (standard deviations normalized to the arithmetic average) must be written; (b) for a cost-effective error-free data reduction, the tabulation (and graphical display) in the statistical representation of various physical quantities for a family of simulations (each one constituted by a set of trajectories evolving from the quantum initiation process) must be automatized with a new computer program, that is written once and for all to handle single- or double-laser simulation; and (c) for new sets of cases, one need not repeat all the amount of work done for manual data reduction, one has only to submit the computerized histogram comparison program.

BIBLIOGRAPHY

Software for the Laser Project

1. P. CADIEUX, M. CORMIER, Y. CLAUDE, C. GOUTIER and F.P. MATTAR, Proc. of the Twelfth Annual Pittsburgh Conference of Modeling and Simulation, Ed. W.G. Vogt and M.H. Mickle, published by Instrument Society of America (May 1981), p. 1527.

2. M. CORMIER, Y. CLAUDE, P. CADIEUX and F.P. MATTAR, Proc. of International Conference for Laser, Dec. 1981, Ed. C.B. Collins, published by S.T.C., McLean, Virginia, 1982.

Cylindrical Laser

3. F.P. MATTAR and M.C. NEWSTEIN, Proc. Seventh Conference on Numerical Simulation of Plasma, Courant Inst. of Math. Studies, New york Univ. (June 1975), p. 223.

4. F.P. MATTAR, Adaptive Stretching & Rezoning as Effective Computational Techniques for Two Level Paraxial Maxwell-Bloch Simulation, Tech. note 65, Laboratory for Laser Energetics, University of Rochester, Rochester, NY.

Adaptive Rezoning

5. F.P. MATTAR, Appl. Phys. 17, 53 (1978).

6. F.P. MATTAR and M.C. NEWSTEIN, Comp. Phys. Commun. 20, 139 (1980); and Comp. Phys. Commun. 32, 225 (1984).

Implicit Laser

7. F.P. MATTAR, Proc. of Ninth Conf. of Numerical Methods in Plasma, Monterey, Calif. (June 1978), Lawrence Livermore Lab. Tech. Rep. LLL-78-004.

Hydrodynamic Laser

8. F.P. MATTAR, J. TEICHMAN, L. BISSONNETTE and R.W. MacCORMACK, Proc. of Second International Symp. on Gas Flow and Chemical Lasers, Ed. by J. Wendt, Western Hemisphere Pub. (1979).

9. F.P. MATTAR and J. TEICHMAN, Comp. Phys. Commun. 22, 1 (1981).

Transistor Laser

10. F.P. MATTAR, Proc. of Eleventh Congress for the International Commission for Optics, Ed. J. Besca, Madrid (1979).

11. F.P. MATTAR, G. MORETTI and R.E. FRANCOEUR, Comp. Phys. Commun. 23, 1 (1981).

Double Laser

12. F.P. MATTAR and J.M. EBERLY, Proc. of the Physics and Chemistry of Laser-Induced Processes in Molecules, Edinburgh (1978), Ed. K.L. Kompa and S.C. Smith, p. 61, Springer-Verlag.

Others

13. F.P. MATTAR and B.R. SUYDAM, A Novel Rezoned Implicity Algorithm for Coherent Propagation in Multi-Level System, Los Alamos National Lab. Tech. Report T-7 LA-UR-82-3376 (nov. 1982), Los Alamos, New Mexico; and B.R. SUYDAM and F.P. MATTAR, Proc. of the Los Alamos Conference on Optics, 1983, pub. SPIE, Vol. 380, p. 439 (1983).

14. F.P. MATTAR, in Optical Bistability, Ed. C.M. Bowden, M. Ciftan and H.R. Robl, Plenum Press, New York (1981), p. 503.

ACKNOWLEDGMENT

This software development would not have been possible without the help of several people who have given us technical help and computer accessibility and who have stimulated and enlightened us with their invaluable advice. Not least among them are Prof. J. Teichman and Prof. R. Zahar. By their hospitality they have made this software project possible in the Centre de Calcul à l' Universite de Montreal. FPM particularly is indebted to Prof. M.S. Feld, Prof. H.M. Gibbs and Dr. S.L. McCall for their assistance in preparing the proposals, guidance in appreciating the physical subletities of Superfluorescence and Optical Bistability and in selecting the relevant modeling parameters to the experimental observations. Their continuous association and hospitality at the Spectroscopy Lab at MIT, the Atomic Physics group at AT&T Bell Lab at Murray Hill respectively is greatly appreciated. FPM has also benefited with the inimitable mentorship of Prof. H.A. Haus, at the Quantum Electronics group of the Dept. of Electrical Engineering and Computer Science at MIT, in the conceptualization of self-action effects associated with light propagation in nonlinear medium. Prof. M. Lax's encouragement, support and sponsorship at the City College of New York is joyfully acknowledged.

As to the Physics, F.P. Mattar wishes to acknowledge extensive discussions with Profs. P.R. Berman, H.M. Gibbs, H.A. Haus, M.S. Feld, M.C. Newstein, J.H. Eberly and Drs. C.M. Bowden and S.L. McCall who helped in conceptualizing the nonlinear light-matter interaction. Whereas for the numerics, F.P.M. joyfully acknowledges the guidance of Prof. C. Moretti and Drs. B.R. Suydam, J. Fleck, M. Lax and R.E. Francoeur who have helped in the development of the computational algorithms used in the laser programs.

The numerical algorithm of the single time-dependent laser propagation and its program implementation was sponsored by the U.S. Joint Services Electronic Program (JSEP-U.S. Air Force, U.S. Army and U.S. Navy) under the auspices of the Microwave Research Institute at the Polytechnic Institute of New York in Brooklyn.

The numerical algorithm of the double laser was initiated under the auspices of the Office of Naval Research and the Department of Energy at the University of Rochester, Rochester, NY. The development of the code applied to this study was sponsored by the Army Research Office DAAG23-79-C-0148, with Army Contract DAAG-29-81-D-0100 and the Office of Naval Research N000-14-80-C0174 at the Polytechnic Institute of New York, Brooklyn, NY. The application to the two-color superfluorescence was sponsored by DAAD (Deutscher Akademisher Austausch Dienst) at the Unisersität Essen-Gesamt Wocshule Essen, F.R. Germany; whereas the Simulton calculations were carried out at the Centre d'Etudes Nucléaires à Saclay, France. FPM's current stipend is supported by the Office of Naval Research N00014-77-C-0553 at NYU, and jointly by the Air Force Office of Scientific Research and the Army Research Office under ARO administered grant DAAG-29-84-K-0137 as well as by the National Science Foundation (NSF-PHY-84-06107 and NSF-PHY-85-12051). Partial support was extended at the City College of New York in 1984/1985 by the Army Research Office Contract DAAG-29-85-0112 and the Department of Energy grant DE-FG02-84-ER45058.

Furthermore, the structured data reduction software has been carried through the years under the sponsorship of a myriad of supporting agencies, the US ARO (at PINY, NYU, CCNY), AFOSR (NYU), ONR (PINY, NYU), NSF (MIT, NYU), DOE (U of R, CCNY), the Research Corporation (PINY); the Canadian Defense Research Establishment at Valcartier DREV (Univ. Montreal), the French Atomic Energy Commission CEA-CEN at Saclay and Battelle Columbus Laboratory for MICOM [0126, 0509, 1180, 1736], NV&EOL [0830] and CRDC [1366].

We also wish to thank W.E. Bashour for the translation from French of the first two sections and M. Storer for the translation of the last two sections of the software description. The skillful editing and word processing effort of M. Storer and C. Devlin is joyfully acknowledged.

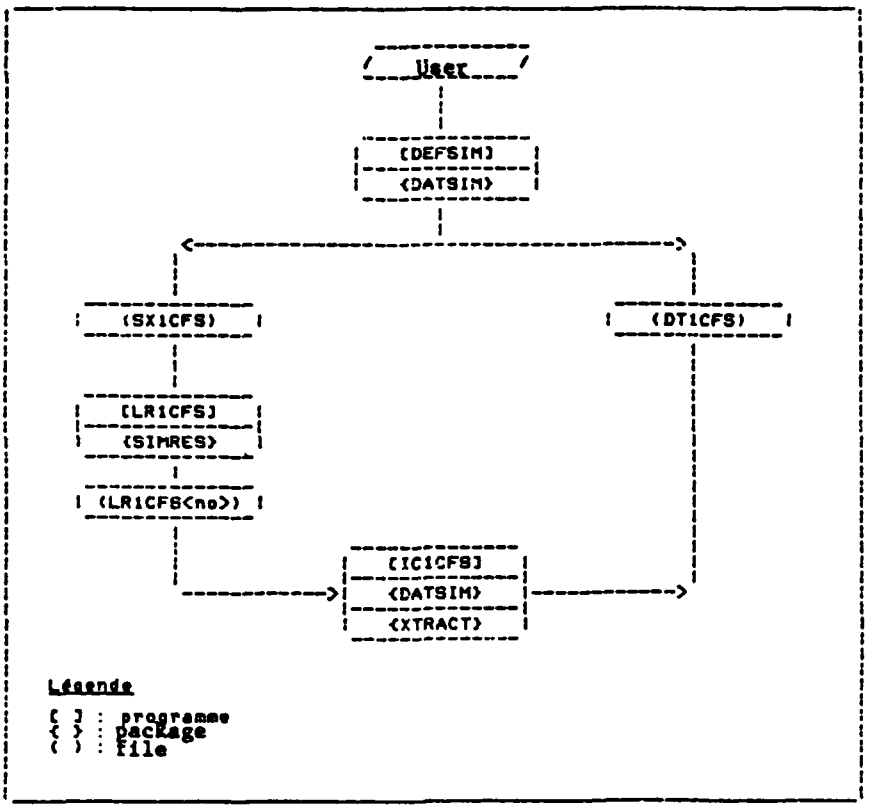

FIGURE 2.1 - Simulation production

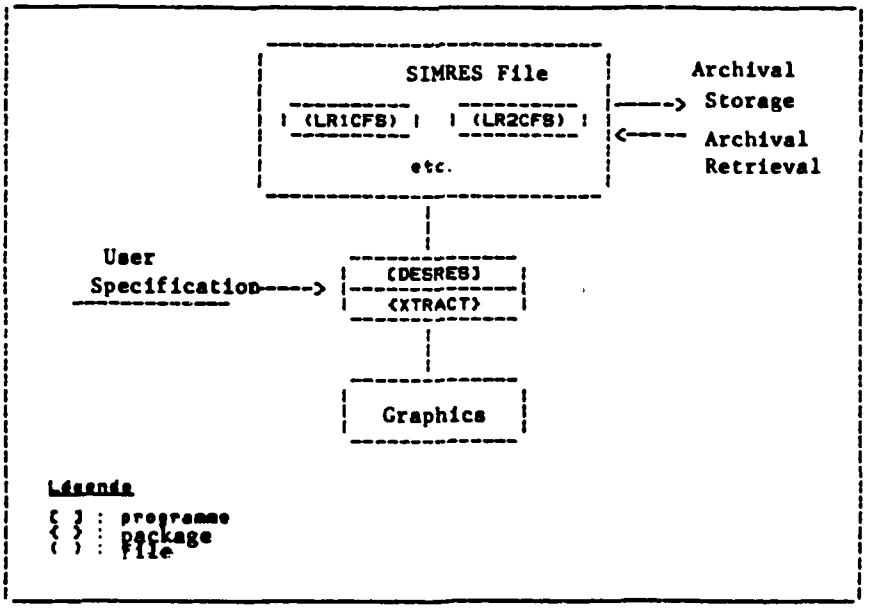

FIGURE 2.2 - Graphics Generation

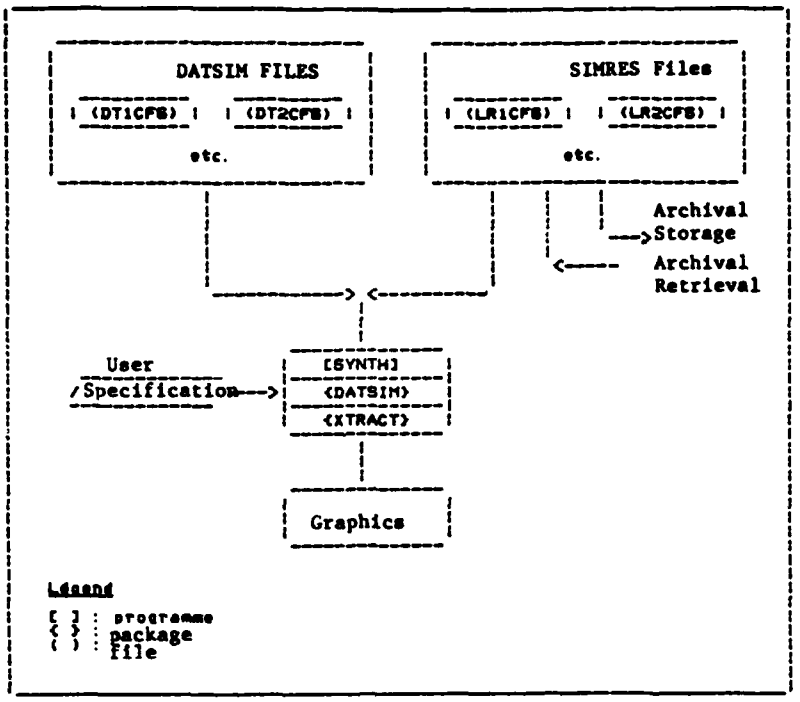

FIGURE 2.3 - Comparison Generation

Explanation of the caption below the plots for section F:

AXIS	TOT. PT.	SYM	RANGE	NB. SEL	RANGE OF VALUES
ORD	3	No	1	1	0.0
Z	801	No	(1,801)	51	(0.0, 8.0)
RHO	151	Yes	(1.125)	32	(0.0, 1.24)

a) The AXIS column indicates the name of the axis:

{STAT / ORD} is a pseudo axis which indicates {which trajectory of the statistical ensemble / which order} the plotted function belongs to.

Z is the longitudinal axis of the propagation

RHO is the radial axis of the cylinder

b) The TOT.PT. column indicates the total number of points used in the calculation of the simulation.

c) The SYM column indicates if an axis has been plotted with symmetry (YES for the RHO axis in the 3-dimensional plots).

d) The RANGE column indicates the lower and upper limits of the point indices (as opposed to the coordinates) used for the plot.

e) The NB.SEL column indicates the total number of points appearing in the plot.

f) The RANGE OF VALUES column indicates the lower and upper limits of the coordinates of the points used for the plot; so, in our example, the value 0.0 corresponding to the ORD axis indicates that it is of order 0; the (0.0, 8.0) values corresponding to the Z axis indicate that the value Z_{min} is 0.0 and that the value Z_{max} is 8.0.

LRPERT SIMULATION NO. 20

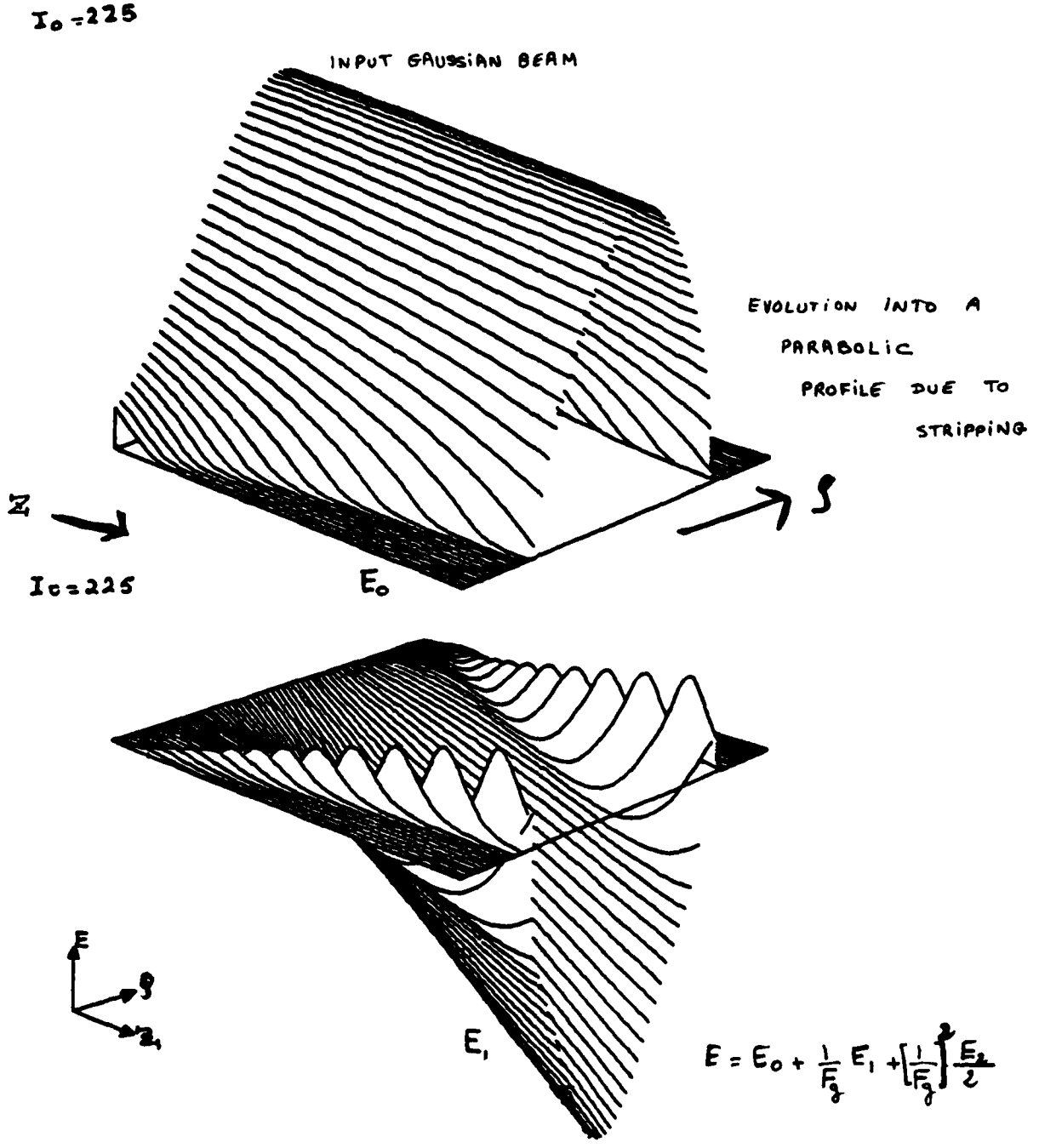

Figure F. 1

DESRES 1.2 86/07/31 00.32.28 PAGE 6

LR1CPC SIMULATION NO. 2

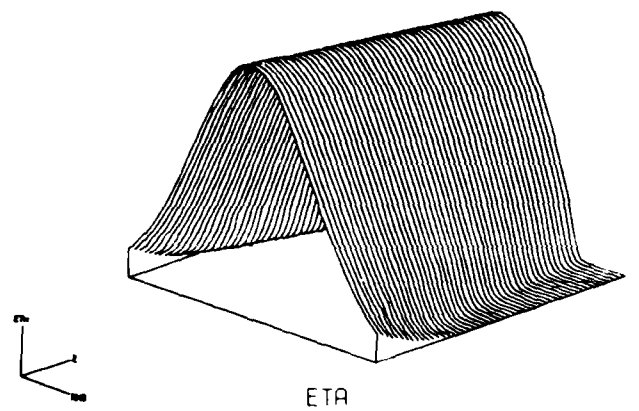

ETA

SCALE	LOCALE	AXIS	TOT.PT	SYM	RANGE	NB.SEL	RANGE OF VALUES
MIN =	.13183667E-04	ORD	3	NO	1	1	0.0
MAX =	10.000000	Z	49	NO	(1.49)	49	(0.0,24.0)
		RHO	64	YES	(1.64)	32	(0.0,1.47619)

DESRES 1.2 86/07/31 00.32.37 PAGE 7

LR1CPC SIMULATION NO. 2

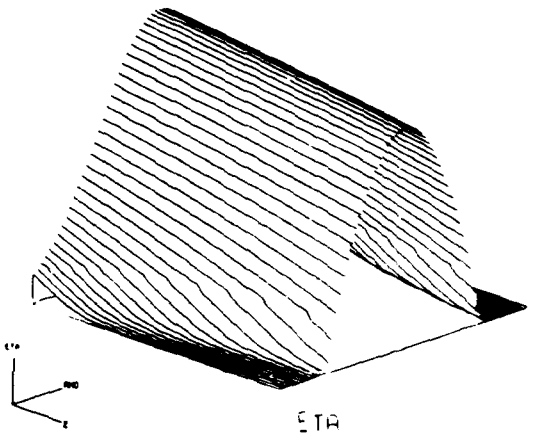

ETA

SCALE	LOCALE	AXIS	TOT.PT	SYM	RANGE	NB.SEL	RANGE OF VALUES
MIN =	.13183667E-04	ORD	3	NO	1	1	0.0
MAX =	10.000000	Z	49	NO	(1.49)	49	(0.0,24.0)
		RHO	64	YES	(1.64)	32	(0.0,1.47619)

DESRES 1.2 86/07/31 00.32.37 PAGE 8

LR1CPC SIMULATION NO. 2

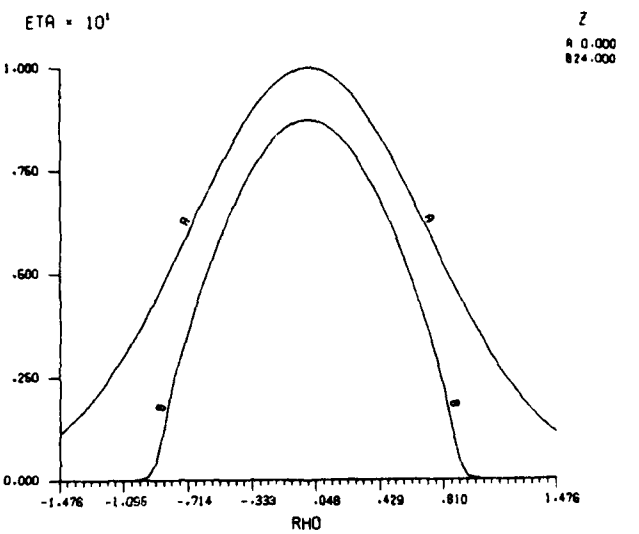

ETA

SCALE	LOCALE	AXIS	TOT.PT	SYM	RANGE	NB.SEL	RANGE OF VALUES
MIN =	.13183667E-04	ORD	3	NO	1	1	0.0
MAX =	10.000000	Z	49	NO	(1.1)	2	(0.0,24.0)
		RHO	64	YES	(1.64)	32	(0.0,1.47619)

Figure F. 1bis

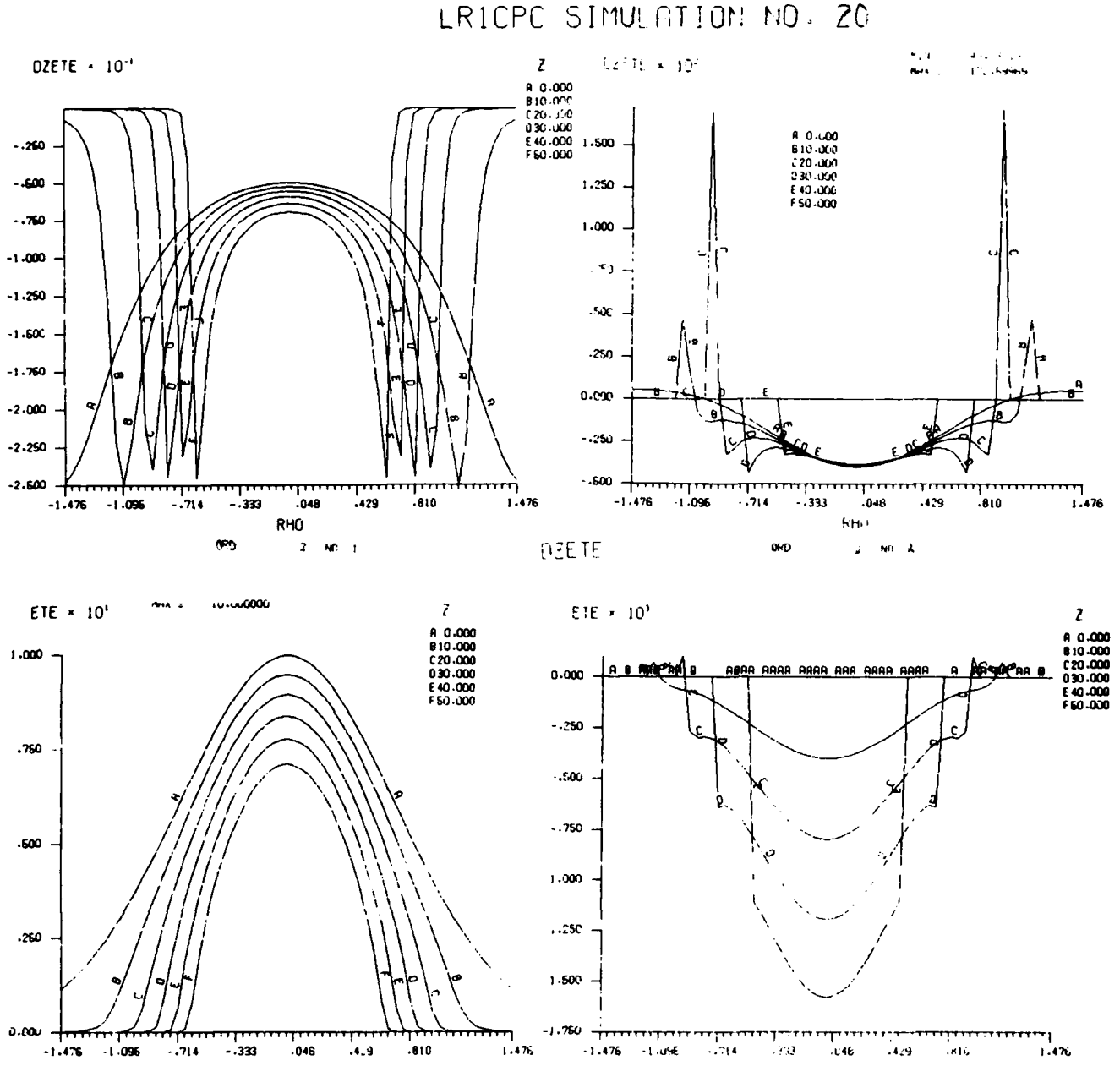
LRICPC SIMULATION NO. 20
RHO
Z
A 0.000
B10.000
C20.000
D30.000
E40.000
F50.000

Figure F. 2

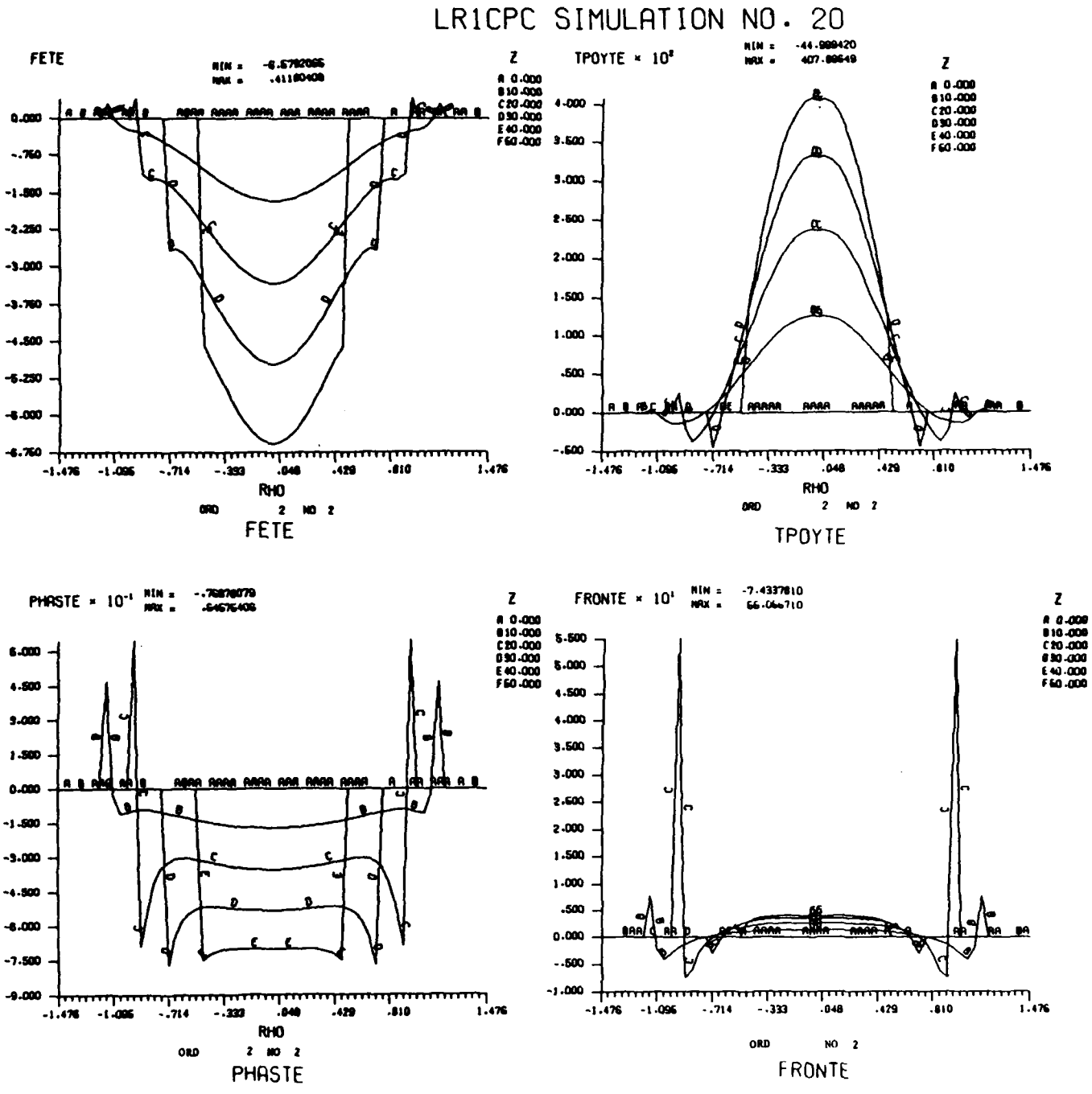
LR1CPC SIMULATION NO. 20
FETE
MIN = -6.5782095
MAX = .41180408
Z
A 0.000
B10.000
C20.000
D30.000
E40.000
F50.000
0.000
-.750
-1.500
-2.250
-3.000
-3.750
-4.500
-5.250
-6.000
-6.750
-1.476 -1.095 -.714 -.333 .048 .429 .810 1.476
RHO
ORD 2 NO 2
FETE
TPOYTE × 10²
MIN = -44.999420
MAX = 407.88649
Z
A 0.000
B10.000
C20.000
D30.000
E40.000
F50.000
4.000
3.500
3.000
2.500
2.000
1.500
1.000
.500
0.000
-.500
-1.476 -1.095 -.714 -.333 .048 .429 .810 1.476
RHO
ORD 2 NO 2
TPOYTE
PHASTE × 10⁻¹ MIN = -.78878079
MAX = .64676406
Z
A 0.000
B10.000
C20.000
D30.000
E40.000
F50.000
6.000
4.500
3.000
1.500
0.000
-1.500
-3.000
-4.500
-6.000
-7.500
-9.000
-1.476 -1.095 -.714 -.333 .048 .429 .810 1.476
RHO
ORD 2 NO 2
PHASTE
FRONTE × 10¹ MIN = -7.4337810
MAX = 66.06e710
Z
A 0.000
B10.000
C20.000
D30.000
E40.000
F50.000
5.500
5.000
4.500
4.000
3.500
3.000
2.500
2.000
1.500
1.000
.500
0.000
-.500
-1.000
-1.476 -1.096 -.714 -.333 .048 .429 .810 1.476
ORD NO 2
FRONTE

Figure F. 3

V. OPTICAL PROPERTIES OF AEROSOLS

VA. Interaction of Radiation and Spherical (Including Layered) Particles

SCATTERING BY ARBITRARILY LARGE HOMOGENEOUS/CONCENTRIC SPHERES -EXACT THEORY WITH USE OF NEW EFFICIENT ALGORITHMS

R.T. Wang and W.X. Wang
Space Astronomy Laboratory, University of Florida
Gainesville, FL 32609

RECENT PUBLICATIONS, SUBMITTALS FOR PUBLICATION AND PRESENTATIONS:

R.T. Wang and W.X. Wang, presented at the 1985 CRDC Scientific Conference on Obscuration and Aerosol Research, Aberdeen, MD (June 1985).

W.X. Wang, Some improvements of scattering theory for spheroid, submitted to Applied Optics (Aug. 1985).

ABSTRACT

Ratio functions of Riccati-Bessel functions and their derivatives are used for exact calculations of the scattering by homogeneous/concentric spheres. New algorithms are developed which are applicable to particles of arbitrary size (large or small), complex refractive index and/or core-to-mantle size ratio, and are especially efficient for computer calculations. Illustrative examples are shown by a series of uniformly formatted graphs. The mathematics are explained in some detail, following a short statement on the necessity of developing such efficient algorithms. In addition to several examples for testing the algorithms, a number of graphs are provided for practical application to concentric-sphere scattering problems. All scattering particles possess realistic complex refractive indexes of water, ice and graphite, with sizes ranging from the resonance to geometrical optics regions. Some hitherto unnoticed, striking/exotic scattering properties of ice-coated graphite spheres and also of water bubbles, as inferred from the computations, are discussed. This work is a part of our theoretical studies linking our microwave-based experimental research to the systematic understanding of the physics of light scattering.

I. INTRODUCTION

Exact calculation of the Lorenz-Mie solution to the problem of scattering by a homogeneous sphere [Refs. 7, 10, 12], or to similar, but more complicated concentric-sphere problems [9, 12, 13] still requires the use of high speed computers. The bulk of these time-consuming tasks is associated with the evaluations of coefficients, a_n's and b_n's, in the series expansion (the so-called Mie series) of the scattered field. The number of terms (n_m) required in such a slow-converging Mie series is a little larger than the size parameter $x=2\pi a/\lambda$ of the sphere, where a is the sphere radius and λ, the incident wavelength. Expressions for a_n's and b_n's involve Riccati-Bessel functions of both real and complex arguments (x and mx; m is the complex refractive index), the evaluations of which appear to be the essential, most difficult part of the scattering problem. As x becomes larger, the time required to evaluate the Mie series increases in such an accelerated manner that the exact calculations often become impractical or even impossible. Thus, ever since the

rigorous mathematical solutions were widely accepted, many researchers have had to develop efficient programs to overcome these difficulties [6, 7, 8, 11, 13, 14, 15]. We have also been motivated to do this in connection with the study of surface waves, rainbow/glory phenomena [4,10] and particle sublimation/evaporation problems, all related to particles too large to be investigated by our microwave-based experiments.

We found that in the a_n, b_n expressions complex Riccati-Bessel functions did not occur irregularly but rather in the forms of ratios. Hence the name 'Ratio function' was summarily given to denote the following ratios:

$$p_n(z) = \psi_n(z)/\psi_{n-1}(z) \tag{1a}$$

$$A_n(z) = \psi_n'(z)/\psi_n(z) \tag{1b}$$

$$B_n(z) = \chi'_n(z)/\chi_n(z) \tag{1c}$$

$$D_n(z) = \zeta'_n(z)/\zeta_n(z) \tag{1d}$$

where $\psi_n(z)$, $\chi_n(z)$ and $\zeta_n(z)$ $[= \psi_n(z) + i\,\chi_n(z)]$ are Riccati-Bessel functions of the first, of the second and of the third kind, respectively, and z is either the real argument x or the complex argument mx. We noticed thereby that:

(1) Simple recursion formulae for these ratio functions, similar to those for the ratio functions of spherical Bessel functions $j_n(z)$, $n_n(z)$ and $h_n^{(2)}(z)$ [1], could be derived from the relations between Riccati-Bessel and spherical-Bessel functions which are:

$$\psi_n(z) = zj_n(z) \tag{2a}$$

$$\chi_n(z) = -zn_n(z) \tag{2b}$$

$$\zeta_n(z) = zh_n^{(2)}(z) \tag{2c}$$

(2) The numerical stability was significantly improved if we employed <u>downward recursion</u> to generate $A_n(z)$ and $p_n(z)$ by judiciously choosing small initial values for $A_n(z)$ and $p_n(z)$ at a sufficiently large starting n, such that $N \gg n_m$; but on the other hand, upward recursions should be employed to generate $B_n(z)$'s and $D_n(z)$'s pertaining to Ricatti-Bessel functions of the second and of the third kind.

In Sec. II we will discuss in more detail the mathematics of the new algorithms, separately for homogeneous and for concentric-sphere cases. Since in both cases the bulk of the calculations needed is for evaluating the much simpler ratio functions rather than the individual Ricatti-Bessel functions, the efficiency/reliability of numerical calculation is considerably improved.

Sec. III gives a number of illustrative examples of using the new algorithms, in extensive but uniform graphical forms. We will also include therein discussions on: (A) The growth function of backscatter, i.e., contribution to backscatter intensity as a function of the number of successive Mie series terms included [4, 12]; (B) Resonances in extinction and backscattering by large spheres in the size range $200.0 \leq x\ (0.001) \leq 201.0$; (C) Effects of core-to-mantle size ratio q (=a/b) and of overall size on scattering properties of concentric spheres. In all cases q spans the range $0.01 \leq q\ (0.01) \leq 1.0$, with overall particle size, $5.0 \leq x_b \leq 2000.0$. Only two distinct, but practical, cases are considered for the core-mantle compositions: ice-coated graphite spheres and water bubbles. We conclude with summary discussions.

II. MATHEMATICAL CONSIDERATIONS

A. For Homogeneous Spheres.

In terms of the ratio functions (Eqs. (1)) the Mie coefficients are [7, 10, 12]

$$a_n = \frac{\psi_n(x)}{\zeta_n(x)} \frac{A_n(mx)-mA_n(x)}{A_n(mx)-mD_n(x)} = \frac{\left[\prod_{i=2}^{n} p_i(x)\psi_{i-1}(x)\right]}{\zeta_n(x)} \frac{A_n(mx)-mA_n(x)}{A_n(mx)-mD_n(x)} \tag{3a}$$

$$b_n = \frac{\psi_n(x)}{\zeta_n(x)} \frac{mA_n(mx)-A_n(x)}{mA_n(mx)-D_n(x)} = \frac{\left[\prod_{i=2}^{n} p_i(x)\psi_{i-1}(x)\right]}{\zeta_n(x)} \frac{mA_n(mx)-A_n(x)}{mA_n(mx)-D_n(x)} \tag{3b}$$

Downward recursions were employed to generate an array of $A_n(z)$'s and $p_n(x)$'s, while upward recursions were used to generate $D_n(x)$'s for computing $\zeta_n(x)$'s. Except for the $p_n(x)$'s, we refer details to the following Sec. II-B on precautions needed in using the recursion relations.

(1) The $p_n(x)$'s, from which all real functions $\psi_n(x)$'s can be obtained successively, are generated by

$$p_{n-1}(x) = 1/\left[(2n-1)/x - p_n(x)\right] \tag{4}$$

starting from a sufficiently large n, so that $N \gg n_m$. If not carefully used, Eq. (4) would lead to $p_1(x) = \infty$ at $x=k\pi$, $k=1,2,3,\ldots$; because at such points the denominator in

$$p_1(x) = \psi_1(x)/\psi_0(x) = (\sin x/x - \cos x)/\sin x \tag{5a}$$

vanishes. Inspection of Eqs. (1) and (3) then suggests that we have to use

$$\psi_1(x) = \sin x/x - \cos x \tag{5b}$$

and p_2 instead of ψ_o and p_1 to avoid such numerical breakdowns in $p_1(x)$. Singularities in $p_n(x)$ for $n \neq 1$ do not exist at $x = k\pi$. (See Appendix.)

(2) $p_n(z)$ goes asymptotically to

$$p_n(z) \sim \frac{z}{(2n+1)} \tag{6}$$

when $n >> |z|$ (see Appendix). The application of this asymptotic property can insure the resultant accuracy of using the downward recursion. Our current experience shows that starting from $n = N = 2|mx| + 10$ is satisfactory for all x and $|mx|$ values in all Mie calculations.

B. Two Concentric Spheres.

(1) Ratio functions $A_n(z)$, $B_n(z)$, $D_n(\nu)$ and their application in the calculation for the Mie coefficients a_n and b_n.

First derived by Aden and Kerker [2], also independently by Güttler [9], and published later in succinct forms by Kerker [12], the explicit formulae for a_n and b_n are:

$$a_n = \frac{(\psi\psi)'_{n,\alpha}\cdot(\chi\psi)'_{n,\nu} - (\chi\psi)'_{n,\alpha}\cdot(\psi\psi)'_{n,\nu}}{(\psi\psi)'_{n,\alpha}\cdot(\chi\zeta)'_{n,\nu} - (\chi\psi)'_{n,\alpha}\cdot(\psi\zeta)'_{n,\nu}} \tag{7a}$$

$$b_n = \frac{(\psi\psi)''_{n,\alpha}\cdot(\chi\psi)''_{n,\nu} - (\chi\psi)''_{n,\alpha}\cdot(\psi\psi)''_{n,\nu}}{(\psi\psi)''_{n,\alpha}\cdot(\chi\zeta)''_{n,\nu} - (\chi\psi)''_{n,\alpha}\cdot(\psi\zeta)''_{n,\nu}} \tag{7b}$$

where ψ, χ and ξ are the Riccati-Bessel functions described earlier, whose order n and pertinent arguments α and ν are indicated by the suffixes attached to the bracketed quantities [p.195, Ref. 12]. α and ν represent the size parameters of core and mantle, respectively; i.e., $\alpha = 2\pi a/\lambda$ (often denoted by x_a) and $\nu = 2\pi b/\lambda$ (often denoted by x_b). Downward recursion generates an array of $A_n(z)$'s, while $B_n(z)$'s and $D_n(\nu)$'s were computed using upward recursions. z is in general a complex argument standing for $m_1\alpha$, $m_2\alpha$ or $m_2\nu$; m_1 and m_2 being the complex refractive indexes of core and mantle, respectively. Instead of customarily taking $A_N(z) = 0$ as the initial value in the downward recursion [1], we found that the better choice would be

$$A_N(z) \sim z/(2N+1) . \tag{8}$$

The initial values $B_0(z)$ and $D_0(\nu)$ for the upward recursion are

$$B_o(z) = \chi'_o(z)/\chi_o(z) = -\sin z/\cos z \tag{9a}$$

$$D_0(\nu) = \zeta'_0(\nu)/\zeta_0(\nu) = -i \ . \qquad (9b)$$

Similar initial value for $A_n(z)$ applies to the previous homogeneous-sphere case.

The recursion relations are as follows:

$$\phi_{n-1}(z)/\phi_n(z) = (2n+1)/z - \phi_{n+1}(z)/\phi_n(z) \qquad (10a)$$

$$F_n(z) = -n/z + \phi_{n-1}(z)/\phi_n(z) \qquad (10b)$$

$$F_n(z) = -n/z + 1/\left[n/z - F_{n-1}(z)\right] \qquad \text{for upward} \qquad (10c)$$

$$F_n(z) = (n+1)/z - 1/\left[(n+1)/z + F_{n+1}(z)\right] \qquad \text{for downward} \qquad (10d)$$

where $\phi_n(z)$ denotes $\psi_n(z)$, $\chi_n(z)$, and $\zeta_n(\nu)$;

$F_n(z)$ denotes $A_n(z)$, $B_n(z)$, and $D_n(\nu)$.

Divided by the common factor $\psi_n(m_1\alpha)\psi_n(m_2\alpha)\chi_n(m_2\alpha)$ in the numerators and denominators, equations (7a) and (7b) can be converted to

$$a_n = \frac{\psi_n(\nu)}{\zeta_n(\nu)} \cdot \frac{\{U_n V_n\left[m_1 A_n(m_2\alpha) - m_2 A_n(m_1\alpha)\right]\cdot\left[B_n(m_2\nu) - m_2 A_n(\nu)\right]}{\{U_n V_n\left[m_1 A_n(m_2\alpha) - m_2 A_n(m_1\alpha)\right]\cdot\left[B_n(m_2\nu) - m_2 D_n(\nu)\right]}$$

$$\frac{-\left[m_1 B_n(m_2\alpha) - m_2 A_n(m_1\alpha)\right]\cdot\left[A_n(m_2\nu) - m_2 A_n(\nu)\right]\}}{-\left[m_1 B_n(m_2\alpha) - m_2 A_n(m_1\alpha)\right]\cdot\left[A_n(m_2\nu) - m_2 D_n(\nu)\right]\}} \qquad (11a)$$

$$b_n = \frac{\psi_n(\nu)}{\zeta_n(\nu)} \cdot \frac{\{U_n V_n\left[m_2 A_n(m_2\alpha) - m_1 A_n(m_1\alpha)\right]\cdot\left[m_2 B_n(m_2\nu) - A_n(\nu)\right]}{\{U_n V_n\left[m_2 A_n(m_2\alpha) - m_1 A_n(m_1\alpha)\right]\cdot\left[m_2 B_n(m_2\nu) - D_n(\nu)\right]}$$

$$\frac{-\left[m_2 B_n(m_2\alpha) - m_1 A_n(m_1\alpha)\right]\cdot\left[m_2 A_n(m_2\nu) - A_n(\nu)\right]\}}{-\left[m_2 B_n(m_2\alpha) - m_2 A_n(m_1\alpha)\right]\cdot\left[m_2 A_n(m_2\nu) - D_n(\nu)\right]\}} \qquad (11b)$$

U_n and V_n are defined by

$$U_n = \psi_n(m_2\alpha)/\psi_n(m_2\nu) \qquad (12a)$$

$$V_n = \chi_n(m_2\nu)/\chi_n(m_2\alpha) \qquad (12b)$$

They obey the following recursion relations

$$U_n = \frac{\psi_n(m_2\alpha)}{\psi_{n-1}(m_2\alpha)} \cdot \frac{\psi_{n-1}(m_2\nu)}{\psi_n(m_2\nu)} U_{n-1} \qquad (13a)$$

$$V_n = \frac{\chi_n(m_2\nu)}{\chi_{n-1}(m_2\nu)} \cdot \frac{\chi_{n-1}(m_2\alpha)}{\chi_n(m_2\alpha)} V_{n-1} \qquad (13b)$$

The ratio functions $\psi_n(m_2\alpha)/\psi_{n-1}(m_2\alpha)$ and $\psi_{n-1}(m_2\nu)/\psi_n(m_2\nu)$ in U_n and $\chi_n(m_2\nu)/\chi_{n-1}(m_2\nu)$ and $\chi_{n-1}(m_2\alpha)/\chi_n(m_2\alpha)$ in V_n are computed using the downward and upward recursions, respectively.

For a large particle, the exponentials $e^{m_1(i)\alpha}$, $e^{m_2(i)\alpha}$, and $e^{m_2(i)\nu}$ (superscript i denotes the imaginary part of refractive index) become extremely large. In order to avoid exponential overflows, we multiplied them by the reducing factors $e^{-m_1(i)\alpha}$, $e^{-m_2(i)\alpha}$ and $e^{-m_2(i)\nu}$. This proved very successful. Remarkably accurate and speedy calculations are now possible for particle sizes up to $\nu = 5000.0$ using our VAX-11/750.

(2) Reduction to homogeneous sphere:

If $q = 1.0$, i.e., $a = b$, and $m_1 = m_2$, then equations (11a) and (11b) reduce to

$$a_n = \frac{\psi_n(\nu)}{\zeta_n(\nu)} \cdot \frac{A_n(m_1\nu)-m_1A_n(\nu)}{A_n(m_1\nu)-m_1D_n(\nu)} \tag{14a}$$

$$b_n = \frac{\psi_n(\nu)}{\zeta_n(\nu)} \cdot \frac{m_1A_n(m_1\nu)-A_n(\nu)}{m_1A_n(m_1\nu)-D_n(\nu)} \tag{14b}$$

No computer program difficulties have been experienced thus far in making this transition to homogeneous-sphere cases.

If q becomes very small, the Riccati-Bessel function of the second kind, $\chi_n(z)$, goes to an extremely large number as fast as $(z/2)^{-n}$. Because of this, our original program for concentric spheres broke down for very small sized cores, i.e., for $q \leq 0.1$. In our new program, we use the ratio function $\chi_n'(z)/\chi_n(z)$ instead of $\chi_n(z)$ itself. Since the following approximate expression holds:

$$\lim_{z\to 0} B_n(z) = \lim_{z\to 0} \frac{\chi_n'(z)}{\chi_n(z)} = \lim_{z\to 0} \left[-\frac{n}{z} + \frac{(n-\frac{3}{2})!/(z/2)^{n-1}}{(n-\frac{1}{2})!/(z/2)^{n}}\right]$$

$$= \lim_{z\to 0} \left(-\frac{n}{z} + \frac{(n-\frac{3}{2})z}{2}\right) \tag{15}$$

we can see that the $B_n(z)$ will become large only as fast as $(-n/z)$ i.e., at a much slower pace than as $(z/2)^{-n}$ Therefore, this program can be used for core size as small as one desires.

If $q = 0$, equations (7a) and (7b) reduce to

$$a_n = \frac{(\psi\psi)'_{n,\nu}}{(\psi\zeta)'_{n,\nu}} \tag{16a}$$

$$b_n = \frac{(\psi\psi)''_{n,\nu}}{(\psi\zeta)''_{n,\nu}} \tag{16b}$$

By using ratio functions, we can express the above equations as

$$a_n = \frac{\psi_n(\nu)}{\zeta_n(\nu)} \cdot \frac{A_n(m_2\nu)-m_2A_n(\nu)}{A_n(m_2\nu)-m_2D_n(\nu)} \tag{17a}$$

$$b_n = \frac{\psi_n(\nu)}{\zeta_n(\nu)} \cdot \frac{m_2A_n(m_2\nu)-A_n(\nu)}{m_2A_n(m_2\nu)-D_n(\nu)} \tag{17b}$$

Eqs. (11a) and (11b) as $q \to 1.0$ and as $q \to 0$ are thus seen to reduce to Eqs. (3a) & (3b), the homogeneous-sphere expressions for a_n's and b_n's; we routinely make these transitions in actual computations.

III. APPLICATION OF THE NEW ALGORITHMS

Figures are used freely, along with explanations/discussions in this section to illustrate the results of scattering calculations using the new algorithms described in the previous Sec. II. Graphical display is one of the easiest ways to visualize the outcome of algorithms.

A. Growth Function of Backscatter.

This function is defined as the total contribution to the backscatter intensity by the first n partial waves in scattering by a spherical particle [4,12]. The absolute magnitude of this function is expressed in terms of Mie coefficients a_n, b_n as:

$$\dot{i}(n) = \left| \sum_{n=1}^{n_m} \frac{2n+1}{n(n+1)} \{a_n\pi_n(\cos\pi) + b_n\tau_n(\cos\pi)\} \right|^2$$

$$= \left| \sum_{n=1}^{n_m} (-1)^{n-1} \frac{2n+1}{2} (a_n-b_n) \right|^2 \tag{18}$$

Thus as n increases the functional dependence on n is characterized by rapid oscillations, due to rapid changes in phase of the partial-wave complex amplitudes a_n and b_n, until the Mie series converges at $n=n_m$ beyond which $\dot{i}(n)$ levels off. Examples are shown in Figs. 1A-1D for homogeneous-sphere cases and in Figs. 2A-2D for concentric spheres. Inspection of Figs. 1A-1D also shows that if one continues to take the contribution by additional partial waves beyond necessity, i.e., $n>n_m$, $\dot{i}(n)$ for homogenous spheres soon resumes oscillatory or even divergent behavior again. Curiously, this tendency appears to be considerably slowed down for concentric-sphere cases (Figs. 2A-2D). By comparing Figs. 2A-2D with corresponding Figs. 1A-1D, we

also notice that coating a sphere by only a one-wavelength-thick mantle significantly changes the backscatter as well as the growth function profile for a large spherical particle.

B. Extinction Efficiency and Backscatter Gain (or Normalized Radar Cross Section)

Figures 3A, 3B, 4A, 4B, 5A, 5B, 6A, and 6B, a total of 8 figures, are to display the particle size dependence of extinction efficiency, Q_{ext}, and backscatter gain $G(\pi)$:

$$Q_{ext} = C_{ext}/G = \frac{4}{x^2} \sum_{n=1}^{n_m} \frac{2n+1}{2} \mathrm{Re}\{a_n+b_n\} \tag{19a}$$

$$G(\pi) = I(\pi)/G = \frac{4}{x^2} \left| \sum_{n=1}^{n_m} (-1)^{n-1} \frac{2n+1}{2} (a_n-b_n) \right|^2 \tag{19b}$$

where G is the geometrical cross section of the sphere, C_{ext} its extinction cross section, $I(\pi)$ the backscatter intensity, and n_m the number of the Mie series terms required for its convergence. These figures are plotted in the particle size range x=200.0 to x=201.0 with a common interval $\Delta x=0.001$: A-figures are for homogeneous spheres and B-figures for the related concentric ones with large core (radius a) mantled (radius b) by one-wavelength-thick foreign material. In particular, Fig. 3A is for water droplets and is to facilitate the direct comparison with other researcher's result [4], while Fig. 3B shows the case when the surface of such water droplets freezes to form 1-λ-thick ice shell. Fig. 4B is for water bubbles; i.e., 1-λ-thick water mantle enveloping spherical void, extended examples of which follow in the next Sec. III-C.

Several outstanding features noted from these figures are: (1) In all cases except for the water bubble, Q_{ext} is close to 2, an asymptotic character exhibited by all spherical particles in the geometrical optics size region. (2) Q_{ext} vs. x profiles for all particles in this size range, however, stay without appreciable magnitude change, and we may have missed narrow but specular resonances reported in the literatures [3,5], due to our choice of $\Delta x=0.001$ being an insufficiently fine interval. (3) On the other hand, resonances of $G(\pi)$ are spectacular for low-absorbing particles, as seen in Figs. 3A-4B, suggesting many intricate interferences between various penetrated and reemerged rays to give rise to the so-called 'glory phenomena'. Absorbing graphite or ice-coated graphite-like spheres

in Figs. 5A and 5B, however, have no such variations of $G(\pi)$ in this size range, except that the magnitude is rather low, i.e., they exhibit low radar echoes. (4) Magnitudes and widths of $G(\pi)$ resonances change with particle size in rather complex ways and can only be explained via the use of exact theories [4,5,12]; the more efficient the theory's algorithms, the easier the explanation. An inference drawn from this work, for example from Figs. 3A-4B, is that if such a spherical particle is allowed to grow or evaporate at a known rate, the backscattered light as seen from the illuminating light source will undergo aperiodical changes in intensity, often spectacularly bright but sometimes quite dark, in a predictable manner. (5) As in the cases of growth functions discussed previously, the effect of even a 1-λ-thick mantle coated on a large spherical particle is such that it may dramatically change the $G(\pi)$ vs. x profile of the uncoated homogeneous sphere (compare Fig. 3A and Fig. 3B).

C. Concentric-sphere Scattering. Effects of q [=a(core radius)/b(mantle radius)], particle size x_b, and compositions, m_{core} and m_{mantle}.

Perhaps the most sensitive way to test our new algorithms is to apply them to problems of concentric spheres. To conduct the test within a manageable extent but in a systematic way, we chose only two sets of material composition where the complex refractive index of the core material, m_{core}, was vastly different from that of the mantle, m_{mantle}. The first set is a graphite core enveloped in a water-ice mantle (m_{core}=1.70-i0.70, m_{mantle}=1.313-i1.9E-9; Figs. 6A, 6B-13A, 13B), while the second is a water bubble (m_{core}=1.000-i0.0, m_{mantle}=1.333-i0.0; Figs. 14A, 14B-19A, 19B). For each set the particle size, or the mantle size x_b, discretely spans the range $5.0 \leq x_b \leq 2000.0$, i.e, from resonance to geometrical optics region. For each x_b the core-to-mantle size ratio q is allowed to change with a common step Δq=0.01 from q=0.01 to q=1.0 or 0.99 (for water bubble) to see the subtle effects of q on net scattering properties. Calculations were made only for those quantities derivable from Mie coefficients (a_n's and b_n's) alone; i.e., efficiencies for extinction (Q_e), scattering (Q_s), absorption (Q_a), radiation pressure (Q_p), single-scattering albedo (Q_s/Q_e) and asymmetry factor $\overline{\cos\theta}$ [10,12]:

$$Q_e = \frac{4}{x_b^2} \sum_{n=1}^{n_m} \frac{2n+1}{2} \mathrm{Re}\{a_n+b_n\} \qquad (20a)$$

$$Q_s = \frac{4}{x_b^2} \sum_{n=1}^{n_m} \frac{2n+1}{2} \{|a_n|^2 + |b_n|^2\} \tag{20b}$$

$$Q_a = Q_e - Q_s \tag{20c}$$

$$\overline{\cos\theta} = \frac{4}{x_b^2 Q_s} \sum_{n=1}^{n_m} \{\frac{n(n+1)}{n+1} \mathrm{Re}(a_n^* a_{n+1} + b_n^* b_{n+1}) + \frac{2n+1}{n(n+1)} \mathrm{Re}(a_n^* b_n)\} \tag{20d}$$

$$Q_p = Q_e - \overline{\cos\theta}\, Q_s \tag{20e}$$

n_m again denotes where the Mie series converges and the summations should be terminated. These efficiences can be normalized with respect to those for the mantle-sized homogeneous sphere possessing the complex refractive index of either the core or the mantle to facilitate the direct comparison of scattering properties of a concentric sphere to those of an equally sized homogeneous one. The former is denoted by $Q_e/Q_{e,c}$, $Q_s/Q_{s,c}$, etc., while the latter, $Q_e/Q_{e,m}$, $Q_s/Q_{s,m}$, etc. All A-figures, Figs. 6A to 19A, refer to such normalized efficiencies, while all B-figures, Figs. 6B to 19B, show the unnormalized, absolute magnitudes of the efficiencies in Eqs. (20).

1. Concentric spheres with graphite core mantled by ice

Figs. 6A, 6B to 13A, 13B are for high-absorbing graphite cores enveloped in very transparent water-ice mantles. They are shown in increasing order of particle size x_b. Outstanding features noted are: (1) Three curves for the normalized efficiencies, $Q_e/Q_{e,c}$, $Q_s/Q_{s,c}$, and $Q_a/Q_{a,c}$ intersect at a single point for every particle size, i.e., at such a point the light energy obscured by the concentric spheres is divided between scattering and absorption in exactly the same proportion as in the case of a homogeneous graphite sphere of the same size. For the larger sized particles ($x_b \geq 100.0$), the above intersecting point occurs at $q = a/b \approx 0.78$, with all normalized efficiencies very close to unity. Further implications of this feature are not yet studied. (2) As the core shrinks in size so that $q \leq 0.1$, absorption becomes negligibly small so that $Q_e \approx Q_s$, i.e.; the absorbing core becomes invisible. (3) On the other hand, as the core grows larger ($q \geq 0.1$) with respect to a fixed mantle size, both Q_a and Q_p increase rather monotonically while Q_s and Q_e develop oscillatory behavior with respect to the variation in q, signifying that more complex wave interferences take place with

increasing core size. (4) More oscillations but less amplitude variations in Q_s and Q_e versus q curves are noted as the overall particle size increases, the most pronounced oscillations occurring in $0.3 \leq q \leq 0.8$. (5) The functional dependences of single-scattering albedo w and asymmetry factor $\overline{\cos\theta}$ on q are equally intriguing. In general, w decreases while $\overline{\cos\theta}$ increases as the graphite core grows in size until $q \approx 0.8$, beyond which this trend may reverse. (6) Oscillations of w and $\overline{\cos\theta}$ versus q curves are also noted for larger particles, which occur in almost perfect synchronism as in Q_s & Q_e vs. q curves except when $q \geq 0.9$, where more enhanced amplitude variations in oscillations are noted for w, $\overline{\cos\theta}$ curves. (7) Not entirely expected is the result that the minimum of albedo w is not at $q = 1.0$ but in the range $0.8 \leq q \leq 0.95$, depending on size, i.e., an ice-coated graphite ball looks even darker than a fully exposed graphite ball of the same overall size, if the thickness of the ice-mantle is about 5 ~ 20% of the particle radius. This decrease in w is more conspicuous for smaller particles.

2. Water bubbles

Figs. 14A, 14B to 19A, 19B are for water bubbles; i.e., each for a water shell with $m_{mantle} = 1.333 - i0.0$ enclosing a spherical void with $m_{core} = 1.0 - i0.0$. Again they are shown in the increasing order of particle size x_b. Such a bubble is characterized by having no absorption, i.e., $Q_a = 0$ hence $Q_e = Q_s$, and the scattering is entirely due to the water mantle. Normalization of efficiencies is therefore made with respect to the efficiencies of an equally sized full water droplet. Core-to-mantle size ratio q is allowed to vary with a constant step $\Delta q = 0.01$ in the range $0.01 \leq q \leq 0.99$. Striking scattering properties noted are: (1) If the size of the bubble cavity is so small that $q \leq 0.2$, the scattering properties of a water bubble are practically the same as those of a full sized water droplet. (2) By increasing the cavity size, i.e. $q \geq 0.2$, oscillatory variations in Q_e ($=Q_s$), Q_p and asymmetry factor vs q curves arise, as also mentioned in the previous ice-coated graphite-sphere case. As q varies, the larger the bubble size, the more frequent the oscillations vary, but the more damped these oscillations are in amplitude. (3) In contrast to the previous ice-coated graphite cases, where the effects of the ice shell on the optical properties diminished as its thickness was reduced, the enhanced effects of the water shell in this case are even more pronounced when it is thin, i.e. when $q \to 1.0$. For this reason, our choice of $\Delta q = 0.01$ was too coarse for large

bubbles ($x_b \geq 400.0$) and might have missed additional oscillations in $0.99 \leq q \leq 1.0$. (4) Examination of the dependences of normalized/unnormalized extinction efficiencies on q further shows that solely by scattering, water in a bubble will tend to obscure much more efficiently than an equal mass of water in a full-water-droplet, particularly when the bubble is large and the bubble shell is appropriately thin, in which case as much as ~ 60% more light may be obscured than with an equally sized (much more massive) full water droplet. Indeed, the absolute magnitude of Q_e (or Q_s) reaching more than 3.0 in such cases is very unusual if compared with a large sphere without interior void. (5) Radiation pressure exerted on a bubble, which follows from inspection of $Q_p/Q_{p,m}$ vs q curves, slowly reaches a maximum at $q \cong 0.5$ (about 25% higher than that of a full droplet), and as q goes to 1.0, it drops thereafter to 0, accompanied by characteristic oscillation similar to $Q_e/Q_{e,m}$ or $Q_s/Q_{s,m}$ curves. This feature is very common to all bubble sizes; therefore, if an aggregate of monodisperse bubbles of various shell thickness was subjected only to the force of radiation pressure, a segregation would take place so that generally thinner bubbles would be left behind in their motion away from the light source.

SUMMARY

In summary, we find:

(1) New algorithms based on the use of ratio functions of Riccati-Bessel functions appear to be applicable to many Mie scattering problems with remarkable efficiency and accuracy. For practical applications it is virtually unrestricted in sphere size, complex refractive index and/or core-to-mantle size ratio for concentric spheres. Although not shown in this paper, we have compared our results with those by other researchers for many specific examples, and we found no significant discrepancies thus far.

(2) A similar ratio-function technique has been employed by us in cylinder-scattering problems for some time, where cylindrical Bessel functions were used in place of the Riccati-Bessel functions. Application to tilted infinite cylinder problems will be reported in the near future. Indeed, the new algorithms are being extended to cover much more complex spheroid problems, whereas most of the other methods impose severe restriction on the ranges of aspect ratio and particle size.

(3) Highlights of this work relate to concentric-sphere scattering, and we have emphasized the effects of mantle thickness for two distinct types of material compositions; i.e., the ice-coated graphite particles and the water bubbles. Examples shown are extensive but not exhaustive. It remains to be seen whether the reported exotic features can be observed in real-world scattering.

ACKNOWLEDGMENT

The authors would like to thank Dr. J.L. Weinberg for critical review of this paper and Dr. G. Eichhorn for computer-interface problems such as communication between VAX-11/750 and our dedicated PDP-11/23. Special thanks are due to the Army Research Office for continued interests and financial support.

REFERENCES

1. M. Abramowitz and I.A. Stegun, eds., Handbook of Mathematical Functions, N.B.S., AMS 55, Chapt. 10, (1955).

2. A.L. Aden and M. Kerker, Scattering of Electromagnetic Waves from Two Concentric Spheres, J. Appl. Phys. 22, 1242 (1951).

3. A. Ashkin and J.M. Dziedzic, Observation of optical resonances of dielectric spheres by light scattering, Appl. Opt. 20, 1803 (1981).

4. H.C. Bryant and A.J. Cox, Mie Theory and the Glory, J. Opt. Soc. Amer. 56, 1529 (1966).

5. P. Chýlek, J.T. Kiel and M.K.W. Ko, Narrow resonance structure in the Mie scattering characteristics, Appl. Opt. 17, 3019 (1978).

6. J.V. Dave, Scattering of Visible Light by Large Water Spheres, Appl. Opt. 8, 155 (1969).

7. D. Deirmendjian, Electromagnetic Scattering on Spherical Polydispersions, Elsevier, N.Y. (1969).

8. G. Grehan and G. Gouesbet, Mie theory calculations: New progress, with emphasis on particle sizing, Appl. Opt. 18, 3489 (1979).

9. A. Güttler, Die Miesche Theorie der Beugung durch dielektrische Kugeln mit absorbierendem Kern und inre Bedeutung für Probleme der interstellaren Materie und des atmosphärischen Aerosols, Ann. der Phys. 11, 65 (1952).

10. H.C. Van de Hulst, Light Scattering by Small Particles, Wiley, N.Y. (1957).

11. G.W. Kattawar and G.N. Plass, Electromagnetic Scattering from Absorbing Spheres, Appl. Opt. 6, 1377 (1967).

12. M. Kerker, The Scattering of Light and other electromagnetic radiation, Academic Press, N.Y. (1969).

13. O.B. Toon and T.P. Ackerman, Algorithms for the calculation of scattering by stratified spheres, Appl. Opt. 20 3657 (1981).

14. A. Ungut, G. Grehan, and G. Gouesbet, Comparison between geometrical optics and Lorenz-Mie theory, Appl. Opt. 20, 2911 (1981).

15. W.J. Wiscombe, Improved Mie scattering algorithms, Appl. Opt. 19, 1505 (1980).

APPENDIX

1. $p_n(x)$ and singularity of $p_1(x)$

Expression of half integral order Bessel function in terms of elementary functions is:

$$J_{n+1/2}(x) = (2/\pi x)^{1/2}\left(\sin(x-n\pi/2)*S_{n+1/2} + \cos(x-n\pi/2)*C_{n+1/2}\right) \qquad (A\text{-}1)$$

where $S_{n+1/2} = \sum_{r=0}^{[n/2]} \frac{(-1)^r(n+2r)!}{(2r)!(n-2r)!(2x)^{2r}}$

$$C_{n+1/2} = \sum_{r=0}^{[n/2-1/2]} \frac{(-1)^r(n+2r+1)!}{(n-2r-1)!(2x)^{2r+1}}$$

For $J_{n-1/2}(x)$, just substitute n-1 instead of n.

Thus $p_n(x)$, as defined by the ratio of $j_n(x)/j_{n-1}(x)$, will be

$$p_n(x) = j_n(x)/j_{n-1}(x) = J_{n+1/2}(x)/J_{n-1/2}(x)$$
$$= \frac{S_{n+1/2}*\sin(x-n\pi/2) + C_{n+1/2}*\cos(x-n\pi/2)}{S_{n-1/2}*\sin(x-(n-1)\pi/2) + C_{n-1/2}*\cos(x-(n-1)\pi/2)} \qquad (A\text{-}2)$$

Now let's discuss the denominator of $p_n(x)$:

For positive integer n, while x is multiple of π, there are the following formulae:

$$\sin(x-(n-1)\pi/2) = \sin(k\pi-(n-1)\pi/2) = (-1)^{k+1}\sin((n-1)\pi/2) \qquad (A\text{-}3)$$

$$\cos(x-(n-1)\pi/2) = (-1)^k\cos((n-1)\pi/2) \qquad (A\text{-}4)$$

If n = 1, $C_{n-1/2} = C_{1/2} = 0$, the sine term becomes zero, and $p_1(x)$ goes to infinity.

Actually, it can be seen from

$$p_1(x) = j_1(x)/j_0(x) = (1/\sin x)(\sin x/x - \cos x) \tag{A-5}$$

2. Asymptotic expression of $p_{n+1}(z)$

From series expansion of half integral order Bessel function

$$J_{n+1/2}(z) = \sum_{k=0}^{\infty} \frac{(-1)^k}{k!\ \Gamma(n+k+3/2)(z/2)^{2k+n+1/2}} \tag{A-6}$$

and from asymptotic expression of Γ function

$$\ell_n\Gamma(n+a) = (n+a-1/2)\ell_n n - n + (1/2)\ell_n(2\pi) + \sum_{m=1}^{r} \frac{(-1)^{m-1}\phi_{m+1}(a)}{m(m+1)n^m} + O(n^{-r-1}) \tag{A-7}$$

where $\phi_{m+1}(a)$ is Bernoulli polynomial and ℓ_n is the natural logarithm.

If $|z|/n < 1$, let $a = k + 3/2$, after some simplification, then

$$J_{n+1/2}(z) \sim \exp\left[(n+1/2) + (n+1/2)\ell_n\left(\frac{z}{2}\right) - (n+1)\ell_n(n+1/2)\right] \cdot \left[C_0 + C_1/(n+1/2) + C_2/(n+1/2)^2 + \ldots\right] \tag{A-8}$$

$$J_{n-1/2}(z) \sim \exp\left[(n-1/2) + (n-1/2)\ell_n\left(\frac{z}{2}\right) - n\ell_n(n-1/2)\right] \cdot \left[C_0 + C_1/(n-1/2) + C_2/(n-1/2)^2 + \ldots\right] \tag{A-9}$$

where $C_0 = 1/(2\pi)^{1/2}$, C_1, C_2,...are constants.

since $p_{n+1}(z) = J_{n+1/2}(z)/J_{n-1/2}(z)$, then we have

$$\lim_{n\to\infty} p_{n+1}(z) = \exp(1)(z/2) \cdot \frac{(1-1/2n)^{(-2n)(-1/2)}}{(1+1/2n)^{(2n)(1/2)}} \cdot \frac{1}{(n+1/2)} = \frac{z}{2n+1} \tag{A-10}$$

FIGURES

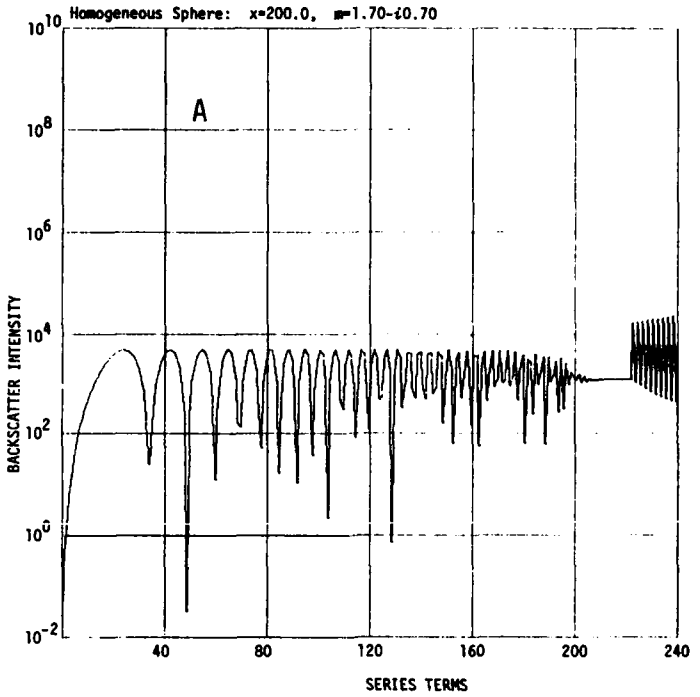

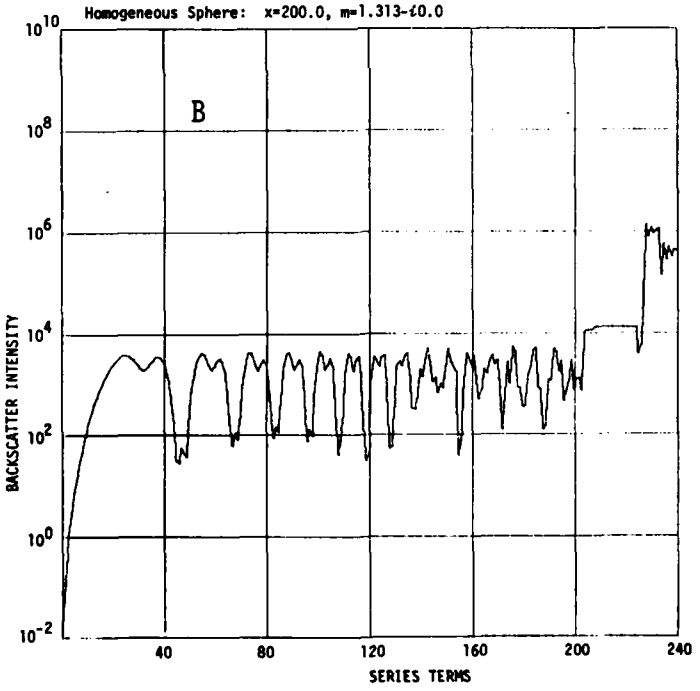

FIGURES 1A & 1B. GROWTH FUNCTIONS FOR HOMOGENEOUS SPHERES. Total contribution to backscatter intensity by the first n terms in Mie series. Fig. 1A is for a graphite sphere, and Fig. 1B is for an ice ball. See also Sec.III-A.

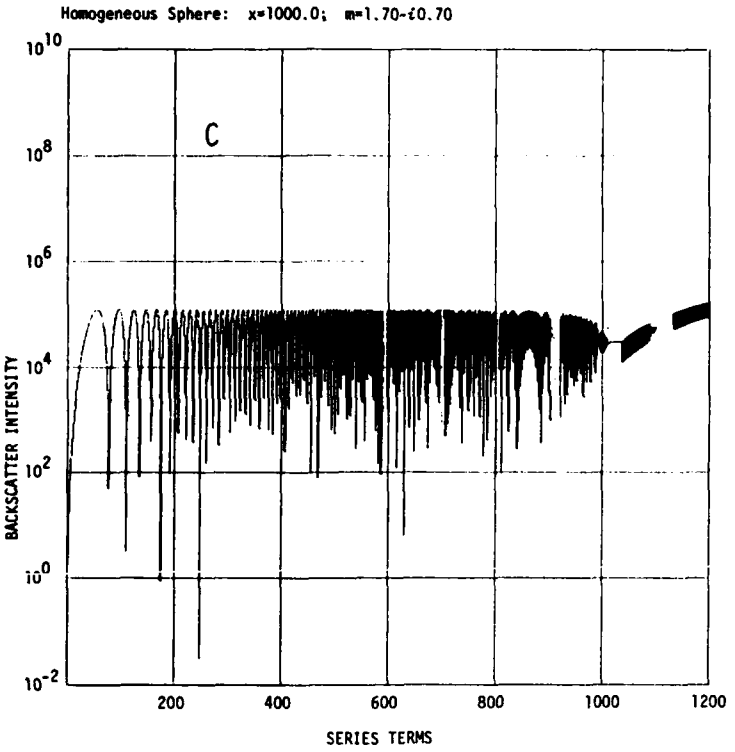

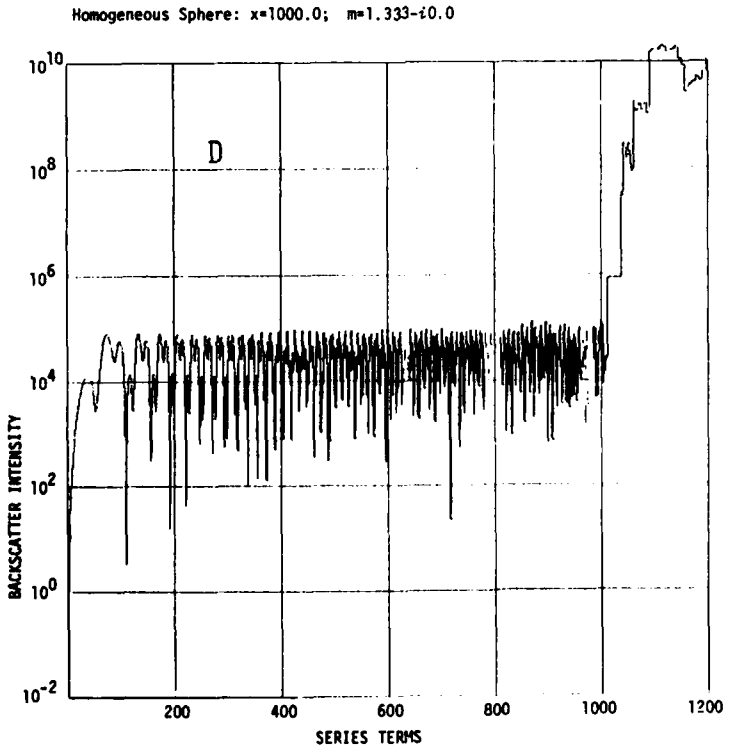

FIGURES 1C & 1D. GROWTH FUNCTIONS FOR HOMOGENEOUS SPHERES. Total contribution to backscatter intensity by the first n terms in Mie series. Fig. 1C is for a graphite sphere, and Fig. 1D is for an ice ball. See also Sec.III-A.

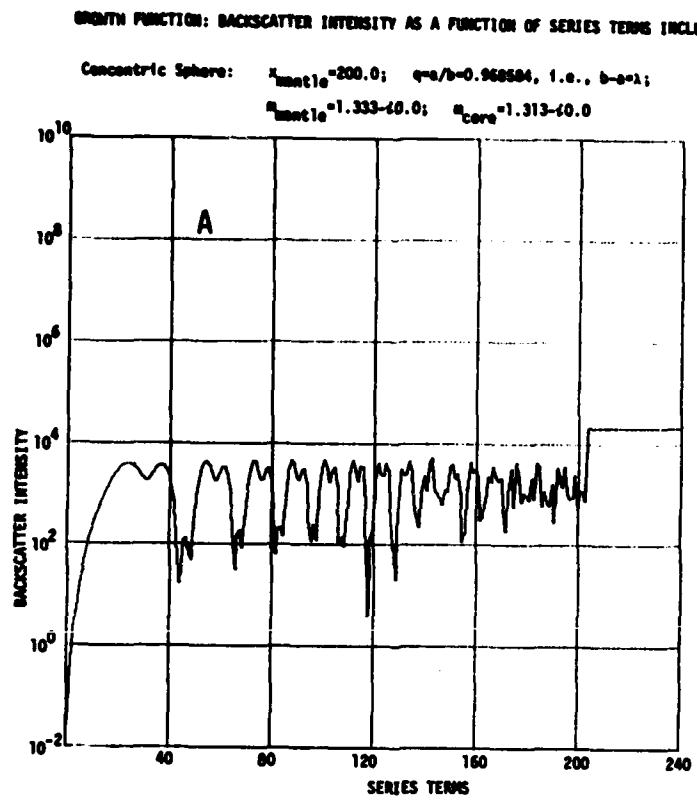

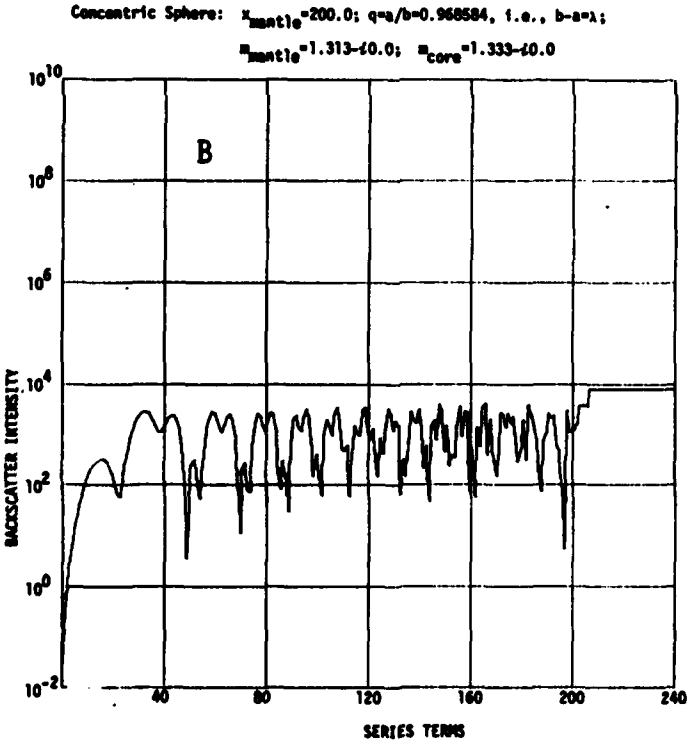

FIGURES 2A & 2B. GROWTH FUNCTIONS FOR CONCENTRIC SPHERES. Total contribution to backscatter intensity by the first n terms in Mie series. Fig. 2A is for an ice ball mantled by one-wavelength-thick water shell, while Fig. 2B is for these core-mantle materials interchanged. See also Sec.III-A.

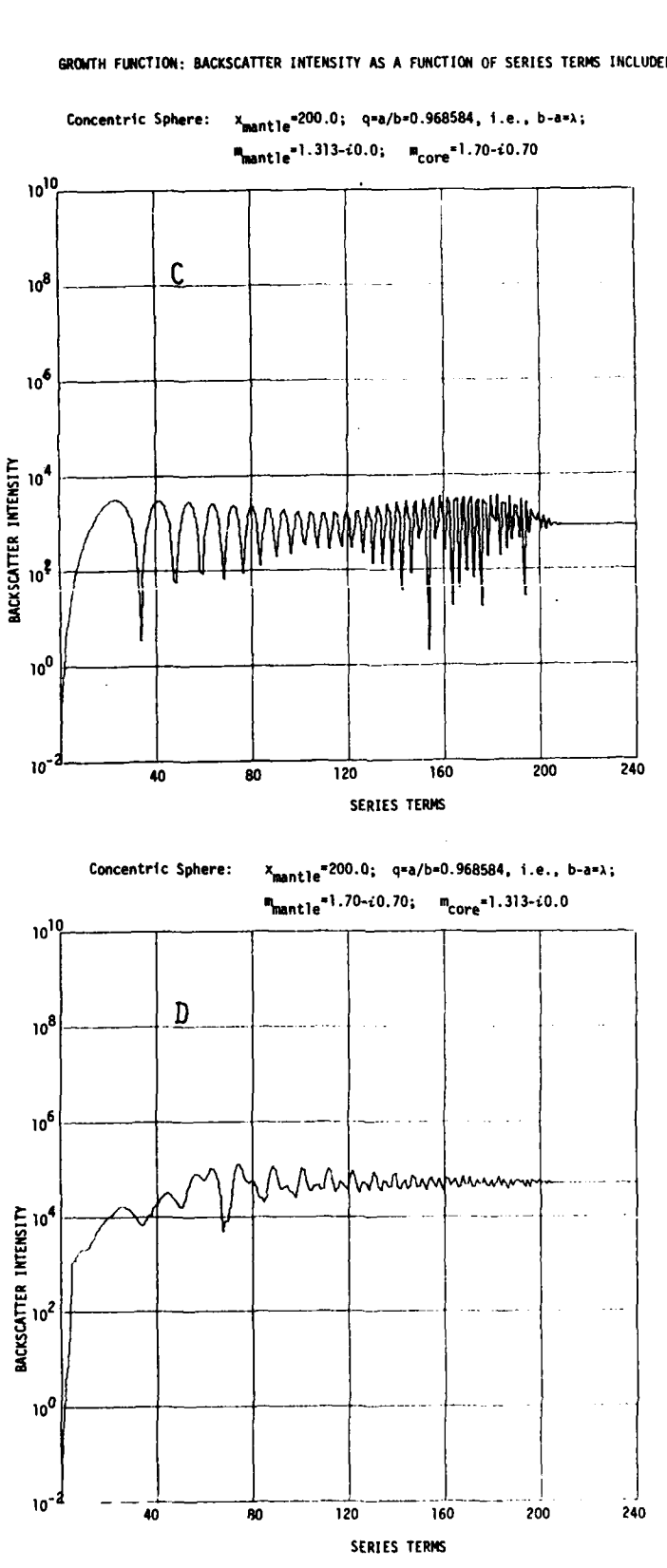

FIGURES 2C & 2D. GROWTH FUNCTIONS FOR CONCENTRIC SPHERES. Total contribution to backscatter intensity by the first n terms in Mie series. Fig. 2C is for the sphere with graphite core and ice mantle, while Fig. 2D is for that with these two materials interchanged. In both cases the mantle thickness is one wavelength. See also Sec.III-A.

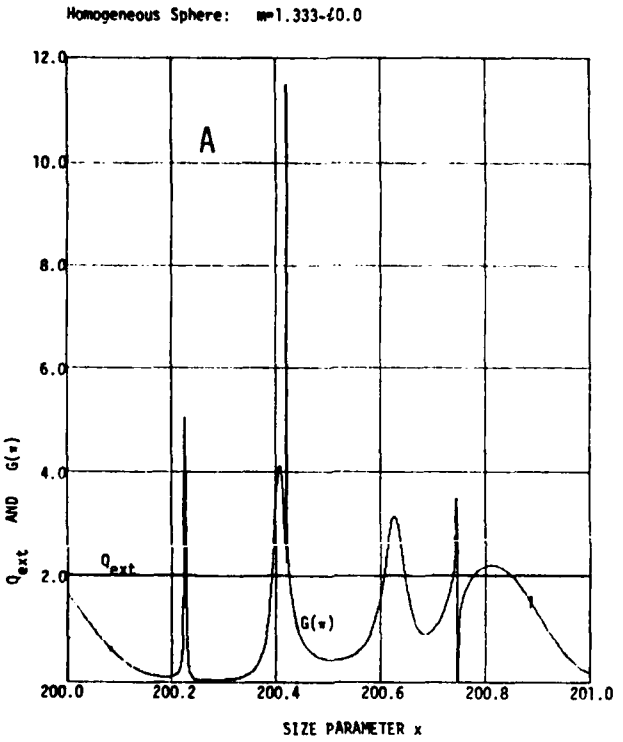

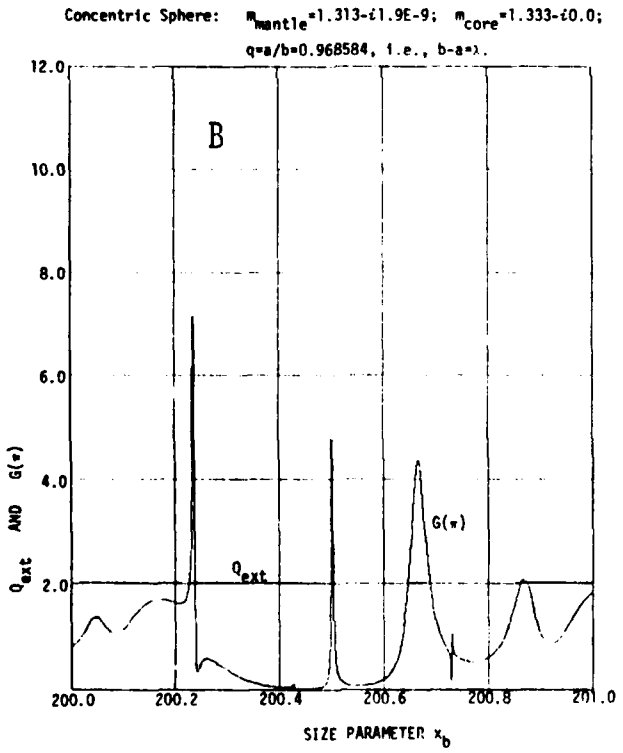

FIGURES 3A & 3B. DEPENDENCE OF EXTINCTION EFFICIENCY AND BACKSCATTER GAIN ON PARTICLE SIZE. Fig. 3A is for a homogeneous water sphere whose growth function is also shown in Fig. 1D. Fig. 3B is for a concentric sphere with water core mantled by 1-λ-thick ice shell (Cf. Fig. 2B). Both are plotted in $200.0 \leq x\ (0.001) \leq 201.0$. See also Sec.III-B.

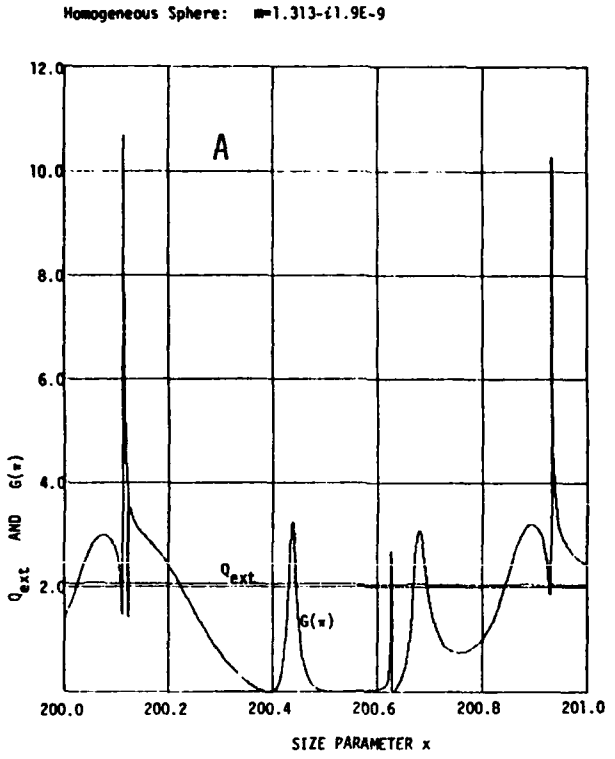

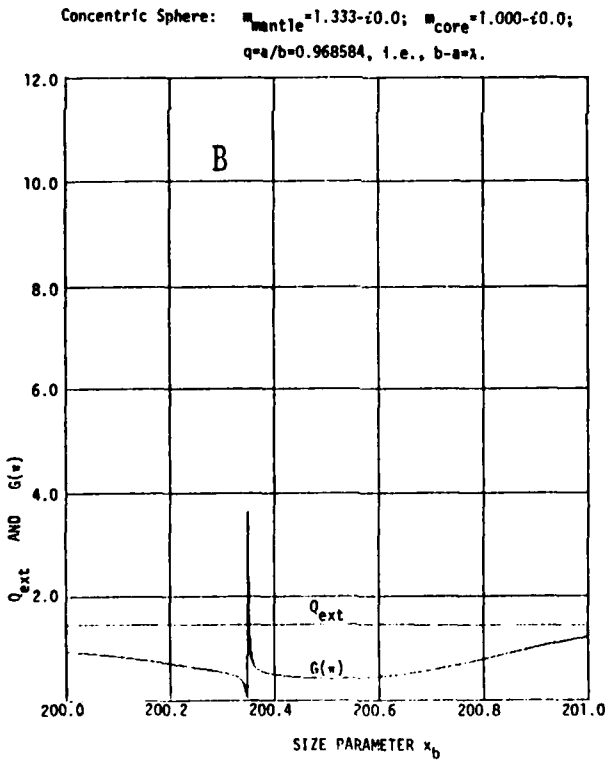

FIGURES 4A & 4B. DEPENDENCE OF EXTINCTION EFFICIENCY AND BACKSCATTER GAIN ON PARTICLE SIZE. Fig. 4A is for a homogeneous ice sphere whose growth function is also shown in Fig. 1B. Fig. 4B is for a water bubble with 1-λ-thick water shell. Both figures are plotted in $200.0 \leq x\ (0.001) \leq 201.0$. See also Sec.III-B.

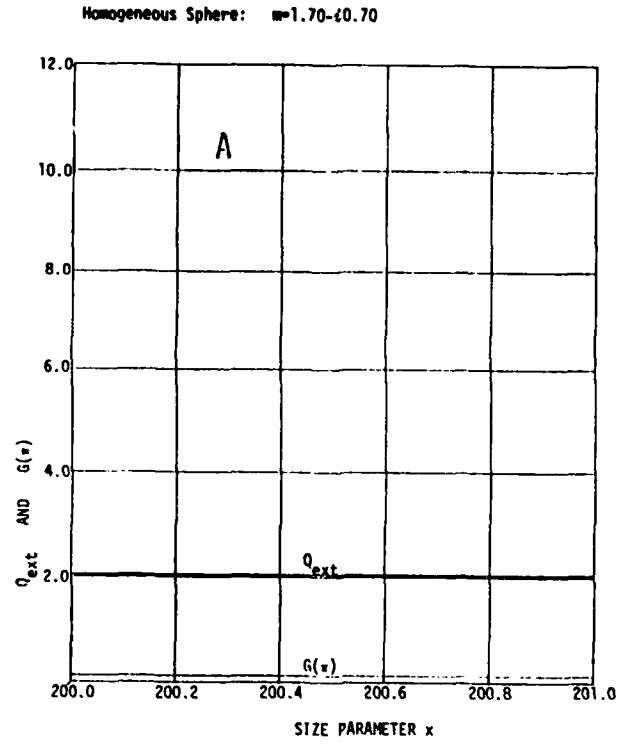

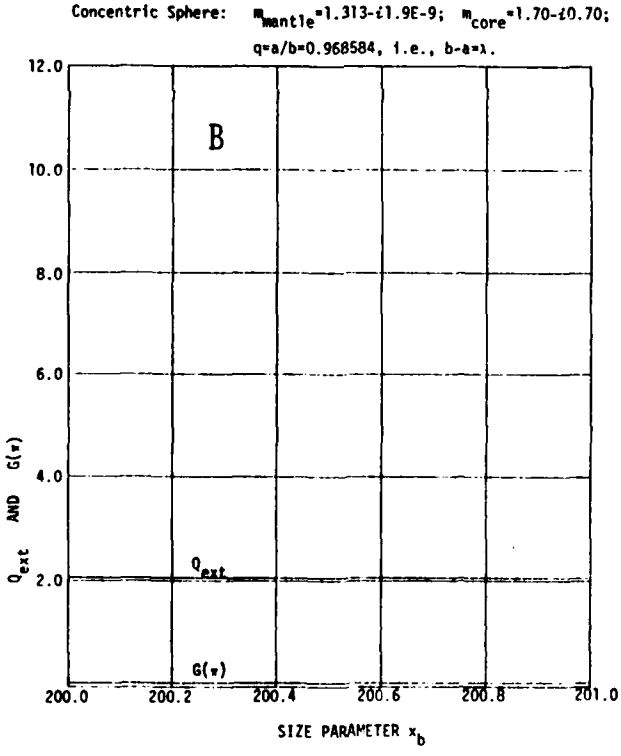

FIGURES 5A & 5B. DEPENDENCE OF EXTINCTION EFFICIENCY AND BACKSCATTER GAIN ON PARTICLE SIZE. Fig. 5A is for a homogeneous graphite sphere whose growth function is also shown in Fig. 1A. Fig. 5B is for a graphite sphere coated by 1-λ-thick ice shell whose growth function is also shown in Fig. 2C. Both figures are plotted in $200.0 \leq x\ (0.001) \leq 201.0$. See also Sec.III-B.

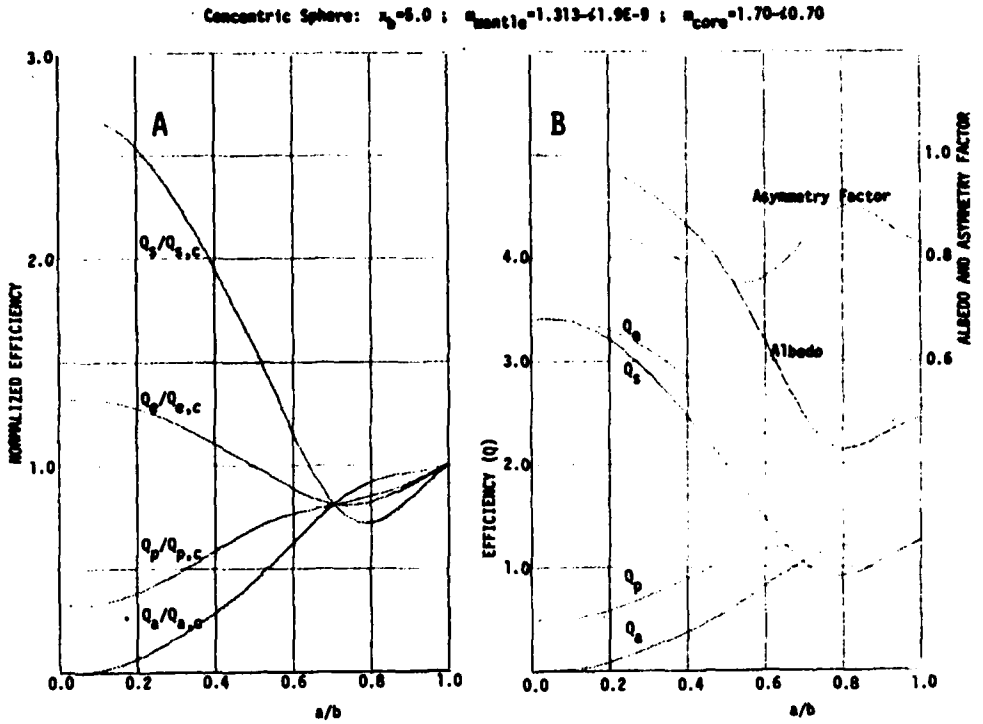

FIGURES 6A & 6B. ICE-MANTLED GRAPHITE. See also Sec. III-C.

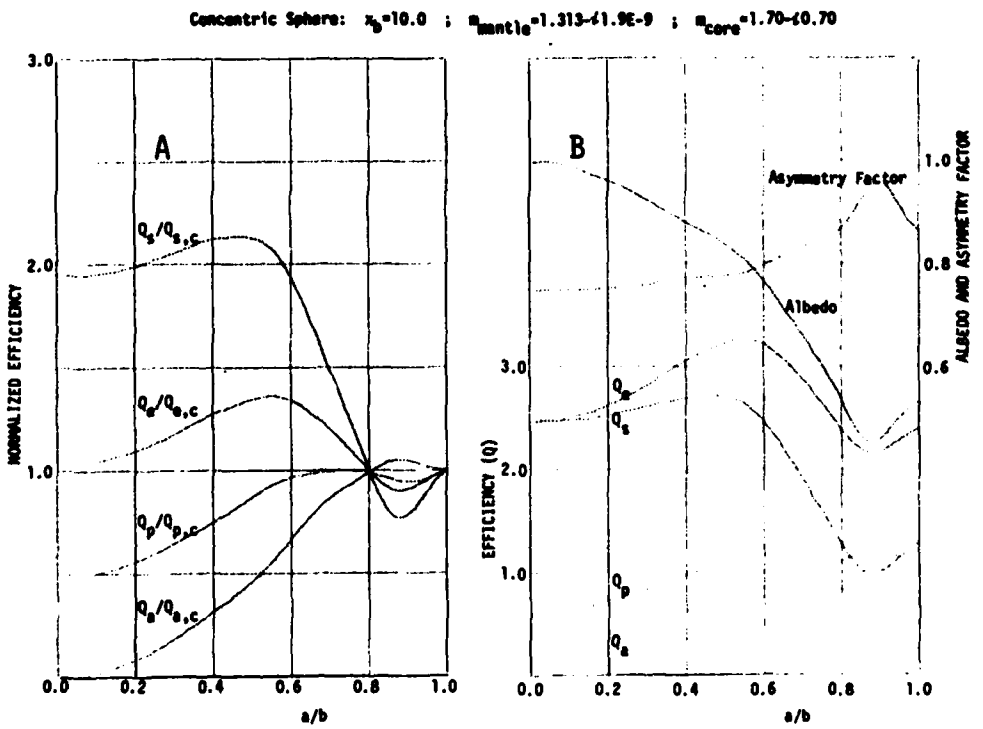

FIGURES 7A & 7B. ICE-MANTLED GRAPHITE. See also Sec.III-C.

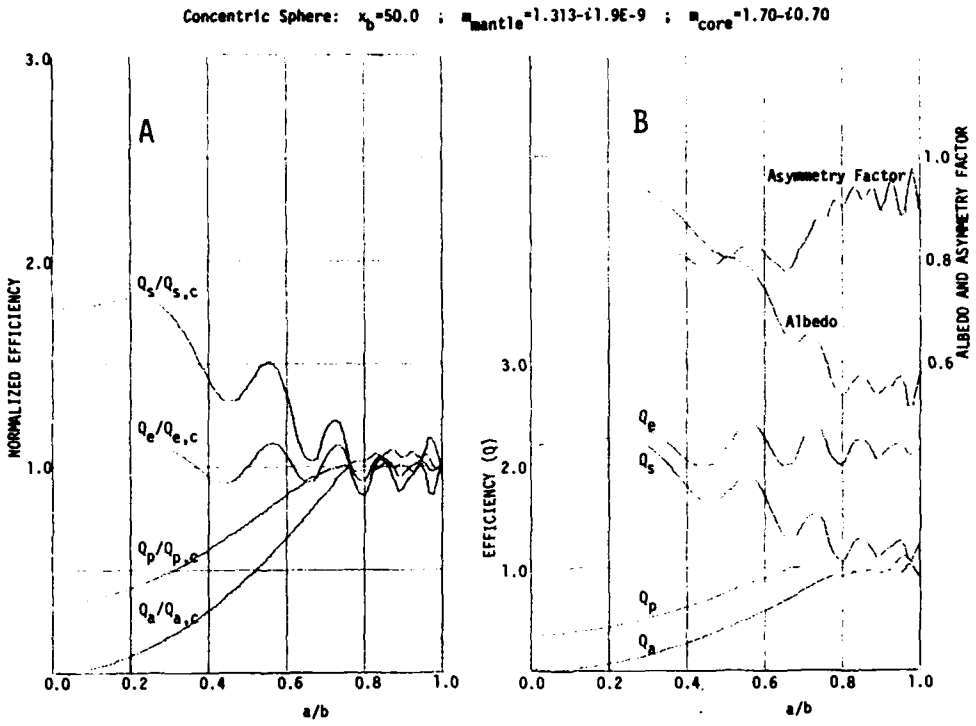

FIGURES 8A & 8B. ICE-MANTLED GRAPHITE. See also Sec.III-C.

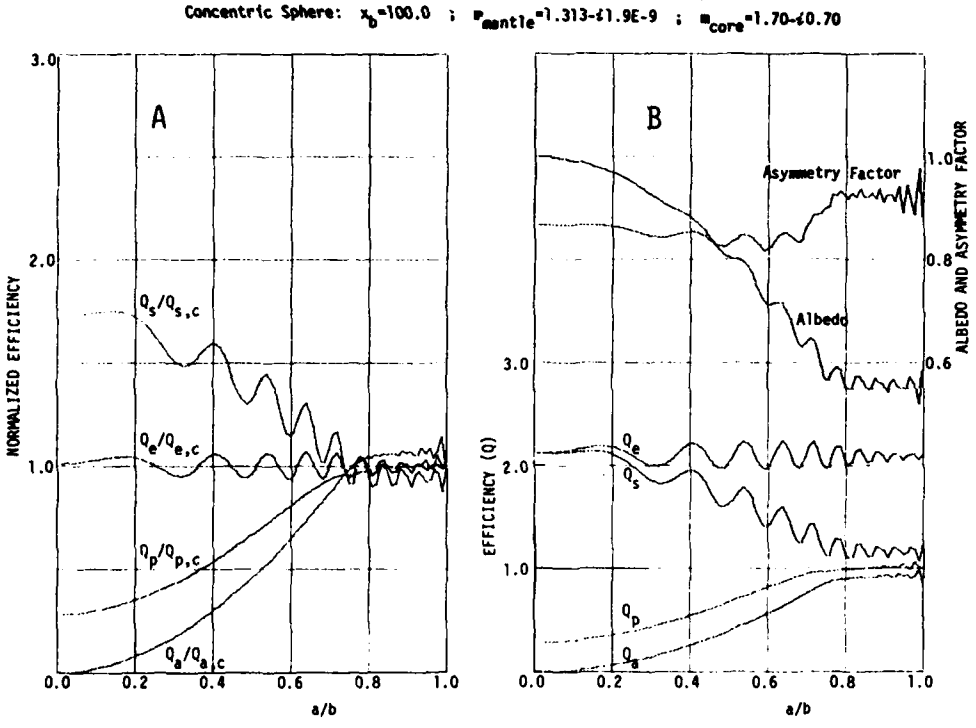

FIGURES 9A & 9B. ICE-MANTLED GRAPHITE. See also Sec.III-C.

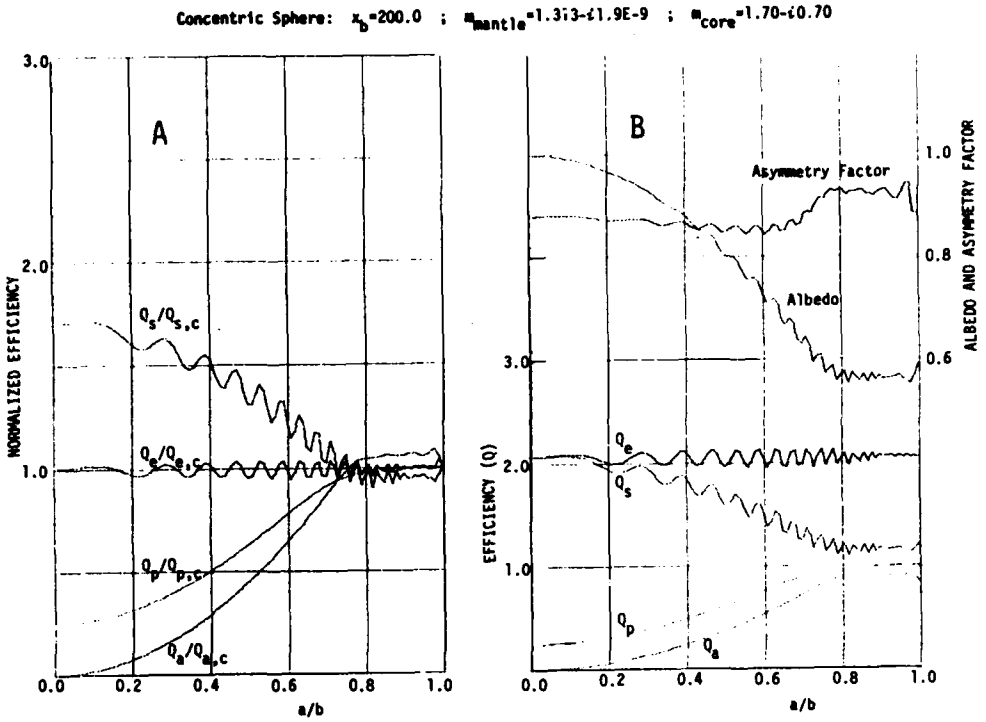

FIGURES 10A & 10B. ICE-MANTLED GRAPHITE. See also Sec.III-C.

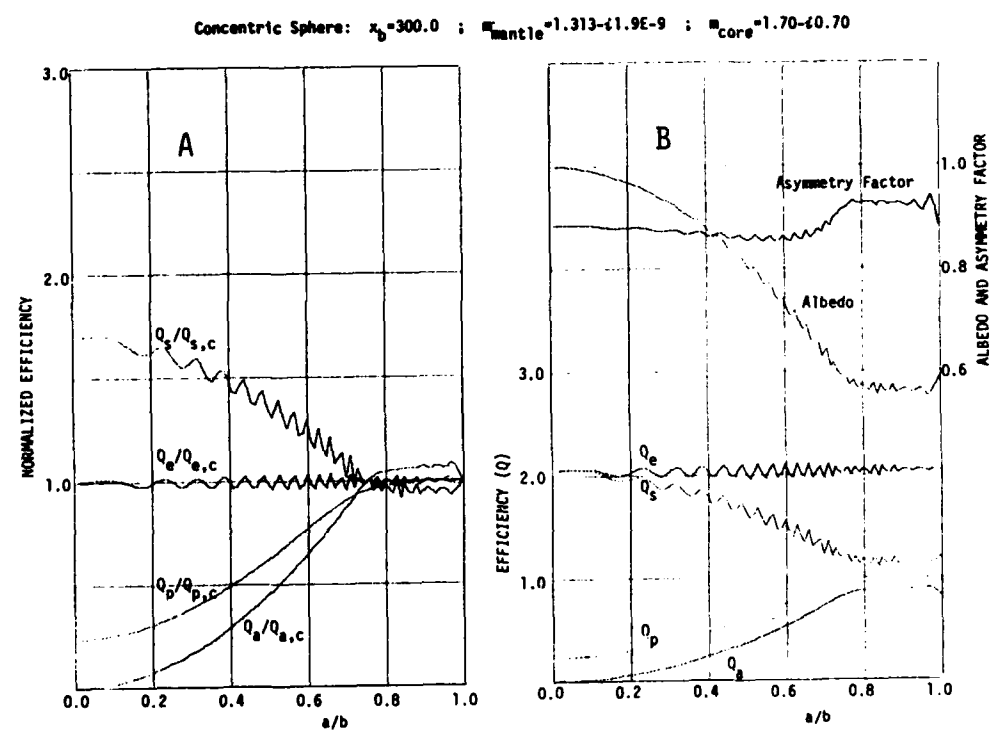

FIGURES 11A & 11B. ICE-MANTLED GRAPHITE. See also Sec.III-C.

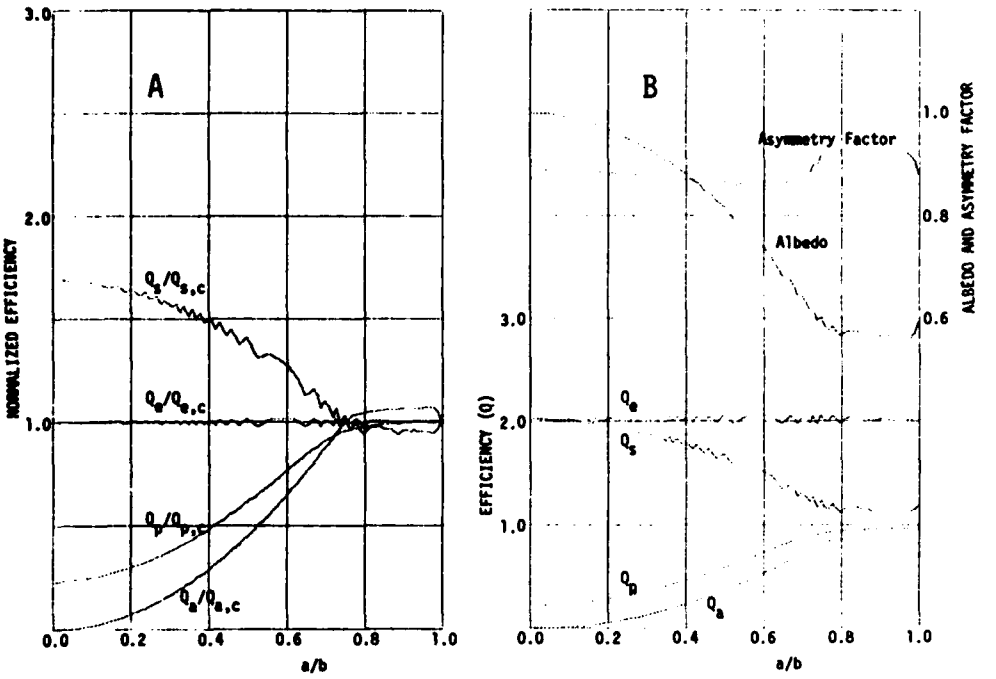

FIGURES 12A & 12B. ICE-MANTLED GRAPHITE. See also Sec.III-C.

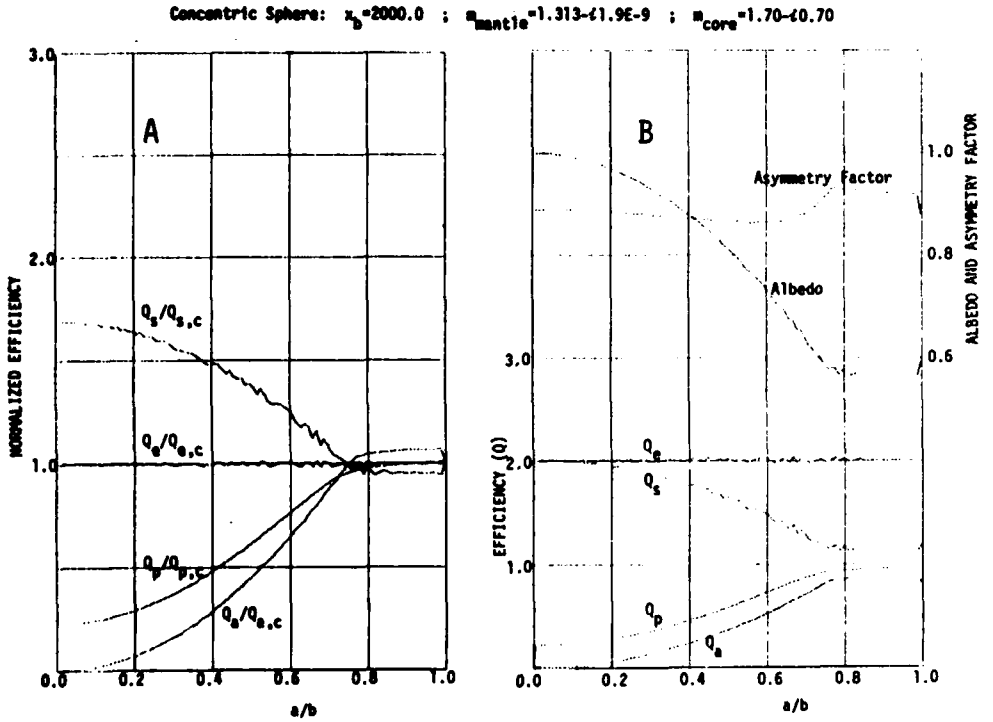

FIGURES 13A & 13B. ICE-MANTLED GRAPHITE. See also Sec.III-C.

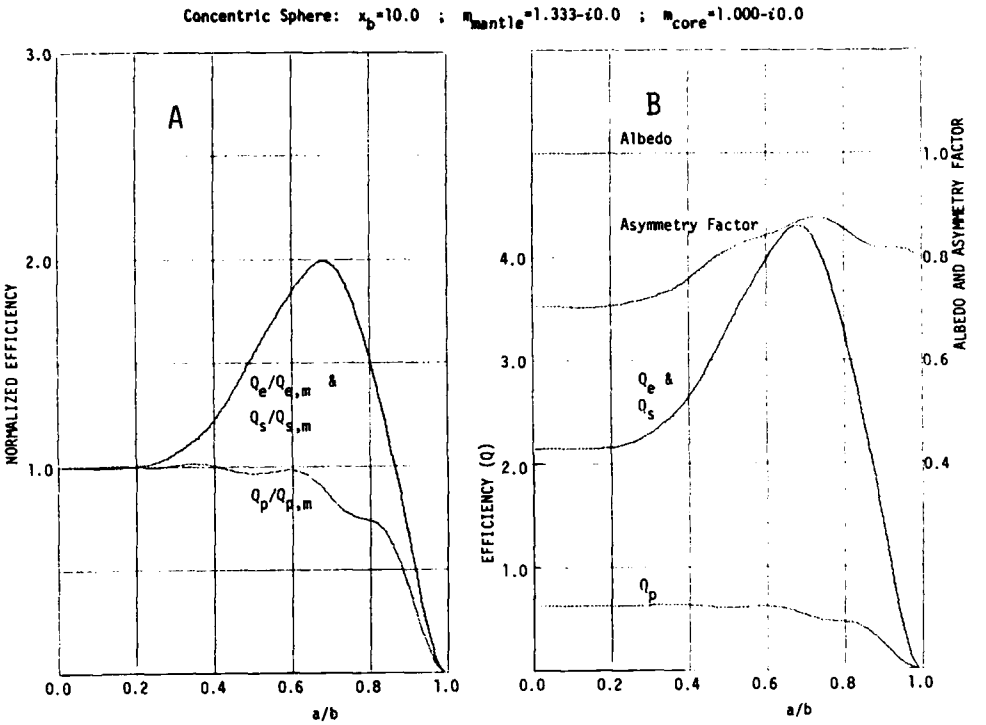

FIGURES 14A & 14B. WATER BUBBLE. See also Sec.III-C.

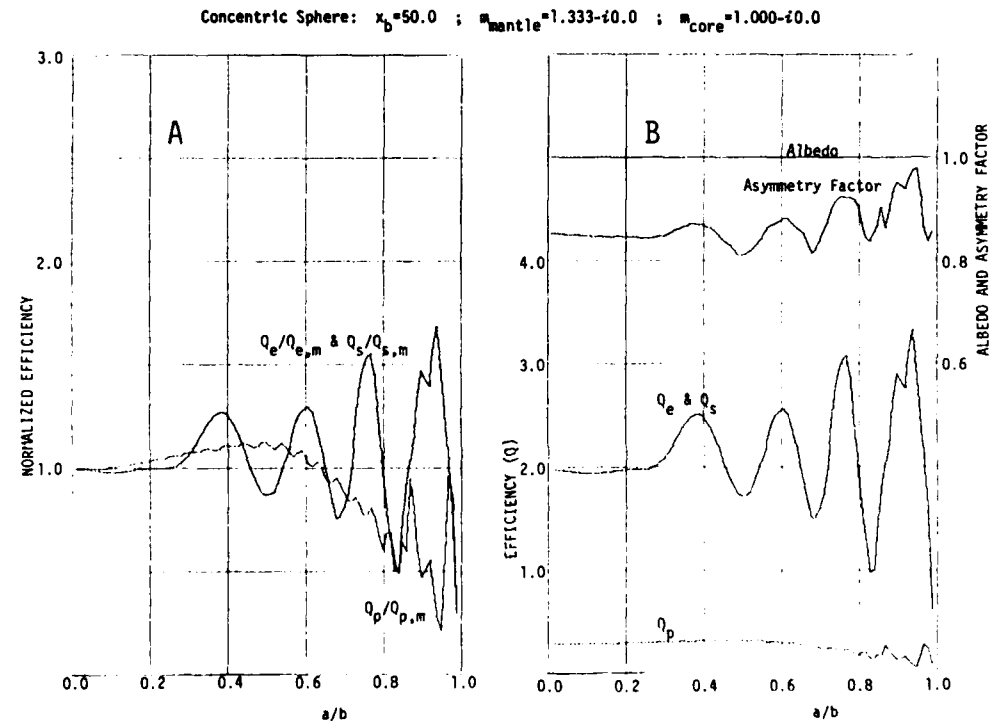

FIGURES 15A & 15B. WATER BUBBLE. See also Sec.III-C.

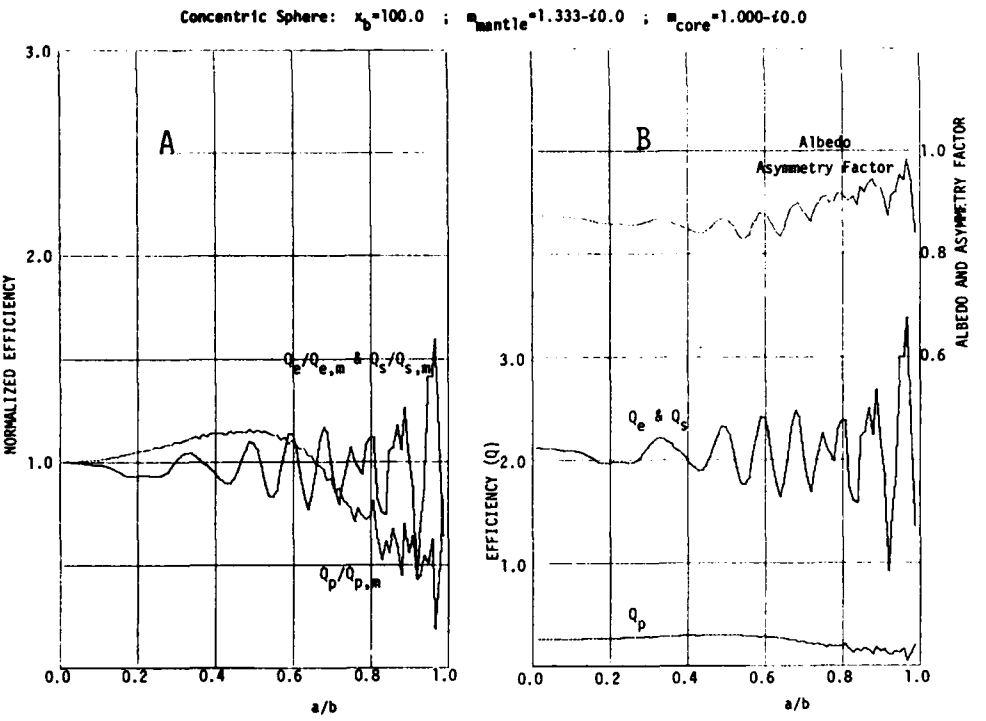

FIGURES 16A & 16B. WATER BUBBLE. See also Sec.III-C.

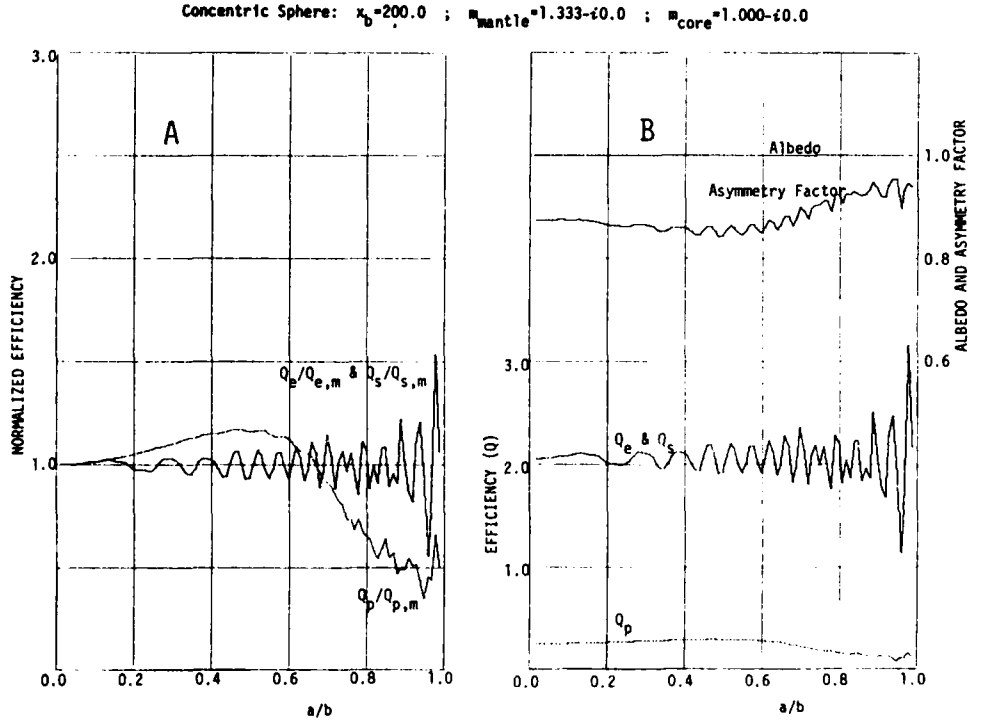

FIGURES 17A & 17B. WATER BUBBLE. See also Sec.III-C.

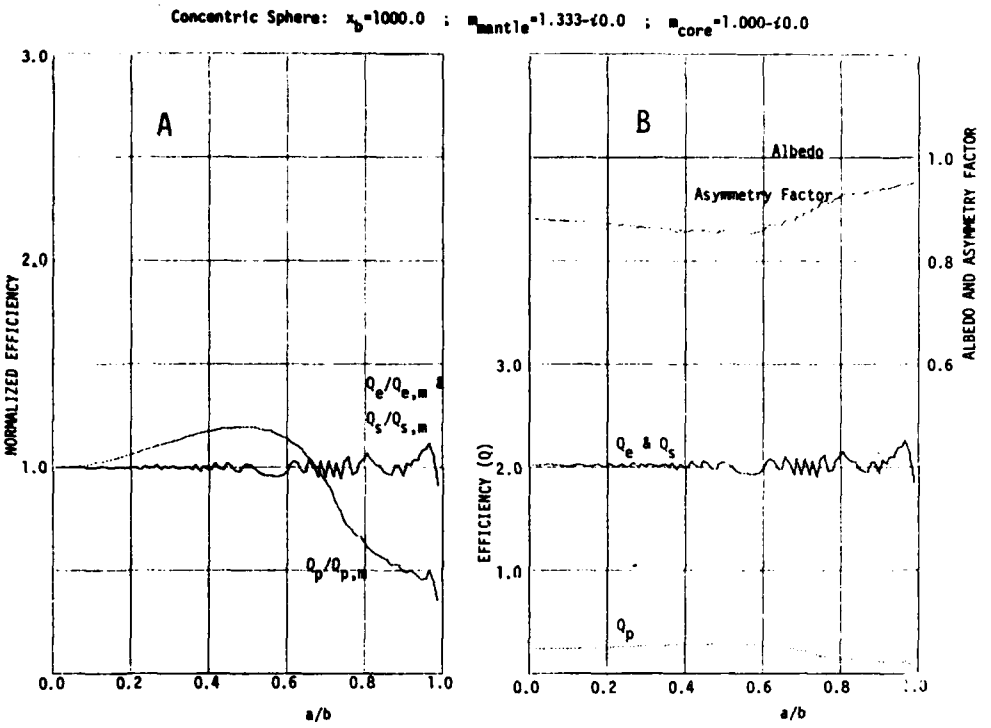

FIGURES 18A & 18B. WATER BUBBLE. See also Sec.III-C.

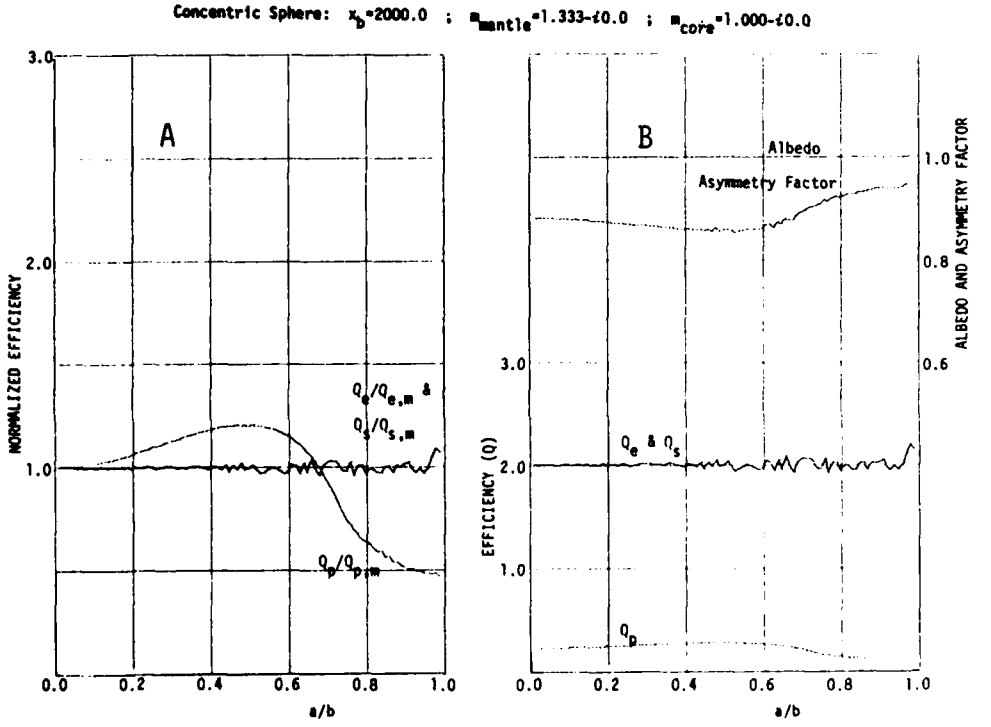

FIGURES 19A & 19B. WATER BUBBLE. See also Sec.III-C.

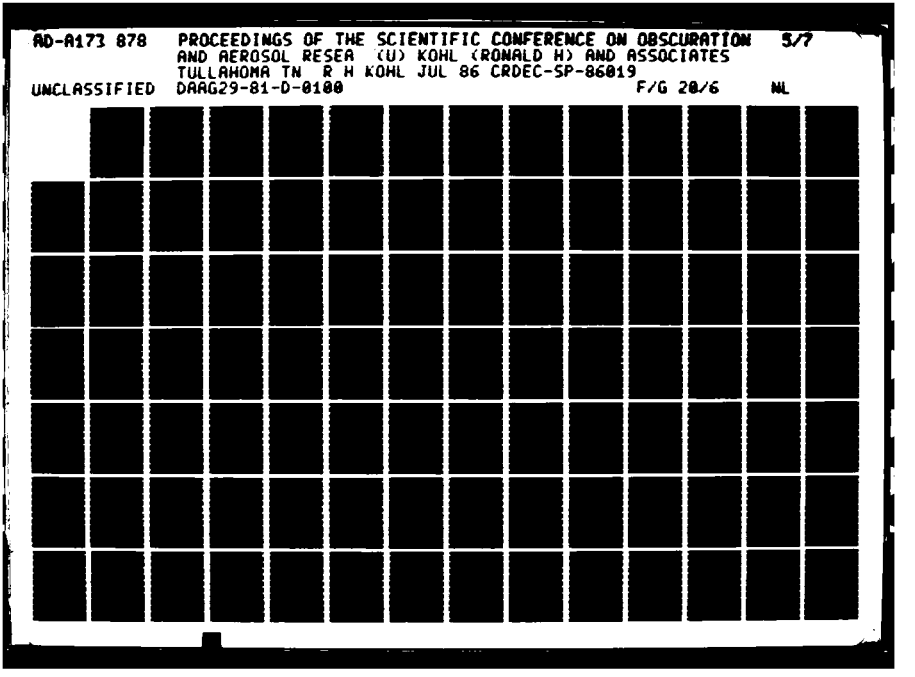
AD-A173 878 PROCEEDINGS OF THE SCIENTIFIC CONFERENCE ON OBSCURATION 5/7
AND AEROSOL RESEA (U) KOHL (RONALD H) AND ASSOCIATES
TULLAHOMA TN R H KOHL JUL 86 CRDEC-SP-86019
UNCLASSIFIED DAAG29-81-D-0100 F/G 20/6 NL

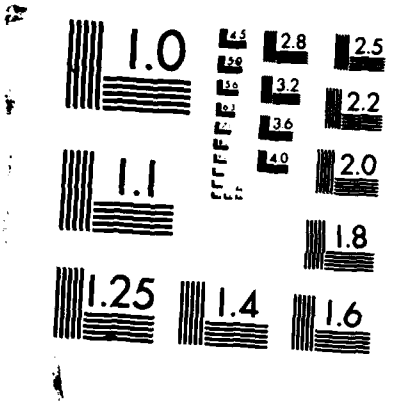

FORWARD OPTICAL GLORY OF BUBBLES: THEORY AND OBSERVATIONS*

Dean S. Langley** and Philip L. Marston
Department of Physics
Washington State University
Pullman, WA 99164-2814

RECENT PUBLICATIONS, SUBMITTALS FOR PUBLICATION AND PRESENTATIONS:

A) P. L. Marston and D. S. Langley, "Forward Optical Glory Scattering from Bubbles (and Clouds of Bubbles) in Liquids and Other Novel Directional Caustics," submitted to the proceedings of the Symposium on Multiple Scattering of Waves in Random Media and Random Rough Surfaces (edited by V. K. and V. V. Varadan) July, 1985.

B) P. L. Marston, "Uniform Mie-theoretic Analysis of Polarized and Cross-Polarized Optical Glories," Journal of Optical Society of America 73, 1816-1818 (1983).

C) P. L. Marston and D. S. Langley, "Transmitted wave and rainbow-enhanced glories of dielectric spheres," in Proceedings of the Chemical Research and Development Center's 1984 Scientific Conference on Obscuration and Aerosol Research, p. 239.

ABSTRACT

The near-forward cross-polarized scattering patterns from gas bubbles in liquids were observed and calculated. Quasi-periodic structures observed are a consequence of glory rays.

SUMMARY

We have photographed the near-forward cross-polarized scattering pattern from individual bubbles and from bubble clouds in liquids.[1,A] The bubbles were large in comparison to the wavelength of light. The quasi-periodic structure present for individual gas bubbles is similar to that previously observed for the cross-polarized near-backward glory of bubbles.[1,C] The observed periodicity is in good agreement with a calculation of diffracted glory wavefronts, and it is clearly not caused by the ordinary forward diffraction which is co-polarized with respect to the illumination.[A,B] The gas bubbles observed were in water or in silicone oil. The dominant toroidal wavefront was associated with the twice-refracted (once-reflected) ray. See Fig. 1 and Ref. 2. Though these experiments may be interpreted using a theory which assumes single scattering, the observed polarization phenomena may be helpful in the understanding of scattering from dense bubble clouds where multiple scattering may be significant. The polarization and structure of glory scattering may be useful in inverse problems.

Since the forward-directed toroidal wavefronts resulted from rays transmitted through the bubbles, the mechanism for glory scattering differs from the one proposed for drops by Nussenzveig and Wiscombe.[3] They calculated the glory contribution to forward scattering from spherical drops of water in air by considering rays which traveled circumferentially along the drop's surface during part of the trajectory. Our calculation of the near-forward glory amplitudes for bubbles is similar instead to our previous models[2,C] of transmitted-wave backward glories.

---

*Research supported by the Office of Naval Research.

**Present address: Department of Physics, Whitman College, Walla Walla, WA 99362.

The measurement configuration used in our experiments is like one of the polarized measurement configurations recently analyzed using Mie theory.[B,4] That analysis gives a description of the far-field scattered irradiances for spheres as seen with co-polarized and cross-polarized measurement configurations. Because of recent interest[5] in such configurations, it is noteworthy that the analysis[B] is uniform with respect to variation of the scattering angle. The cross-polarized scattering from spheres vanishes in the exact forward and backward directions.

SUPPLEMENTAL REFERENCES

1. D. S. Langley, "Light Scattering from Bubbles in Liquids," Ph.D. thesis, Washington State University, 1984 (available from the Defense Technical Information Center, Alexandria, VA: Accession Number AD-A158736).
2. P. L. Marston, D. S. Langley, and D. L. Kingsbury, "Light scattering by bubbles in liquids: Mie theory, physical-optics approximations, and experiments," Appl. Sci. Res. 38, 373-383 (1982).
3. H. M. Nussenzveig and W. J. Wiscombe, "Forward optical glory," Opt. Lett. 5, 455-457 (1980).
4. Inspection of Eq. (2) of Ref. B reveals a trivial misprint. The rightmost quantity of the upper line should have been printed as $h_5[\hat{e}_x - (\hat{e}_r \cdot \hat{e}_x)\hat{e}_r]$.
5. J. T. Brown and F. V. Kowalski, "Polarization effects in the scattering of light by spherical particles," presented at this CRDC Conference, June 1985.

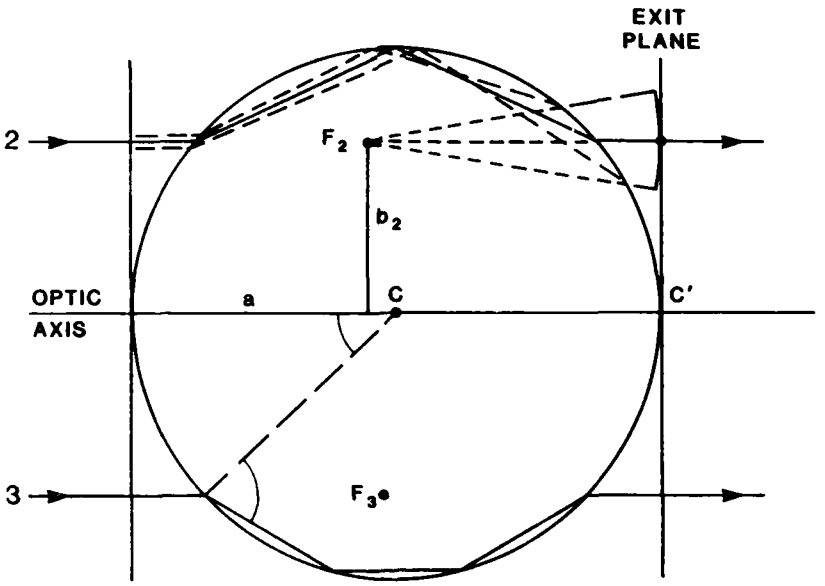

FIGURE 1. SOME FORWARD DIRECTED GLORY RAYS FOR BUBBLES. The ray families shown have 2 and 3 chords. The resulting toroidal wavefronts appear to diverge from ring-like sources which cut the plane at F_2 and F_3, respectively. The largest contribution to the cross-polarized near-forward scattering is due to the 2-chord family.

ELECTROMAGNETIC INTERACTION--ENERGY TRANSFER AND TRANSIENT RESPONSE

D. K. Cohoon
Temple University Department of Mathematics 038-16
Philadelphia, Pennsylvania 19122

RECENT SUBMITTAL

A) D. K. Cohoon, "Dispersive and geometric electromagnetic pulse distortion effects--Lorentzian and Debye Materials," to appear in IEEE Transactions on Antennas and Propagation, August, 1985.

ABSTRACT

We have developed analytical methods and computer algorithms treating the problem of describing electromagnetic interaction with a single particle which will help us describe the propagation of electromagnetic radiation through an aerosol of particles. One of our concerns is that the ringing or internal reflections of a ducting nature that have been shown by computer computations to occur when an electromagnetic pulse interacts with an individual particle whose index of refraction has a small imaginary part or that purely dispersive effects such as that which engenders the Sommerfeld-Brillouin precursor waves [1] will alter the transmission properties of a cloud of these particles in a manner that could not have been predicted with a traditional time-harmonic analysis. Another concern is that an intense coherent source of radiation might, by heating or other energy transfer, do such things as explode the droplet, create a plasma around it, or change the droplets electrical properties during the course of the electromagnetic radiation so that the transmission properties of the aerosol of droplets depends on the precise history of its exposure to radiation. We have predicted with computer codes the thermal response of spherically symmetric particles and cylindrically symmetric obstacles with circular cross sections; these objects may be multi-layer in nature and the layers may have different heat sink and source characteristics. For the case of a homogeneous spherical ball the computer code was verified by experimental measurement using Vitek non-field perturbing thermal probes. This comparison is described in Cohoon et al. [2]; in a microwave simulation a homogeneous spherical ball was encased in a styrofoam mold and was exposed to 1.2 Gigahertz and 2.4 Gigahertz radiation for times ranging from 0 to 180 seconds with the temperature being measured along three perpendicular axes, one of which was parallel to the direction of propagation of the radiation. Excellent agreement was found between theory and experiment. No comparisons have been made for the cylindrical structures or for any multilayer structures. We have developed a hybrid method of evaluating the spherical and cylindrical harmonics used in these two programs that could conceivably be used to improve EBCM codes that are applicable to particles with a general shape. For example, in the cylindrical harmonics code we use series to compute $J_0(z)$ and $J_1(z)$ when $|z|$ is small, Neumann series for $Y_0(z)$ and $Y_1(z)$ for moderate values of $|z|$, asymptotic expansions when $|z|$ is large, and continued fraction expansions for $J_n(z)/J_{n+1}(z)$ (c.f. Gian Carlo Rota (ed) Encyclopedia of Mathematics. Volume 11, page 162) and a careful use of recurrence relations. A similar analysis and algorithm testing was carried out for the spherical Bessel and Hankel functions of arbitrary order and complex argument that arise naturally in Mie-solution, spheroidal-harmonics, and EBCM computer codes. An effort is underway to improve these codes and then to attempt to predict the electromagnetic pulse response of spheroidal particles to transient electromagnetic radiation and to predict the thermal response of spheroidal objects to time harmonic radiation.

INTRODUCTION

We treat in this report the problem of predicting the transient and thermal responses of penetrable particles such as orthophosphoric acid droplets (e.g. Rubel [3]), methylene blue particles (Liu [4], p 40), or zirconium dioxide(Rabbe [5], p 92) that have been subjected to electromagnetic radiation. The basic equations under consideration are

$$\text{curl}(E) = -\frac{\partial B}{\partial t}, \tag{1}$$

$$\text{curl}(H) = \frac{\partial D}{\partial t} + J, \tag{2}$$

$$D(x,y,z,t) = \int_{-\infty}^{\infty} F^{-1}(\varepsilon)(x,y,z,\tau)E(x,y,z,t-\tau)d\tau \ , \tag{3}$$

$$J(x,y,z,t) = \int_{-\infty}^{\infty} F^{-1}(\sigma)(x,y,z,\tau)E(x,y,z,t-\tau)d\tau \ , \tag{4}$$

$$B(x,y,z,t) = \int_{-\infty}^{\infty} F^{-1}(\mu)(x,y,z,\tau)H(x,y,z,t-\tau)d\tau \ , \tag{5}$$

$$\rho c\frac{\partial u}{\partial t} = -bu + \text{div}(K\text{grad}(u)) + Q_r(\vec{E},\vec{H}) \tag{6}$$

where

b = a cooling law coefficient of the -bu distributed heat sink term with units of calories per cubic centimeter per second with the units of b therefore being $(L^{-3}T^{-1})$,

B = the magnetic induction vector or magnetic flux density in Webers per square meter$(MT^{-1}Q^{-1})$,

c = the specific heat in calories per gram per degree centigrade(M^{-1}),

D = the electric flux density in coulombs per square meter(QL^{-2}),

E = the electric field strength in volts per meter$(Q^{-1}MLT^{-2})$,

F^{-1} = the inverse Fourier transform operator which transforms functions of the spatial variables (x,y,z) and frequency ω into functions of the spatial variables (x,y,z) and time t,

H = the magnetic field intensity in amperes per meter$(QT^{-1}L^{-1})$,

J = the current density in amperes per meter$(QT^{-1}L^{-2})$,

K = the thermal conductivity in calories per centimeter per second per degree centigrade $(L^{-1}T^{-1})$,

(L,M,Q,T) is a four tuple containing our symbols, L for length, M for mass, Q for charge, and T for time, for the basic units in which the physical quantities discussed in this paper are expressed,

$Q_r(E,H)$ = the radiative heat transfer term which defines the energy transfer by the electromagnetic field, defined by the vector valued functions E and H, into a penetrable scattering body with prescribed electrical and thermal properties and constitutive relations. This is commonly referred to as a power density distribution and is expressed in calories per cubic centimeter per second$((ML^2T^{-2})L^{-3}T^{-1} = ML^{-1}T^{-3})$,

t = the time of observation of the fields and temperature excursions(T),

(x,y,z) = the laboratory coordinates of an observation point(L,L,L),

ε = the permittivity at a point in the scattering body when the incoming radiation is time-harmonic and has frequency ω and where we assume that the permittivity function ε is a temperate distribution(Hormander [6], p 19) whose units at each point are farads per meter$(Q^2M^{-1}L^{-3}T^2)$

μ = the complex permeability, a temperate distribution of the spatial and frequency variables, whose value at each point has units of Henry's per meter$(Q^{-2}ML)$

σ = the complex conductivity in mhos per meter$(M^{-1}L^{-3}TQ^2)$

u = the temperature in degrees centigrade (ML^2T^{-2})

ρ = the mass density (ML^{-3})

We developed in Cohoon et al [2] and in Bell et al [7] a computer program which uses hybrid methods of evaluating higher order spherical harmonics and in particular the spherical Bessel functions, j_0, j_1, y_0, y_1, $h_0^{(1)}$, $h_1^{(1)}$, and the ratios j_n/j_{n+1} and which makes use of Taylor series, Neumann series, asymptotic expansions, and recursion relations to enable us to compute in a very accurate manner the thermal response of and electromagnetic power density distribution within lossy-dielectric-multilayer-spherically-symmetric scatterers. In a microwave simulation we find in Cohoon et al [2] a comparison between computer predictions of microwave induced thermal excursions and actual measurements with a Vitek non-field perturbing thermal probe.

The derivation of the formula for the radiative heat transfer term $Q_r(E,H)$ which serves as a source term for the energy balance equation (6) is related to a proper understanding of the analysis of transient responses which might result from stimulating a scatterer with an electromagnetic pulse. The analysis of the pulse response of a scatterer can be obtained from the response of the scatterer to time harmonic radiation of many frequencies in an efficient manner if we correctly represent the ratio $k(\omega)/k_0(\omega)$ of the propagation constant of the material within the scatterer and the propagation constant $k_0(\omega) = \omega/v_0$ of free space, where ω is the frequency of the incoming radiation and v_0 is the frequency-independent velocity of light in the material containing the scatterer. We make use of what we know about solving scattering problems when the incoming radiation is time harmonic to develop an expression or at least an algorithm for computing the Fourier transform $\hat{E}$ of the induced electric field vector. While normally we think of the inverse Fourier transform as an integral

$$E(x,y,z,t) = \left(\frac{1}{2\pi}\right)\int_{-\infty}^{+\infty}\hat{E}(x,y,z,\omega)\exp(i\omega t)d\omega \qquad (7)$$

over the entire real line from minus infinity to plus infinity which is, to say the least, a difficult task on any computer, we can, by extending the frequency variable ω to complex values and by defining $\mathrm{Arg}(\xi + i\eta) = \theta$, where $\xi = r\cos(\theta)$, $\eta = r\sin(\theta)$, and $r^2 = \xi^2 + \eta^2$, and $r > 0$ and $0 \leq \theta < \pi$ and by using the argument function Arg to define the complex propagation constant $k(\omega)$ as a member of an algebraic extension(Cohoon [8]) of the field([8], page 723) of meromorphic functions, reduce the problem to evaluating a finite number of residues and to carrying out an integral around a contour of finite length for many pulse interaction problems that arise in a natural way. One important case is that of the interaction of a planar electromagnetic pulse with a Lorentz medium. An example of a Lorentz medium of interest to the U. S. Army is a phosphorus derived smoke droplet which is subjected to infrared radiation(Milham et al [9]). In the case of a Lorentz medium the ratio of the propagation constants is given by

$$(k/k_0)(x,y,z,\omega) = \left|\frac{(\omega - \omega_0^+)(\omega - \omega_0^-)}{(\omega - \omega_\infty^+)(\omega - \omega_\infty^-)}\right|^{1/2}\left[\frac{\exp((i\mathrm{Arg}(\omega - \omega_0^+) + i\mathrm{Arg}(\omega - \omega_0^-))/2)}{\exp((i\mathrm{Arg}(\omega - \omega_\infty^+) + i\mathrm{Arg}(\omega - \omega_\infty^-))/2)}\right] \quad (8)$$

for the simple case of a Lorentz medium whose charge moieties have a single characteristic oscillation frequency ω_j where

$$\omega_0^+ = +\sqrt{\omega_j^2 + a_j^2 - \rho_j^2} + i\rho_j , \quad (9)$$

$$\omega_0^- = -\sqrt{\omega_j^2 + a_j^2 - \rho_j^2} + i\rho_j , \quad (10)$$

and

$$\omega_\infty^+ = +\sqrt{\omega_j^2 - \rho_j^2} + i\rho_j , \quad (11)$$

$$\omega_\infty^- = -\sqrt{\omega_j^2 - \rho_j^2} + i\rho_j , \quad (12)$$

where

a_j^2 = the density of the charge moiety with characteristic oscillation frequency ω_j multiplied by the (e/m) charge to mass ratio and divided by the free space permittivity ε_0 $(T^{-2} = (QL^{-3})(Q/M)/(Q^2M^{-1}L^{-3}T^2))$, .

ρ_j = $(g_j/2)$ which is half of the damping constant associated with field induced oscillations of the charge moieties of mass m and charge e which oscillate with characteristic oscillation frequency ω_j (T^{-1}),

and where the vector displacement x of the charge moiety of mass m and charge e satisfies the ordinary differential equation

$$m\left(\frac{d^2x}{dt^2}\right) + mg_j\left(\frac{dx}{dt}\right) + m\omega_j^2 x = eE \quad (13)$$

where E is the stimulating electric vector. Thus, if

N = the charge per unit volume in the Lorentz medium(QL^{-3}),

so that the polarization vector is

$$P = Nx \quad (14)$$

then the fact that the polarization vector P is also given by

$$P = (\varepsilon - \varepsilon_0 - i\sigma/\omega)E \quad (15)$$

implies that if $a_j^2 = (e/m)N/\varepsilon_0$ where $\varepsilon_0 = 8.854\text{x}10^{-12}$ and if x has an $\exp(i\omega t)$ time dependence, then equations (13), (14), and (15)--and the fact that $k_0^2 = \omega^2\mu_0\varepsilon_0$ and the relation, $k^2 = \omega^2\mu_0\varepsilon - i\omega\mu_0\sigma$, where $\mu_0 = 4\pi\text{x}10^{-7}$ is the permeability of the ambient space--imply that

$$(k/k_0)^2 = 1 + \frac{a_j^2}{-\omega^2 + ig_j\omega + \omega_j^2} , \quad (16)$$

which gives the relationship (8).

To begin to understand the relationship between these developments and the radiative energy transfer term $Q_r(E,H)$ we multiply both sides of equation (13) by $\frac{\partial P^*}{\partial t}$, where $\frac{\partial P}{\partial t}$ is

the complex conjugate of the time derivative $\frac{\partial P}{\partial t}$ of the polarization vector P, add the conjugate of this relation to itself and divide by 2 obtaining the relationship,

$$\left(\frac{1}{2}\right)\left(E^{*}\cdot\frac{\partial P}{\partial t} + E\cdot\frac{\partial P^{*}}{\partial t}\right) = \frac{\partial}{\partial t}\left(\left(\frac{1}{2}\right)\left(Nm\left|\frac{dx}{dt}\right|^2 + Nm\omega_j^2|x|^2\right)\right) + Nmg_j\left|\frac{dx}{dt}\right|^2 = \frac{\partial U}{\partial t} + Q_r(E,H), \tag{17}$$

where in this case U represents kinetic plus potential energy and $Q_r(E,H)$ represents the rate at which energy is transfered into heat. This derivation implies that the dissipative term $Q_r(E,H)$ is given by

$$Q_r(E,H) = \left(\frac{1}{2}\right)(\omega\varepsilon'' + \sigma')|\bar{E}|^2/(4.1x10^6) \tag{18}$$

where

$\varepsilon' - i\varepsilon''$ = the complex permittivity ε in farads per meter$(Q^2M^{-1}L^{-3}T^2)$ where ε' and ε'' are both real valued functions of (x,y,z) and frequency ω,

$\sigma' + i\sigma''$ = the complex conductivity σ in mhos per meter$(M^{-1}L^{-3}TQ^2)$ where σ' and σ'' are both real valued functions of the spatial variables (x,y,z) and the frequency ω,

and

$|\bar{E}|$ = a locally time averaged electric vector$(Q^{-1}MLT^{-2})$ length.

The electromagnetic field or the electric field vector(if the scatterer is nonmagnetic)can be obtained by solving electric field integral equations. One can show by elementary calculus that if

E^i = the electric field vector of an incident electromagnetic wave that is traveling in a direction parallel to the unit vector in the direction of the positive z-axis and which is normally incident on an aerosol or composite material bounded by the planes $z = 0$ and $z = L$ $(Q^{-1}MLT^{-2})$

and if we define a coupled system of integral equations involving E and H by the rule,

$$E = E^i - \left(\frac{\omega\mu_0}{2k_0}\right)TE, \tag{19}$$

and

$$H - H^i = \text{curl}\left(\left(\frac{-i}{2k_0}\right)TE\right), \tag{20}$$

where

$$TE = \int_0^L (i\omega(\varepsilon - \varepsilon_0) + \sigma)(z',\omega)E(z',\omega)\exp(-ik_0|z - z'|)dz' \tag{21}$$

so that if $0 < z < L$, then we can transform TE into a form that can be readily differentiated, obtaining the relation,

$$TE = \int_0^z (i\omega(\varepsilon - \varepsilon_0) + \sigma)(z',\omega)E(z',\omega)\exp(-ik_0(z - z'))dz' +$$

$$\int_z^L (i\omega(\varepsilon - \varepsilon_0) + \sigma)(z',\omega)E(z',\omega)\exp(-ik_0(z' - z))dz'. \tag{22}$$

If $z < 0$, then TE has the representation

$$TE = \exp(ik_0 z)\int_0^L (i\omega(\varepsilon - \varepsilon_0) + \sigma)(z',\omega)E(z',\omega)\exp(-ik_0 z')dz' = A_r \exp(ik_0 z), \qquad (23)$$

which represents a left going or reflected wave. If $L < z$, then TE can be put in the form,

$$TE = \exp(-ik_0 z)\int_0^L (i\omega(\varepsilon - \varepsilon_0) + \sigma)(z',\omega)E(z',\omega)\exp(ik_0 z')dz' = C_t \exp(-ik_0 z) , \qquad (24)$$

which represents a right going or transmitted wave. This enables us to easily show that any solution of the integral equations (19) and (20) is automatically a solution of the Maxwell equations (1) and (2). Furthermore, one can show that in view of the fact that we have used the same integral equations in the three regions $0 < z < L$, $z < 0$, and $L < z$, that solutions of the integral equations (19) and (20) satisfy the boundary conditions which say that the tangential components of the electric field vector E and the magnetic field vector H are continuous across the boundaries $z = 0$ and $z = L$ of the slab. Furthermore, equations (23) and (24) show that any solution of the integral equations (19) and (20) satisfy a kind of radiation condition in that $E - E^i$ is a left going wave when $z < 0$ and $E - E^i$ is a right going wave when $z > L$. Also, by using Dyadic expansions of the free space Green's functions associated with the Helmholtz operator in two and three dimensions, the same results can be obtained for the two and three dimensional integral equations. By using the volume integral equations one can develop a procedure which will permit us to predict the electromagnetic interaction with heterogeneous particles of a general shape. The dyadic expansion of the free space Green's functions shows us that if we substitute the solution in Bell et al [7] into the integral equation describing scattering by a multilayer sphere that the integral equation is satisfied exactly. Because the Mie solution describing the scattering by a sphere is the only exact solution to a three-dimensional scattering problem that can be easily computed, there has been a heavy reliance on this solution in a variety of efforts to describe the propagation of radiation through clouds. As more powerful computers become available, the integral equation methods and other methods applicable to bodies with a general shape will be used more widely to model the interaction of radiation with aerosols. These methods coupled with powerful methods of solving the heat equation in a body with a general shape and contour integration schemes for computing the inverse Fourier transform of the Fourier transform of the electromagnetic field will help us determine both the thermal response and the pulse response of scatterers with a general shape.

If a spherical droplet has a complex index of refraction, then in view of the representation (18) of the heat source term $Q_r(E,H)$, we can expect the droplet to be heated by the radiation source. In a microwave simulation a spherical ball with a permittivity of $50.4\varepsilon_0$ and a conductivity $\sigma = 1.52$ mhos per meter when exposed to 1.2 Gigahertz radiation and having a density of .970 grams per cubic centimeter, a specific heat of $c = .84$ calories per gram per degree and a thermal conductivity of $K = .0012$ calories per centimeter per second per degree gave the following result when the temperature was measured at the center of the sphere and the radiation with a power of 70 milliwatts was on for 5.5 minutes and was then shut off.

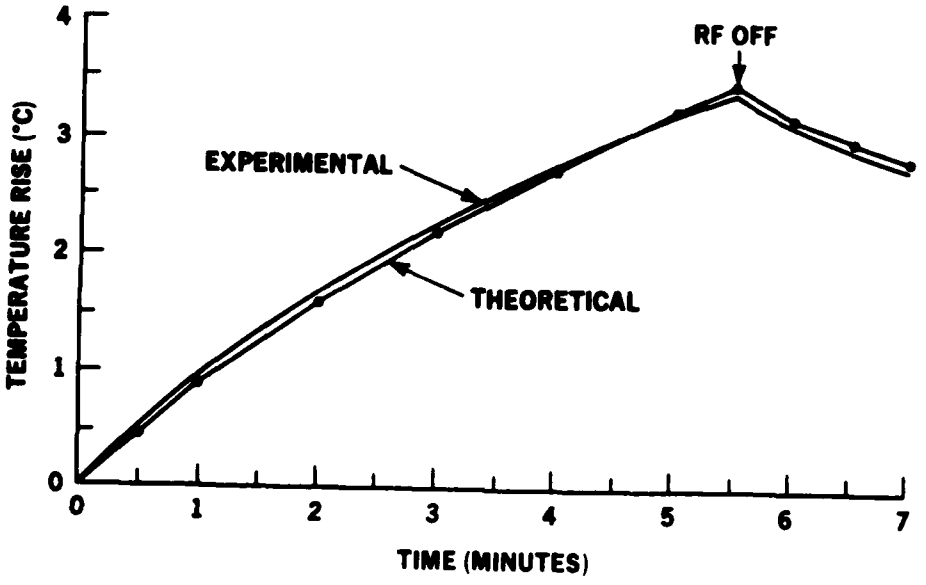

Figure 1. The predicted and measured temperature increase versus time at the center of a 3.3 cm radius homogeneous sphere of muscle equivalent material exposed to 1.2 GHz radiation with a power of 70 milliwatts per square centimeter.

The temperature excursions shown in Figure 1 were measured with a Vitek, Inc., Model 101, electrothermia monitor with output to a Data Precision, Model 3500, Digital Multimeter, Microwave Labs ML1200 scanner, and a Hewlett-Packard HP9830A computing calculator. The sphere was encased in a 8 cm by 8 cm block of Dupont HD 300 closed cell styrofoam. Because of probe placement we estimated that there would be approximately a 5 percent error in measurement when the probe was moved during the course of the measurement process. The following Figure shows the results of exposing a 3.3 centimeter sphere for 3 minutes when measurements were made along an axis which was parallel to the direction of propagation of the radiation.

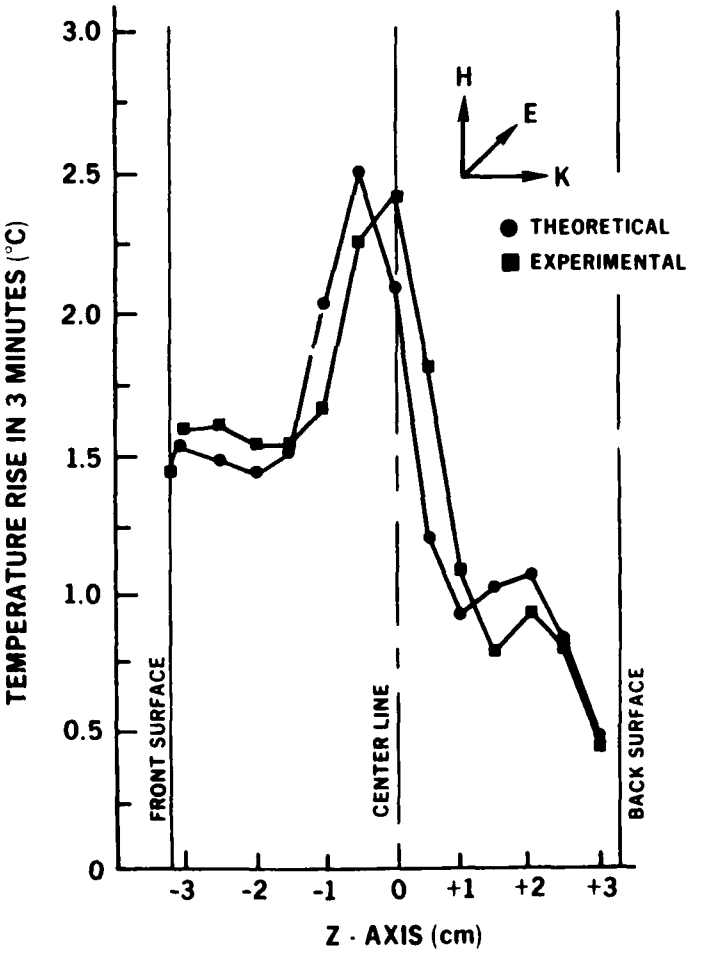

Figure 2. Temperature rise along the z-axis of a 3.3 cm homogeneous muscle-equivalent sphere exposed for three minutes to 70 milliwatt per square centimeter radiation with a frequency of 1.2 Gigahertz.

In what follows we will consider the interaction of planar electromagnetic pulses of the form

$$E^i = E_0(Y(t-x/c) - Y(t-x/c-T))\sin(\omega_0(t-x/c))e_y, \qquad (25)$$

where $Y(u) = 0$ for negative values of u and $Y(u) = 1$ if u is nonnegative, ω_0 is the central frequency of the pulse, e_y is the unit vector in the direction of the positive y-axis, and $T/5$ is the period of the incoming radiation, with dielectric bodies of interest to the U. S. Army. Figure 3 shows the time profile of the electromagnetic signal induced at a point just inside a spherical ball filled with a low loss dielectric material when the stimulating pulse is of the form defined by equation (25), and Figure 4 shows the time profile of the electromagnetic signal induced at a point just inside a dielectric slab bounded by the planes $x = 0$ and $x = \lambda$ where λ is the wavelength of the radiation of frequency ω_0 in a slab or ball filled with material whose relative permittivity is $\varepsilon/\varepsilon_0 = 70$ and whose conductivity σ is .01. Since both the initial and total time profiles are distinct we see that we cannot assume that data concerning radiative transfer into a half-space or slab can be used to infer how radiation might be transferred into a spherical particle if the wavelength λ of the radiation and the slab or sphere diameter are nearly the same. Figure 3 shows that there is a considerable ringing when transient radiation is passed into a low loss spherical particle. This may help explain the lasing or fluorescence transfer that occurs when a spherical ball that is doped with one or two types of chromophores at such a low density that the expected intra-chromophore distance is larger than the accepted maximum separation distance for chromophore to chromophore energy transfer is irradiated by an external source of laser light. Figure 5 illustrates the purely geometric quarter-wavelength interference phenomena in a simple way; the plane wave given by equation (25) interacts with a slab bounded by the planes $x = 0$ and $x = \lambda$ where λ is the wavelength of the radiation in the material filling the slab when the point at which the field is being observed is $x = \lambda/4$. In the example described in Figure 5 which is a microwave simulation the relative permittivity of the material was 64 and the conductivity was 0; this calculation is related to the problem of making structures invisible to radar through coatings which is of interest to the U.S. Army. Figure 6 shows the induced electric field vector 5 wavelengths into a half space filled with a Lorentzian type material; the Lorentz medium half space is being irradiated by a plane wave defined by equation (25). Figure (7) shows the Sommerfeld Brillouin precursor wave at the same point considered in Figure (6) but starting at a time equal to the travel time of a wave whose velocity is the vacuum speed of light. The main wave begins at a time equal to the travel time of a wave whose velocity is the speed of a wave of frequency ω_0 in the material filling the half space.

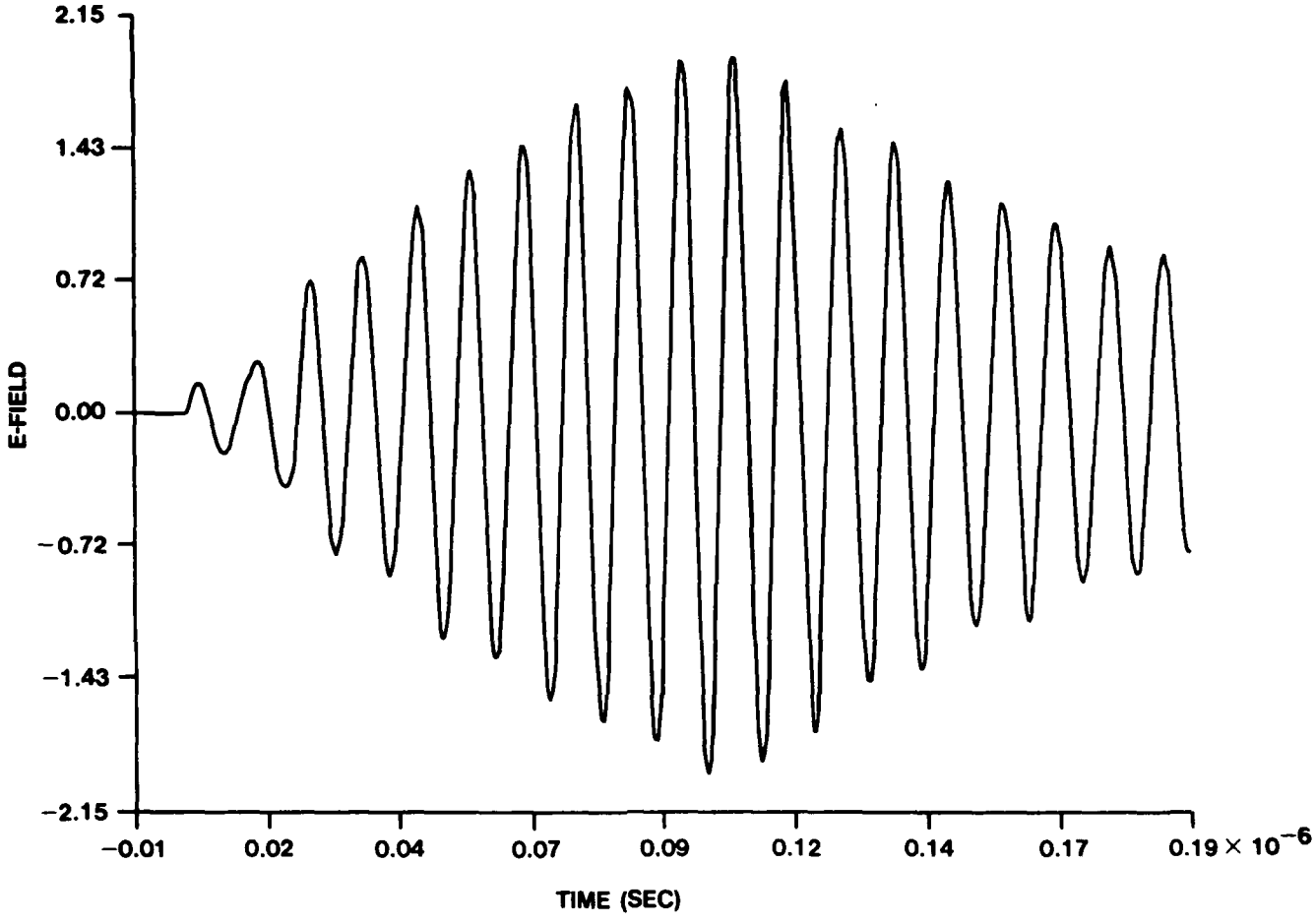

Figure 3. The response of a one-wavelength diameter ball with a relative permittivity of 70 and a microwave conductivity of .01 to a planar, five cycle, truncated sinusoidal pulse with a central frequency of 100 megahertz. (Tic-mark labels on this and following figures suffer from round-off error.)

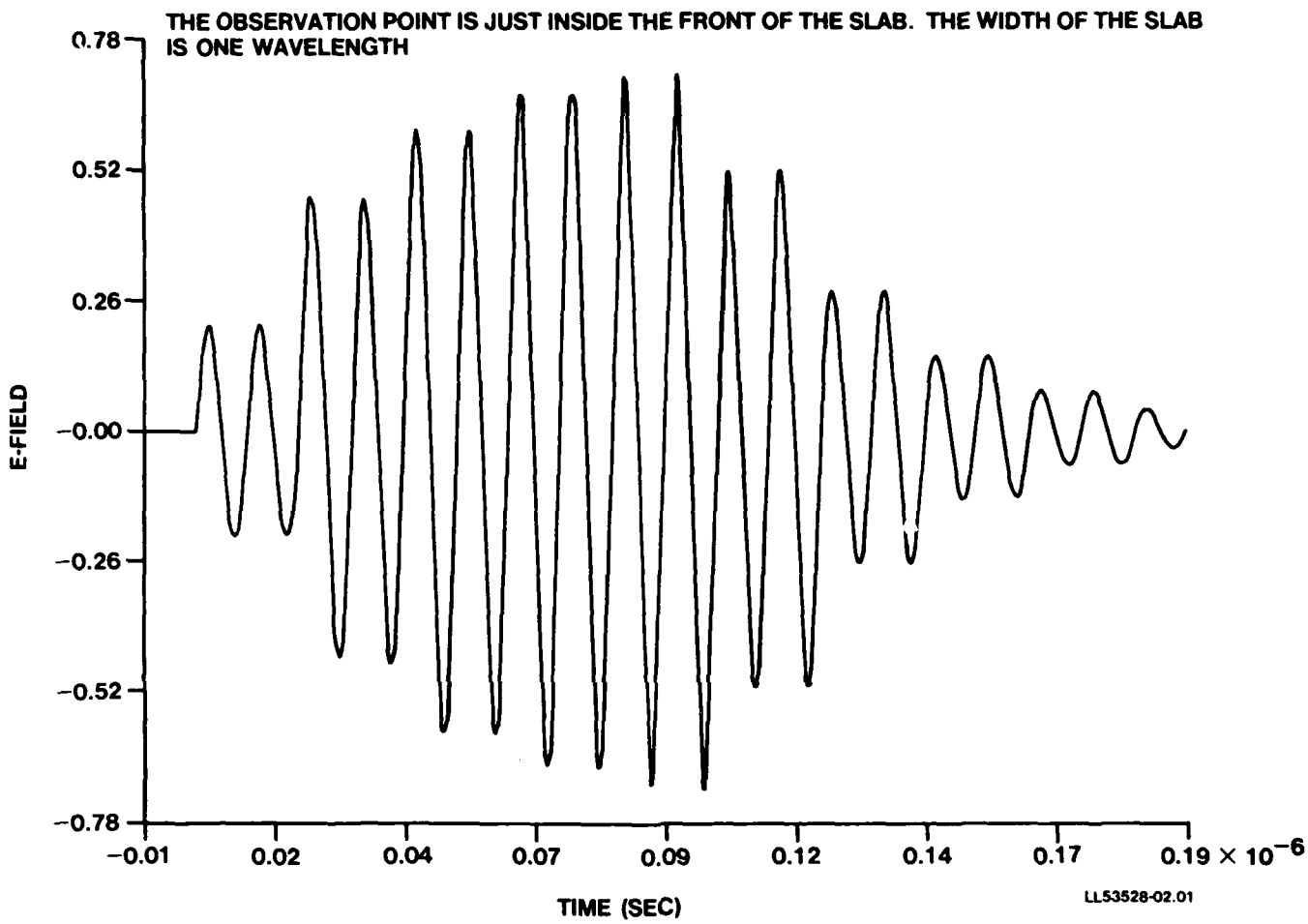

Figure 4. The response of a one-wavelength thick slab with a relative permittivity of 70 and a microwave conductivity of .0i to a planar, truncated sinusoidal pulse of 5 cycles when the central frequency of the pulse is 100 megahertz.

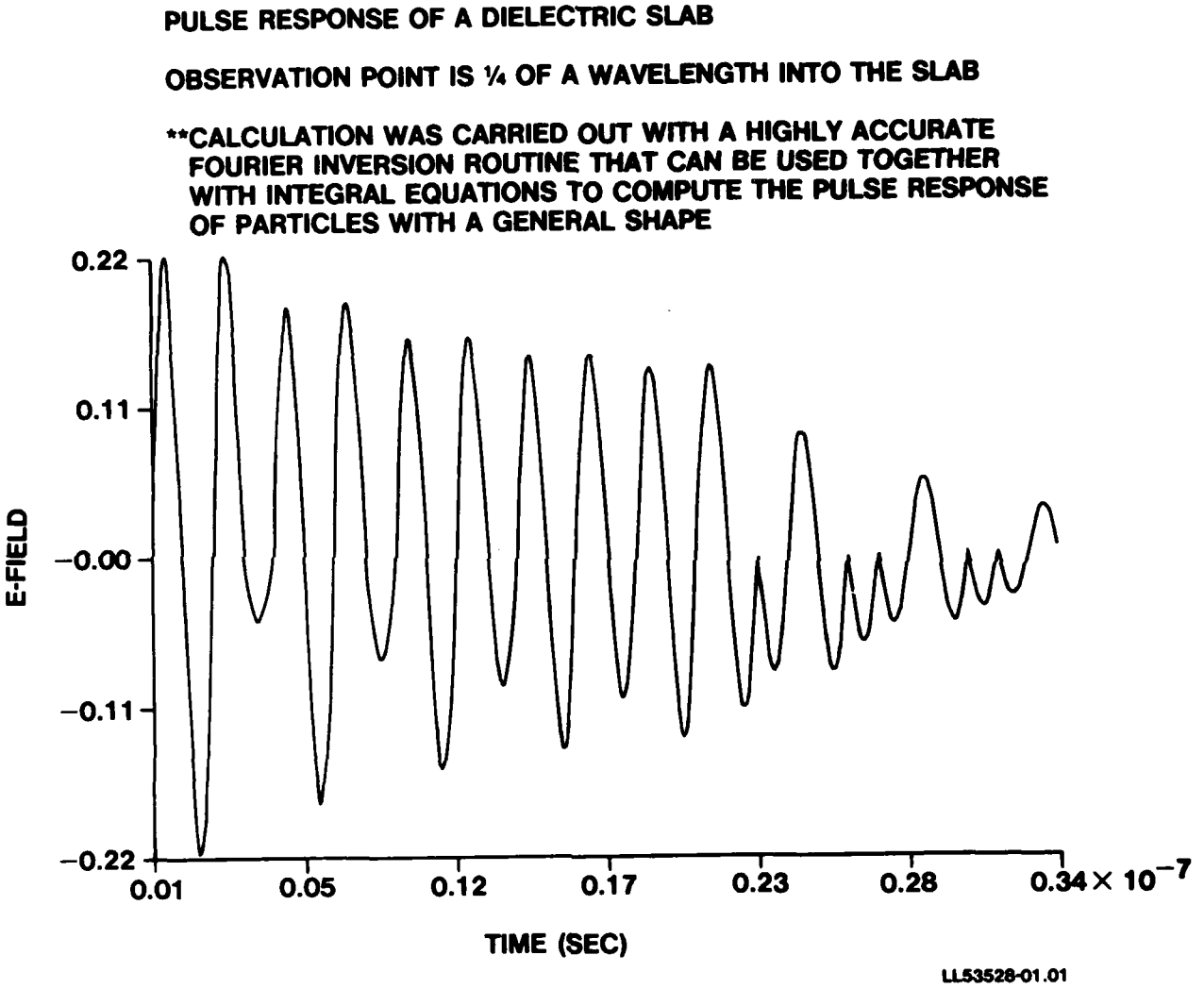

Figure 5. The pulse response of a one-wavelength thick loss-free dielectric slab with a relative permittivity of 64, when the observation point is one-quarter of a wavelength into the slab which is stimulated by a truncated sinusoidal pulse with a central frequency of 1 GHz and exactly 5 cycles.

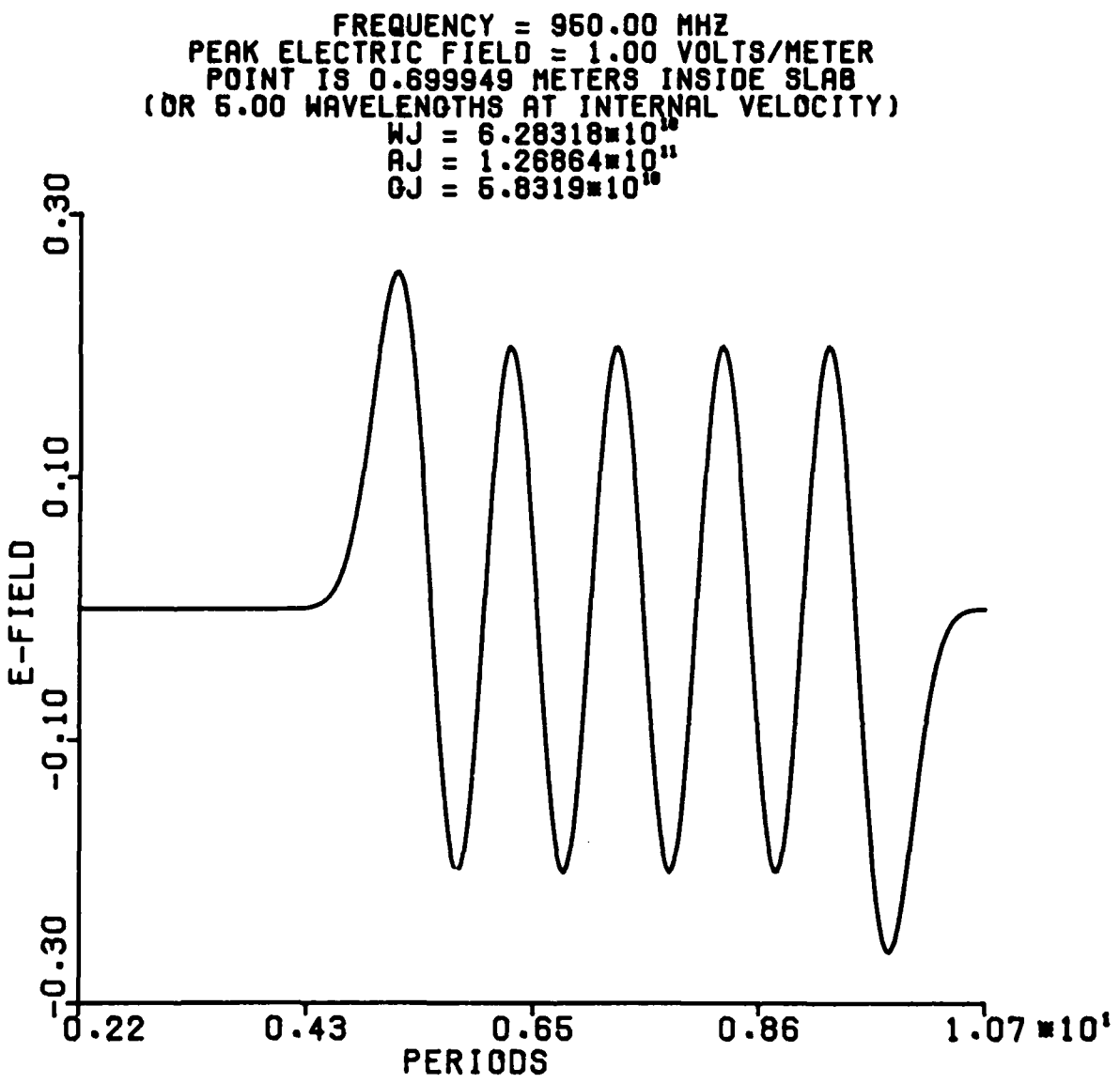
FREQUENCY = 960.00 MHZ
PEAK ELECTRIC FIELD = 1.00 VOLTS/METER
POINT IS 0.699949 METERS INSIDE SLAB
(OR 5.00 WAVELENGTHS AT INTERNAL VELOCITY)
WJ = 6.28318*10^10
AJ = 1.26864*10^11
GJ = 5.8319*10^10
E-FIELD
0.30
0.10
-0.10
-0.30
0.22
0.43
0.65
0.86
1.07*10^1
PERIODS

Figure 6.

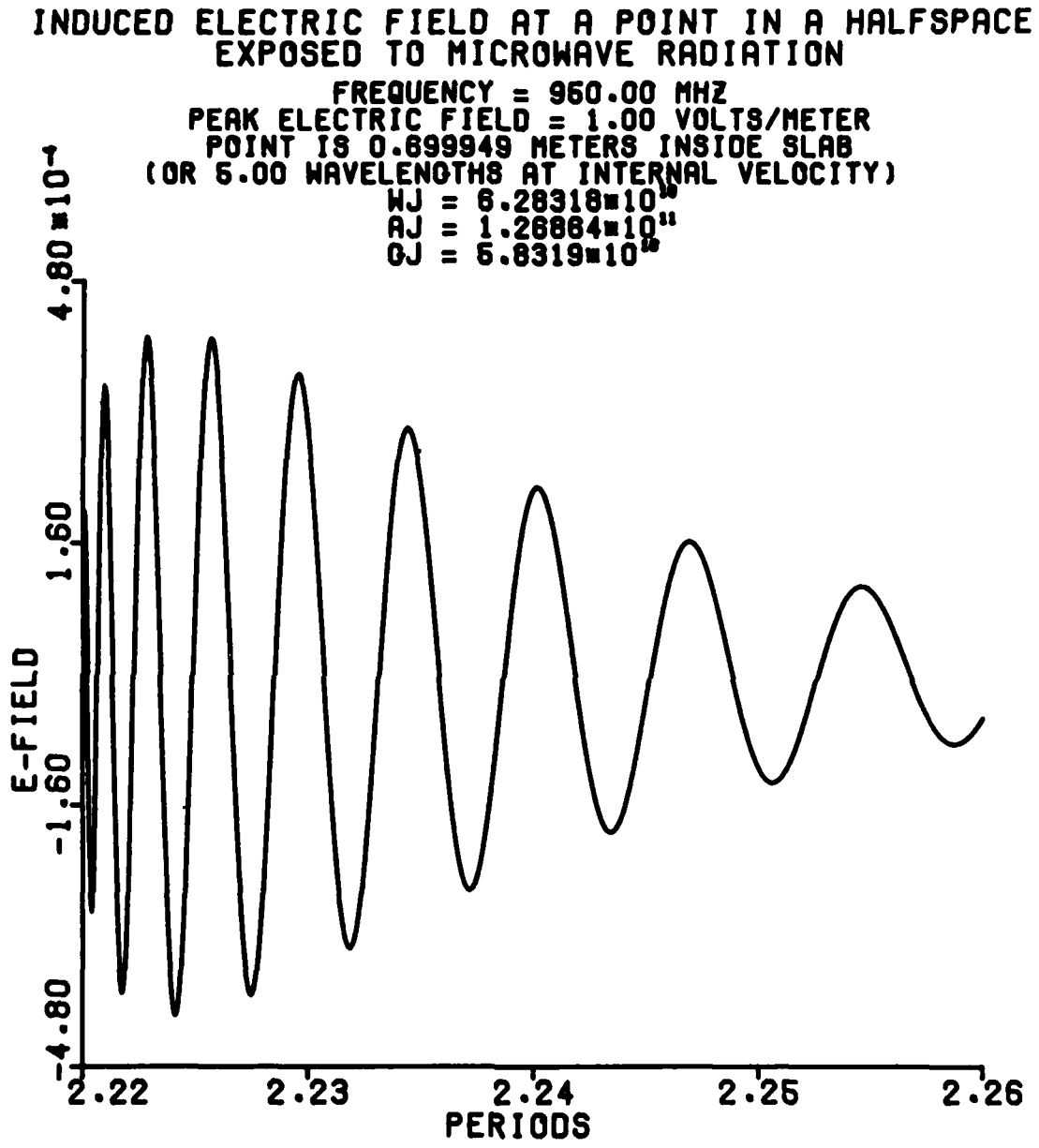
INDUCED ELECTRIC FIELD AT A POINT IN A HALFSPACE
EXPOSED TO MICROWAVE RADIATION
FREQUENCY = 960.00 MHZ
PEAK ELECTRIC FIELD = 1.00 VOLTS/METER
POINT IS 0.699949 METERS INSIDE SLAB
(OR 5.00 WAVELENGTHS AT INTERNAL VELOCITY)
WJ = 6.28318*10^10
AJ = 1.26664*10^11
QJ = 5.8319*10^12
E-FIELD
4.80*10^-4
1.60
-1.60
-4.80
2.22
2.23
2.24
2.25
2.26
PERIODS

Figure 7.

Some final notes follow.

David Colton [11] describes some theorems regarding surface integral equations which permit one to prove uniqueness theorems associated with the problem of describing scattering from electromagnetically hard surfaces. By using volume integral equations one can describe scattering by penetrable and internally heterogeneous bodies.

The precursor waves are described in [12] and integral equations can be used to describe their occurrence in heterogeneous bodies.

Haken [13] describes possible nonlinear interactions and the variational methods of Mizohata and Lions ([14] and [15]) could be used to describe them.

REFERENCES

1 . Cohoon, D.K. Dispersive and geometric electromagnetic pulse distortion effects--Lorentzian and Debye Materials," Submitted to IEEE Transactions on Antennas and Propagation, August, 1985.

2 . Cohoon, D.K., J.W. Penn, E.L. Bell, D.R. Lyons, and A.G. Cryer.
A Computer Model Predicting the Thermal Response to Microwave Radiation.
SAM-TR-82-22(1982) Brooks AFB, Tx 78235(1982)

3 . Rubel, Glenn O. Physical constants of standard military smokes.
ARCSL-TR-83025. Aberdeen Proving Ground, Maryland(June, 1983)

4 . Liu, Benjamin Y.H. "Standardization and Calibration of Aerosol Instruments" In Liu, Benjamin Y. H. (ed) Fine Particles. Aerosol Generation, Measurement, Sampling, and Analysis. New York: Academic Press (1976).

5 . Rabbe, Otto G. "The Generation of aerosols of fine particles" In Liu, Benjamin Y. H.(ed) Fine Particles. Aerosol Generation Measurement, Sampling and Analysis. New York: Academic Press(1976).

6 . Hormander, Lars. Linear Partial Differential Operators. New York: Springer Verlag (1962)

7 . Bell, Earl L. David K. Cohoon, John W. Penn.
Electromagnetic energy deposition in a concentric spherical model of the human or animal head.
SAM-TR-79-6.

8 . Cohoon, D.K. and S.A. Burr.
A Theorem on Difference Equations and its Generalization to Operator Equations, Journal of Mathematical Analysis and Applications. Vol. 30 No.3 (June, 1970) pp 715-729.

9 . Milham, M.E. D.H. Anderson and R.H. Frickel. Infrared optical properties of phosphorous derived Smoke. Applied Optics, Vol 21 No. 14 (July 15, 1982) pp 2501-2507.

10 . Cohoon, D.K. The electromagnetic pulse response of structures with frequency dependent electrical properties. Submitted to SIAM REVIEW.

11 . Colton, David and Rainer Kress. Integral Equation Methods in Electromagnetic Theory.
New York: John Wiley and Sons (1983).

12 . Brillouin, Leon. Wave propagation and group velocity.
New York: Academic Press (1960).

13 . Haken, H. Cooperative Phenomena in Systems far from thermal equilibrium and in nonphysical systems.
Reviews in Modern Physics. Volume 47 (1975) pp 67-120.

14 . Mizohata, Sigeru. The Theory of Partial Differential Equations. London: Cambridge at the University Press (1973).

15 . Lions, J.L. Equationes Differentielles Operationnelles et Problemes aux Limites.
New York: Springer Verlag (1961).

V. OPTICAL PROPERTIES OF AEROSOLS

VB. Interaction of Radiation and Nonspherical Particles Including Aggregates

NEAR AND FAR FIELD SCATTERING FROM TWO INTERACTING SPHERES

K. A. Fuller and G. W. Kattawar
Department of Physics, Texas A&M University
College Station, Texas 77843

ABSTRACT

This paper provides a summary of some preliminary work that has been conducted on three rather disparate aspects of the physics of dependent scattering by a bispherical system. The first type of phenomenon to be investigated here is that of structure resonances in the scattered fields at the surface of a two-sphere particle. Secondly, the effects of the orientation of such a particle on its scattering properties (*viz.*, the Müller matrix) in the radiation zone are considered. Lastly, we present comparisons between the exact solution of the dependent scattering problem and two methods of approximation. This latter endeavor provides a bit more physical insight into the effects and range of the crosstalk that is set up between two closely spaced scattering centers.

INTRODUCTION

The modal expansion technique developed by Bruning and Lo[1] is an excellent vehicle through which one may address the problem of light scattering by two interacting spheres. In principle the scattered fields may be obtained to any desired accuracy for any combination of constituent sphere characteristics, and for any orientation or state of polarization of the incident beam. Computational limits do exist, of course, and we are currently restricted to a maximum size parameter of eight for the individual spheres.

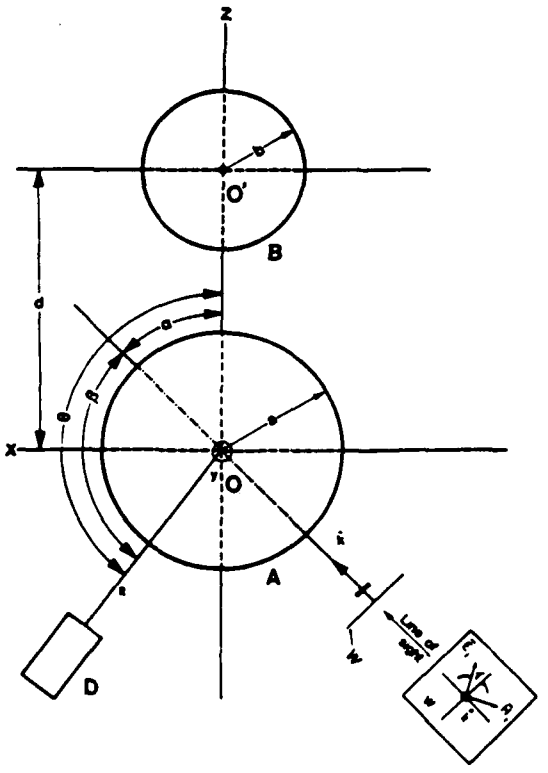

Fig. 1 The scattering geometry.

The scattering geometry is depicted in Figure 1. All calculations were made with the incident beam lying in the $\phi = \pi$ semiplane and the point of observation is restricted to the x-z plane. The quantities used in this presentation which do not appear in Figure 1 are defined as follows:

$$kx = 2\pi x/\lambda,$$

$$S_r(kr,\theta,\phi) = Re(E_\theta H_\phi^* - E_\phi H_\theta^*);$$

for $\phi = 0$ or $\phi = \pi$, the Müller matrix of the two-sphere system assumes the form

$$\tilde{P} = \begin{pmatrix} P_{11} & P_{12} & 0 & 0 \\ P_{12} & P_{11} & 0 & 0 \\ 0 & 0 & P_{33} & P_{34} \\ 0 & 0 & -P_{34} & P_{33} \end{pmatrix}$$

where

$$P_{11} = 0.5(|S_2|^2 + |S_1|^2),$$

$$P_{12} = 0.5(|S_2|^2 - |S_1|^2),$$

$$P_{33} = Re(S_1 S_2^*), \text{ and } P_{34} = Im(S_2 S_1^*).$$

The amplitude functions S_1 and S_2 are elements of the scattering matrix which is defined by the equation

$$\begin{pmatrix} E_{s\parallel} \\ E_{s\perp} \end{pmatrix} = \frac{e^{ikr}}{ikr} \begin{pmatrix} S_2 & S_3 \\ S_4 & S_1 \end{pmatrix} \begin{pmatrix} E_{i\parallel} \\ E_{i\perp} \end{pmatrix}.$$

For the two-sphere system, $S_3 = S_4 = 0$ *provided* that the observations are made in the x-z plane.

Two approximations have also been considered. One is made by simply adding the scattered fields of two non-interacting spheres and is labeled 'Mie+Mie'. The second approximation is taken from the work of Bruning and Lo[2]. It is labeled 'Fib' and consists of adding a "far-field" interaction term to the superposed non-interacting Mie field of the form

$$i(s^a S_1(kr,\pi-\theta,0) + s^b S_1(kr,\theta,\pi)e^{i\delta})$$

where

$$s^a = \frac{\Phi^* S_1(kd,\alpha,\pi) - S_1(kd,\pi-\alpha,0)S_1(kd,\pi,\pi)}{1 - |S_1(kd,\pi,\pi)|^2},$$

$$s^b = \frac{\Phi S_1(kd,\pi-\alpha,0) - S_1(kd,\alpha,\pi)S_1(kd,\pi,\pi)}{1 - |S_1(kd,\pi,\pi)|^2},$$

$$\Phi = exp(i\,kd\cos\alpha),$$

and

$$\delta = kd(\cos\alpha - \cos\theta).$$

This form of the approximation assumes that the spheres have identical radii and optical constants.

THE NATURAL MODES OF STRONGLY REFRACTING BISPHERES

As a partial test of the reliability of our computer program we ran some preliminary calculations in which the refractive index N2 of the second sphere was set to unity. By so doing, selected portions of a study conducted in the near zone by Kamiuto[3,4] were easily reproduced. In addition, we also regenerated one of the single-sphere resonance spectra calculated by Barber *etal.*[5] with our code before proceeding to the case of two spheres. For the case of transparent dielectric spheres, size-dependent resonances of appreciable strength do not appear at optical frequencies for any reasonable value of refractive index unless ka>4. Detailed studies of the normal modes of spheres of this size are computationally expensive if cooperative scattering is involved. Although the refractive indices of dielectrics are <2.5 in the visible region, refractive indices of $\approx$ 10 are not uncommon at centimeter wavelengths. By employing such values to our present study, rather strong and very sharp resonances can be obtained for size parameters as small as 0.30.

The resonance spectra of the radial component of the Poynting vector as calculated for a selection of points *on* the surface of a two-sphere system with N1=N2=10 are presented in Figure 2. For the case of N2=1, resonances occur at ka$\approx$0.305, 0.444, and 0.447 which correspond to the TE_{11}, TM_{11}, and TE_{21} modes, respectively. At no time do the resonances for the single sphere rise above 250 nor do they fall below -10. Thus the interaction between the spheres tends to break the singlets in the spectra of the individual spheres into a rather complicated set of multiplets, the peaks of which may be enhanced by as much as a factor of 400. It should be noted that, due to the scales involved in some of the graphs, not all of the spectral signatures of the two-sphere particle are discernable in the plots presented here.

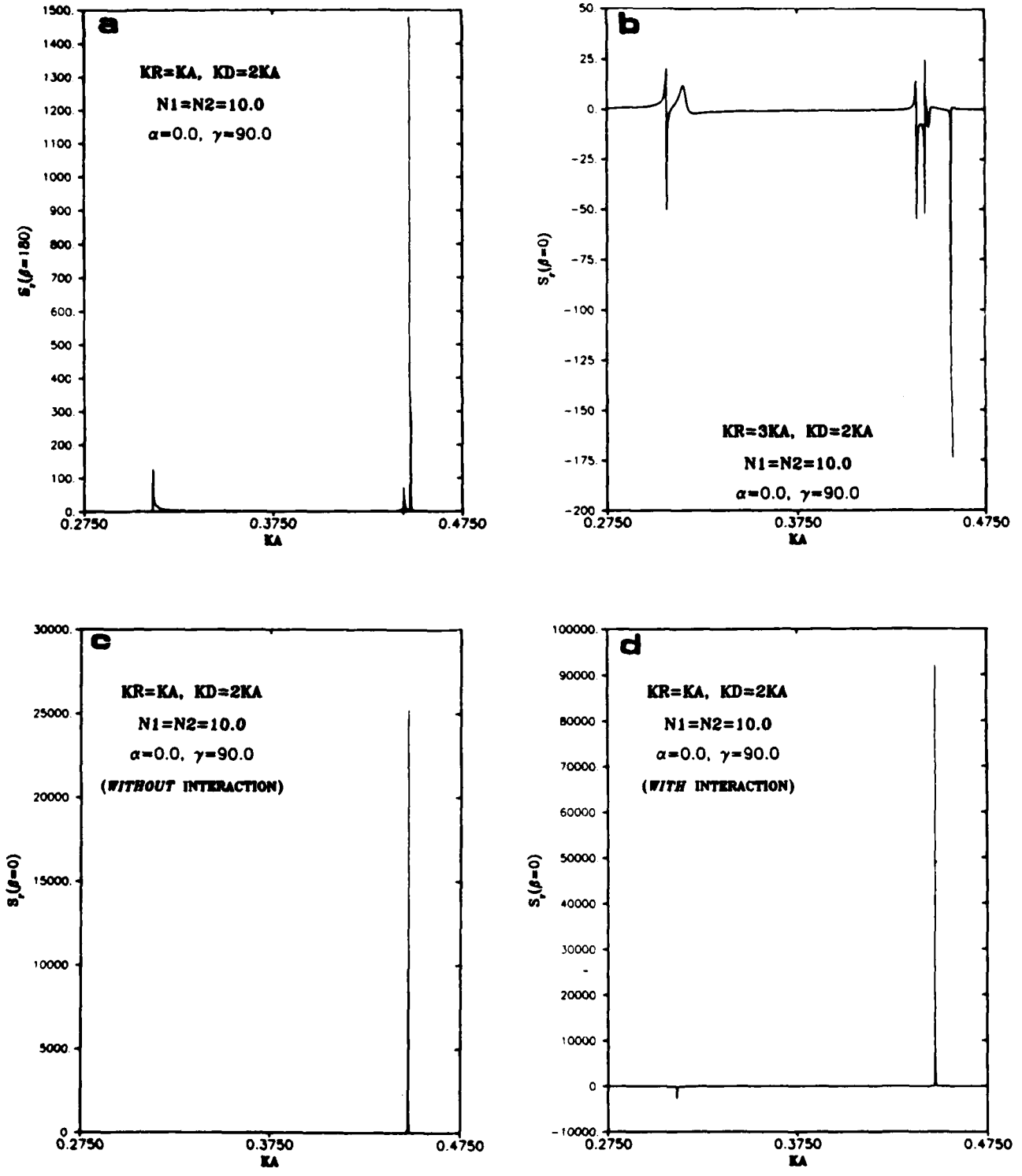

Fig. 2 The structure resonances produced at selected points on the surface of a two-sphere particle. Figure 2.c is the calculated effect of a simple superpositioning of the fields scattered by noninteracting spheres, *i.e.* the Mie · Mie approximation.

THE EFFECTS OF ORIENTATION ON THE MÜLLER MATRIX

The Müller matrix elements have been calculated for $\alpha = 0, \pi/4$, and $\pi/2$, and the orientation-averaged elements arising from these three sets of data have also been determined. These results will appear in the reference that is cited in the final section of this paper; only the results of the orientation-average are presented here. It should be noted that $< P_{11} >$ is the field-averaged phase function and not a simple amplitude-averaged quantity. In this study, the observation point remained in the x-z plane, and hence there is no predicted depolarization of the scattered fields. The elements in the upper right and lower left quadrants of the 4×4 Müller matrix are therefore equal to zero. The results of this calculation are displayed in Figure 3. The characteristics of the constituent spheres match those studied by Thompson *et al.*[6] and the Müller matrix obtained in the course of the present research for a single sphere agrees with calculations that were employed in their work.

THE APPROXIMATIONS

The nature of the approximations has already been outlined in the introduction. Although the Mie+Mie approximation is certainly a naive one, it serves to help distinguish those features that appear in the phase functions of a two-sphere system which are primarily due to simple interference effects from those which arise from the interactions. The multiple reflection approach ignores the extended size of the scatterers, their proximity to one another, and the fact that a different set of boundary conditions must be applied with each successive reflection. For the case of small ($ka \leq 1.0$) spheres, however, this approximation can be surprisingly accurate, and it may also be employed to yield qualitative predictions for moderately separated spheres of larger relative size. Both approximations converge to the exact solution as the separation becomes large. The multiple reflection approximation is in best agreement with the exact solution when one is calculating the backscatter produced from broadside incidence. Some representative results of the application of these estimates are provided in Figure 4. Attention is called to the close agreement between them and the exact solution when the center to center distance between the spheres is only ten radii.

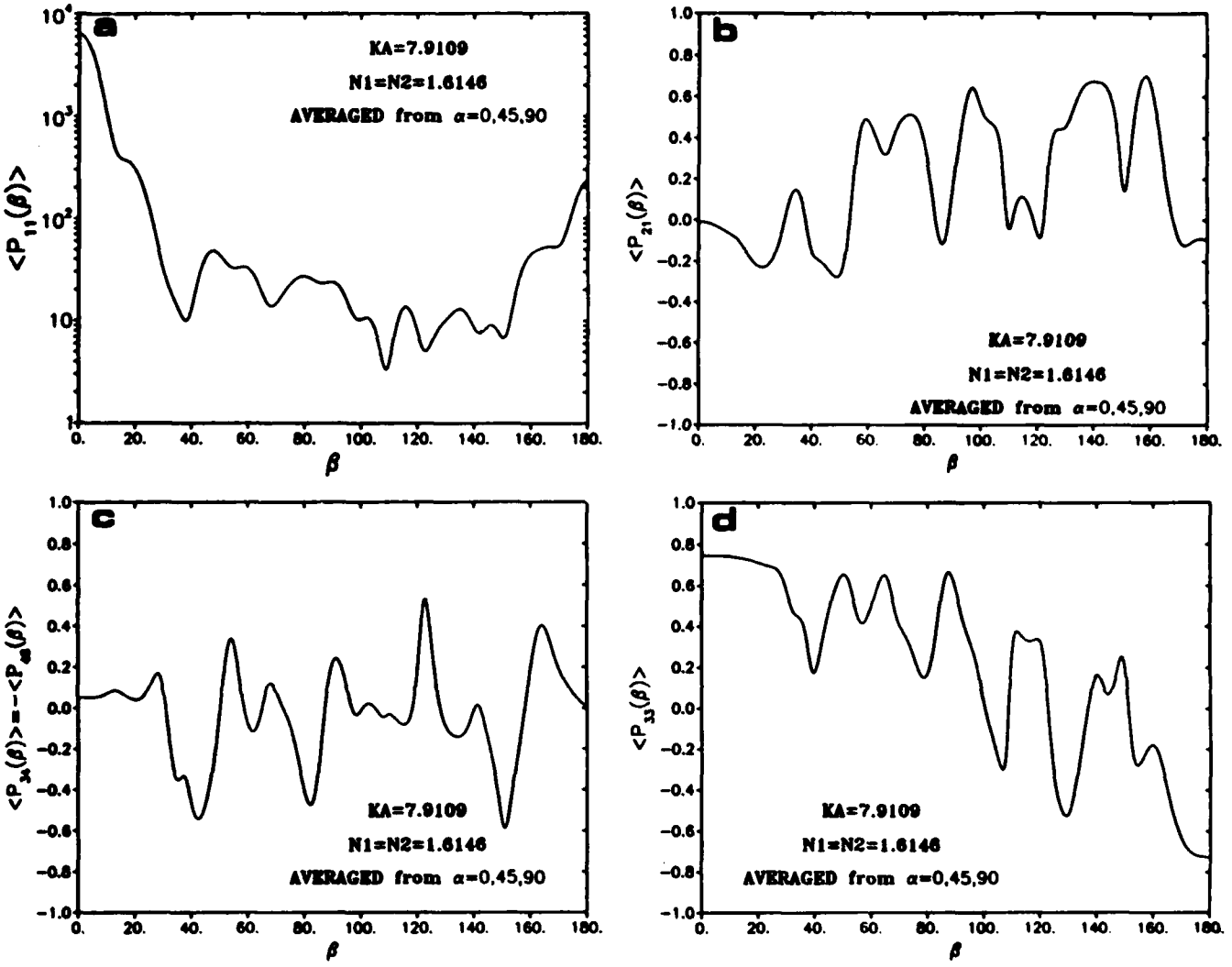

Fig. 3 The orientation-average of the Müller matrix elements. $< P_{11} >$ was obtained from an average of scattered *fields* for orientation angles α=0, $\pi/4$ $\pi/2$ whereas all other elements were obtained from an average of the matrix elements that correspond to these orientations and then normalized against $< P_{11} >$. For all orientations it was found that, as in the case of a single sphere, $P_{43} = -P_{34}$ and $P_{22} = P_{11}$ when the field point remained in the x-z plane.

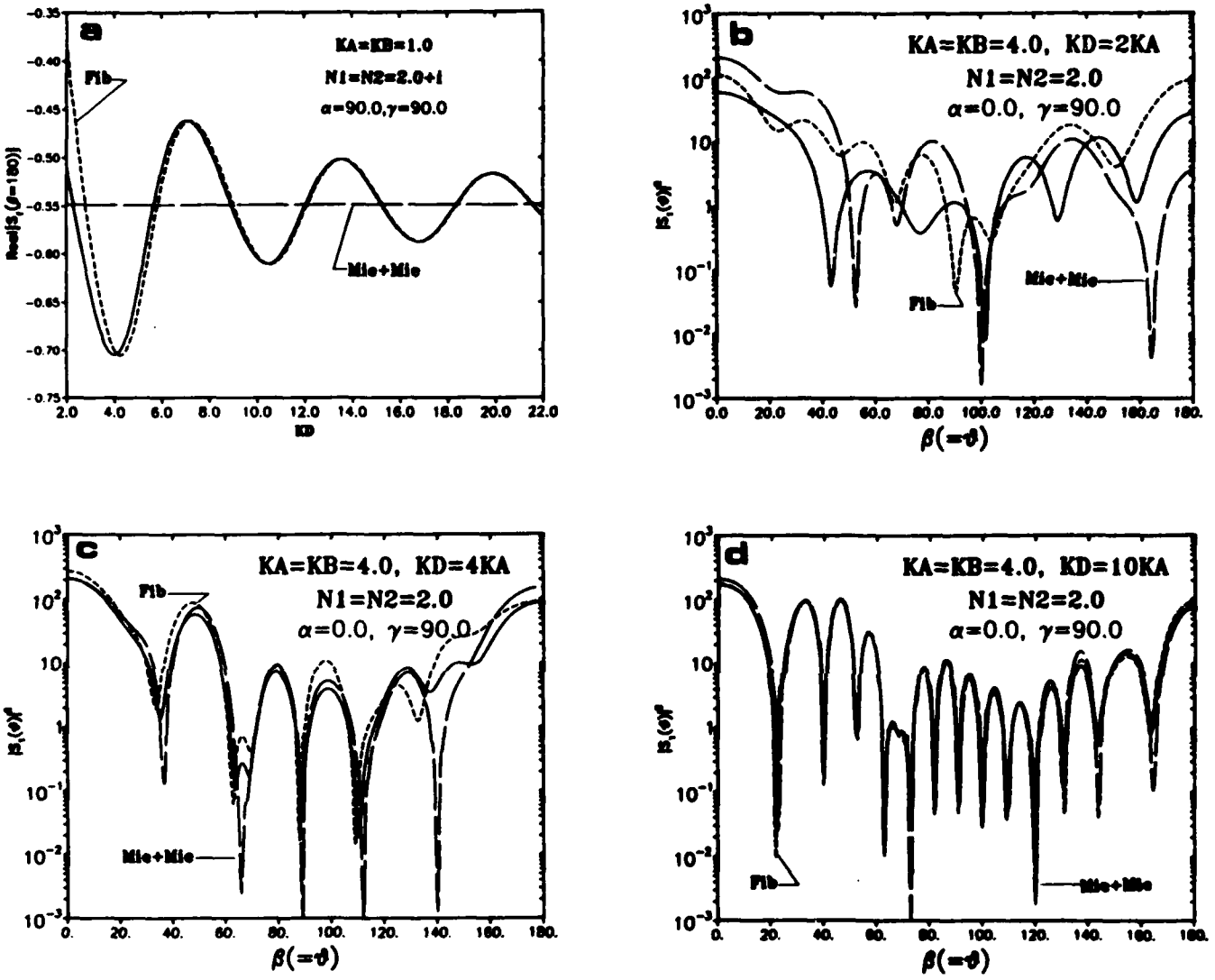

Fig. 4 A comparison of the approximations to the exact theory. Figure 4.a contrasts the backscatter efficiency as calculated by the multiple reflection approximation to that of the exact solution when the separation between the spheres is varied. The remaining graphs are characteristic of the behavior of the phase function of a two-sphere particle as the separation is increased.

FUTURE WORK

The results of the Müller calculations will be submitted presently as part of a collaborative effort with R. T. Wang to Applied Optics.

A modification of our computer code that will allow the study of larger particles is to be implemented as soon as possible. We also plan to study the effects of interactions between small metalic spheres on the phenomenon of surface-enhanced Raman spectroscopy (SERS). Finally, we will engage in the rather formidable task of extending our calculations to the case of cooperative scattering by three or more spheres.

ACKNOWLEDGMENT

This research was supported by the U. S. Army Research Office under contract No. DAAG29-83-K-0074.

REFERENCES

1. J. H. Bruning and Y. T. Lo, "Multiple scattering by spheres," Tech. Rep. 69-5(Antenna Laboratory, University of Illinois, Urbana, Ill., 1969).
2. J.H. Bruning and Y.T. Lo, IEEE Trans. Antennas Propag. **AP-19**, 378(1971).
3. K. Kamiuto, J. Opt. Soc. Am. A **1**, 840(1984)
4. K. Kamiuto, J. Opt. Soc. Am. **73**, 1819(1983)
5. P. W. Barber, J. F. Owen, and R. K. Chang, IEEE Trans. Antennas Propag., **AP-30**, 168(1982)
6. R. C. Thompson, J. R. Bottiger, and E. S. Fry, Appl. Opt. **19**, 1323(1980)

DIFFRACTION CATASTROPHES AND INVERSE SCATTERING FROM SPHEROIDAL DROPS

Philip L. Marston*
Department of Physics
Washington State University
Pullman, WA 99164-2814

and Eugene H. Trinh**
Jet Propulsion Laboratory
California Institute of Technology
Pasadena, CA 91109

RECENT PUBLICATIONS, SUBMITTALS FOR PUBLICATION AND PRESENTATIONS:

A) P. L. Marston and E. H. Trinh, "Hyperbolic umbilic diffraction catastrophe and rainbow scattering from spheroidal drops," Nature (London) 312, 529-531 (1984).

B) P. L. Marston, "Cusp diffraction catastrophe from spheroids: generalized rainbows and inverse scattering," Optics Letters (accepted for publication).

C) P. L. Marston and D. S. Langley, "Forward optical glory scattering from bubbles (and clouds of bubbles) in liquids and other novel directional caustics," submitted to the proceedings of the Symposium on Multiple Scattering of Waves in Random Media and Random Rough Surfaces (edited by V. K. and V. V. Varadan) July, 1985.

ABSTRACT

The scattering into the rainbow region from spheroidal drops of water manifests hyperbolic-umbilic and cusp diffraction catastrophes not previously known to be present. The angular location of the cusp diffraction catastrophe in the far-field scattering from a spheroid was used to determine the axis ratio of drops of water.

SUMMARY

It is well known that large spherical drops of water in air give enhanced scattering at angles close to the rainbow angle $\theta_R \simeq 138^o$. Near θ_R, diffraction provides an essential correction to geometric optics and the scattering is a simple example of a fold diffraction catastrophe.[1] We observed[A] the scattering from spheroidal drops into the rainbow region and we find other diffraction catastrophes can be produced depending on the drop's axis ratio $q = D/H$. Here the drop's diameter is D in the horizontal equatorial plane and it is H along the vertical axis of rotational symmetry. An acoustic standing wave was used to levitate the drop and to control q. The drops were oblate ($q > 1$) and they were horizontally illuminated. With $q \simeq 1.31$, the observed scattering pattern corresponds to the focal section of a hyperbolic-umbilic diffraction catastrophe. For q differing somewhat from this value, the pattern was observed to separate into fold and cusp diffraction catastrophes.[B]

The hyperbolic-umbilic and cusp catastrophes arise because, in addition to the usual set of equatorial rays, skew rays contribute to the scattering near the horizontal plane. Nye[2] has calculated the critical $q \simeq 1.31$ from the condition that two infinitesimal-skew rays merge with

---

*Supported by the Office of Naval Research.

**Supported by N.A.S.A.

two equatorial rays at the rainbow angle $\theta_R \simeq 138^\circ$. We find that the cusp in the unfolded catastrophe occurs where the skew rays merge with a single equatorial ray having a scattering angle $\theta > \theta_R$. Ray tracing formalism was used to relate q to the θ of the cusp.[B] This calculation was confirmed by observations with q from 1.21 to 1.37 and D ~ 1 mm.

The analysis[B] facilitates the determination of the shape of drops of water from the angular location of the cusped rainbow. The shape and size information in the scattering pattern are in effect decoupled. The present analysis is limited, however, to oblate drops oriented with their axis of rotational symmetry perpendicular to the propagation direction of the incident light. Since the existence and angular locations of cusp and hyperbolic-umbilic diffraction catastrophes may be predicted, these catastrophes may be useful as benchmarks for testing computer algorithms based on the partial-wave series for scattering from spheroids.[3] Recall that the computation of rainbow patterns was useful for verification of computer algorithms for Mie scattering from spheres.[4] Diffraction catastrophes are examples of directional caustics[C] and as such, they are characterized by bright, localized scattering patterns when the drop is much larger than the wavelength.

The experiments were carried out while P. L. Marston was on a sabbatical visit to the Microgravity Science and Applications Laboratory (supported by N.A.S.A.) of Jet Propulsion Laboratory. The subsequent data analysis and development of theory has been supported by O.N.R.

SUPPLEMENTAL REFERENCES

1. M. V. Berry and C. Upstill, "Catastrophe Optics: Morphologies of Caustics and Their Diffraction Patterns," Prog. Opt. 18, 257-346 (1980).
2. J. F. Nye, "Rainbow scattering from spheroidal drops--an explanation of the hyperbolic umbilic foci," Nature (London) 312, 531-532 (1984).
3. S. Asano and G. Yamamoto, "Light scattering by a spheroidal particle," Appl. Opt. 14, 29-49 (1975).
4. J. V. Dave, "Scattering of visible light by large water spheres," Appl. Opt. 8, 155-164 (1969) (see Fig 4).

Absorption and Scattering by Conductive Fibers:

Basic Theory and Comparison with Asympototic Results

N. E. Pedersen
P. C. Waterman
J. C. Pedersen

Panametrics, Inc.
221 Crescent Street
Waltham, Massachusetts 02254

ABSTRACT

This paper considers electromagnetic scattering and absorption by thin conductive fibers. Earlier related work was supported by CRDC, as described in

[N. E. Pedersen, J. C. Pedersen and P. C. Waterman, Final Report on Theoretical Study of Single and Multiple Scattering by Cylinders, prepared by Panametrics, Inc. for U.S. Army Chemical Systems Laboratory (Sept. 27, 1984).]

The present work is supported by the U.S. Air Force Office of Scientific Research, and includes further refinements to the theory (Drude equations, size dependence of conductivity) and a comparison with approximate formulas in the long and short wavelength limits.

1.0 INTRODUCTION

During the course of the past several years, a theory based on the variational method, along with associated computer codes, has been developed at Panametrics for analyzing the electromagnetic scattering and absorption from thin conductive fibers of arbitrary size, conductivity and orientation.[1] Extensions and refinements of this theory have now been completed and programmed, as described herein.

We begin by summarizing the basic equations used in the variational computation for arbitrary fibers. The quasistatic model appropriate at long wavelengths is then derived, followed by the infinite cylinder computation which should be accurate for wavelengths short compared with cylinder length.

In order that the computations may be extended into the infrared and visible regimes, it is necessary to incorporate the optical properties of the fibers. We do this by employing the Drude model for conductivity (or complex dielectric constant), and also introducing the dependence of conductivity on both fiber diameter and electron mean free path.

Numerical results are then presented for copper and lead fibers, and the approximate methods are seen to agree very well with the variational computation in those limiting regions where they should apply.

2. THEORY

2.1 The Variational Equations

The variational method has been discussed often;[1-4] we will simply summarize the important equations here. The basic integral equation is

$$E_o \sin\theta_i e^{jkz\cos\theta_i} = I(z)\,Z + \frac{1}{2\pi}\int_0^{2\pi}\frac{j\eta k}{4\pi}\int_{-\ell}^{\ell} I(z')\left(1+\frac{\partial^2}{k^2\partial z'^2}\right)\frac{e^{-jkR}}{R}\,dz'd\phi' \qquad (1)$$

with surface impedance Z given by

$$Z = \frac{g\,I_o(ga)}{2\pi k_o a\,(\varepsilon''+i\varepsilon')\,I_1(ga)} \qquad (2)$$

$$g^2 = k_o{}^2 = [(\cos^2\theta_o - \varepsilon') + i\varepsilon'']$$

For the current I(z) one assumes

$$I = I_o\,\{f_c(z) + Af_s(z)\}, \qquad (3)$$

where

$$f_c(z) = \cos kz\cos qx - \cos x\cos qkz$$

$$f_s(z) = \sin kz\sin qx - \sin x\sin qkz \qquad (4)$$

$$q = \cos\theta_i \qquad x = k\ell\,.$$

For the constant A appearing in Eq. (3), the variational method then gives

$$A = \frac{g_s(\gamma_c - \lambda_c)}{g_c(\gamma_s - \lambda_s)}, \tag{5}$$

in terms of the coefficients

$$\gamma_c = \frac{k}{2\pi} \int_0^{2\pi} d\phi \int_{-\ell}^{\ell}\int_{-\ell}^{\ell} f_c(z) f_c(z') \left(1 + \frac{1}{k^2}\frac{\partial^2}{\partial z'^2}\right) \frac{e^{-jkR}}{R} \, dz' dz$$

$$\gamma_s = \frac{k}{2\pi} \int_0^{2\pi} d\phi \int_{-\ell}^{\ell}\int_{-\ell}^{\ell} f_s(z) f_s(z') \left(1 + \frac{1}{k^2}\frac{\partial^2}{\partial z'^2}\right) \frac{e^{-jkR}}{R} \, dz' dz$$

$$\lambda_c = \frac{4\pi\, jZ_i}{\eta} \int_{-\ell}^{\ell} f_c^2(z) dz$$

$$\lambda_s = \frac{4\pi\, jZ_i}{\eta} \int_{-\ell}^{\ell} f_s^2(z) dz$$

$$g_c = k \sin\theta_i \int_{-\ell}^{\ell} f_c(z) e^{jkz \cos\theta_i} dz$$

$$g_s = k \sin\theta_i \int_{-\ell}^{\ell} f_s(z) e^{jkz \cos\theta_i} dz \tag{6}$$

all of which can be evaluated explicitly.

The extinction, absorption and scattering cross-sections are then given explicitly by

$$\sigma_e(\theta_i) = \frac{4\pi}{k^2} \operatorname{Im}\left(\frac{g_c^2}{\gamma_c - \lambda_c} - \frac{g_s^2}{\gamma_s - \lambda_s}\right)$$

$$\sigma_a(\theta_i) = \frac{4\pi}{k^2} \frac{\operatorname{Re}(Z)}{|Z|} \left(\left|\frac{g_c}{\gamma_c - \lambda_c}\right|^2 |\lambda_c| + \left|\frac{g_s}{\gamma_s - \lambda_s}\right|^2 |\lambda_s|\right)$$

$$\sigma_s(\theta_i, \theta) = \frac{4(1-p^2)}{k^2} \left|\left(\frac{g_c}{\gamma_c - \lambda_c}\right)\left[\frac{\cos qx}{(1-p^2)}(\sin x \cos px - p\cos x \sin px)\right.\right.$$

$$\left.\left. - \frac{\cos x}{(q^2 - p^2)}(q \sin qx \cos px - p\cos qx \sin px)\right]\right.$$

$$+ j\left(\frac{\delta_s}{\gamma_s - \lambda_s}\right)\left[\frac{\sin qx}{(1-p^2)}\,(p\sin x\cos px - \cos x\sin px)\right.$$

$$\left. - \frac{\sin x}{(q^2 - p^2)}\,(p\sin qx\cos px - q\cos qx\sin px)\right]\Bigg|^2 \qquad p = \cos\theta \quad x = k\ell \tag{7}$$

2.2 The Quasistatic Model

In the following, we re-derive the equations of Ref. 5 and 6 for absorption, scattering, and extinction worked out in 1965. Although the previous equations are satisfactory at radar frequencies, one must consider the relaxation effects of Sections 2.4 and 2.5 when calculating optical and infrared electromagnetic interactions.

First consider the electric field E_i inside a long, thin spheroid, given by

$$E_i = E_o - L\,4\pi\,P, \tag{8}$$

where L = depolarizing factor, P = polarization, and E_o = homogeneous applied field. In the case of a long, thin spheroid, which is a good approximation to our conductive filament, the depolarizing factor is

$$L = 4\left(\frac{a}{\ell}\right)^2\left[\ell n\left(\frac{\ell}{a}\right) - 1\right], \tag{9}$$

where a = particle radius and ℓ = particle length.

The definition of the polarization is

$$P = \frac{(\varepsilon - 1)\,E_i}{4\pi} \tag{10}$$

where ε = normalized dielectric constant. Combining (9) and (10) we see that the internal field is given by

$$E_i = \frac{E_o}{1 + L\,(\varepsilon - 1)} \tag{11}$$

We next take ε to be complex, i.e., $\varepsilon = \varepsilon' + i\varepsilon''$. The internal field then becomes

$$E_i = E_o \frac{1 + L(\varepsilon'-1)\ L\varepsilon - iL\varepsilon - iL\varepsilon''}{[L(\varepsilon'-1) + 1]^2 + [L\varepsilon]^2} \tag{12}$$

and we see that, in the quasistatic approximation, we have both an in-phase and a quadrature component of the internal field.

The electric dipole moment of our Rayleigh particle is defined in terms of the polarization as

$$p^{(1)} = PV_p \tag{13}$$

where V_p = particle volume. The polarizability α of the particle is related (by definition) to the dipole moment as follows:

$$p^{(1)} = \alpha E_o\ . \tag{14}$$

Combining (12), (13), and (14), we obtain the needed expression for the complex electric polarizability of the particle:

$$\alpha = \frac{V_p}{4\pi} \frac{(\varepsilon'-1)[1 + L(\varepsilon'-1)] + L\varepsilon^2 + i\varepsilon''}{[L(\varepsilon'-1) + 1]^2 + [L\varepsilon]^2} \tag{15}$$

The well known Extinction Theorem[6] relates the extinction cross section of any scatterer to its normalized forward scattering amplitude, S(0) by the following relation:

$$\sigma_{ext} = \frac{4\pi}{k^2}\ \mathrm{Re}\ [S(0)], \tag{16}$$

where σ_{ext} = extinction cross section, $k = 2\pi/\lambda_o$, λ_o = free space wavelength of the incident wave.

To order k^6, S(0) is related to the polarizability by[6]

$$S(0) = ik^3 \alpha + \frac{2}{3} k^6 \alpha^2, \tag{17}$$

where the complex polarizability is given by Eq. (15).

The absorption and scattering cross sections are, respectively, given by

$$\sigma_{abs} = 4\pi k \, \mathrm{Re}\,(-i\alpha) \tag{18}$$

and

$$\sigma_{sca} = \frac{8}{3} \pi k^4 |\alpha|^2, \tag{19}$$

where α is given by Eq. (15). After considerable manipulation, the following expressions for the cross sections emerge:

$$\sigma_{ext} = kV_p[B + \frac{k^2 V_p}{6\pi} (B^2 + A^2)] \tag{20}$$

$$\sigma_{abs} = kV_p B \tag{21}$$

$$\sigma_{sca} = \frac{k^4 V_p^2}{6\pi} (A^2 + B^2) \tag{22}$$

$$A = \frac{(\varepsilon'-1) + L[(\varepsilon'-1)^2 + \varepsilon''^2]}{[1 + L(\varepsilon'-1)]^2 + [L\varepsilon'']^2} \tag{23}$$

$$B = \frac{\varepsilon''}{[1 + L(\varepsilon'-1)]^2 + [L\varepsilon'']^2} \tag{24}$$

and, in summary from the preceding sections plus Secs. 2.4 and 2.5,

$$\varepsilon' = 1 - \frac{\sigma\tau}{\varepsilon_o}\left(\frac{1}{1 + (\omega\tau)^2}\right) \tag{25}$$

$$\varepsilon'' = \frac{\sigma}{\omega\varepsilon_o}\left(\frac{1}{1 + (\omega\tau)^2}\right) \tag{26}$$

$$L = 4\left(\frac{a}{\ell}\right)^2 \left[\ell n\left(\frac{\ell}{a}\right) - 1\right] \tag{27}$$

$$\sigma = \sigma_o \left[1 - \frac{3}{8}(1-\varepsilon)\left(\frac{\Lambda}{a}\right)\right] \tag{28}$$

In an attempt to analyze the effects of Eqs. (25) and (26) on the absorption cross section, we have substituted these expressions into Eq. (24), and then inserted Eq. (24) into Eq. (21). The resulting expression for absorption cross section is too complicated for easy analysis. However, there is no doubt that in the regime of $(\omega\tau)^2 \ll 1$, the absorption cross section is, in general, diminished from its value without the inclusion of relaxation effects. It turns out that, for copper, $\omega\tau = 1$ corresponds to $\lambda_o \doteq 30$ microns.

We have recently shown that (at least, for the filament types of interest here), we can greatly extend the region of applicability of the quasistatic theory by letting $\ell = 1/k_o$ in the $k_o\ell > 1$ regime. We do this only in the depolarizing factor, L', given by

$$L' = 4(k_o a)^2 \left[\ell n\left(\frac{1}{k_o a}\right) - 1\right] \tag{29}$$

Note that this substitution cannot be used to predict the scattering cross section when $k_o\ell > 1$, and is good only for absorption. We will comment shortly on the use of this formula.

2.3 The Infinite Cylinder Approximation

Using the results of Wait[7,8] for scattering by infinitely long cylinders of arbitrary dielectric constant, we have derived the expression for absorption cross section per unit length of the infinite cylinder. The general expression, obtained by

considering the inward radial component of the Poynting vector on the lateral surface of the cylinder, is

$$\sigma_a = \frac{2\pi a\ell \sqrt{\frac{\mu_o}{\varepsilon_o}} \sin^2 \theta_o \, \mathrm{Re}\left[\left(\frac{ik}{\omega\mu_o}\right) J_o(k^* a) J_o'(ka)\right]}{\left|J_o(ka) - \left(\frac{1}{\mu}\right) \sin^2 \theta_o \left[\ell n \left(\frac{k_o a \sin \theta_o}{2}\right) + \gamma + \frac{i\pi}{2}\right](ka) J_o'(ka)\right|^2} \qquad (30)$$

$$k^2 = \mu\varepsilon k_o^2$$

$$\gamma = .5772$$

We have compared the results of our high frequency asymptotic quasistatic expression for the absorption cross section with this expression. The results in all (six or seven) cases were in close ($\approx$ 20%) agreement, as will be shown below. This close agreement was both surprising and gratifying to us. It is now evident that we have a quasistatic theory which can predict the <u>absorption</u> cross section of <u>thin</u> conductive filaments over a very wide range of $k\ell$, and which predicts the <u>scattering</u> cross section in the region $k_o\ell < 1$.

2.4 The Drude Model

Our early work[5,6] in the area of target obscuration was restricted to the microwave range of incident electromagnetic energy. We did not at that time anticipate that the infrared and visible regions of the spectrum would be pertinent in the absorbing particle cloud techniques which we developed. Although, during our theoretical programs with the U.S. Army Chemical Systems Lab, such applications were being explored, we were so involved in developing a comprehensive theory that we did not include the <u>optical</u> properties of the (metallic) filaments whose cross sections we were calculating. Indeed, it has not been until the present AFOSR program that we have included these properties. In this and the following sub-section we deal with (1) the inclusion of the optical properties in both theories, and (2) the inclusion of the dependence of electrical conductivity upon particle radius and the electron mean-free-path.

In a recent paper by Ordal, et al[9], the application of the Drude model for the prediction of complex optical dielectric constant was compared with measured values of the real and imaginary parts of the optical dielectric constant for a number of metals (Al, Cu, Au, Pb, Ag, and W). Tabular experimental results are also given for Fe, Pt, Co, Ni, Ti and Pd. This model, which is based on the Free Electron Theory of Metals, is in surprisingly good agreement with the observed experimental results. We realize that, for certain transition elements such as Fe, the model has drawbacks. For such cases, one must resort to the use of tabular experimental data. For our present discussion, we will choose Cu as the substance comprising our fibers, and will utilize the Drude model in the calculation of the various electromagnetic cross sections. A good exposition of this is given in Wooten's book[10], in which the normalized complex dielectric constant is derived (note that Eq. (32) corrects a mistake on p. 53 of Wooten's book):

$$\varepsilon = \varepsilon' + i\varepsilon'' \tag{31}$$

$$\varepsilon' = 1 - \frac{\omega_p^2 \tau^2}{1 + (\omega\tau)^2} \tag{32}$$

$$\varepsilon'' = \frac{\omega_p^2 \tau}{\omega[1 + (\omega\tau)^2]} \tag{33}$$

Using MKS units, the plasma frequency ω_p is given by

$$\omega_p^2 = \frac{Ne^2}{m\varepsilon_0} \tag{34}$$

in which N = electron density (m^{-3}), e = electronic change, m = effective mass of the electron, and ε_0 = permittivity of free space = $(1/3/6\pi \times 10^{-9}$ mho/m.

The quantity τ is the electron relaxation time, which is the time required for randomization of the momentum vector of an electron in the (metallic) lattice. For our

purposes, it is instructional to cast the dielectric constant in terms of the electrical conductivity, σ, given by

$$\sigma = \frac{Ne^2\tau}{m} \tag{35}$$

From (34) and (35), we obtain

$$\omega_p^2 = \frac{\sigma}{\tau\varepsilon_o} \tag{36}$$

Using Eq. (36) in (31) and (32), we have

$$\varepsilon' = 1 - \frac{\sigma\tau}{\varepsilon_o}\left(\frac{1}{1 + (\omega\tau)^2}\right) \tag{37}$$

$$\varepsilon'' = \frac{\sigma}{\omega\varepsilon_o\,[1 + (\omega\tau)^2]} \tag{38}$$

Typical values of the relaxation time τ are on the order of 10^{-14} sec.

It is easily shown that Eq. (37) can be written in terms of ε'':

$$\varepsilon' = 1 - \varepsilon''(\omega\tau) \tag{39}$$

This equation shows us that, for all frequencies significantly below the visible and infrared (i.e. the microwave region), $|\varepsilon'| << |\varepsilon''|$. And, from Eq. (38), we see that ε'' goes to its low frequency value $\varepsilon'' = \sigma/\omega\varepsilon_o$ for $(\omega\tau)^2 << 1$.

The reason for the above analysis is to determine whether or not the Drude model can be utilized at ''low'' frequencies. Although the low frequency asymptotic value of ε' differs significantly from a value of unity, which is normally assumed for metals at ''low'' frequency, the ratio $|\varepsilon''/\varepsilon'|$ will always be very large when $(\omega\tau)^2 << 1$. Therefore, the use of the Drude model throughout the region 10^{-6} m $\leq \lambda_o \leq 10^{-1}$ m appears to be justified, and we feel confident in using Eqs. (37) and (38) in the derivation of the electromagnetic cross sections throughout this entire wavelength range.

2.5 The Reduced Conductivity

When one or more dimensions of a conductive material (metal or semiconductor) are on the order of the mean free path of the conduction electrons, electron collisions with the surface will significantly reduce the mean free time, and hence the mean free path Λ given by

$$\Lambda = v_F \tau \tag{40}$$

where v_F = Fermi velocity and τ = relaxation time discussed previously. Since the electrical conductivity is proportional to τ (Eq. (35)), the conductivity will be reduced.

The classic work on this subject was done in 1938 by Fuchs.[11] In a more recent paper, Dingle[12] reviews the subject and provides some useful numerical computations. The key equation in Dingle's paper is his Eq. (2.3) which relates the effective conductivity σ to the bulk conductivity σ_o, as a function of the mean free path Λ, the wire radius, a, and the quantity ε that is the probability of an elastic collision at the surface:

$$\sigma = \sigma_o \left[1 - \frac{3}{8} (1-\varepsilon) \left(\frac{\Lambda}{a}\right)\right] \tag{41}$$

A value of $\varepsilon = 1/2$ is frequently used as the surface scattering coefficient. Taking this, we have

$$\sigma = \sigma_o \left[1 - \frac{3}{16} \left(\frac{\Lambda}{a}\right)\right] \tag{42}$$

We have had difficulty in obtaining numerical values for mean free paths from the literature. However, Kittel[13] provides a good background as well as quantitative data for a number of metals. Taking copper as the subject material, a value of $\Lambda = 4.2 \times 10^{-8}$m is given in Table 10.1 of Kittel's book. Using Eq. (40), and taking the Fermi velocity $v_F = 1.6 \times 10^6$ m/sec (Kittel, p. 240), we obtain a mean free time of $\tau = 2.6 \times$

10^{-14} sec. This is in fairly good agreement with the value $\tau = 1.9 \times 10^{-14}$ sec, which we obtain from Ref. 3 for copper.

Utilizing the above value, we obtain for copper

$$\sigma = \sigma_0 \left[1 - \frac{7.9 \times 10^{-9}}{a}\right] \tag{43}$$

where the radius a has the unit of meters. This equation shows that, if $a = 1.6 \times 10^{-8}$ m (160 Angstroms), the conductivity is roughly half its bulk value. If the radius is 0.1 micron, the conductivity is 92% of the bulk value.

This exercise was done to show that, indeed, one must consider the particle size effect upon electrical conductivity, when computing the absorption and extinction properties of thin metallic fibers or films.

3.0 NUMERICAL RESULTS

All of the above work has been reduced to operating computer codes with quantitative graphical outputs. It should be noted that, as a part of our present AFOSR contract, we expect to receive a Hewlett Packard Model 9020AS computer. This machine will replace our present HP9835 computer, which presently requires 50 hours to complete a full set of scattering, absorption, and extinction data on a given particle over a wavelength range from 10 cm to 1 micron. The new machine will reduce this time by a factor of between 100X and 1000X.

As a first example, consider copper. We take fiber radius of 5×10^{-8} m, unreduced bulk conductivity of 5.8×10^{7} mho/m, relaxation time 1.9×10^{-14} sec, mean free path of 3×10^{-8} m. The reduced conductivity can now be computed from Eq. (42), and using that result the complex optical dielectric constant is obtained from Eqs. (37) and (38). Results of this computation are plotted in Fig. 1 vs. wavelength over the range from 10 cm to 1 micron.

Knowing ϵ' and ϵ'', the surface impedance of the fiber may be computed from Eq. (2). The results, which are again frequency-dependent, are shown in Fig.2 .

Choosing a fiber length of 5×10^{-4} m, the extinction, absorption and scattering cross-sections may now be obtained from Eq. (7) of the variational method, and are plotted vs. wavelength in Fig. 3. Note that both the scattering and absorption cross-sections rise to peak values at $\lambda \sim 10^{-3}$ m, then fall off. The extinction cross-section must equal the sum of the scattering and absorption cross-sections, and this is seen to be accurately obeyed except at the shorter wavelengths $\lambda \lesssim 10^{-4}$ m, where we believe that σ_s is in error due to employing too few points in the numerical integration (which affects only σ_s).

In Fig. 4 we show the cross-sections obtained using the quasistatic theory, for the same example. As expected, both σ_a and σ_s are in excellent agreement with the previous values at the longer wavelengths. The absorption cross-section moreover, is seen to agree with that of Fig. 3 for the shorter wavelengths also, providing good confirmation of the ''high frequency'' depolarizing factor proposed in Eq. (29).

In Fig. 5 σ_a is plotted using the infinite cylinder approximation Eq. (30) appropriate for short wavelengths. Almost exact agreement is found with both preceding results, for $\lambda \lesssim 10^{-3}$ m, and hence for $k\ell \gtrsim 3$, about as one would expect.

Figures 6 and 7 give respectively the variational and quasistatic results for the same cylinder shortened by a factor of ten. The peaking and crossover behavior from long to short wavelength is now seen to occur at $\lambda \sim 10^{-4}$ m as one would anticipate. Agreement between the two figures is analogous tc that of the first example, although the peak height predicted by the quasistatic theory for σ_a is seen to be somewhat low in this case. For the infinite cylinder approximation, the curve of Fig. 5 applies without change, and again σ_a is in excellent agreement with the variational values at the shorter wavelengths for which $k\ell \gtrsim 3$.

Next, consider lead fibers. The resulting dielectric constant and impedance are shown vs. wavelength in Figs. 8 and 9, with fiber parameters as listed in the figures. The variational results, along with the long and short wavelength approximations, are shown in Figs. 10-12, respectively. Agreement is analogous to that obtained with copper. Note that in these cases σ_a shows saturation effects for wavelengths $\gtrsim 10^{-5}$ m.

Figures 13 and 14 show that upon increasing the fiber radius by a factor of 10, the dielectric constant is substantially unchanged, while the surface impedance decreases at all wavelengths by about two orders of magnitude. The resulting cross-sections, given in Figs. 15-17, again show the same pattern of agreement between the variational (Fig. 15) and approximate results.

Finally, Figs. 18 and 19 (which should be compared with the short wavelength approximation of Fig. 17) give the corresponding values when the fiber length is decreased by a factor of ten. This time the absorption cross section peaks at $k\ell \sim 3$, precisely as observed originally with copper.

4.0 DISCUSSION

Excellent agreement has been demonstrated in the case of absorption cross section between the variational technique and the quasistatic approximation over virtually the entire range of kh. Both of these techniques provide excellent agreement with the infinite-cylinder results in the range of validity of these latter results.

The above comparisons provide substantial confirmation that (a) the modified quasistatic theory can be used over a much wider range of kh than had been previously anticipated, and (b) the rather primitive current trial function (see Eq. 4 and Ref. 1) used in the variational technique appears to be giving results that are in good agreement with both the quasistatic and the infinite cylinder theories in their strict limits of validity. Further work is underway to improve the numerical integration accuracy in the variational code for the case of the total scattering cross section at large values of kh.

The calculation of ε' and ε'' should be thought of as preliminary. Actually, one is dealing with two relaxation times, one due to bulk conductivity effects, and the other due to surface scattering. We are, at this writing, as a part of our ongoing AFOSR work, reformulating the calculation of the complex dielectric constant, taking into account multiple relaxation times. Note that, since the same complex dielectric constant is used in all three (variational, quasistatic, and infinite cylinder) electromagnetic calculations, the conclusions given above still appear to be valid.

REFERENCES

1. N. E. Pedersen, J. C. Pedersen and P. C. Waterman, Final Report on Theoretical Study of Single and Multiple Scattering by Cylinders, prepared for U.S. Army Chemical Systems Laboratory (September 27, 1984).

2. C. T. Tai, Electromagnetic Backscattering from Cylindrical Wires, J. Appl. Phys. 23, 909-916 (1952).

3. E. S. Cassedy and J. Fainberg, Electromagnetic *Cross* Sections of Finite Conductivity Wires, The Johns Hopkins Laboratory Technical Report No. AF-81, August 1960.

4. J. R. Wait, Exact Surface Impedance for a Cylindrical Conductor, Electr. Lett. 15, 659-660 (1979).

5. N. E. Pedersen and J. C. Pedersen, Theoretical, Experimental and Systems Studies on a New Technique for Radar Cross Section Reduction, (Secret), AVCO RADTN-65-67, 8 December 1965.

6. N. E. Pedersen, J. C. Pedersen and H. A. Bethe, ''A New Method of Radar Target Concealment,'' Proc. Tri-Service Radar Symposium, San Diego, 1969 (Secret).

7. J. R. Wait, Scattering of a plane wave from a circular dielectric cylinder at oblique incidence, Can. J. Phys. 33, 189 (1955).

8. J. R. Wait, The long wavelength limit in scattering from a dielectric cylinder at oblique incidence, Can. J. Phys. 43, 2212 (1965).

9. M. A. Ordal et al., Appl. Optics 22, 1-99 (1983).

10. F. Wooten, Optical Properties of Solids (Academic Press, New York, 1972).

11. K. Fuchs, Proc. Camb. Phil. Soc. 34, 100 (1938).

12. R. B. Dingle, Proc. Roy. Soc. A201, 545 (1950).

13. C. Kittel, Introduction to Solid State Physics (Wiley, New York, 1956), Chap. 10.

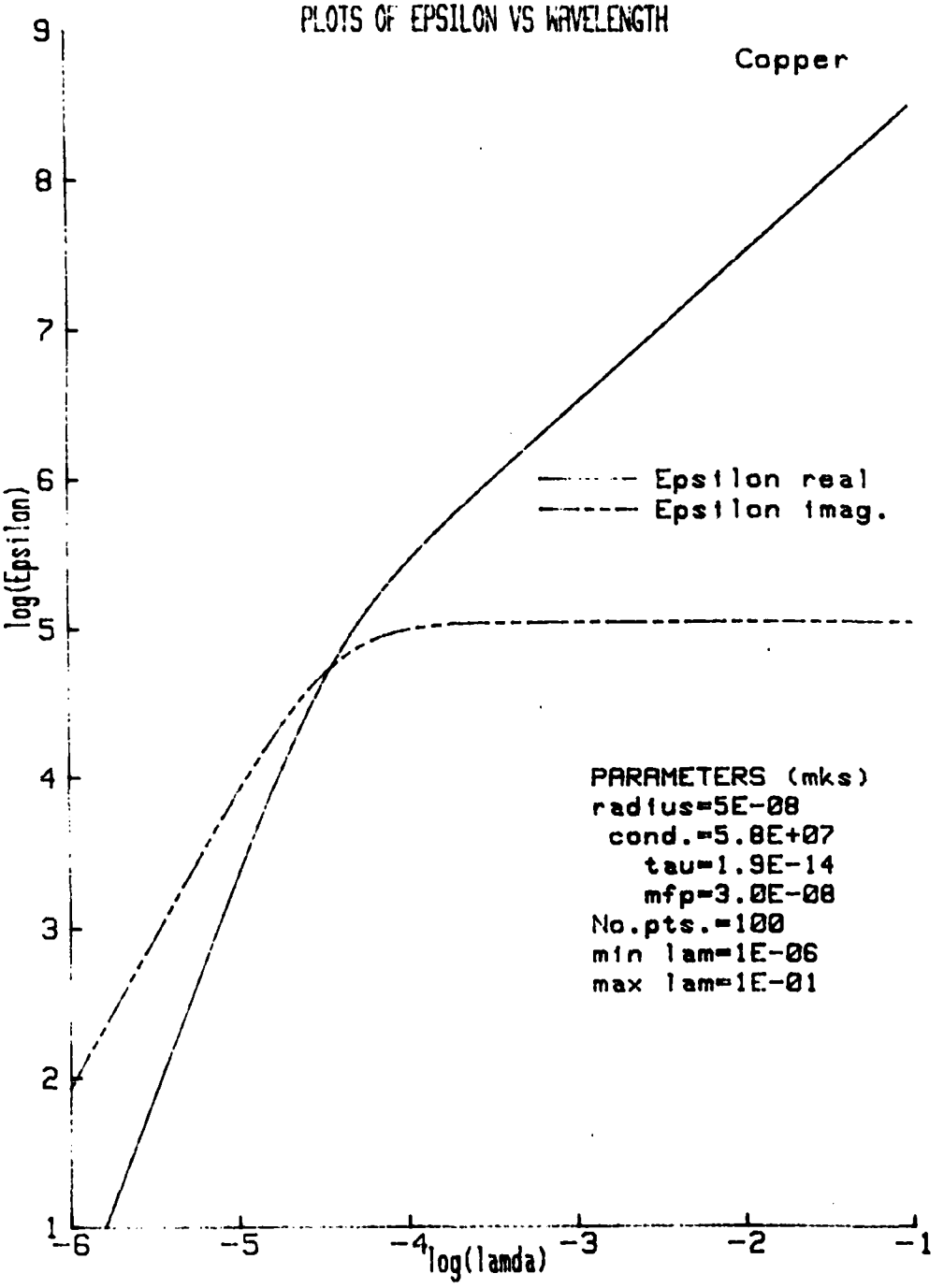

FIGURE 1. Complex dielectric constant vs. wavelength for copper.

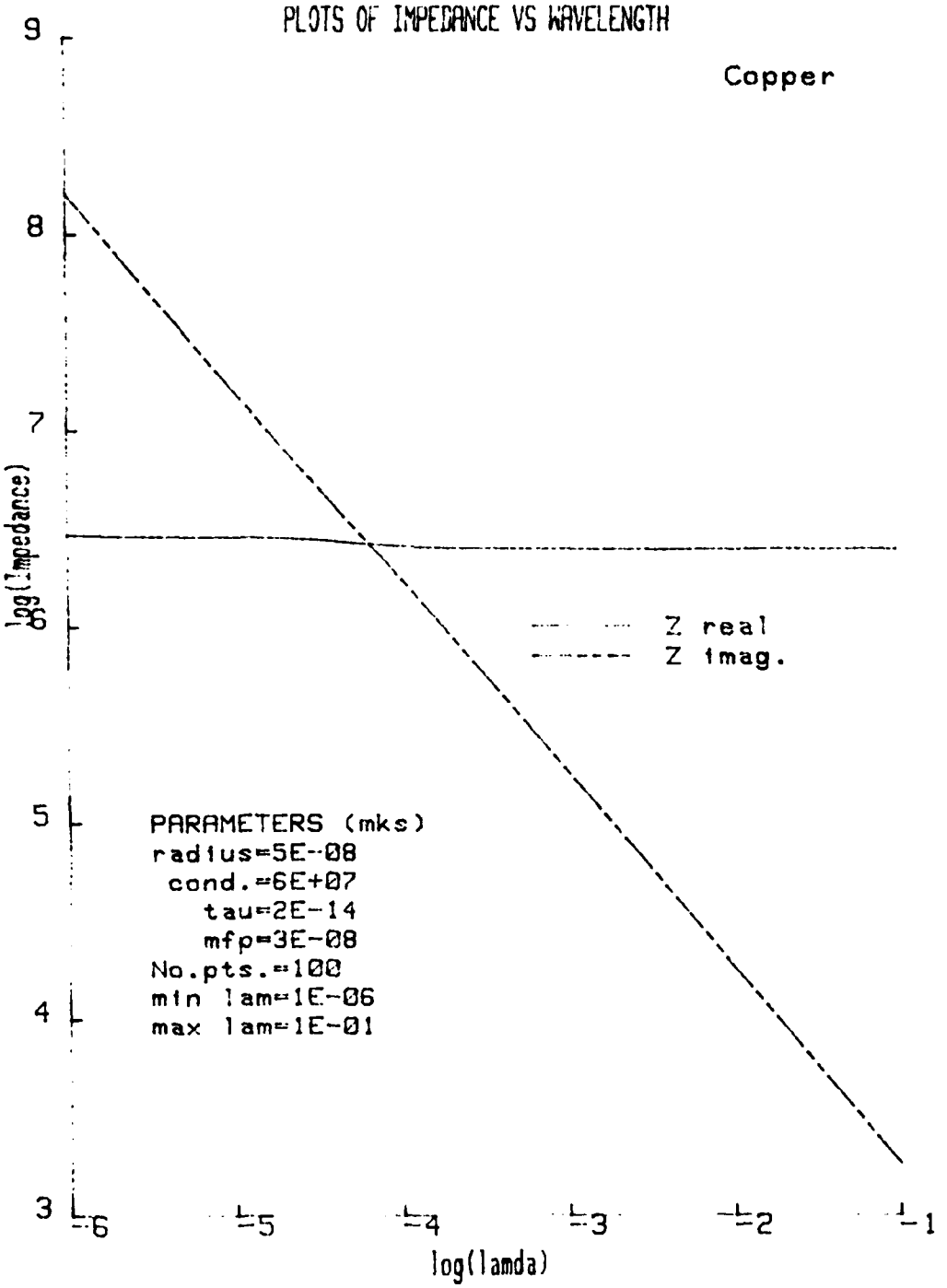

FIGURE 2. Complex surface impedance vs. wavelength for copper.

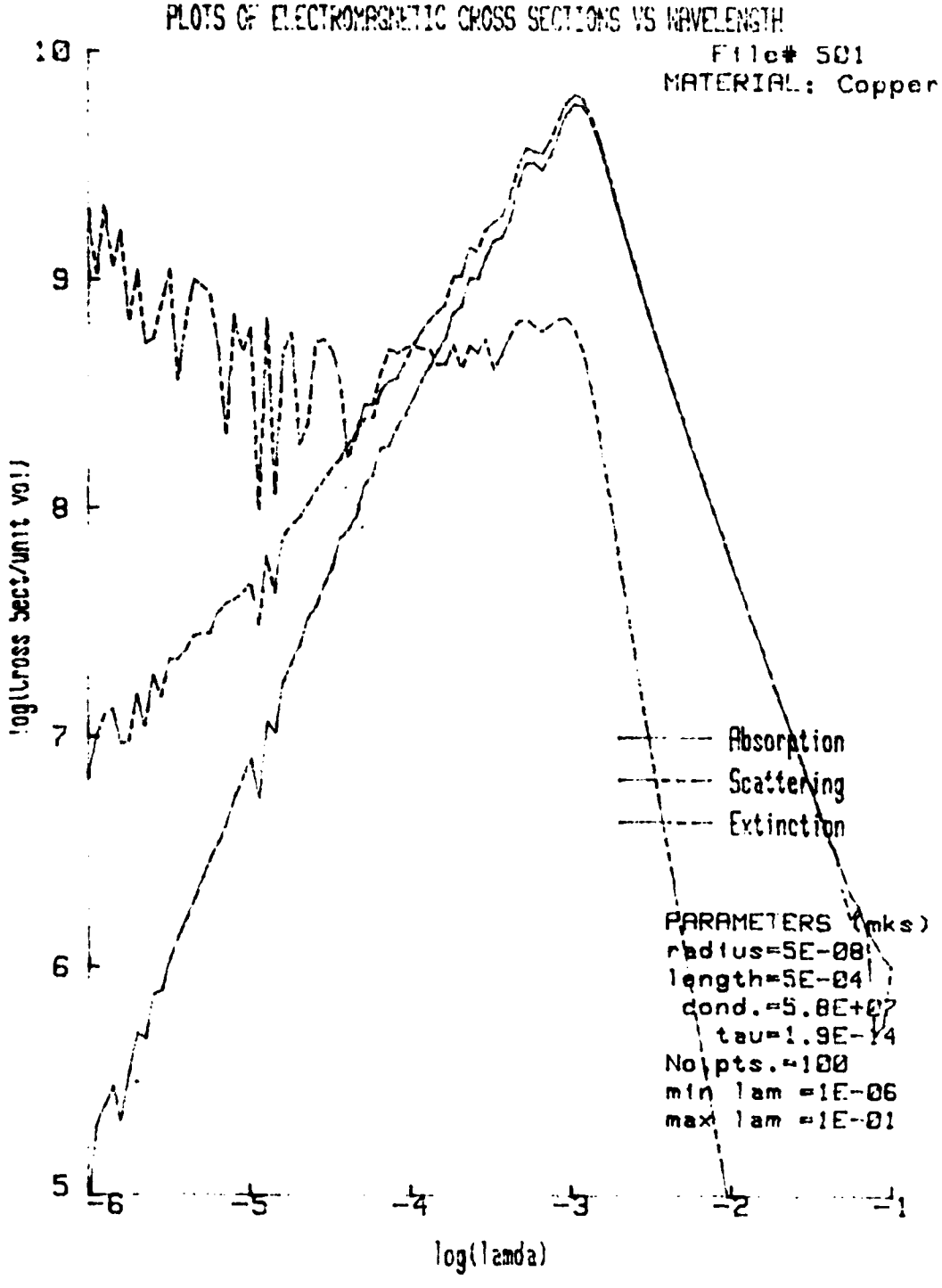

FIGURE 3. Cross-sections vs. wavelength for copper (variational method).

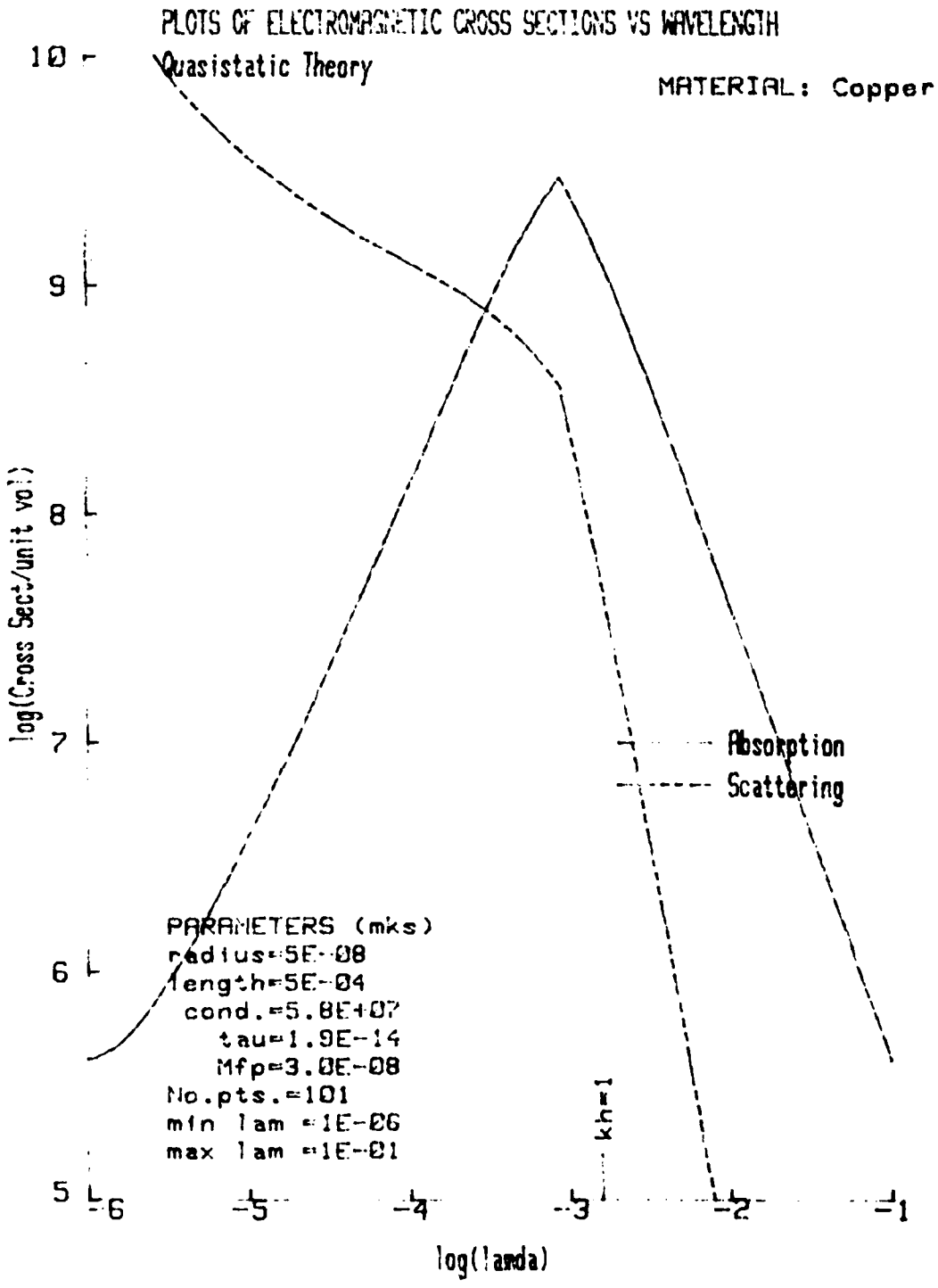

FIGURE 4. Cross-sections vs. wavelength for copper (quasistatic theory).

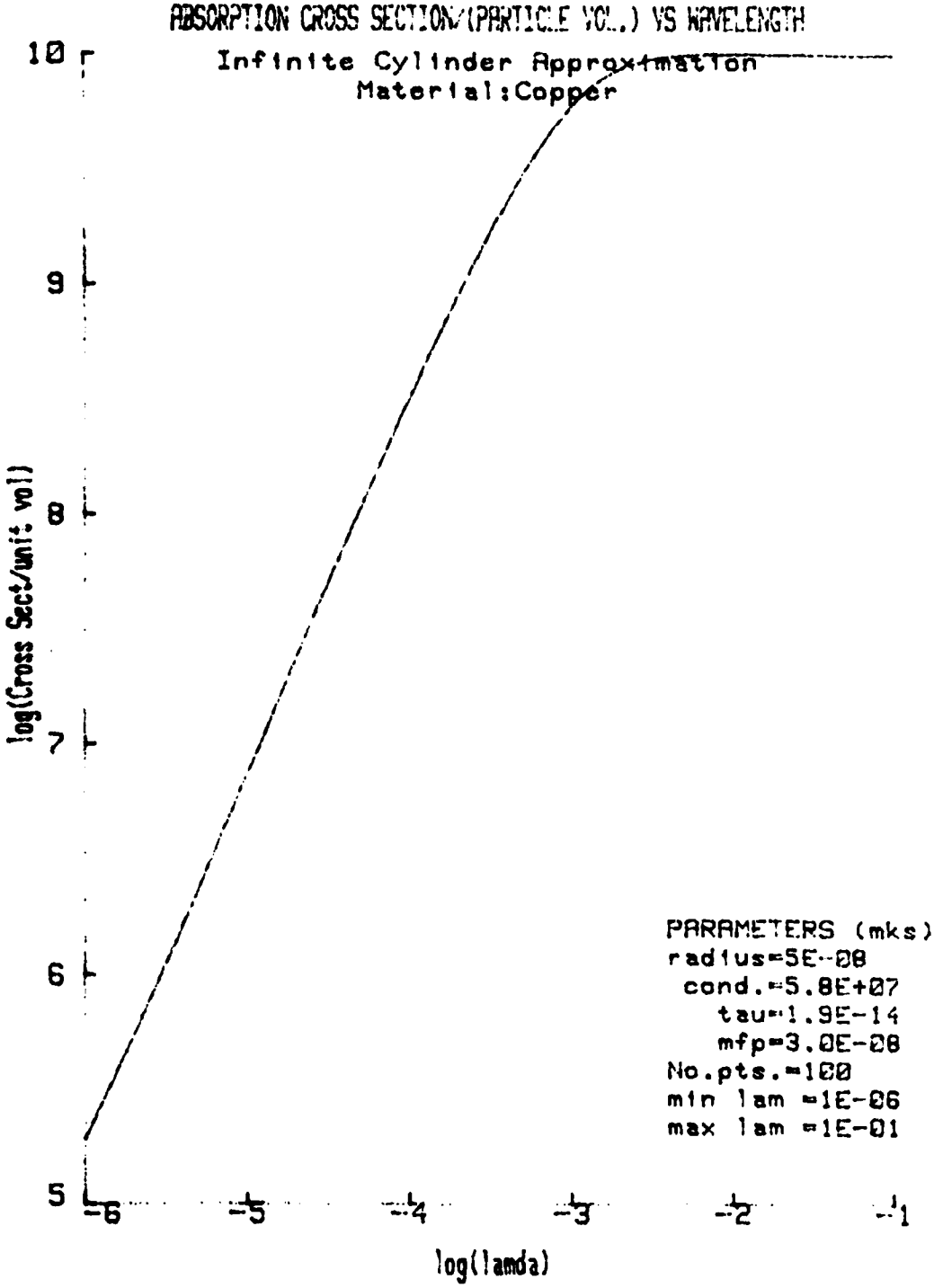

FIGURE 5. Absorption cross-section vs. wavelength for copper (infinite cylinder approximation).

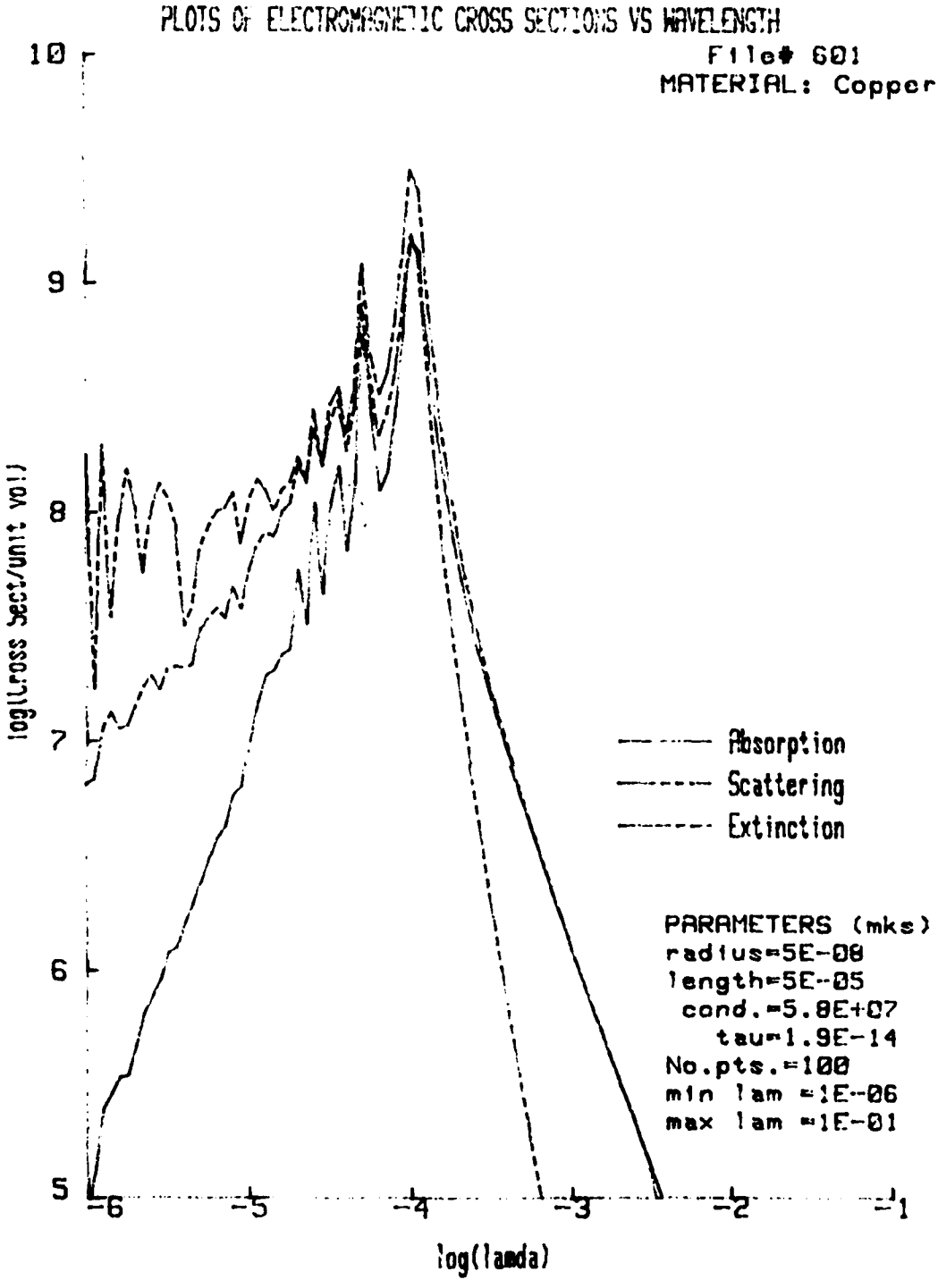

FIGURE 6. Cross-sections vs. wavelength for copper (variational method).

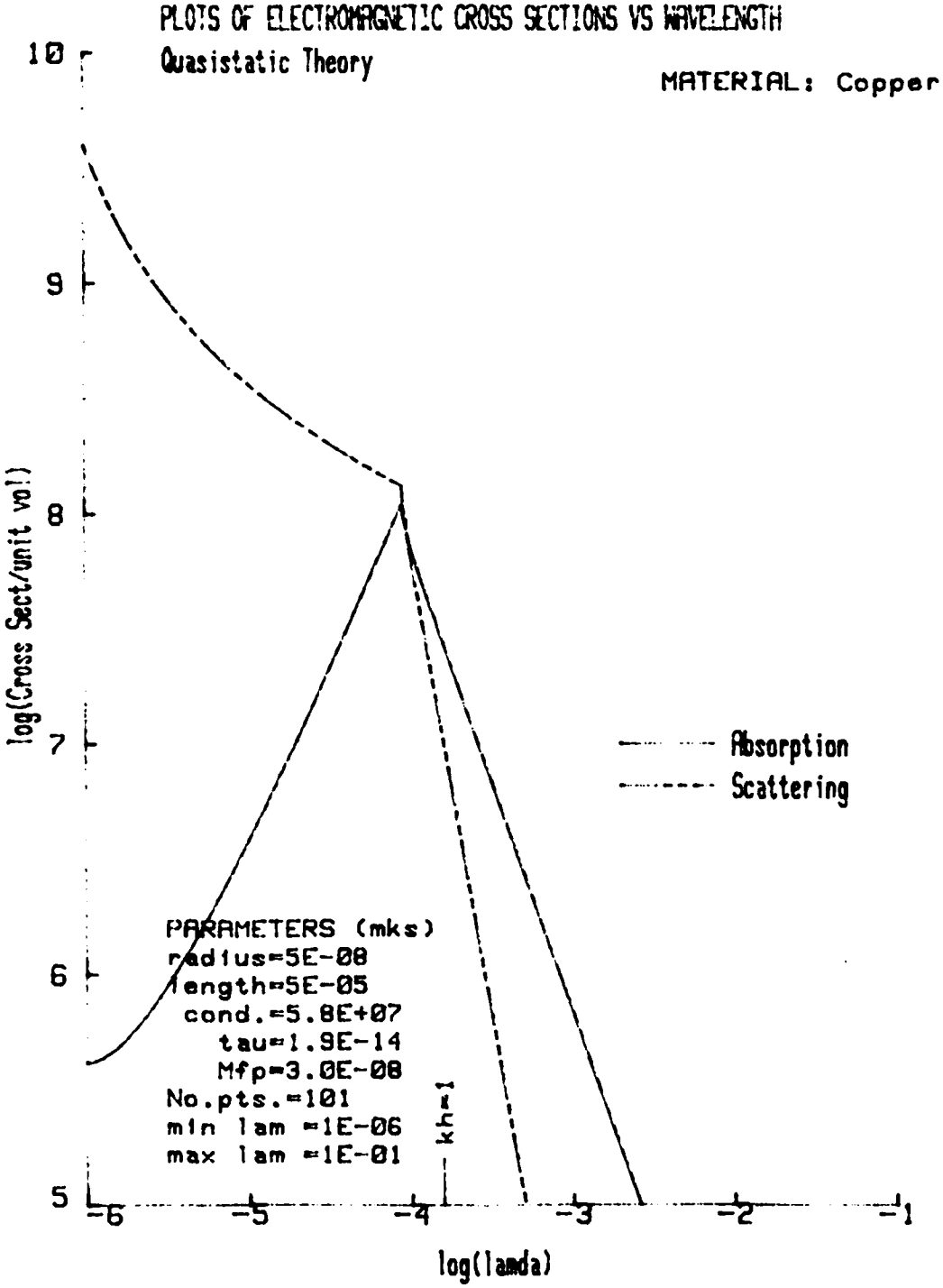

FIGURE 7. Cross-sections vs. wavelength for copper (quasistatic theory).

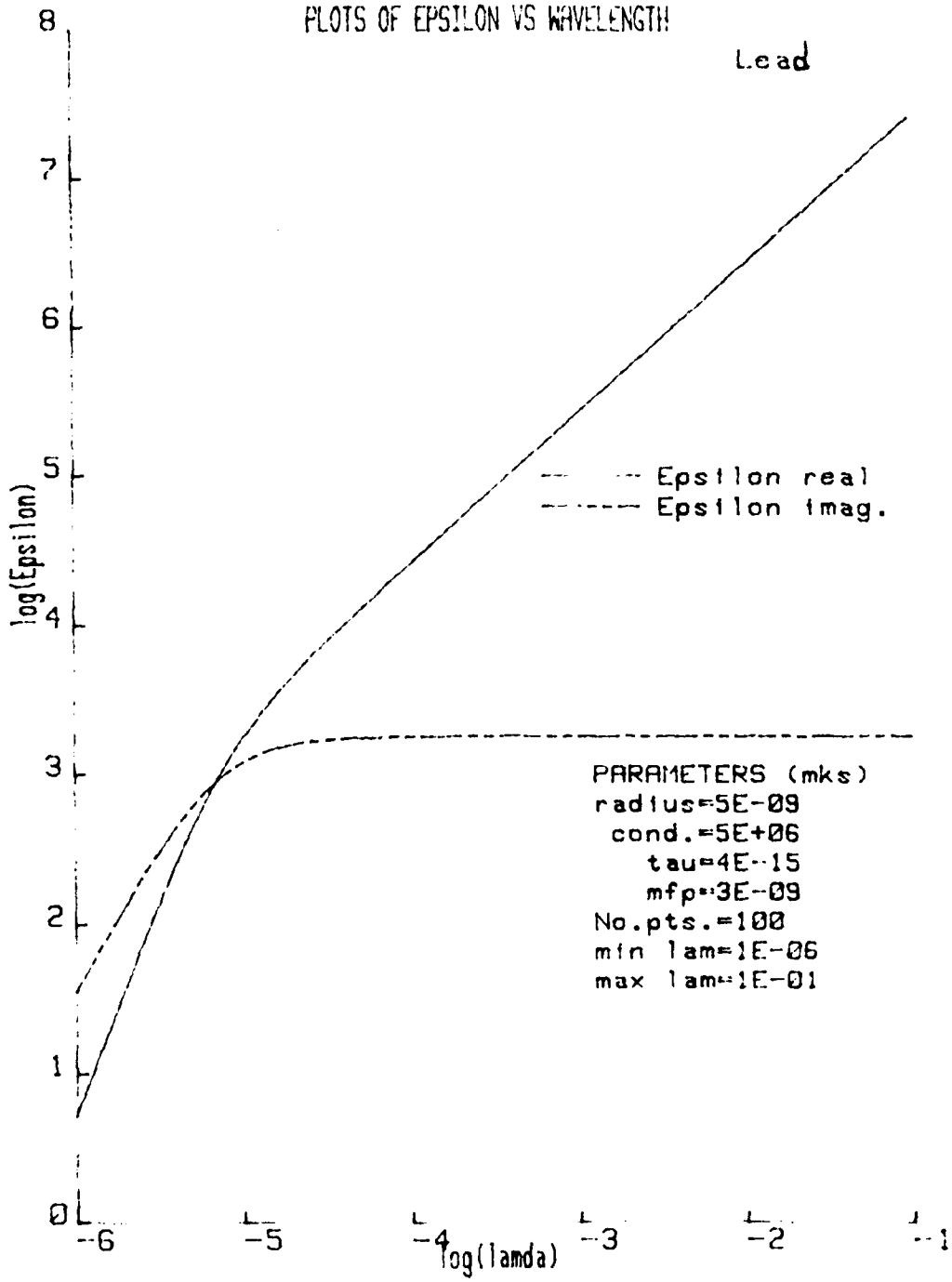

FIGURE 8. Complex dielectric constant vs. wavelength for lead.

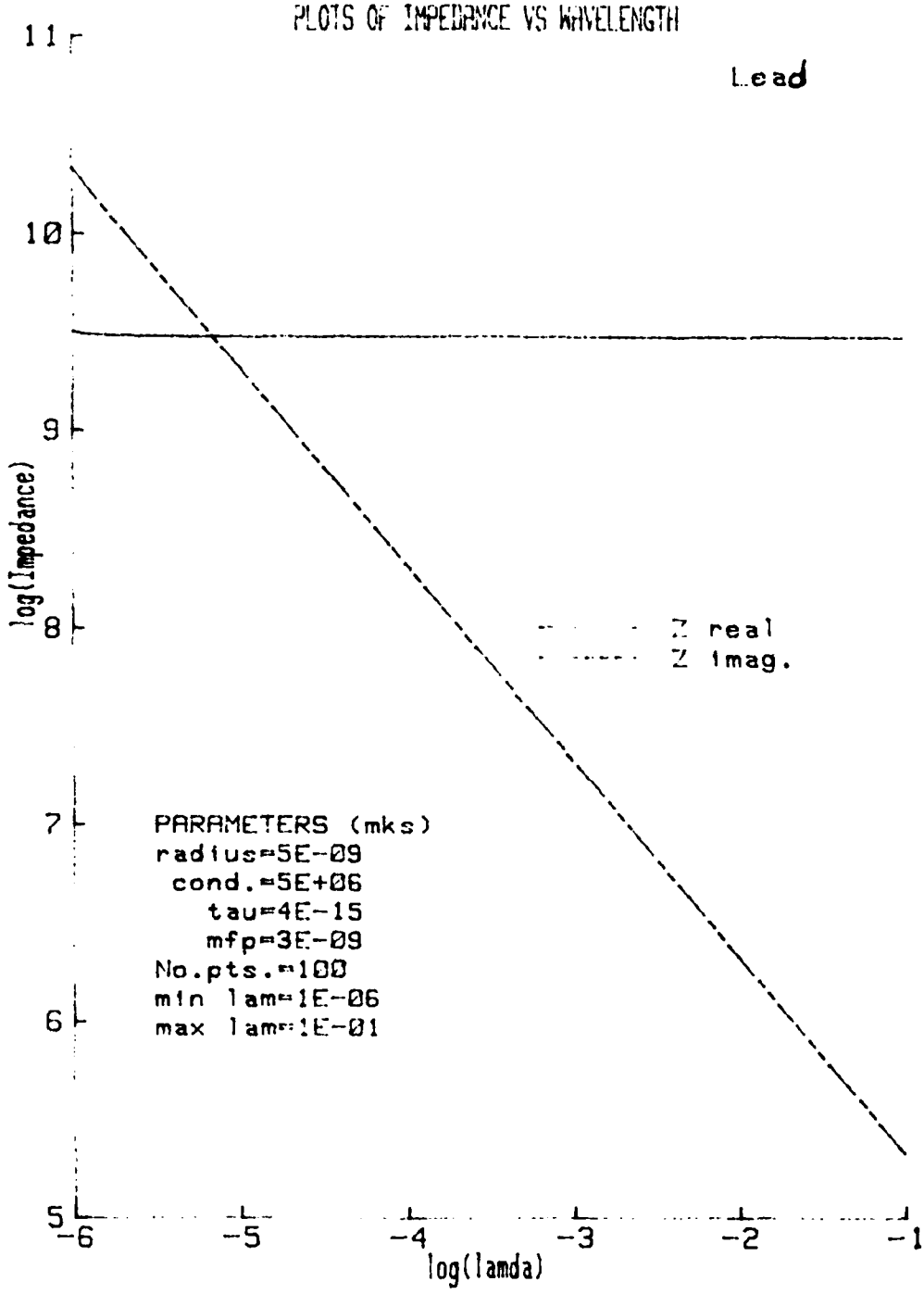

FIGURE 9. Complex surface impedance vs. wavelength for lead.

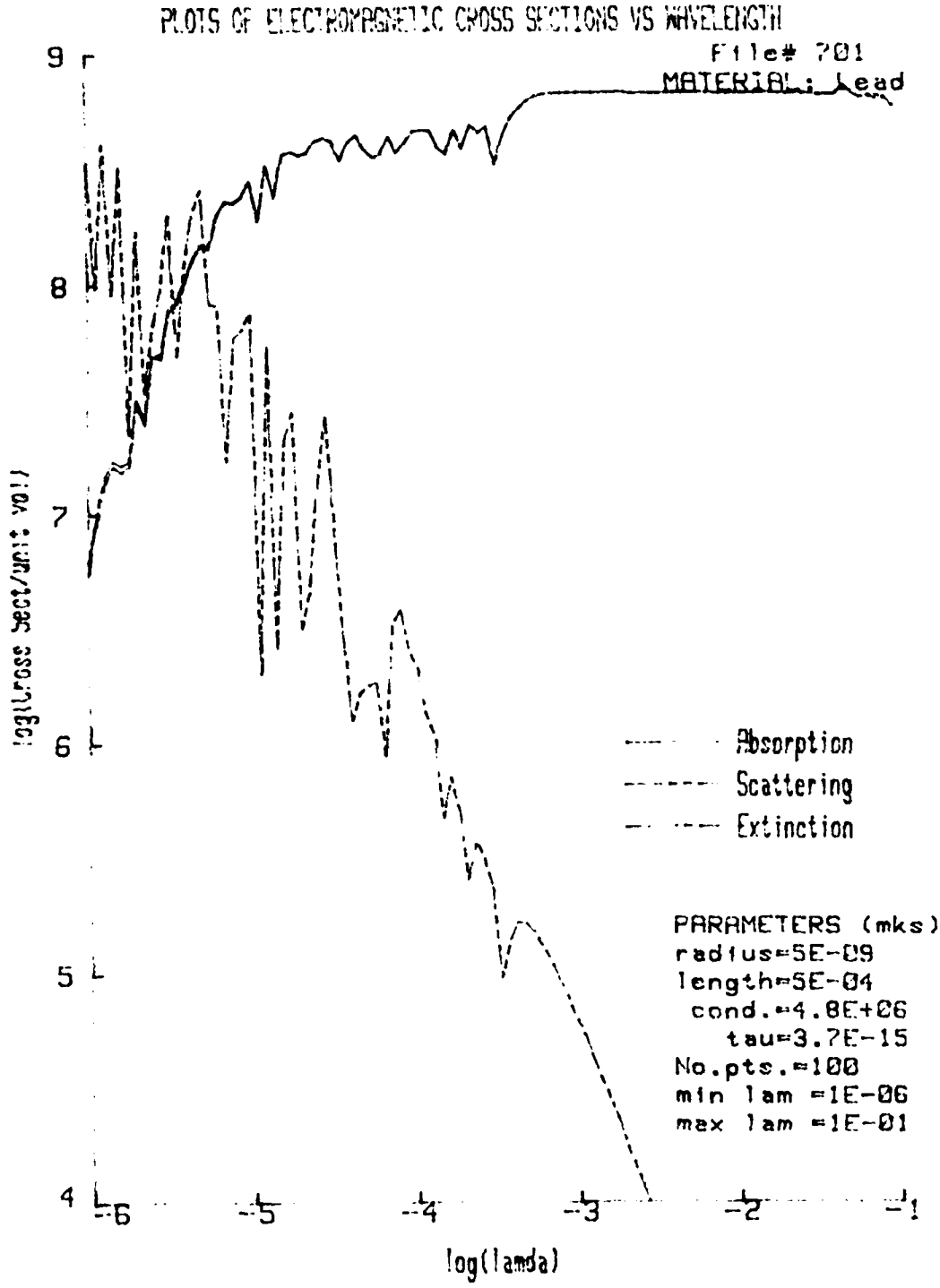

FIGURE 10. Cross-sections vs. wavelength for lead (variational method).

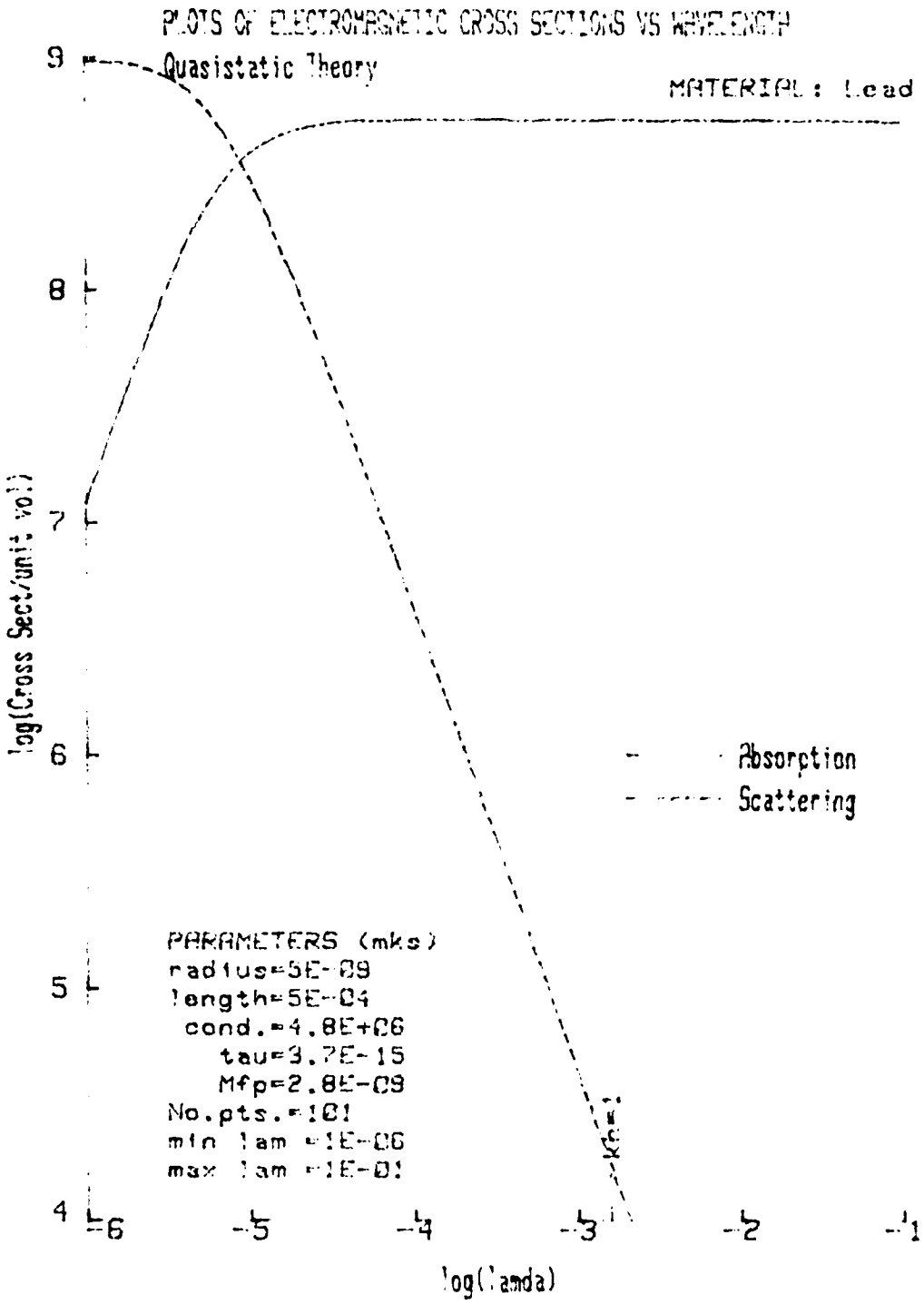

FIGURE 11. Cross-sections vs. wavelength for lead (quasistatic theory).

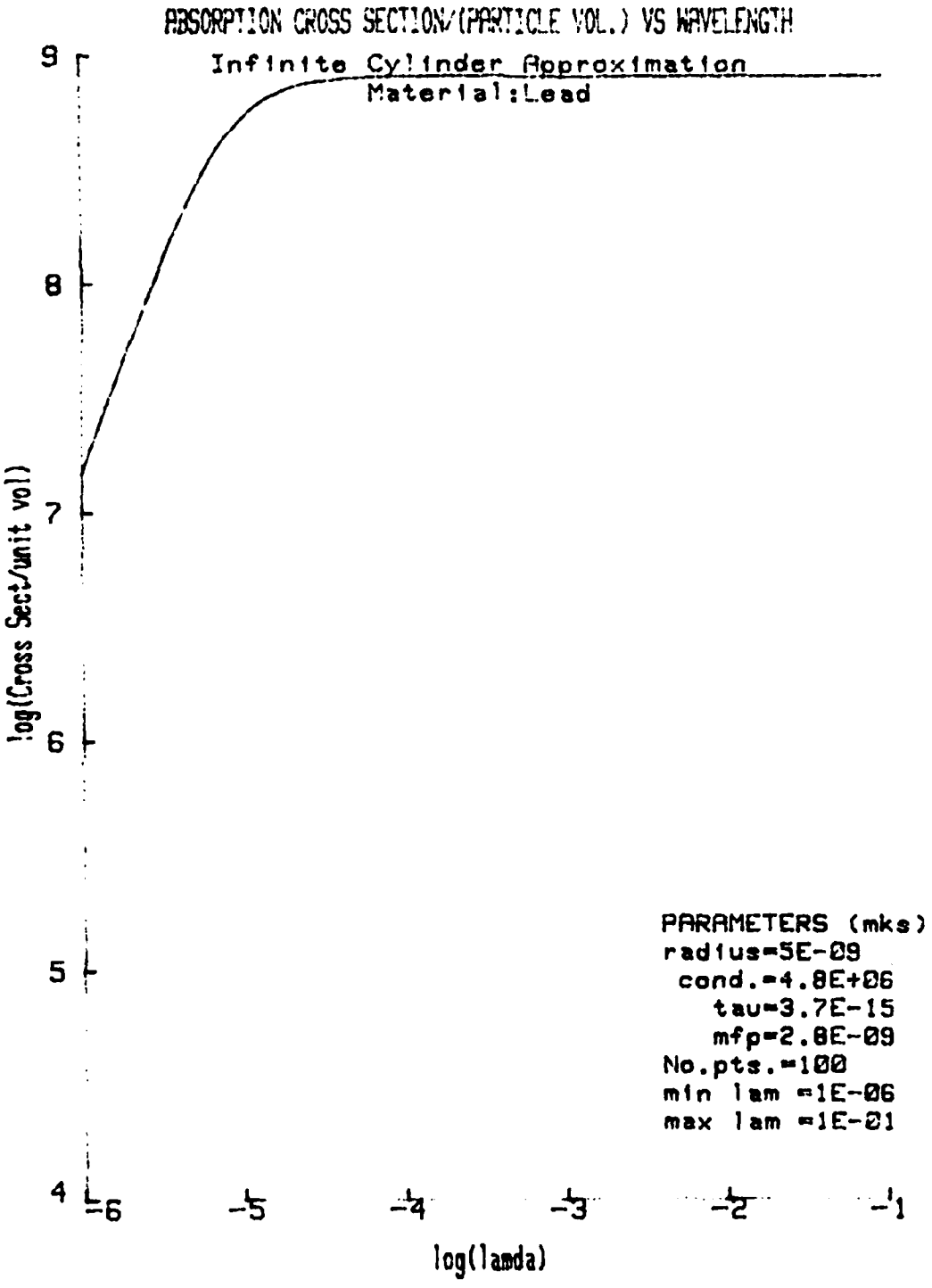

FIGURE 12. Absorption cross-section vs. wavelength for lead (infinite cylinder approximation).

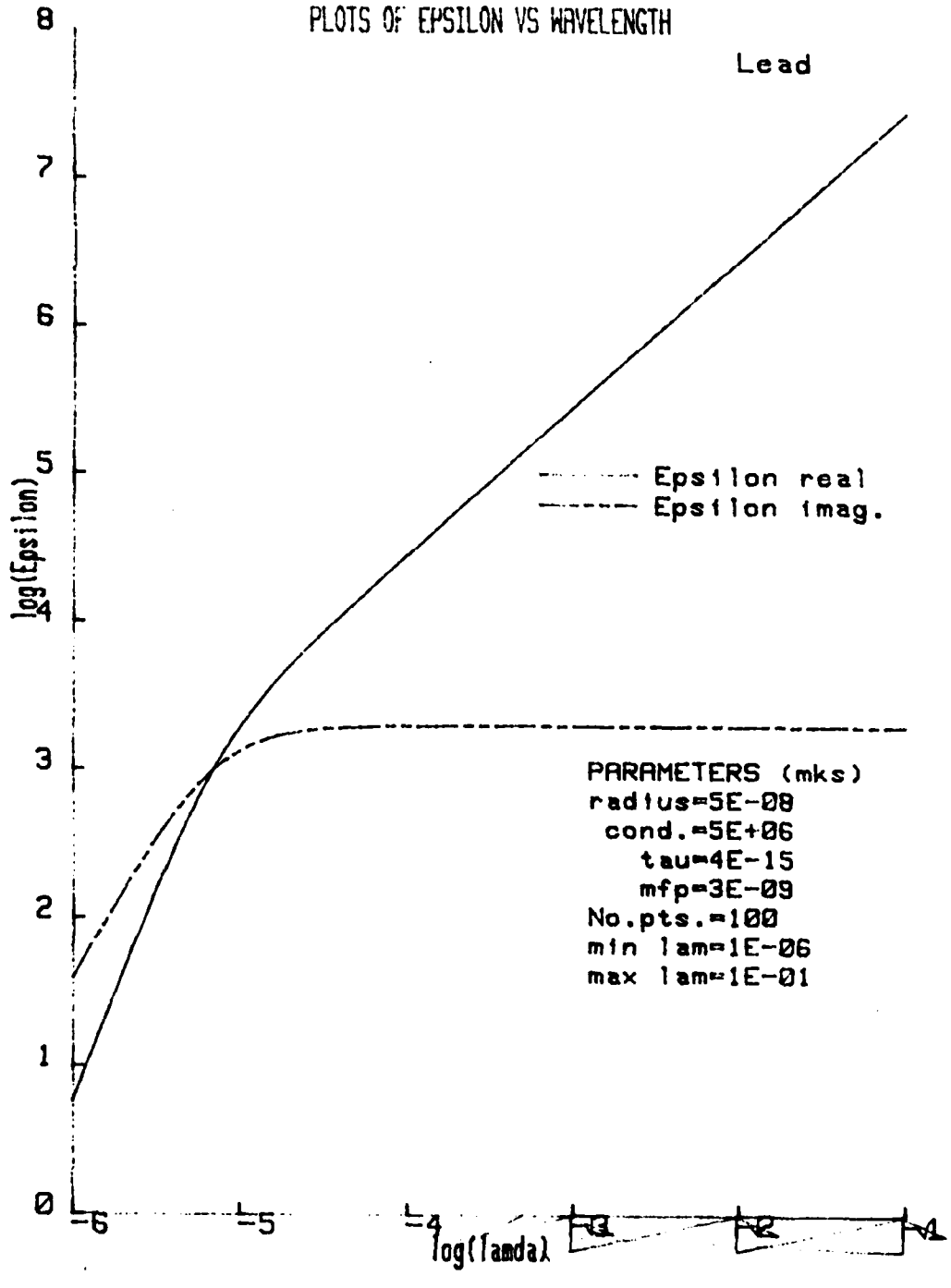

FIGURE 13. Complex dielectric constant vs. wavelength for lead.

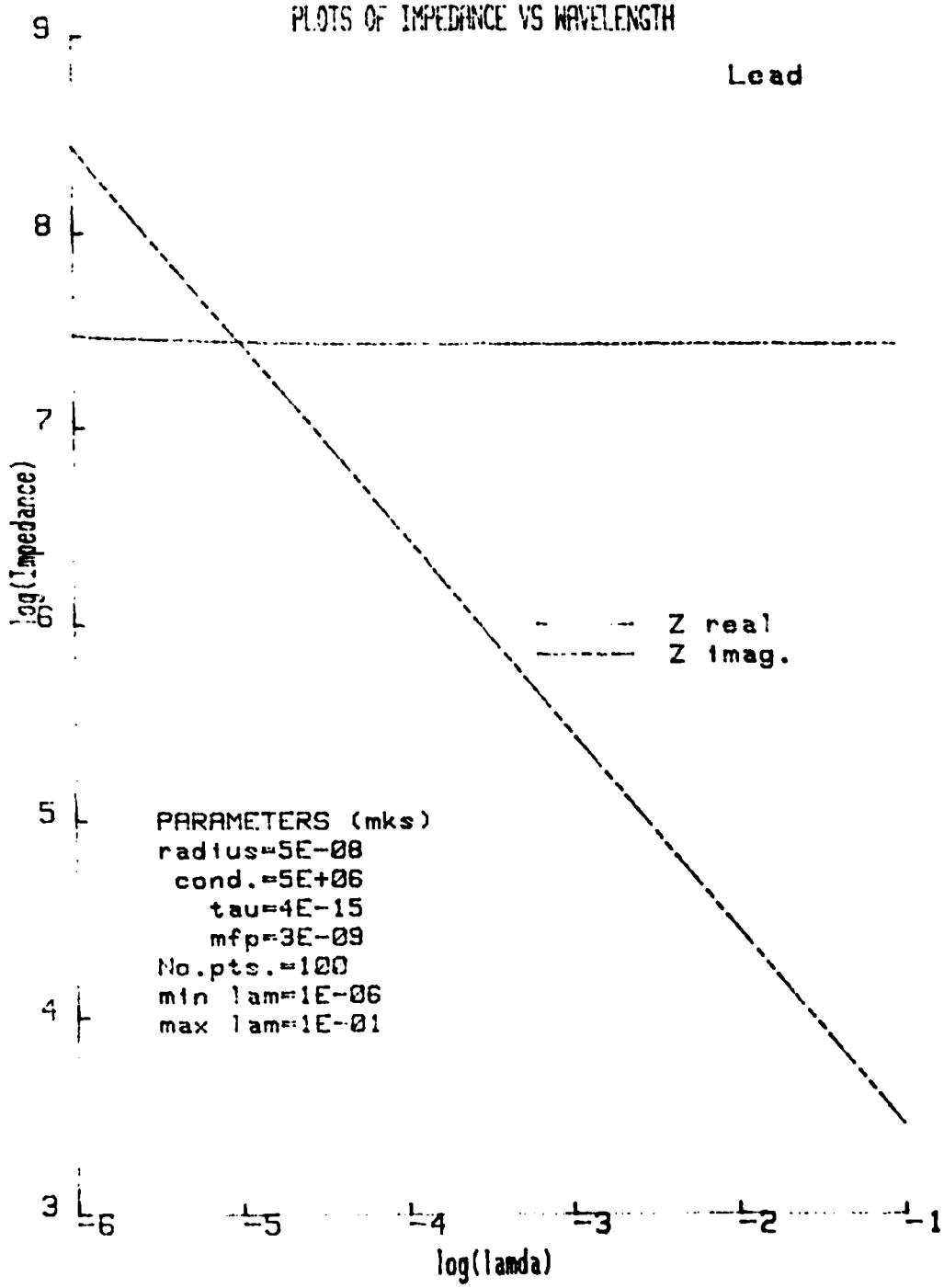

FIGURE 14. Complex surface impedance vs. wavelength for lead.

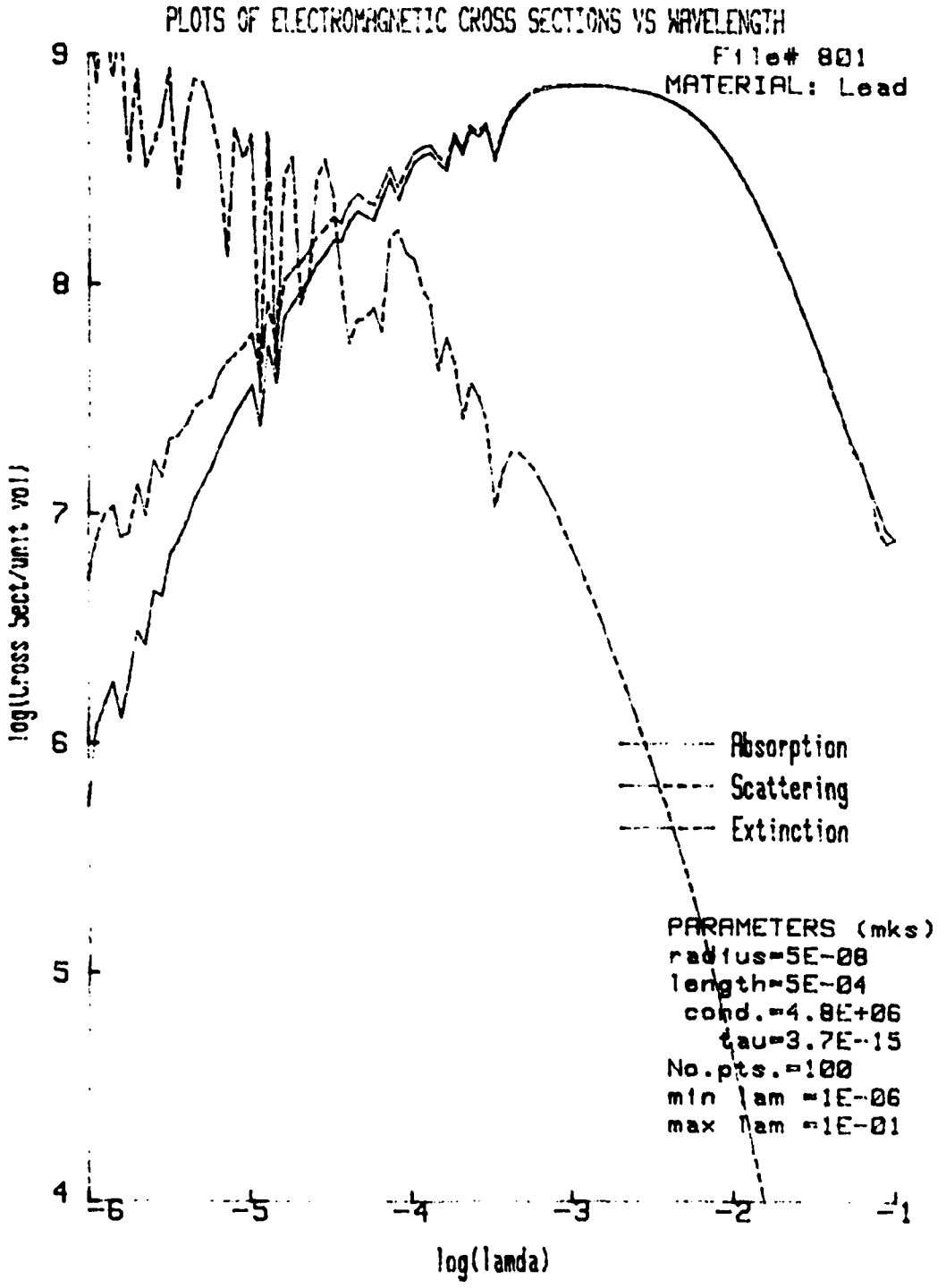

FIGURE 15. Cross sections vs. wavelength for lead (variational method).

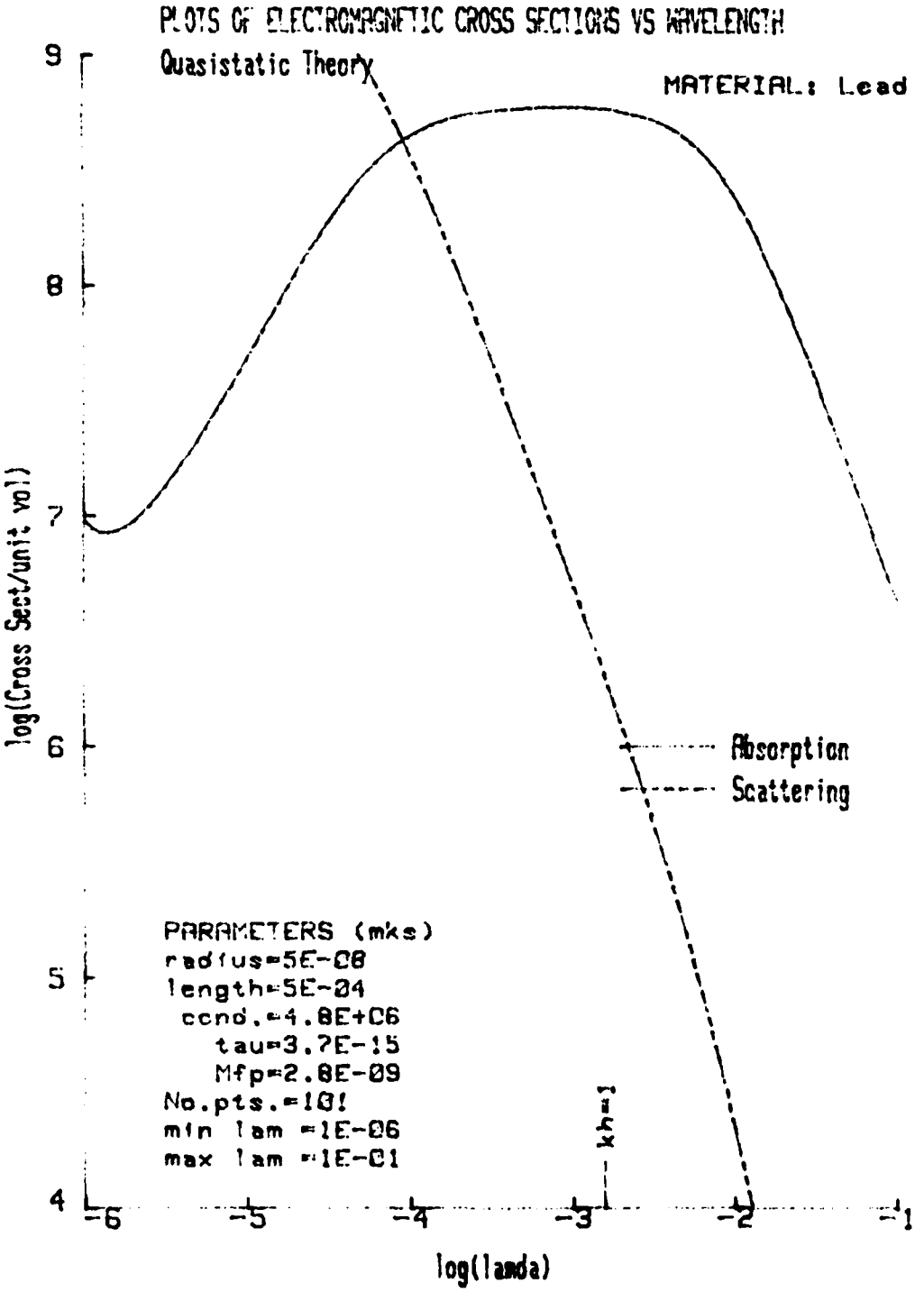

FIGURE 16. Cross sections vs. wavelength for lead (quasistatic theory).

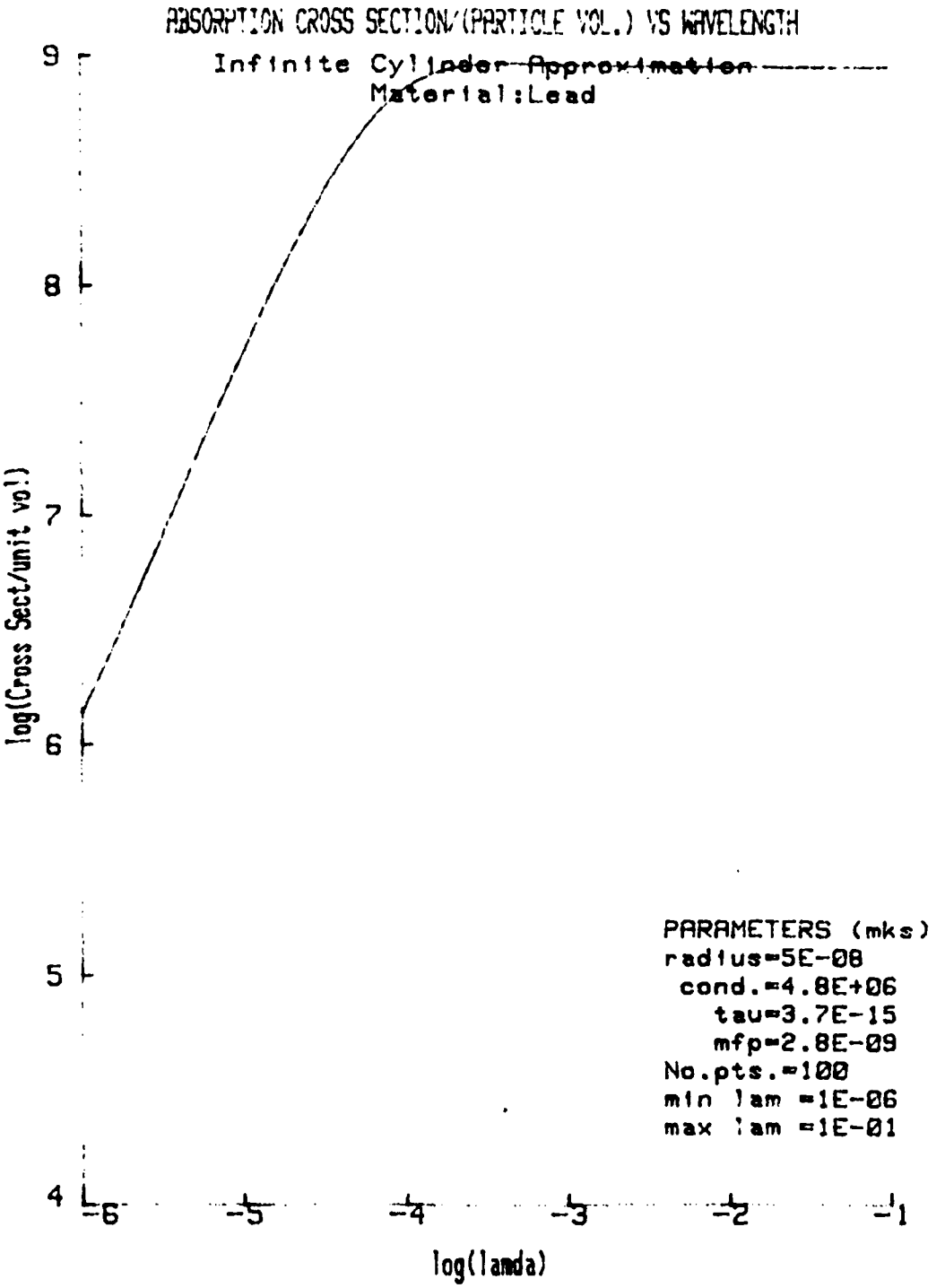

FIGURE 17. Absorption cross-section vs. wavelength for lead (infinite cylinder approximation).

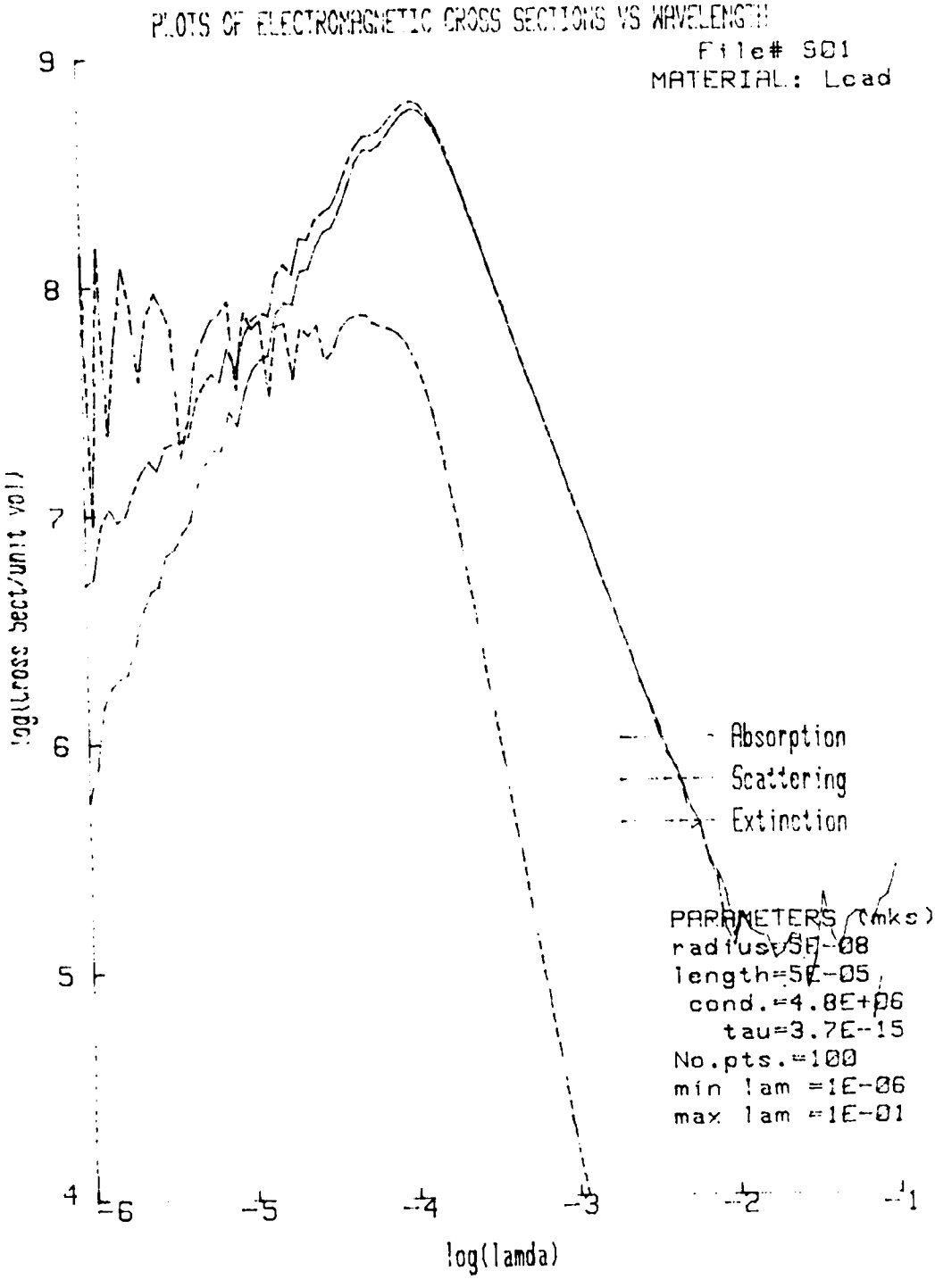

FIGURE 18. Cross-sections vs. wavelength for lead (variational method).

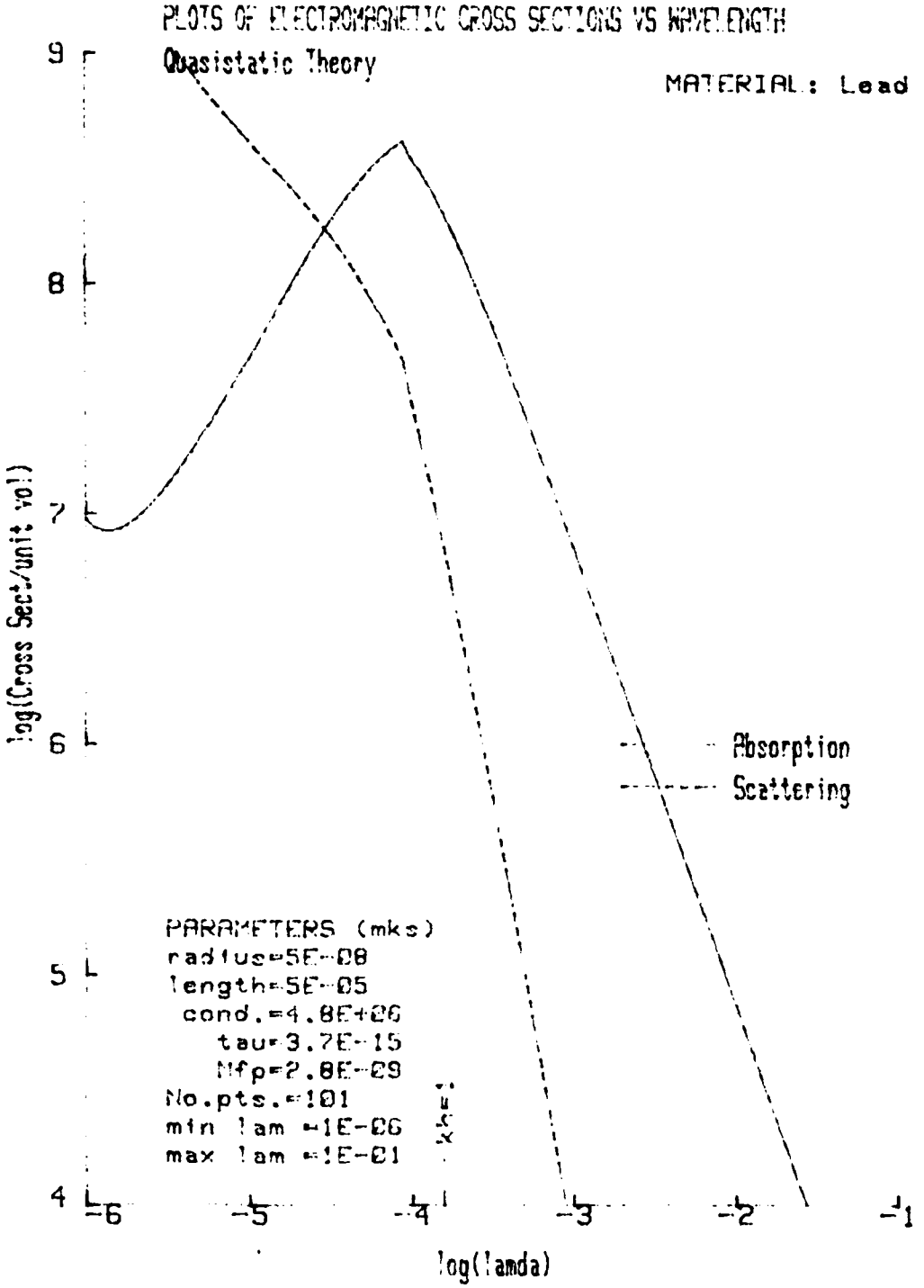

FIGURE 19. Cross-sections vs. wavelength for lead (quasistatic theory).

SPECULAR SCATTERING BY ORIENTED FINITE CYLINDERS

R.T. Wang and Y.L. Xu
Space Astronomy Laboratory, University of Florida
Gainesville, FL 32609

RECENT PUBLICATION, SUBMITTALS FOR PUBLICATION AND PRESENTATIONS:

R.T. Wang and Y.L. Xu, Presented at the 1985 CRDC Scientific Conference on Obscuration and Aerosol Research, Army CRDC, Aberdeen, MD (June 1985)

R.T. Wang, Angular Scattering by Rough Particles, in Proc. of the 1984 CRDC Scientific Conference on Obscuration and Aerosol Research, R. Kohl and D. Stroud, Eds., Army CRDC-SP-85007, pp. 327-363 (June 1985)

D.W. Schuerman and R.T. Wang, Experimental Results of Multiple Scattering, Army CSL Contractor Report, ARCSL-CL-81003 (Nov. 1981)

ABSTRACT

Stimulated by our earlier findings on resonant scattering by two oriented, neighboring spheres [Refs. 8,10], we have performed a similar investigation for the case of finite cylinders using our now computer-controlled microwave analog technique. Three resonance-sized finite cylinders of aspect ratios 12:1, 4:1 and 2:1, whose refractive indexes simulate those of ice or silicate at visible wavelengths, were prepared for this study. The scattering intensities, all calibrated in absolute magnitudes and observed at scattering angles θ = 50°, 70°, and 90°, were plotted versus the azimuth angle χ as each cylinder was continuously rotated through 180° from the beam direction (χ = 0) in the horizontal scattering plane. This plane contains both the transmitting and receiving antennas which are simultaneously polarized either vertical or horizontal, the respective scattering intensities being denoted by i_{11} or i_{22}, respectively. Several striking features are discussed. Preliminary theoretical analysis of these data has also led us to the new finding that surprisingly close predictions of these features were possible via the use of the well-known Rayleigh-Gans-Debye approximation theory [5,6], especially for ice-like cylinders having low refractive indexes. The results of these experimental/theoretical findings are shown in uniformly formatted figures. This work is an integral part of our ARO-supported research program to better the understanding of the physics of light scattering by irregularly shaped particles.

INTRODUCTION

Long, active research by a number of people [2,4,5,6,7,9] has made possible the quantitative prediction of light scattered from an infinitely long, but arbitrarily oriented, cylindrical object. An outstanding feature in such a process is that the scattered light is observable only when sighted from the directions defined by a circular cone and toward its apex [4,6]. This particular cone is dependent only on the angle of incidence and is formed by rotating the incident ray around the cylinder axis with a constant angle in between. For example if a long straight spider web is fully illuminated only by collimated light, only a particular spot along its length can be seen. This spot is the apex of the cone just mentioned. Thus, it is seen that the scattering by a very long cylinder is extremely narrow in its angular spread, being almost delta-function-like.

What if the unrealistic restriction that the cylinder be infinitely long is removed? This question in realistic scattering problems has not yet been answered in sufficient generality

despite the existence of a number of promising, yet highly involved theories [1,3]. On the other hand, experimental investigation is extremely difficult other than using microwave-analog techniques - mainly due to the lack of knowledge/precise controls of particle parameters such as size, shape, refractive index and orientation in the beam. In the next section (Sec. II) we shall describe in some detail the measurement procedures of this investigation using our microwave facility. An important mathematical symmetry relation which is independent of the cylinder size and material, but which proves very useful in the interpretation of cone profile, is also discussed. Sec. II also includes a brief explanation of the Rayleigh-Gans-Debye approximation theory (abbreviated hereafter by RGD), which gave unexpectedly close predictions for the observed phenomena. Sec. III presents the experimental results along with the comparisons with RGD theory in uniform comprehensive graphical forms. Most of the significant scattering properties are discussed. This paper then concludes with the summary.

II. EXPERIMENTAL/THEORETICAL CONSIDERATIONS

A. Experimental Considerations

The parameters of the three plastic, circular target cylinders are listed at the top of each of the figure pages, Figs. 1A-3F. Two cylinders of these three have aspect ratios 1:12.263 and 1:4.0 and were machined from expanded polystyrene material to simulate the refractive index of water-ice at visible wavelengths. The third cylinder, which has a 1:2.008 aspect ratio, was similarly prepared from plexiglass material to simulate silicate. The choice of cylinder diameters and lengths was made to systematically investigate the change in the scattering-cone profile as the cylinder was shortened, to be compatible with the antenna-wave-front size and the level of accurately measurable scattering intensity, and to obtain mechanical rigidity of the particle shape.

Scattering intensities $i_{11}(\chi)$ and $i_{22}(\chi)$ were measured at each azimuth angle χ as each cylinder was rotated in the horizontal scattering plane that contains both the transmitting and receiving antennas. χ is the angle between the cylinder axis and the incident beam. It was varied in the common range $0^\circ \leq \chi \leq 180^\circ$ either by an interval $\Delta\chi = 1^\circ$ or by $\Delta\chi = 2^\circ$. i_{11} and i_{22} are the intensities (in absolute magnitude) when both antennas are polarized vertical and horizontal, respectively. The absolute magnitude calibration of i_{11} and i_{22} was made by comparing intensities with those of a standard sphere run immediately following each azimuth sweep. Each of these scattering-cone profiles was measured at three angular positions of the receiving antenna - scattering angles $\theta = 50^\circ$, $\theta = 70^\circ$, $\theta = 90^\circ$--and are depicted, respectively, in the A & B figures, C & D figures, and E & F figures of Figs. 1A-3F. (They are labeled "Expt".) Separate runs to measure the intensities averaged over random particle orientations, the $\overline{i_{11}}$ and $\overline{i_{22}}$, were also made. (See our previous report

[11] to facilitate the direct comparison between i_{11} and $\overline{i_{11}}$ and between i_{22} and $\overline{i_{22}}$.) The levels as well as the numerical magnitudes of $\overline{i_{11}}$ and $\overline{i_{22}}$ are shown at the lower left corner of each figure.

All measured scattering intensities are calibrated in absolute magnitude to facilitate direct comparisons with the necessarily complex theoretical results. In the summer, when these measurements were performed, the high indoor temperature of our large anechoic chamber may have caused appreciable system gain changes (in the transistor/integrated circuitry) during target azimuth sweeps (typically 12-25 minutes). Maximum error in the absolute magnitude calibration is estimated to be about 10% if the magnitudes of i_{11} and i_{22} are larger than about 5. Below magnitude 5, the error may climb to about 20% because an additional factor of fluctuating residual background has to be considered.

B. Scattering Properties Resulting from Particle Shape Symmetry

All cylinderical particles used here are of course axisymmetric in shape. As the axis of such a particle is confined to rotate in the scattering plane, the $i_{11}(\chi)$ or $i_{22}(\chi)$ profiles should be symmetrical about the bisectrix $(\pi - \theta)/2$ with a half period $\pi/2$. Equivalently, $i_{11}(\chi)$ and $i_{22}(\chi)$ are also symmetrical about the bisecting angular position of the scattering angle, $\theta/2$, as the azimuth χ is varied. These remarkable symmetry relations follow from examination of the transformation properties of the complex scattering amplitude matrix $\tilde{S}$ under particle rotations/inversions. van de Hulst explained [5] that there exist four related particle positions in which $\tilde{S}$ at each position can be represented by the same set of matrix elements S_1, S_2, S_3, S_4:

$$\begin{array}{cccc} \text{Position a} & \text{Position b} & \text{Position c} & \text{Position d} \\ \tilde{S}_a = \begin{pmatrix} S_2 & S_3 \\ S_4 & S_1 \end{pmatrix} & \tilde{S}_b = \begin{pmatrix} S_2 & -S_4 \\ -S_3 & S_1 \end{pmatrix} & \tilde{S}_c = \begin{pmatrix} S_2 & -S_3 \\ -S_4 & S_1 \end{pmatrix} & \tilde{S}_d = \begin{pmatrix} S_2 & S_4 \\ S_3 & S_1 \end{pmatrix} \end{array} \qquad (1)$$

Only two of the above transformations, $\tilde{S}_a \rightarrow \tilde{S}_c$ and $\tilde{S}_a \rightarrow \tilde{S}_b$, lead to the proof of our beginning statements. These two positions c and b are obtained from the particle position a by mirroring the particle with respect to the scattering plane, and 180° particle rotation about the bisectrix, respectively. Immediate consequences of Eqs. (1) are

(1) $\tilde{S}_a \rightarrow \tilde{S}_c$. Since our cylinder axis is always in the scattering plane, the positions (a) and (c) are identical. Equating the $\tilde{S}$-matrix elements for both positions we have $S_3 = -S_3$ and $S_4 = -S_4$, which are true if and only if $S_3 = S_4 = 0$; i.e., there are no cross-polarized components.

(2) $\tilde{S}_a \rightarrow \tilde{S}_b$. The above consequence, $S_3 = S_4 = 0$, further results in $\tilde{S}_a = \tilde{S}_b$; i.e., the matrix elements at position a are identical to the corresponding elements at position b, the reciprocal position. Thus, as χ is varied, both S_1 and S_2 vary periodically with the half period $\pi/2$ and with symmetrical patterns about the bisectrix.

Since the intensity components i_{11}, i_{22}, i_{12} and i_{21} (i_{12} & i_{21} are called the cross-polarized intensity components) are by definition simply related to the amplitude matrix elements by

$$i_{11} = |S_1|^2 \ , \ i_{22} = |S_2|^2 \ , \ i_{12} = |S_3|^2 \text{ and } i_{21} = |S_4|^2 \ , \tag{2}$$

the symmetry properties of i_{11} and i_{22} follow those of the $\tilde{S}$-matrix elements shown above.

These symmetry properties, which are independent of the target size/material, allow us to check the precision with which we orient each particle in the beam, the homogeneity/symmetry of the product particle, and/or even the reliability of theoretical algorithms employed to analyze the experimental results. It is also interesting to note that when the cylinder axis is aligned to the $\theta/2$ direction, i.e., when $\chi = \pi - \theta/2$, an extremum (in general a maximum) in i_{11} or i_{22} is observed at θ, the intersecting direction of the scattering plane and the scattering cone.

C. Rayleigh-Gans-Debye (RGD) Approximation Theory

This classical theory in light scattering is known as the Born approximation in its wave mechanical counterpart. It was developed to treat the scattering by particles larger in size than in the Rayleigh region (where $x \ll 1$ and $|mx| \ll 1$; $x = 2\pi a/\lambda$, $m = m' - im''$ = complex refractive index). The physics in the RGD theory is the same as in the Rayleigh scattering theory, except that the scattering particle is subdivided into a number of Rayleigh-sized particulates each of which contributes a scattered wavelet (in the familar Rayleigh pattern) at the observation point. Each particulate therein is assumed to scatter the <u>unperturbed</u> incident wave as if other particulates were absent, but only the phase relationships between these wavelets are taken into account to assess the resultant RGD pattern. Even though the basic assumptions in the RGD theory imply that $2x|m' - 1| \ll 1$ (i.e., m has to be very close to 1), this approximation has been applied to many practical problems far beyond its validity mainly because of its relative simplicity in the qualitative explanation of scattering by irregularly shaped particles. Furthermore, the angular scattering patterns of many nonspherical shapes can be expressed in closed analytical forms. For more detailed expositions of the RGD theory, we refer to other texts [chapt. 7, Ref. 5; Chapt. 8, Ref. 6], and describe here only those formulae employed in this investigation.

For a finite cylinder of radius a and length L, the particle azimuth and scattering-angle dependences of scattering intensities i_{11} and i_{22} by RGD theory are

$$i_{11} = \frac{9}{4} \left| \frac{m^2 - 1}{m^2 + 2} \right|^2 \left(\frac{L}{2a} \right)^2 x^6 P(\Theta, \beta) \tag{3a}$$

$$i_{22} = i_{11} \cos^2 \Theta, \tag{3b}$$

respectively, where

$$x = ka = 2\pi a/\lambda \tag{3c}$$

$$m = m' - im'' = \text{complex refractive index} \tag{3d}$$

$$\beta = \chi - (\pi - \theta)/2 = \text{angle between cylinder axis and bisectrix} \tag{3e}$$

and $P(\theta, \beta)$ is called the "Form Factor" of the oriented cylinder:

$$P(\theta,\beta) = \left(\frac{\sin(v\cos\beta)}{v\cos\beta} \quad \frac{2J_1(u\sin\beta)}{u\sin\beta}\right)^2 \tag{3f}$$

in which

$$u = 2\,k\,a\,\sin(\theta/2) \tag{3g}$$

$$v = k\,L\,\sin(\theta/2) \tag{3h}$$

and J_1 is the first order Bessel function of the first kind. i_{11} and i_{22} are dimensionless quantities representing the absolute magnitudes of the perpendicular and parallel components of the scattering intensities, respectively. They are also plotted as a function of χ and are shown in each of the figures Figs. 1A - 3F for direct comparison with experimental results.

III EXPERIMENTAL RESULTS AND COMPARISONS WITH RGD THEORY

The easiest and most efficient way to evaluate the outcome of microwave experiments is to present the experimental data in a carefully selected set of graphs. This not only facilitates the visualization of actual light scattering phenomena but also provides an adequate link to the theoretical interpretations needed to better understand the underlying physics. We present 18 figures (Figs. 1A - 3F; note that Figs. 1A & 1B for $\theta = 50°$ data are shown twice to facilitate comparisons with $\theta = 70°$ and $\theta = 90°$ data, Figs. 1C & 1D and Figs. 1E & 1F, respectively).

Outstanding features:

(1) The larger the aspect ratio, the more pronounced is the specular scattering from a finite cylinder - in the sense that narrower, sharper peaked light beams are scattered into the directions of a cone predicted by the infinite cylinder theory.

(2) What is not known by the infinite cylinder theory is that one such main scattered beam is accompanied by several side lobes symmetrically surrounding it. Again, the larger the aspect ratio, the narrower is the side lobe and the lower the intensity level compared to the main beam. Indeed, for the 2:1 cylinder the side lobe level becomes comparable to that of the main lobe and is so displaced in angular position (Fig. 3E) that these two may become indistinguishable.

(3) The profile of scattering intensity versus cylinder azimuth angle changes markedly with respect to the incident polarization. For the longer cylinders the peaks of i_{11} are in general higher than those of i_{22} at all scattering angles. In an extreme case such as shown in Fig. 2F, the extremum of i_{22} at the cone direction may even become a trough!

(4) For long and short cylinders alike, i_{11} and i_{22} vs χ profiles follow the mathematical symmetry described in the beginning paragraph of Sec. II-B; i.e., the profile is symmetrical about the bisectrix position $\chi = (\pi - \theta)/2$ or half-scattering angle position $\chi = \pi - \theta/2$ and repeats itself with a period π.

(5) The degree of specular scattering may also be quantitatively expressed by the ratios $r_{11} = (i_{11})_{max} / \overline{i_{11}}$ and $r_{22} = (i_{22})_{max} / \overline{i_{22}}$, where $(i_{11})_{max}$ and $(i_{22})_{max}$ are the maximum intensities of i_{11} and i_{22} while $\overline{i_{11}}$ and $\overline{i_{22}}$ are the corresponding intensities averaged over random cylinder orientations, respectively. r_{11} and r_{22} are seen to give the measure of flashing scattered light in a constant background of light scattered by randomly oriented cylinders. There are no simple correlations between r_{11} or r_{22} and either polarization or scattering angle, but in general longer cylinders have larger r_{11} or r_{22}; i.e., they exhibit more enhanced twinklings. The maximum value observed was $r_{22} = 34$ for the 12:1 cylinder shown in Fig. 1B at $\theta = 50°$.

(6) Away from the azimuth $\chi = \pi - \theta/2$ where specular scattering occurs, scattering by an oriented cylinder is considerably reduced in intensity, and the larger the aspect ratio the more conspicuous is this contrast.

(7) The RGD approximation for finite-cylinder scattering gave surprisingly good predictions for those with ice-like refractive indexes (see Figs. 1A-2F); e.g., as regards the angular locations and widths of the major and neighboring scattering lobes. Even the quantitative agreement with experiment in intensity versus azimuth profiles is unexpectedly close.

(8) According to Eq. (3b) there is no scattering at $\theta = 90°$ by RGD theory when both antennas are polarized parallel to the scattering plane. While this is roughly borne out by experiment for the two longer cylinders with lower refractive indexes (Figs. 1F & 2F), it is not the case for the 2:1 cylinder with higher refractive index (Fig. 3F).

(9) Despite the fact that RGD theory gives the worst predictions for the higher-refractive-index targets by overestimating (Fig. 3A) or underestimating (Figs. 3C, 3D, 3E, 3F) the absolute magnitudes of scattering intensities, it still foretells the occurrences and angular locations of major scattering lobes and in some cases the minor lobes as well (Fig. 3B).

SUMMARY

(1) An oriented finite cylinder may also specularly scatter the incident light in the same cone-shaped directions as the similarly oriented very long cylinder.

(2) The aspect ratio, or the length/diameter ratio, is a dominant determining parameter of such a cone profile, in that the larger the aspect ratio, the narrower is the angular width and the more sharply

peaked is this major scattering lobe. The lobe profile is also strongly dependent on both the incident polarization and the scattering angle.

(3) This main scattering lobe is accompanied by side lobes symmetrically surrounding it, the widths, intensity levels and angular positions of which again depend strongly on the aspect ratio. For shorter cylinders these side lobes, as well as the main lobe itself, become wider and less specular in intensity levels; i.e., the cone profiles are more smeared out.

(4) The Rayleigh-Gans-Debye approximation theory is seen to provide unexpectively good predictions of the above scattering features if the cylinder's refractive index is low. This argues strongly for development of even better theoretical methods.

ACKNOWLEDGMENT

The authors thank Dr. J.L. Weinberg for critical review of this article. This work was supported in part by the Army Research Office and the Army CRDC, Aberdeen, MD.

REFERENCES

1. P. Barber and C. Yeh, Scattering of electromagnetic waves by arbitrarily shaped dielectric bodies, Appl. Opt. 14 2864 (1975).

2. A. Cohen and C. Acquista, Light Scattering by tilted cylinders: properties of partial wave coefficients, J. Opt. Soc. Amer. 72 531 (1982).

3. L.D. Cohen, R.D. Haracz, A. Cohen and C. Acquista, Scattering of light from arbitrarily oriented finite cylinders, Appl. Opt. 22, 142 (1983).

4. D.D. Cooke and M. Kerker, Light Scattering from Long Thin Glass Cylinders at Oblique Incidence, J. Opt. Soc. Amer 59, 43 (1969).

5. H.C. van de Hulst, Light Scattering by Small Particles, Wiley, N.Y. (1957).

6. M. Kerker, The Scattering of Light and Other Electromagnetic Radiation, Academic Press, N.Y. (1969).

7. A.C. Lind and J.M. Greenberg, Electromagnetic Scattering by Obliquely Oriented Cylinders, J. Appl. Phys. 37, 3195 (1965).

8. D.W. Schuerman and R.T. Wang, Experimental Results of Multiple Scattering, Army CSL Contractor Rept., ARCSL-CR-81003 (Nov. 1981).

9. J.R. Wait, Scattering of a Plane Wave from a Circular Dielectric Cylinder at Oblique Incidence, Can. J. Phys. 33, 189 (1955).

10. R.T. Wang, J.M. Greenberg and D.W. Schuerman, Experimental Results of Dependent Light Scattering by Two Spheres, Opt. Lett. 6, 543 (1981).

11. R.T. Wang, Angular Scattering by Rough Particles, in Proc. of the 1984 CRDC Scientific Conference, R. Kohl and D. Stroud, eds., Army CRDC-SP-85007 pp. 327-363 (June 1985).

FIGURES

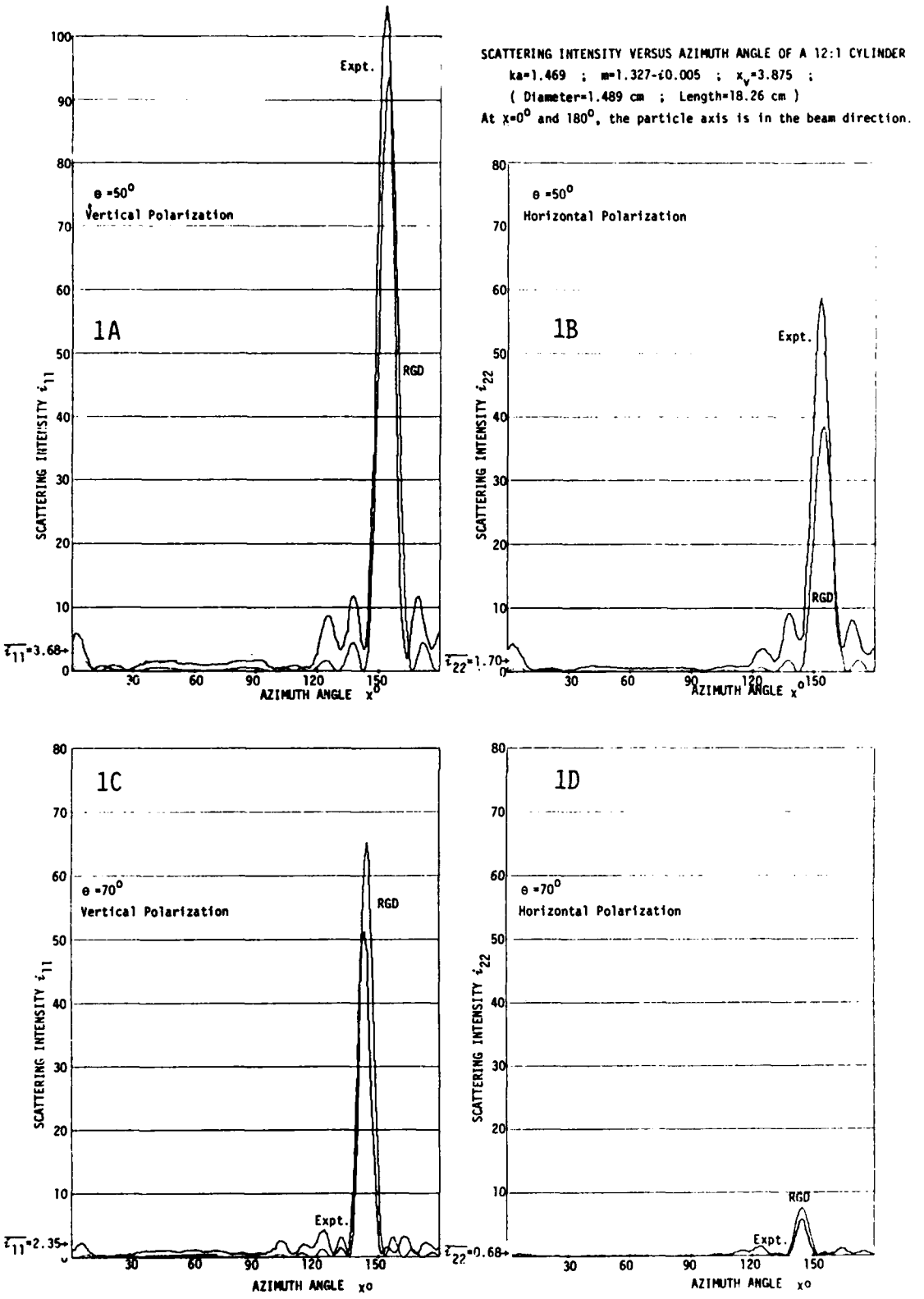

FIGURES 1A-1D. SCATTERING INTENSITY VERSUS PARTICLE AZIMUTH ANGLE. Experimental (marked Expt.) and theoretical (marked RGD) curves depicting the azimuth dependence of the scattering intensity for a 12:1 cylinder as its axis was continuously rotated through 180° in the scattering plane. Target parameters are shown on the upper right corners of this page. $\overline{i_{11}}$ or $\overline{i_{22}}$ on the lower left corner of each figure is the intensity averaged over *random cylinder orientations*, as measured by separate runs. See also Sec.II.

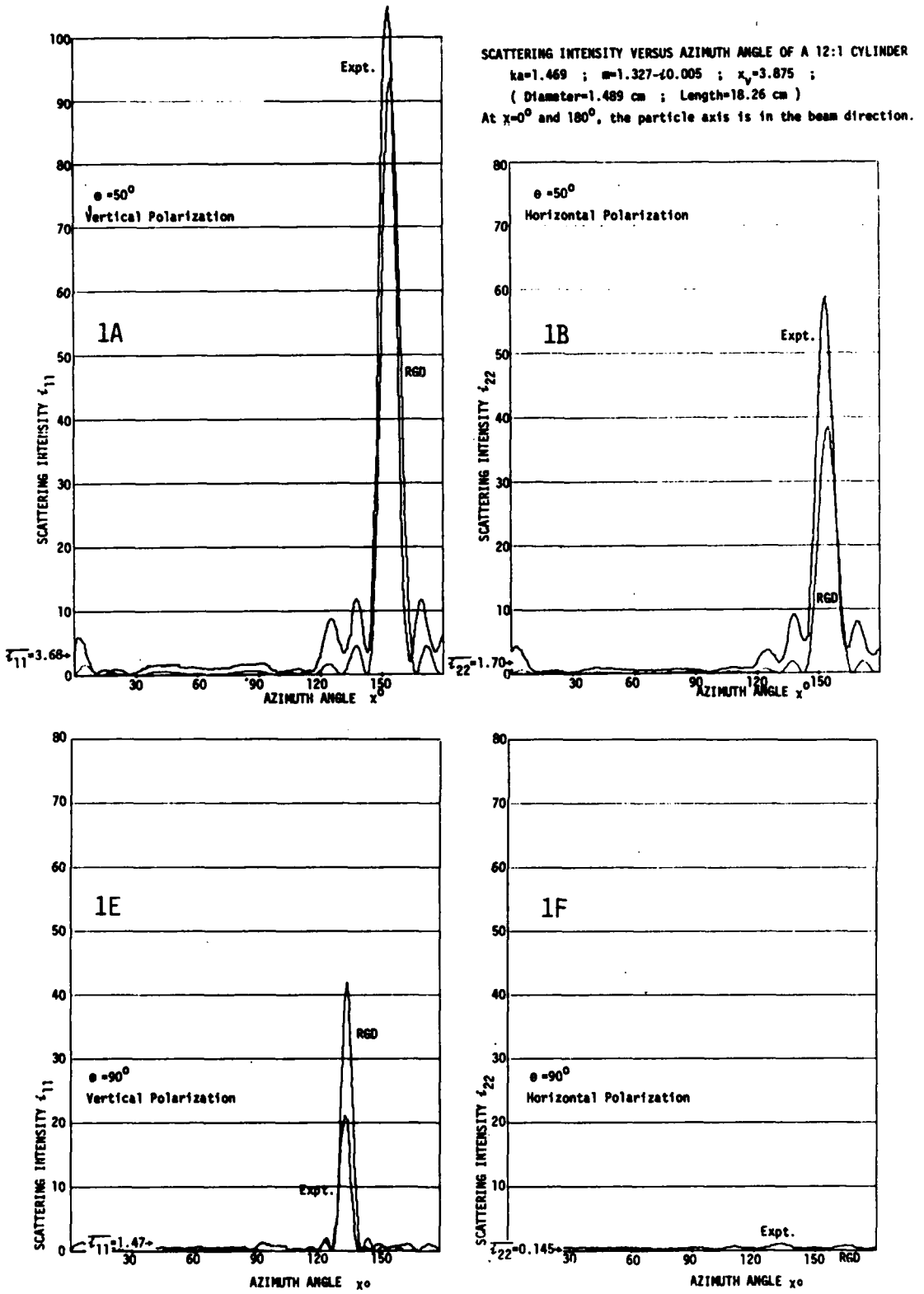

FIGURES 1A, 1B, 1E & 1F. SCATTERING INTENSITY VERSUS PARTICLE AZIMUTH ANGLE. Same as in the Figures 1A-1D.

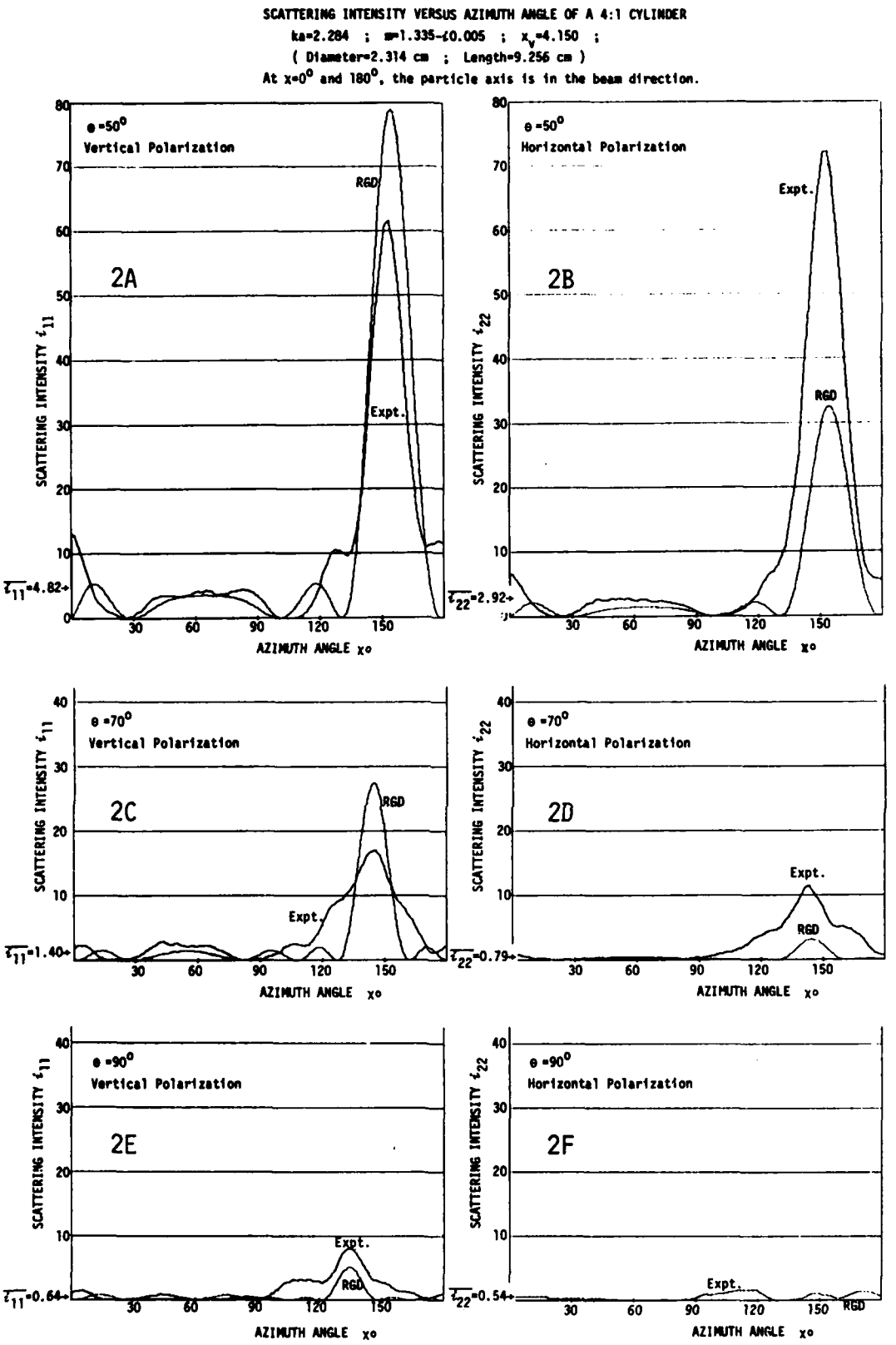

FIGURES 2A-2F. SCATTERING INTENSITY VERSUS PARTICLE AZIMUTH ANGLE. Experimental (marked Expt.) and theoretical (marked RGD) curves depicting the azimuth dependence of the scattering intensity for a 4:1 cylinder as its axis was continuously rotated through 180° in the scattering plane. Target parameters are shown on the top of this page. $\overline{i_{11}}$ or $\overline{i_{22}}$ on the lower left corner of each figure is the intensity averaged over random cylinder orientations, as measured by separate runs. See also Sec. II.

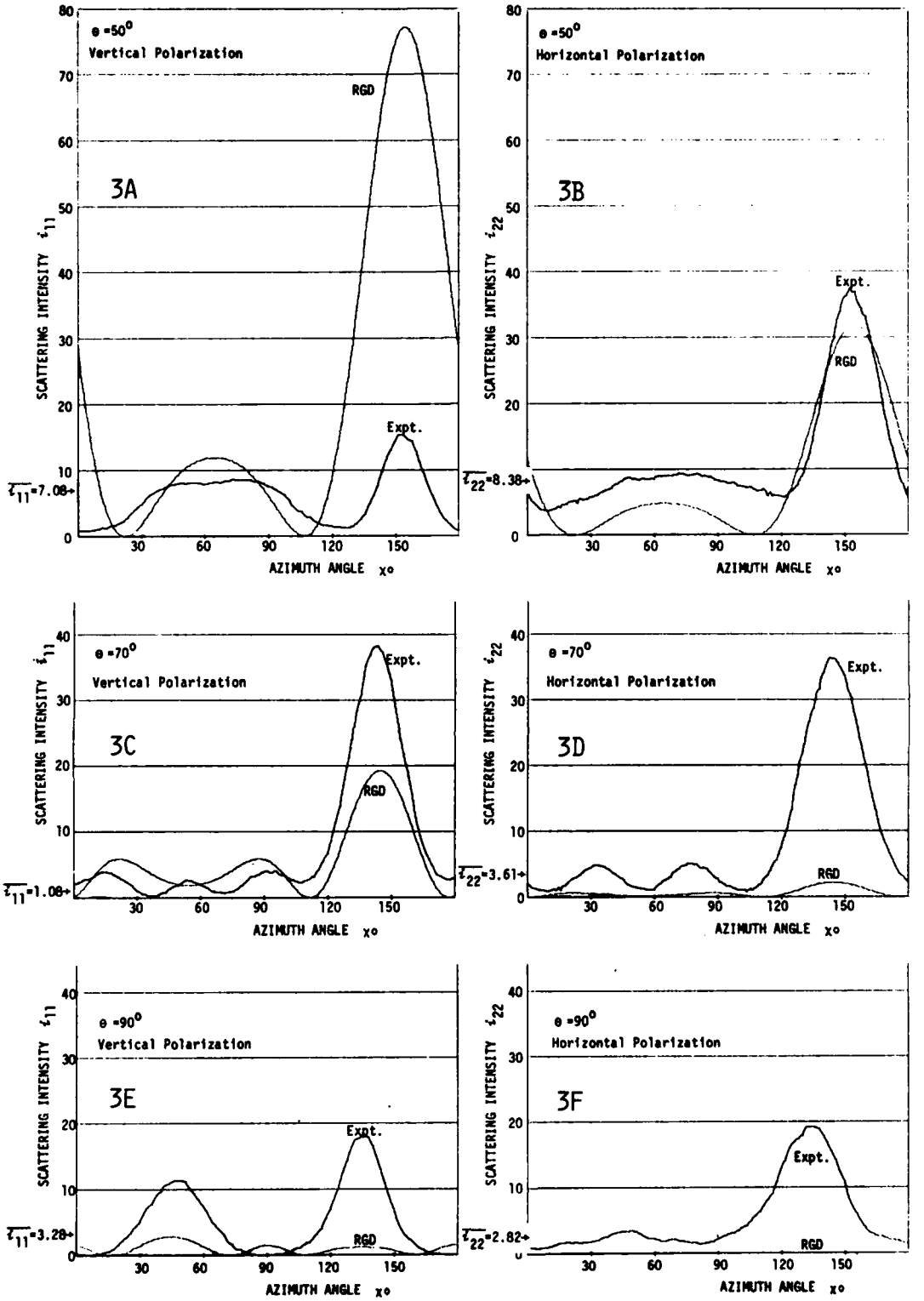

FIGURES 3A-3F. SCATTERING INTENSITY VERSUS PARTICLE AZIMUTH ANGLE. Experimental (marked Expt.) and theoretical (marked RGD) curves depicting the azimuth dependence of the scattering intensity for a 2:1 cylinder as its axis was continuously rotated through 180° in the scattering plane. Target parameters are shown on the top of this page. $\bar{i}_{11}$ or $\bar{i}_{22}$ on the lower left corner of each figure is the intensity averaged over *random cylinder orientations*, as measured by separate runs. See also Sec. II.

ANGULAR SCATTERING CURVES AND ASYMMETRY FACTORS FOR A CLUSTER OF RANDOMLY ORIENTED INFINITE CYLINDERS

Ariel Cohen*, Richard D. Haracz and Leonard D. Cohen

Department of Physics and Atmospheric Science

Drexel University

Philadelphia, Pennsylvania 19104

Recent Publications and Submittals for Publication and Presentations:

A) A. Cohen, R.D. Haracz and L.D. Cohen, 'Asymmetry Factors for Randomly Oriented Infinite Cylinders', Appl. Phys. 58, 1135 (1985).

B) R.D. Haracz, L.D. Cohen and A. Cohen, 'Scattering of Linearly Polarized Light from Randomly Oriented Cylinders and Spheroids', Appl. Phys. Nov. (1985).

C) A. Cohen, L.D. Cohen and R.D. Haracz, 'On the Optical Properties of Fibrous Insulation', Submitted to Appl. Phys. Communication

*On leave from the Dept. of Atmos. Sci., Hebrew Univ., Jerusalem

Abstract

The special geometry required for obtaining the optical scattering intensities for a cluster of randomly oriented fibers is discussed.

The geometry is also used to generalize the concept of asymmetry factor to include nonspherical long cylinders in order to calculate the ratio of the power of radiated light into the forward direction to the power of backscattering light.

Theory

The determination of the scattering intensity for the scattering of light from randomly-oriented long cylinders into a given direction in space requires the integration over all possible tilt angles between the incident direction of light and the cylinder axis. However, due to the unique properties of the scattering pattern of light from infinitely long cylinders, the integration cannot be performed by numerical integration over all possible orientations equally weighted. Account must be taken of the fact that very long cylinders, with aspect ratios exceeding 200 (aspect ratio = diameter/length), scatter light primarily along the surface of a cone whose vertex angle equals the angle between the direction of incidence and the cylinder axis.[6]

Let ϕ be the tilt angle between the direction of incidence and the axis of the cylinder. The angle between the incident light and the scattered light is denoted $2\phi_0$. It is customary to define the scattering angle θ as being measured in a plane perpendicular to the cylinder axis as shown in Fig. 2. If $2\phi_0$ is fixed, there are only two values of θ, (θ and $-\theta$) for which the cylinder contributes to the scattering. All other orientations of the same tilt angle ϕ produce negligible scattering as these orientations correspond to scattering off the cone. As a consequence, when determining the average intensity for the various possible orientations, care must be taken to select only those orientations that produce scattering along the cone. Inclusion of orientations that do not produce such scattering, as may occur when the integral is done in constant steps in the averaging process over all orientations, will result in erroneous results.

The scattering intensities of light obliquely incident on an infinite cylinder are given by

$$I_1 = \text{const.}\ |[b_{0I} + 2\sum_{n=1}^{\infty} b_{nI}\cos(n\theta)]\cos\gamma^{*} - i[2\sum_{n=1}^{\infty} b_{nII}\sin(n\theta)]\sin\gamma^{*}|^2. \quad (1)$$

$$I_2 = \text{const.}\ |[a_{oII} + 2\sum_{n=1}^{\infty} a_{nI}\cos(n\theta)]\sin\gamma^* - i[2\sum_{n=1}^{\infty} a_{nI}\sin(n\theta)]\cos\gamma^*|^2. \quad (2)$$

where b_{nI}, b_{nII}, a_{nI}, and a_{nII} are the scattering coefficients and γ^* is the polarization angle (see below). I_1 and I_2 are the polarized intensities in, and normal to the cylinder-scattering plane (formed by the cylinder axis and the direction of scattering).

The coefficients are dependent on the size parameter of the cylinder, $x = 2\pi a/\lambda$, the complex index of refraction $m = n - ik$ and the tilt angle ϕ. Here λ is the wavelength of the incident light and "a" the radius of the cylinder.

In order to solve the problem of the scattering of light by randomly oriented cylinders, five angles are used (see Fig. 1 of Haracz, Cohen and Cohen):

1) The scattering angle $2\phi_0$.

2) The angle of incident linear polarization α. This is measured relative to the scattering plane. (Note that the scattering plane containing the incident and the scattering light is different for each cylinder - the scattering plane is defined above).

3) The tilt angle 0 between the cylinder axis and the direction of incidence. We note that $\phi >= \phi_0$.

4) The scattering angle θ, measured on a plane normal to the cylinder axis.

5) The orientation angle γ, the azimuthal angle of the cylinder axis in the reference plane. This frame places z in the direction of incidence, and x in the scattering plane. Thus, the orientation angles of the cylinder axis in the reference frame are γ and ϕ. The angle γ^* appearing in eqs.(1) and (2) is is defined by

$$\gamma^* = \gamma + \alpha \quad (3)$$

As a direct result of the fact that light is scattered on the envelope of a cone, the angles θ, ϕ and ϕ_0 are related

$$\theta = 2 \sin^{-1}(\sin\phi_0 / \sin\phi) \tag{4}$$

The angles ϕ, ϕ_0 and γ are also related as

$$\phi = \tan^{-1}(\tan\phi_0 / \cos\gamma) \tag{5}$$

with $\phi \geq \phi_0$.

The summation over all tilt angles can now be performed by multiplying each intensity obtained for a particular tilt angle ϕ by a probability factor corresponding to this tilt angle:

$$P(\phi, \phi_0) = \sin 2\phi / \sin\phi_0 \tag{6}$$

where $\phi = \phi(\gamma)$ by Eq.(5), and it is shown that

$$\int_0^{\pi/2} P(\phi, \phi_0)\, d\gamma = \pi/2 \ , \tag{7}$$

for any value of ϕ_0 .

This result reflects the important fact that the same number of cylinders is participating in the scattering of light in any given direction. (References for equation 6 and 7 - see (B)).

Angular Scattering Curves

We calculate the intensities for the wavelength 10 microns incident on cylinders with the complex index of refraction m = 1.85 - i0.033 i. The size parameter x = 7.3513. These values are used by N.L. Mckay el al. (J.A. P.55, 1984), in which a different averaging process was used that required a compensation factor for a singularity in the averaging integral. Our averaging process is nonsingular and requires no compensation factor. The intensities I_1 and I_2 in relative units are plotted against the scattering angle $2\phi_0$ in Fig. 1 for $\alpha = 0$. (incident light linearly polarized in the scattering plane). Fig. 1 also contains these intensitites for $\alpha = \pi/2$ (incident light linearly polarized perpendicular to the scattering plane). It is important to point out that each point in these curves involves calculations of contributions of several tilted cylinders which are not necessarily in the scattering plane and for which cross-component terms (see eqs. (1) and (2)) must be taken into account. The curves have a few of the basic characteristics of the intensities for the scattering of light from a sphere with a similar size parameter. These characteristics are

1) A strong forward scattering value.
2) A minimum in the region of 70 to 120 degrees of scattering angle.
3) A backscatter value approximately one order of magnitude smaller than the forward scattering value.
4) The number of maxima roughly equal to the value of the size parameter.

We note that no divergence appears,as is physically expected. This leads to the conclusion that our method of averaging over cylinders using the constraints imposed by scattering on the envelope of a cone overcomes the difficulties reported by Mckay et al.

Asymmetry Factor for Infinite Cylinders.

One of the main optical parameters in the study of heat transport through fibrous media is the amount of radiative power scattered into the forward hemisphere versus the power scattered in the backward direction. In the case of spherical particles, this ratio is called the asymmetry factor f and for spheres larger that the wavelength of light [$x = (2\pi a/\lambda) > 1$] it's form is

$$f(x) = \int_0^1 I(\mu, x, m)\, d\mu \Big/ \int_{-1}^1 I(\mu, x, m)\, d\mu > 1/2 \qquad (8)$$

where $\mu = \cos\theta$, θ is the scattering angle and m is the complex relative index of refraction.

This equation cannot be used for the definition of the asymmetry factor for cylinders since the scattering angle 0 is not defined relative to the direction of the incident light. We shall therefore define the scattering angle for light scattering from a long cylinder and the geometry required for a proper definition of the asymmetry factor.

Consider Fig. 2 where the incident light is along the z-axis, the target axis is z_c, and the scattered direction is z'. The direction of incident polarization defines the x axis and the incident polarization frame xyz. We can then orient the target axis z_c relative to the frame xyz using the spherical angles ϕ (tilt or polar angle) and y (azimuthal angle).

For long cylinders, the scattering is along the surface of a cone whose apex is at the origin (Figs. 2 and 3), and whose base has its center, denoted 0_c, on the target axis z_c. This geometry is illustrated in Fig. 3. Any line from the origin to the periphery of the base of the cone is a possible scattering direction. Thus, the lines OA (forward scattering) and OB (arbitrary) are possible scattering

directions. The direction OB can then be defined by the angle 0, measured in the conic base counterclockwise about z_c.

The base of the cone intersects the xy plane along the line CD, as shown in Fig. 3. Thus, the lines OC and OD are scattering directions perpendicular to the incident direction, and their respective scattering angles are $\theta = \theta_A$ and $\theta = -\theta_A = 2\pi - \theta_A$. Forward scattering then corresponds to the range of scattering angles

$$0 < \theta < \theta_A , \qquad 2\pi - \theta_A < \theta < 2\pi$$

and backward scattering corresponds to the range $0_A < \theta < (2\pi - 0_A)$.

We can now proceed to the definition of the observable quantities. The scattered plane is defined by z and z', and the intensities for the scattering of light parallel and perpendicular to the scattering plane are given by eqs. (1) and (2). As mentioned above (eq. (4)) the scattering angle θ, the tilt anlge ϕ and ϕ_o, where $2\phi_o$ is the angle between z and z' are related. We are interested in forward scattering for which the scattered light is in the forward hemsiphere (above the xy plane). If the tilt angle 0 of the cylinder axis is less than 45°, all scattering directions will be forward. For $\phi > 45^\circ$, the critical scattering angles $-\theta_A$ for scattering perpendicular to the direction of incidence are shown in Fig. 3. These are found from Eq. (4) be setting $\phi_o = 45^\circ$:

$$\theta_A = +-|2 \sin^{-1}[1/\sqrt{2} \sin \phi)]| \qquad (9)$$

The asymmetry factor for a long cylinder can now be defined as the ratio of the power scattered into the forward hemisphere to the total power.

$$\rho(\phi, \gamma') = \int_{-\theta_A}^{\theta_A} (I_1 + I_2)\, d\theta \Big/ \int_{-\pi}^{\pi} (I_1 + I_2)\, d\theta \qquad (10)$$

For a cloud of randomly oriented cylinders, the average value of this factor is found by summing the effects of scattering for all possible values of the orientation angles and

$$\rho_{ave} = \left(\int_0^{2\pi} d\gamma' \int_0^{\pi/2} \sin\phi\, d\phi \int_{-\theta_A}^{\theta_A} (I_1 + I_2)\, d\theta\right) \Big/ \left(\int_0^{2\pi} d\gamma' \int_0^{\pi/2} \sin\phi\, d\phi \int_{-\pi}^{\pi} (I_1 + I_2)\, d\theta\right) = I_I / I_{II} \qquad (11)$$

Asymmetry Factors - Calculations

Denoting,

$$A = \int_{-\theta_A}^{\theta_A} I_1\, d\theta, \quad B = \int_{-\theta_A}^{\theta_A} I_2\, d\theta,$$

we get

$$A = \int_{-\theta_A}^{\theta_A} \cos^2\gamma^* \left|b_{0I} + 2\sum_{n=1}^{\infty} b_{nI} \cos(n\theta)\right|^2 d\theta$$

$$+ \int_{-\theta_A}^{\theta_A} \sin^2\gamma^* \left|2\sum_{n=1}^{\infty} b_{nII} \sin(n\theta)\right|^2 d\theta$$

$$- \int_{-\theta_A}^{\theta_A} \sin 2\gamma^* \operatorname{Im}\left[\left(b_{0I} + 2\sum_{n=1}^{\infty} b_{nI} \cos(n\theta)\right) \times \left(2\sum_{n=1}^{\infty} b_{nII}^{*} \sin(n\theta)\right)\right] d\theta \qquad (12)$$

The quantity A is the power radiated into the forward hemisphere for scattered light polarized parallel to the scattering plane, and it is more compactly expressed as

$$A = A_1 \cos^2\gamma^* + B_1 \sin^2\gamma^* - C_1 \sin(2\gamma^*) \tag{13}$$

where A_1, B_1 and C_1 are evident from the preceding equation, and are not dependent on γ^*. Therefore, for a cloud of randomly oriented fibers, the integration over γ^* results in averaging $\cos^2\gamma^*$, $\sin^2\gamma^*$, and $\sin(2\gamma^*)$.

Similarly

$$\begin{aligned} B = & \int_{-\theta_A}^{\theta_A} \sin^2\gamma^* \left| a_{0\perp} + 2\sum_{n=1}^{\infty} a_{n\perp\perp} \cos(n\theta) \right|^2 d\theta \\ & + \int_{-\theta_A}^{\theta_A} \cos^2\gamma^* \left| 2\sum_{n=1}^{\infty} a_{n\parallel} \sin(n\theta) \right|^2 d\theta \\ & - \int_{-\theta_A}^{\theta_A} \sin(2\gamma^*) \operatorname{Im}\left[\left(a_{0\perp\perp} + 2\sum_{n=1}^{\infty} a_{n\perp\perp} \cos(n\theta)\right) \right. \\ & \left. \times \left(2\sum_{n=1}^{\infty} a_{n\parallel}^* \sin(n\theta)\right)\right] d\theta \\ = & A_2 \sin^2\gamma^* + B_2 \cos^2\gamma^* - C_2 \sin(2\gamma^*) \end{aligned} \tag{14}$$

The quantities A_i, B_i, C_i ($i = 1,2$) can be integrated in closed form,

$$A_1 = 2|b_{0\perp}|^2 \theta_A + 4\sum_{n=1}^{\infty} |b_{n\perp}|^2 [\theta_A + \sin(2n\theta_A) / (2n)]$$

$$+ \sum_{n=1}^{\infty} (8\mathrm{Re}(b_{0I} b_{nI}^{*}] \sin(n\theta_A) / n + \sum_{m=n+1}^{\infty} 8\mathrm{Re}[b_{nI} b_{mI}^{*}]$$

$$x\,[\sin(n-m)\theta_A/(n-m) + \sin(n+m)\theta_A/(n+m)]) \qquad (15)$$

As B_1 does not contain zero-order partial waves its integrated form is

$$B_1 = 4 \sum_{n=1}^{\infty} |b_{nII}|^2 [\theta_A + \sin(2n\theta_A)/(2n)]$$

$$+ \sum_{n=1}^{\infty} \sum_{m=n+1}^{\infty} 8\mathrm{Re}[b_{nII} b_{mII}^{*}][\sin(n-m)\theta_A/(n-m)$$

$$- \sin(n+m)\theta_A/(n+m)]. \qquad (16)$$

Finally, the quantity C_1 contains integrals of $\sin(n\theta)$ and $\sin(n\theta)\cos(n\theta)$ which vanish when the limits are $-\theta_A$ and θ_A. However, for integrating the amount of light scattered between θ_A and θ_B, C_1 has the form

$$C = 2 \sum_{n=1}^{\infty} \mathrm{Im}(-[b_{0I} b_{nII}^{*}] \cos(n\theta)/n + \sum_{\substack{m=1 \\ m \neq n}}^{\infty} [b_{nII} b_{mII}^{*}][\cos(n-m)\theta/(n-m)$$

$$- \cos(n+m)\theta/(n+m)] - 2[b_{nI} b_{nII}^{*}]\cos(2n\theta)/2n)) \qquad (17)$$

and $C_1 = C(\theta_B) - C(\theta_A)$.

The expressions for A_2, B_2, and C_2 can be obtained from these by replacing

b_{nI} and b_{nII} by a_{nII} and a_{nI}, respectively.

Results

Fig.4 shows the asymmetry factor ρ_{ave} averaged over the possible orientations of the cylinder as defined above. This parameter is plotted against the size parameter. The behavior is seen to be highly oscillatory with a period of about 15 units that damps as x increases. It is also observed that the mean value of ρ_{ave} decreases with x.

The results should be of value in applications involving the transmission of electromagnetic radiation through media that contain randomly oriented long cylinders, for example, fibrous insulating material.

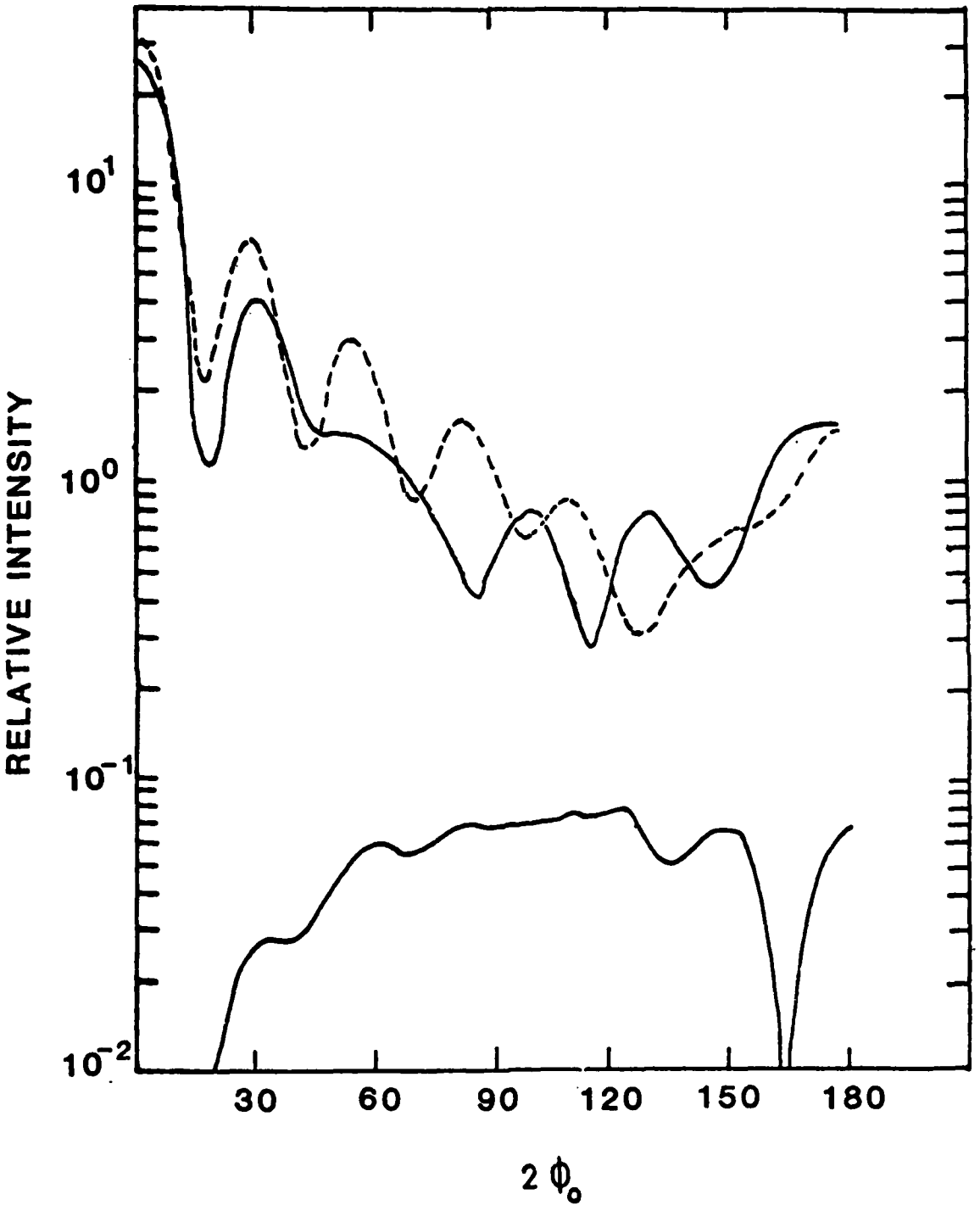

Fig.1. Relative intensities of randomly oriented cylinders versus the scattering angle $2\phi_0$. The top curves are I_1 for $\alpha = 0$ (solid) and I_2 for $\alpha = \pi/2$ (dashed). The bottom curve is I_2 for $\alpha = 0$ and I_1 for $\alpha = \pi/2$.

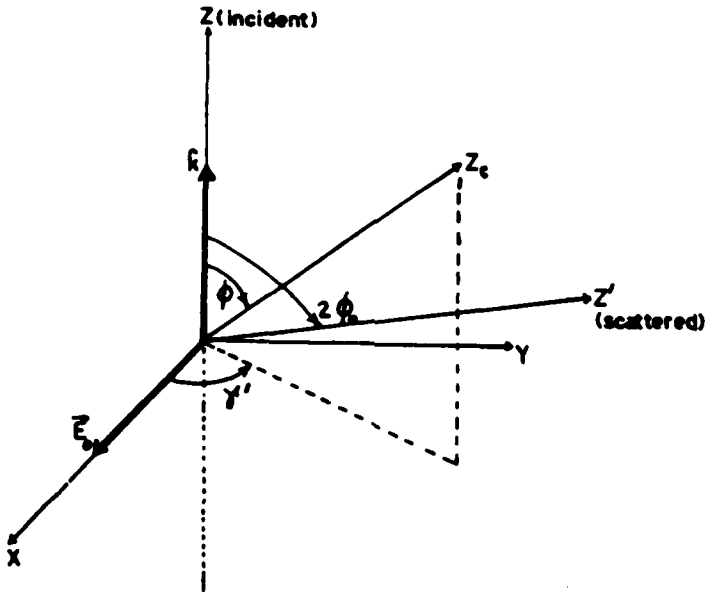

Fig.2. The geometry for the scattering process. The light is incident along the z-axis, and polarized along the x-axis. The light is then scattered along the z'-axis and $2\phi_0$ is the angle between the incident and scattered directions. The cylinder axis is denoted z_c, and its orientation angles with respect to xyz are ϕ (tilt angle) and γ'(azimuthal angle).

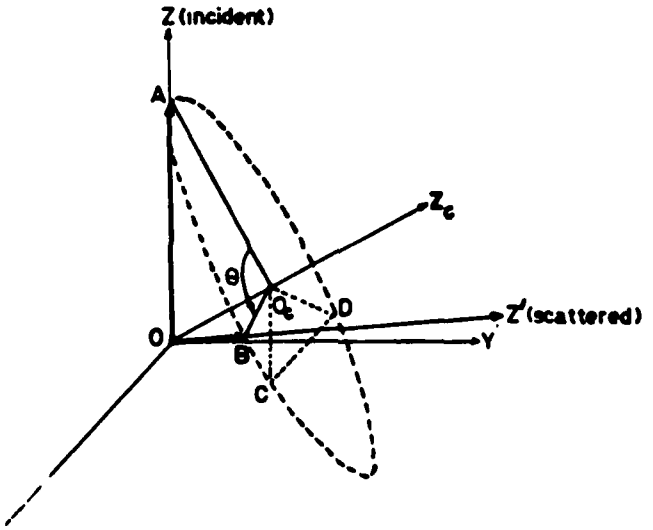

Fig.3. For scattering of light from an infinite cylinder, the scattering is along the element of a cone as shown. The scattering angle θ is measured on the base of the cone counterclockwise from A (forward direction).

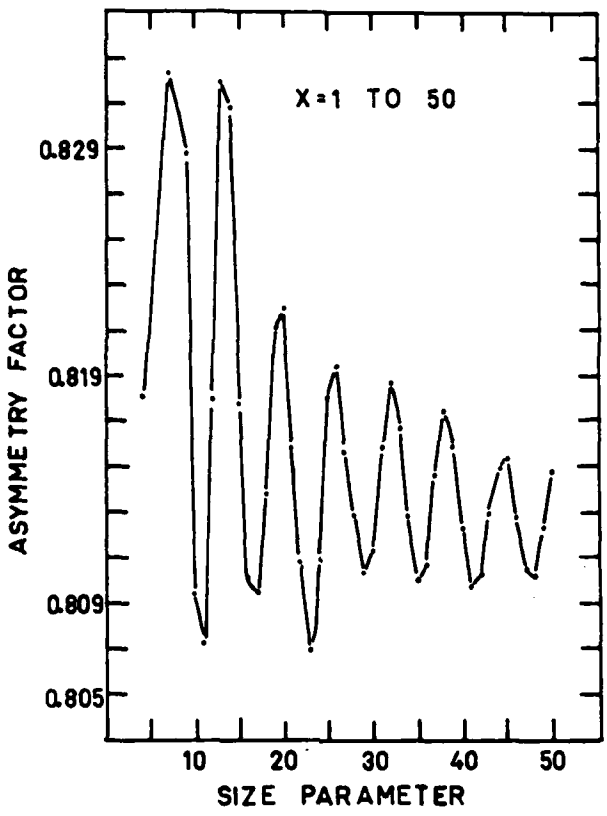

Fig.4. The asymmetry factor averaged over all possible orientations of the scattering cylinder versus size parameter.

SUPERPOSITION PRINCIPLE FOR CIDS BY HEIRARCHICAL MOLECULAR STRUCTURES

Chris W. Patterson, Shermila B. Singham, Gary C. Salzman
University of California
Los Alamos National Laboratory
Los Alamos, New Mexico 87545

and

Carlos Bustamante
Department of Chemistry
University of New Mexico
Albuquerque, New Mexico 87131

RECENT SUBMITTALS FOR PUBLICATION:

A) C. W. Patterson, S. B. Singham, G. C. Salzman, and C. Bustamante, "Circular Intensity Differential Scattering of Light by Heirarchical Molecular Structures," submitted to J. Chem. Phys., August 1985.

B) S. B. Singham and G. C. Salzman, "Evaluation of the Scattering Matrix of an Arbitrary Particle Using the Coupled Dipole Approximation," submitted to J. Chem. Phys., August 1985.

ABSTRACT

We show that circular intensity differential scattering (CIDS) of light by macromolecules with different levels of chiral structure is the superposition of the CIDS from each individual level. As an example, we treat a model superhelix with anisotropic polarizability.

INTRODUCTION

The theory of the circular intensity differential scattering (CIDS) has previously been considered for molecules with one level of chiral structure.[1-8] In this paper we study the CIDS for a model superhelix with two levels of chiral structure. Because we are most often dealing with macromolecules in solution, we will only consider the CIDS resulting from an orientational average. We show that the CIDS of the orientationally averaged superhelix is the superposition of the CIDS for each of the two separate orientationally averaged helices which comprise the superhelix. We give heuristic arguments to show that this superposition principle is quite general and applies to any number and type of chiral structure for which orientational averaging is appropriate.

The consideration of hierarchical structure of molecules also provides an understanding of the theoretical basis for using effective polarizabilities for the 'aggregates' which comprise the last level of a macromolecule's structure. It is important to know whether it is possible to average the polarizability of lower order structures in order to obtain effective polarizabilities for higher order structures. In this paper we give examples which help to confirm this averaging principle for anisotropic polarizabilities.

The theory of CIDS for orientationally averaged structures with anisotropic polarizabilities has been developed extensively by Bustamante, Maestre, and Tinoco.[4] We describe this theory briefly below and refer the reader to the referenced works above for more detail.

CIDS THEORY

We wish to determine the far electric field due to a radiating dipole $\vec{p}_n$ at point $\vec{r}_n$,

$$\vec{p}_n = \vec{\vec{\alpha}}_n \cdot \vec{E}_o, \tag{1}$$

induced by the incident field $\vec{E}_0$ where the polarizability at point $\vec{r}_n$ is given (on principal axes)

$$\vec{\vec{\alpha}}_n = \alpha_i^n \vec{e}_i \vec{e}_j \delta_{ij} \tag{2}$$

The scattered field at $\vec{r}'$ with wave vector $\vec{k}'$ and incident wave vector $\vec{k}$ from a collection of such radiating dipoles is given (using the first Born approximation) by

$$E(\vec{r}') = Ce^{ik'r'}(\hat{1}-\vec{k}'\vec{k}')\cdot\Sigma_n e^{i\Delta\vec{k}\cdot\vec{r}_n}\vec{\vec{\alpha}}_n\cdot\vec{E}_o \tag{3}$$

where

$$\Delta\vec{k} = \vec{k}'-\vec{k}. \tag{4}$$

The orientational average for the difference in total scattered intensity, I_L-I_R, with left and right circularly polarized light incident, given by Bustamante et al,[4] is then of the form

$$I_L - I_R = \frac{C'}{2}\sum_{i,j}\alpha_i^*\alpha_j(\vec{e}_i\times\vec{e}_j)\cdot\hat{R}_{ij}\{[(\vec{e}_i\cdot\vec{e}_j)(j_2/q-j_1) - (\vec{e}_i\cdot\hat{R}_{ij})(\vec{e}_j\cdot\hat{R}_{ij})(5j_2/q-j_1)](\sin\beta + \sin^3\beta)\} \tag{5}$$

where the argument of the spherical Bessel functions (j_1 and j_2),

$$q = 4\pi R_{ij}/\lambda, \tag{6}$$

is omitted for simplicity, and

$$\vec{R}_{ij} = \vec{r}_j-\vec{r}_i \tag{7}$$

is the distance vector between dipoles. The angle β is half the scattering angle and is 90° for backward scattering. All components of all dipoles are included in the sums of Eq. (5).

Eq.(5) is the starting point for all our calculations of CIDS arising from helices and superhelices. Although normally the CIDS signal is normalized to the total scattered intensity I_L+I_R, we shall see that such a normalization conceals the superposition principle which we develop below As a result, we shall identify CIDS as synonymous with the orientationally averaged I_L-I_R given in Eq.(5). When calculating CIDS using Eq.(5) we let C=1 and α_i=1.

SUPERPOSITION PRINCIPLE

We now apply Eq.(5) to calculate the CIDS from the superhelix shown in Fig.1a. The result is shown in Fig.1b where we have assumed the polarization is everywhere tangential to the superhelix ($\vec{e}_1$=tangent vector). One can observe in Fig.1b a high frequency oscillation superimposed on a low frequency one. In general, the higher frequency oscillation in reciprocal $\vec{k}$-space of CIDS corresponds to the larger structure in real $\vec{r}$-space. One might expect, then, that the observed high and low frequency oscillations in Fig.1b might correspond to the CIDS of the large and small helices, respectively, in Fig.1a.

In order to see this behavior, we calculate the CIDS separately for the small and large helices which comprise the superhelix. In Fig.2a we show the small helix and in Fig.2b its resulting CIDS using tangential polarizability as before. In Fig.3a we show the large helix and in Fig.3b its resulting CIDS. The question arises as to what polarizability one uses for the large helix. We simply place the dipoles on the large helix by translating the respective dipoles we used for the superhelix. This is possible when the radius of the small helix is much less than the radius and pitch of the large helix comprising the superhelix.

Calculations show that further simplification is possible. We may average the dipole vector over the turns of the small helix when its pitch is much less than the radius and pitch of the large helix comprising the superhelix. Such an average results in only a tangential component of the induced dipole on the large helix. We have indeed used this approximation to find the CIDS for the large helix shown in Fig.3b.

In Fig.4 we compare the CIDS from the superhelix in Fig.1b with the sum of the CIDS for the separate small and large helices in Fig.2b and Fig3b. The agreement is quite good and confirms the superposition principle. Note that, in general, the superposition principle would not work had we followed standard procedure and normalized the CIDS with the total intensity I_L+I_R.

Comparing Fig.1b and Fig.2b it is evident that the CIDS of the superheli· oscillates about the CIDS of the small helix. This is just a representation in reciprocal space of the fact that the superhelix oscillates about the large helix in real space! Thus the difference of scales of hierarchical levels in real space implies different scales of hierarchical levels in CIDS as well.

The existence of a discernible hierarchy in CIDS allows one to apply a smoothing function to extract the CIDS arising from the small structure component. For multiple levels of structure, such a smoothing function can be applied repetitively and the CIDS signal at each level can be extracted sequentially until only the CIDS from the largest structural component remains. Conversely, if there is

no visually discernible hierarchy in real space, there will be none in the CIDS. Signal smoothing will not work and the superposition principle will not apply.

We have shown that the CIDS arising from chiral molecules with hierarchical levels of structure is the superposition of CIDS from each of the individual levels. This principle allows us to treat the different levels of structure of a macromolecule on an equal footing. We contrast this with the situation in crystal diffraction where the different levels of structure result in a signal product instead of a signal sum. For the superposition principle to be valid, it is necessary that the CIDS result from an orientational average of the macromolecule and that the different levels of structure be readily discernible.

ACKNOWLEDGMENTS

This work was carried out under the auspices of the U. S. Department of Energy and was supported in part by Mesa Diagnostics, Inc., Los Alamos, New Mexico.

REFERENCES

1. C. Bustamante, M. F. Maestre, and I. Tinoco, Jr., J. Chem. Phys. 73, 4273 (1980).
2. C. Bustamante, M. F. Maestre, and I. Tinoco, Jr., J. Chem. Phys. 73, 6046 (1980).
3. C. Bustamante, I. Tinoco, Jr., and M. F. Maestre, J. Chem. Phys. 74, 4839 (1981).
4. C. Bustamante, I. Tinoco, Jr., and M. F. Maestre, J. Chem. Phys. 76, 3440 (1982).
5. S. Zietz, A. Belmont, and C. Nicolini, Cell Biophys. 5, 163 (1983).
6. W. M. McClain, J. A. Schauerte, and R. A. Harris, J. Chem. Phys. 80, 606 (1984).
7. C. Bustamante, M. Maestre, D. Keller, and I. Tinoco, Jr., J. Chem. Phys. 80, 4817 (1984).
8. D. Keller, C. Bustamante, M. Maestre, and I. Tinoco, Jr., Biopolymers 24, 783 (1985).

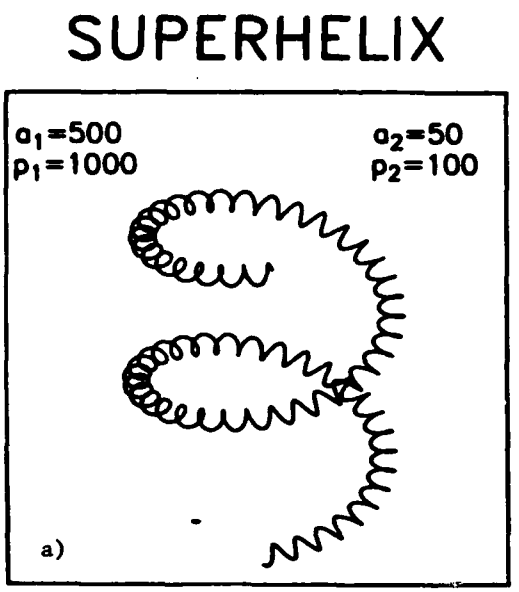

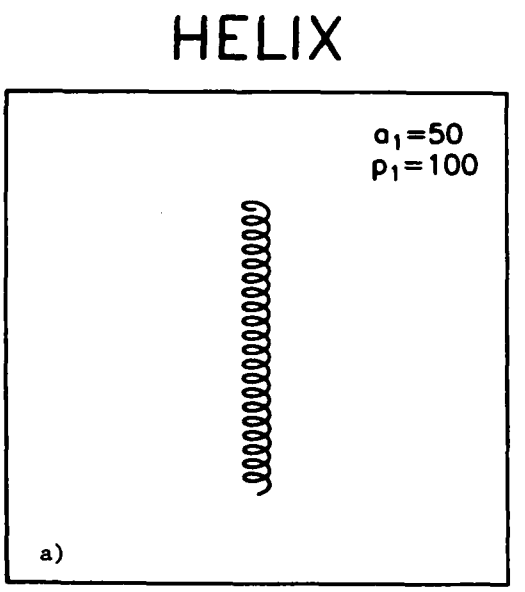

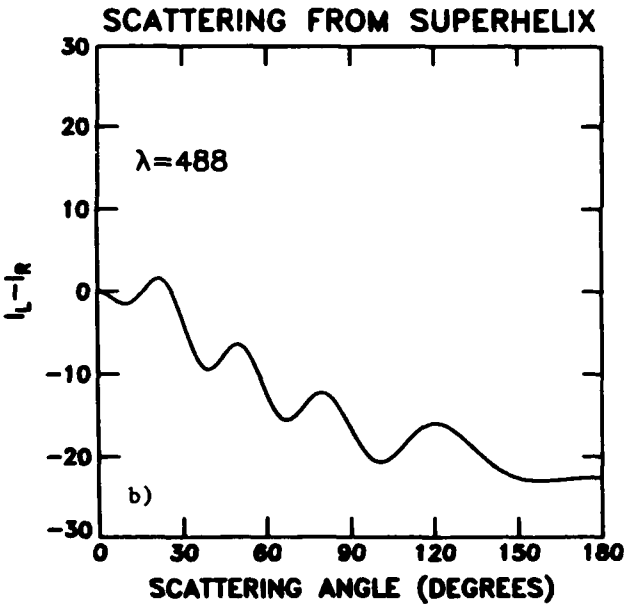

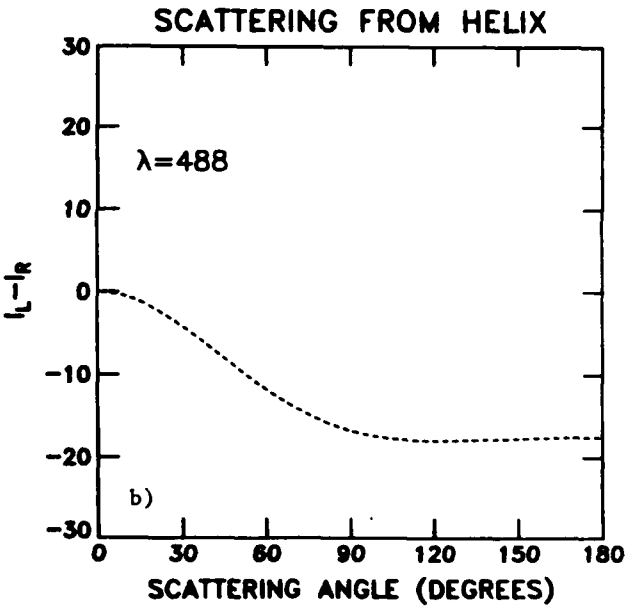

FIGURE 1. CIDS FROM SUPERHELIX. a) Superhelix with radius and pitch dimensions shown. There are ≈32 turns of the small helix per turn of the large helix. b) CIDS from 1 turn of superhelix with 3 dipoles per turn of small helix. The dipoles are directed tangential to the superhelix. A total of 96 dipoles were used.

FIGURE 2. CIDS FROM SMALL HELIX a) Small helix of the superhelix with radius and pitch dimensions shown. b) CIDS from 32 turns of the small helix with 3 dipoles per turn. The dipoles are directed tangential to the small helix.

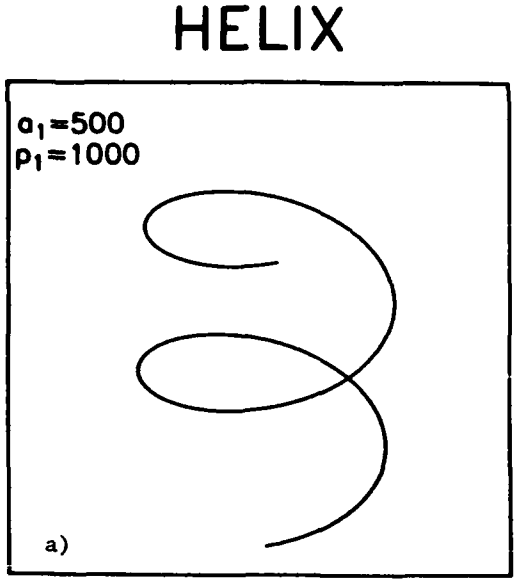

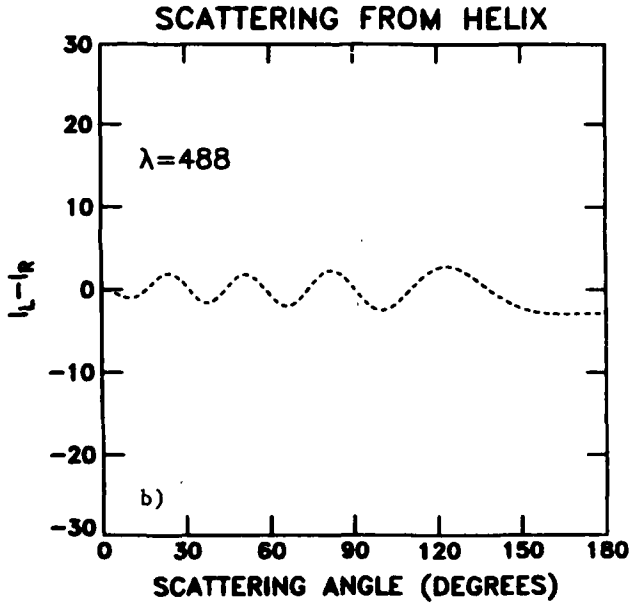

FIGURE 3. CIDS FROM LARGE HELIX. a) Large helix of the superhelix with radius and pitch dimensions shown. b) CIDS from 1 turn of the large helix with 96 evenly spaced dipoles corresponding to those translated from the superhelix.

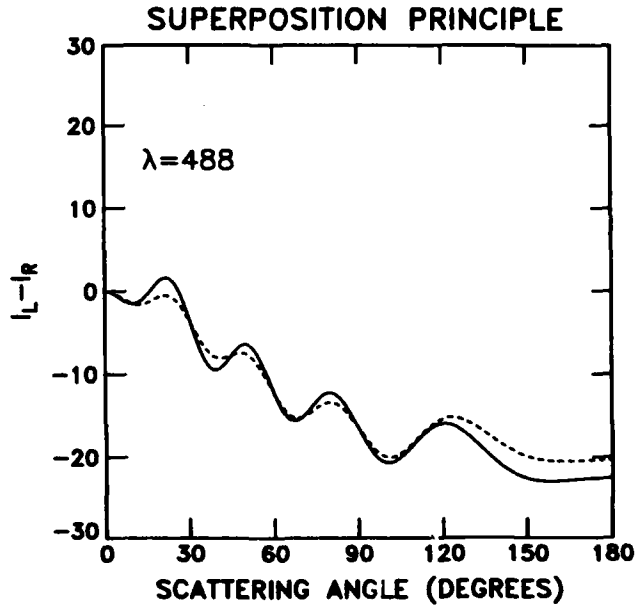

FIGURE 4. SUPERPOSITION PRINCIPLE. Comparison of the CIDS from the superhelix in Fig. 1b (solid line) with the sum of the CIDS from the individual small and large helices (dashed line) comprising the superhelix. The dashed line here is the sum of the dashed lines in Fig. 2b and Fig. 3b.

The Scattering of Linearly Polarized Light from a Dielectric Spiral.

Leonard D. Cohen

Richard D. Haracz

and

Ariel Cohen

Department of Physics and Atmospheric Science

Drexel University

Philadelphia, Pennsylvania 19104

Recent Publications and Submittals for Publication and Presentations:

A) A. Cohen, R.D.Haracz, and L.D. Cohen, 'Asymmetry Factors for Randomly Oriented Infinite Cylinders,' Appl. Phys. 58, 1135 (1985).

B) R.D.Haracz, L.D.Cohen, and A. Cohen, 'Scattering of Linearly Polarized Light from Randomly Oriented Cylinders and Spheroids,'Appl. Phys., Nov. 1985.

C) A. Cohen, L.D.Cohen, and R.D.Haracz, 'On the Optical Properties of Fibrous Insulation,' submitted to Appl. Phys. Communications.

D) R.D.Haracz, L.D. Cohen, and A. Cohen, 'The Scattering of Light by a Dielectric Helix of Finite Cross Section in the Shifrin Approximation,' in progress.

ABSTRACT

The integro-differential equation developed by Shifrin for scattering by tenuous particles and extended by Acquista is used as the basis for a model for scattering by a dielectric spiral. In order to develop the model it is necessary to carefully delineate the scattering geometry and the geometry of the spiral.

Introduction

Shifrin's approach to the solution of Maxwell's equations for the scattering of a plane wave from an isotropic and non-magnetic medium can be expressed by the

integro-differential equation

$$\vec{E}(\vec{r}) = \vec{E}_0 \exp(i\vec{k}_0 \cdot \vec{r}) + (\text{grad div} + k_0^2) \int d^3r' \exp(ik_0|\vec{r}-\vec{r}'|)(m^2-1)\vec{E}(\vec{r}')$$

where $\vec{E}(\vec{r})$ is the electric field far from the scattering medium,

$\vec{E}_0 \exp(i\vec{k}_0 \cdot \vec{r})$ represents the incident plane wave,

and m is the index of refraction.

A direct solution to this equation might be obtained by evaluating $\vec{E}(\vec{r})$ at many points inside the scatterer and solving for these values by a matrix inversion technique. This would be a prohibitively complicated approach. Another more manageable possibility is to estimate the E field inside the target medium and use this as the start of an iterative approach. In fact, in the Rayleigh-Gans-Rocard approximation the external plane wave is used for the internal field.

Shifrin's approach adopts a more realistic choice for the lowest order approximation to the internal field, specifically, the internal solution for the scatterer placed in a uniform electrostatic field. Acquista found that Shifrin's solution, which was appropriate for values of $ka < 1$ was unnecessarily restrictive on theoretical grounds. Another drawback of Shifrin's approach is that his derivation of the scattered fields depends heavily on the geometry of the scattering particle. Thus, for scatterers of different shapes, the entire derivation must be repeated.

Acquista used a Fourier-transform technique which changed the integro-differential equation of Shifrin into a pure integral equation. Futhermore, the scatterer's shape dependence can be extracted as a separate integral over the volume of the scatterer provided the electric field is constant throughout the target. This leaves the rest of the formulation independent of the scatterer's shape. Thus, in principle, scattering by a dielectric helix involves determining the "pupil"(or shape) function for sections of the helix where the field can be assumed constant and then multiplying this function by the general first order scattering solution. The second order solution in the iterative scheme used necessarily involves a much more complex integration.

As mentioned above, the Shifrin-Acquista technique provides an improvement over the Rayleigh-Gans-Rocard calculation in the first iterate by assuming an internal solution which is the solution of the equivalent electrostatic problem. This approach has produced quite accurate results for spheres, spheroids, and cylinders for which the equivalent electrostatic problems are soluable. In the case of the helix the authors are unaware of any solution of a dielectric helix in a uniform electrostatic field. Thus, one must appeal to other notions to obtain the first order estimate of the internal field. What has been done is to break the spiral into a number of disks. The electrostatic solution for a disk arbitrarily oriented with respect to a uniform field is known. This internal field does of course vary from disk to disk. In the sections to follow , the details of the somewhat complex geometry is presented along with the integral formulation of the spiral shape function.

The geometry of scattering

The reference frame is shown in Fig.1. It indicates the incident direction, the scattered direction, and the direction of polarization. Fig.2 indicates the spiral coordinate system and it s relation to the reference frame. The spiral frame is related to the reference frame by two rotations:

$$\begin{vmatrix} x_S \\ y_S \\ z_S \end{vmatrix} = R_{\hat{k}_s}(\phi_s)\, R_{\hat{j}_o}(\gamma_s) \begin{vmatrix} x_o \\ y_o \\ z_o \end{vmatrix}$$

$$\hat{k}_S = \sin\phi_s \cos\gamma_s \hat{i}_o + \sin\phi_s \sin\gamma_s \hat{j}_o + \cos\phi_s \hat{k}_o$$

$$\hat{i}_S = \cos\phi_s \cos\gamma_s \hat{i}_o + \cos\phi_s \sin\gamma_s \hat{j}_o - \sin\phi_s \hat{k}_o$$

$$\hat{j}_S = -\sin\gamma_s \hat{i}_o + \cos\gamma_s \hat{j}_o$$

AD-A173 878 PROCEEDINGS OF THE SCIENTIFIC CONFERENCE ON OBSCURATION 6/7
AND AEROSOL RESEA (U) KOHL (RONALD H) AND ASSOCIATES
TULLAHOMA TN R H KOHL JUL 86 CRDEC-SP-86019
UNCLASSIFIED DAAG29-81-D-0100 F/G 20/6 NL

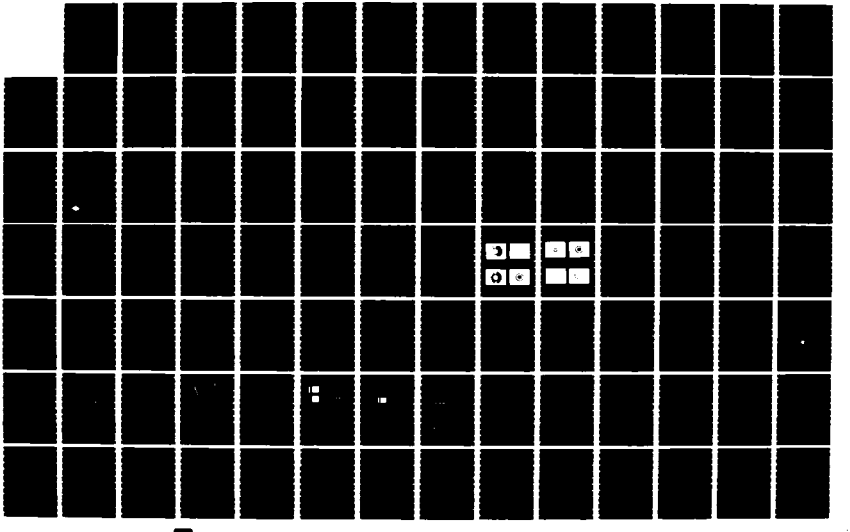

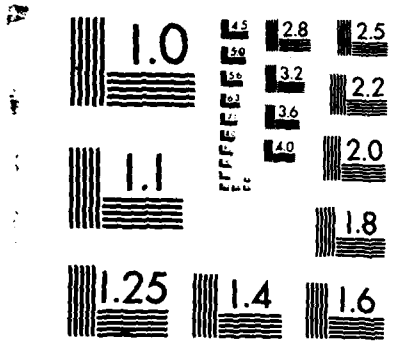

where ($\hat{i}_o, \hat{j}_o, \hat{k}_o$) and ($\hat{i}_s, \hat{j}_s, \hat{k}_s$) are the cartesian unit vectors for the reference and spiral frames respectively.

The Geometry of the Spiral

The radius of the spiral is R. The location of a point on its axis is given by the vector

$$\vec{h}(\phi) = R\cos\phi\,\hat{i}_s \pm R\sin\phi\,\hat{j}_s + (P/2\pi)\,\phi\,\hat{k}_s$$

in the spiral frame, where ϕ is shown in Figure 4, and P is the distance of rise of the spiral in one cycle and is shown in Figure 3. The "+" corresponds to the right handed helicity shown in Fig.3, while "-" corresponds to a left handed spiral. The vector $\vec{h}$ locates the point "O" shown in Fig.5, which is at the center of a disk of radius "a" (the radius of the helical wire). The direction z_ϕ is the direction of the helical wire at the point "O".

$$d\vec{S}_\phi = (d\vec{h}/d\phi)\,d\phi = [-R(\sin\phi\,\hat{i}_s - \cos\phi\,\hat{j}_s) + (P/2\pi)\hat{k}_s]\,d\phi$$

$$|d\vec{S}_\phi| = [R^2 + (P^2/4\pi^2)]^{1/2}\,d\phi$$

$$\hat{k}_\phi = d\vec{S}_\phi/|dS_\phi| = \frac{1}{\sqrt{R^2 + \frac{P^2}{4\pi^2}}}[-R(\sin\phi\,\hat{i}_s \mp \cos\phi\,\hat{j}_s) + (P/2\pi)\hat{k}_s]$$

We complete the right hand triad with

$$\hat{i}_\phi = \cos\phi\,\hat{i}_s + \sin\phi\,\hat{j}_s,$$

$$\hat{j}_\phi = \hat{k}_\phi \times \hat{i}_\phi = \frac{1}{\sqrt{R^2 + \frac{P^2}{4\pi^2}}}[(P/2\pi)(\cos\phi\,\hat{j}_s \mp \sin\phi\,\hat{i}_s) \mp R\hat{k}_s]$$

Scattering of Light from a Spiral in the First Order Shifrin Approximation

The scattered field is to first order

$$\vec{E}_S(\vec{r}) = \alpha[k_o^2 + \text{div grad}]\int d^3r_s\, U(\vec{r}_s)\,\vec{E}_{o\phi}\,e^{i\vec{k}_o\cdot\vec{r}_s}\,G(\vec{r},\vec{r}_s)$$

where $\alpha = 3(m^2-1)/(4\pi(m^2+2))$

m= index of refraction

$\vec{r}_s$= locates points relative to the spiral frame (x_s, y_s, z_s)

$U(\vec{r}_s)$ is 1 within the target and zero elsewhere.

The spiral is divided into disks as shown in Figures 4 and 5. We assume that $\vec{E}_{o\phi}$ is constant within an elemental disk. Then

As mentioned above, the Shifrin-Acquista technique provides an improvement over the Rayleigh-Gans-Rocard calculation in the first iterate by assuming an internal solution which is the solution of the equivalent electrostatic problem. This approach has produced quite accurate results for spheres, spheroids, and cylinders for which the equivalent electrostatic problems are soluable. In the case of the helix the authors are unaware of any solution of a dielectric helix in a uniform electrostatic field. Thus, one must appeal to other notions to obtain the first order estimate of the internal field. What has been done is to break the spiral into a number of disks. The electrostatic solution for a disk arbitrarily oriented with respect to a uniform field is known. This internal field does of course vary from disk to disk. In the sections to follow , the details of the somewhat complex geometry is presented along with the integral formulation of the spiral shape function.

The geometry of scattering

The reference frame is shown in Fig.1. It indicates the incident direction, the scattered direction, and the direction of polarization. Fig.2 indicates the spiral coordinate system and it s relation to the reference frame. The spiral frame is related to the reference frame by two rotations:

$$\begin{vmatrix} x_S \\ y_S \\ z_S \end{vmatrix} = R_{\hat{j}_o}(\phi_s)\, R_{\hat{i}_o}(\gamma_s) \begin{vmatrix} x_o \\ y_o \\ z_o \end{vmatrix}$$

$$\hat{k}_S = \sin\phi_s \cos\gamma_s \hat{i}_o + \sin\phi_s \sin\gamma_s \hat{j}_o + \cos\phi_s \hat{k}_o$$

$$\hat{i}_S = \cos\phi_s \cos\gamma_s \hat{i}_o + \cos\phi_s \sin\gamma_s \hat{j}_o - \sin\phi_s \hat{k}_o$$

$$\hat{j}_S = -\sin\gamma_s \hat{i}_o + \cos\gamma_s \hat{j}_o$$

$$\vec{E}_S(\vec{r}) = [k_o^2 + \text{grad div}] \sum_{i=1}^{N} \int_{\text{disk}} d^3 r_s \, U(\vec{r}_s) \, \vec{E}_{o\phi_i} e^{i\vec{k}_o \cdot \vec{r}_o} G(\vec{r}, \vec{r}_o)$$

where

$$\vec{E}_{o\phi} = [\vec{E}_o \cdot \hat{i}_\phi \hat{i}_\phi + \vec{E}_o \cdot \hat{i}_\psi \hat{i}_\phi] a_{TE} + \vec{E}_o \cdot \hat{k}_\phi \hat{k}_\phi a_{TM}$$

here

a_{TE} and a_{TM} are constants taken to be the same as in the static infinite cylinder case,

$$a_{TE} = 2/(m^2+1), \quad a_{TM} = 1 .$$

Using the far-field approximation

$$\vec{E}_S(\vec{r}) = \alpha \frac{\exp(ikr)}{r} k_o^2 \sum_i u_i(k_o \hat{r} - \vec{k}_o)[\vec{E}_{o\phi_i} - \vec{E}_{o\phi_i} \cdot \hat{r}\hat{r}]$$

where $u_i(k_o \hat{r} - \vec{k}_o)$ is the Fourier transform of the pupil function for the ith disk.

Evaluation of the Pupil Function $u_i(k_o \hat{r} - \vec{k}_o)$

The pupil transform is

$$u_i(\vec{\gamma}) = \int_{\text{all space}} d^3 r_s \, U_i(\vec{r}_s) \exp(i\vec{\gamma} \cdot \vec{r}_s)$$

where $\vec{\gamma} = k_o \hat{r} - \vec{k}_o$.

We have (Acquista) evaluated this transform in a previous paper with

$$\vec{r}_s = \vec{h} + \vec{r}' ,$$

giving,

$$u_i(\vec{\gamma}) = \int_{\text{all space}} d^3 r' \, U_i(\vec{r}' + \vec{h}) \exp(i\vec{\gamma} \cdot \vec{r}') \exp(i\vec{\gamma} \cdot \vec{h})$$

$$= \int_{\text{disk } i} d^3 r' \exp(i\vec{\gamma} \cdot \vec{r}') \exp(i\vec{\gamma} \cdot \vec{h})$$

$$= 2\pi a^2 dS_{\phi_i} \frac{J_1(\gamma_\perp a)}{\gamma_\perp d} \exp(i\vec{\gamma} \cdot \vec{h})$$

$$= 2\pi a^2 \sqrt{R^2 + P^2/4\pi} \; \frac{J_1(\gamma_\perp a)}{\gamma_\perp d} \exp(i\vec{\gamma} \cdot \vec{h}) \, d\phi_i$$

where

$J_1(\gamma_\perp a)$ is a Bessel function and

$$\gamma_\perp = [(\gamma_{x\phi_i} \cos\phi_i + \gamma_{y\phi_i} \sin\phi_i)^2 + \gamma_{z\phi_i}^2]^{1/2}$$

$$\vec{\gamma} \cdot \vec{h} = \gamma_{x\phi_i} R \cos\phi_i - \gamma_y R \sin\phi_i$$

It follows that the first order scattered electric field is

$$\vec{E}_s(\vec{r}) = \alpha \frac{\exp(ik_o r)}{r} k_o^2 2\pi a \sqrt{R^2 + \frac{P^2}{4\pi^2}} \int_0^{2\pi} d\phi \left[\frac{J_1(\gamma_\perp a)}{\gamma_\perp} \right.$$
$$\left. \exp(i\vec{\gamma}\cdot\vec{\rho}) \times (\vec{E}_{o\phi} - \vec{E}_{o\phi}\cdot\hat{r}\hat{r}) \right]$$

We write

$$\vec{E}_\perp(\phi) = \vec{E}_{o\phi} - \vec{E}_{o\phi}\cdot\hat{r}\hat{r}$$

Expression of $\vec{E}_\perp(\phi)$ in the reference frame ($x_o y_o z_o$)

The unit vector $\hat{r}$ is in the scattered direction z', and $\hat{r}\cdot\vec{k}_o = \cos 2\phi_o$ as seen in Fig. 1.

$$\vec{E}_{o\phi} = [\vec{E}_o\cdot\hat{i}_\phi\hat{i}_\phi + \vec{E}_o\cdot\hat{j}_\phi\hat{j}_\phi]\, a_{TE} + \vec{E}_o\cdot\hat{k}_\phi\hat{k}_\phi a_{TM}$$

$$\vec{E}_o = E_o\cos\alpha_p\hat{i}_o + E_o\sin\alpha_p\hat{j}_o$$

We first need $\hat{i}_\phi$, $\hat{j}_\phi$, $\hat{k}_\phi$ in the reference frame

$$\hat{i}_\phi = \cos\phi[\cos\phi_s\cos\gamma_s\hat{i}_o + \cos\phi_s\sin\gamma_s\hat{j}_o - \sin\phi_s\hat{k}_o] \pm \sin\phi[-\sin\gamma_s\hat{i}_o + \cos\gamma_s\hat{j}_o]$$
$$= a_{11}\hat{i}_o + a_{12}\hat{j}_o + a_{13}\hat{k}_o$$

$$\hat{j}_\phi = \frac{1}{\sqrt{R^2 + P^2/4\pi^2}}\left[\frac{P}{2\pi}(\cos\phi[-\sin\gamma_s\hat{i}_o + \cos\gamma_s\hat{j}_o]\right.$$
$$\mp\sin\phi[\cos\phi_s\cos\gamma_s\hat{i}_o + \cos\phi_s\sin\gamma_s\hat{j}_o - \sin\phi_s\hat{k}_o] \mp R[\sin\phi_s\cos\gamma_s\hat{i}_o + \sin\phi_s\sin\gamma_s\hat{j}_o + \cos\phi_s\hat{k}_o]]$$
$$= a_{21}\hat{i}_o + a_{22}\hat{j}_o + a_{23}\hat{k}_o$$

$$\hat{k}_\phi = \frac{1}{\sqrt{R^2 + P^2/4\pi^2}}[-R\sin\phi[\cos\phi_s\cos\gamma_s\hat{i}_o + \cos\phi_s\sin\gamma_s\hat{j}_o - \sin\phi_s\hat{k}_o] \mp R\cos\phi[-\sin\gamma_s\hat{i}_o + \cos\gamma_s\hat{j}_o]$$
$$+ \frac{P}{2\pi}[\sin\phi_s\cos\gamma_s\hat{i}_o + \sin\phi_s\sin\gamma_s\hat{j}_o + \cos\phi_s\hat{k}_o]]$$
$$= a_{31}\hat{i}_o + a_{32}\hat{j}_o + a_{33}\hat{k}_o .$$

thus

$$\begin{vmatrix} x_\phi \\ y_\phi \\ z_\phi \end{vmatrix} = \begin{vmatrix} a_{11} & a_{12} & a_{13} \\ a_{21} & a_{22} & a_{23} \\ a_{31} & a_{32} & a_{33} \end{vmatrix} \begin{vmatrix} x_o \\ y_o \\ z_o \end{vmatrix}$$

We may then write

$$\vec{E}_{o\phi} = E_o[\cos\alpha_p([\hat{i}_o\cdot\hat{i}_\phi\hat{i}_\phi + \hat{i}_o\cdot\hat{j}_\phi\hat{j}_\phi]\, a_{TE} + \hat{i}_o\cdot\hat{k}_\phi\hat{k}_\phi a_{TM}) + \sin\alpha_p([\hat{j}_o\cdot\hat{i}_\phi\hat{i}_\phi + \hat{j}_o\cdot\hat{j}_\phi\hat{j}_\phi]\, a_{TE} + \hat{j}_o\cdot\hat{k}_\phi\hat{k}_\phi a_{TM})$$
$$= E_o[\cos\alpha_p([a_{11}(a_{11}\hat{i}_o + a_{12}\hat{j}_o + a_{13}\hat{k}_o) + a_{21}(a_{21}\hat{i}_o + a_{22}\hat{j}_o + a_{23}\hat{k}_o)]a_{TE} + a_{31}(a_{31}\hat{i}_o + a_{32}\hat{j}_o + a_{33}\hat{k}_o)a_{TM})$$
$$+ \sin\alpha_p([a_{12}(a_{11}\hat{i}_o + a_{12}\hat{j}_o + a_{13}\hat{k}_o) + a_{22}(a_{21}\hat{i}_o + a_{22}\hat{j}_o + a_{23}\hat{k}_o)]a_{TE} + a_{32}(a_{31}\hat{i}_o + a_{32}\hat{j}_o + a_{33}\hat{k}_o)a_{TM})]$$

$$\vec{E}_{o\phi} = (E_{o\phi})_{x_o}\hat{i}_o + (E_{o\phi})_{y_o}\hat{j}_o + (E_{o\phi})_{z_o}\hat{k}_o$$

This form is next used to get the vector portion of the scattered wave

$$E_\perp(\phi) = [(E_{o\phi})_{x_o}\hat{i}_o + (E_{o\phi})_{y_o}\hat{j}_o + (E_{o\phi})_{z_o}\hat{k}_o] - (\hat{i}_o \sin 2\phi_o + \hat{k}_o \cos 2\phi_o)((E_{o\phi})_{x_o}\sin 2\phi_o + (E_{o\phi})_{y_o}\cos 2\phi_o)]$$

$$E_\perp(\phi) = \hat{i}_o[(E_{o\phi})_{x_o}\cos^2 2\phi_o - (E_{o\phi})_{y_o}\sin 2\phi_o \cos 2\phi_o] + \hat{j}_o(E_{o\phi})_{y_o} + \hat{k}_o[(E_{o\phi})_{z_o}\sin^2 2\phi_o - (E_{o\phi})_{x_o}\sin 2\phi_o \cos 2\phi_o]$$

The scattered wave is therefore given by

$$\vec{E}_s(\vec{r}) = \alpha \frac{\exp(ik_o r)}{r} k_o^2 2\pi a \sqrt{R^2 + P^2} \times \int_0^{2\pi} d\phi \frac{[J_1(\gamma_\perp(\phi)a)\exp(i\vec{\beta}(\phi)\cdot\vec{h})\vec{E}_\perp(\phi)]}{\gamma_\perp(\phi)}$$

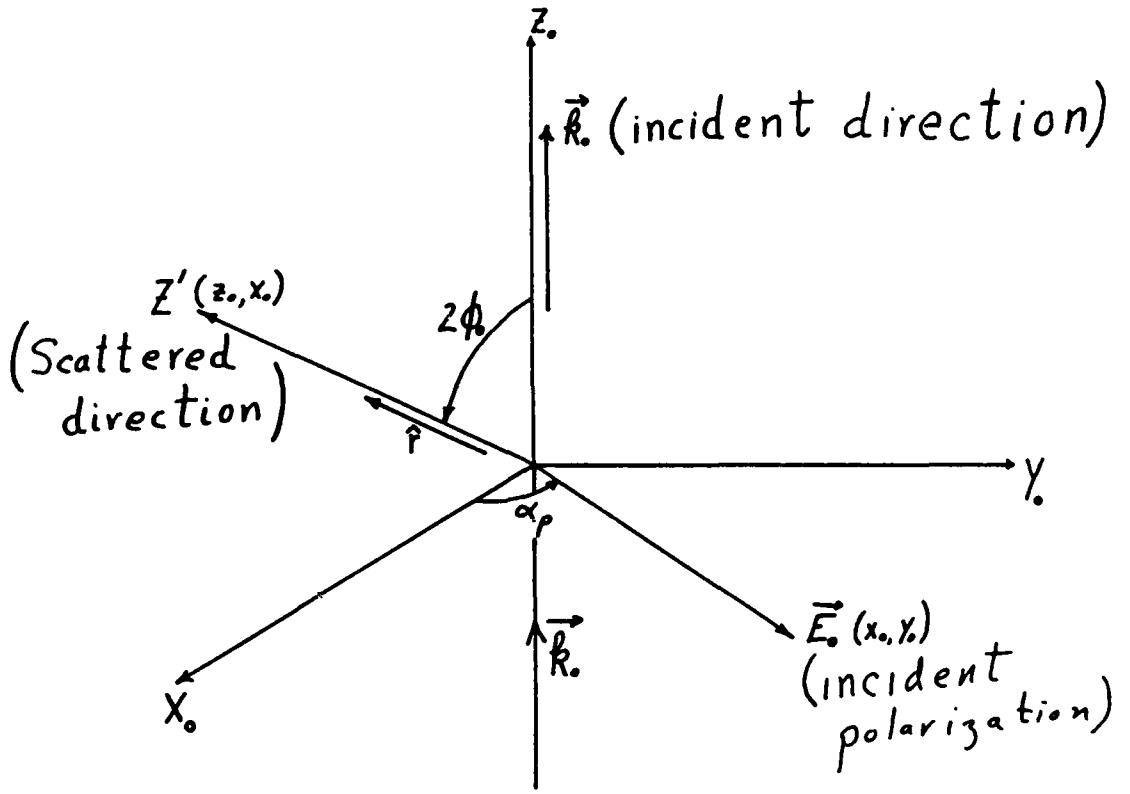

Figure 1.

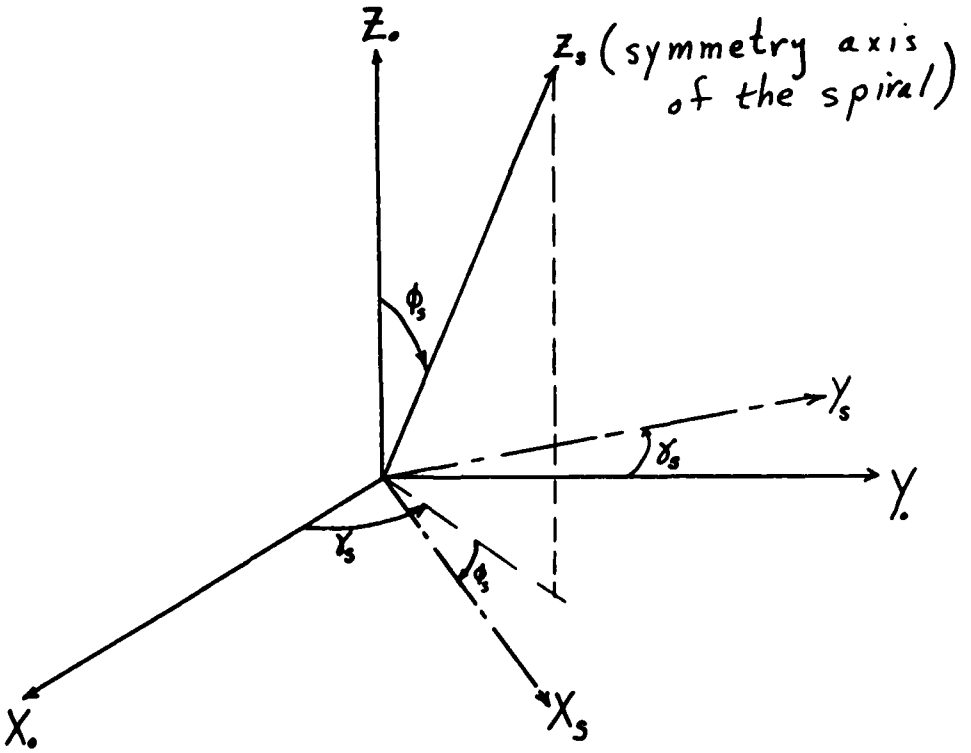

Figure 2.

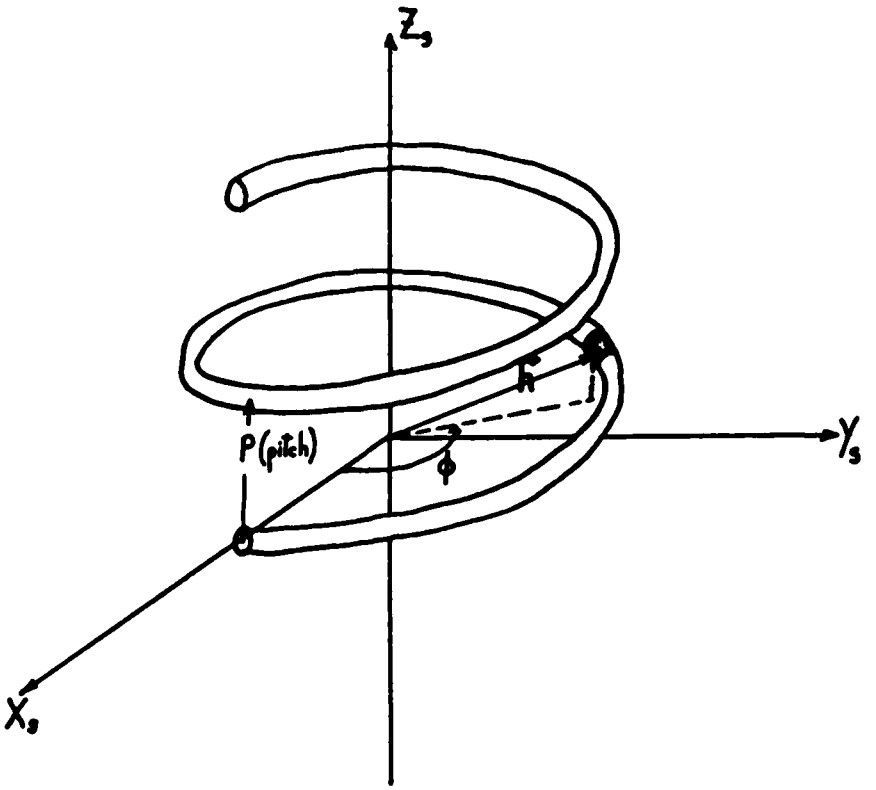

Figure 3 .

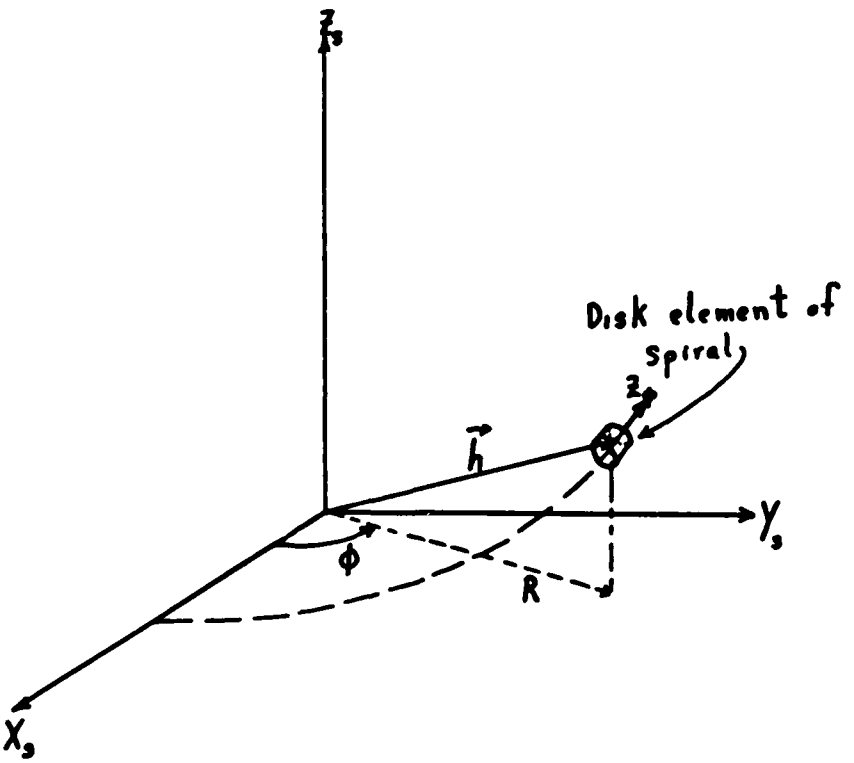

Figure 4 .

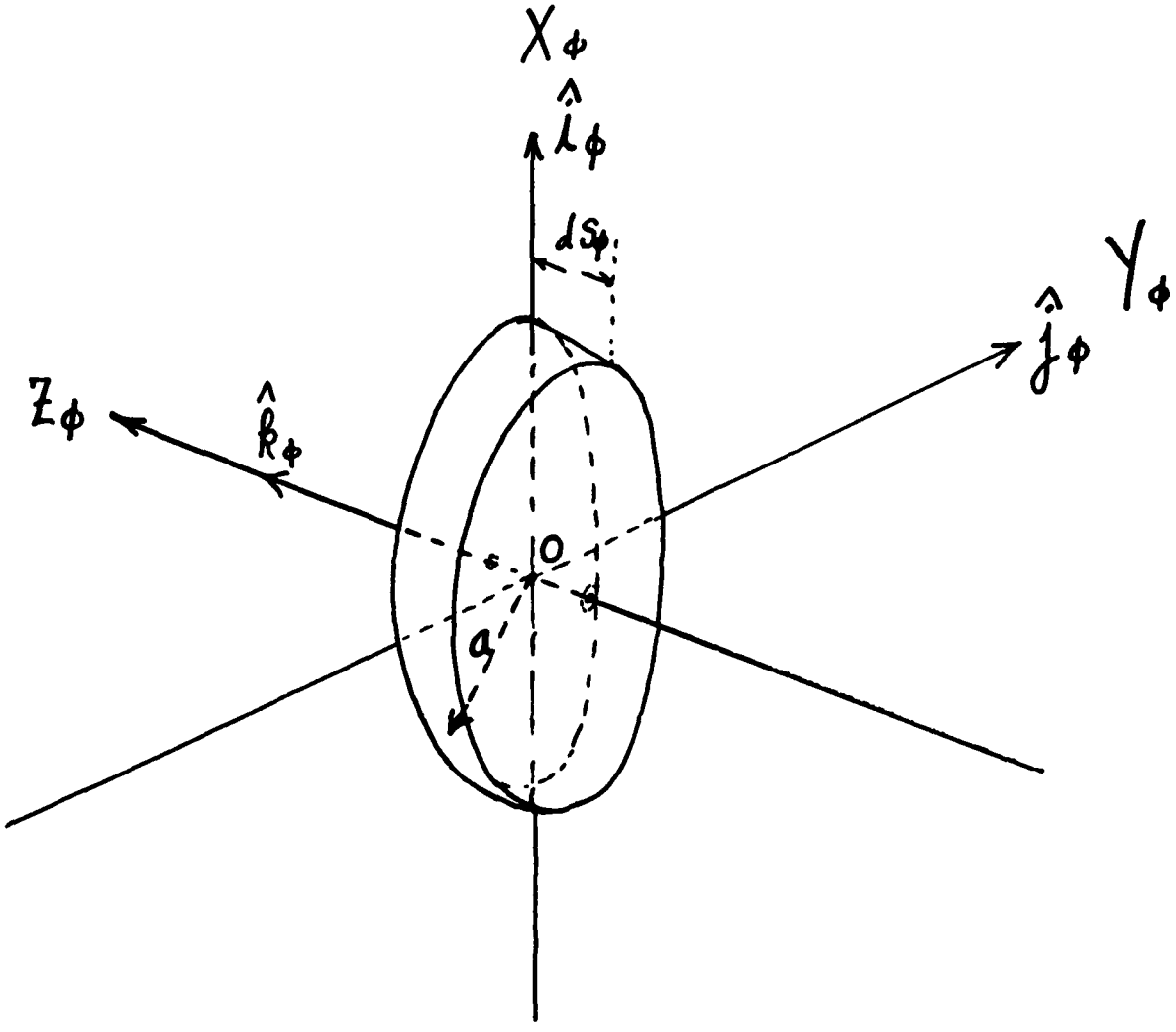

Figure 5. Disk of radius a and thickness dS_ϕ with its local coordinate system.

The Scattering of Light from Targets of Varying Orientation

Richard D. Haracz
Leonard D. Cohen
and
Ariel Cohen

Department of Physics and Atmospheric Science
Drexel University
Philadelphia, Pennsylvania 19104

Recent Publications and Submittals for Publication and Presentations:

A) A. Cohen, R. D. Haracz, and L. D. Cohen, 'Asymmetry Factors for Randomly Oriented Infinite Cylinders,' Appl. Phys. 58, 1135 (1985).

B) R. D. Haracz, L. D. Cohen, and A. Cohen, 'Scattering of Linearly Polarized Light from Randomly Oriented Cylinders and Spheroids,' Appl. Phys. , Nov., 1985.

C) A. Cohen, L. D. Cohen, and R. D. Haracz, 'On the Optical Properties of Fibrous Insulation,' submitted to Appl. Phys. Communications.

D) R. D. Haracz, L. D. Cohen, and A. Cohen, 'The Scattering of Light by a Dielectric Helix of Finite Cross Section in the Shifrin Approximation,' in progress.

ABSTRACT

The scattering of polarized light from targets of either random or constrained orientation is discussed with emphasis on the special geometrical considerations involved. Application is made to randomly oriented short cylinders and spheroids, and it is shown that the different shapes of equal volume produce different intensities when the plane of polarization is changed by the scattering process. The Shifrin theory is applied and extended to a continuous spiral modelled as a sequence of adjacent disks.

GEOMETRY

We want to be able to find scattering intensities for light incident on a target whose symmetry axis is arbitrarily oriented relative to the direction of incidence, and the incident light is arbitrarily polarized. To this end, we first establish a reference frame defined by the direction of incidence and the direction of scattering.

Let z_o be an axis in the direction of incidence and z be an axis in the direction of scattering, as shown in Fig. 1. The plane formed by z_o and z is called the reference plane. The x_o axis is perpendicular to z_o and in the reference plane, and the y_o axis is perpendicular to the reference plane. This defines the reference frame - the x_o, y_o , z_o axes. The angle between the directions of incidence and scattering is denoted 2ϕ .

Application of the scattering matrix is done in the target frame, where z_t is the symmetry axis of the target. The target plane is formed by z_t and z_o, and x_t is perpendicular to z_t in the target plane. The right-hand triad is completed, and x_t, y_t , z_t is the target frame.

The reference frame and the target frame are then related by two rotations:

$$A_t = \begin{bmatrix} A_{z_t} \\ A_{y_t} \\ A_{z_t} \end{bmatrix} = R_{y_t}(\phi)\, R_{z_o}(\gamma) \begin{bmatrix} A_{x_o} \\ A_{y_o} \\ A_{z_o} \end{bmatrix} , \qquad (1)$$

where the transformation matrix is

$$R_{o \to t} = \begin{bmatrix} \cos\phi\cos\gamma & \cos\phi\sin\gamma & -\sin\phi \\ -\sin\gamma & \cos\gamma & 0 \\ \sin\phi\cos\gamma & \sin\phi\sin\gamma & \cos\phi \end{bmatrix} \qquad (2)$$

AVERAGE SCATTERING INTENSITIES FOR RANDOMLY ORIENTED SHORT CYLINDERS AND SPHEROIDS

Our first application is to finite cylinders and spheroids of equal volume. The incident light has the electric field

$$\vec{E}_o = E_{ox_o}\, \hat{i}_o + E_{oy_o}\, \hat{j}_o \qquad (3)$$

and hence it is linearly polarized.

To apply the scattering matrix, this field must be transformed to the target frame by the application of the rotation matrix given in Eq. (2):

$$E_{ot} = R_{o \to t} \quad E_o \tag{4}$$

The scattered electric field is perpendicular to the scattered direction $\hat{r}$,

$$\vec{E}_{sc} = \vec{E}_{sc} - \hat{r} \cdot \vec{E}_{sc} \quad \hat{r} \quad , \tag{5}$$

where the vector $\vec{E}_{sc}$ is obtained by the application of the Shifrin-Acquista perturbation theory, so the first order contribution to $\vec{E}_{sc}$ in the target frame is

$$E_{st} = S \; E_{ot} \; , \tag{6}$$

where the scattering matrix is

$$S = C \, k_o^2 \; e^{ik r} \; u(k_o \hat{r} - \vec{k}_o) \begin{bmatrix} a_{TE} & 0 & 0 \\ 0 & a_{TE} & 0 \\ 0 & 0 & a_{TM} \end{bmatrix} . \tag{7}$$

It is assumed that the polarization matrix is constant over the target volume (not quite true in the case of a finite cylinder as shown in our paper in Appl. Opt. 23 (1984)). In Eq. (7), the constant $C = (m^2 - 1)/ 4\pi$ and is the expansion constant of the perturbation theory. The function $u(\vec{\gamma})$ is the Fourier transform of the pupil function for the target.

Two intensities are defined in relation to the reference frame (parallel and perpendicular). Each assumes that the incident electric field is in the reference plane, and

$$\begin{aligned} I_{\parallel} &= k_o^2 \; r^2 \; (\; |E_{scx_o}|^2 \; + \; |E_{scz_o}|^2 \;) \; / \; |E_o|^2 \; , \\ I_{\perp} &= k_o^2 \; r^2 \; |E_{scy_o}|^2 \; / \; |E_o|^2 \; . \end{aligned} \tag{8}$$

The average intensity is found by integrating these intensities over all possible target orientations:

$$I_{ave} = 1/4\pi \int_0^{2\pi} d\gamma \int_0^{\pi} d\phi \; \sin\phi \; I(\gamma, \phi) \tag{9}$$

The results are shown in Figs. 2-5 for aspect ratios of 10, 2, 1, and 0.1, respectively. In these figures, the volume of each target is 1 $(\mu m)^3$, the index of refraction is 1.5, and the wave number of the incident light is $k_0 = 1\ (\mu m)^{-1}$. In each figure, the results for a sphere is given as a reference (dashed line).

The intensity $I_{\parallel}$ has both the incident and the final directions of polarization in the reference plane, and we see that the intensity patterns for each shape are quite similar with small but discernable differences in the position of the minima. Thus, for spheroids and cylinders, the scattering pattern for $I_{\parallel}$ is controlled by the volume of the target.

On the other hand, the intensity $I_{\perp}$ corresponds to the situation where the incident polarization is in the reference plane and the final direction of polarization is perpendicular to the reference plane. For an aspect ratio of 10, the cylinder and spheroid have similar values of $I_{\perp}$, while the sphere has $I_{\perp} = 0$. For an aspect ratio of 2, $I_{\perp}$ for a spheroid is nearly an order of magnitude smaller than $I_{\perp}$ for a finite cylinder of the same volume. For an aspect ratio of 0.1, $I_{\perp}$ for a spheroid is more than an order of magnitude smaller and does not appear on the figure. One then concludes that these various shapes can be distinguished through measurements of $I_{\perp}$.

AVERAGE SCATTERING FROM LONG CYLINDERS WITH CONSTRAINED ORIENTATIONS CONSISTENT WITH SCATTERING ON A CONE

In the above discussion, the average intensities were found by including all orientations of target axes, equally weighted. On the other hand, for a given direction of incidence and scattering, the orientation of a long cylinder must be constrained in order for the scattering to be along an element of one of a family of cones. The orientation angles of the cylinder must satisfy the constraining equation

$$\phi = \mathrm{Tan}^{-1} (\tan\phi_0 / \cos\gamma) \qquad (10)$$

(as given in reference A). This condition places the axis of the cylinder on a great circle (as described in reference A), and the result is that the average intensity depends on an integration over only one of the orientation angles:

$$I_{ave} = 2/\pi \int_0^{\pi/2} d\gamma \, (\sin^2\phi(\gamma)/\sin\phi_0 \ ) \, I(\gamma, \phi(\gamma)). \qquad (11)$$

SCATTERING OF LIGHT FROM AN ARBITRARILY ORIENTED CYLINDRICAL SPIRAL

This problem is treated as coherent scattering from specially positioned dielectric disks.

The relationship between the target and reference frames is given in Eq. (1). As shown in Fig. 6, the spiral axis in the target frame is located by the vector $\vec{h}(\phi)$, where ϕ is the azimuthal angle of the spiral as shown in the figure. The equation of the axis is

$$\vec{h}(\phi) = R\cos\phi\ \hat{i}_t + (-)R\sin\phi\ \hat{j}_t + P/2\pi\ \hat{k}_t \qquad (12)$$

where R is the radius of the spiral, P is the pitch, and $\hat{i}_t$, $\hat{j}_t$, and $\hat{k}_t$ are the unit vectors of the target frame. The sign of the second term determines the "handedness" of the spiral.

The cylindrical spiral is next divided into disks of infinitesimal length and radius a. The length of the disk located by the angle ϕ is

$$ds_\phi = |dh/d\phi|\ d\phi = \sqrt{R^2 + P^2/4\pi^2}\ d\phi \qquad (13)$$

If the components of a vector in the disk frame are A_{x_ϕ}, A_{y_ϕ}, and A_{z_ϕ}, these are related to the corresponding components in the target frame as

$$\begin{bmatrix} A_{x_\phi} \\ A_{y_\phi} \\ A_{z_\phi} \end{bmatrix} = \begin{bmatrix} \cos\phi + (-)\sin\phi & 0 & 0 \\ \alpha(-(+)\sin\phi)P/2\pi & \alpha P/2\pi\cos\phi & -(+)\alpha R \\ -\alpha R\sin\phi & -(+)\alpha R\cos\phi & \alpha P/2\pi \end{bmatrix} \begin{bmatrix} A_{x_t} \\ A_{y_t} \\ A_{z_t} \end{bmatrix}, \qquad (14)$$

i.e., $A_\phi = R_{t\to\phi}\ A_t$, with $\alpha \equiv \sqrt{R^2 + P^2/4\pi^2}$. The reference and disk frames are then related as

$$A_\phi = R_{t\to\phi}\ R_{o\to t}\ A_o \qquad (15)$$

The incident wave can have any polarization, and when this incident wave scatters off the disk, the scattered wave obeys

$$d\vec{E}_{sc} = d\vec{E}_{sc} - \hat{r}\cdot d\vec{E}_{sc}\ \hat{r} \qquad (16)$$

The vector $d\vec{E}_{sc}$ is obtained from the first-order perturbation theory in the disk frame as

$$d\vec{E}_{s\phi} = S\,(R_{t\to\phi}\ R_{o\to t}\ E_o) \qquad (17)$$

where this vector is in the disk frame of reference and S has the form of Eq. (7), but

$du(k_o r - k_o)$ is the Fourier transform of the pupil function for the disk. This Fourier transform is obtained as

$$
\begin{aligned}
du(\vec{\gamma}) &= \int d^3 r_\phi \; U(\vec{r}_\phi) \; e^{i \vec{\gamma} \cdot \vec{r}_\phi} \\
&= \int_{disk} d^3 r'_\phi \; \exp(i \vec{\gamma} \cdot \vec{r}'_\phi) \; \exp(i \vec{\gamma} \cdot \vec{h}) \\
&= 2\pi a^2 \sqrt{R^2 + P^2/4\pi^2} \; J_1 (\gamma_\perp(\phi) \, a) / (\gamma_\perp(\phi) \, a) \\
&\qquad \times \exp(i \vec{\gamma} \cdot h(\phi)) \; d\phi \quad , \qquad (18)
\end{aligned}
$$

where we have used $\vec{r}_\phi = \vec{h} + \vec{r}'_\phi$. In this last equation J_1 is a Bessel function, and $\gamma_\perp$ is the component of the vector $\vec{\gamma}$ perpendicular to the axis of the disk.

It is noted that each disk contribution is constructed from an internal electric field that follows the orientation of the disk and varies with the angle ϕ . The total scattered electric field is the coherent sum of these disk contributions:

$$
\vec{E}_{sc} = \int_{spiral} d\vec{E}_{sc} \qquad (19)
$$

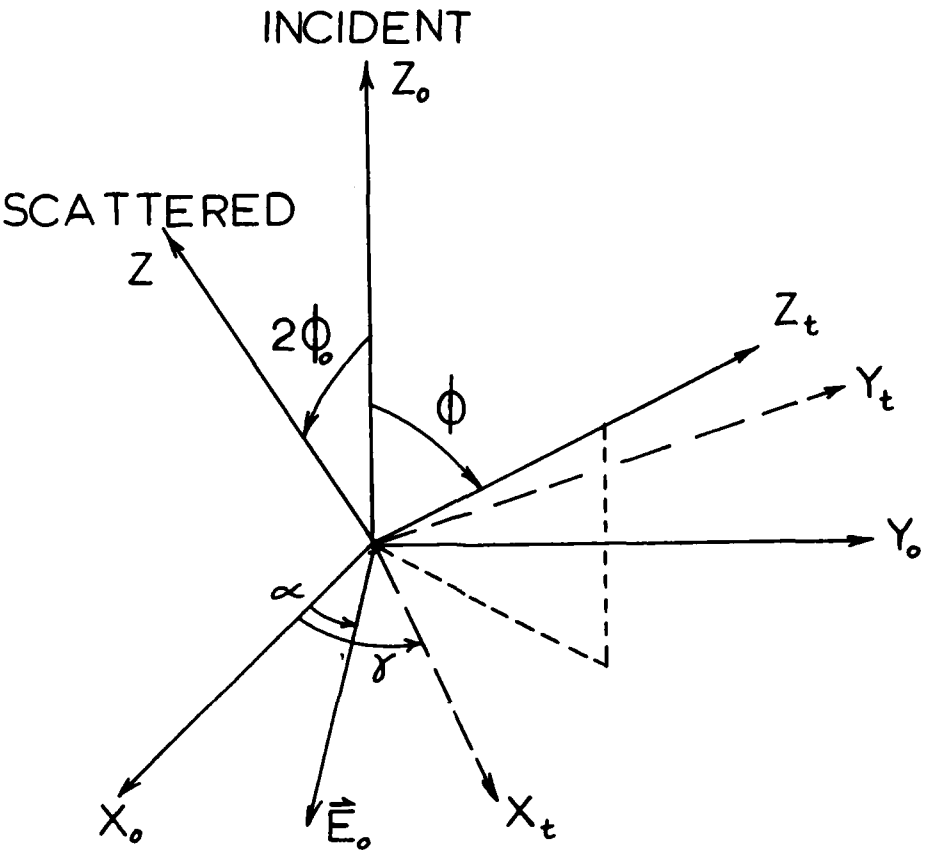

Figure 1. The geometry for the scattering process. The direction of incidence is z_o, the direction of scattering is z, the symmetry axis of the target is z_t, and incident electric field is $\vec{E}_o$.

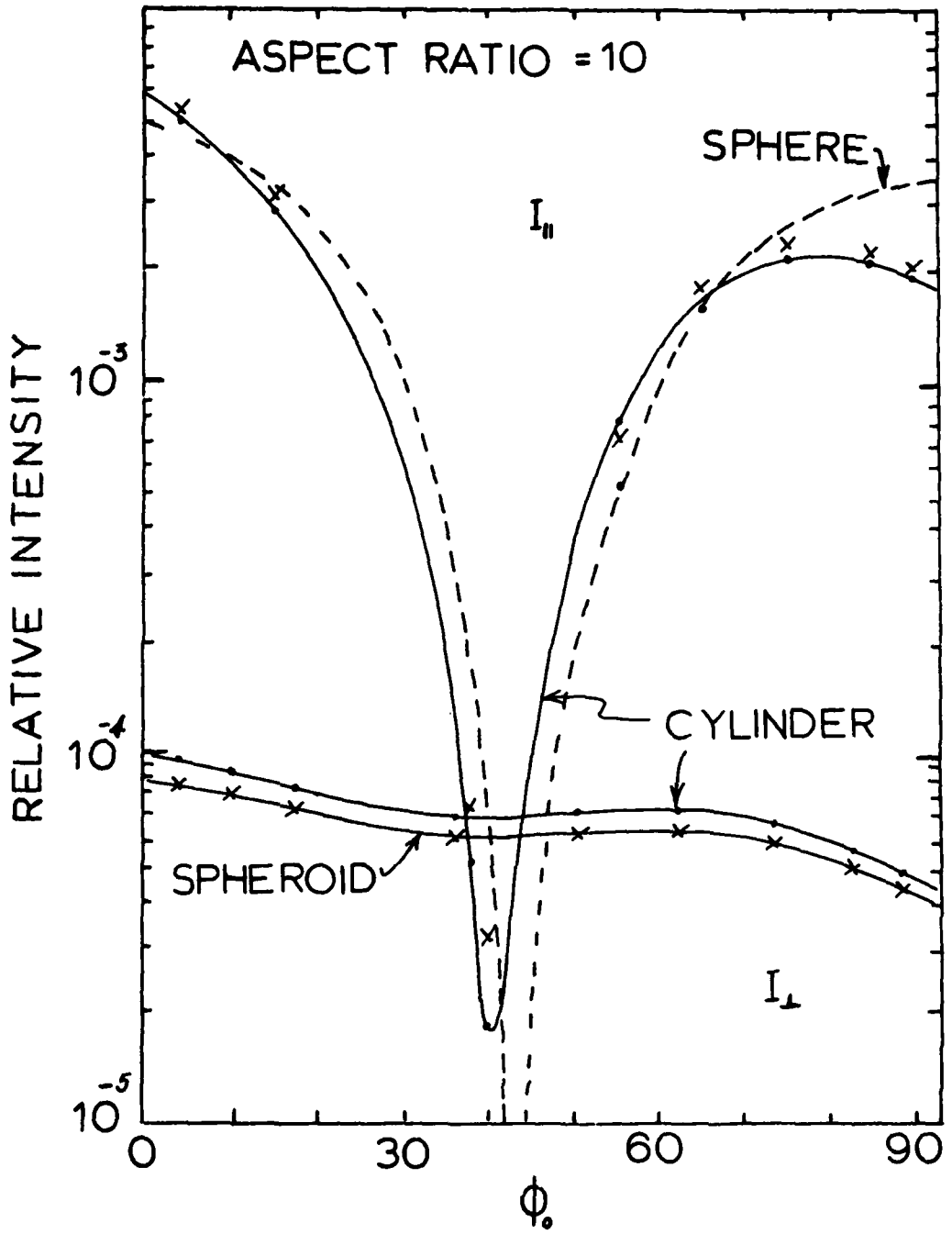

Figure 2. The intensities $I_{\parallel}$ and $I_{\perp}$ for targets of various shapes all with volume 1 (μm^3). The results for a sphere are shown as dashed lines, and the results for cylinders and spheroids of the same aspect ratio are shown as solid lines (with dots for the cylinder and crosses for the spheroid). The aspect ratio = 10. (The solid curve for $I_{\parallel}$ for the spheroid is not drawn in, in Figures 2 and 3, but its close proximity to the curve from the cylinder is indicated by the crosses.)

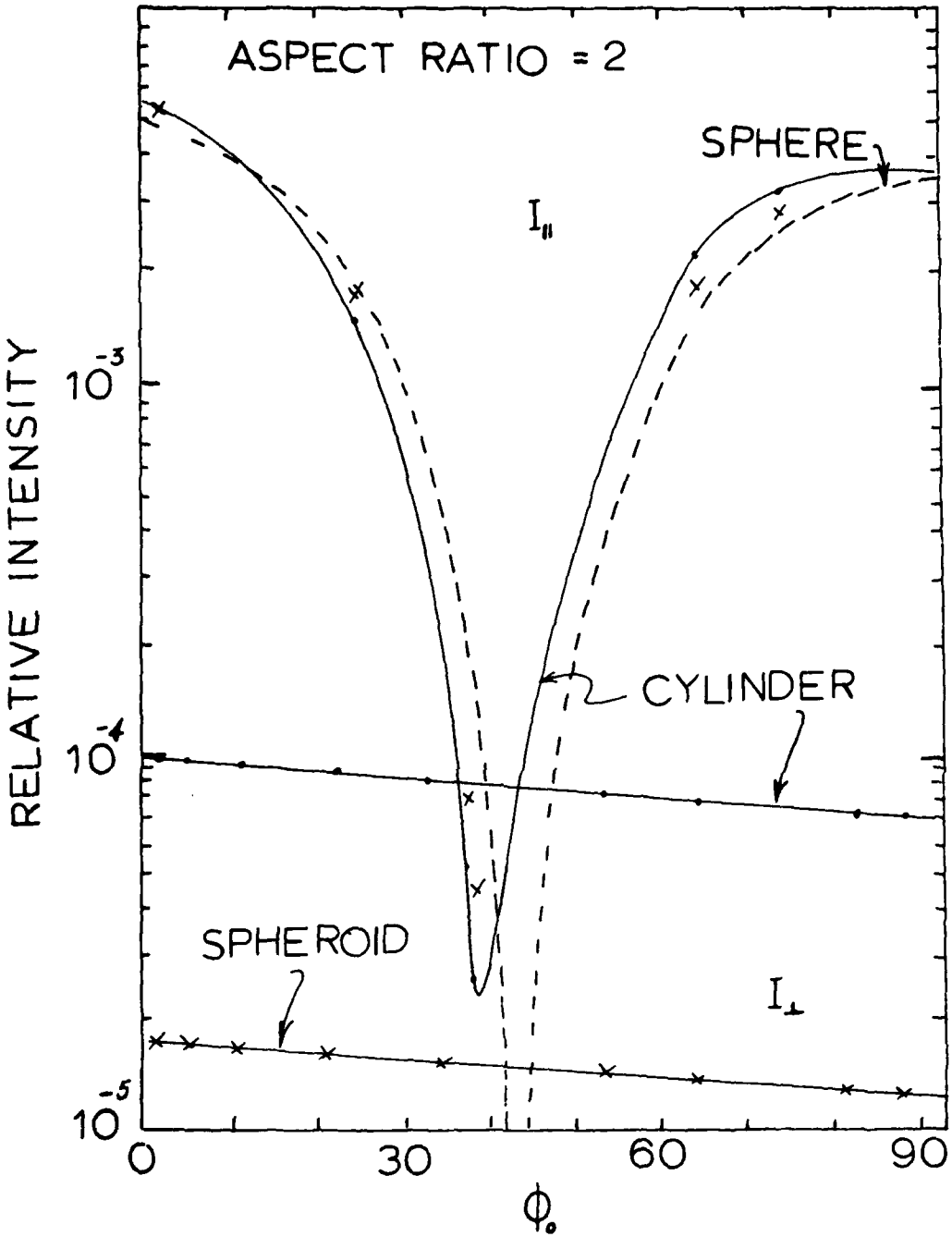

Figure 3. The same as Figure 2 with aspect ratio = 2.

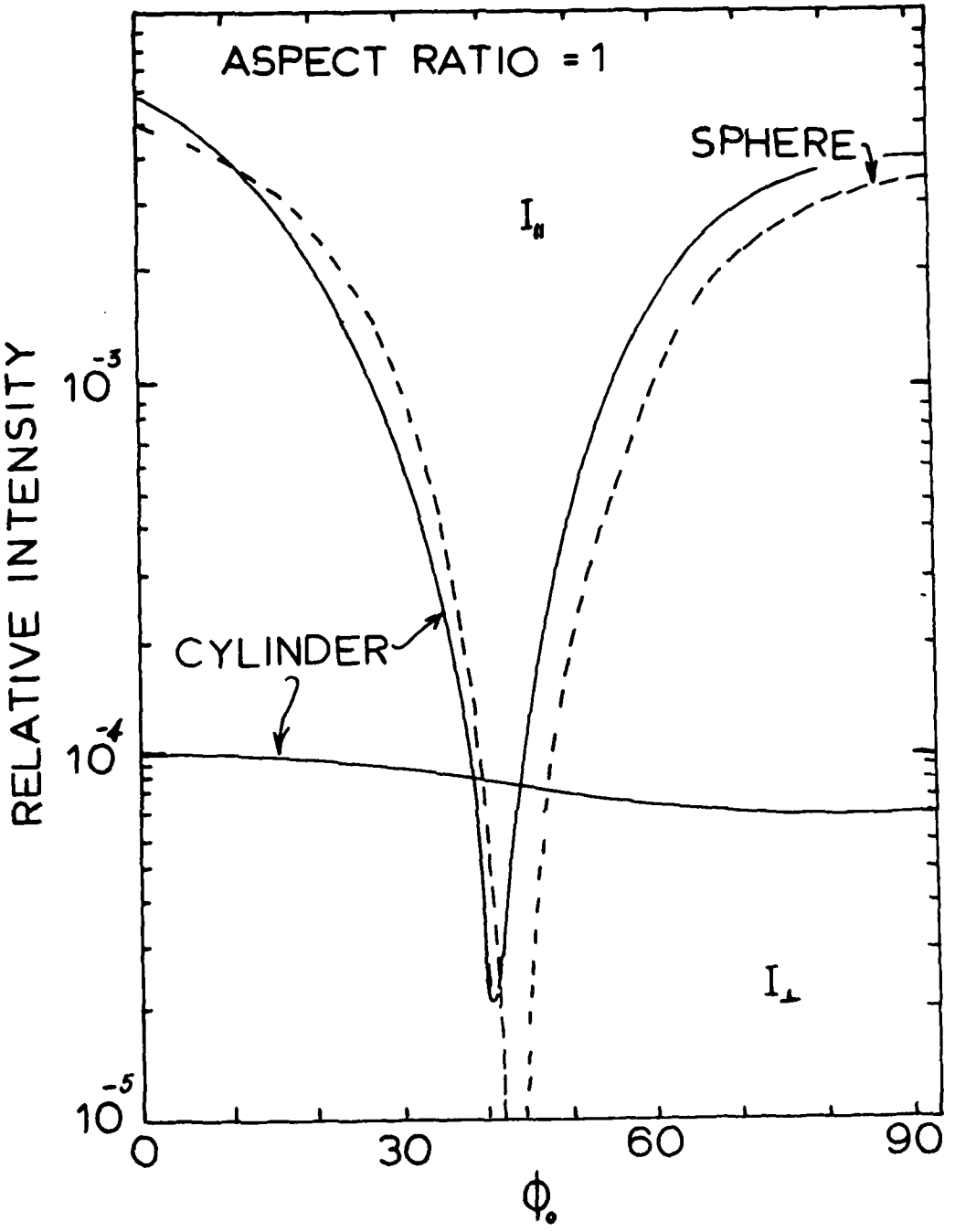

Figure 4. The same as Figure 2 with aspect ratio = 1.

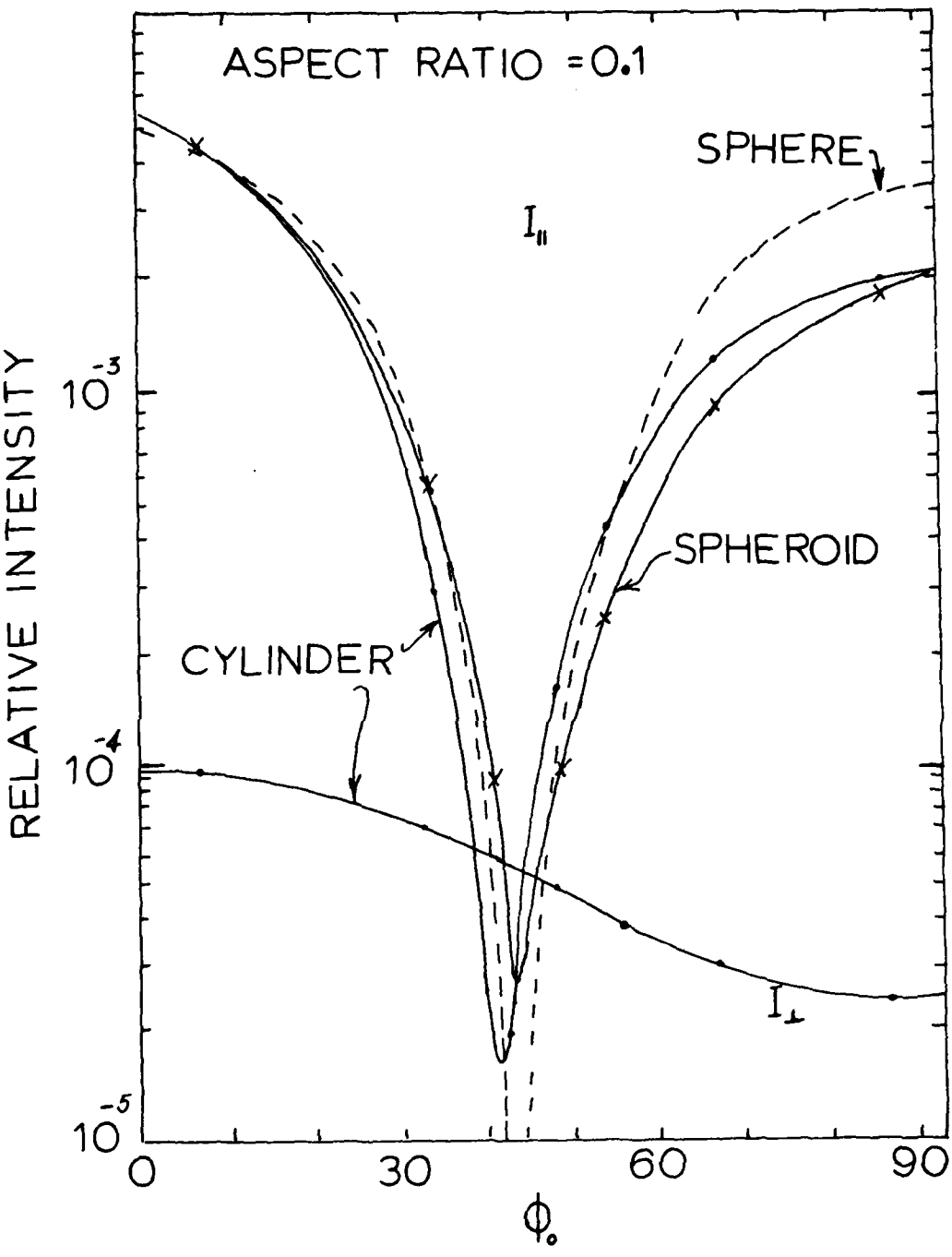

Figure 5. The same as figure 2 with aspect ratio = 0.1. Note that the intensity $I_{\perp}$ for the spheroid is less than 10^{-5} and does not appear on the figure.

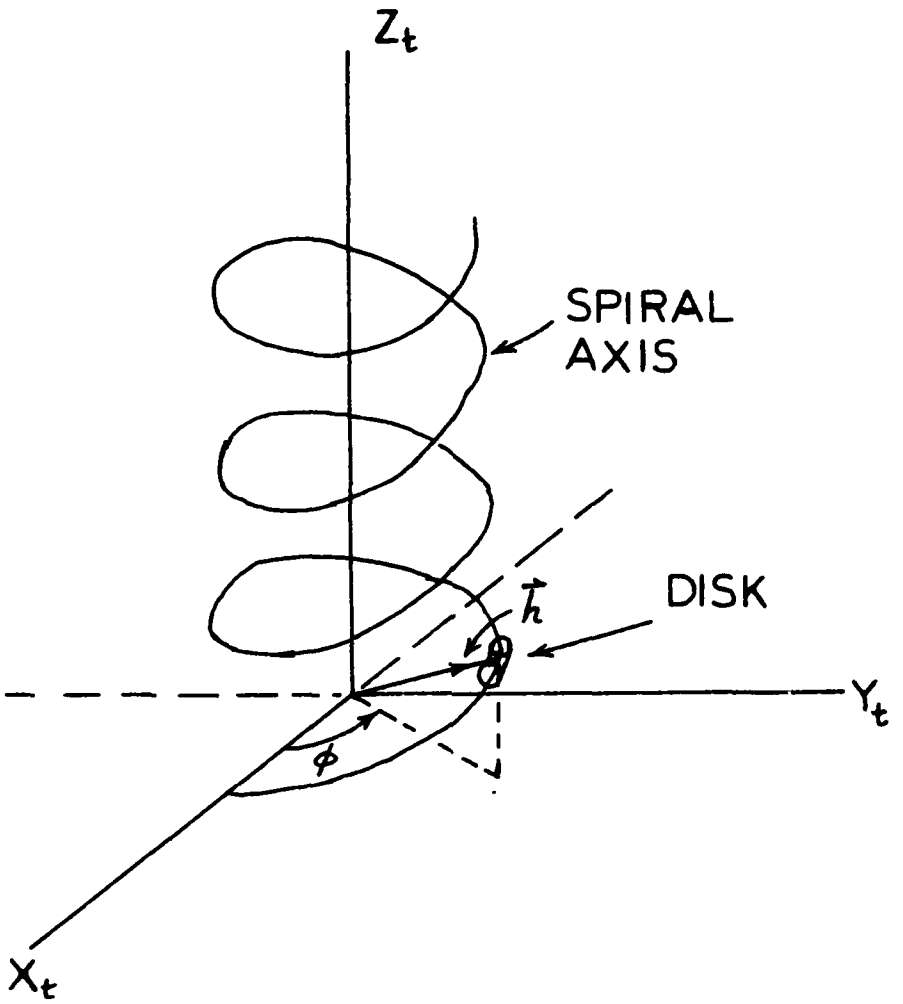

Figure 6. The geometry for a spiral in the target frame of reference. Note that points on the axis of the spiral are located by the vector $\vec{h}(\phi)$, with ϕ the azimuthal angle of the spiral.

ORIENTATION OF ONE MICRON SIZE CUBES SUSPENDED IN A QUADRUPOLE TRAP

Edward S. Fry, Pascal Herb and William E. White
Physics Department, Texas A&M University
College Station, TX 77843

RECENT PUBLICATIONS, SUBMITTALS FOR PUBLICATION AND PRESENTATIONS:

A) Edward S. Fry, Pascal Herb and William E. White, "Laser Based Orientation of a Micron Size Cube Suspended in a Quadrupole Trap," to be submitted to Appl. Opt., Dec. (1985).

ABSTRACT

Single cubes whose dimensions are of the order of one micron have been suspended in a quadrupole trap and oriented by using a laser beam with a non-uniform azimuthal intensity distribution. This is a major step forward in our program to measure the complete Mueller matrix of small cubes and to compare the results with theoretical calculations. The orientation phenomenon itself is very interesting and provides new research directions such as studies of the dynamics of gas-particle interactions. The ability to hold and hence also turn a small particle by optical means provides the possibility of spinning a non-absorbing particle at very high speeds. Future work in these areas as well as complete analysis of the torques and intensity distributions in the orientation process are being planned. The orientation scheme is being engineered to fit into our Mueller matrix measuring apparatus and data for oriented cubes will be obtained.

I. Introduction

A major part of our work on measurements of the complete electromagnetic scattering properties of small particles is to hold a single particle in a fixed orientation while making the measurements. This is required for a rigorous comparison of theoretical calculations with the experimental results. One possibility is to use a fine spider web[1] to hold the particle. However, even for the smallest webs, the electromagnetic scattering properties will be affected in an undetermined way since the effects will depend on the relative positions of web, particle, and scattered light detector. Consequently, a much more elegant way to orient the suspended particle has been sought.

The physical idea upon which our method is based can be understood as follows. Consider a laser beam which has a non-uniform azimuthal intensity distribution about the laser beam axis. If such a beam is incident on a particle, it will exert forces and torques on the particle due to radiation pressure. If the direction of incidence corresponds to an axis with respect to which the particle has the same azimuthal symmetry as the laser beam, then there will be an orientational potential energy function with well defined minima. If the minima are deep enough, the particle will be trapped in a fixed orientation. A pertinent example is a laser beam with three azimuthal intensity maxima spaced 120° apart incident on a cube along a body diagonal, i.e. the cube presents a three-fold symmetry when

viewed along a body diagonal - See Fig 1.

II. Experimental

An apparatus has been assembled for the specific purpose of studying orientation schemes. A schematic is shown in Fig. 2. A laser beam of wavelength, 488 nm, is passed through a two lens beam expander to obtain a 1" diameter collimated beam. A third lens of 15 cm focal length focuses this beam onto the particle which is suspended at the center of a quadrupole trap.[2] A fourth lens, also 15 cm focal length, recollimates the beam. A mirror reflects the beam back through the fourth lens, refocusing it onto the particle. For successful orientation the transverse positions of the foci of the direct and reflected beams must be superimposed.

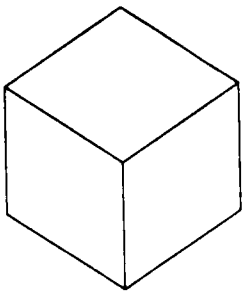

FIGURE 1. A CUBE VIEWED ALONG A BODY DIAGRAM.

Light scattered at 90° by the particle is detected by a photomultiplier (RCA 921A). The output is Fourier analyzed using a Spectral Dynamics Model SD340 Fast Fourier Transform Analyzer. If the particle is spherical the intensity of the light scattered at 90° has a constant amplitude and the

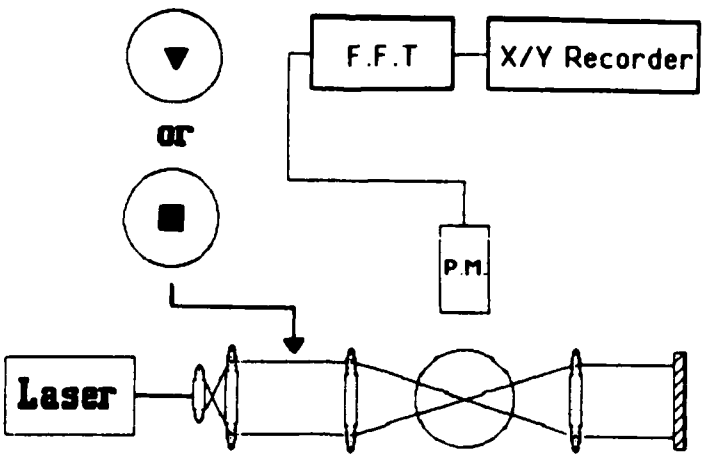

FIGURE 2. SCHEMATIC OF THE ORIENTATION APPARATUS.

Fourier spectrum is flat as shown in Fig. 3. The two spikes at 270 Hz and 540 Hz are the fundamental and first harmonic of the trap drive frequency.

If the particle is non-spherical, for example, a cube, then the light scattered at 90° has a fluctuating amplitude due to the tumbling motion of the particle and the Fourier spectrum shows significant amplitudes below 1 KHz as shown in Fig. 4. (The shape of the tail is a Lorentzian.[3]) If the cube is fixed in orientation then the light scattered at 90° should have a constant intensity and the spectrum should be flat as for the case of a sphere, Fig. 3.

FIGURE 3. FOURIER ANALYSIS OF THE LIGHT INTENSITY SCATTERED AT 90° BY A SPHERE.

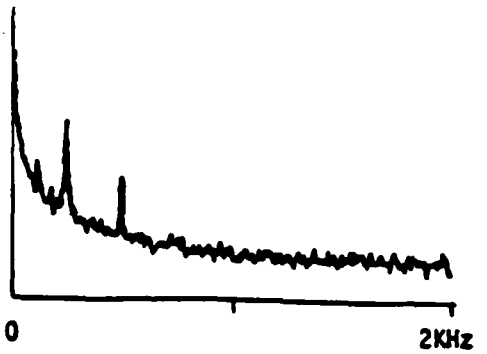

FIGURE 4. FOURIER ANALYSIS OF THE LIGHT INTENSITY SCATTERED AT 90° BY A CUBE.

To orient the particle, the laser beam must be given the appropriate azimuthal symmetry. This is accomplished by blocking the center of the laser beam with an appropriate geometry in the region where it has a collimated 1" diameter. (See Fig. 2.) We have found that either a triangular block or square block will successfully orient the cube as indicated by the Fourier spectra of Fig. 5.

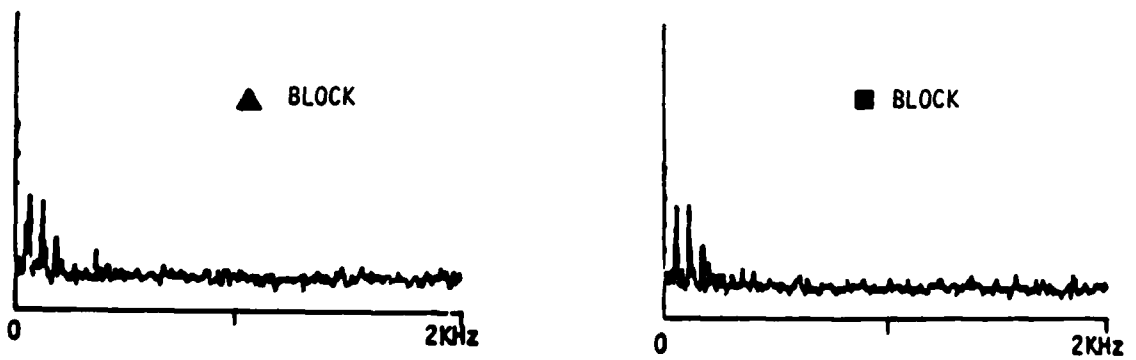

FIGURE 5. FOURIER SPECTRUM FOR AN ORIENTED CUBE.
a) a triangular block, b) a square block.

For these data the dimensions of the blocks were approximately the radius of the Gaussian beam waist. The low frequency spikes are noise pickup at the line frequency and its harmonics. Fig. 6 shows some data for a triangular block with side of length 1.2 cm. The laser power focussed into the trap is varied from 0.01 mW to 0.5 mW. As the intensity increases the low frequency contributions decrease until the spectrum is relatively flat, indicating a fixed orientation.

An important systematic check is to use a circular block. Indeed, for such a block the spectrum is unchanged from that in Fig. 4. A particle has not yet been oriented using a mono-directional laser beam. Whether this is in fact possible has not yet been determined, but we believe that counterpropagating beams may be necessary so that longitudinal forces will cancel, leaving only orientation producing torques. Experimentally it is essential to overlap the transverse positions of the focuses of the counterpropagating beams in order to effect orientation.

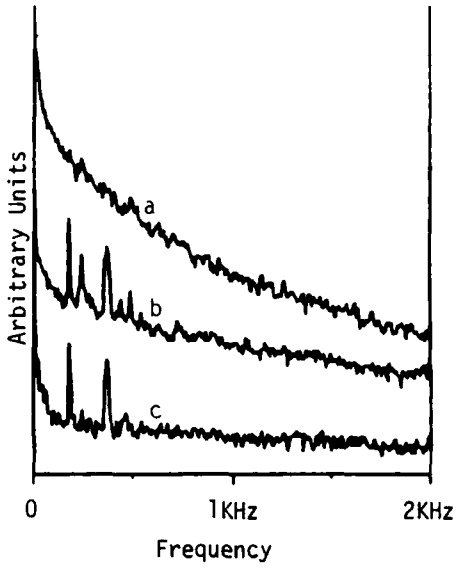

FIGURE 6. SPECTRA FOR A CUBIC PARTICLE. a) no block, b) and c) a triangular block with 0.11 mW and 0.3 mW respectively. Note the ordinates are offset for clarity.

III. Theoretical

Only the triangle block will be considered here. Some general observations about the expected intensity distributions in the region of the focus are in order. First, even though the center of the beam is removed, at the focus the intensity will be a maximum. In fact, the standard procedure to generate a smooth Gaussian profile is to insert a pinhole at the focus. However, slightly off axis the triangle block is expected to produce an azimuthal intensity distribution with three maxima separated by 120°.

After passing through the focus, the orientation of the triangular hole in the beam will be inverted. Thus near the focus, the reflected beam will also have three azimuthal intensity maxima separated by 120°, but they will be halfway between the maxima of the direct beam. The inversion of the triangle matches exactly the physical requirement, since for a cube observed along a body diagonal the triangular symmetry observed from one end of the diagonal is inverted with respect to that observed from the opposite end.

Even for a single beam, due to the fact that the triangle inverts on passing through the focus, the three azimuthal intensity maxima on each side of the focus must pass smoothly into each other. Since they are offset by 60° from each other, there must be a point between them at which there is either a smooth azimuthal distribution or one with six maxima separated by 60°. Our theoretical results give the latter.

The calculations of the intensity distributions use the Kirchoff integral approximation[4] for the field.

$$\Psi(\vec{x}) = \frac{k}{2\pi i} \int_S \frac{e^{ikR}}{R} \Psi'(\vec{x}')da' \tag{1}$$

where we have set the obliquity factor equal to unity and used $R >> \lambda$. The relevant geometry is shown in Fig. 7.

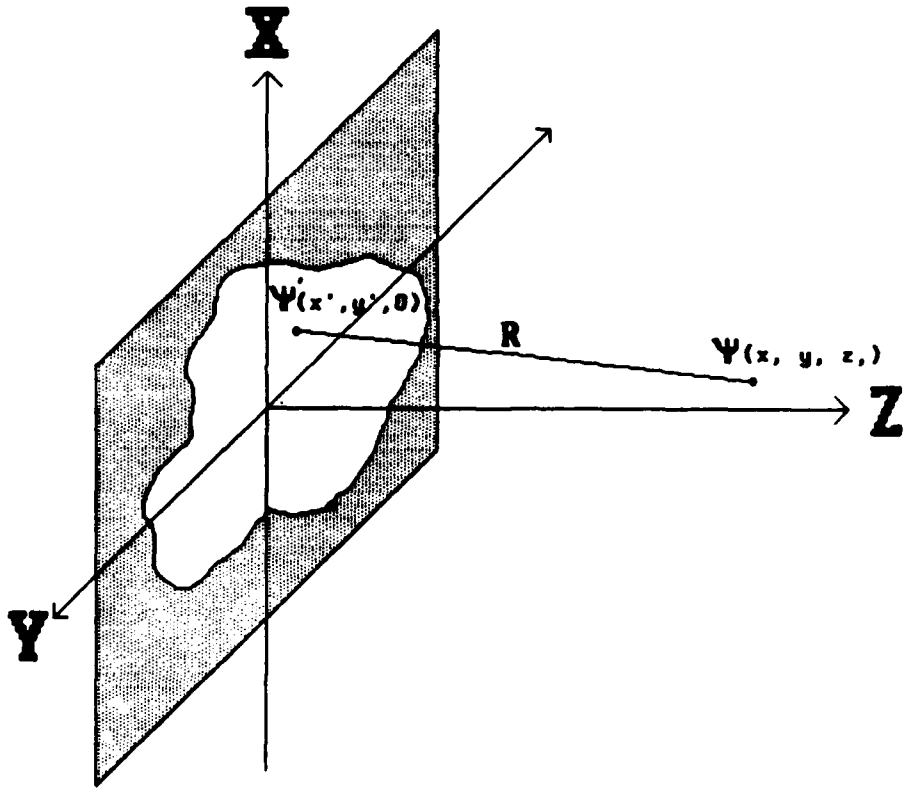

FIGURE 7. GEOMETRY FOR THE KIRCHOFF INTEGRAL APPROXIMATION.

The integration is over the clear aperture in the x-y plane, $\psi'(x',y',0)$ is the field in the aperture, $\psi(x,y,z)$ is the field at the observation point, and the parameter R is,

$$R = \sqrt{(x - x')^2 + (y - y')^2 + z^2} \tag{2}$$

Due to the rapidly varying phase neither the Fraunhofer norFresnel approximations are accurate in our experimental situation. Consequently, we have directly integrated Eq. 1 numerically. Typical results using a triangle block are shown in Fig. 8. As expected there are three intensity maxima separated by 120° which evolve into six maxima and then into three again as one proceeds down the z-axis.

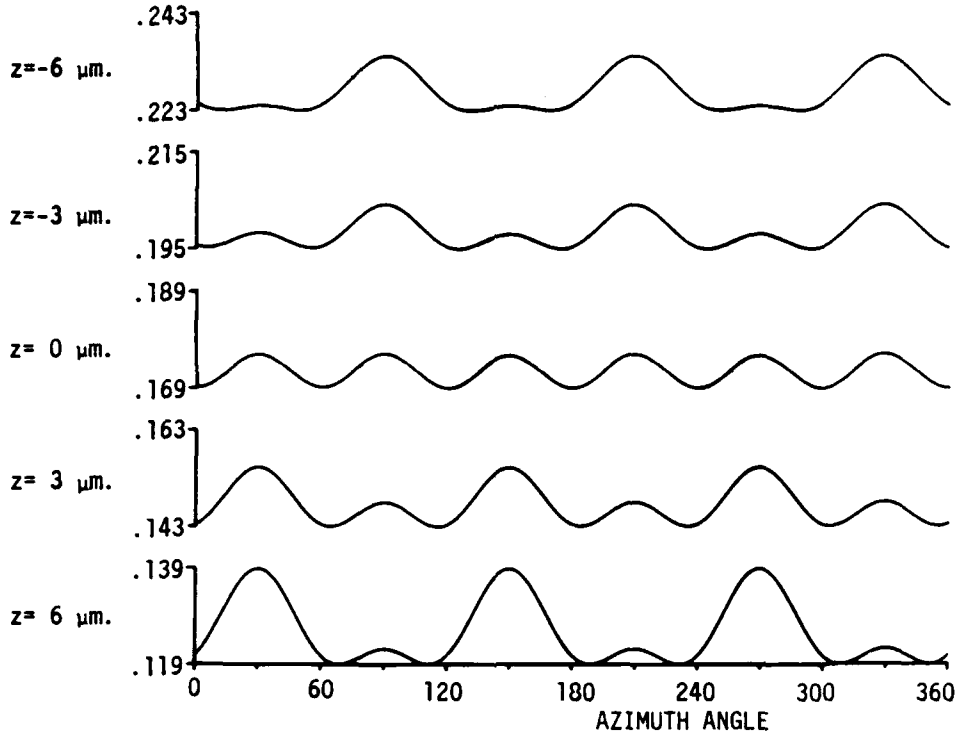

FIGURE 8. NUMERICAL RESULTS FOR THE AZIMUTHAL INTENSITY VARIATION. The relative intensity is given as a function of azimuthal angle at a distance of 1 μm from the axis for 5 successive points on the z axis separated by 3 μm. Note the ordinates are offset to show the variations. Parameters are: focusing lens, f = 15 cm; input gaussian beam waist = 1.2 cm; edge length of triangle block = 1.7 cm and focussed beam waist = 2 μm.

SUMMARY

Single cubes whose edge lengths are approximately 1 μm have been successfully suspended and oriented. Orientation has been achieved by using a laser beam whose intensity has an azimuthal symmetry that matches the projected symmetry of a cube about some axis. Both triangular and square symmetries introduced into the laser beam have provided successful orientation. If the center of a Gaussian laser beam is blocked by an opaque triangle or square, then calculations of the intensity distribution near the focus show the required azimuthal variations.

ACKNOWLEDGMENTS

The authors would like to thank Professors Chia-Ren Hu and George Kattawar for many helpful discussions and Kelly Thieme for assistance with data acquisition. This work was supported by the Army Research Office, Contract DAAG29-83-K-0074.

REFERENCES

1. M. J. Saunders and P. E. Prettyman, Science 155, 1124 (1967).
2. R. F. Wuerker, H. Shelton and R. V. Longmuir, J. Appl. Phys. 30, 342 (1959) or M. A. Philip, F. Gelbard and S. Arnold, J. Coll. Int. Sci. 91, 507 (1983).
3. B. J. Berne and R. Pecora, "Dynamic Light Scattering," Wiley-Interscience, New York (1976).
4. M. Born and E. Wolf, "Principles of Optics," Pergamon Press (1975).

MUELLER MATRIX CALCULATIONS FOR DIELECTRIC CUBES: COMPARISON WITH EXPERIMENTS

George W. Kattawar, Chia-Ren Hu and Mark E. Parkin
Texas A&M University, Dept. of Physics
College Station, Texas 77843

RECENT PUBLICATIONS, SUBMITTALS FOR PUBLICATION AND PRESENTATIONS:

A) Chia-Ren Hu, George W. Kattawar, and Mark E. Parkin, "Complete Mueller Matrix Calculations for Light Scattering from Dielectric Cubes of Dimensions of the Order of a Wavelengtn," Proceedings of the 1984 CRDC Conference on Obscuration and Aerosol, P307.

B) George W. Kattawar, Chi-Ren Hu and Mark E. Parkin, "Mueller Matrix Calculations for Dielectric Cubes: Comparison with Experiments," (to be submitted to Applied Optics).

C) Kirk A. Fuller, George W. Kattawar, and Ru T. Wang, "Electromagnetic Scattering from two Dielectric Spheres: Further Comparisons Between Theory and Experiment," (to be submitted to Applied Optics).

D) Chia-Ren Hu, George W. Kattawar, Mark E. Parkin and Paskel Herb, "Symmetry Theorems on the Forward- and Backward-Scattering Muller Matrices for Light scattering from a Non-Spherical Dielectric Scatterer," (to be submitted to Applied Optics).

ABSTRACT

The resolvent kernel technique[1] was used to calculate the complete Mueller matrix for a cube in random orientation. For experimental comparison we used the microwave analog results of Zerull.[2] In this article he presented the results for a monodisperse mixture of cubes whose edge to wavelength ratio $L/\lambda=0.96209$. This size cube corresponds to an equivalent volume shpere whose size parameter $\rho=2\pi a/\lambda=3.75$ where a and λ are the radius and wavelength respectively. We were also able to obtain some unpublished results of Zerull provided to us by Dr. Ru T. Wang for a similar monodispersion of randomly oriented cubes where $L/\lambda=0.76967$ giving an equivalent volume sphere whose size parameter $\rho=3.00$. The complex refractive index was N=1.57-.006i. In order to emulate the measurements we calculated the resolvent kernel for a single cube of the appropriate size and refractive index. This was done by partitioning the cube into 125 subcubes which yielded a resolvent kernel matrix of order 375. Once the resolvent kernel matrix is obtained, the scattered field for any orientation of the incident beam can be obtained. To obtain the Mueller matrix for a randomly oriented cube we used a Monte Carlo sampling of the three Euler angles (Φ,Θ,Ψ)[3] consistent with the scattering geometry shown in Fig. 1. To cover the unit sphere uniformly, the angles Φ and Ψ were selected randomly in the intervals $0 < \Phi < \pi/2, 0 < \Psi < \pi/2$, whereas the angle Θ was selected according to $\Theta=\cos^{-1}(1-2R)$ where R is a random number uniformly distributed between zero and unity. This selection in Θ assures that the mirror image of the particle in the scattering plane is obtained. For the randomization program we used 250 orientations. If the selection is adequate the upper right and lower left 2x2 sub-

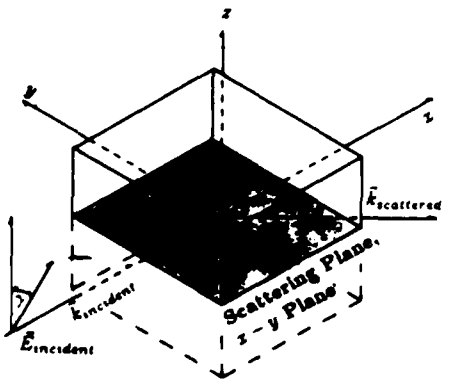

Fig. 1 Scattering geometry for the cube.

matrices of the Mueller matrix should be zero. Our tests always produced zeros in these elements within a few percent. In addition, for a cube in random orientation $P_{12}=P_{21}$ and $P_{43}=P_{34}$. These equalities were also satisfied to within a few percent.

In Figs. 2a and 2b we show a comparison of the element P_{11} for both cubes where L/λ = 0.76967 and and 0.96209 corresponding to spheres whose equivalent volumes have size parameters of ρ=3.00 and 3.75 respectively. Also shown are the results of the unpublished microwave analog measurements of Zerull. The first interesting feature to note is that for scattering angles up to ~60° there is very little difference between the randomly oriented cube and the sphere. This is of course suggestive that this lobe is primarily due to diffraction effects. For scattering angles between ~60° and ~130° the cube calculations produce a better shape dependence than the sphere when compared to the measurements. Unfortunately there were no error bars presented on the data. Another interesting feature is that the cube calculations give more backscattering than the equivalent volume sphere. In Figs. 2c and 2d we show similar comparisons for the element P_{12}. Again we see the small difference between the cube calculation and the equivalent volume sphere for scattering angles up to ~60°. The behavior of the data in this region seems to suggest that there may be a slight calibration problem in the measurements. The cube calculation produces better agreement with the data than the sphere calculations. In Figs. 2e and 2f we show the element P_{22}. The element P_{22} is quite interesting since it is unity for a monodispersion or polydispersion of spheres whereas the randomly oriented cube gets as low as 0.4 at a scattering angle of ~125°. This element is a true test of asphericity.

In Figs. 3a and 3b we show comparisons between the sphere and the randomly oriented cube for the element P_{34}. For the larger size cube (Fig. 3b) there are very large differences between the sphere and the cube particularly at the larger scattering angles. In Figs. 3c and 3d we show a simultaneous plot of P_{33} and P_{44} compared to the sphere. What is extremely important about these results is that $P_{33}\neq P_{44}$ for a randomly oriented cube, whereas $P_{33}=P_{44}$ for either a monodispersion or polydispersion of spheres.

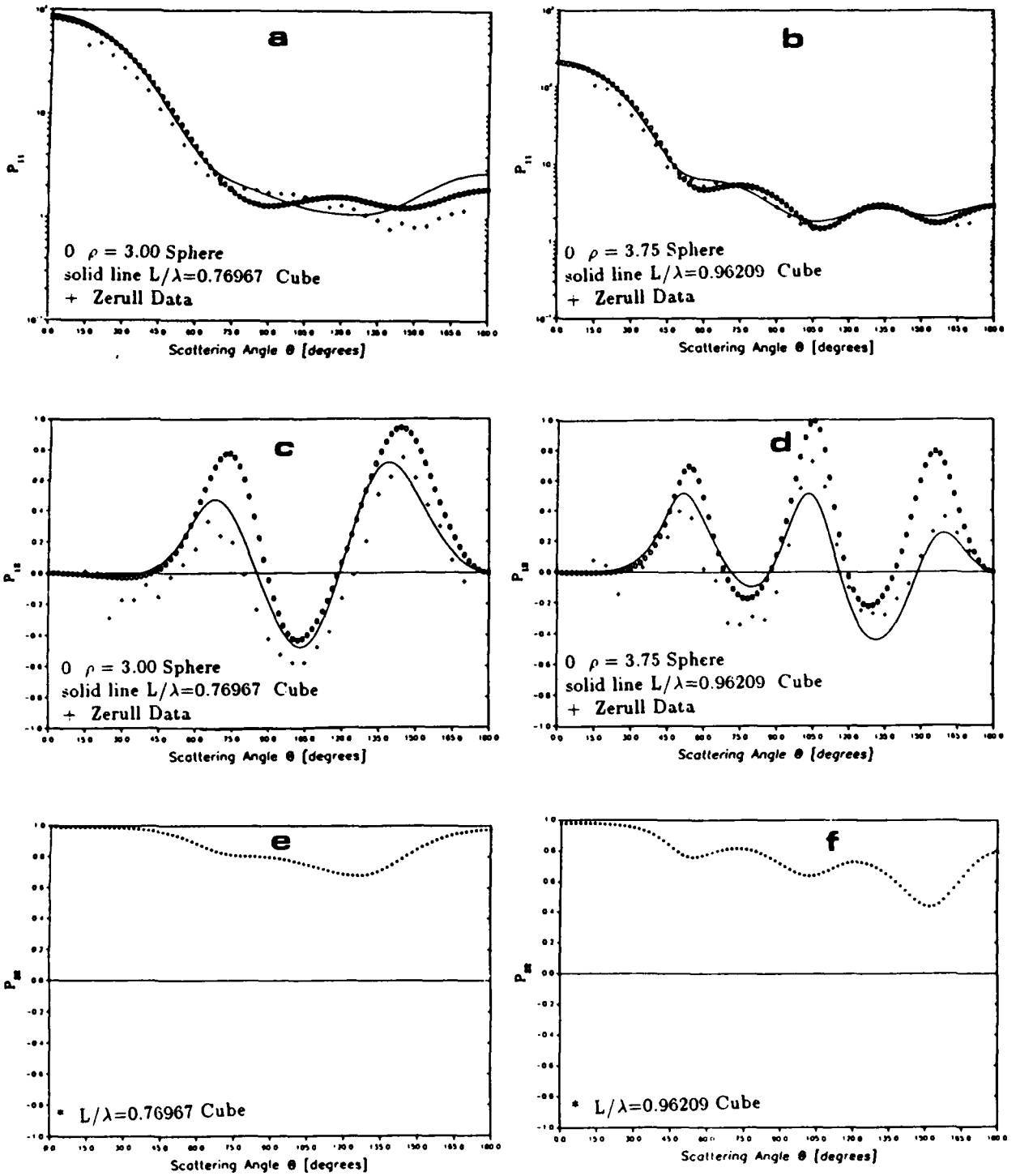

FIGURE 2. A comparison of the Mueller matrix elements P_{11}(a and b), P_{12}(c and d), P_{22}(e and f) for a cube in random orientation. The edge to wavelength ratios were 0.76967 and 0.96209 corresponding to equivalent volume spheres of size parameters ρ=3.00 and 3.75 respectively. The refractive index was N=1.57-0.006i. The microwave analog measurements of Zerull are also shown for comparison. [The scattering angle runs from 0 to 180 degrees; the vertical axis runs from 10^{-1} to 10^{+2} in (a), 10^{-1} to 10^{+3} in (b), and -1.0 to +1.0 in the rest.]

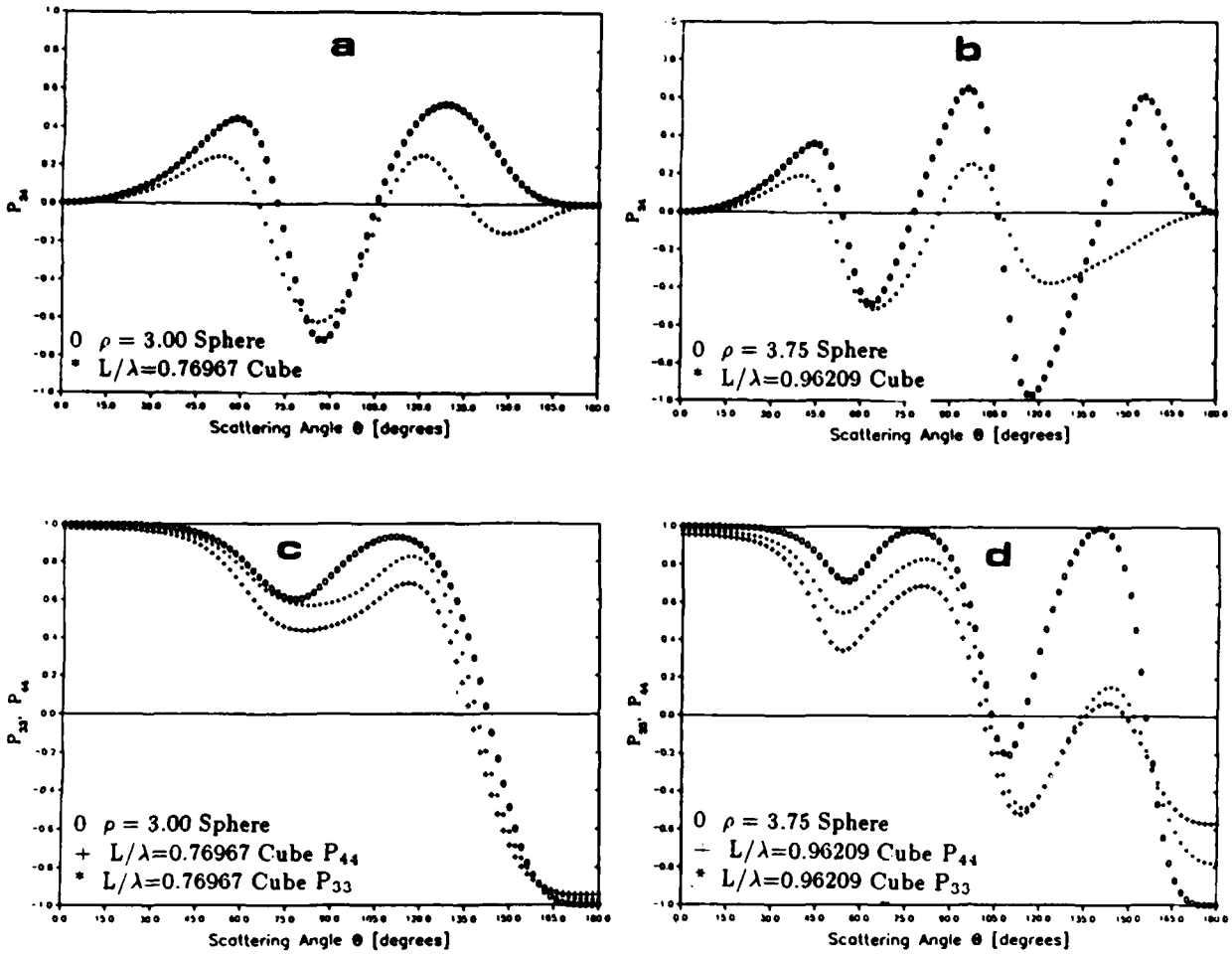

FIGURE 3. Same as Fig. 2 except for elements P_{34}(a and b) and P_{33}, P_{44}(c and d). [Vertical axis run from -1.0 to +1.0.]

FUTURE WORK

Dr. Edward Fry and coworkers have managed to orient a single cube whose edge length is of the order of a micron. We will soon be able to compare complete Mueller matrix calculations with experimental measurements for cubes.

Dr. Ru Wang has recently obtained some new data for randomly oriented cubes using his microwave analog technique. We will perform the theoretical calculations and check with his new data, however the microwave analog technique at present gives only the upper left 2x2 submatrix of the 4x4 matrix. We are also planning to calculate the forces and torques exerted on the particle by using the Maxwell stress tensor.

ACKNOWLEDGEMENT

This research was supported by the U.S. Army Research Office under Contract No. DAAG29-83-K-0074.

REFERENCES

1. Chie-Ren Hu, George W. Kattawar and Mark E. Parkin, "Complete Mueller Matrix Calculations for Light Scattering from Dielectric Cubes of Dimensions of the Order of a Wavelength," Proceedings of the 1984 CRDC Conference on Obscuration and Aerosol Research, P307.

2. R. H. Zerull, "Scattering Measurements of Dielectric and Absorbing Nonspherical Particles," Beitr. zur Physik der Atmos. 49, Band 168 (1976).

3. H. Goldstein, Classical Mechanics (Addison-Wesley Publishing Co., Inc., 1959).

4. H. C. van de Hulst, Light Scattering by Small Particles (John Wiley & Sons, New York, 1957).

SYMMETRY THEOREMS ON THE FORWARD- AND BACKWARD-SCATTERING MÜLLER MATRICES FOR LIGHT SCATTERING FROM A NON-SPHERICAL DIELECTRIC SCATTERER.

Chia-Ren Hu, George W. Kattawar, Mark E.Parkin and Pascal Herb
Texas A&M University, Dept. of Physics
College Station, Texas 77843

ABSTRACT

In this work we have systematically analyzed the symmetry theorems for the complete forward- and backward-scattering Müller matrices for light scattering from a single dielectric scatterer (as opposed to an ensemble of scatterers). Such an exhaustive analysis has not been done previously. From the symmetry theorems on the forward-scattering matrices, we have also deduced a symmetry theorem on the total extinction cross section. This work was motivated by our recent effort to calculate the complete Müller matrix for light scattering from a dielectric cube, at various orientations. (For a progress report of that work, see references 1 and 2)

In those studies, we found that the complete forward- and backward-scattering Müller matrices for light scattering from a dielectric cube at face-, edge-, and corner-on incidences show clear signatures of the symmetry properties of the scatterer relative to the incident wave vector $\vec{k}_i$, which cannot be fully understood in terms of the symmetry theorems discussed in the literature. A complete set of such symmetry theorems can not only help us understand our calculations of light scattering properties from a dielectric cube, it can also have a wide range of applications, including: (i) Consistency checks for numerical methods, approximation schemes and experimental measurements on light scattering from a non-spherical scatterer, (ii)providing a simple, fast, non-destructive method for identifying certain types of objects, etc. These considerations have motivated us to undertake the present thorough study of the symmetry theorems for forward and backward light

scattering.

In this study, we find that there are four basic symmetry operations that are relevent to the analysis of the forward scattering of light. They are: (i) a mirror plane parallel to $\vec{k}_t$, but not necessarily coinciding with the scattering plane, (ii) an n-fold discrete rotation about $\vec{k}_t$ with $n > 2$, (iii) a 180°-rotation about an axis perpendicular to $\vec{k}_t$, but not necessarily lying in the scattering plane, and (iv) a mirror plane perpendicular to $\vec{k}_t$. Through various combinations of these four symmetry operations, including the possibility of screw-like symmetries (i.e., a symmetry with respect to a product of two or more basic symmetry operations, but not with respect to any of the factor operations), we find that there are sixteen different symmetry shapes for analyzing the forward scattering of light, [named (1),(1′),(2),(3),(3′),(4),(5),(6),(7),(8a),(8b),(9),(10),(11),(12a) and (12b),] , which may be classified into five symmetry classes [named (A),(B),(C),(D) and (E)]. The reductions in the forward-scattering Müller matrix are identical for all symmetry shapes that fall in the same symmetry class, so that they are actually indistinguishable by the forward scattering of light alone. Not included in this list is a general shape with no *relevant* symmetries at all, which falls into a class of its own, which may be called the "symmetry class" (X). Including this shape and class we would have seventeen symmetry shapes and six symmetry classes for analyzing the forward scattering of light. Only for the shapes in the class (E), is the forward-scattering Müller matrix diagonal (and proportional to a unit matrix).

For backward scattering, there are only two relevant symmetry operations (i.e., the first two for forward scattering), which may be combined in various ways to give only four different symmetry shapes, [named $(\bar{1})$, $(\bar{1}')$, $(\bar{2})$ and $(\bar{3})$]. (Again not included is a general shape with no relevant symmetries at all.) These symmetry shapes may be grouped into only two symmetry classes, [named $(\bar{A})$ and $(\bar{B})$,] with again identical predictions on the backward-scattering matrices for all the symmetry shapes that fall in the same symmetry class. (Again to these symmetry classes one may add a "symmetry class" (X), corresponding to no symmetry reductions in the backward-scattering matrices at all). Only for the shapes in class $(\bar{B})$ is the backward-scattering Müller Matrix diagonal (and proportional to the diagonal matrix with elements 1,1,-1,-1). We also find that by combining the predictions for both the forward and the backward scatterings, one

has a slightly better distinction between the different symmetry shapes, but many of the different symmetry shapes are still not distinguishable, and one must rely on other methods for their distinction. Thus the symmetry theorems deduced in this work allow one to understand the maximum information that can be obtained from forward and backward light scattering alone. The clear distinction of many different symmetry shapes by this method should suggest many practical applications, especially when partial information is already available about an unknown system to be identified. This method may then provide a quick and convenient non-destructive method for its identification. One promising such application is in the area of automated cytology where, for example, normal blood cells could be distinguished from sickle cells due to the fact that they belong to clearly different symmetry classes in the sense discussed in this work, even at random orientations! It should also provide exciting possibilities for LIDAR use in determining aerosol shapes. Radar applications will also be possible. Measurement of light scattering properties in the exact forward and backward directions may be difficult, but this difficulty may be easily circumvented by measuring the scattering properties at small deviations from the exact forward and backward directions, and then performing simple extrapolations. Small errors caused by such extrapolation procedures will not be of concern, if the main task is to distinquish between a small set of possible objects, which belong to clearly distinguishable symmetry classes in the sense discussed here, such as to distinguish between sickle cells and normal blood cells. Applications of this type should be quite abundant, and in a wide range of fields, such as in medicine, in various types of industries, and in pollution analysis, etc. The availability of lasers, optical fibers, and various sentitive light detection devices, etc. should make such applications quite feasible and of practical value. The essential common feature of such applications is the measurement of *a few crucial* elements of the forward- and/or backward-scattering Müller matrices, and then cross-checking the results with the predictions of the symmetry theorems deduced here.

In order to enhance our confidence in these symmetry theorems, we have also performed extensive numerical tests of all of the symmetry theorems deduced here, using our cube scattering program. We subdivided the cubic scatterer into 64 subcubes, and then deleted the appropriate subcubes, in order to emulate all of the different symmetry shapes

discussed in this work. We obtained excellent agreement with all of the conclusions in these theorems, except that in some cases, some crucial quantities may turn out to be very small and can thus become misleading if plotted on ordinary scales. This is of course unavoidable, since the symmetry theorems cannot say anything about the magnitudes of the nonvanishing elements of the forward- and backward-scattering Müller matrices, except to provide certain relations among these elements. The theoretical part of this phase of our research is essentially completed. It is currently being prepared for publication in Applied Optics.

ACKNOWLEDGMENT

This work is supported by the U.S. Army Research Office under Contract No.DAAG29-83-K-0074.

REFERENCES

(1) C.-R. Hu, G. W. Kattawar and M.E. Parkin, "Complete Mueller Matrix Calculations for Light Scattering From Dielectric Cubes of Dimensions of the Order of a Wavelength", Proceedings of the 1984 CRDC Scientific Conference on Obscuration and Aerosol Research, R. H. Kohl and D. Stroud, eds., RHK & Associates, Tullahoma, Tenn., P. 307.

(2) G. W. Kattawar, C.-R. Hu and M. E. Parkin, "Mueller Matrix Calculations for Dielectric Cubes: Comparison With Experiments" In This Issue of The Proceedings.

SURFACE ROUGHNESS, CLUSTERING AND MATERIAL EFFECTS IN ABSORPTION AND SCATTERING BY ELECTRICALLY SMALL PARTICLES

Herschel Weil
Radiation Laboratory
Department of Electrical Engineering and Computer Science
The University of Michigan
Ann Arbor, Michigan 48109

RECENT PUBLICATIONS, SUBMITTALS FOR PUBLICATION AND PRESENTATIONS:

A) H. Weil, T.B.A. Senior, "Structure of Surface Polariton Modes in and Near Small Particles", presented to U.S. Nat. Comm. of URSI, Radio Science Meeting, Boulder, CO, January 1984.
B) T.B.A. Senior and D. A. Ksienski, "Determination of a Vector Potential", Radio Sci., 19, pp. 603-607, March-April 1984.
C) T.B.A. Senior and M. Naor, "Low Frequency Scattering by a Resistive Plate", IEEE Trans. Antennas and Propagat., Vol. AP-21, pp. 272-275, March 1984.
D) D. A. Ksienski, "Scattering by Distributions of Small Particles", Ph.D. Dissertation, University of Michigan, December 1984.
E) H. Weil, "Transmission and Absorption of Radiation in Particle Clouds,", Final Report on CSL Contract DAAK11-82-K-0007, May 1985.
F) H. Weil, T.B.A. Senior and T. M. Willis III, "Internal and Near Fields of Small Particles Irradiated in Spectral Absorption Bands", J. Opt. Soc. Amer. A, Vol. 2, pp. 989-996, June 1985.
G) H. Weil and T.B.A. Senior, "Absorption and Scattering by Small Particles; Structure of Internal and Near Fields", Proc. 1984 CSL Conference on Obscuration and Aerosol Research, pp. 295-296, June 1985.
H) T.B.A. Senior and D. A. Ksienski, "Low Frequency Scattering by Dielectric Platelets", Applied Physics B (to appear) Vol. 38, pp. 3160-3166 (provisional page numbers), 1985.

ABSTRACT

Resonance absorption and scattering by polariton modes for Rayleigh particles and particle clusters are studied numerically. The effects on the resonance frequencies and resonance strengths of particle shape and contiguity and of surface grooves and ridges are illustrated for a number of particle configurations.

INTRODUCTION

The resonances we are concerned with occur in absorption bands of the bulk material of which the particles are composed. The absorption is due to combined electromagnetic-vibrational modes of excitation; i.e., polariton modes. The resonances occur even in particles wnich are much smaller than the wavelength of the purely electromagnetic incident wave, so-called Rayleigh particles. Since the results we present are all based on the theory, computational techniques and computer programs presented in Refs. A), E), F) and G) listed above, as well as in an older related paper [Senior and Weil, Appl. Phys. B 29, 117, 1982]; we simply quote without proof the theoretical formulas essential to understand the significance of the present results. A requirement on the applicability of the results is that the entire group of one or more scatterers must lie within a region small compared to the free space wavelength. We shall consider such a group of particles to be a single disjoint scatterer. To simplify the problem, while still retaining the effects we wish to demonstrate, we assume that all the scatterers are rotationally symmetric about an axis which we take to be the x_3 axis of a Cartesian or cylindrical system. The polarization tensor, $\bar{\bar{X}}$, which relates the

unperturbed incident electric field $\bar{E}_0$ to the dipole moment of the induced field via

$$\bar{p} = \varepsilon_0 V \bar{\bar{X}} \bar{E}_0$$

then has a diagonal matrix with $X_{11} = X_{22}$. Element X_{11} is proportional to the dipole moment when $\bar{E}_0$ is transverse to the symmetry axis, X_{33} to the dipole moment when $\bar{E}_0$ is parallel to the symmetry axis. X_{11} and X_{33} are functions of the complex dielectric constant $\varepsilon = \varepsilon' + i\varepsilon''$ of the bulk material composing the scatterer(s) (which are assumed to be homogeneous and nonmagnetic) and of their geometrical configuration. The absorption and total scattering cross-section σ_A and σ_T are expressible in terms of the X_{ii}. Thus if one averages over all orientations of the scatterer, considering all orientations to be equally likely, the resulting average cross sections are

$$\langle \sigma_T \rangle = \frac{k_0^4 V^2}{18\pi} (2|X_{11}|^2 + |X_{33}|^2)$$

$$\langle \sigma_A \rangle = \frac{k_0 V}{3} \mathrm{Im}(2X_{11} + X_{33}) \quad .$$

At the polariton resonances of X_{11} or X_{33} both absorption and scattering are enhanced.

The absorption bands of the bulk materials are characterized by a range of frequencies wherein $\varepsilon' < 0$ ($\varepsilon'' > 0$ always). The particle resonances occur for $\varepsilon' < 0$ and their strength depends on ε''. If $\varepsilon'' \equiv 0$, there is no damping and Im X_{ii} and $|X_{ii}|$ are infinite. Our procedures locate the important resonance values of ε' by searching for those values which give clear maxima of Im X_{ii} as a function of ε' while ε'' is held fixed (independent of ε') at a non-zero value small enough so as to avoid excessive damping. Of course for physically real materials ε' and ε'' are both frequency dependent; ε'' varies with ε'. This is illustrated for Cu and SiC in Fig. 1 which plots ε'' vs ε' for these materials while showing values of wavelength along the curve for Cu or normalized frequency ν = f/23.8 THz along the curve for SiC. We shall use these data to bring into account realistic material effects.

A good object with which to illustrate the resonance effects is the isolated sphere for which a simple formula exists for X_{ii}:

$$X_{11} = X_{33} = 3(\varepsilon - 1)/(\varepsilon + 2) \quad .$$

Hence there is one true resonance and this is for $\varepsilon' = -2$, $\varepsilon'' = 0$. To explore the effect of non-zero ε'' one can write

$$\varepsilon = -2 + \Delta + i\varepsilon''$$

so that

$$\text{Im } X_{11} = \text{Im } X_{33} = \frac{9\varepsilon''}{\Delta^2 + \varepsilon''^2}$$

which at resonance ($\Delta = 0$) shows that

$$\text{Im } X_{11} = 9/\varepsilon'' \quad .$$

RESULTS

1. Pairs of Spheres and Partial Spheres

We first consider the sequence of bodies shown in Fig. 2. This begins with a single sphere and then follows a sequence as though two superimposed spheres were being pulled apart, finally becoming a pair of separate spheres. For each configuration Fig. 2 also shows the location on the $-\varepsilon'$ axis of the resonances which are not damped out when $\varepsilon'' = 0.01$. Resonances for both X_{11} and X_{33} are shown. X_{33} tends to have a larger number of appreciable resonances than X_{11}. There is also a sudden shift to an extremely large value of $-\varepsilon'$ for one of the X_{33} resonances, occurring just as the two spheres separate.

Next, to illustrate the relative peak strengths and resonance widths of the various resonances, we plot $-\varepsilon'$ vs Im X_{11} in Fig. 3 for one of the configurations in Fig. 2. We do this for the three materials; the unphysical one in which $\varepsilon'' = 0.01$ for all ε', and for Cu and SiC. One might think of the resonances obtained for $\varepsilon'' = 0.01$ as putative resonances which may or may not be damped out by the ε'' values of a true material. We see that most, but not all such potential resonances are in fact removed by damping for Cu and SiC.

2. Circular Disks and Pairs of Circular Disks

Results similar to those of Fig. 2 are given in Fig. 4 for a sequence made by "pulling apart" two superposed disks until they become separate pairs. The results are in some ways similar to those of spheres but note that a single disk, unlike a single sphere, possesses many potential resonances.

3. Surface Perturbations

In this section we illustrate how small scale perturbations of the surface can modify the strengths of the resonances as well as the ε' values at which they occur. The perturbations also introduce new resonances. As an unperturbed prototype shape, we use a circular cylinder, spherically capped at both ends, of five to one length to diameter ratio. Again, we show the X_{11} and X_{33} resonances for the unphysical ($\varepsilon'' = 0.01$) material and for Cu and SiC. In Fig. 5(a) the X_{11} results are shown for the unperturbed cylinder while Fig. 5(b) displays the results for surface modified as illustrated

with alternate ridges and grooves. Additional potential resonances are generated by the perturbations. Some, but not all, of these are suppressed by damping in the real materials. Figures 6(a) and 6(b) present similar results for X_{33} and point up again that the number of resonances for X_{33} is greater than for X_{11}.

COMMENTS

Matrix elements X_{11} and X_{33} were each computed numerically from an integral equation based on the unperturbed field being, respectively, radially or axially directed. The limitation to rotational symmetry not only limited the matrix to only two non-zero elements, it enabled analytic reduction of the integrals from surface to line integrals before any numerical procedure had to be introduced. When the particle is not rotationally symmetric the same type of diagonal matrix still exists for mirror symmetry of the body shape in the $x_1 x_3$ and $x_2 x_3$ planes.

Finally, we mention that Refs. D and H describe a completely different technique to handle thin disks of arbitrary shape. The method is a finite element one and gives identical results, when applied to thin circular Rayleigh disks, as the integral equation mode used here, but it is not applicable in the polariton resonance regions without further refinement.

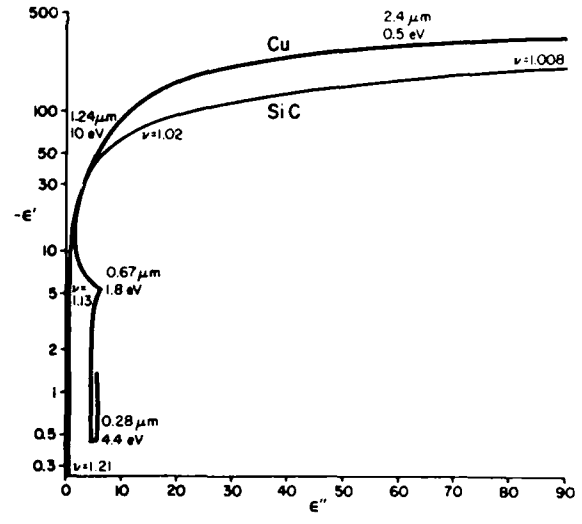

Fig. 1: The relationship ε" (ε') for Cu and SiC; wavelength or frequency as parameter. Data for Cu from Physik Daten; Part II, Fachinformationzentrum Energie, Physik, Mathematik, GMBH, Karlsruhe, 1981. Data for SiC from W. G. Spitzer, D. Kleinman and D. Walsh, Phys. Rev. 113, 127, January 1, 1959.

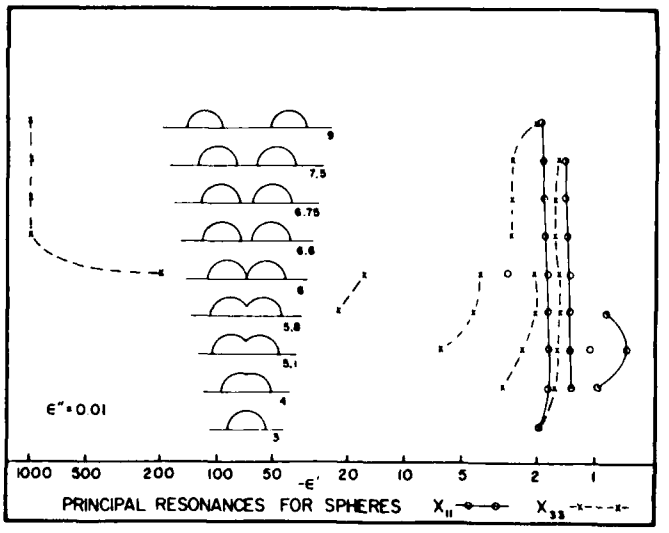

Fig. 2: Sphere sequence and associated principal resonance values of -ε' for both radial (X_{11}) and axial (X_{33}) $\bar{E}$ excitations.

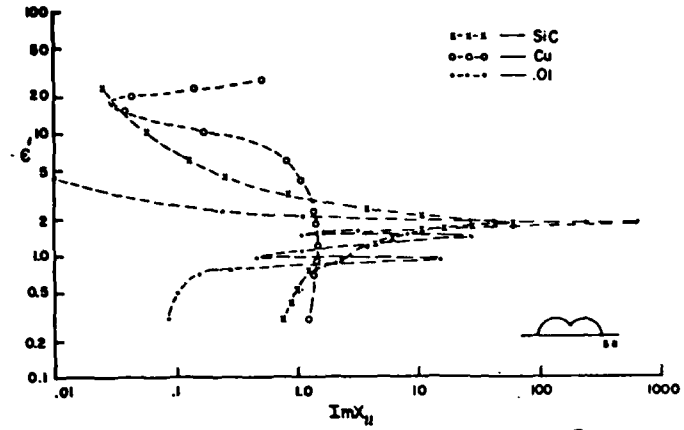

Fig. 3: Resonance strength for transverse $\bar{E}$ excitation of the configuration shown in the insert. This figure illustrates the damping effects of real materials Cu and SiC compared to the $\varepsilon' = 0.01$ hypothetical low damping material.

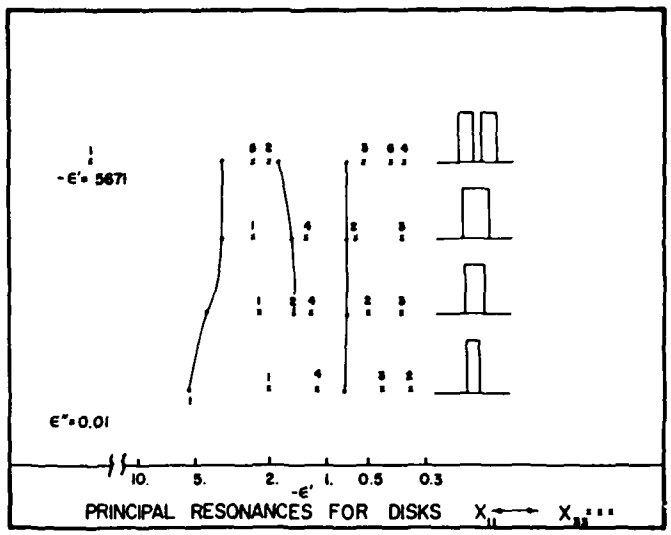

Fig. 4: Disk sequence and associated principal resonance values of $-\varepsilon'$ for both radial X_{11} and axial X_{33} $\bar{E}$ excitations.

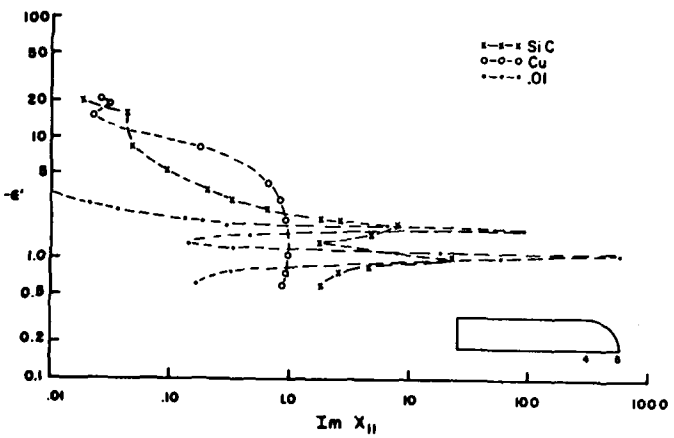

Fig. 5(a): Unperturbed surface.

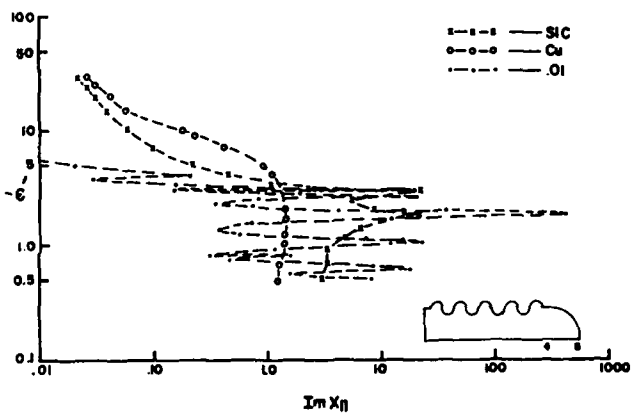

Fig. 5(b): With ridge and groove perturbations.

Resonance strengths for transverse excitation of a 5:1 hemispherically capped cylinder illustrating real material damping effects and surface perturbation effects.

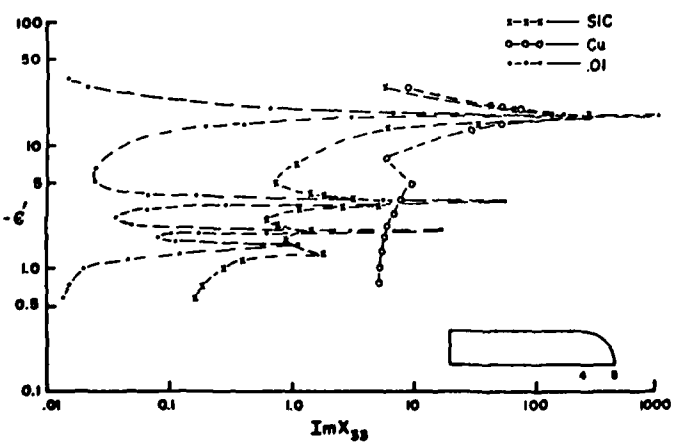

Fig. 6(a): Unperturbed surface.

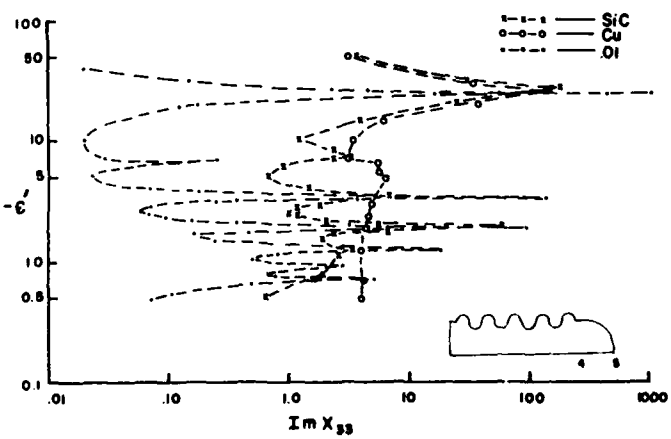

Fig. 6(b): With ridge and groove perturbations.

Resonance strengths for axial excitation of a 5:1 hemispherically capped cylinder illustrating real material damping effects and surface perturbation effects.

ON INVERSE SCATTERING AND OBJECTS OF COMPLEX SHAPE

D.L. Jaggard and K. Schultz
Moore School of Electrical Engineering
University of Pennsylvania
Philadelphia, PA 19104

RECENT PUBLICATIONS, SUBMITTALS FOR PUBLICATION AND PRESENTATIONS:

A) P.V. Frangos and D.L. Jaggard, "Inverse Scattering for One-Dimensional Dielectrics," presented at the 1984 Benjamin Franklin Symposium on Advances in Antennas and Microwave Technology, Philadelphia (May 5, 1984).

B) D.L. Jaggard, K.E. Olson and P.V. Frangos, "Inverse Scattering for One-Dimensional Dispersionless Dielectrics," presented at the 1985 IEEE/AP Symposium and National Radio Science Meeting, Boston (June 25-28, 1985).

C) D.L. Jaggard, N.H. Farhat, K. Schultz and T.H. Chu, "Three-Dimensional Tomographic Microwave Imaging," presented at the XXI General Assembly of URSI, Florence, Italy (Aug. 28-Sept. 5, 1984).

D) D.L. Jaggard, "Microwave Imaging of Dielectric Bodies," invited talk, SOHIO, Dallas Texas (April 18, 1985).

E) Y. Kim and D.L. Jaggard, "Inverse Blackbody Radiation: An Exact Closed-Form Solution," 1985 Benjamin Franklin Symposium on Advances in Antennas and Microwave Technology, Philadelphia (May 4, 1985).

F) D.L. Jaggard, P. Frangos and Y. Kim, "Some Nonlinear Methods for Inverse Scattering," 1985 Benjamin Franklin Symposium on Advances in Antennas and Microwave Technology, Philadelphia (May 4, 1985).

G) D.L. Jaggard and Y. Kim, "Inverse Blackbody Radiation," US-France Conference on Near Field Microwave Imaging, Georgia Tech., Atlanta, Georgia (June 10-11, 1985).

H) D.L. Jaggard, P.V. Frangos and Y. Kim, "Nonlinear Inversion Techniques for One-Dimensional Inhomogeneous Dielectrics," US-France Conference on Near Field Microwave Imaging, Georgia Tech., Atlanta, Georgia (June 10-11, 1985).

I) D.L. Jaggard and K. Schultz, "Imaging of Multiply Connected Dielectrics for Nondestructive Evaluation," US-France Conference on Near Field Microwave Imaging, Georgia Tech., Atlanta, Georgia (June 10-11, 1985).

J) D.L. Jaggard, K. Schultz, Y. Kim and P.V. Frangos, "Inverse Scattering for Dielectric Media," presented at the Annual Meeting of the Optical Society of America, Washington, D.C. (October 14-18, 1985).

K) D.L. Jaggard and A.K. Jordan, "Inversion Theory for Almost Periodic Media," Radio Science 19 1333-1341 (1984).

L) Y. Kim and D.L. Jaggard, "Inverse Black Body Radiation: An Exact Closed-Form Solution," IEEE Trans. Ant. AP-33, 797-800 (1985).

M) D.L. Jaggard and K.E. Olson, "Numerical Reconstruction for Dispersionless Refractive Profiles," to appear in the special issue on Inverse Problems, J. Opt. Soc. Am. (Nov. 1985).

N) D.L. Jaggard and Y. Kim, "Accurate One-Dimensional Inverse Scattering Using a Nonlinear Renormalization Technique," to appear in special issue on Inverse Problems, J. Opt. Soc. Am. (Nov. 1985).

O) D.L. Jaggard and P. Frangos, "Numerical Profile Reconstructions for Incomplete and Noisy Data," submitted for publication.

ABSTRACT

Inverse scattering methods are used to characterize and/or image diaphanous refractive scatterers. These methods provide high quality images of singly-connected and multiply-connected structures such as those that might be encountered in aerosols. Several reconstruction methods are employed using both simulated and experimental data.

This work, which is in progress, will be concerned with reconstructions or characterizations of lossy and optically large structures in the future.

I. INTRODUCTION

The Fourier transform relation between the shape of a diaphanous object and its scattered field has been known since the original work in this area by Lord Rayleigh [1], circa 1880. Subsequent calculations by Born, Gans and many others after the turn of the century have produced similar confirming calculations which are appropriate for a variety of wave-scattering problems. Since the Fourier transform possesses an inverse, certain formulations of the inverse-scattering problem also make use of the Fourier relation between the known scattered field and the desired,but unknown,characteristics of an unknown object. These methods, both direct and inverse, linearize the inherently nonlinear nature of the problem. However, though approximate in nature, these methods provide useful insights in their regime of validity. Exact methods for multidimensional problems, such as the Gel'fand-Levitan approach [2] or the methods involving integral equations of the first-kind [3] have not been implemented to date due to their almost overwhelming complexity and/or difficulty in computation.

Here we examine a solution to the scalar inverse problem in which the shape and internal structure of a multiply-connected tenuous dielectric object is determined from the electromagnetic backscatter data. This method is applied both to experimental data taken from our laboratory measurements and to simulated data. The resulting images or reconstructions will be seen to be accurate,(band-pass) filtered replications of the original object and are very similar to the corresponding imagery created from simulated data. Fourier transform and backprojection techniques [4] are both used to process the swept-frequency backscatter data collected in the experiment. The interest here is in testing the limits of the appropriate scalar theory and in the comparison of several processing schemes. The work is currently in progress.

II. FORMULATION

Consider the problem where a lossless refractive object of finite support in the volume V is illuminated by an incident electromagnetic or optical wave. The appropriate Helmholtz equation for the total scalar field component $\psi^{tot}(\underline{x},k)$ is given by

$$[\nabla^2 + k^2\, n(x)]\, \psi^{tot}(\underline{x},k) = 0 \qquad (1)$$

where k is the vacuum wavenumber and n the (real) refractive index. The integral equation satisfied by the total field at a point $\underline{x}$ outside the scatterer can be divided into incident and scattered fields as expressed by

$$\psi^{tot}(\underline{x},\underline{k}^{inc},\underline{k}^{sc}) = \psi^{inc}(\underline{x},\underline{k}^{inc}) + \psi^{sc}(\underline{x},\underline{k}^{inc},\underline{k}^{sc}) \tag{2}$$

where the superscripts identify the appropriate field ψ or wavevector $\underline{k}$. In the far zone the scattered field can be written as

$$\psi^{sc}(\underline{x},\underline{k}^{inc},\underline{k}^{sc}) \xrightarrow[kr>>1]{} \frac{k^2 e^{ikr}}{4\pi r}\int_V [n^2(\underline{x}')-1]\, e^{-i\underline{k}^{sc}\cdot\underline{x}'}\, \psi^{tot}(\underline{x}',\underline{k}^{inc},\underline{k}^{sc})\, d\underline{x}' \tag{3}$$

where $r=|\underline{x}|$ is the distance from the center of the object located at the origin to the observer located at $\underline{x}$. Expression (3) is exact but is not easily inverted for the refractive index $n(\underline{x})$ unless the perturbation approximation is made. For plane wave illumination the incident field becomes

$$\psi^{inc}(\underline{x},\underline{k}^{inc}) = \psi_o\, e^{i\underline{k}^{inc}\cdot\underline{x}} \tag{4}$$

while for diaphanous objects, the total field in the integrand of (3) can be replaced by the incident field of (4) in the perturbation approximation. This yields the scattered field result

$$\psi^{sc}(\underline{x},\underline{q}) = \frac{k^2 e^{ikr}}{4\pi r}\,\psi_o \int_V [n^2(\underline{x}') - 1]\, e^{-i\underline{q}\cdot\underline{x}'}\, d\underline{x}' \tag{5}$$

where

$$\underline{q} \equiv \underline{k}^{sc} - \underline{k}^{inc} = \frac{\omega}{c}(\hat{e}^{sc} - \hat{e}^{inc}) = q_x\hat{e}_x + q_y\hat{e}_y + q_z\hat{e}_z \tag{6}$$

which is valid for optically small, diaphanous refractive objects and for observers in the far zone. Here ω is the radian frequency of the illuminating wave and c is the vacuum speed of light.

Clearly (5) can be exactly inverted in principle for the unknown refractive index if the scattered field is known in all of $\underline{q}$-space, that is, for all frequencies and all orientations of $\hat{e}^{inc}$ and $\hat{e}^{sc}$ such that the three dimensional manifold of $\underline{q}$ is covered. This result can be written in compact form as

$$\Gamma(\underline{q}) = \int \gamma(\underline{x})\, e^{-i\underline{q}\cdot\underline{x}}\, d\underline{x} \tag{7}$$

where $\Gamma(\underline{q})$ is proportional to the scattered field as indicated by

$$\Gamma(\underline{q}) \equiv \left[\frac{k^2 e^{ikr}}{4\pi r}\,\psi_o\right]^{-1} \psi^{sc}(\underline{x},\underline{q}) \tag{8}$$

and the object function $\gamma(\underline{x})$ is defined by

$$\gamma(\underline{x}) = \begin{cases} [n^2(\underline{x}) - 1] & \underline{x} \in V \\ 0 & \underline{x} \notin V \end{cases} \tag{9}$$

These expressions can be inverted to find the desired object function

$$\gamma(\underline{x}) = (2\pi)^{-3} \int \Gamma(\underline{q}) e^{i\underline{q}\cdot\underline{x}} \, d\underline{q} \tag{10}$$

Of course $\Gamma(\underline{q})$ is not known for all $\underline{q}$ since that requires an infinite number of measurements and a measurement system with infinite bandwidth. In practice, a set of measurements are made in a plane of $\underline{q}$, say the q_x-q_y plane, over a desired spatial frequency bandwidth Δq so that $\Gamma(\underline{q})$ is known in an annular disk of $\underline{q}$-space. This results in a bandpass-filtered projection image of $\gamma(\underline{x})$ in the x-y plane with a spatial resolution on the order of $2\pi/\Delta q$. The ideal projection image is

$$\gamma^{proj}(x,y) = \int_{-\infty}^{\infty} \gamma(x,y,z) \, dz \tag{11}$$

or equivalently

$$\gamma^{proj}(x,y) = \iint_{-\infty}^{\infty} \Gamma(q_x,q_y,0) \, e^{i(q_x x + q_y y)} \, dq_x \, dq_y \tag{12}$$

where (12) also gives the bandpass-filtered projection image if $\Gamma(q_x,q_y,0)$ is the measured data in the q_x - q_y plane.

A vector formulation of this problem is given by Farhat et. al. [5]. However, for the diaphanous objects examined here, the role of polarization is not expected to play a significant role. This expectation is verified by experimental results for the cases considered. Other objects or materials may cause polarization effects to become more prominent. This occurs in particular for the perfectly conducting case.

III. EXPERIMENTS

The scattered field and hence $\Gamma(\underline{q})$ are measured in a backscatter configuration such that (6) becomes

$$\underline{q} = 2\underline{k}^{sc} = 2\,\frac{\omega}{c}\,\hat{e}^{sc} \tag{13}$$

To access the desired annulus of data in the q_x - q_y plane, measurements are taken with a swept-frequency microwave source and coherent receiver with the object to be imaged rotated around the q_z axis. This is shown schematically in Fig. 1. The object rotation, frequency sweeping and data acquisition are under the control of a DEC MINC computer. Data processing takes place on a DEC VAX 750. In the experimental results shown here, 64 frequencies, equispaced from 6.1 to 17.1 GHz, are used for

180 angles spanning 2π radians. The objects are constructed of 0.25 cm thick plexiglass (n=1.6) with maximum dimension 30 cm. The approximate resolution of the system is 1.5 cm. Initial experiments with dielectrics can be found in [6].

In Fig. 2, the experimental results for a thin-walled plexiglass cylinder containing two plates is shown. On the left the relative magnitude of $\Gamma(q_x,q_y)$ is displayed in the q_x - q_y plane. Large specular reflections due to the interior dielectric plates produce the characteristic bright lines in the data at the 11 o'clock and 3 o'clock positions. The reconstruction is shown on the right where relative values of the object function $\gamma^{proj}(x,y)$ are displayed. This reconstruction uses a 2-D discrete Fourier transform (DFT) implemented through the use of the fast Fourier transform (FFT). The result is an excellent band-pass image of the original, multiply connected object.

In Fig. 3, the reconstruction of three eccentric cylinders is shown. Again, the left side shows the magnitude of the experimental values of $\Gamma(q_x,q_y)$ while the FFT reconstruction is shown on the right. It is a surprisingly excellent result in that all three dielectric cylinders are evident even though the two assumptions inherent in the perturbation expression are violated. In Fig. 4 the simulation and the experimental reconstruction are compared for the same case. The simulation result is found by taking the inverse FFT of the object in image space, bandlimiting the result to correspond to the experiment values of 6.1 to 17.1 GHz and taking the FFT of the bandlimited data to obtain a band-pass filtered object. The resolution of the experimental image is very close to that of the simulation. Some loss of detail of the object at the 6 o'clock and 12 o'clock positions is due to a slender dielectric rod which holds all of the cylinders in place. (The effect of this rod can also be noted in the experimental data shown on the left side of Fig. 3.)

Finally, we note that backprojection methods as well as 2-D FFT techniques may also be used to carry out the two-dimensional Fourier transform inherent in (12). In Fig. 5 a comparison of these two signal processing schemes is shown for the cylinder-enclosing-two-plates object first shown in Fig. 2. Here similar results are shown in each case although the interior plates are emphasized more clearly in the backprojection reconstruction method (left side) as opposed to the FFT technique (right side). This is more clearly shown for cases in which the number of views is restricted (not shown) and suggests that backprojection methods may possess some slight advantage in the reconstruction of objects containing high spatial frequencies such as edges or corners.

IV. CONCLUSION

Inversion or imaging of multiply connected diaphanous objects is possible from swept frequency measurements by use of a perturbational approximation. This method is robust as evidenced by the fact that excellent reconstructions are performed with band-limited and imprecise experimental data and that these results compare favorably with reconstructions due to simulated data. Furthermore, the images are qualitatively accurate even for cases in which the approximations inherent in the theory are seriously violated. This latter effect is the subject of continuing investigation and the present methods are being extended to objects of larger optical size.

In closing we note the usefulness of using microwave modelling and measurements to examine the scattering and inversion of optical scattering phenomena.

ACKNOWLEDGEMENTS

We appreciate the helpful discussions with N.H. Farhat and C.L. Werner (Univ. of Pennsylvania) and the use of the computational facilities of the GRASP Laboratory (Univ. of Pennsylvania). This work was supported by the Air Force Office of Scientific Research under grant AFOSR-81-0240 and the Army Research Office under grant DAAG29-83-K-0120.

REFERENCES

[1] Lord Rayleigh (J.W. Strutt), "On the Electromagnetic Theory of Light", Phil. Mag. 12, 81-101 (1881).

[2] See e.g., R.G. Newton, "Inverse Scattering IV. Three Dimensions: Generalized Marchenko Construction with Bound States and Generalized Gel'fand-Levitan Equation", J. Math. Phys. 23, 594-604 (1982) and the references listed therein.

[3] See e.g., D.S. Jones, Methods in Electromagnetic Wave Propagation, Clarendon Press, Oxford, (1979 .

[4] General backprojection techniques are summarized in G.T. Herman, Image Reconstruction from Projections, Academic Press, New York (1980) with suggestions for application to microwaves given by N.H. Farhat and T.H. Chu, "Tomography and Inverse Scattering", International Commission on Optics, Sapporo, Japan (1984).

[5] N.H. Farhat, T.H. Chu and C.L. Werner, "Microwave Diversity Imaging", to appear in Proc. IEEE (1986).

[6] T.H. Chu, "Optimal Methodoligies in Inverse Scattering", Ph.D Thesis, Moore School of Electrical Engineering, University of Pennsylvania (1983).

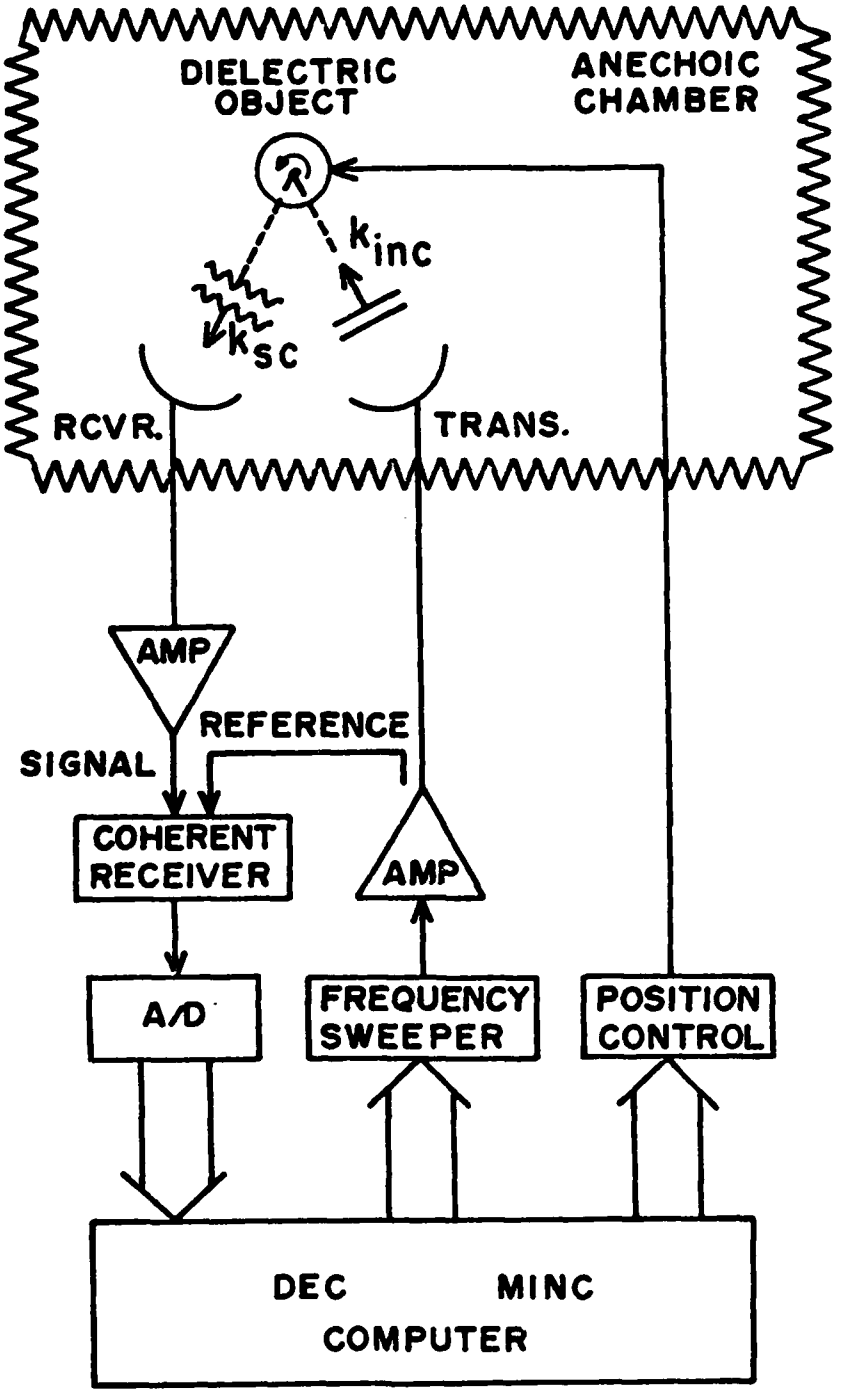

FIGURE 1. Schematic diagram of swept-frequency measurement facility for microwave imaging.

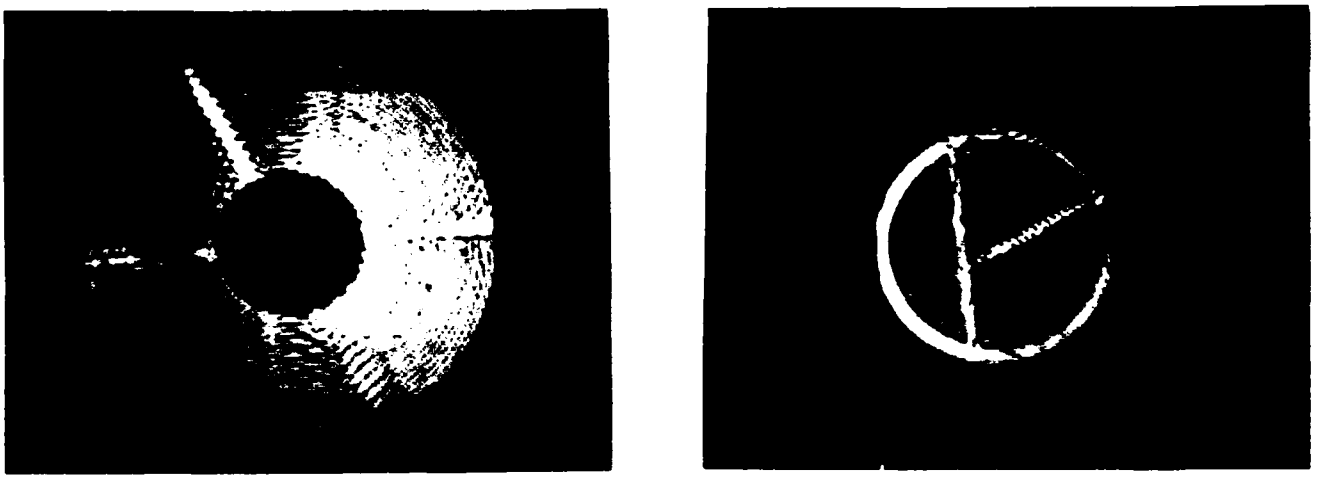

FIGURE 2. Experimental data for $|\Gamma(q_x,q_y)|$ (left) in an annulus of q_x-q_y plane of Fourier space and resulting image (right) of thin-walled plexiglass cylinder containing two dielectric plates in x-y plane of image space.

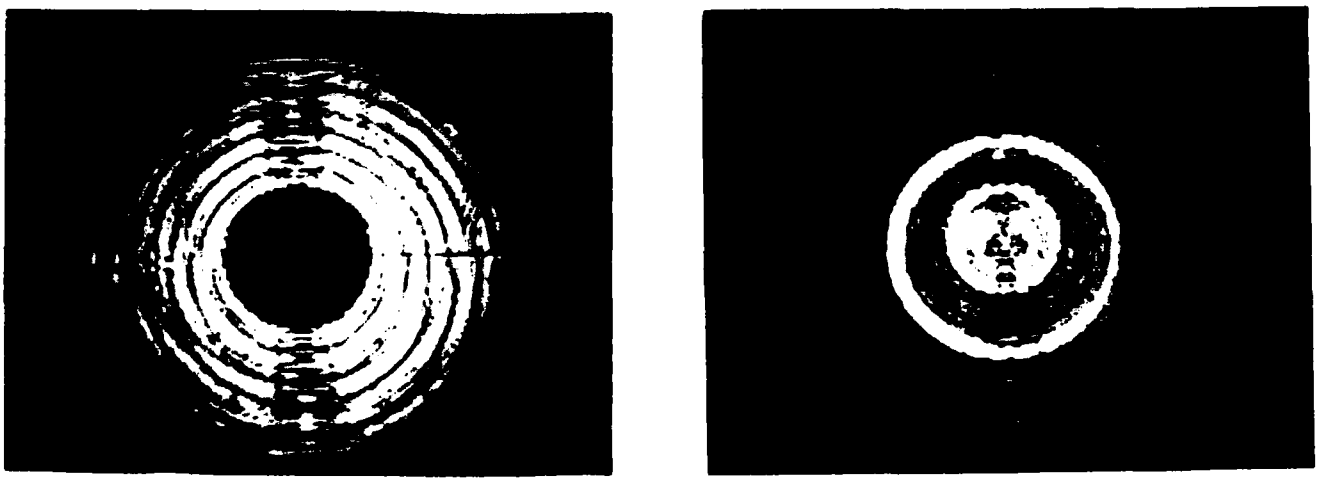

FIGURE 3. Experimental data for $|\Gamma(q_x,q_y)|$ (left) in an annulus of q_x-q_y plane of Fourier space and resulting image (right) of three thin-walled plexiglass cylinders in x-y plane of image space.

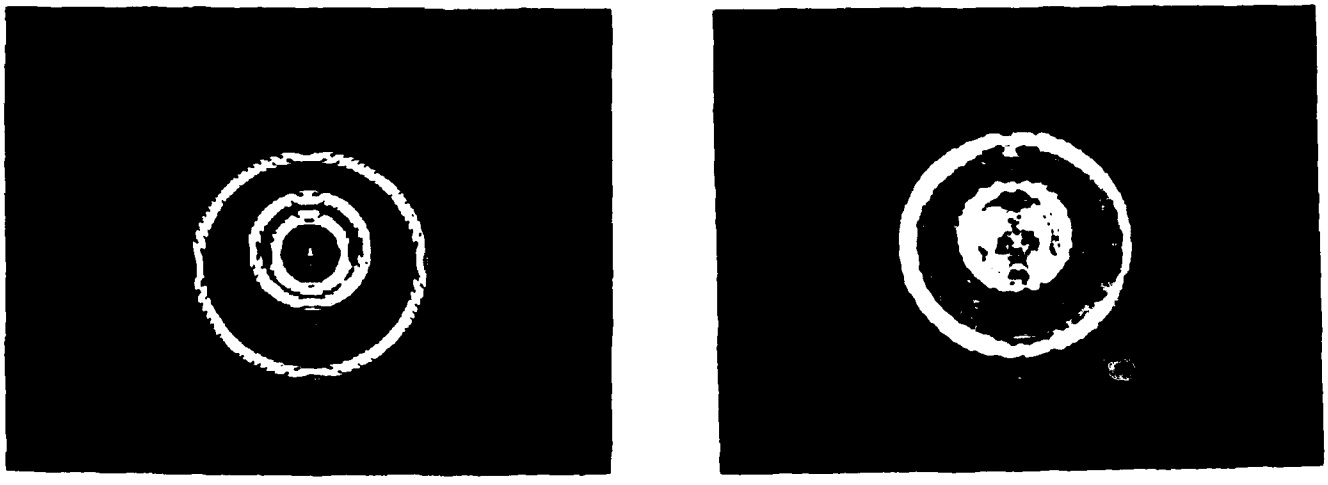

FIGURE 4. Comparison of reconstructions of the three plexiglass cylinders using bandlimited simulated data (left) and bandlimited experimental data (right).

FIGURE 5. Comparison of reconstructions of the plexiglass cylinder with plexiglass plates using backprojection (left) and two dimensional discrete Fourier transform method (right).

POLARIZED LIGHT SCATTERING FROM SURFACES

William S. Bickel and Vince Iafelice
Physics Department, University of Arizona
Tucson, Arizona 85721

RECENT PUBLICATIONS, SUBMITTALS FOR PUBLICATION AND PRESENTATIONS:

A) W. A. Gilliar, W. S. Bickel and W. M. Bailey, "Light Diffraction Studies of Single Muscle Fibers as a Function of Fiber Rotation," Biophys. J., Vol. 45, June 1984, 1159-1165

B) W. S. Bickel, "The Mueller Scattering Matrix Elements for Rayleigh Spheres," Proceedings of the Workshop on Applications of Circularly Polarized Radiation, Albuquerque, NM, May 17-20, 1984.

C) W. S. Bickel and W. M. Bailey, "Stokes Vectors, Mueller Matrices and Polarized Scattered Light," Am. J. Phys., Vol. 53, May 1985, 468-478.

D) W. S. Bickel and R. R. Zito "Light Scattering from Metal Surfaces," submitted to J. Phys. B.

E) W. S. Bickel, "Information Content and Sensitivity of Matrix Elements to Structural Changes in Complex Scattering Systems," ARO DAAK 11-80-Q-0106 Final Report, March 1983.

F) W. S. Bickel, "Masking of Light Scattering Information on Matrix Elements from Complex Scatterers," ARO DAAK-11-82-0008 Final Report, Nov. 1984.

G) K. Nahm, "Light Scattering by Polystyrene Spheres on the Conducting Plane," Ph.D. Dissertation, Physics Dept., Univ. of Arizona, 1985.

H) V. Iafelice, "The Polarized Light Scattering Matrix Elements for Select Perfect and Perturbed Optical Surfaces," M.S. Thesis, Physics Dept., Univ. of Arizona, 1985.

I) D. Abromson, "Ring Cavity Decay Lifetimes as a Function of Small Fiber Scattering and Extinction," M.S. Thesis, Physics Dept., Univ. of Arizona, 1985.

J) H. A. Yousif, "Light Scattering from Parallel Tilted Fibers," Ph.D. Dissertation, Physics Dept., Univ. of Arizona, 1985.

ABSTRACT

A highly motivated, systematic and fundamental approach to surface scattering requires that the initial surfaces be fundamental (perfect or ideal) and that the contamination to produce surface scattering be known and controlled. Rough surfaces are considered to be perturbed perfect surfaces that have reached their final condition through some continuum contamination process. This approach permits the classification of surfaces according to the light scattering response to the surface as it is perturbed away from its initial condition. All light scattering data are reported in the context of the Stokes vector and Mueller matrices.

INTRODUCTION

The powerful Stokes-vector/Mueller-matrix light scattering techniques used to study suspended particulates (spheres and fibers) can be extended directly to study surfaces. Scattering from "perfect" spheres and fibers can be theoretically predicted and experimentally tested in the laboratory to an arbitrarily high degree of accuracy. The word "perfect" is the key. The experimentalist cannot make perfect (ideal) spheres and fibers which are homogeneous in optical properties. Nor can the theorist solve in closed form the scattering fields for a slightly perturbed sphere or fiber. Nevertheless the experimental fits to theory are so close that small deviations do not endanger the validity of Maxwell's equations or the speed of light. Because theory and experiment agree for perfect particles, attention is directed to imperfect particles and particle systems, i.e., snowflakes, "bird nests" and mixtures of complex particles. Closed-form theoretical scattering solutions for truly

complex particles like snowflakes do not exist. Some solutions that come close work because the complex particle is an only slightly perturbed perfect system (ellipse) or possesses symmetry (cube, etc.). However, scattering from any arbitrarily random complex particle can be solved exactly by a brute force calculation, point by point throughout the particle.

Experimentalists have an advantage. Everything scatters. They can measure what the theorists cannot calculate, and it is just as easy to measure the light scattering from a perfect particle system as it is from a collection of snowflakes. If the data are used to check theory the experimentalist must relate the light scattering (S_{ij}) signal to both the exact structure and orientation that scattered. This is not easy because test particles are not perfect and so-called cubes often have rounded corners, etc.

With these observations and limitations in mind, it is important to review why light scattering research is done. What are the motivations and main goals? Five are listed below:

1. Test Theory: Rayleigh, Rayleigh-Gans, and Mie theory for spheres and fibers is valid and can predict the far-field scattered polarizations and intensities to a high degree of accuracy.

2. Obtain a Signature: A set of 16 matrix elements S_{ij} obtained from any scattering system can be called a signature of that system. If the signature is unique, it will identify the system and be empirically related to the structure.

3. Obtain a Change in Signature: A change in any optical, geometrical, or stochastic property of the particle (system) should cause a change in the signature. This feature is probably the most important application of light scattering -- its use as a probe for change.

4. Quantify the Signature Change: Relate a specific change in the signature S_{ij} to a specific parameter change of the system.

5. Obtain an Inversion: Measure all 16 matrix elements for a scattering system and computer invert the signals to obtain the exact (best) fit to all the system parameters. This is the final goal of many light scattering experiments. It is ambitious and it is impossible since light scattering signals are not unique. However, partial inversions are sometimes possible and useful. This involves extracting either an exact value for one parameter of the system for which all other properties are known or an approximate value whose uncertainty is related to the inversion procedure and the amount of other information known about the system.

Our work with surfaces follows the same novel and powerful procedures we used to study perfect

and imperfect particles. They are as follows:

First, start with perfect systems (spheres and fibers) that are exactly amenable to theory and experimental verification.

Second, slightly perturb the perfect system, and measure how the S_{ij} respond to the perturbation. Some perturbations are reversible, some amenable to theory, some are fundamental and some useful. A small perturbation is expected to cause a small change in some feature of the S_{ij}. (Some very large pertubations cause no change at all).

Third, increase the perturbation until the S_{ij} become nonlinear, or oscillate (multivalued) or become nonresponsive (saturated).

We have studied extensively the threshold, sensitivity, and response of S_{ij} to all forms of simply perturbed perfect systems, experimentally and theoretically. The simplest perturbations are fundamental parameter changes which leave the new system amenable to theory.[1] These involve changes in radius r, refractive index n, and absorption μ, but not shape. The larger perturbations which can significantly change the structure, effectively create a new scatterer whose shape and structure have only a tenuous connection to its initial starting point.[2] This observation is important to our approach to surface scattering. Some examples of these ideas are demonstrated in Figures 1, 2 and 3.

Figure 1 shows the four light scattering curves from a two component sphere system as a function of relative concentration. The system containing mostly large spheres is characterized by the S_{ij} for 0.7 micron spheres. We now "contaminate" the system with small spheres. As more and more small 0.3 micron spheres are added to the 0.7-micron sphere system, the original S_{ij} gradually lose phase information and finally become equal to the S_{ij} for 0.3 micron spheres. At certain angles, where both particles have the same polarization, all curves pass through the same point. These crossing points are independent of the population ratio and do not occur at the same angle for all S_{ij}. The single-component 0.3 and 0.7 micron S_{ij} curves bound all curves that result from any other population ratio. Data taken at certain (crossing point) angles will show no response to population changes, whereas data obtained at other "well chosen" angles will give large monotonic responses represented by the well known S-shaped masking curve. These are the angles that must be selected if the matrix element is to be used as a probe for change.

Figure 2 illustrates how phase information from large perfect spheres can be lost as the particles become irregular or mixed with different particles. As the particle systems in rows, B, C, D, and E progress to the right, they become more complex causing their light scattering curve, row A, to

become less complex. This is why light scattering data can be unreliable as a diagnostic tool. We examined the polydispersive systems of perfect spherical particles (which are exactly solvable theoretically and attainable experimentally) and irregular particles -- both of which give smooth light scattering curves.[3] This procedure can be used to test exactly the validity of inversion techniques.

When phase loss is severe, information is lost and the light scattering data are not unique to the scattering interaction. Inversion will then yield wrong or highly uncertain values for the optical and geometrical constants. In some cases, however, the remaining data are sufficient to partially characterize the scattering system.

Figure 3 shows an example of extreme phase loss in the four matrix element signals for Arizona road dust. This is a log-normal system of irregular particles polydispersed in all optical and geometrical constants. All matrix elements are smooth. Matrix elements S_{12} and S_{33} appear almost Rayleigh except that the minimum of S_{12} and the zero crossing point of S_{33} are shifted approximately 20 degrees toward the backscatter. S_{34} is almost zero as it is for Rayleigh spheres. S_{11}, varying by more than 2.5 orders of magnitude and increasing in the backscatter, is the only signal that suggests that the particles are large with high refractive index and low absorption.

SURFACE SCATTERING

How do these ideas for particulates carry over to light scattering from surfaces? What questions do we ask and what starting points do we choose for a highly motivated, systematic and fundamental study of surface scattering?

A surface is characterized by its surface properties as well as by its orientation with respect to the input-exit beam. Since surface appearance depends on how it is viewed, the S_{ij} are not unique to the surface alone. Since we consider surface scattering to be an extension of sphere and fiber scattering, similiar questions arise.

1. What kinds of surfaces should be studied?
2. What do the matrix elements S_{ij} look like?
3. What kinds of perturbations should be applied?
4. How is the S_{ij} information related to structure and its perturbation?
5. How important is the input-output-surface geometry?
6. How are various surfaces related?

THE STARTING POINT -- THE FUNDAMENTAL SURFACE

Of the infinite number of surfaces available for study, we choose to start with perfect surfaces just as we started with perfect spheres and fibers for particulate study. The first choice is an ideally flat surface such as a thin film, glass plate or mirror. However perfect surfaces do not scatter. They reflect and transmit. The reflection and refraction properties (directions, intensities and polarizations) of such surfaces are predicted exactly by electromagnetic theory (Fresnel equations and Snell's law), and they can be experimentally measured. Some results for the two polarizations refelected from glass, gold, and silver are shown in Fig 4. These well-known Fresnel curves exist for virtually every flat, high polished, natural and man-made material. However, since no scattering occurs, the curves are measured only for the special case of reflection (I = R) and transmission. There seems to be a dilemma. Unlike perfect particles, perfect surfaces do not scatter -- except into the special angles R and T. Nevertheless, we choose the reflecting "perfect surface" for the starting point for surface scattering. We will see that all scattering that does occur must come from imperfect surfaces, i.e., surfaces with imperfections and impurities.

How perfect is a perfect surface? Careful measurements of even the "best surfaces" show that the scattered light intensity at angles other than I = R is not zero but decreases rapidly by several orders of magnitude on each side of the reflected peak. Different "perfect surfaces" can be characterized by this θ-dependent intensity (and other S_{ij}) function. The residual scattering from "perfect surfaces" comes from uncontrolled defects or impurities on the surface and perhaps quantum mechanical fluctuations in the dielectric constant at the atomic level. Whatever its cause, this residual scattered light is the "zero baseline" starting point for perfect surfaces. Any surface, perturbed even more, will scatter more. The same consideration holds for particulates (spheres and fibers) in suspension. The air or liquid medium is considered to be non-scattering, although even perfectly clean fluids show Rayleigh scattering. This is taken as the zero baseline for particulates. Therefore scattering from any surface will consist of two components -- scattering from the perfect surface and scattering from the added perturbation.

Our research starts with the basic premise that any scattering surface is a "perturbed" perfect surface. A completely scratched aluminum surface is considered to be a perfect aluminum surface completely perturbed by scratches. We plan to follow the S_{ij} as a function of perturbation -- from the first scratch to final "saturation." Since a scratch is a nonfundamental (nonsolvable) perturbation, the addition of the first scratch to a perfect surface immediately generates a scattering system that is not amenable to theory. We are therefore faced with the possibility that no scattering surface can be fundamental. Although this is true for most surfaces, a number of fundamental scattering surfaces

can be experimentally created that are amenable to exact theory. Since there are so few, they are worthy of careful consideration. They are shown in Fig. 5.

The mirror, bi-mirror and line (A, B, C) are perfect flat surfaces with boundaries that separate surfaces of different refractive index. The mirror has surface index n_1; the bi-mirror -- a particular case of edge diffraction -- contains two regions, n_1 and n_2, separated by an "infinitely narrow" boundary line; the line consists of a straight line of width w, index n_3 separating two boundaries with index n_1 and n_2. These three surfaces are flat planes with no geometrical surface structure. The scattering comes only from the boundaries (discontinuity) between the different indices.

The mirror has been discussed earlier; the bi-mirror can be solved exactly using Fresnel edge diffraction. We are studying the line to see how the S_{ij} respond to changes in n_1, n_2, and n_3, w and orientation.

The grating, fiber-plane and multifiber-plane (D, E, F) have geometrically perturbed surfaces. The grating is completely characterized by the surface index n, the blaze angles α and β and by the grating constant d. The fiber-plane, consisting of two exactly characterized fundamental systems, is also fundamental. The multifiber-plane is more complex, where d_i and x_i can be specified for any number of fibers near the surface.

The interference filter (G) is a special surface made up of multilayers. Its function is to select a certain wavelength through constructive and destructive interference of the incident radiation. All of its surfaces (boundary layers) are assumed to be smooth and flat, to minimize scattering.

The Lambertian surface (I) is the "opposite case" of the perfect mirror (A) because its rough surface perturbations scatter isotropically any light incident on it. Just as there are no perfect mirrors, there are no perfect Lambertian scatterers, yet it represents the ideal and final end point --- a completely saturated perturbation of an initially perfect surface. We are trying to determine if all initially perfect surfaces can be driven to Lambertian by "enough" of the "right kind" of surface perturbations.

The rough surface (H) represents "real world" surfaces all of which lie somewhere between the perfect mirror and the perfect Lambertian. The roughness is caused by perturbations which can be any particulate -- above, on or under the surface, any kind of crack, scratch, hole, bump or other geometrical defect or a mixture of all of them. There are an infinite number of imperfect surfaces and an infinite number of ways to destroy a perfect one. Much theoretical work needs to be done to predict the scattering from these perfect surfaces. Special attention should be given to the role of polarization in the context of the Mueller matrices and Stokes vectors.

Experimentally we will find out how well the light scattering S_{ij} can characterize various classes of these surfaces and detect changes in them as more of the same or other perturbations are added.

SURFACE ORIENTATION

As mentioned earlier, the geometrical orientation of the rough surface with respect to the input exit beam is important. This problem must be addressed early because there are an infinite number of possible orientations all of which might give a different S_{ij} for the same surface. Figure 6 shows some of the geometrical parameters involved in surface scattering studies. The laser beam, after preparation into a definite polarization state, strikes the surface at angle α and is scattered into all 4π. The light scattering into angle θ is analyzed with the polarization exit optics and detected by a photomultiplier. The angle τ is a surface tilt measured in the surface plane. Initially we thought that the geometric effects were like scaling factors or convolutions which could somehow be folded out of the S_{ij} to leave information only about the structure. We hoped to find the optimum geometry to enhance or perhaps subdue certain surface effects or find that certain S_{ij} are independent of geometry.

Our work and that of others show that geometry is important and that no best orientation exists for all cases. Harvey[4] shows how a total intensity spread function becomes distorted by the θ-dependent measuring arm that moves the detector along the circumference of a circle. See Fig. 7. This spread function, when projected onto a circle, generates a set of intensity curves whose shape depends on the illumination angle of the surface. Conversely, when the curves are deconvoluted, from the circle to the plane, all spread functions are identical.[4] See Fig. 8. This shows that at some angles the total intensity matrix element S_{11} is orientation independent.

The polarization curves S_{ij} do not scale this way. Figure 9 shows the four matrix elements from a random sanded brass surface as a function of illumination angle α. The S_{11} all appear different but can be related through the spread function. S_{12} gives a different curve for each α. S_{33} is independent of geometry for $\theta \leq 80$ degrees, S_{34} is independent of geometry at all scattering angles. To detect orientation changes of a surface with fixed structure, we would choose S_{12}. To detect structure changes on surfaces, independent of orientation, we would choose S_{34}. Since these conclusions might be specific to this sample only, more experimental work has to be done. We have also found that the detectability of one component (defect) in a two or more component system depends on illumination angle. In fact, at some angles a particular defect can be invisible!

Figure 10 shows how the matrix element S_{33} responds to a geometrical surface line ($h=0.8\ \mu$, $w=2.2\ \mu$) when illuminated at two different angles: normal incidence ($\alpha=90$) and grazing incidence ($\alpha \neq 0$).

The normal incidence illumination gives a smooth S_{33} similiar to that from a Rayleigh particle. The grazing incidence illumination reveals an oscillatory structure indicative of a single fiber. As the angle of illumination varies from grazing to normal, the structure gradually disapppears. Other S_{ij} respond similarly showing that no simple geometrical or scaling function can generate an α independent S_{ij}.

SCATTERING FROM SURFACES UNDERGOING CONTROLLED CONTAMINATIONS WITH QUANTIZED COUNTABLE PARTICLES (DEFECTS)

We now get to the main part of our experimental approach to surface scattering. Basically we will follow the response of all θ-dependent matrix elements (for all angles of illumination) as a perfect surface is contaminated with known particulates. Our first contamination choice is spheres since a sphere and surface represent an exactly solvable system. The experimental procedure is described with the help of Fig. 11.

A perfect clean mirror (situation A) when illuminated with laser light (wavelength λ, intensity I_0, width w, cross sectional area A)reflects light according to the law of reflection I=R. Since ideally no scattering occurs into angles other than θ_R a delta-function shaped intensity peak I_R occurs at the reflected angle θ_R as indicated in the graph at lower right.

As spheres begin to contaminate the surface (situation B), increased scattering occurs into all angles θ_S (at the expense of light removed from θ_R). This is single, independent particle scattering since each individual sphere is far ($D >>> \lambda$) from other spheres. The scattered intensity will increase linearly with increasing contamination (neglecting localized speckle).

Further contamination (situation C) increases the scatter at all angles and drives the scattering system into the non-linear region. Here non-independent scattering occurs from those spheres that touch or lie close to one another ($D \sim \lambda$ or $D=0$).

Still further contamination (situation D and E) occurs until the surface is completely covered by the particles. Situation D represents a "geometrical" covering of the surface (no ray of incident light at any angle can hit the surface or leave the surface without interacting with at least one particle). Situation E represents the final result, the complete masking of the initial surface. The particles form a new surface which is thick enough to ensure that no radiation leaving it carries any information about the initially perfect mirror surface underneath. Adding even more particles to this surface does not affect the scattering. We say the initial surface is completely masked out (at this wavelength) by the new particles. The final surface is saturated. The light scattering signal is flat or rigid.

As the situation moves from A to E, scattering increases at all angles until saturation occurs. This is indicated by the θ-dependent intensity curve E in the graph. (NOTE: For simplicity the scattering intensities have all been normalized to the reflected intensity for the mirror. Conservation of energy requires that the areas under each curve remain constant, i.e., scattering occurs at the expense of the main reflected peak intensity.) If the final surface were perfectly Lambertian, the scattered intensity would be independent of the scattering angle. The controlled contamination would have created from a perfect mirror a new surface which scatters isotropically.

THE SURFACE MASKING CURVE

Contamination of any surface with particles will change the <u>initial</u> surface scattering properties into the <u>final</u> surface scattering properties. During the process intermediate but related surfaces are created. Continuous contamination will generate an intensity function whose initial response is linear with contamination number N. It goes over to a final flat response at saturation. The theory describing this response is shown in Fig. 12.

Spherical particles with a geometrical cross-section area a randomly contaminate an illuminated surface of area A_o. The surface suffers the "raindrop effect" where the most likely value of the fraction of the surface remaining uncovered is

$$e^{-\frac{Na}{A_o}} ,$$

where N is the number of particles on the surface.

The fraction of the area covered is

$$1 - e^{-\frac{na}{A_o}}$$

so that

$$A_{covered} = A_c = A_o(1 - e^{-\frac{na}{A_o}}) = A_o - A_{uncovered} .$$

In the geometrical limit the scattering intensity is proportional to the area covered (the total particle-covered area) so .

$$I_S = I_o A_o \varepsilon(1 - e^{-\frac{Na}{A_o}}) ,$$

where ε is the efficiency for particle scattering. We note that for large N (as $N \to \infty$)

$$I_S = I_o A_o \varepsilon$$

Also, for small N (as N→0)

$$I_S = I_o A_o \varepsilon \frac{Na}{A_o} = I_o \varepsilon Na \quad .$$

The response curve for the scattered intensity I_S is shown in Fig. 12. Initially, scattering is zero for the perfect mirror. Adding a few particles that scatter (independent scattering) causes the scattered intensity increase linearly with N. The intermediate non-linear region occurs when non-independent scattering from near-neighbor or touching spheres start to dominate. Here ε changes also. Finally the surface is completely covered (new surface) giving no response to additional contamination. We say the initial surface is totally masked or saturated by non-independent multiple scattering particles which make up the new final surface. The light scattering response is rigid.

The above discussion deals only with the reflected scattered intensity I_{RS}. A complete experimental measurement will measure the scattering into all angles as a function of all angles of incidence. Whether this will create redundant information remains to be seen. However, there is an advantage in measuring other intensities in addition to I_{RS}.

Figure 13 shows the experimental setup of the θ-dependent light scattering and response curves for four important interactions. Here small particles contaminate a thin glass plate so that transmission occurs also. Specifically the detector scans through θ to measure the transmitted beam I_T, the transmitted scatter I_{TS}, the reflected scatter I_{RS} and the reflected beam I_R. Note that the angles for I_T and I_R are dictated by the geometry whereas the angles for I_{TS} and I_{RS} can be arbitrary. The expected response of the four intensities to increasing contamination is as follows:

I_T will start from an initial high value and asymptotically approach zero.

I_R somewhat lower than I_T will decrease asymptotically to approach a non-zero limit.

I_{RS} will start from zero, and increase asymptotically to approach a non-zero limit.

I_{TS} will start from zero, reach a maximum and then asymptotically approach zero.

These curves are shown on the Intensity-Number (I-N) plot at the bottom of Fig. 13. Some important conclusions can be drawn from these experiments.

1. If the final surface is a perfect Lambertian, $I_R = I_{RS}$ for all α and θ so that $\Delta I = 0$.
2. If the final surface is opaque, $I_T = I_{TS} = 0$.
3. For large enough N, the surface is totally masked or saturated and all curves are flat (non-responsive, rigid).
4. I_{TS} is the only signal to change the sign of its slope.
5. The curves I_T and I_{TS} will never cross.

6. I_R and I_{RS} will never be zero.
7. The I_T and I_{RS} curves will always cross once.
8. The I_R and I_T curves will always cross once.
9. The I_{TS} and I_{RS} can cross no more than once.
10. Initially , for small N, all curves have a linear (small exponential) response. Finally, at large N, they are constant.

Figure 14 shows the expected S_{11} total intensity response to contamination number N (perturbation strength). In general the vertical axis can represent any matrix element S_{ij}. The polarization responses are not as obvious as the S_{11} and are therefore receiving a great deal of experimental attention. Note that a particular set of response curves are obtained for a single wavelength λ and illumination angle α and for preselected fixed scattering angles θ_R, θ_T, θ_{RS}, and θ_{RT}. A particular perturbation strength N_i therefore gives four S_{ij} values to characterize the surface. Whether or not these will be unique or contain "enough information," requires more experimental study.

CONCLUSIONS

With the help of Figure 14 we can speculate about the kinds of response curves that can be generated by different surface contaminations.

Any surface in the universe is a point on the S_{ij}-N curve (curve A). However, the one data point is only a small part of the complete "history line" for a particular contamination process (curve B). Some contaminations will cause "thin film" interference effects as their thickness passes through various $m\lambda$ (curve C). The removal of a contamination by some process might not follow the contamination curve backward. This will cause repeated contamination and removal to show hysteresis (curve D).

Contaminating an already contaminated surface with another different contamination will cause a discontinuity in the S_{ij}-N curve (curve E). The system is driven from a to b by the first contamination. It is driven from b to c by the second and from c to d by the third. These different contaminations create a final S_{ij}-N point at d which is intimately related to the order, nature and strength of each contaminant.

THIS CURVE EXPLAINS WHY ANY SURFACE, REGARDLESS OF ITS ORIGIN, HISTORY OR STRUCTURE, OR WHETHER IT IS SATURATED OR NOT, WILL RESPOND AGAIN TO A DIFFERENT CONTAMINATION AND AFFECT THE LIGHT SCATTERED FROM IT. ALL THAT IS REQUIRED IS THAT THE NEW CONTAMINATION DIFFER FROM THE FIRST IN SOME OPTICAL OR GEOMETRICAL PROPERTY. THEREFORE, ANY S_{ij} WILL RESPOND TO ANY CHANGE IN ANY SURFACE, REGARDLESS OF WHAT THE SURFACE IS OR WHAT THE CHANGE IS.

A word of caution is in order here, since unrelated surfaces will give S_{ij} points through which a smooth line can be drawn. However, the fact that a smooth curve can be drawn through the points 1, 2, and 3 does not imply that the three surfaces are related by the same contamination that varies only in strength. For example, the strength of an S_{ij} signal at some angle might monotonically increase for three different samples, each with a different kind of surface roughness, one caused by scratches, one by pot holes, the third by pimples. The response curve of any one of the three perturbations will not necessarily follow the smooth curve that arbitrarily connects the three samples.

FINAL COMMENTS

These comments summarize some important observations concerning light scattering from surfaces.

1. The different shapes that occur for S_{11} as a function of illumination angle α can be normalized to a single angle-independent shape through a geometrical spread function. The other S_{ij} for polarized light do not scale in a simple way.
2. The detection of defects on a rough surface depends strongly on illumination angle α. Certain angles can increase the light scattering sensitivity to the defect. At other angles, the defect can be invisible.
3. All S_{ij} depend significantly on the laser spot size used to illuminate small localized defects on a larger irregular surface. Scattering occurs from defect and surface. As the laser spot size decreases, the scattering from the defect increases with respect to the scattering from the surface.
4. Rough surfaces are multiple non-independent scatterers.
5. Certain matrix elements can be sensitive to surface structure independent of orientation, while others can be sensitive to orientation but independent of structure.
6. Multiple component surfaces give polarization curves that are dominated by the component that scatters the most light.

REFERENCES

1. B. W. Bell and W. S. Bickel, "Single Fiber Light Scattering Matrix - an Experimental Determination," Appl. Opt. 20, 3874 (1981).
2. G. Videen and W. S. Bickel, "Quartz Fiber Scattering as a Function of Contamination by MgO Crystals," to be submitted to Appl. Opt.
3. W. S. Bickel, H. A. Yousif and W. M. Bailey, "Masking of Information in Light Scattering Signals from Complex Scatterers," Aerosol Science and Technology 1, 329-335 (1982).
4. J. E. Harvey, "Light Scattering Characteristics of Optical Surfaces," Ph.D. Dissertation, Univ. of Arizona, 1976.

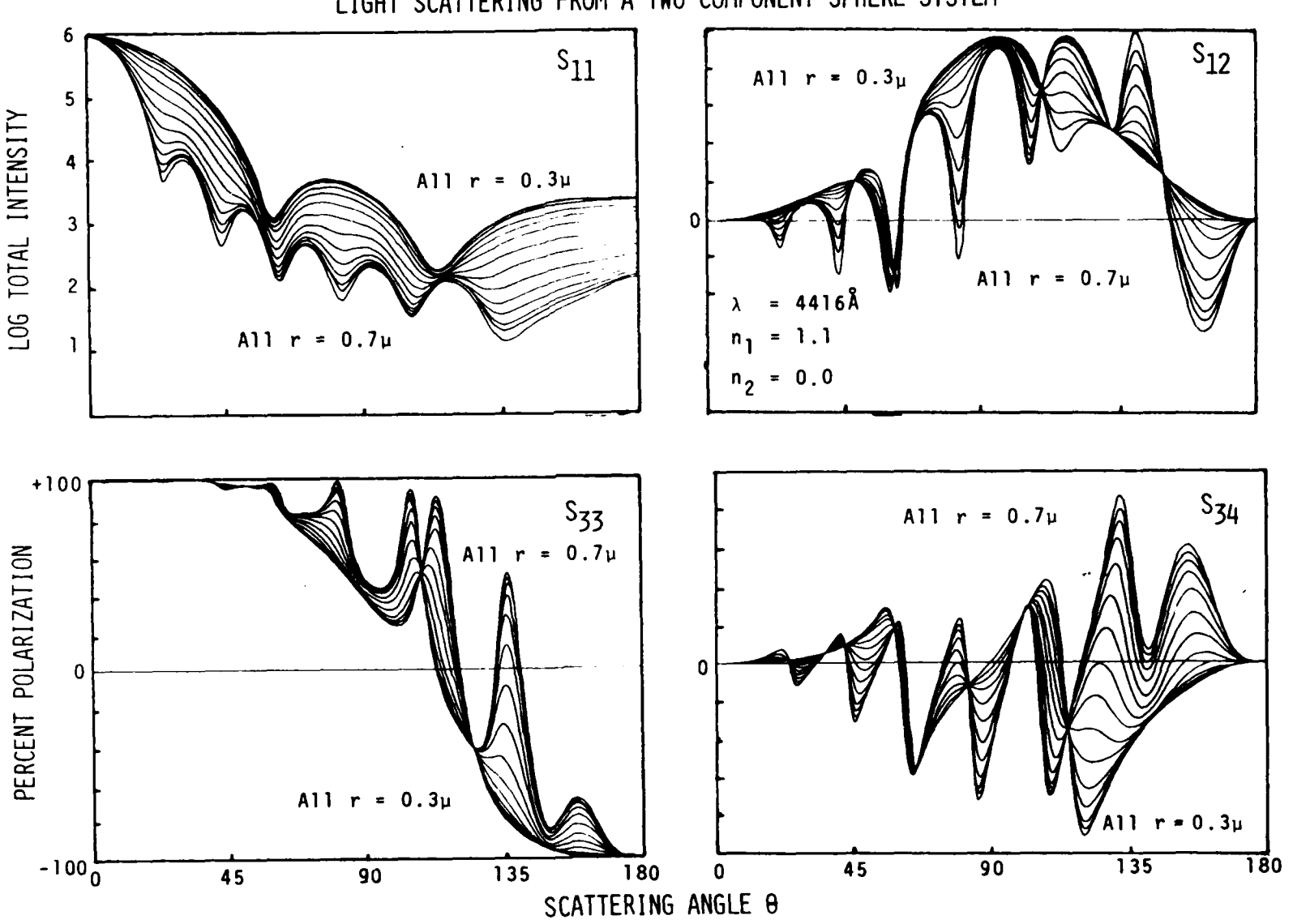

FIGURE 1. TWO COMPONENT SPHERE MIXTURE. The four S_{ij} scattering matrix elements from a two component (0.3 and 0.7 micron) sphere system as a function of relative component concentration.

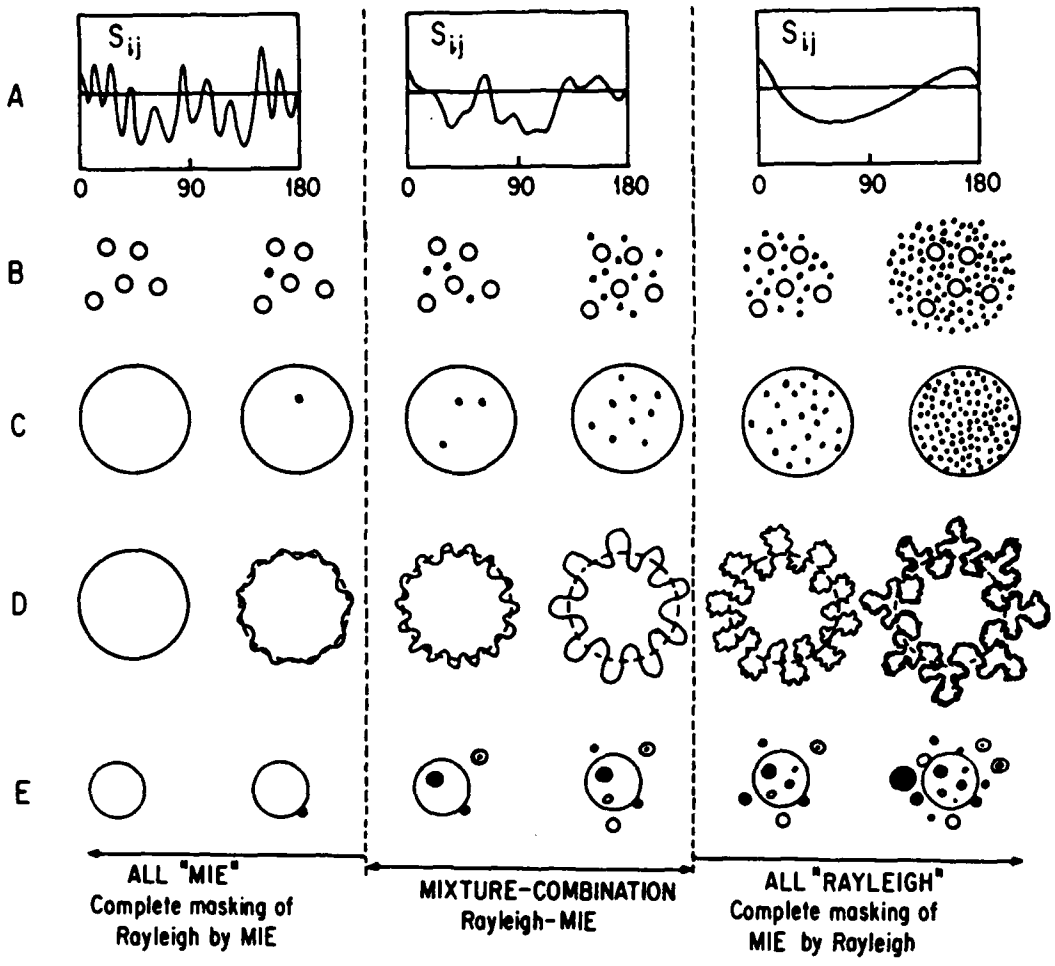

FIGURE 2. PHASE LOSS. The relationship between phase information on matrix elements S_{ij} and the complexity of the scatterer (rows C, D, and E) or as complexity of a perfect particle mixture (row B).

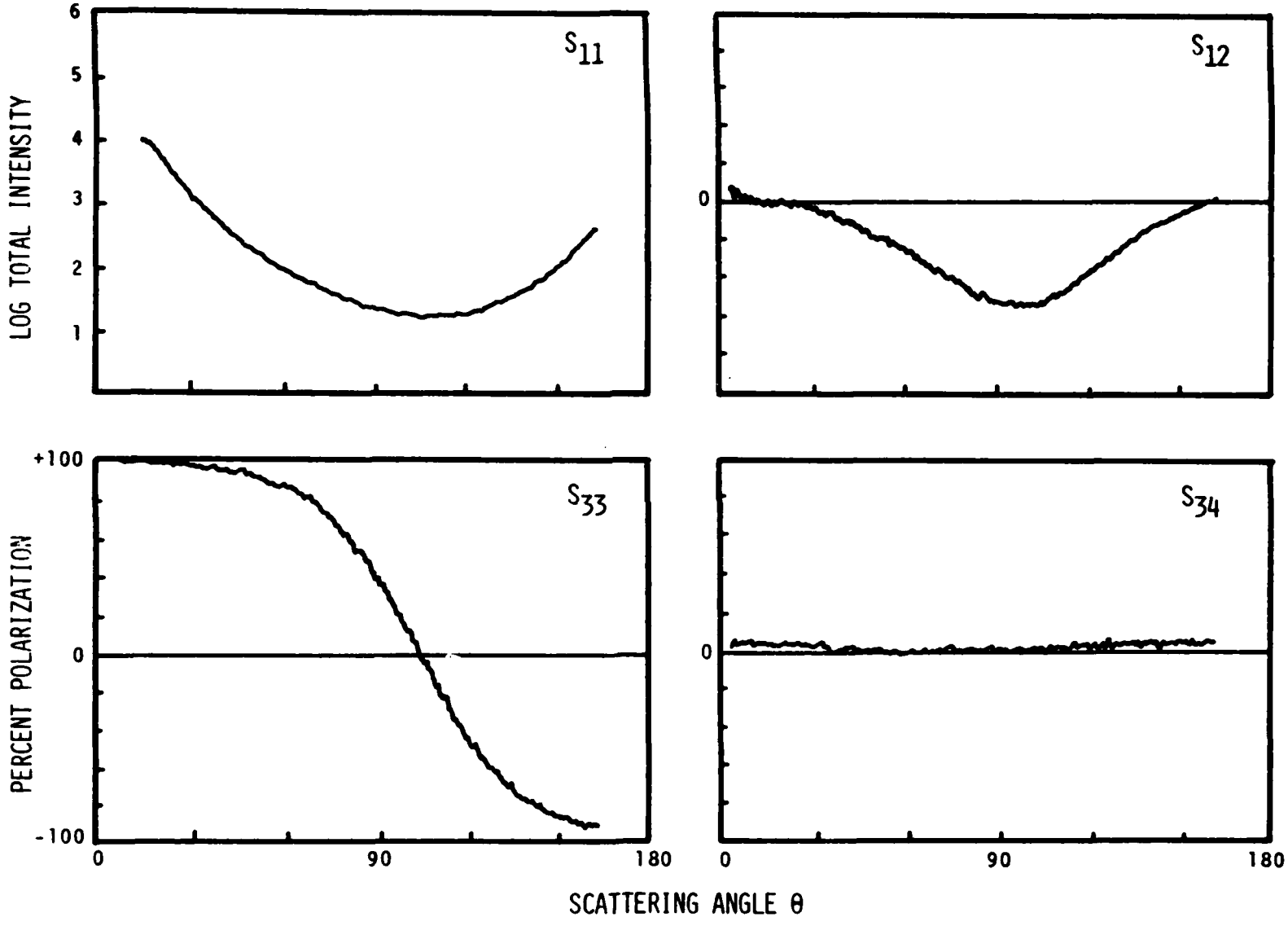

FIGURE 3. ARIZONA ROAD DUST. The four matrix elements for Arizona Road Dust, a log-normal system of irregular particles, polydispersed in all optical and geometrical constants.

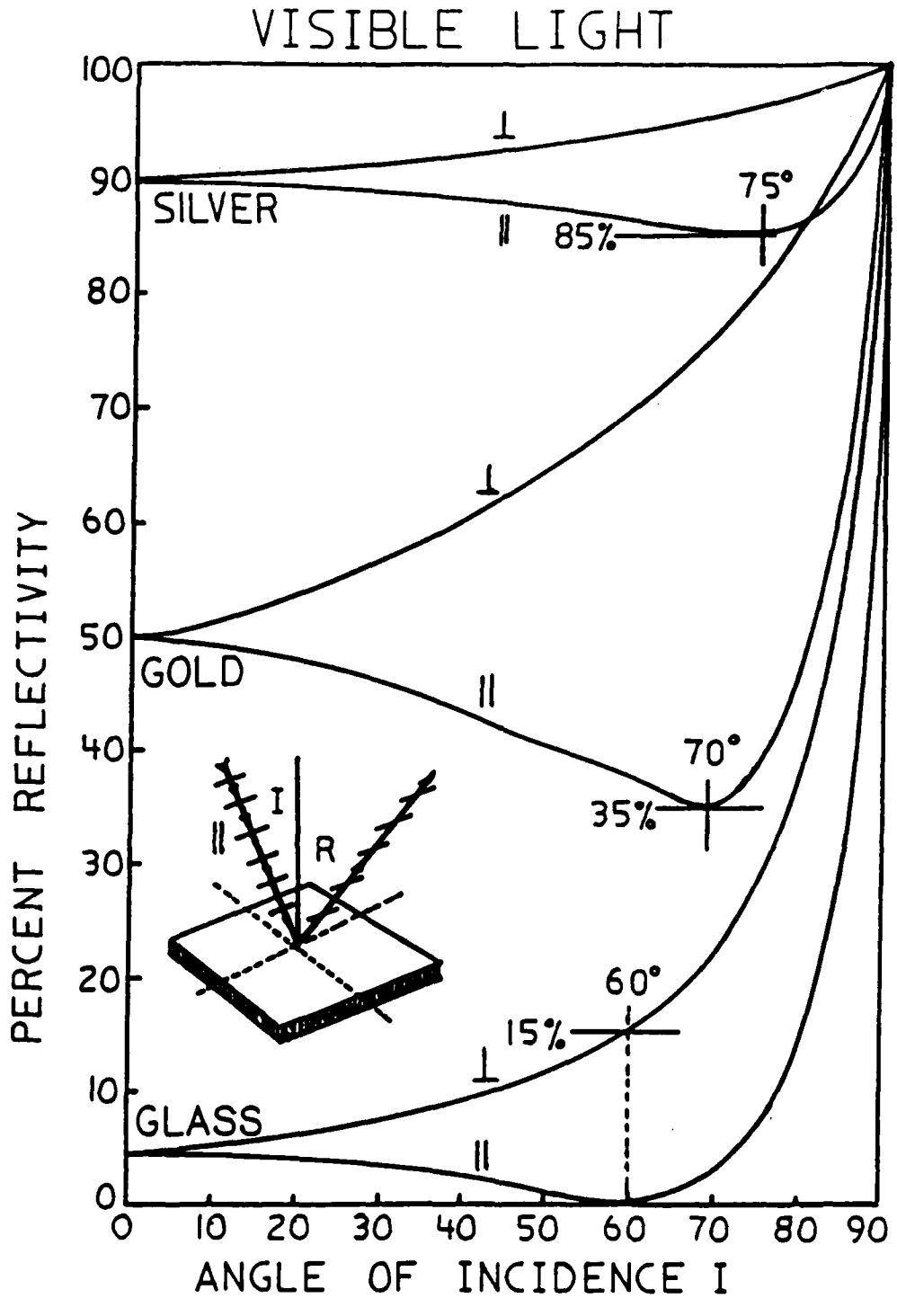

FIGURE 4. FRESNEL CURVES. The well known Fresnel polarized reflection curves as a function of incident and reflecting angle for glass, gold, and silver.

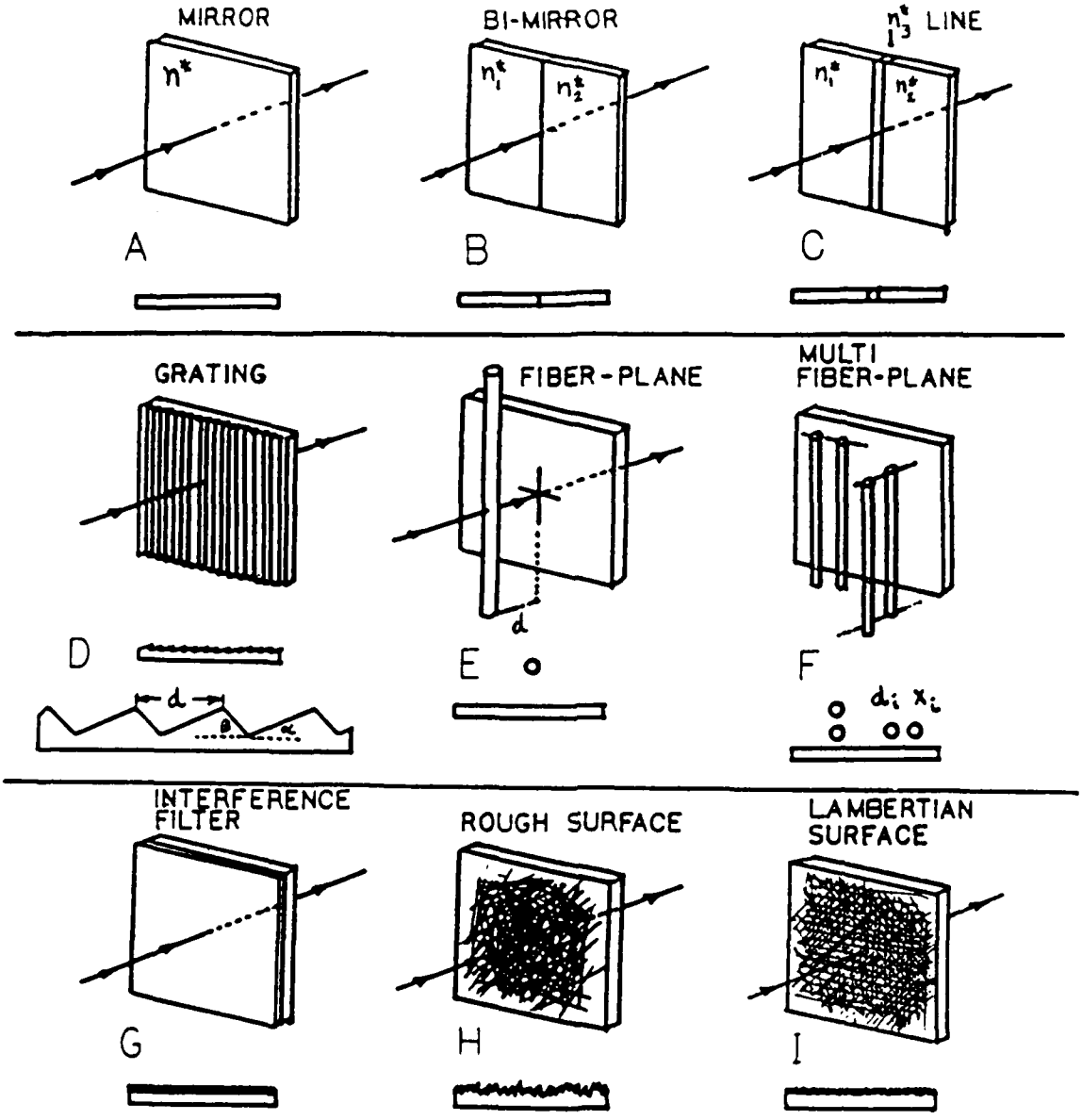

FIGURE 5. FUNDAMENTAL SURFACES. Some fundamental scattering systems involving perfect fibers (or spheres) and known surface geometry. Surfaces H and I are statistical (nonfundamental) scatterers.

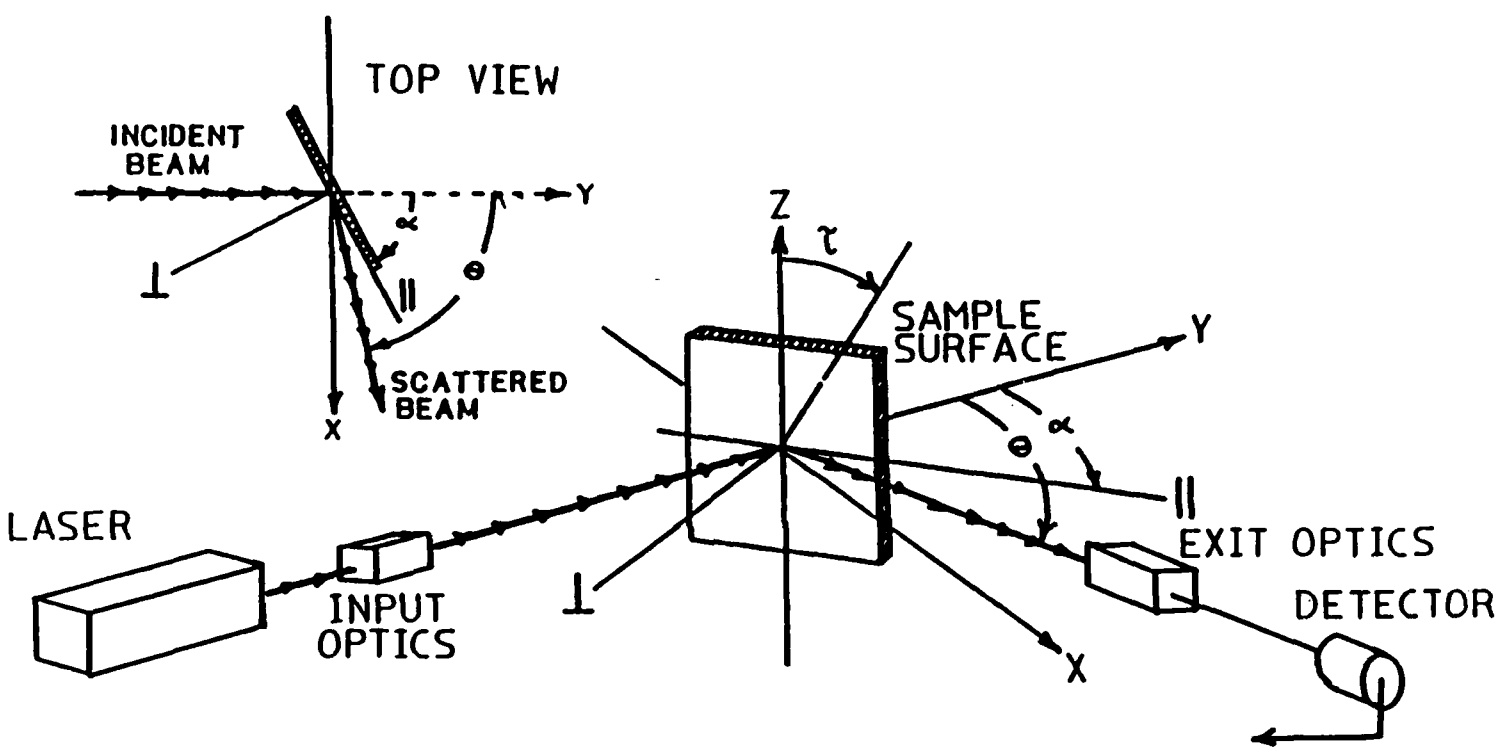

FIGURE 6. EXPERIMENTAL SET UP. The arrangement of surface, input, and exit optics used to study all the light scattering matrix elements from surfaces as a function of incident angle α, scattering angle θ, and surface tilt τ. In Figures 7 and 8, β is the surface-orientation angle in the yz plane corresponding to α in the yx plane. Here $\beta = 90°$.

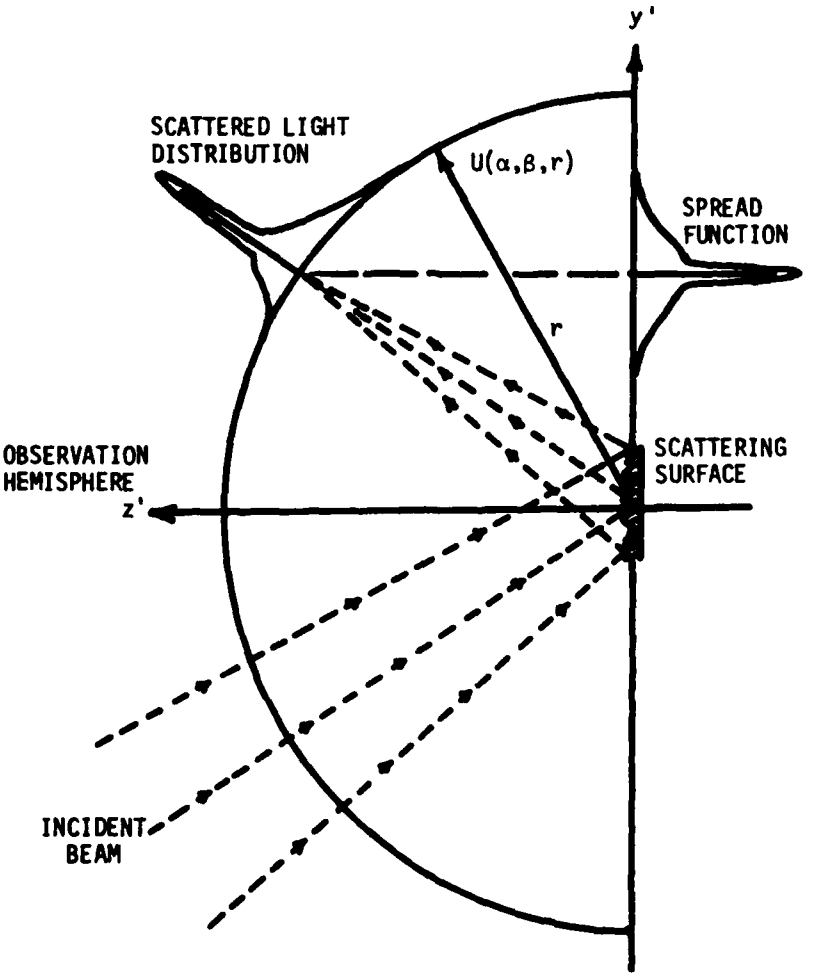

FIGURE 7. DISTORTED SPREAD FUNCTION. The distortion of the total intensity (S_{11}) spread function due to the surface orientation with respect to the angle of incidence α and scattering angle θ.

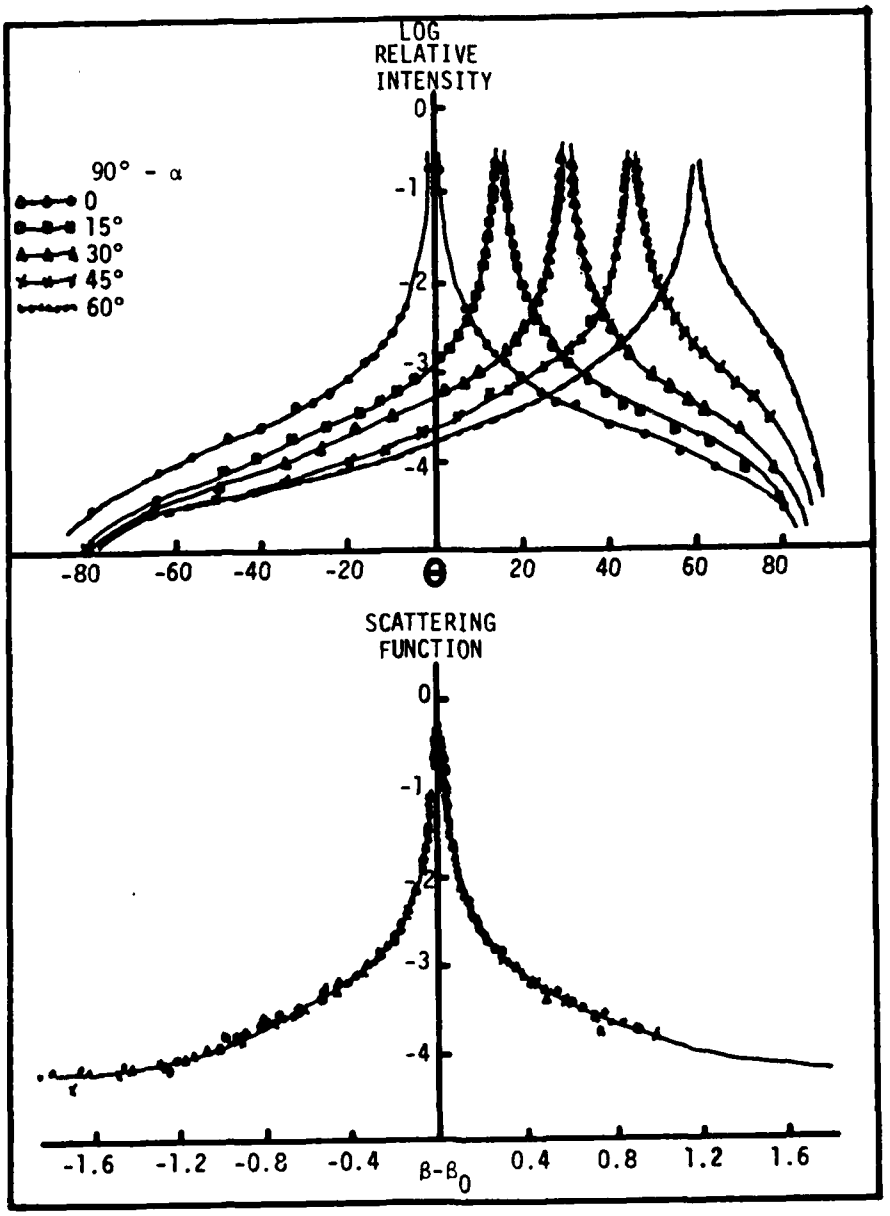

FIGURE 8. DECONVOLUTED SPREAD FUNCTION. The deconvolution of the distorted spread function giving a total intensity S_{11} signal independent of the incident angle α. Bold θ is $90° + \alpha - 0$.

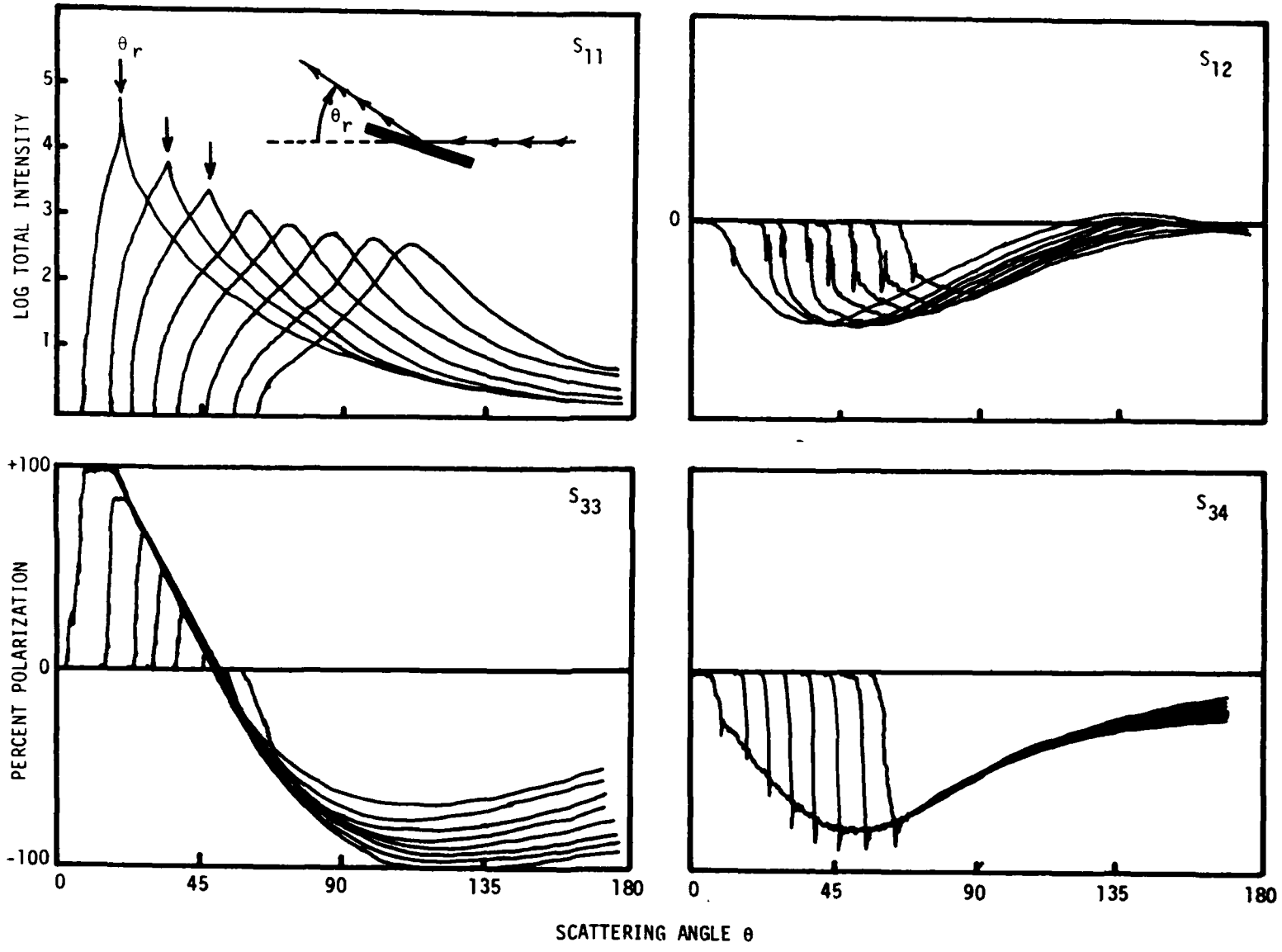

FIGURE 9. SANDED BRASS SURFACE. The four matrix elements from a random sanded brass surface as a function of illuminating angle α.

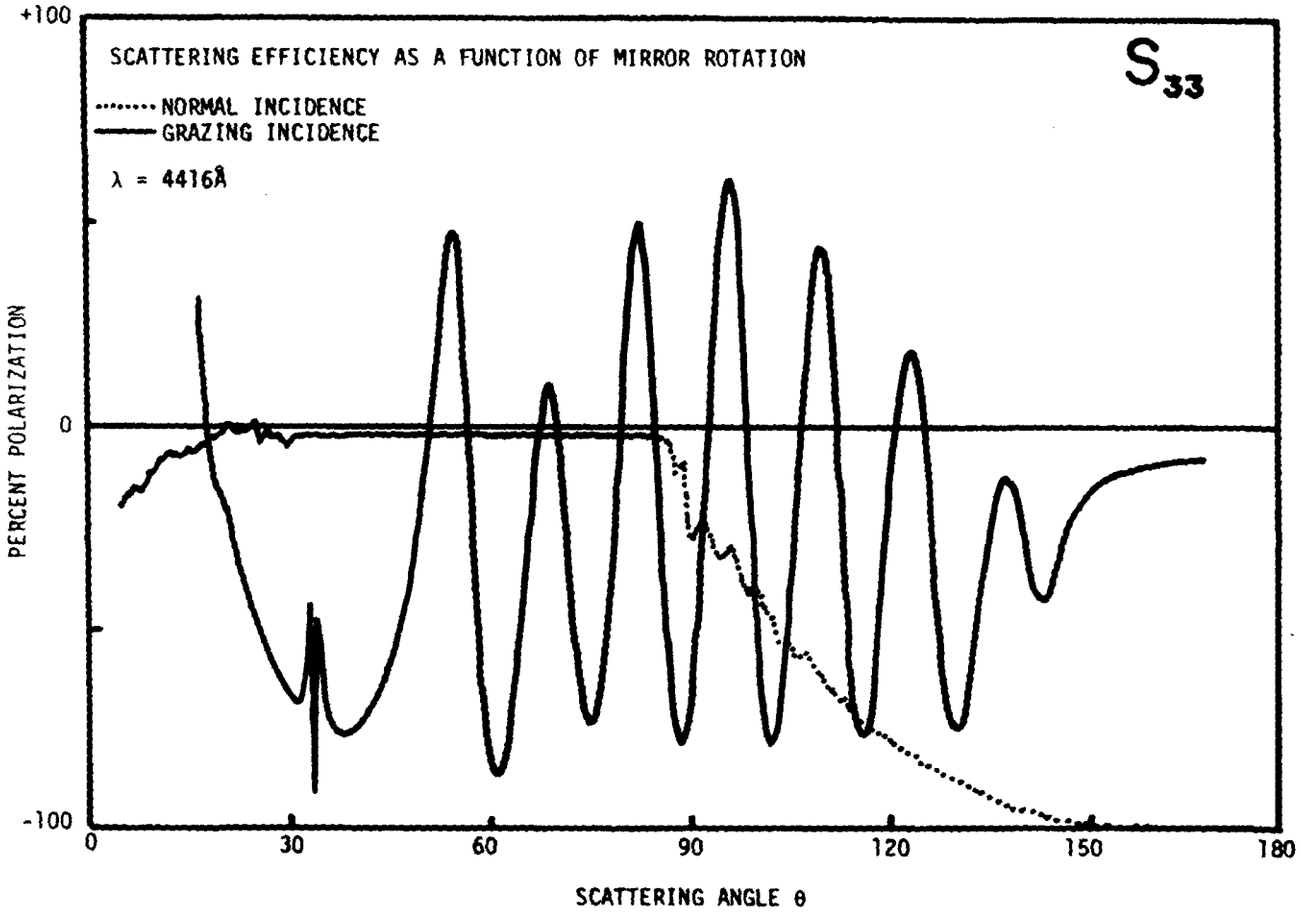

FIGURE 10. SURFACE-LINE SCATTERING. The matrix element S_{33} from a line (h = 0.8 micron, w = 2.2 micron) on an aluminum surface as a function of illuminating angles α = 90 degrees (normal incidence) and α = 0 degrees (grazing incidence).

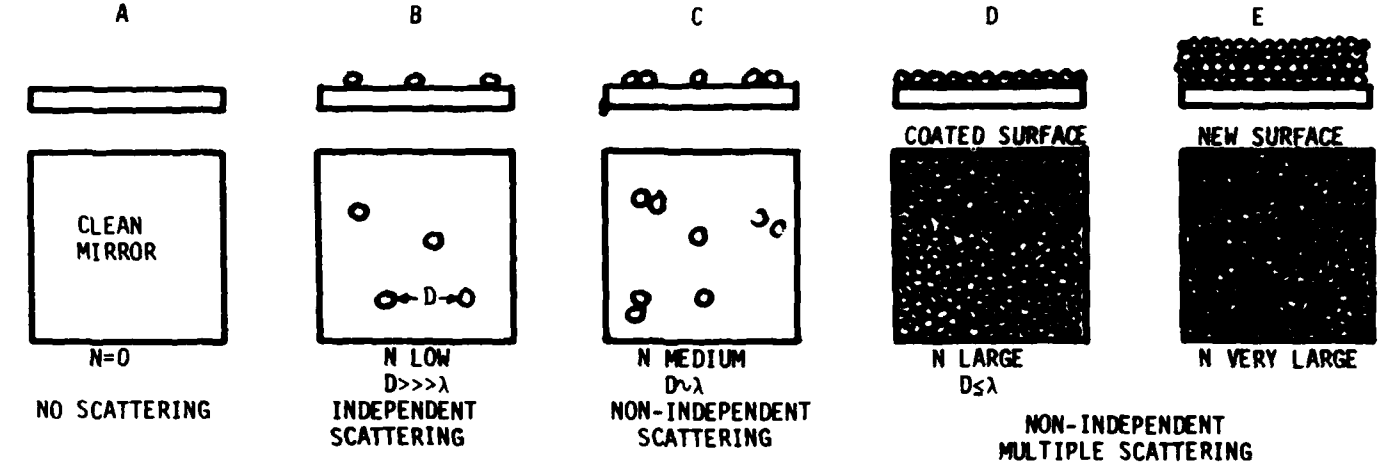

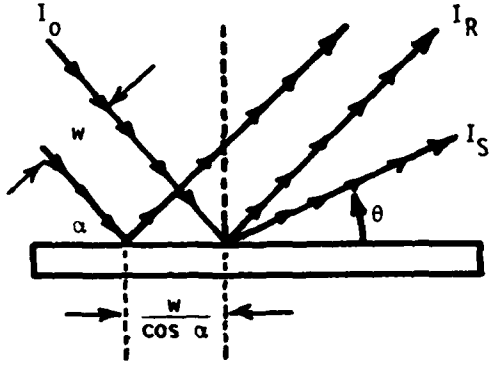

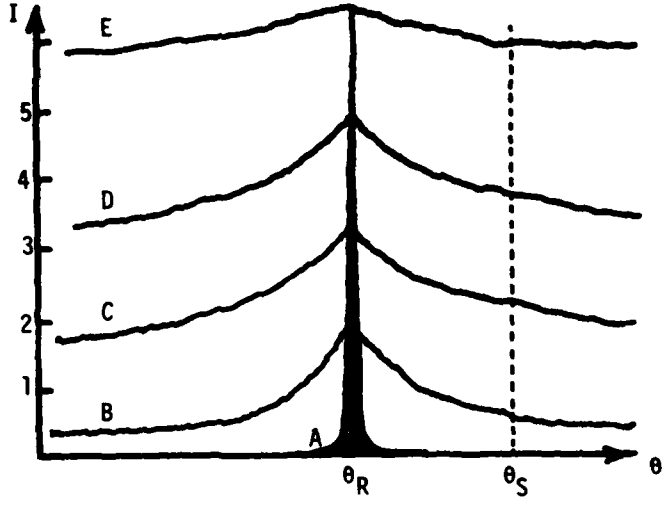

FIGURE 11. CLEAN MIRROR CONTAMINATION. The response of light scattering to contamination of a perfect clean mirror. Contamination starts at B where independent scattering occurs from a few particles and ends at E where total contamination has created a new surface. The light scattered into θ_s increases with contamination until saturation occurs.

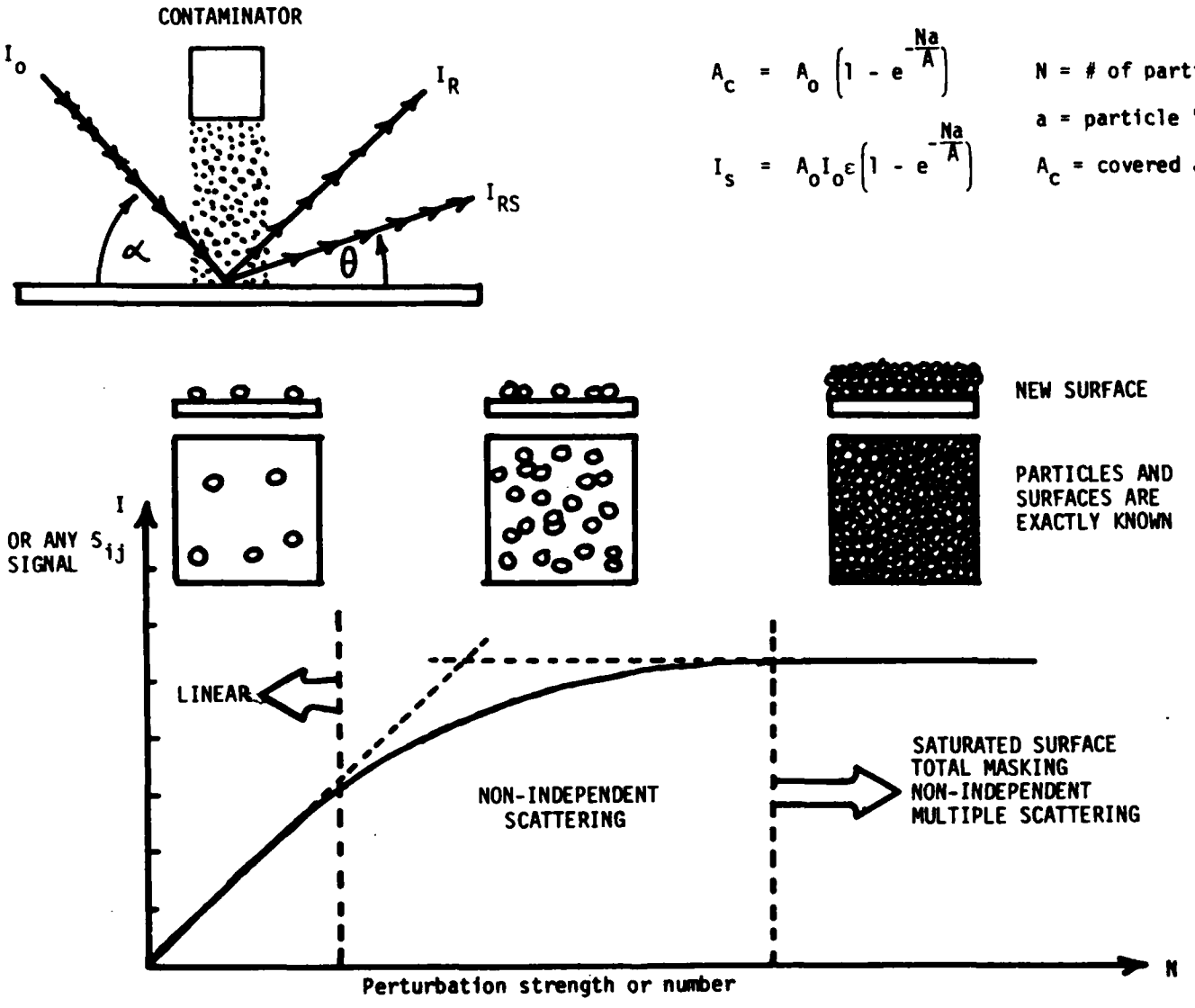

FIGURE 12. RESPONSE TO CONTAMINATION. The response curve of an S_{ij} matrix element as a function of surface contamination strength. The curve becomes flat when the surface becomes totally saturated with the contaminating particles.

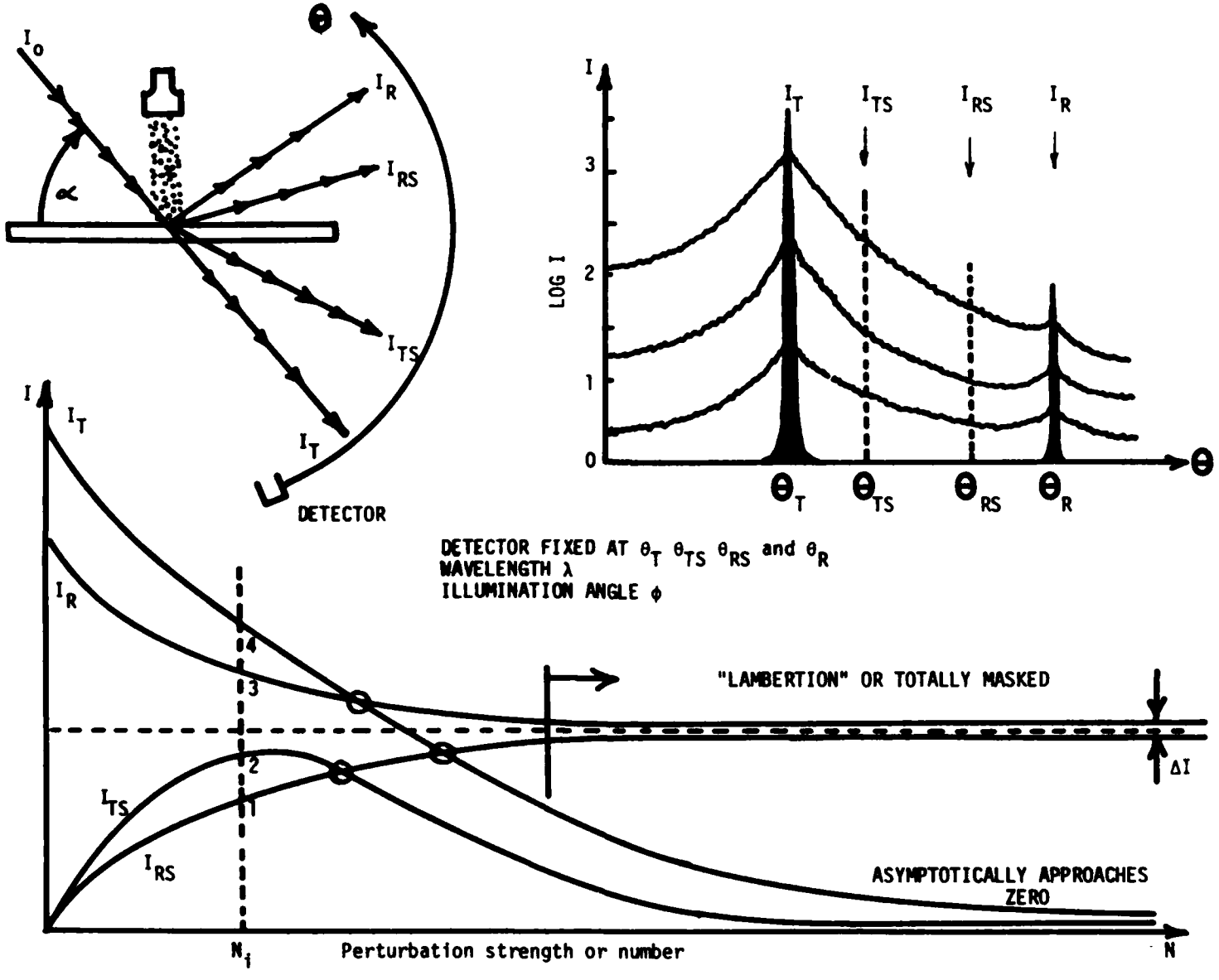

FIGURE 13. REFLECTED AND TRANSMITTED SCATTER. The response of any matrix element at four important angles as a function of surface contamination.

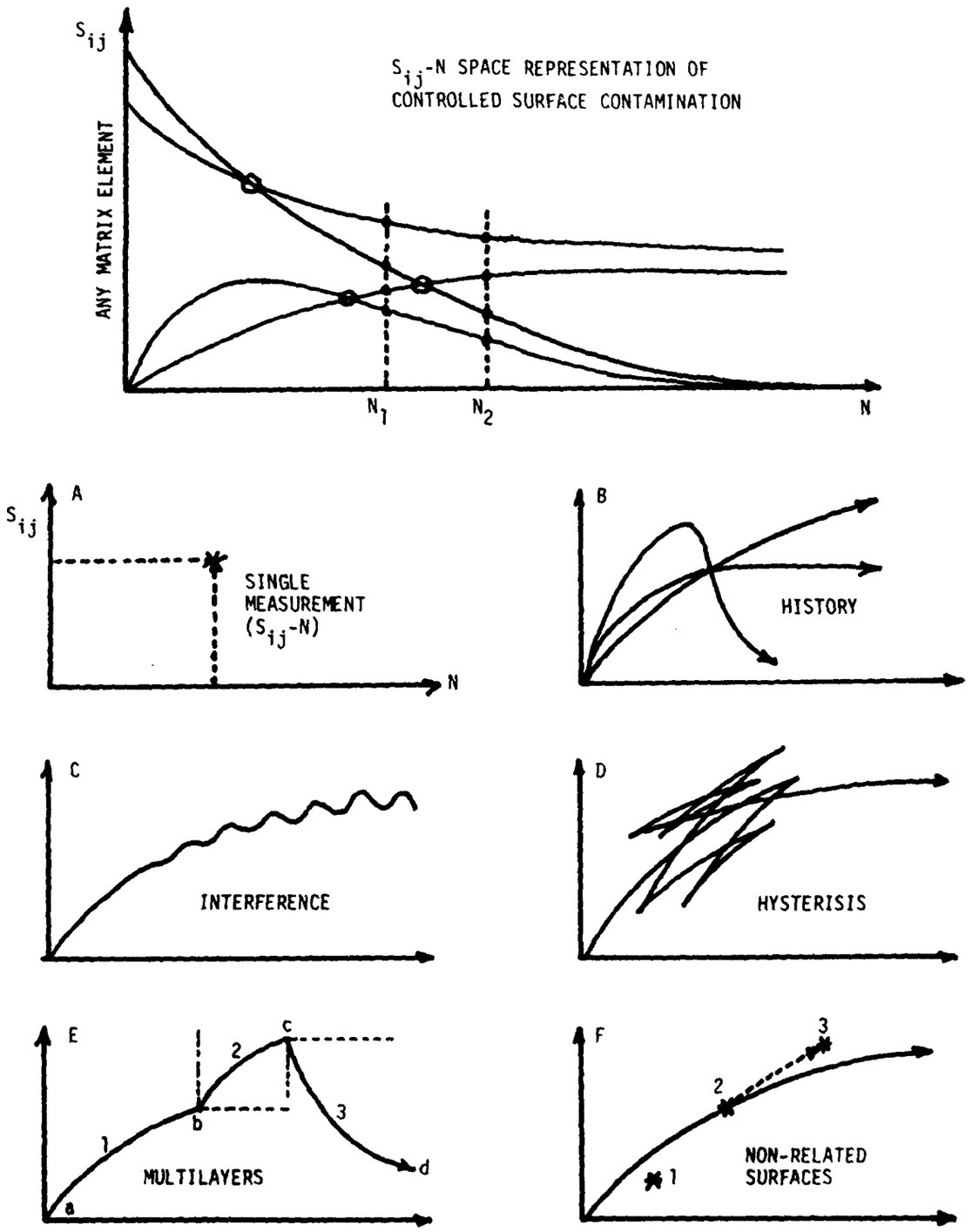

FIGURE 14. RESPONSE CURVES. Various S_{ij}-N responses that can be expected from different kinds of surface contaminations.

V. OPTICAL PROPERTIES OF AEROSOLS (CONTINUED)

VC. Propagation/Multiple Scattering in Aerosol Media and Radiative Transfer

DIFFUSION APPROXIMATION FOR MODELING OF 3-D RADIATION DISTRIBUTIONS

A. Zardecki and S. A. W. Gerstl
Theoretical Division, MS P371
Los Alamos National Laboratory
Los Alamos, NM 87545

and

R. E. De Kinder, Jr.
Project Manager, Smoke/Obscurants
Aberdeen Proving Ground, MD 21105

RECENT PUBLICATIONS, SUBMITTALS FOR PUBLICATION AND PRESENTATIONS:

A) A. Zardecki, S. A. W. Gerstl, and J. F. Embury, "Imaging through a Multiple Scattering Medium," Proceedings of the 1984 CRDC Scientific Conference on Obscuration and Aerosol Research, Chem. Res. and Devel. Center report CRDC-SP-85007, 491-494, June 1985.

B) A. Zardecki, S. A. W. Gerstl, and J. F. Embury, "Multiple Scattering Effects in Spatial Frequency Filtering," Appl. Opt. 23, 4124-4131 (1984).

C) S. A. W. Gerstl and A. Zardecki, "Discrete-Ordinates Finite-Element Method for Atmospheric Radiative Transfer and Remote Sensing," Appl. Opt. 24, 81-93 (1985).

D) A. Zardecki and S. A. W. Gerstl, "Screening and Shielding Effectiveness of Aerosols Against Laser Beams: An Optimization Study," Los Alamos National Laboratory report LA-10359-MS, May 1985.

E) A. Zardecki and C. Simmer, "Satellite-Based Detection of Visible Radiation from a Nuclear Fireball," Los Alamos National Laboratory report LA-UR-85-1488, June 1985.

F) L. D. Duncan, R.C. Shirkey, and A. Zardecki, "ILUM Code: Solar and Lunar Flux Calculations for Multi-Cloud Layered Atmospheres," Proceedings of the Fifth Annual EOSAEL/TWI Conference, White Sands Missile Range, April 1985.

G) A. Zardecki, S. A. W. Gerstl, W. G. Tam, and J. F. Embury, "Image Quality Degradation in a Turbid Medium under Partially Coherent Illumination," submitted to J. Opt. Soc. Am., February 1985.

H) R. L. Armstrong, S. A. W. Gerstl, and A. Zardecki, "Nonlinear Pulse Propagation in the Presence of Evaporating Aerosols," submitted to J. Opt. Soc. Am., February 1985.

ABSTRACT

A three-dimensional transport code DIF3D, based on the diffusion approximation, is used to model the spatial distribution of radiation energy arising from volumetric isotropic sources. Future work will be concerned with the determination of irradiances and modeling of realistic scenarios, relevant to the battlefield conditions.

INTRODUCTION

Light propagation through an optically thick particulate medium is basically a multiple-scattering problem in which rays or photons traverse a medium of scatterers and undergo many scattering events before escaping. A natural framework to deal with this type of problem is provided by the theory of radiative transfer. The linear Boltzmann equation--in the context of radiative energy also termed the equation of transfer--governs the radiation field in a medium that absorbs, emits, and scatters radiation.[1]

The complexity of the equation of transfer forces one to implement numerical methods of solution. The most direct procedure is the discrete-ordinates approach, in which the radiance distribution function $I(\vec{r},\vec{\Omega},\lambda)$ is replaced by a discrete set of values at a discrete set of points $(\vec{r}_i,\vec{\Omega}_j,\lambda_k)$. Unfortunately, such a calculation becomes a rather formidable task even on the most powerful supercomputer available today.[2]

Because of the numerical complexities, an important aspect of transport theory involves the development of simpler approximate descriptions. There are some special cases where simple and useful solutions

are available.[3] For isotropic scattering the irradiance distribution function can be represented as a sum of two terms, the residue term and the branch cut integration. If the particles are mostly scattering (albedo $\omega \to 1$) the residue term whose behavior is identical to a diffusion process dominates over the branch cut integration for optical depth greater than unity.[4]

In this paper, we employ the diffusion approximation to model the spatial distribution of radiative energy density due to a collection of volumetric, isotropic sources. After outlining the essence of the diffusion approximation and discussing the limits of its validity, we give numerical results in the form of 3-D isosurface plots, representing the surfaces of constant energy density. It will be shown that as the detector sensitivity decreases, the individual radiation sources cannot be spatially distinguished, thus leading to a false target effect.[5]

DIFFUSION APPROXIMATION

The diffusion approximation, which corresponds to the lowest-order truncation in the spherical harmonics expansion of the radiance distribution function, was employed by Tam and Zardecki[6] to examine the role of non-small-angle scattering for off-axis beam propagation. To gain insight into the approximation in question, we write the radiance distribution function for any given wavelength λ, whose index will be dropped, in the form

$$I(\vec{r},\vec{\Omega}) = \frac{1}{4\pi}\left[\rho(\vec{r}) + 3\vec{\Omega}\cdot\vec{J}(\vec{r})\right] \quad , \tag{1}$$

where $\vec{J}(\vec{r})$ is the flux, $\vec{\Omega}$ is a unit direction vector, and where the function $\rho(\vec{r})$, proportional to the energy density, satisfies a diffusion equation

$$-\nabla D\nabla\rho + (\sigma_t - \sigma_s)\rho = q_o \tag{2}$$

In Eq. (2), σ_t and σ_s denote the total extinction and scattering coefficients, and q_o is the isotropic source term. If $\langle\mu\rangle$ denotes the mean cosine of the scattering angle, which can be identified with the asymmetry parameter g, then the diffusion coefficient D is given in terms of the transport coefficient

$$\sigma_{tr} = \sigma_t - \sigma_s\langle\mu\rangle \quad , \tag{3}$$

as

$$D = \frac{1}{3\sigma_{tr}} \tag{4}$$

Eq. (2) should be solved with the boundary condition demanding that the radiant flux directed inward at the scattering boundary be zero.

To delineate the range of validity of the diffusion approximation, we have compared the results for 1-D geometry obtained with the transport code ONEDANT[7] with the results obtained with the diffusion-based code DIF3D.[8] Figures (1) and (2) contain the results of computations referring to a 100 m wide slab, divided into 200 meshes of equal size. The isotropic source of unit strength, located in the

first mesh with the boundaries 0. and 0.5 m generates the radiation field. As can be seen from Fig. 2, the diffusion theory leads to a degeneracy with respect to the single scattering albedo $\omega = \sigma_s/\sigma_t$. The perfect-scattering case, however, where $\omega = 1.0$, is described correctly within the diffusion approximation. This implies that the diffusion theory can be applied to model radiation distribution and multiple scattering in dense, non-absorbing media, such as inventory smokes in the visible range of the spectrum.

FALSE TARGET EFFECTS

In Ref. 5, we addressed the resolution problem that arises for a distant observer attempting to distinguish spatially between two thermal sources radiating into a turbid medium. Since our analysis was based on the transport theory, the results--especially for low optical depths--suffered from the ray effect distorting the spatial form of the radiation distribution. With the aid of the diffusion theory, we are in a position to entirely bypass the problem of ray effect; in addition the code DIF3D allows us to model 3-D situations, an unrealistic undertaking within the framework of the transport theory.

Our model scenario involves a cube 100x100x100 m in size. The lower half of the cube, $z < 50$, is filled with haze having the optical thickness 2.0 in the x or y direction. The upper half, $z > 50$, contains water cloud aerosol with optical thickness 8.0. Two isotropic point sources of equal strength located at $S_1 = (20,20,20,)$ and $S_2 = (80,80,80)$ produce the volumetric radiation distribution. By solving the diffusion equation (2) for ρ, we can compute the radiation energy density inside our scattering volume. For the wavelength of 0.55μm we show in Figs. 3 and 4 the isosurface plots representing surfaces of equal energy density. Choosing a fixed value for the maximum energy density, set by the source strength of the point sources, the resulting plots vary drastically with the value of the detectable energy density. Thus for a detector registering 4% or more of the maximum energy density the sources appear well separated, Fig. 3. On the other hand, for a detector registering 2% of the maximum energy distribution function, the individual sources appear to overlap, Fig. 4, leading to a false target effect. Similar results have been obtained with a larger number of sources both for homogeneous and inhomogeneous media.

CONCLUSIONS

Contrary to popular belief, the diffusion approximation is susceptible to yielding erroneous results when the single scattering albedo is smaller than 0.95. On the other hand, this approximation becomes a powerful tool to model complicated 3-D scenarios, which is today outside the scope of conventional approaches based on transport theory. Since diffusion theory does not deal with directional quantities, but with angle-integrated energy density, it does not suffer from the ray effect distortion. For these reasons, the false target problem finds a natural setting within the framework of the diffusion theory.

Our future investigation will largely focus on two as yet unsolved problems. First, using the diffusion approach, we intend to study the spatial detectability of radiating or reflecting objects placed in the vicinity of a smoke screen. When the radiation field is described in terms of irradiances, this becomes a problem of optical imaging. Second, to describe multiple scattering of laser beams in the off-axis regime, a novel approach valid for a wide range of size parameters needs to be formulated. A combination of the small-angle scattering approximation with diffusion theory should provide the desired computational base.

REFERENCES

1. J. J. Duderstadt and W. R. Martin, Transport Theory, (Wiley, New York, 1979).
2. A. Zardecki, S. A. W. Gerstl, and J. F. Embury, "Application of the 2-D Discrete-Ordinates Method to Multiple Scattering of Laser Radiation", Appl. Opt. 22 1346-1353 (1983).
3. W. G. Tam and A. Zardecki, "Laser Beam Propagation in Particulate Media", J. Opt. Soc. Am., 69, 68-70 (1979).
4. A. Ishimaru, Wave Propagation and Scattering in Random Media, (Academic Press, New York, 1978).
5. A. Zardecki, S. A. W. Gerstl and J. F. Embury, "Multiple-Scattering-Induced False Targets", Proceedings of the 1983 Scientific Conference on Obscuration and Aerosol Research, edited by J. Farmer and R. H. Kohl, July 1984.
6. W. G. Tam and A. Zardecki, "Off-Axis Propagation of a Laser Beam in Low Visibility Weather Conditions", Appl. Opt. 19, 2822-2827 (1980).
7. R. D. O'Dell, F. W. Brinkley Jr. and D. R. Marr, "User's Manual for ONEDANT", Los Alamos National Laboratory report LA-9184-M, February 1982.
8. K. L. Derstine, "DIF3D: A Code to Solve One-, Two-, and Three-Dimensional Finite-Difference Diffusion Theory Problems", Argonne National Laboratory report ANL-82-64, April 1984.

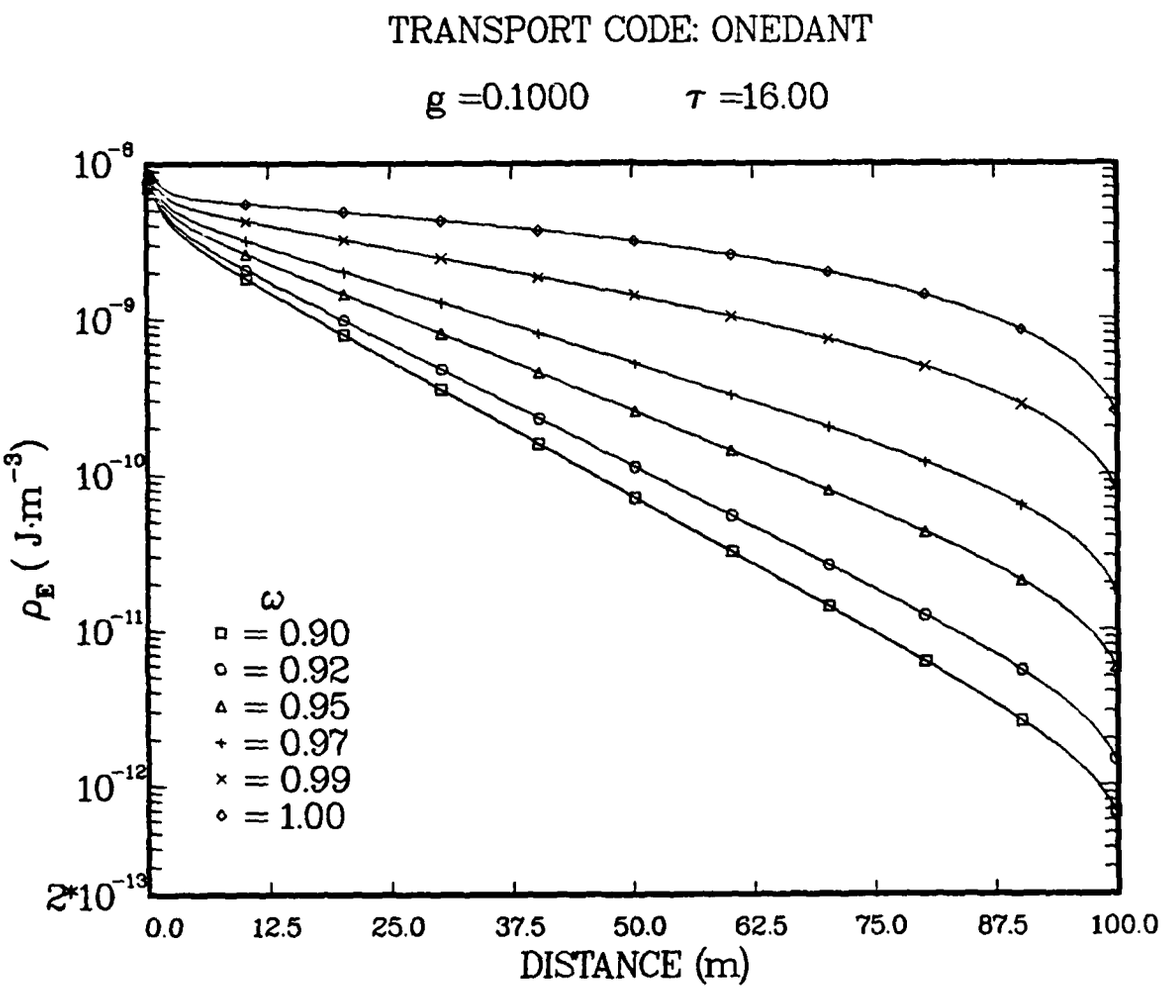

FIGURE 1. ENERGY DENSITY DISBRIBUTION PREDICTED BY TRANSPORT THEORY. Optical depth = 16, asymmetry parameter = 0.1.

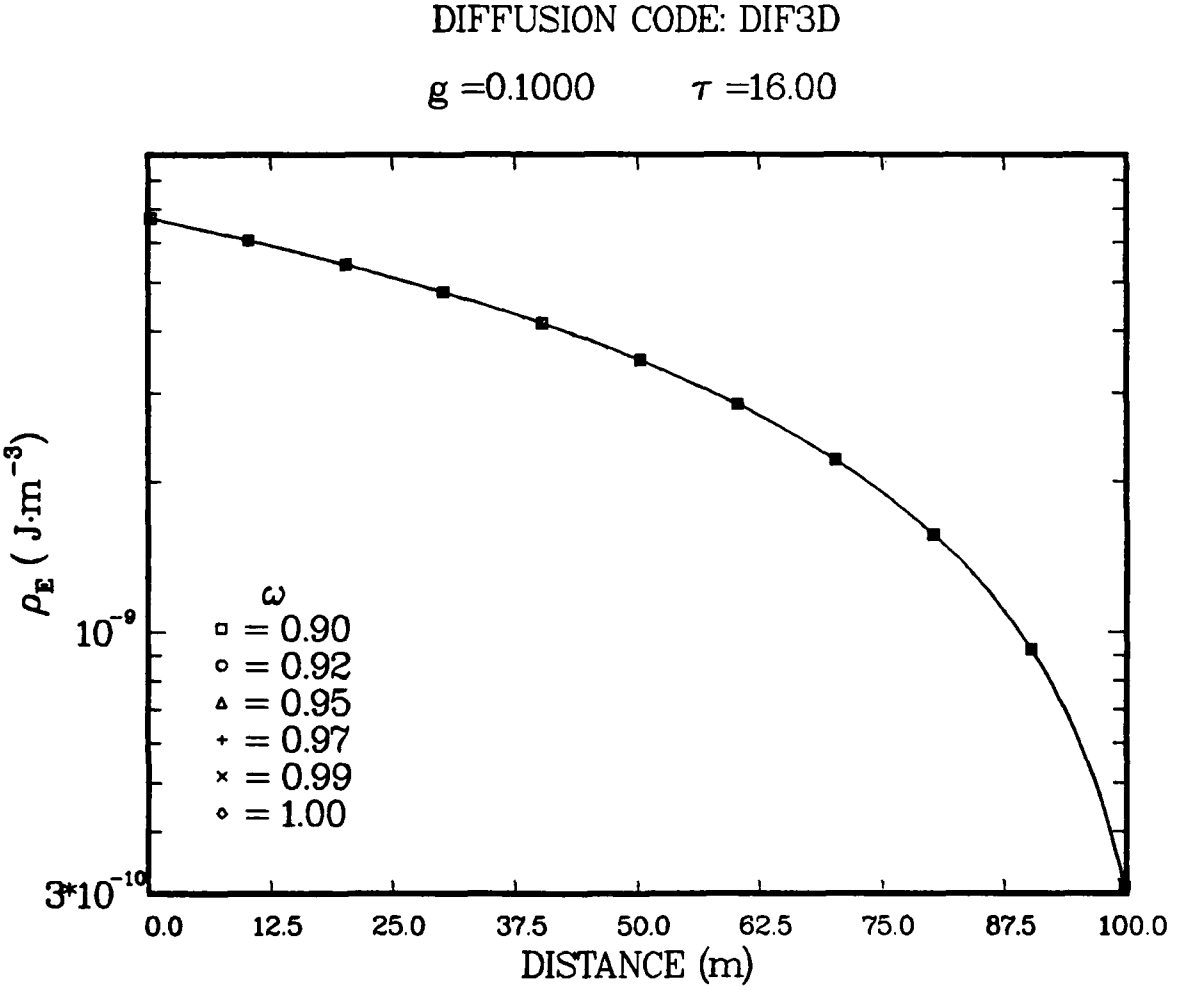

FIGURE 2. ENERGY DENSITY DISTRIBUTION PREDICTED BY DIFFUSION THEORY. Parameters as in Fig. 1. Note the degeneracy with respect to the single scattering albedo.

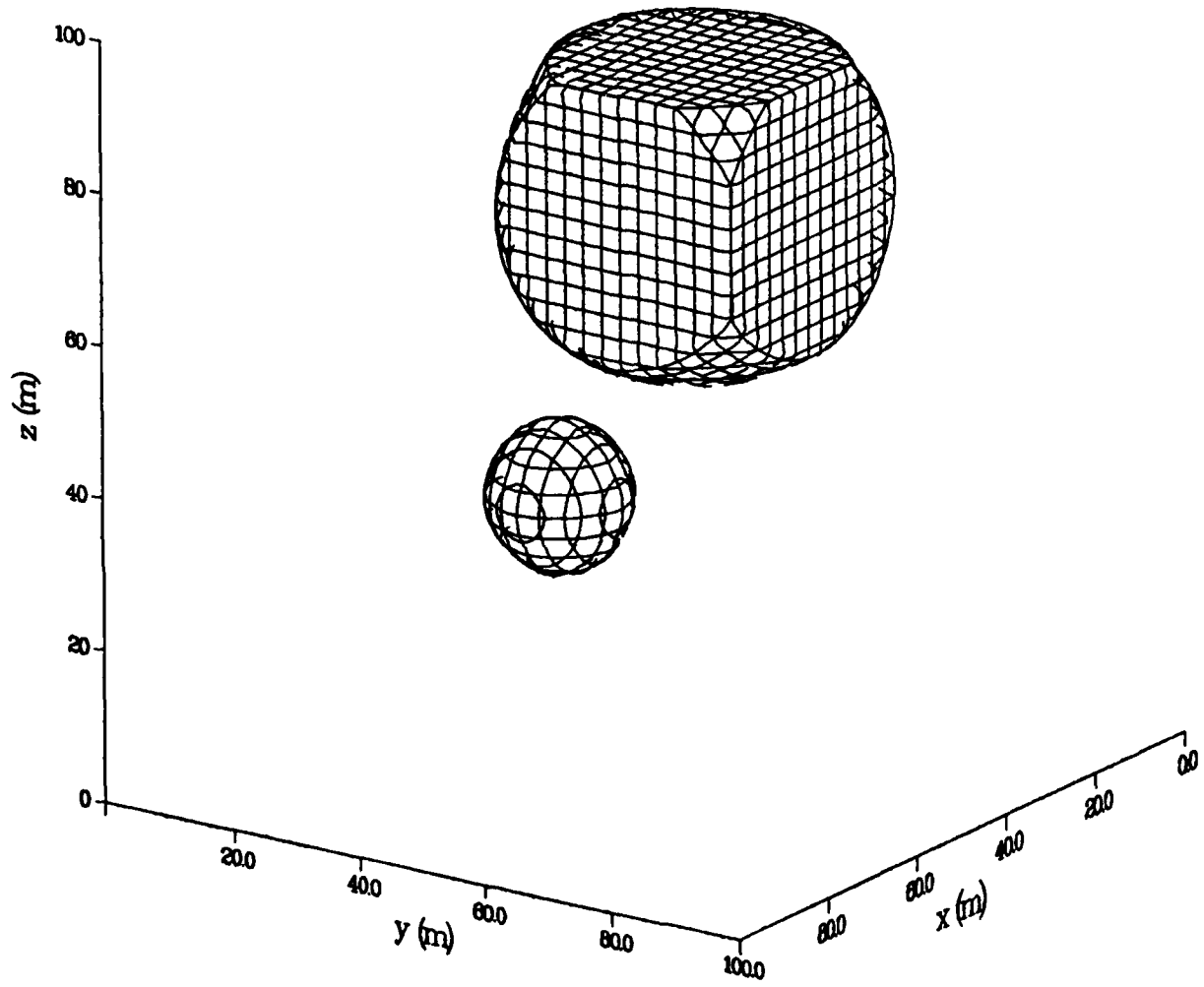

FIGURE 3. ISOSURFACE PLOT AT 4% OF MAXIMUM ENERGY DENSITY. Radiation fields from individual sources well separated.

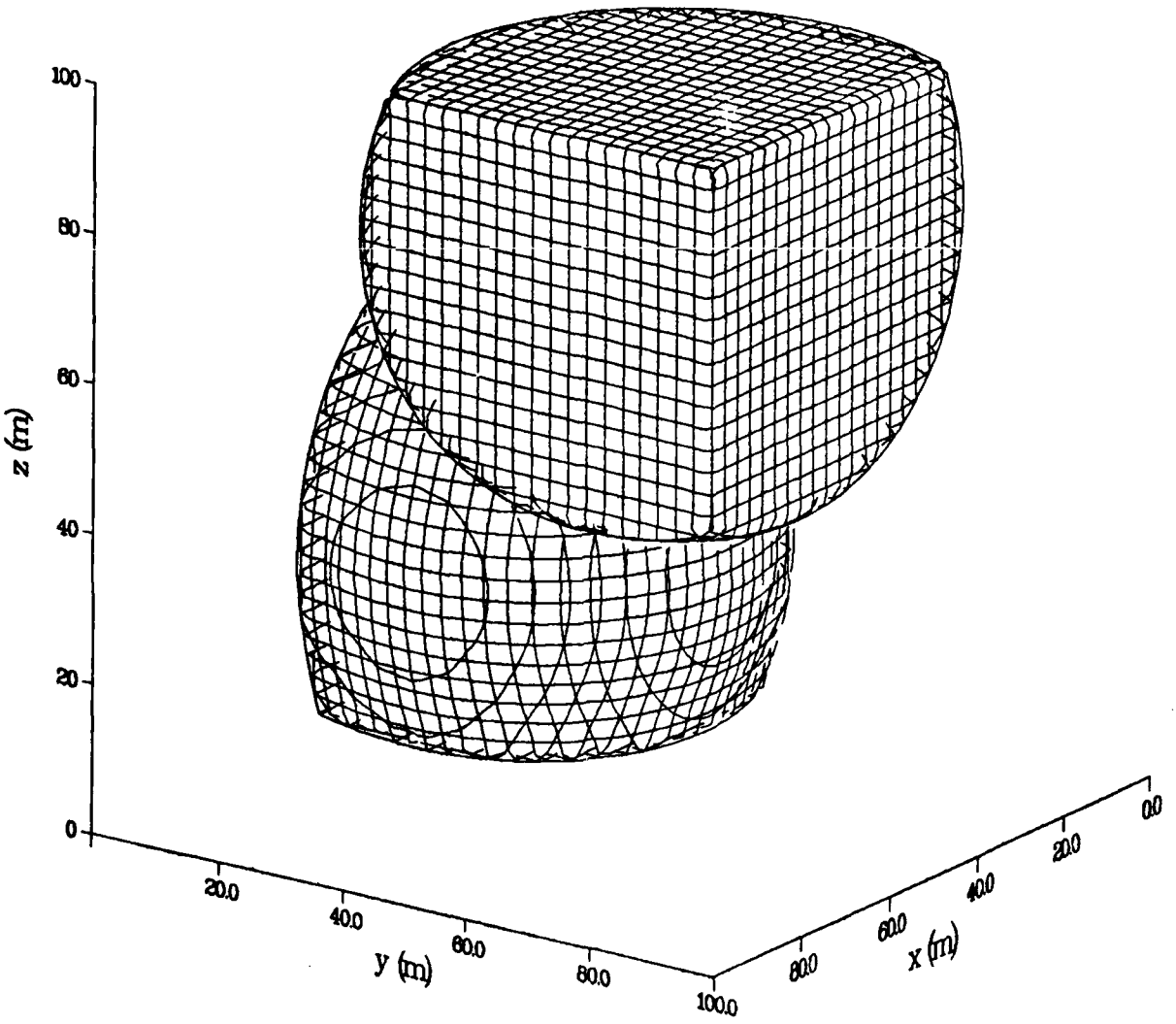

FIGURE 4. ISOSURFACE PLOT AT 2% OF MAXIMUM ENERGY DENSITY. Radiation fields from individual sources overlap, showing a false target effect.

COHERENT AND INCOHERENT INTENSITY OF THE ELECTROMAGNETIC FIELD IN A DISCRETE RANDOM MEDIUM

V. V. Varadan and V. K. Varadan
Laboratory for Electromagnetic and Acoustic Research
Department of Engineering Science and Mechanics
The Pennsylvania State University
University Park, PA 16802

ABSTRACT

In this paper, work reported in the 1984 CRDC proceedings concerning a propagator model for multiple scattering of waves in a discrete random medium is extended to include higher order terms of the multiple scattering series for both the coherent and incoherent intensities. The list below provides references to papers that have been submitted for publication based on the 1985 presentation and other related presentations.

V. K. Varadan and V. V. Varadan, "Progress in Research on Wave Propagation and Scattering in Discrete Random Media Using Multiple Scattering Theory", 1984 CRDC Proceedings.

V. V. Varadan, Y. Ma and V. K. Varadan, "Propagator Model Including Multipole Fields for Discrete Random Media", J. Optical Society of America, scheduled for publication in December 1985.

V. K. Varadan, Y. Ma and V. V. Varadan, "Coherent Electromagnetic Wave Propagation Through Randomly Distributed Pair-Correlated Dielectric Scatterers", Radio Science 19, Pp. 1445-1449, 1984.

EXTENDED SUMMARY

In the previous CRDC Proceedings, a propagator model to describe propagation and scattering of multipole fields in a discrete random medium containing a distribution of inclusions was described using a T-matrix to characterize the single scatterer response and a propagation matrix to describe wave propagation between scatterers. Since the T-matrix is represented in a basis of vector spherical functions, the propagator is simply the translation matrix for vector spherical functions. Although the explicit expressions for the elements of the translation matrix are quite complicated, the formalism is quite compact and general.

Let r_i denote the portion of the i-th scatterer, $\sigma_{nn'}$, $(\vec{r}_i-\vec{r}_j)$ denote the propagation matrix for propagation from $\vec{r}_j$ to $\vec{r}_i$, $T^i_{nn'}$ is the T-matrix of the ith scatterer and E^o is the incident field. The total field at any point $(\vec{r})$ in the host medium can be written as

$$\vec{E}(\vec{r}) = \vec{E}^o(\vec{r}) + \Sigma_i \; Ou \; \vec{\psi}_n \; (\vec{r}-\vec{r}_i) \; T^i_{nn'} \; A^i_{n'}$$

$$+ \Sigma_j \; \Sigma_{i\neq j} \; Ou \; \vec{\psi}_n \; (\vec{r}-\vec{r}_i) \; T^i_{nn'} \; \sigma_{n'n''} \; (\vec{r}_i-\vec{r}_j) \; T^j_{n''n'''} \; A^j_{n'''}$$

$$+ - - - -$$

where

$$\vec{E}^o \; (\vec{r}) = \hat{p} e^{i \; k \; \hat{k}_o . \vec{r}} = \Sigma_n \; A^i_n \; Re \; \vec{\psi}_n \; (\vec{r}-\vec{r}_i)$$

with

$$A_n^i = e^{i\,k.\hat{k}_o.r_i}\,(i^{-n}\,\hat{p}.\vec{A}_n(\hat{k}_o));\ \hat{p}.\hat{k}_o = 0 \qquad (2b)$$

where $\hat{p}$ is the polarization of the incident wave, $\hat{k}_o$ its direction of propagation, $\underset{Re}{Ou}\,\vec{\psi}_n$ are vector spherical functions and $\vec{A}_n$ are vector spherical harmonics, definitions of which can be found in Ref. 1.

The configurational average of the series retaining only certain types of multiple scattering processes permitted by the Quasi-Crystalline approximation, using a diagrammatic representation, was shown to be

$$\langle \vec{E}(\vec{r})\rangle_{QCA} = \vec{E}^o(\vec{r}) +$$

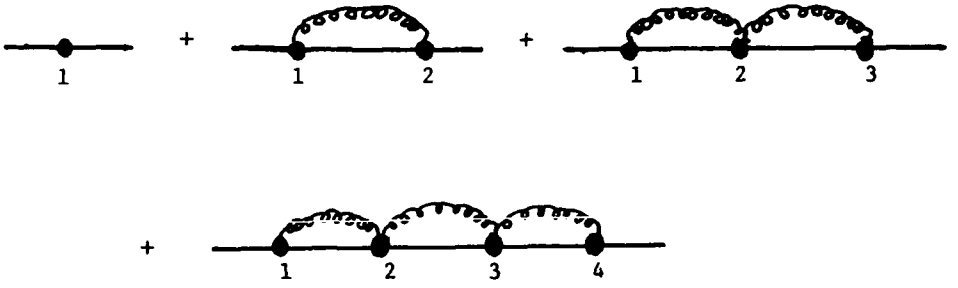

$$+ - - - - . \qquad (3)$$

where $_1\!\bullet\!\!-\!\!-$ denotes $T^1 A^1_n$;  denotes $T^1 \int \sigma(\vec{r}_1-\vec{r}_2)\ T^2\ p(\vec{r}_2|\vec{r}_1)$; and $\!\!-\!\!-\!\!\bullet_1$ denotes $\int Ou\ \vec{\psi}(\vec{r}-\vec{r}_1)\ T^1\ p(\vec{r}_1)$.

The coherent field in the QCA, satisfies a dispersion equation of the form

$$\left|\ 1 - n_o T \int c(\vec{r}_{12})\ p(\vec{r}_2|\vec{r}_1)\ e^{-i\vec{k}.\vec{r}_{12}}\ d\vec{r}_{12}\ \right| = 0\ . \qquad (4)$$

To here $|\ |$ denotes a matrix determinant and the roots of the above equation yields the effective, complex propagation constant $K = K_1(n_o,T,\omega) + i\,K_2(n_o,T,\omega)$.

Similarly one can keep restricted classes of terms in the definition of the incoherent intensity and represent it as

$$I_u(\vec{r}) = \langle \hat{u}.(\vec{E} - \langle \vec{E} \rangle)\ (\vec{E} - \langle \vec{E} \rangle)^{*}.\hat{u} \rangle$$

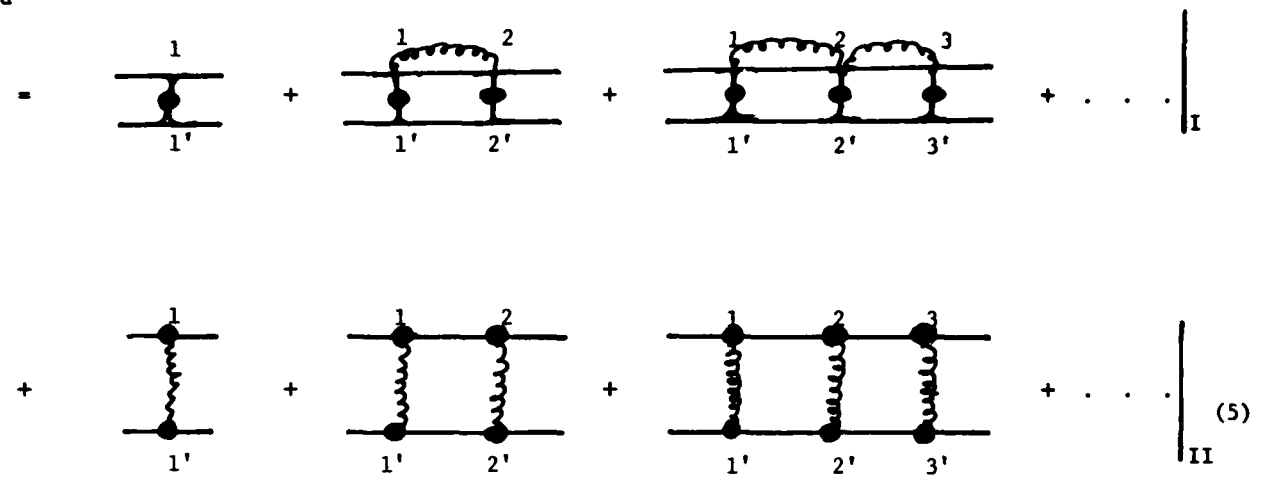

(5)

where $\hat{u}$ is a particular polarization component of the incoherent intensity. In the above expression, the first series is the intensity of the multiple scattered field when both field contributions arise from the same scatterer or scatterers (in the language of the diagrams in Eq. (5), both field lines pass through the same scatterers). In the second sequence of terms the two field contributions arise from different scatterers (the field lines pass through distinct scatterers). There are several other types of terms which have been neglected because they do not lend themselves to resummation and require a knowledge of higher order correlations.

Results are presented for the incoherent intensity computed from the lowest order terms and the order of magnitudes of the terms are compared. Only single and double scattering terms from both sets were considered and the results plotted in the figures below. In Fig. 1, the normalized incoherent intensity is plotted resulting from diagrams of the form  (B),  (A) and  (C). The nonzero value of A essentially shows the effect of pair correlations which is more noticeable at higher values of ka and is a considerable fraction of the uncorrelated single scatterer values even at a scatterer concentration, c, of five percent.

In Fig. 2 the (correlated) different-scatterer (A) and same-scatterer (B), single scattered intensities are plotted as a function of the angle of observation, θ, for a concentration of c = 10% at ka = 2.0. It is seen that the effect of correlations as a function of θ is due to the angular dependence of the expression for the single scattered intensity. For example at $\theta = 90°$ and 155°, the curve A has a minimum, but near the forward direction A is a considerable fraction of B. In the back scattered direction, A is not a minimum, but it is only a small fraction of B.

In Fig. 3, the contribution from single () and double () scattering are compared as a function of ka at a concentration of 10% for $\theta = 90^{o}$. The double scattering contribution is anywhere from 0 to 40% of the single scattered value. In Fig. 4, the effects are compared as a function

of the angle of observation at $c \approx 0.15$. Unlike Fig. 2, in the forward direction the contribution of the simpler process, the single scattering contribution, is several orders of magnitude higher than the contribution of the more complicated process, the double scattered results, whereas at other angles, especially in the backscattering direction, double scattering cannot be neglected.

CONCLUSIONS

In this summary, we have essentially tried to compare the order of magnitude of the different orders of multiple scattering and the effect of pair correlations. Our results indicate that both are important and it is only in certain preferred directions or at certain values of ka that simple approximations to the incoherent intensity will agree well with experimentally observed values. Further studies will focus on resummations of the diagrams presented in Eq. (5) that can be called the ladder approximation to the incoherent intensity. In this connection we note that recently just the summation of terms (I), neglecting pair correlations in Eq. (5), has been referred to as the ladder approximation by some authors.[2] This is incorrect; it is the sum of I and II including the effect of pair correlations that leads to the so-called ladder approximation or the Bethe-Salpeter equation.

REFERENCES

1. V. N. Bringi, T. A. Seliga, V. K. Varadan and V. V. Varadan, "Propagation Characteristics of Discrete Random Media" in Multiple Scattering and Waves in Random Media, P. C. Chow, W. E. Kohler and G. C. Papanicolaou (eds.), North Holland Publishing Company (1981).
2. L. Tsang and A. Ishimaru, "Theory of Backscattering Enhancement of Random Discrete Isotropic Scatterers Based on the Summation of all Ladder and Cyclical Terms", J. Opt. Soc. Am. A2, pp. 1331-1338 (1985).

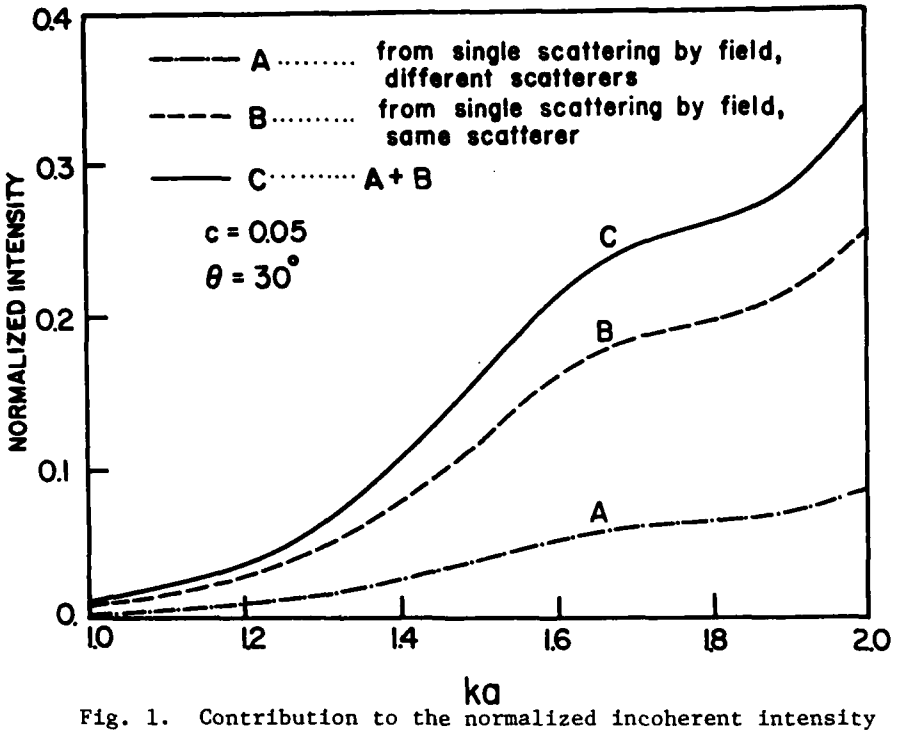

Fig. 1. Contribution to the normalized incoherent intensity as a function of the non-dimensional wavenumber ka for randomly distributed spherical ice particles (ε_r = 3.17) due to terms (B), (A) and C = A + B.

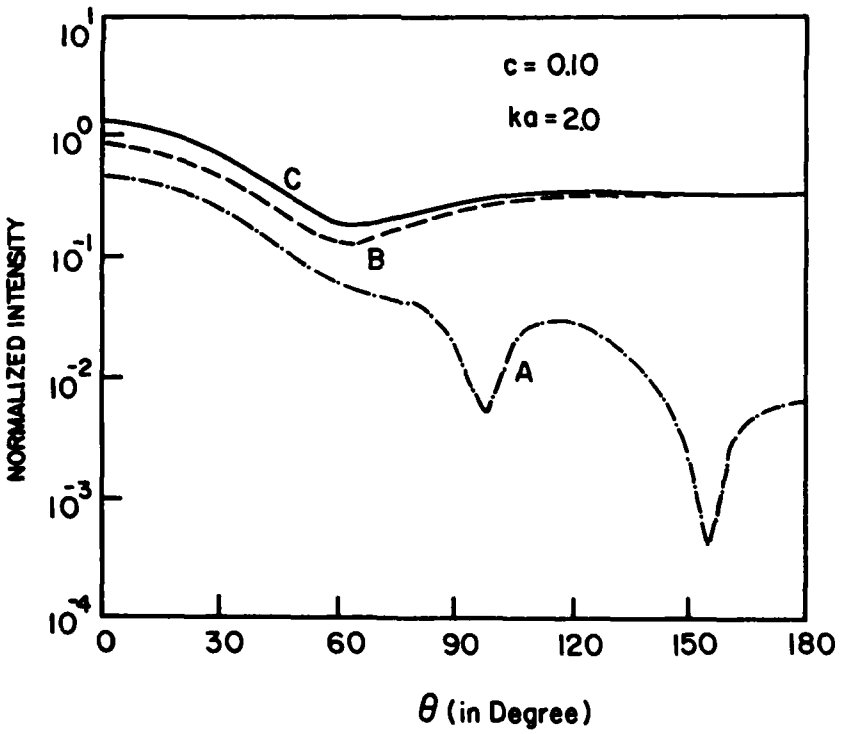

Fig 2. Same as Fig. 1, but intensity versus angle of observation θ.

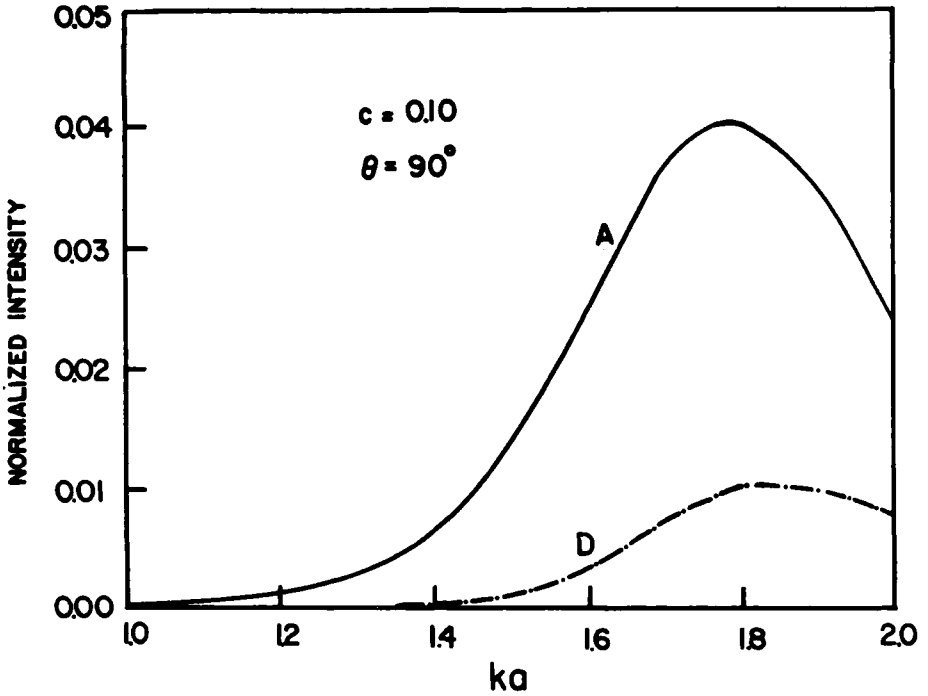

Fig 3. Comparison versus ka of single and double scattering contributions  (A) and 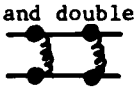 (D) for spherical particles.

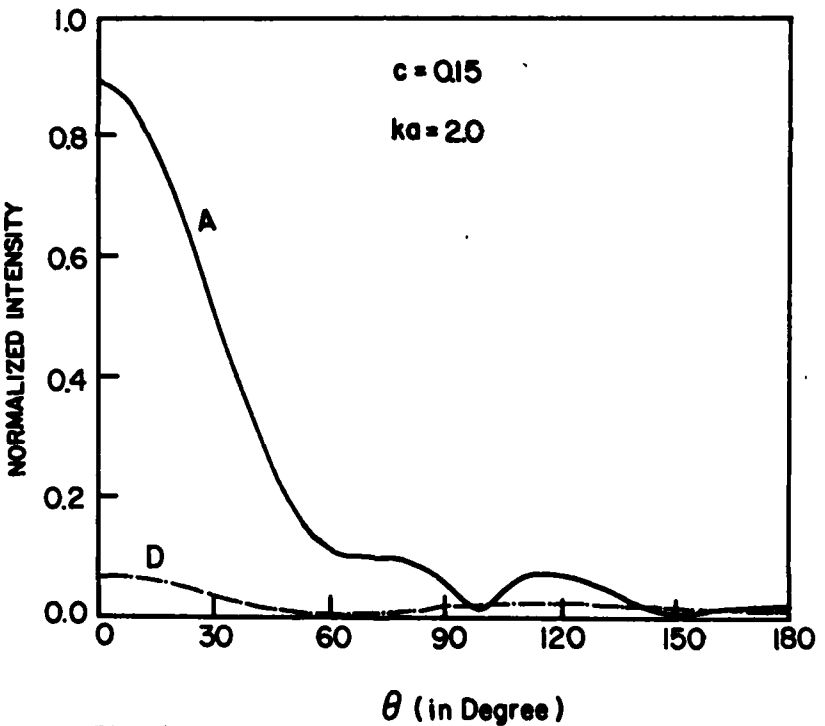

Fig. 4. Comparison versus angle of observation θ for single (A) and double scattering (D) contributions for spherical ice particles.

INDEXES FOR PAPERS IN THESE PROCEEDINGS

INDEX A

INDEX OF AUTHORS
OF PAPERS IN THESE PROCEEDINGS

INDEX B

INDEX OF AUTHORS' ORGANIZATIONS
AND COUNTRIES (IF NOT U.S.A.)
FOR PAPERS IN THESE PROCEEDINGS

AD-A173 878 PROCEEDINGS OF THE SCIENTIFIC CONFERENCE ON OBSCURATION 7/7
AND AEROSOL RESEA (U) KOHL (RONALD H) AND ASSOCIATES
TULLAHOMA TN R H KOHL JUL 86 CRDEC-SP-86019
UNCLASSIFIED DAAG29-81-D-0100 F/G 20/6 NL

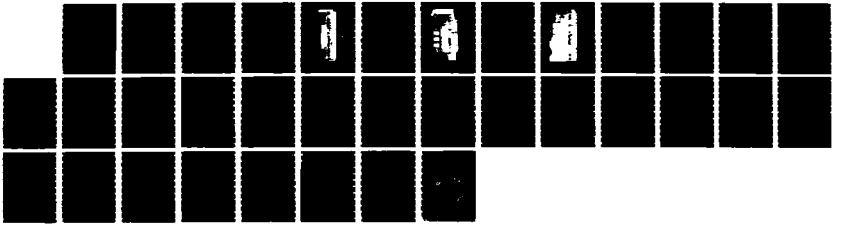

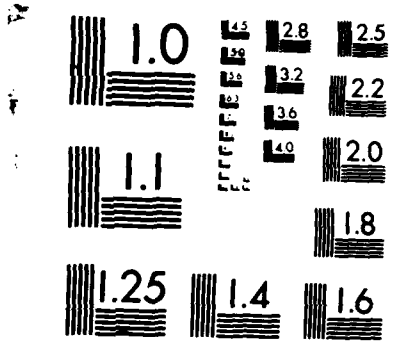

APPENDIXES

APPENDIX A

PHOTOGRAPHS OF CONFERENCE ATTENDEES
(Taken MidWeek)

Group with Elaine Kohl at left:

Third Row: Paul Yager, Kirk Fuller, John Green, Stan Abramowitz, Bill Curry, Alan Snelson, Robert Frickel, S. M. Chitanvis, B. Yudanin, Robert Jolliffe, Jya Wang, T. Majoch Bob Keesee

Second Row: Mark Orman, Chris Evoniuk, Robert Spreng, Martin Richardson, Dick Haracz, Ariel Cohen Ben Herman, Robert Bell, Tony Pluchino, David Capps, William Flood, J. A. Reagan, Steve Druger, Sterling Beck

First Row: Elaine Kohl, Burt Bronk, Leonard Cohen, Bill Bickel, Gregg Adams, Hugh Carlon, Ram Srivastav, Eldon Burgess, Richard Reitz, Jim Brown, Marvin Querry, Dave Pendleton Phil Lawless, Robert Benner, Merrill Milham, William Pearce, R. A. Elliott

1985 CRDC SCIENTIFIC CONFERENCE ON OBSCURATION AND AEROSOL RESEARCH

Group with Ed Stuebing at left center:

Second Row: Petr Chylek, Philip Wyatt, Morris Morgan, Herschel Weil, Dennis Alexander, Alessandro Coletti, Ed Fry, Richard Chang, Ron Pinnick Philip Marston

First Row: Steve Arnold, Wan-Xian Wang, Howard Littman, Edward Stuebing, Dick Baker, H. E. Wilhelm, Kwan Im, George Kattawar, Chia-Ren Hu, Ru Wang, David Cohoon

Group with Ron Kohl at left:

Second Row: Tate Tsang, J. R. Brock, John Glissmeyer, Brent Smith, Jim Hanley, Tom Buckley, Bill Dunn, Don Huffman, Roger Davis, August Miller, Robert Armstrong, Mel Lax

First Row: Ron Kohl, Keng Leong, Isaiah Gallily, Alan Evans, George Sehmel, Ralph Alexander, Avishi Ben-David, Dwight Jaggard, Edward Burlbaw, Mike Farmer, Young Kim, Michael Ligotke, Orazio Sindoni, Robert Platz

APPENDIX B

ATTENDEES LIST

1985 CRDC Scientific Conference
On Obscuration and Aerosol Research

ABRAMOWITZ, STANLEY DR.
National Bureau of Standards
Center for Chemical Physics
Gaithersburg, MD 20899
(301) 921-2131

ADAMS, GREGG DR.
Chemical Research & Development Center
SMCCR-RSC-A
Aberdeen Proving Ground, MD 21010-5423
(301) 671-3753

ALEXANDER, DENNIS PROF.
Mechanical Engineering Department
255 WSEC
University of Nebraska-Lincoln
Lincoln, NE 68588
(402) 472-3091

ALEXANDER, RALPH W., JR. PROF.
Physics Department
University of Missouri-Rolla
Rolla, MO 65401
(314) 341-4781

ARMSTRONG, ROBERT L.
Department of Physics, 3D
New Mexico State University
Las Cruces, NM 88003
(505) 646-4308

ARNOLD, STEPHEN PROF.
Department of Physics
Polytechnic Institute of New York
333 Jay Street
Brooklyn, NY 11201
(718) 643-4371

BACH, WALTER
US Army Research Office
P.O. Box 12211
Research Triangle Park, NC 27709
(919) 549-0641

BAHAR, EZEKIEL DR.
Dept. of Electrical Engineering
University of Nebraska-Lincoln
Lincoln, NE 68588
(402) 488-4074

BAKER, RICHARD
The Aerospace Corp.
Bldg. D8-MS-MY 965
2350 E. El Segundo Blvd.
El Segundo, CA 90245
(213) 416-8916

BECK, STERLING R.
Boeing Aerospace Company
P.O. Box 3999, MS 87-50
Seattle, WA 98124
(206) 773-9951

BELL, ROBERT J. DR.
Physics Department
University of Missouri-Rolla
Rolla, MO 65401
(314) 341-4796 or 4878

BEN-DAVID, AVISHAY
University of Arizona
Institute of Atmospheric Physics
Tucson, AZ 85721

BENNER, ROBERT PROF.
Dept. of Electrical Engineering
3054 Merrill Engineering Building
University of Utah
Salt Lake City, UT 84112
(801) 581-6684

BICKEL, WILLIAM DR.
Department of Physics
University of Arizona
Tucson, AZ 85721
(602) 621-6820/2524

BOBO, WILLIAM S.
Chemical Research & Development Center
SMCCR-
Aberdeen Proving Ground, MD 21010-5423

BOHREN, CRAIG PROF.
Department of Meteorology
Pennsylvania State University
University Park, PA 16802
(814) 865-2951

BOTTIGER, JEROLD
Chemical Research & Development Center
SMCCR-RSP-B
Aberdeen Proving Ground, MD 21010-5423
(301) 671-2395

BOWERS, CHARLES
Department of Physics
Colorado State University
Fort Collins, CO 80523
(303) 491-6076

BRADLEY, BRAD
Director
US Army Material Systems Analysis Activity
Attn: DRXSY-CS
Aberdeen Proving Ground, MD 21005
(301) 278-6231

BROCK, JAMES R. PROF.
Dept. of Chemical Eng.
University of Texas
Austin, TX 78712
(512) 471-3348

BRONK, BURT
Clemson University
Clemson, SC 29631
(803) 656-3417

BROWN, JAMES
Dept. of Physics
Colorado School of Mines
Golden, CO 80401
(303) 273-3835

BUCKLEY, THOMAS J.
National Bureau of Standards
Building 222, Room A261
Gaithersburg, MD 20899
(301) 921-2783

BURGESS, ELDON W.
US Army Dugway Proving Ground
MT-DA-O
Dugway, Utah 84022
(801) 522-5346 AU 789-5346

BURLBAW, EDWARD
Science & Technology Corporation
Suite 940
First National Tower
Las Cruces, NM 88005
(505) 523-8541

CAPPS, C. DAVID DR.
Boeing Aerospace Company
P.O. Box 3999, MS 87-50
Seattle, WA 98124
(206) 773-9949

CARLON, HUGH
Chemical Research & Development Center
SMCCR-RSP-P
Aberdeen Proving Ground, MD 21010-5423
(301) 671-4106

CASTLEMAN, W.A.
Department of Chemistry
152 Davey Lab
Pennsylvania State University
University Park, PA 16802
(814) 865-7242

CHITANVIS, SHIRISH DR.
Physics Department
City College of New York
New York, NY 10031
(212) 690-6865

CHYLEK, PETR DR.
Department of Physics
New Mexico State University
Las Cruces, NM 88003
(505) 646-4308

COHEN, ARIEL PROF.
Department of Atmospheric Sciences
Hebrew University
Jerusalem
ISRAEL
972-2-423886
OR
Summer Address
Department of Physics & Atmos. Sciences
Drexel University
Philadelphia, PA 19104
(215) 895-2707

COHEN, LEN DR.
Dept. of Physics & Atmospheric Sciences
Drexel University
Philadelphia, PA 19104
(215) 895-2710

CHANG, RICHARD K. PROF.
Applied Physics Department
Yale University
P.O. Box 2157, Yale Station
New Haven, CT 06520
(203) 436-0992

COHOON, DAVID DR.
Temple University
43 Skyline Drive
Glen Mills, PA 19342
(215) 358-5725

COLETTI, ALESSANDRO
Georgia Institute of Technology
School of Geophysical Sciences
Atlanta, GA 30332
(404) 894-3890

CURRY, William
VKF/SP Calspan, Inc.
MS 650
Arnold Air Force Station, TN 37389
(615) 455-2611, ext. 7200

DAVIS, E.
Commandant
US Army Chemical School
ATZN-CM-CS
Ft. McClellan, AL 36205

DAVIS, ROGER E.
Science & Technology Corp.
Suite 940
First National Bank Tower
Las Cruces, NM 88005
(505) 523-8541

de WOLF, DAVID
Dept. of Electrical Engineering
Virginia Tech
Blacksburg, VA 24061
(703) 961-6646

DRESSELHAUS, MILDRED S.
Massachusetts Institute of Technology
Department of Electrical Engineering Rm 13-3005
Cambridge, MA 02139
(617) 253-6864

DRUGER, STEPHEN
Department of Chemistry
Northwestern University
Evanston, IL 60201

DUNN, BILL
University of Illinois
1206 W. Green Street
Urbana, IL 61801
(217) 333-6896 (lab) 3832 (office)

ELLIOTT, R.A. DR.
Oregon Graduate Center
19600 N.W. Von Neumann Drive
Beaverton, OR 97006-1999
(503) 690-1135

EMBURY, JANON DR.
Chemical Research & Development Center
SMCCR-RSP-B
Aberdeen Proving Ground, MD 21010-5423

ENSOR, DAVID S.
Research Triangle Institute
P.O. Box 12194
Research Triangle Park, NC 27709
(919) 541-6000

ERICKSON, NILS E.
National Bureau of Standards
Chem-B248
Gaithersburg, MD 20899
(301) 921-2789

EVANS, ALAN J. MR.
Chemical Defense Establishment
C.D.E. Porton Down
Salisbury, Wiltshire SP4 0JQ
ENGLAND
0980-610211 Ext. 420

EVONIUK, CHRIS
3M Company
Building 202-1
St. Paul, MN 55144
(612) 733-1918

FARMER, W. MICHAEL
Science & Technology Corp.
FNB, Suite 940
Las Cruces, NM 88005
(505) 523-8541

FLOOD, W. A. DR.
Army Research Office
P.O. Box 12211
Research Triangle Park, NC 27709
(919) 549-0641

FREUND, DAVID
Johns Hopkins Applied Physics Lab
Johns Hopkins Road 2-211
Laurel, MD 20707
(301) 953-7100

FRICK, GLENDON
Naval Research Lab
Washington, DC 20375
(202) 767-3589

FRICKEL, ROBERT MR.
Chemical Research & Development Center
SMCCR-RSP-B
Aberdeen Proving Ground, MD 21010-5423
(301) 671-3854

FRY, EDWARD PROF.
Department of Physics
Texas A&M University
College Station, TX 77843
(409) 845-1910

FULLER, KIRK
Texas A&M University
Department of Physics
College Station, TX 77843

GALLILY, ISAIAH PROF.
Dept. of Atmospheric Sciences
Hebrew University
Jerusalem 91904
ISRAEL
02-639003

GLISSMEYER, JOHN
Battelle Pacific Northwest Lab
P.O. Box 999
Richland, WA 99352
(509) 376-7913

GOLDBERG, HARRIS A.
Celanese Research Co.
86 Morris Avenue
Summit, NJ 07901
(201) 522-7523

GREEN, JOHN J.
Project Manager, Smoke/Obscurants
AMCPM-SMK-E
Aberdeen Proving Ground, MD 21005
(301) 298-3536

GRODZKA, PHILOMENA DR.
Lockheed Missiles & Space Co.
Huntsville Research & Engineering Center
P.O. Box 1103
Huntsville, AL 35807
(205) 837-1800

GUINN, JOHN DR.
General Dynamics, Fort Worth Division
P.O. Box 748 ; Mail Zone 2814
Fort Worth, TX 76101

HAGAR, JOE MAJ
Air Force Office of Scientific Research
AFOSR/NE
Building 410
Bolling AFB, DC 20332
(202) 767-4909

HANLEY, JAMES T.
Calspan Corporation
P.O. Box 400
Buffalo, NY 14225
(716) 631-6917

HARACZ, DICK
Dept. of Physics & Atmospheric Sciences
Drexel University
Philadelphia, PA 19104
(215) 895-2709

HARRISON, LEE
Battelle Pacific Northwest Lab
P.O. Box 999
Richland, WA 99352
(509) 376-1516

HERMAN, BENJAMIN M. PROF.
Institute of Atmospheric Physics
Building No. 81
University of Arizona
Tucson, AZ 85721
(602) 621-6846/6831

HOPPEL, WILLIAM
Naval Research Lab
Washington, DC 20375
(202) 767-2362

HU, CHIA-REN PROF.
Dept. of Physics
Texas A&M University
College Station, TX 77843
(409) 845-3531

HUFFMAN, DONALD R. PROF.
Dept. of Physics
University of Arizona
Tucson, AZ 85721
(602) 621-4804 or 3634

IM, K. H.
Argonne National Laboratory
Building 207
9700 South Cass Avenue
Argonne, IL 60439
(312) 972-5979

ISKANDER, MAGDY PROF.
Dept. of Electrical Engineering
3054 Merrill Engineering Bldg.
University of Utah
Salt Lake City, UT 84112
(801) 581-6944

JAGGARD, DWIGHT L. PROF.
Moore School of Electrical Engineering
University of Pennsylvania
Philadelphia, PA 19104
(215) 898-4411

JENKINS, WILHELMINA
Lincoln University
Dept. of Physics
Lincoln University, PA 19352
(215) 932-8300 X4777

JOLLIFFE, ROBERT V.
Chemical Research & Development Center
SMCCR-RSP-P
Aberdeen Proving Ground, MD 21010-5423

KAGAN, JEFF
Chemical Research & Development Center
SMCCR-RSP-B
Aberdeen Proving Ground, MD 21010-5423
(301) 671-2326

KAHN, MARVIN J.
SRI International
P.O. Box 757
Brooklandville, MD 21022
(301) 823-2828

KAPLAN, CAROLYN
Naval Research Lab
4555 Overlook Avenue, SW
Washington, DC 20375
(202) 767-2476

KATTAWAR, GEORGE PROF.
Dept. of Physics
Texas A&M University
College Station, TX 77843
(409) 845-7717

KEESEE, ROBERT G. DR.
Department of Chemistry
The Pennsylvania State University
University Park, PA 16802
(814) 863-3574

KENNEDY, JOHN R. Dr.
Naval Weapons Support Center
Code: 5063
Crane, IN 47401

KERKER, MILTON PROF.
Clarkson University
Potsdam, NY 13676
(315) 268-2390

KIECH, E.L.
VKF/SP Calspan Corp.
MS 650
Arnold Air Force Station, TN 37389
(615) 455-2611, ext. 7669

KIM, YOUNG J. DR.
Aerosol Science Laboratory
Wedding & Associates, Inc.
Box 572
Fort Collins, CO 80522

KLIMEK, WALTER G.
Project Manager, Smoke/Obscurants
AMCPM-SMK-T
Aberdeen Proving Ground, MD 21005
(301) 278-5411

KNISELY, RALPH F.
Chemical Research & Development Center
SMCCR-CBN
Aberdeen Proving Ground, MD 21010-5423
(301) 671-3358

KOHL, RONALD H. DR.
Ronald H. Kohl & Associates
P.O. Box 1298
Tullahoma, TN 37388
(615) 454-9060

KOLASA, EMILY
AAI Corporation
P.O. Box 6767
Baltimore, MD 21204
(301) 628-3471

LATHAM, JOHN PROF.
Dept. of Pure & Applied Physics
U.M.I.S.T.
P.O. Box 88
Manchester M60 IQD
ENGLAND
061-236-3311, ext. 2962

LAWLESS, PHIL. A.
Research Triangle Institute
Box 12194
Durham, NC 27709
(919) 541-6782

LAX, MELVIN DR.
12 High Street
Summit, NJ 07901
(201) 273-6188

LEONG, KENG H. DR.
3207 Newmark Civil Eng.
University of Illinois
208 N. Romine
Urbana, IL 61801
(217) 333-8064

LETTIERI, THOMAS
National Bureau of Standards
MET-A117
Gaithersburg, MD 20899
(301) 921-2157

LIGOTKE, MICHAEL W.
Battelle Pacific Northwest Laboratory
P.O. Box 999
Richland, WA 99352
(509) 375-2933

LITTMAN, HOWARD PROF.
123 Ricketts Building
Rensselaer Polytechnic Institute
Dept. of Chemical Engineering
Troy, NY 12180-3590
(518) 266-6039

MACK, EUGENE J.
Calspan Corporation
P.O. Box 400
Buffalo, NY 14225
(716) 631-6782 or 632-7500

MAJOCH, T. R.
Boeing Aerospace Company
P.O. Box 3999, MS 87-50
Seattle, WA 98124
(206) 773-9943

MARSTON, PHILIP
Physics Department
Washington State University
Pullman, WA 99164-2814
(509) 335-5343

MILHAM, MERRILL
Chemical Research & Development Center
SMCCR-RSP-B
Aberdeen Proving Ground, MD 21010-5423
(301) 671-3854

MILLER, AUGUST PROF.
Department of Physics
New Mexico State University
P.O. Box 3D
Las Cruces, NM 88003

MORGAN, MORRIS H. PROF.
Dept. of Chemical Eng.
Rensselaer Polytechnic Institute
Troy, NY 12180-3590
(518) 266-6059

MULLINS, MICHAEL
RTT
P.O. Box 12194
RTP, NC 27709

NOLAN, PAT MR.
Dept. of Chemistry
Drexel University
32nd & Market Streets
Philadelphia, PA 19104
(215) 895-2642

ORMAN, MARK
Riverside Research Institute
330 W. 42nd Street
New York, NY 10036
(212) 563-4545 Ext. 717

PATTERSON, CHRIS
Los Alamos National Lab
P.O. Box 1663
Los Alamos, NM 87545
(505) 667-7795

PEARCE, WILLIAM A. DR.
EG&G
Washington Analytical Services Center
5000 Philadelphia Way, Suite J
Lanham, MD 20706
(301) 731-2044

PEDERSEN, JEANNE DR.
Panametrics
221 Crescent Street
Waltham, MA 02154
(617) 899-2719 / 462-7682

PEDERSEN, NORMAN DR.
Panametrics
221 Crescent Street
Waltham, MA 02154
(617) 899-2719 / 462-7682

PENDLETON, J. DAVID DR.
Atmospheric Sciences Laboratory
P.O. Box 236
White Sands Missile Range, NM 88002
(505) 678-5634

PENG, SHENG DR.
Teledyne Micronetics
P.O. Box 20396
San Diego, CA 92120
(619) 583-3525

PFAFF, GERALD A.
Teledyne Micronetics
7155 Mission Gorge Road
San Diego, CA 92120
(619) 583-3525

PINNICK, RONALD DR.
Atmospheric Sciences Laboratory
DELAS-EO-ME
White Sands Missile Range, NM 88002
(505) 678-5634

PLATZ, ROBERT
SRI International
333 Ravenswood Avenue
Menlo Park, CA 94025
(415) 859-4622

PLUCHINO, ANTONINO
Aerospace Corporation
Building A 6-1647
P.O. Box 92957
Los Angeles, CA 90009
(213) 648-7060

PODZIMEK, JOSEF PROF.
Graduate Center for Cloud
Physics Research
109 Norwood Hall
University of Missouri-Rolla
Rolla, MO 65401
(314) 341-4338

POREH, MICHAEL
Department of Civil Engineering
Colorado State University
Fort Collins, CO 80523
(303) 491-6696

POZIOMEK, ED
Chemical Research & Development Center
SMCCR-RS
Aberdeen Proving Ground, MD 21010-5423
(301) 671-3250

QUERRY, MARVIN PROF.
Dept. of Physics
University of Missouri
Kansas City, MO 64110
(816) 276-1604

RANADE, MADHAV B.
RTI
P.O. Box 12194
Research Triangle Park, NC 27709
(919) 541-6000

REAGAN, JOHN A. PROF.
Dept. of Electrical & Computer Eng.
Engineering Bldg #20
University of Arizona
Tucson, AZ 85721
(602) 621-6203

REITZ, RICHARD
TECOM
Aberdeen Proving Ground, MD 21005
(301) 278-2170 AV 298-2170

RICHARDSON, MARTIN DR.
Atmospheric Sciences Laboratory
DELAS-AE-O
White Sands Missile Range, NM 88002
(505) 678-6780

RILEY, ERICA PETERSON
Chemical Research & Development Center
SMCCR-RSP-B
Aberdeen Proving Ground, MD 21010-5423

RIN, CHUN-HSUN DR.
Chemical Research & Development Center
SMCCR-CBB
Aberdeen Proving Ground, MD 21010-5423
(301) 671-3884

RUBEL, GLENN O. DR.
Chemical Research & Development Center
SMCCR-RSP-B
Aberdeen Proving Ground, MD 21010-5423
(301) 671-2760

SCHIRMER, ROGER E. DR.
Battelle Pacific NW Lab
P.O. Box 999
Richland, WA 99352
(509) 376-5247

SEHMEL, GEORGE
Battelle Pacific NW Lab
SIGMA 5 Bldg 3000 Area
Richland, WA 99352
(509) 376-8527

SHAW, DAVID DR.
Dept. of Electrical Engineering
State University of New York
330 Bonner
Buffalo, NY 14226
(716) 636-3112

SINDONI, ORAZIO I. DR.
Chemical Research & Development Center
SMCCR-RSP-B
Aberdeen Proving Ground, MD 21010-5423
(301) 671-4256

SMITH, R.B.
Optech, Inc.
701 Petrolia Road
Downsview, Ontario
CANADA M3J 2N6
(416) 661-5904

SNELSON, ALAN
IIT Research Institute
10 W. 35th Street
Chicago, IL 60616
(312) 567-4260

SPAIN, IAN L. DR.
Department of Physics
Colorado State University
Fort Collins, CO 80523
(303) 491-6076 or 6206

SPRENG, BOB
3M Company
3M Center Building 220-4E-01
St. Paul, MN 55110
(612) 733-6723

SRIVASTAV, RAM
Army Research Office
Mathematical Sciences Division
Research Triangle Park, NC 27709-2211
(919) 549-0641

STUEBING, EDWARD W. DR.
Research Area Coordinator,
Aerosol Science
Chemical Research & Development Center
SMCCR-RSP-B
Aberdeen Proving Ground, MD 21010-5423
(301) 671-3089

TSANG, T. H. DR.
Dept. of Chemical Eng.
University of Kentucky
Lexington, KY 40506
(606) 257-2825

VARADAN, V. K.
Dept. of Eng. Science & Mech.
Hammond Building
Pennsylvania State University
University Park, PA 16802
(814) 865-4523

VARADAN, V. V.
Dept. of Eng. Science & Mech
Pennsylvania State University
227 Hammond Building
University Park, PA 16802

WANG, JYA
Dept. of Chemical Engineering
University of Maryland
College Park, MD 20742
(301) 454-5098

WANG, WAN-XIAN DR.
Space Astronomy Laboratory
University of Florida
1810 N.W. 6th Street
Gainesville, FL 32609
(904) 392-5450

WATERMAN, PETER DR.
Panametrics
8 Baron Park Lane
Burlington, MA 01803
(617) 272-4494

WEIL, HERSCHEL PROF.
Dept. of Electrical & Computer Science
University of Michigan
Ann Arbor, MI 48109
(313) 764-0500

WILHELM, H. E. PROF.
Naval Weapons Center
Code 381
China Lake, CA 93555
(619) 939-1428

WORLEY, GARY G.
FWG Associates, Inc.
Rt. 2, Box 271-A
Tullahoma, TN 37388
(615) 455-1982

YAGER, PAUL
Bio/Molecular Engineering
Naval Research Laboratory
Attn: Code 6190
Washington, DC 20375-5000
(202) 767-4301

YEH, CAVOUR PROF.
EMtec Engineering, Inc., Suite 2032
1100 Glendon Avenue
Los Angeles, CA 90024
(213) 825-2970

YUDANIN, BORIS
Physics Department
City College of New York
New York, NY 10031

ZARDECKI, ANDREW
Los Alamos National Laboratory
MS P371
Los Alamos, NM 87545
(505) 667-0954

WANG, RU T. DR.
Space Astronomy Lab
University of Florida
1810 N.W. 6th Street
Gainesville, FL 32609
(904) 392-5450

WYATT, PHILIP DR.
Wyatt Technology Company
P.O. Box 3003
Santa Barbara, CA 93130-3003
(805) 963-5904

APPENDIX C

17 June 1985

AGENDA*

1985 CRDC SCIENTIFIC CONFERENCE ON OBSCURATION AND AEROSOL RESEARCH

17-21 June

Bldg. E4810 (Post Theater) Edgewood Area

OR

Bldg. 3074 (Dickson Hall) Aberdeen Area

Each presentation is listed with the appropriate session topic, and, if it is scheduled for presentation at a different time, it is listed a second time at the appropriate place in the schedule. The second listing for scheduling purposes is set off by carets in the margins.

MONDAY 17 June

9:15 Registration Opens

10:00 Opening of Conference

Welcome - Dr. B. Richardson, Technical Director, CRDC
Administrative Remarks - R. Kohl

10:15 Overview of Aerosol Research Program - E. Stuebing, G. Rubel, J. Bottiger, and O. I. Sindoni

11:45 LUNCH

I. PHYSICAL AND CHEMICAL PROPERTIES OF AEROSOLS

Moderator: Glen Rubel

A. Particle Formation, Evolution and Composition

Post.* R. G. Keesee and A. W. Castleman, Jr. (Pennsylvania State Univ.), The Interaction of Clusters with Reactive Species: Initial Stages in the Evolution of Particle Composition

1:00 J. R. Brock and S. G. Kim (Univ. of Texas-Austin), Nucleation and Growth of Aerosol Particles (15)

*"Post." indicates a presentation in the all-topic poster session on Wednesday, late afternoon and evening.
Presenters are underlined. Where only the presenter's name appears, other authors may be indicated during the presentation.

MONDAY 17 June (continued)

I. A. (continued)

1:20 R. K. Ahluwalia and K. H. Im (Argonne National Lab.), Boundary Layer Nucleation (15)

1:40 K. H. Im and R. K. Ahluwalia (Argonne National Lab.), Evolution and Transport of Aerosols Formed from Vapor Condensation (15)

Post. Michael Ligotke (Battelle, Northwest), Generation and Characterization of Phosphorus Smokes in a Wind Tunnel

Tu.AM Roger Schirmer (Battelle, Northwest), Changes in Phosphorus Smoke Chemistry with Environmental Conditions

Post. P. A. Lawless, A. S. Damle, and P. C. Reist (Research Triangle Institute), An Experimental Study of Gas Pressure Effects on the Coagulation Growth of Metallic Aerosols

2:00 Philomena Grodzka (Lockheed-Huntsville), Mechanisms of Solid Particle Formation (15)

Post. Paul Yager and Paul Schoen (NRL), Structure of Polymerized Lipid Tubules

2:20 Keng H. Leong (Univ. of Illinois), Generation of Nonspherical Aerosol Particles (15)

Post. John Glissmeyer and W. Rudy Allaman (Battelle, Northwest), Maximum Containment Aerosol Chamber

2:40 BREAK

B. Plume Mechanics (and Particle Fluidization)

Post. Morris Morgan and Howard Littman (Rensselaer Polytechnic Institute), The Mechanics of Fluid Particle Jets and Their Stability

3:10 Howard Littman and Morris Morgan (Rensselaer Polytechnic Institute), The Fluidization of Fine Particles (15)

3:30 John Latham (U.M.I.S.T.- England), Mixing/Phase-Change Processes in Wet-Aerosol Clouds (15)

3:50 J. R. Brock (Univ. of Texas-Austin), Dispersion of Thermal and Chemical Aerosol Plumes (15)

4:10 Tate T. H. Tsang (Univ. of Kentucky), Numerical Techniques in Aerosol Plume Simulation (15)

MONDAY 17 June (continued)

I. B. (continued)

Post. Michael Poreh and J. E. Cermak (Colorado State Univ.), Diffusion in an Atmospheric Layer with an Elevated Inversion

4:30 Michael Poreh and J. E. Cermak (Colorado State Univ.), Wind Tunnel Simulation of Dispersion of a Particle Plume with Appreciable Settling Velocities Diffusing in a Neutrally Buoyant Surface Layer (15)

C. Particle Dynamics: Including Orientation Effects, Concentration Sampling, and Size/Shape Analysis

4:50 Carolyn Kaplan and J. W. Gentry (Univ. of Maryland), Use of Condition Numbers in Interpreting Atmospheric Aerosol Size Distributions

5:10 ADJOURNMENT
Cocktails and Dinner at The Bayou Restaurant, Havre de Grace, MD (casual)

TUESDAY 18 June

I. PHYSICAL AND CHEMICAL PROPERTIES OF AEROSOLS (continued)

A. Particle Formation, Evolution and Composition (additional presentation)

8:15 Roger Schirmer (Battelle, Northwest), Changes in Phosphorus Smoke Chemistry with Environmental Conditions (15)

C. Particle Dynamics: Including Orientation Effects, Concentration Sampling, and Size/Shape Analysis (continued)

8:35 Robert M. Platz and Daryl L. Roberts (SRI International), Simulation of Particle Deposition of Phosphorus Smokes Based on MAEROS Model of Particle Dynamics (15)

8:55 W. E. Dunn (Univ. of Illinois), Field Study of Fog-Oil Smokes (15)

Mo.PM Carolyn Kaplan and J. W. Gentry (Univ. of Maryland), Use of Condition Numbers in Interpreting Atmospheric Aerosol Size Distributions

9:15 David T. Shaw (State Univ. of New York), Measurement Techniques for Obscuring Smokes - A Review (15)

9:35 Keng H. Leong (Univ. of Illinois), Sizing of Moderately Nonsperical Aerosol Particles (15)

Post. Chris Evoniuk (3M Company), Methods of Size Measurement & Evaluation of Whisker Aerosols

9:55 BREAK

Post. H. E. Wilhelm (Naval Weapons Center), Diffusion and Coagulation of Magnetic Dipole Particles in Magnetic Fields

10:25 Isaiah Gallily and Moshe Goldenberg (Hebrew Univ.-Israel), Determination of the Orientation of Nonspherical Particles in a Turbulent Field; Experimental (15)

I. C. (continued)

10:45 Ehud Gavze and Isaiah Gallily (Hebrew Univ.-Israel), On the Nonsteady Motion of an Arbitrary Particle in a Stokes Flow (15)

Post. Jya Wang and J. W. Gentry (Univ. of Maryland), Survey of Filtration in Idealized Membrane Filters

D. Aerosol Elimination

11:05 Josef Podzimek (Univ. of Missouri-Rolla), A Realistic Assessment of Clearing Smoke Cloud by Scavenging Technique (15)

11:25 LUNCH

II. AEROSOL CHARACTERIZATION METHODS (Other than Aerodynamic Methods - See Session I. C.)

Moderator: Jerald Bottiger

A. Optical Inversion Methods for Size, Size Distribution and Other Particle Properties

Post. Robert E. Benner, S. C. Hill, C. K. Rushforth, and P. R. Conwell (Univ. of Utah), An Automated Algorithm for Sizing Dielectric Microspheres by Aligning Multiple Orders of Measured and Computed Resonance Locations

Post. Lee Harrison (Battelle, Northwest), Optimization of Single Particle Optical Sizers: Prospects for Improvement in Minimum Size Resolution and Reduction of Size Uncertainty

12:25 Earl Kiech (Calspan), Optimization of Mie Scattering Wavelengths and Angles for Particle Sizing (15)

12:45 [combined presentations] An Empirical, Orthogonal Function Approach to the Inversion of Backscattered Data:

Benjamin Herman, A. Ben-David and John Reagan (Univ. of Arizona), I. Theory (10)

A. Ben-David, Benjamin Herman and John Reagan (Univ. of Arizona), II. Results (10)

1:10 D. L. Jaggard, P. Frangos and Y. Kim (Univ. of Pennsylvania), Non-Linear Methods for the Inversion of Refractive Index Profiles (15)

II. A. (continued)

Post. Edward Burlbaw (Science & Technology Corp.), An Advanced Fiber Array Polar Nephelometer: FAN I

1:30 Philip J. Wyatt and Jeffrey M. Reece (Wyatt Technology Corp.), Trolling for Single Particles in an Ocean Environment (15)

1:50 S. R. Beck, C. D. Capps, N. E. Carroll, T. R. Majoch, and A. R. Tokuda (Boeing Aerospace Co.), Multichannel Nephelometer - System Overview (15)

Post. S. R. Beck, C. D. Capps, N. E. Carroll, T. R. Majoch, and A. R. Tokuda (Boeing Aerospace Co.), Multichannel Nephelometer - Aerosol System Capabilities and Operations

Post. S. R. Beck, C. D. Capps, N. E. Carroll, T. R. Majoch, and A. R. Tokuda (Boeing Aerospace Co.), Multichannel Nephelometer - Light Scattering Chamber and Data Acquisition

2:10 CONVERSATION/DISCUSSION BREAK (1½ hours)

B. Optical Constants of Liquids and Powders

3:40 K. D. Moeller (Fairleigh Dickinson Univ.), and J. Heaney (NASA), [Read by E. Stuebing] Millimeter Wave Spectroscopy at FDU, NASA and BNL (15)

4:00 H. H. Chung, G. A. Pfaff, and S. Y. Peng (Teledyne Micronetics), X-Band *Multiple-Position Cavity Method for Determining Complex Permeability* and Permittivity (15)

Post. Ralph W. Alexander, Jr., R. J. Bell and L. L. Long (Univ. of Missouri-Rolla), Optical Constants of Natural Mineral Powders and Single Crystals in the Millimeter and Submillimeter Spectral Range

Post. R. J. Bell, R. W. Alexander, M. A. Ordal, L. L. Long (Univ. of Missouri-Rolla) and M. Querry (Univ. of Missouri-Kansas City) Graphite Research at Low Frequencies

4:20 R. J. Bell, R. W. Alexander, M. A. Ordal, and L. L. Long (Univ. of Missouri-Rolla), Optical Properties of Ni; Cavity Measurements at FIR and Submillimeter Wavelength Ranges; Resistivity Ratios; and Linkage Equations

Post. Ronald G. Pinnick (Atmospheric Sciences Lab.), Attenuated Total Reflectance Measurements of the Complex Refractive Index of Aerosol Constituents at CO_2 Laser Wavelengths

4:40 Marvin R. Querry (Univ. of Missouri-KC), Optical Constants of Selected Materials (15)

TUESDAY 18 June (continued)

(Session III, the Tutorial Review: Intercalation, is scheduled on Wednesday at 9:15)

IV. NONLINEAR EFFECTS AT HIGH ENERGY

Moderator: O. I. Sindoni

Post. Dave Pendleton (Atmospheric Sciences Lab.), Water Droplets Irradiated by a Pulsed CO_2 Laser: Fluence Requirements for the Initiation of Explosive Vaporization

5:00 Mel Lax and Boris Yudanin (City College of New York), Shock Waves in Aerosol Droplets at Early Times (15)

Post. Mel Lax and Shirish Chitanvis (City College of New York), Automatic Conversion of a Huge Non-Standard Fortran66 Hydrocode (TOODY4) to Standard Fortran77

5:20 Dennis R. Alexander and John Armstrong (Univ. of Nebraska), Experimental System for Real-Time Observation of Particle Dynamics at High Energy (15)

5:40 ADJOURNMENT
Cocktails and Dinner at Giovanni's, Edgewood, MD (casual) or
Cocktails and Dinner at Hausner's Restaurant, Baltimore, MD

WEDNESDAY 19 June

IV. (continued)

8:15 Stanley Abramowitz (National Bureau of Standards), Overview of NBS Program in Support of AFOSR's Spacecraft Survivability Program [Aerosol Related Aspects] (15)

8:35 Richard K. Chang, Shi-Xiong Qian, and Judith B. Snow (Yale Univ.), Laser Emission and Stimulated Raman Scattering from Liquid Droplets (15)

8:55 J. R. Brock and J. C. Carls (Univ. of Texas-Austin), Aerosol Interaction with Laser Radiation (15)

(Session IV is continued after Session III.)

III. TUTORIAL REVIEW: INTERCALATION ("Small Needle-Shaped Filaments Based on Carbon")

Organized and Moderated by Ian Spain

9:15 Ian L. Spain (Colorado State Univ.), Chemistry & Physics of Intercalation (25)

9:45 Mildred S. Dresselhaus (MIT), Intercalated Fibers Derived from Benzene (25)

10:15 BREAK

10:45 Harris A. Goldberg (Celanese Research Co.), Properties and Applications of Modified PAN Fibers (25)

IV. NONLINEAR EFFECTS AT HIGH ENERGY (resumed)

11:15 [combined presentations] On the Propagation of Intense Optical Pulses through Vaporizing Aerosols:

Andrew Zardecki (Los Alamos), R. L. Armstrong (New Mexico State Univ.), and S. A. W. Gerstl (Los Alamos), An Algortihm for the Radiative Transfer Equation (10)

Robert L. Armstrong (New Mexico State Univ.), A. Zardecki (Los Alamos), and S. A. W. Gerstl (Los Alamos), Solutions of the Aerosol-Beam Equations (10)

11:40 Withdrawn

12:05 LUNCH (Film Withdrawn)

V. OPTICAL PROPERTIES OF AEROSOLS

Moderator: Ed Stuebing

A. Interaction of Radiation and Spherical (Including Layered) Particles

Post. David K. Cohoon (CRDC and Temple Univ.), Energy Transfer of Electromagnetic Radiation to Spherically Symmetric Penetrable Bodies

WEDNESDAY 19 June (continued)

V. A. (continued)

1:05 Steve Arnold (Polytechnic Inst. of New York), Primary Events in Energy Transfer within an Aerosol Particle (15)

(Session V. A. is continued Thursday Morning)

1:25 [combined presentations] from Session V. B. (each continues as a poster presentation this evening):

Chia-Ren Hu and George W. Kattawar (Texas A&M Univ.), Symmetry Theorems for Forward and Backward Scattering of Light from a Non-Spherical Particle (10)

George W. Kattawar, Chia-Ren Hu, and Mark E. Parkin (Texas A&M Univ.), Mueller Matrix Calculations for Dielectric Cubes: Comparison with Experiments (10)

William White, Pascal Herb, and Edward Fry (Texas A&M Univ.), Suspension and Orientation of 1 μm Cubic Particles and Measurement of Their Mueller Matrices (10)

PREVIEWS OF PRESENTATIONS in the ALL-TOPIC POSTER SESSION

I. PHYSICAL AND CHEMICAL PROPERTIES OF AEROSOLS

A. Particle Formation, Evolution and Composition

2:05 red R. G. Keesee and A. W. Castleman, Jr. (Pennsylvania State Univ.), The Interaction of Clusters with Reactive Species: Initial Stages in the Evolution of Particle Composition (2)

2:08 blue Michael Ligotke (Battelle, Northwest), Generation and Characterization of Phosphorus Smokes in a Wind Tunnel (2)

2:11 red P. A. Lawless, A. S. Damle, and P. C. Reist (Research Triangle Institute), An Experimental Study of Gas Pressure Effects on the Coagulation Growth of Metallic Aerosols (2)

2:14 blue John Glissmeyer and W. Rudy Allaman (Battelle, Northwest), Maximum Containment Aerosol Chamber (2)

B. Plume Mechanics (and Particle Fluidization)

2:17 red Morris Morgan and Howard Littman (Rensselaer Polytechnic Institute), The Mechanics of Fluid Particle Jets and Their Stability (2)

2:20 blue Michael Poreh and J. E. Cermak (Colorado State Univ.), Diffusion in an Atmospheric Layer with an Elevated Inversion (2)

PREVIEWS (continued)

I. (continued)

C. Particle Dynamics: Including Orientation Effects, Concentration Sampling, and Size/Shape Analysis

2:23 red — Presented as a talk

2:26 blue — H. E. Wilhelm (Naval Weapons Center), Diffusion and Coagulation of Magnetic Dipole Particles in Magnetic Fields (2)

2:29 red — Jya Wang and J. W. Gentry (Univ. of Maryland), Survey of Filtration in Idealized Membrane Filters (2)

II. AEROSOL CHARACTERIZATION METHODS (Other than Aerodynamic Methods - See Session I. C.)

A. Optical Inversion Methods for Size, Size Distribution and Other Particle Properties

2:32 blue — R. E. Benner, S. C. Hill, C. K. Rushforth, and P. R. Conwell (Univ. of Utah), An Automated Algorithm for Sizing Dielectric Microspheres by Aligning Multiple Orders of Measured and Computed Resonance Locations (2)

2:35 red — Lee Harrison (Battelle, Northwest), Optimization of Single Particle Optical Sizers: Prospects for Improvement in Minimum Size Resolution and Reduction of Size Uncertainty (2)

2:38 blue — Edward Burlbaw (Science & Technology Corp.), An Advanced Fiber Array Polar Nephelometer: FAN I (2)

2:41 red — S. R. Beck, C. D. Capps, N. E. Carroll, T. R. Majoch, and A. R. Tokuda (Boeing Aerospace Co.), Multichannel Nephelometer - Aerosol System Capabilities and Operations (2)

2:44 blue — S. R. Beck, C. D. Capps, N. E. Carroll, T. R. Majoch, and A. R. Tokuda (Boeing Aerospace Company), Multichannel Nephelometer - Light Scattering Chamber and Data Acquisition (2)

B. Optical Constants of Liquids and Powders

2:47 red — Ralph W. Alexander, Jr., R. J. Bell and L. L. Long (Univ. of Missouri-Rolla), Optical Constants of Natural Mineral Powders and Single Crystals in the Millimeter and Submillimeter Spectral Range (2)

2:50 blue — Ronald G. Pinnick (Atmospheric Sciences Lab.), Attenuated Total Reflectance Measurements of the Complex Refractive Index of Aerosol Constituents at CO_2 Laser Wavelengths (2)

PREVIEWS (continued)

IV. NONLINEAR EFFECTS AT HIGH ENERGY

2:53 red — J. D. Pendleton (Atmospheric Sciences Lab.), Water Droplets Irradiated by a Pulsed CO_2 Laser: Fluence Requirements for the Initiation of Explosive Vaporization (2)

2:56 blue — Mel Lax and Shirish M. Chitanvis (City College of New York), Automatic Conversion of a Huge, Nonstandard Fortran66 Hydrocode (TOODY4) to Standard Fortran77 (2)

V. OPTICAL PROPERTIES OF AEROSOLS

A. Interaction of Radiation and Spherical (Including Layered) Particles

2:59 red — D. K. Cohoon (CRDC and Temple University), Energy Transfer of Electromagnetic Radiation to Spherically Symmetric Penetrable Bodies (2)

3:02 blue — Dean S. Langley (Whitman College), and Philip L. Marston (Washington State Univ.), Forward Optical Glory of Bubbles: Theory and Observations (2)

3:05 red — Ru Wang and Wan-Xian Wang (Univ. of Florida), Scattering by Arbitrarily Large Homogeneous/Concentric Spheres and Spheroids - Exact Theory with use of New Efficient Algorithms (2)

3:08 blue — Withdrawn

B. Interaction of Radiation and Nonspherical Particles Including Aggregates

3:11 red — Kirk A. Fuller and George W. Kattawar (Texas A&M Univ.), Near and Far Field Scattering from Two Interacting Spheres (2)

3:14 blue — David Capps (Boeing Aerospace Co.), Analysis of Scattering Cross Sections of Nonspherical Particles (2)

3:17 red — Leonard D. Cohen, Richard D. Haracz, and Ariel Cohen (Drexel Univ.), Scattering of Linearly Polarized Light by a Dielectric Spiral (2)

3:20 blue — Chia-Ren Hu and George W. Kattawar (Texas A&M Univ.), Symmetry Theorems for Forward and Backward Scattering of Light from a Non-Spherical Particle (2)

3:23 red — George W. Kattawar, Chia-Ren Hu, and Mark E. Parkin (Texas A&M Univ.), Mueller Matrix Calculations for Dielectric Cubes: Comparison with Experiments (2)

PREVIEWS (continued)

V. (continued)

B. Interaction of Radiation and Nonspherical Particles (continued)

3:26 blue — William White, Pascal Herb, and Edward Fry (Texas A&M Univ.), Suspension and Orientation of 1 μm Cubic Particles and Measurement of Their Mueller Matrices (2)

3:29 red — Withdrawn

3:32 blue — Alessandro Coletti (Georgia Institute of Technology), Angular Light Scattering as Measured with a Fisheye Lens Photographic Camera (2)

C. Propagation/Multiple Scattering in Aerosol Media and Radiative Transfer

3:35 red — William A. Pearce (EG&G), Optical Spread Function Dependence on the Aerosol Size Distribution (2)

3:38 blue — Brent Smith (Optech, Inc.), Laboratory Measurements of the Forward and Backscattering of Laser Beams in Dense Aerosol Clouds (2)

3:41 red — Richard A. Elliott (Oregon Graduate Center), Time Resolved Measurements of Irradiance Backscattered from Optically Thick Media (2)

3:44 blue — Withdrawn

3:47 — Paul Yager & Paul Shoen (NRL), Structure of Polymerized Lipid Tubules (2)

3:50 — Chris Evoniuk (3M Company), Methods of Size Measurement and Evaluation of Whisker Aerosols (2)

3:53 — R. J. Bell, R. W. Alexander, M. A. Ordal, L. L. Long (Univ. of Missouri-Rolla) and M. Querry (Univ. of Missouri-Kansas City), Graphite Research at Low Frequencies

3:56 BREAK

ALL - TOPIC POSTER SESSION at (Edgewood Area) Officers Club during the Social Hour, Breaking for Beef and Burgundy Dinner, continuing with Dessert and Coffee.

4:15 (approximately) Beginning of Poster Session

5:00 Emphasis RED [Red boards are manned, blue presenters may view other posters.]

5:45 Emphasis BLUE [Blue boards are manned, red presenters may view other posters.]

6:30 Break for Dinner, followed by

Resumption of Poster Session over Dessert and Coffee [Both Red and Blue boards manned.]

THURSDAY 20 June

V. OPTICAL PROPERTIES OF AEROSOLS (resumed)

A. Interaction of Radiation and Spherical (Including Layered) Particles (continued from 1:25 Wednesday)

8:15 Petr Chylek (New Mexico State Univ.), Ron Pinnick, D. Pendelton, J. Cruncleton, and V. Srivastava (Atmospheric Sciences Lab.), Surface Waves, Sturctural Resonances and Surface Heating of Spherical Particles (15)

Post. Dean S. Langley (Whitman College), and Philip Marston (Washington State Univ.), Forward Optical Glory of Bubbles: Theory and Observations

Post. Ru Wang and Wan-Xian Wang (Univ. of Florida), Scattering by Arbitrarily Large Homogeneous/Concentric Spheres - Exact Theory with Use of New Efficient Algorithms

8:35 Milton Kerker (Clarkson Univ.), Some New Surface Plasmon Phenomena: Photoelection Emission from Small Silver Particles; Light Emission from Tunnel Junctions in Layered Particles (15)

Post. Withdrawn

8:55 James T. Brown and F. V. Kowalski (Colorado School of Mines), Polarization Effects in the Scattering of Light by Spherical Particles (15)

B. Interaction of Radiation and Nonspherical Particles Including Aggregates

Post. Kirk A. Fuller and George W. Kattawar (Texas A&M Univ.), Near and Far Field Scattering from Two Interacting Spheres

9:15 Donald R. Huffman (Univ. of Arizona), Spectroscopy from Atoms to Small Particles Using Light Scattering and Absorption (15)

9:35 Craig Bohren (Pennsylvania State Univ.), On the Applicability of Effective-Medium Theories to Problems of Scattering and Absorption by Inhomogeneous Particles (15)

Post. David Capps (Boeing Aerospace Co.), Analysis of Scattering Cross Sections of Nonspherical Particles

9:55 BREAK

10:25 Philip Marston (Washington State Univ.), and E. H. Trinh (Jet Propulsion Lab.), Diffraction Catastrophes and Inverse Light Scattering from Spheroidal Drops (15)

10:45 Tony Pluchino (Aerospace Corp.), and Steve Arnold (Polytechnic Institute of New York), Structure Resonances of Nonspherical Particles (15)

V. B. (continued)

Post. Leonard D. Cohen, Richard D. Haracz, and Ariel Cohen (Drexel Univ.), Scattering of Linearly Polarized Light by a Dielectric Torroid

11:05 M. F. Iskander, S. C. Olson, and D. E. Yoshida (Univ. of Utah), Optical Scattering by Metallic and Carbon Aerosols of High Aspect Ratio (15) [presented at end of the day]

11:25 Norman E. Pedersen, Peter C. Waterman, and Jeanne Pedersen (Panametrics), Calculation of Scattering and Absorption in the Infrared and Visible by Specific Metallic Fibers with Comparison to Asymptotic Results (20)

11:50 LUNCH (Videotape of Diffraction Catastrophes--See 10:25 paper above)

12:50 Richard D. Haracz, Leonard D. Cohen, and Ariel Cohen (Drexel Univ.), Light Scattering from Randomly Oriented Finite Cylinders and Spheroids (15)

1:10 Ariel Cohen, Leonard Cohen, and Richard D. Haracz (Drexel Univ.), Hemispherical Scattering and Angular Distributions by a Cloud of Randomly Oriented Infinite Cylinders (15)

1:30 Ru Wang and Yu-Lin Xu (Univ. of Florida), Extinction by Finite Cylinders (Microwave Results & Preliminary Analysis) (15)

We.PM & Post. [combined presentations]:

Chia-Ren Hu and George W. Kattawar (Texas A&M Univ.), Symmetry Theorems for Forward and Backward Scattering of Light from a Nonspherical Particle

George W. Kattawar, Chia-Ren Hu, and Mark E. Parkin (Texas A&M Univ.), Mueller Matrix Calculations for Dielectric Cubes: Comparison with Experiments

William White, Pascal Herb, and Edward Fry (Texas A&M Univ.), Suspension and Orientation of 1 μm Cubic Particles and Measurement of Their Mueller Matrices

1:50 Chris Patterson, Shermela Singham, and Gary Salzman (Los Alamos National Lab.), Superposition Principle for Hierarchical Structure in Light Scattering (15)

Post. Withdrawn

2:10 William S. Bickel and Vincent Iafelice (Univ. of Arizona), Polarized Light Scattering from Surfaces (15)

2:30 CONVERSATION/DISCUSSION BREAK (1½ hours)

THURSDAY 20 June (continued)

V. B. (continued)

4:00 Herschel Weil (Univ. of Michigan), Surface Roughness and Clustering Effects in Absorption and Scattering by Electrically Small Particles (15)

4:20 Withdrawn

4:40 D. L. Jaggard and K. Schultz (Univ. of Pennsylvania), Using Scattering Information to Determine Object Shape for Objects of Complex Shape (15)

Post. Alessandro Coletti (Georgia Institute of Technology), Angular Light Scattering as Measured with a Fisheye Lens Photographic Camera

5:00 Alessandro Coletti (Georgia Tech), The Angular Light Scattering from Nonspherical Particles Generated with the Berglund Liu Vibrating Orifice Generator (15)

5:20 [Ishkander talk presented. See 11:05 above.]

5:40 ADJOURNMENT
Crab Feast at Gabler's Shore Restaurant on the Bush River (very casual)
[chicken and hamburgers also available]

FRIDAY 21 June

V. OPTICAL PROPERTIES OF AEROSOLS (continued)

B. Interaction of Radiation and Nonspherical Particles Including Aggregates (continued)

8:15 Ezekiel Bahar (Univ. of Nebraska-Lincoln), Multiple Scattering in Media Consisting of Nonspherical Finitely Conducting Particles (15)

C. Propagation/Multiple Scattering in Aerosol Media and Radiative Transfer

8:35 Richard K. Chang, Burghard Schlicht, and Kevin F. Wall (Yale Univ.), Light Scattering from a Fiber Placed near a Mirror: Case Study of Multiple Scattering (15)

8:55 D. A. de Wolf (Virginia Tech), Large-Angle Scattering in the CFSB Approximation: A Numerical Result (15)

Post. William A. Pearce (EG&G), Optical Spread Function Dependence on the Aerosol Size Distribution

Post. Brent Smith (Optech, Inc.), Laboratory Measurements of the Forward and Backscattering of Laser Beams in Dense Aerosol Clouds

FRIDAY 21 June (continued)

V. C. (continued)

Post. Richard A. Elliott (Oregon Graduate Center), Time Resolved Measurements of Irradiance Backscattered from Optically Thick Media

9:15 A. Zardecki, S. Gerstl (Los Alamos), and R. E. DeKinder, Jr. (PM Smoke), Diffusion Approximation for Modeling of 3-D Radiation Distribution (15)

9:35 V. V. Varadan and V. K. Varadan (Pennsylvania State Univ.), Coherent and Incoherent Intensity of the Electromagnetic Field in a Discrete Random Medium (15)

9:55 BREAK

10:25 A. Ishimaru and C. Yeh (EMtec), Multiple Scattering of Beam Waves by an Ensemble of Nonspherical Particles - First Order Theory (15)

Post. Withdrawn

10:45 David L. Mott and August Miller (N.M. State Univ.), Contrast Prediction in the Presence of Multiple Scattering (15)

VI. DISCUSSION: DIRECTIONS FOR FUTURE RESEARCH IN THE CRDC AEROSOL SCIENCE PROGRAM

Moderator: E. Stuebing

11:05 Discussion (1½ hours)

Approximately 12:35 END OF CONFERENCE

☆U.S GOVERNMENT PRINTING OFFICE: 1986-491-024 40367

END

12-86

DTIC